Edited by Arvind Kumar, Dinesh K. Aswal, and Nirav Joshi

1D Semiconducting Hybrid Nanostructures

Synthesis and Applications in Gas Sensing and Optoelectronics

1D Semiconducting Hybrid Nanostructures

1D Semiconducting Hybrid Nanostructures

Synthesis and Applications in Gas Sensing
and Optoelectronics

Edited by Arvind Kumar, Dinesh K. Aswal, and Nirav Joshi

WILEY-VCH

Editors

Dr. Arvind Kumar
Chaman Lal (P.G.) College
Department of Physics
Chaman Lal Mahadidhyalaya
Haridwar
India

Dr. Dinesh K. Aswal
CSIR-National Physical Laboratory
New Delhi
India

Dr. Nirav Joshi
University of Sao Paolo
Sao Caro Institute of Physics
Sao Paolo
Brazil

Cover Image: © Inkoly/Shutterstock

Contents

Preface

In recent years, the progress in the gas-sensing and optoelectronic fields has swiftly escalated because of their exceeding utilization in applications having high technological throughputs. Avant-garde gas sensors are now commercially available as a result of emerging electronic technologies backed up by novel and innovative ideas, which do not only offer superior advancements like increased portability and size miniaturization but also feed on minimized power while offering prolonged durability. In such a case, one-dimensional (1D) semiconducting nanostructures, such as nanowires, nanopillars, and nanorods, have shown promising potential for scientific and technological fields in many ways. These structures offer several unique advantages, such as high specific surface area, smaller diameter, efficient charge transport, and excellent light trapping capability. It also explores the functional optoelectronic features that emerged at the interface when 1D semiconducting nanostructures were coupled with other low-dimensional materials. The topics discussed in the book are critical to a wide spectrum of modern and new nanotechnologies used or to be used in most industries, academics, healthcare, food, the environment, energy, and research institutes, and thus have a significant impact on our society. This book primarily focuses on providing breakthrough research developments and trends in a variety of 1D hybrid nanostructures for chemiresistive gas-sensing and optoelectronics applications. Further, it highlights the applicability of the developed sensors using 1D hybrid nanostructures in a wide range of modern nanotools and nanodevices deployed in the electronic, healthcare, biomolecules detection, food, pharmaceutical, and medical industries that have a significant impact on our society.

The field of gas sensors and optoelectronic devices is indeed experiencing fast and consistent growth. There is an incredibly wide range of materials, and almost all known materials, including metal oxides, polymers, dichalcogenides, and ferrites, can be utilized in designing gas sensors and optoelectronic devices. However, the desired application-oriented selection of these materials is a challenging and multivariate task. While taking this situation into account, a comprehensive analysis of the available sensing materials with respect to their design and development strategies that are compatible with modern semiconductor fabrication technology has been concluded in this book. Besides, superior and/or additional electronic, mechanical, electrical, and thermal properties offered by these 1D hybrid

nanostructured materials in contrast to pristine 1D nanostructures are also discussed herein. Close attention is given to the problems associated with the stability, selectivity, and functionalizing of these nanostructures. This book consolidates up-to-date information on every aspect of these 1D hybrid nanostructured materials, including their sensing mechanisms, device performance, and state-of-the-art applications, covering the entire spectrum of the most recent literature citations, current market, and patents in a very detailed manner. In a nutshell, this book is an effort made in the quest to unravel the recent advances in the gas-sensing and optoelectronic worlds, while simultaneously suggesting potential solutions to tackle the limitations in this field. This book will be a valuable and accessible guide to the material scientists and researchers from universities and national laboratories working in this phenomenal and exciting field of functional materials.

1

One-Dimensional Semiconducting Hybrid Nanostructure: Gas Sensing and Optoelectronic Applications

Jyoti Rawat, Himani Sharma, and Charu Dwivedi

Doon University, School of Physical Sciences, Department of Chemistry, Kedarpuram Dehradun, Uttarakhand, 248001, India

1.1 Introduction

The study and manipulation of matter on the nanoscopic scale is known as nanotechnology. It involves nanoparticles within the size range of 100 nm [1]. The nanomaterial comprises two-dimensional (2D) nanofilms, one-dimensional (1D) nanowires (NWs), and zero-dimensional (0D) nanoparticles [1]. It is widely acknowledged that 1D nanomaterials are quintessential method for investigating a wide range of unique systems at the nanoscale as well as to study the size and dimensional dependency of their functional properties [2]. They are expected to play a key role as both interconnect and fundamental components in nanoscale, optoelectronic, electrochemical, and electromechanical devices. 1D semiconductor nanostructures can be systematically and consistently manufactured in a single-crystalline form with precise control over their chemical composition, diameter, length, and doping level [3, 4]. Nanostructures have made it possible to develop a wide range of prototype devices and integration methodologies [5].

Hybrid nanostructures are made up of at least two unique elements, both of which have as minimum as 1D nanometer scale [6]. Hybrid nanostructures have the ability to combine the benefits of distinct components while overcoming their flaws, resulting in increased efficiency in certain applications or possibly the generation of unique characteristics and/or functions [7]. The shape, crystalline form, exposed facet, spatial organization, component distribution, and interface between components all contribute to the features and functionality of a hybrid nanostructure [8, 9]. As a result, coherent design and controlled manufacturing of hybrid nanostructures are vital for optimizing material performance in specialized applications as well as improving our knowledge of key framework interactions [10].

In general, there are two types of synthetic approaches for constructing 1D nanostructures: top-down and bottom-up. The top-down technique necessitates

horizontal sequencing of bulk materials using either subtractive or additive procedures in order to make nanosized structures [11]. Several technologies, such as gas-phase condensation and wet ball milling, are employed to produce nanostructures utilizing a top-down approach [12]. Although the top-down method has been crucial in the fabrication of nanostructures, it has various disadvantages, including the formation of defects in treated materials, high prices, the necessity for high-surface-finish materials, and longer etching durations. Nanostructures are also built from single atoms or molecules in a bottom-up manner. During the construction of desirable nanostructures (2–10 nm in size range), regulated segregation of atoms or molecules occurs [13]. Some of the technologies used in the bottom-up approach are molecular beam epitaxy (MBE), chemical vapor deposition (CVD), sol–gel technique, laser pyrolysis, metal–organic decomposition, self-assembly processes, and wet synthesis [14].

The application of 1D hybrid nanostructure is also being explored in gas sensing and optoelectronic devices. Regulated development of carbon nanotube (CNT) arrays may be used to fabricate electrical and optoelectronic devices such as field-effect transistors (FETs), photodetectors, and light-emitting diodes (LEDs) for applicability in optoelectronics of 1D nanostructures LED [15, 16]. Y. Zhao et al. explain current advancement on the construction of organic 1D nanostructures and their distinctive optical and electronic properties, along with their use as basic components in optoelectronic functions and devices such as tunable emission, multicolor emission, optical waveguides, lasing, and modulators. The design and manufacturing techniques of structured 1D nanostructures and their possible implementations in optoelectronic devices such as photovoltaic (PV) cells and switches, and the synthesis of 1D organic nanostructures utilizing a range of organic functional materials spanning from polymers to small molecules, are also documented in the literature [17]. Type II antimonide-based superlattices in 1D, for instance, can be employed in infrared photon detectors for implementations in electronics, sensing, biosciences, and plasmonics [18, 19].

This chapter describes 1D hybrid nanostructure such as nanotube, NW, and nanotube and their unique properties. The method of fabrication for such nanostructures is also discussed in brief. Furthermore, this chapter also sheds light on the application of 1D nanostructure in the field of gas sensing and optoelectronic devices.

1.2 Synthesis of 1D Hybrid Nanostructures

1.2.1 Top-Down Approach

The top-down strategy necessitates horizontal sequencing of bulk materials, using either subtractive or additional processes, to build nanosized morphology [20]. Wet ball milling, gas-phase condensation, and lithography as well as other top-down strategies have been employed by researcher to fabricate nanostructures [21]. The most cost-efficient methods for mass-producing nanomaterials are mechanical techniques. Wet ball milling appears to be the most fundamental of all. Wet ball

milling produces nanomaterials by transmitting kinetic energy from a grinding medium to a material being reduced [21].

Chen et al. employed wet ball milling method to produce hexagonal boron nitride powder which are extremely noncrystalline or amorphous nanoparticles. Boron nitride nanotubes (BNNTs) and nanostructures similar to the bamboo-shaped BN have been developed [22]. When vaporized materials collide with inert gas molecules in the gaseous phase, they dissipate kinetic energy and condense in the form of nanoscopic crystals which can be accumulated on the substrate as an extremely fine powder [23]. Chepkasov et al. reported an experimental investigation of copper nanoparticles condensation from the gas phase, as well as molecular dynamic modeling of a system with 8500 typical copper atoms. The digital model was established to accurately represent the mechanism of vaporization as well as condensation in significant studies. Lithography is a more adaptable and simple approach for generating self-assembled 1D nanostructures on various substrates [24]. Lithography is also a quick and efficient method of surface mapping that is applicable for a large variety of substrates. Lithography refers to a variety of surface processing techniques that include projecting a pattern from a photomask onto a substrate's surface, allowing many duplicates to be created from a single exposure [25]. To complement lithographic techniques for the fabrication of 1D semiconductor nanostructures, several other lithographic techniques such as extreme ultraviolet (EUV) and X-ray lithography (XRL) are being developed [25]. XRL has been extensively explored using radiations in the wavelength range of 0.1–10 nm, as this narrow wavelength range was deemed promising for high-resolution applications [26]. Despite this, quality imaging UV lithography with a 13.5 nm wavelength irradiation is insufficient [27]. However, considering EUV sources have restricted power, enhancing the sensitivity of resists while maintaining design integrity and consistency is a crucial problem for addressing high-volume production throughput demands [27].

1.2.2 Bottom-Up Approach

Bottom-up approach have proven to be advantageous over the top-down method as they stands to benefit the preparation of self-assembled nanostructures that exhibit distinctive interdisciplinary characteristics which are distinguishable from the characteristics demonstrated by the independent constructing constituent [28]. CVD process, sol–gel method, MBE process, molecular self-assembly (MSA) process, and wet synthesis are some ways utilized in the bottom-up approach. The method which is broadly used in the semiconductor industrial field for the deposition of thin layers in various substances is CVD [29]. The subjection of the surface to more than one unstable precursors is involved in this process. The reactant is decomposed by the precursors, which interact with it to produce the desirable deposition. In this method, volatilized precursors at the beginning are adsorbed on a surface at a high temperature, which subsequently interact with one another or disintegrate to form crystals [29]. MBE is another method of physical evaporation that does not require any chemical reactions. MBE varies from conventional epitaxy systems because it depends on a simple physical evaporation process rather than chemical

Table 1.1 1D hybrid nanostructures, types, method of synthesis, analyte gas molecules, and detection limit.

Methods of syntheses	1D nanostructures type	Analyte gas	Detection limit	References
Hydrothermal	ZnO nanowire	H_2S	5 ppb	[34]
Electrospinning	SnO_2 BNNT	NO_2	250 ppb	[35]
Electrochemical anodization	TiO_2 nanotube	Ethanol	100 ppm	[36]
Electrodeposition	CuO nanowire	H_2S	2.5 ppb	[37]
Solvothermal	ZnO nanotube	NO_2	500 ppm	[38]
Oxidation	Fe_2O_3 nanowire	NH_3	0.95 ppm	[39]
Hydrothermal	TiO_2 nanoparticles	Acetone	500 ppb	[40]
Sol–hydrothermal	$Ag-In_2O_3$ nanorod	H_2S	0.005 ppm	[41]
Electrospinning	In_2O_3/reduced graphene oxide nanofiber	NH_3	44 ppb	[42]

interactions. The notion of vacuum evaporation is used in this process, in which hot molecules and atomic rays collide directly with a hot substrate under ultrahigh vacuum conditions [30, 31]. The MBE process has the benefit of operating at a lower temperature than vapor-phase epitaxy. The MSA method excels in producing nanoparticles in the 1–100 nm range [32]. Critical characteristics like distinct geometry and precise interactions between the basic units must be taken into account when creating complex nanostructures utilizing the MSA method. MSA is a noncovalent binding process in which atoms and molecules assemble in a stable and distinct nanophase [33]. Several 1D TiO_2 nanostructures (such as nanorods, NWs, nanotubes, and nanobelts) have been produced for optoelectronic and gas sensor applications throughout, which will be briefly reviewed in the next section (Table 1.1) [43]. The sol–gel method entails merging scattered solid nanoparticles (sols with diameters ranging from 1 to 100 nm) in a homogenous liquid medium and aggregating them to form a coherent three-dimensional (3D) structure in the liquid phase with pore dimensions in the sub-micrometer range [44].

1.2.2.1 Nanotubes

CNTs were found soon after fullerenes were successfully synthesized in one experiment. CNTs have been a subject of investigation since their discovery in 1991, owing to their distinctive structural qualities and properties, as well as their potential technological applications [38]. They resemble a cylinder constructed of a graphite sheet (hexagonal carbon lattice). Nanotubes exhibit a variety of electrical, structural, and thermal properties that vary depending on length, diameter, and chirality or twist of the nanotube [45]. To further the interest, nanotubes can have multiple walls (MWNTs) cylinders inside cylinders in addition to a single cylindrical wall (SWNTs) [46]. Sen et al. pyrolyzed adequate components to create boron carbide nitride (B–C–N) and C–N nanotubes. When aza-aromatics, like pyridine, are

pyrolyzed over cobalt catalysts, CN nanotubes are produced. Thermal decomposition of the 1 : 1 addition compound of BH_3 with $(CH_3)_3N$ yields B–C–N nanotubes. $C_{33}N$ is believed to be the usual composition of C–N nanotubes [46]. Unusual structural morphologies, such as bamboo or nested-cone-shaped cross sections, and others with unique morphologies, such as coiled nanotubes, are commonly observed in doped nanotubes. The B–C–N nanotubes composition changes depending on their mode of synthesis. Moreover, single-walled nanotubes (SWNTs) are the most common product in terms of diameter [47, 48].

1.2.2.2 Nanowires

Over the last years, a broad range of physicochemical methods have been reported the fabrication of semiconducting NWs [49]. These strategies might be classified using both bottoms-up and top-down approaches [50]. To create NWs, the physical process relies on cutting bulk single-crystalline materials (such as Si, Ge, and GaAs) with high-energy plasma species [51, 52]. Since Wagner and associates created Au-catalyzed Si micro-whiskers in 1964, the catalyst particle aided vapor–liquid–solid (VLS) growth process, first reported by the production of NWs from diverse materials utilizing a range of physical sputtering, e-beam, MBE, and CVD methods, has been intensively studied [53]. By using traditional methodologies for the development of the epitaxial structure through this VLS method, a precision alignment system may be obtained throughout NW formation. Inside the regulated fabrication of heavy nanofiller arrays and single-wire devices, the approach VLS epitaxy proves to be advantageous [54]. If ZnO is grown multilayered on a flat crystal framework, it tends to enlarge in dimension and readily generates highly oriented arrangements (Figure 1.1a). For the GaN (Figure 1.1b) and Si/Ge structures, a comparable level of epitaxial regulation may be accomplished [55, 56]. This VLS approach may be used to create NW structures with strict shape control (<20 nm) [57, 58]. Advances in scanning and transmission electron microscopy (TEM) provided essential analytical tools for characterizing these materials in the following decades, paving the way for the fabrication of NWs in the field of advanced materials.

(a) (b)
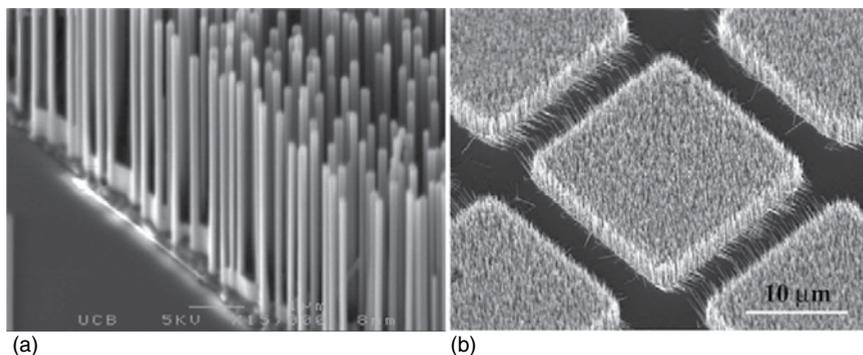
Figure 1.1 SEM image (a) on a plane sapphire wafer, ZnO nanowires, and (b) GaN nanowire arrays on plane $LiAlO_2$ part. Source: Pauzauskie and Yang [56], Elsevier.

1.2.2.3 Nanorods

Nanorods are an appealing component for research and often good alternatives for various applications due to their form anisotropy. Due to the increased stimulation of surface plasmons in nanoparticles produced by an increase in particle aspect ratio, nanorods have been shown to be more efficient than spherical particles. The strength of the dipole moment is notably significant within a nanoparticle due to the rise in surface plasmons [59]. As a result, the electrical field in nanorods increases in comparison with spherical particles. Significantly well-oriented CdSe nanorods, according to Alivisatos and coworker, provided an effective, guided path for charge transporters to pass through the photoelectric device and be collected [60]. Inserting nanorods into P3HT films boosted extrinsic quantum yield by three times when the aspect ratio was raised from 1 to 10 nm [61]. While researching Ag nanorods for polystyrene composites by Winey et al., they discovered that the electrical conductivity of polymer composites is influenced by the aspect ratio of anisotropic nanoparticles. Particularly, because rod-shaped particles have a lower percolation threshold than spherical particles [62], percolation threshold was discovered to be affected by both the form and size of nanoparticles. Many advantages in the underlying features of nanorods are projected to be shared by larger rod-shaped particles, both in diameter and length. In conclusion, the aspect ratio, polydispersity, volume fraction, and alignment of nanorods have a significant impact on their efficacy [62].

In general, the development of nanorods in arrays requires a platform supplied by the substrate, which can be constructed of a variety of materials [63]. According to Oh et al., electrochemical gas sensors based on vertically oriented ZnO nanorod arrays (average length and diameter were 500 and 50 ppm, respectively) were successfully created (Figure 1.2a,b) [64, 65]. The devices can be made by introducing 39.5 W/cm ultrasound vibrations at 20 kHz into a solvent (such as 0.1 M zinc nitrate

(a)   (b)
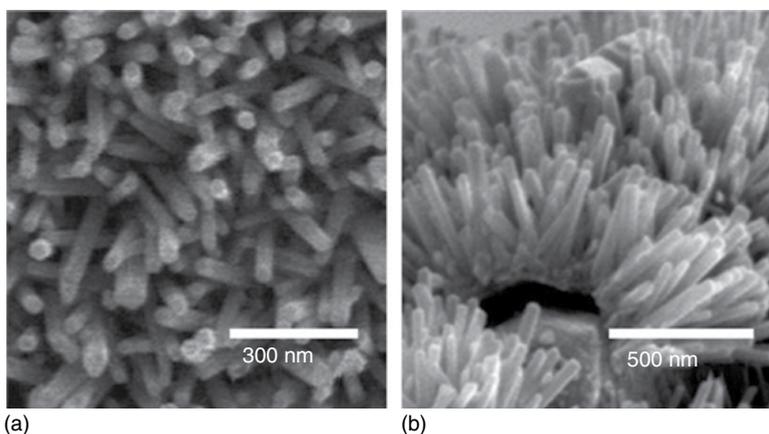
Figure 1.2 SEM picture of ZnO nanorod (a) upper view and (b) oblique view. Source: Yuan et al. [64], MDPI, CC BY 4.0.

hexahydrate and 0.1 M hexamethylenetetramine) so that the organic material is submerged in the Al_2O_3 substratum, where the Pt conductor is stored, and Zn thin films are formed immediately [65].

1.3 Applications of 1D Hybrid Nanostructures

1.3.1 Gas Sensing

The need for the detection of the small extent of explosive, combustible, and poisonous gases and screening of environmental contamination has given way to the development of various gas sensors [66]. Medicine, agriculture, industrial refining, and environmental studies are the fields that have found the great application of these sensors. Among such highly flammable gases, sensing of lightest element hydrogen is one such case of implementation of gas sensors. It is undetectable by the human eye. Hydrogen on reaction with oxygen results in an inflammable compound that can be ignited with a flame or a spark. The fuel- for hydrogen-powered vehicles and aeronautical operations are being provided by hydrogen [67]. Hydrogen screening is useful for a variety of reasons, from pollution detection to early warning indications of fires or nuclear reactor safety to presenting proof of certain diseases. Detecting the presence and quantity of hydrogen is useful in the manufacturing of semiconductors and the identification of imminent transformer failure in electric power plants. Other examples include volatile organic compounds (VOCs), which as the name suggests have a high vapor pressure [68]. VOCs are plentiful and omnipresent, with some posing a health risk to humans and others being damage to the environment. Hazardous VOCs are not usually dangerous, but if they are created within homes, they might cause sick building syndrome. VOCs can be found in human bodies, and on the other hand, some of the VOCs have intensified long-term health consequences and some are even proven carcinogens [69]. A good sensor should have a high susceptivity, quick response, and good selectivity. The development of low-cost and reliable gas sensors that can function at room temperature continues to be a significant scientific and technological obstacle. The detection methodology of the gas sensors can serve as a basis for the classification of various sensing materials and methods. Alterations in electric characteristics, visual, chromatographic, and calorimetric gas sensing are various methods of detection. When gas interacts with the surface of semiconductor gas sensor (metal chalcogenides, CNTs, and conducting polymer), it alters the main physical properties such as the electrical conductivity and work function of the sensing material [66]. Yang and coworkers used thermal oxidation in an oxygen atmosphere within a horizontal tube furnace to manufacture oriented ZnO nanobelt configurations natively on Zn substrates. The coverage of the ZnO nanobelt array on the substrate seems to be reasonably homogenous, with an aerial density of around 1014 nanobelts/m^2 [70]. These nanobelts have a root diameter of 100–300 nm, a length of 10–20 mm, and a thickness of 3–4 nm. ZnO nanobelt balls grow directly from Zn microparticles to

generate a thick sheet, with the nanobelts precisely aligned on the microparticle surface, when a layer of micrometer-sized Zn particles is used as the growth medium instead of Zn foil. The ammonia gas sensor made from such as-grown ZnO nanobelt ball arrangements on Si substrates has a high sensitivity and quick responsiveness at room temperature [70, 71].

1.3.1.1 Safety Monitoring of Exhaust Gases in Automobile

Gas sensors are commonly found in modern automobiles and serve as either a commodity or a critical engine component [72]. Based on the concentrations of atmospheric gases detected in the air intake manifold, it is becoming increasingly common for a vehicle's electronic control unit (ECU) to naturally close and open the outside air flaps [73]. The most monitored gases are those which are combustible [74]. A pair of CO- and NO_2-sensitive sensors is commonly mounted to determine the air quality. Automobiles must now strictly adhere to rules to maintain adequate air quality index and, therefore, the gas sensors are now a part of their machinery [75]. The decrease in atmospheric contamination and increase in the fuel efficacy must be the aim of the automotive industries, and modern-day gas sensors can help in achieving this goal by offering flexibility in the design and high sensitivity [72].

Electric car fires, chemically dangerous gas leaks and gas pipeline leaks, and explosions have occurred all around the world, and they are nearly typically caused by combustible and explosive gases such as hydrogen, carbon monoxide, hydrogen sulfide, and others [76]. Resistive gas sensors based on 1D nanomaterials have been thoroughly explored for monitoring common gases such as hydrogen, carbon monoxide, and hydrogen sulfide in order to avoid probable explosion and combustions [77]. These gas sensors offer excellent electronic transmission routes, high susceptibility, and chemical and thermal stability [78, 79]. Kumar et al. constructed Nb nanofibers (NFs) and a reversible and selective resistive gas sensor for room-temperature CO gas detection. At room temperature, these sensors demonstrated CO responses of 22% for 2 ppm and 91% for 400 ppm and were more beneficial with fast response/recovery durations [80].

Wang and coworkers used two-step procedures of VLS and atomic layer deposition (ALD) to create 1D SnO_2/NiO core–shell nanowires (CSNWs) (Figure 1.3a). The SnO_2/NiO-100 sensor (with 100 ALD cycles) showed a substantial sensitivity of 114–500 ppm hydrogen below 500 °C, that is nearly fourfold more than virgin SnO_2 NWs, and excellent selectivity even in a complex gas environment (ethanol, acetone, hydrogen, and NH_3) (Figure 1.3b,c). SnO_2/NiO CSNWs' increased hydrogen-sensing performance was attributed to their high surface-to-volume ratio, the p–n heterojunction that evolved at the p-NiO-shell/n-SnO_2 core interface, and the effective modification of the NiO shell layer [81, 82]. Nikfarjam and coworkers used a unique electrospinning process with secondary electrostatic fields on electrodes with extremely sharp triangular and rectangular edges to create single-aligned pure TiO_2 NFs and gold nanoparticle (GNP)-TiO_2 NFs for gas-sensing devices (Figure 1.3d,e). GNPs-TiO_2 NFs had a lower working temperature (250 °C) than pure TiO_2 NFs and had high susceptibility (70–30 ppb CO) and a lower limit of detection (70 ppt) (Figure 1.3f,g). Through the local Surface Plasmon Resonance (LSPR)
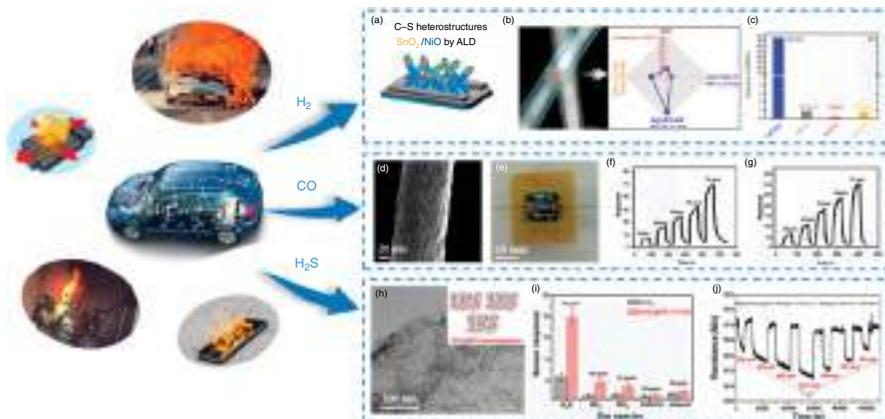
Figure 1.3 (a) Diagrammatic illustration of SnO$_2$/NiO-X CSNWs; (X is the number of atomic layer deposition cycles) (b) SEM image and sensing response of the SnO$_2$/NiO-X CSNWs heterostructures toward 200 ppm of H$_2$ at 50 °C as a function of the NiO–shell layer thickness; (c) at 500 °C, the SnO$_2$/NiO-100 sensor response to 200 ppm H$_2$ and additional interfering gases (300 ppm ethanol, 50 ppm acetone, and 20 ppm NH$_3$); (d) TEM image of TiO$_2$ NFs; (e) picture of the GNP–TiO$_2$ sensor, time-dependent response; (f) pristine TiO$_2$ at 300 °C; (g) GNP–TiO$_2$ at 250 °C in various concentration levels, (h) SEM image of SnO$_2$–GO composites with schematic diagram; (i) at 700 °C, the detection performance of the SnO$_2$ gas sensor and SnO$_2$–GO gas sensor to various gases (10 ppm H$_2$S, 10 ppm SO, 10 ppm NH$_3$, 50 ppm acetone, and 50 ppm ethanol); and (j) the SnO$_2$–GO gas sensor (70 °C, RH85%) was used to detect a lower content of H$_2$S ranging from 200 to 1000 ppb in acetone (500 ppb) and ethanol (500 ppb) mixture. Source: Wang et al. [81]/MDPI/Public Domain CC BY 4.0.

phenomenon, visible light can activate GNPs, decreasing the reaction's activation energy in the process. It is observed that, when GNPs came into proximity of TiO_2 nanograins, a Schottky barrier formed between them, and electrons passing from the TiO_2 nanograins to the GNPs enlarged the TiO_2 nanograins' depletion zone, reducing sensor conductivity. H_2S is also one of the combustible and dangerous gases that, when subjected to heat or introduced to open flames, it can form an explosive mixture with air, resulting in combustion. More interestingly, it showed a ppb-level H_2S reaction in a gas combination containing H_2S, acetone, and ethanol, with 85% humidity (Figure 1.3j). Pure SnO_2 quantum wires and the GO nanosheet cooperated together to increase transducer performance and chemical reception, resulting in high responsiveness and specific gas sensing. Due to its room-temperature fabrication, low-temperature operation, and great compatibility with the paper substrate, the SnO_2–GO sensor is a potential adaptable gas sensor. Song et al. used a simple mechanical stirring approach to make SnO_2 quantum wire/GO nanosheets (Figure 1.3h). At low temperatures, the SnO_2–GO sensor outperformed a pure SnO_2 sensor in terms of responsiveness and specificity to H_2S (Figure 1.3i) [83].

1.3.1.2 Health Monitoring

Gas sensors which are made up of semiconductors are used in practically every industry and have a wide range of applications. Underground miners are vulnerable to combustible gas, asphyxiates, lower oxygen levels, and other poisonous gases [84]. Anchored and transportable sensors are utilized to ensure that in the event of an emergency gas leak, audiovisual alerts are activated, allowing for a safe and quick evacuation of the manpower [85]. Similarly, many different gas detectors are used in the gas and oil industries because of the existence of dangerous random moving molecules, whether during production, transportation, processing, storage, or near distribution pipes [86]. Chemical facilities in almost every sector around the globe are responsible for the release of dangerous gases as by-products during their processes which includes benzene, ethylene, propylene, and toluene produced by the petrochemical sector, H_2S, and SO_2 produced by the drilling and extraction industries, exposing people living near companies to harmful gases [87]. That makes the availability of highly efficient gas-sensing systems in such sectors imperative.

In the food industry, smart food packaging involves a variety of gas sensors to determine the optimal food/meat aging time, monitor the quality of meat, and control food quality in general [87]. The clever packaging approach allows us to monitor the state of edibles as well as the package's surroundings [88]. As a result, using gas sensors in the food manufacturing and packing industries might dramatically minimize food waste while also lowering the annual number of food poisonings, therefore, enhancing food safety [89]. However, a few of the chemicals found in the body may be used for medical diagnostics, and detection of these unique gases has been proved to be useful in the diagnostic industry. Toluene (lung cancer), isoprene (heart disease), formaldehyde (lung cancer), and NH_3 (hemodialysis) are few examples of such type of chemicals [89]. Ama et al. used nanocomposites including 1D KWO ($K_2W_7O_{22}$) nanorods and 2D $Ti_3C_2T_x$ nanosheets to construct a novel acetone
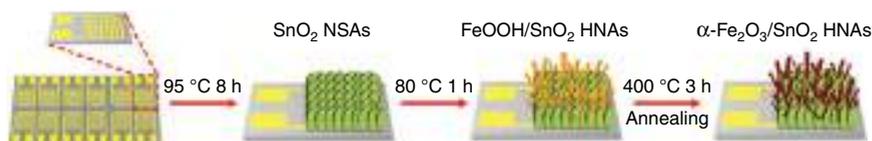
Figure 1.4 The advancement of Fe_2O_3/SnO_2 reaction. Source: [92] Research A Science Partner Journal / Public Domain CC BY 4.0.

sensor. These nanocomposites have a high acetone sensitivity (10 times that of a KWO-based sensor), a considerable higher atmospheric condition tolerance, and months of increased stability, showing its promising application as a highly accurate as well as precise methanol detecting element in medical care and insulin treatment [90]. Wang et al. developed a poly(styrene-butadiene-styrene)/carbon nanotubes (SBS/CNT) hybrid fiber detector that used a modular wet spinning method to increase selectivity (19–10% solvent) across the entire sensing distance of 100–400 ppm, as well as a quick response (40 seconds) or brilliant mechanical dependability. This sensor showed a lot of potential for health monitoring in wearable and flexible electronic devices [91]. In an easy two-stage CVD process, Gong et al. created a biosensor for alcohol depending on α-Fe_2O_3/SnO_2 heterogeneous structure. There was an increase in sensitivity with outstanding alcohol characteristics in systems based on solid SnO_2 nanosheets or Fe_2O_3 nanorods. A heterojunction using 1D/2D hybridization designs (Fe_2O_3) could explain the higher productivity (SnO_2). Furthermore, the Fe_2O_3/SnO_2 had remarkable reproducibility, indicating these materials might be used in exhalation testing (Figure 1.4) [92].

1.3.1.3 Environmental Monitoring

Poor air quality index in the urban areas are posing a threat to the health of the living beings in such areas. Many respiratory disorders and environmental issues can be tracked down to the emission of harmful gases from chemical power plants and petroleum and mining industries [93]. Natural, synthetic, and anthropogenetic gases are the three types of gaseous contaminants [94]. Natural causes of air pollution include volcano eruptions, wildfires, and lightning, whereas synthetic sources include emissions from human activities such as automobile exhaust gases, chemical disasters, or commercial activity, for example transformers and land disposal [95]. As a direct consequence of climate change due to the increase in the greenhouse gases, the need for monitoring such pollutants is more than ever [95]. The predominant objective of air pollution control is improvement in the air quality index and, therefore, reduced respiratory illness [96]. This includes a screening of gases like CO_2, NO_2, SO_2, and O_3 through befitting gas sensors [89]. Suh et al. developed an edge-exposed WS_2 manufactured on SiO_2 NRs that can detect NO_2 extremely accurately as well as precisely. It reacted to 5 ppm NO_2 with a response that was significantly greater than the reaction to interfering gases at ambient temperature (3.44 ppm to CO and 0.47 ppm to H_2S) [97]. The excellent performance of WS_2 is largely due to its very porous 1D nanomaterials as well as highly sensitive interface regions, which serve as beneficial catalyst surfaces for immediate contact with specific atoms [98].

Lim et al. developed Au-SnO$_2$ NFs that can detect NO$_2$ gas at low conditions while exposed to photons (Figure 1.5a). The sensor's exceptional transparency (93%) was aided by the incredibly minimal coverage of sensing materials (approximately 0.3%), allowing the substance to be completely open to the gas and, therefore, facilitate thermal detection as well as photosensibility process (Figure 1.5b). The packed Au particles amplified the reactivity to NO$_2$ due to the surface plasmon resonance effect of Au. The sensor had increased responsiveness (300) in daylight to 5 ppm NO$_2$, consistent response to sub-ppm NO$_2$, and a low activation range of 6 ppb with a high NO$_2$ reaction in all dried or slightly moist atmospheres (50% and 70%, respectively) (Figure 1.5d,e). A gas sensor with high visibility and ambient temperature functionality would assist in improving transparent digital gadgets and optoelectronic devices which are directly connected to the Internet of Things (IoT) (Figure 1.5) [99]. To synthesize silver nanocrystal (NC)-functionalized multiwalled carbon nanotubes (Ag NC-MWCNTs), Cui et al. employed a simple mini-arc plasma technique combined with an electromagnetic pressure assembling method (Figure 1.5f). When Ag NCs were added to MWCNTs, the susceptibility to NH$_3$ gas was greatly enhanced (Figure 1.5g). The performance of the gas sensor is significantly influenced by the oxidized Ag surface. NH$_3$ particles bind to Ag hollow areas on the AgO interface when H is directed against Ag. A positive energy exchange from NH$_3$ to the Ag NC-MWCNTs hybrid results in a conductance change. The sensor also had high selectivity for various gases and was easy to maintain over time (Figure 1.5h,i) [100].

1.3.2 Optoelectronic Application

Optoelectronics is among the most intriguing areas of applicability for hybrid nanostructures due to the ocular and electrical attributes of isolated semiconductors and metal nanoparticles [101]. Indeed, hybrid designs hold the possibility of combining greater potentiality, superior performance, and scaling down of optoelectronic devices, hence enhancing the performance of the device, speed, and power efficiency [101, 102]. The expanded features of hybrid nanostructures might have a significant impact on the disciplines of photodetection and PVs in particular. PV systems are often regarded as among the most efficient and essential strategies for meeting the rising world's energy demands [103]. From the many existing approaches, PVs are deemed being the safest technique to accomplish the desired results through solar energy conversion. Because of their capacity to cost-effectively change conventional catalyst PV radiation as a supply of solar energy, small-molecule and polymer-based PVs have attracted much interest in both industry and academia [104]. Nanoscopic proportions and quicker carrier collection owing to short transit routes are some of the restrictions resolved by semiconductor NWs [55]. Decreasing dimensions underneath the typical absorption depth, on the other hand, impede effective light trapping, lowering overall efficacy. Metal nanostructures can be included in optoelectronics as well as PV-nanostructured methods to improve optical absorbance by enhancing electrical charge [104]. For comparison, near-field coupling between plasmonic nanostructures in close proximity to GaAs NWs was
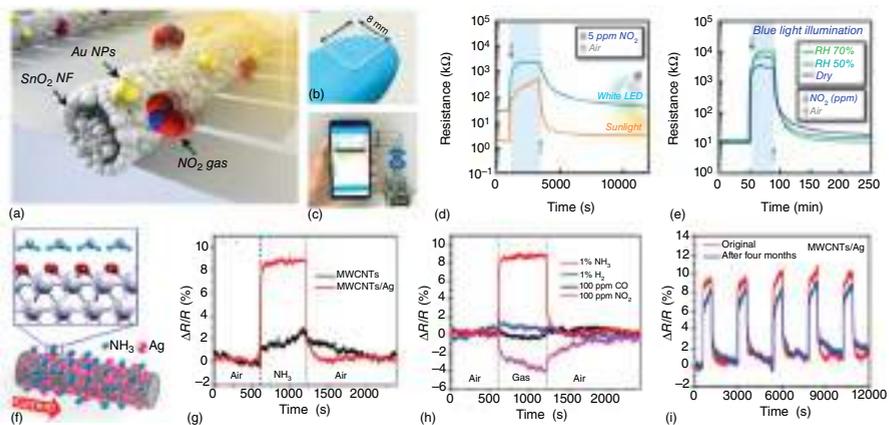
Figure 1.5 (a) Au-SnO$_2$ NFs diagrammatic representation; (b) transparency detector images; (c) smart sensor component that can interact with smart phones; (d) resistivity shift in reaction to 5 ppm NO$_2$ with white LED and sunshine; (e) for various environments; (f) Ag NC MWCNTs graphic demonstration; (g) room-temperature multidimensional sensitivity reaction during Ag NCs decoration; (h) analysis of sensor responses to different chemicals; and (i) characterization of sensing reaction to 1% NH$_3$ during four months of storage in air. Source: Wang et al. [81], MDPI, CC BY 4.0.

used to reroute electromagnetic waves into the semiconductor and increase intensity up to 20 times for the chosen wavelength and polarization, allowing for the customization of the nonlinear optical response of a single NW [55].

Hyun and coworkers used scanning visible light spectroscopy to correct a localized photocatalytic activity increase of 20% across a Si nanostructure coated with nanocomposite with the horizontal direction. The interaction with the electromagnetic spectra was improved by narrowing the gap between the metallic nanoparticles as well as the Si nanostructure to the semi-region, leading to a twofold increase in photocurrent over the unprotected NWs [105]. Grinblat et al. created ZnO nanostructure by inserting a gold qualitative oligomer within the electric current hotspots. The author has also reported the interplay between leaky-mode resonances (LMRs) in NWs and limited interface vibrational modes. LMRs are electronic patterns provided by a dielectric cavity in a single silicon-based nanostructure, wherein absorbance is resonance increased. The leaky nature of all these phases aided the interfacial resonances of metallic nanoparticles on the NW substrate. The ensuing coupling allows for the suppression, enhancement, and shifting of absorption resonances, greatly increasing the amount of control over tenability and optical characteristics modulation [106]. Knight et al. investigated the alternative mechanism of hot electron emission through plasmonic degeneration for sensor applications for the first time [107]. Using temperatures beyond the optoelectronic visible region, this indicated system, which was composed of such an arrangement of Au nanostructures constructed atop an n-type Si surface, produced a vibrational frequency and isotropic photon energy with a maximum value of 0.01%. This concept was recently accomplished in near-infrared photodetection devices made of Au nanorods and ZnO NWs. Au nanorod surface plasmons were utilized as reactive ingredients in the suggested idea to create or transmit hot electrons into the huge absorption coefficient ZnO NW, functioning as an inactive material for electronic conductivity. Kawawaki and coworkers enhanced the near-infrared absorbance of PbS QD/ZnO NW PV by integrating Ag nanotubes, improving the electrical properties from 4.5% to 6%. Inside the solid-state p–n power generation system, core–shell silicon NW PVs ornamented with single silver nanomaterials indicated short-wave progression of the short-circuit current (i.e. absorption) emerging both from near-field and far-field coupling with dipolar and quadrupolar nanocrystalline spectra [108]. Weiwei et al. established a solution-phase technique to create a $CsPbX_3$/ZnS QDs heterodimer with improved chemical stability and systematic density functional theory-based first-principles calculations backed up this claim. When combined with ZnS, $CsPbX_3$ exhibits excellent charge dispersion, which is advantageous for PV employments [109].

1.3.2.1 Photodetector
Quantum confinement effects can extend bandgaps in nanostructures, and direct bandgaps in semiconductors vary from 1.5 eV (CdTe) to 3.7 eV (ZnS). As a result, nanostructures have a lot of promise for applications such as near infrared (NIR) to UV nanophotodetectors (nano-switches) [55]. Nanostructures are estimated to

have substantially greater efficiency and economics than standard film and bulk devices due to their higher absorption coefficient and chemical stability. Several proof-of-concept composite NW photocatalysts were produced due to the increased optical emission in modified nanomaterials [110, 111]. Luo et al. showed a considerable improvement in photodetection effectiveness of CdSe nanoribbons decorated with Au hollow nanoparticles when compared to bare CdSe nanoribbons and nanoribbons adorned with solid nanoparticles [112]. In addition, Au-decorated CdSe and CdTe NWs, Au-decorated ZnO/ZnCdSeTe CSNWs, Ag-decorated ZnO nanorod array LEDs, and Si NW arrays covered with Au nanomaterial-coated graphene sheets all demonstrated superior plasmon increased light transfer efficiency [112].

Dong and Huang et al. utilized a large bandgap hole transport layer with perovskite photoactive layers to create a highly efficient PV-type photodetector [113]. A photodetector with a ZnSe nanoribbon/Si p–n heterojunction was built by Wang and coworkers to augment the functioning of the ZnSe nanoribbon/Si p–n heterojunction system for which Ag nanoparticles were added (Figure 1.6a–c). The system with Ag nanoparticles had a receptivity and detectivity of 184.8 mA/W and 9.201 cm Hz$^{1/2}$ W^{-1}, respectively, compared to 117.2 mA/W and 5.86 cm Hz$^{1/2}$ W^{-1} for the system without silver nanomaterial [114]. The very kinetic hot electrons from regionalized surface plasmon resonance stimulation of metallic plasmonic nanoparticles may swiftly migrate to the surrounding ZnSe nanoribbon with a comparable high energy once the heterojunction is illuminated by light [114]. High-performance photodetectors based on hybrid perovskite PV cells have been disclosed by Dou et al. Under standard circumstances, these PV panels seem to have an electrical performance of around 12% [115].
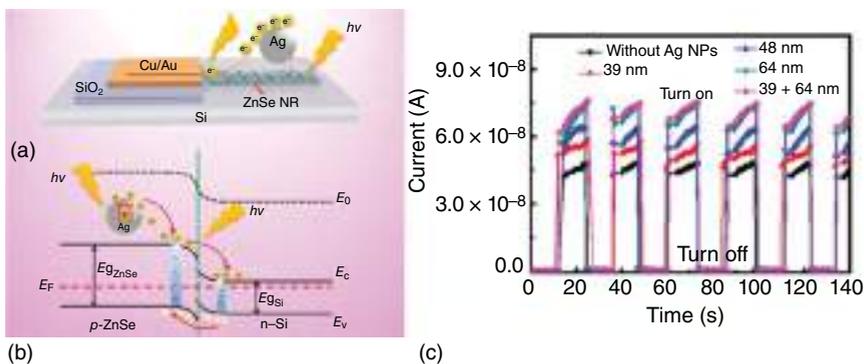
Figure 1.6 (a) Schematic depiction of localized surface plasmon resonance induced e-transfer from nanomaterials in ZnSe nanoribbon, (b) schematic diagram of the energy bandgap of ZnSe nanoribbon Si heterostructure enhanced with Ag nanomaterial with visible light, and (c) at low voltages, time-domain spectra of the circuit with and without decorating nanomaterials. Source: Zhang [102] / MDPI / Public Domain CC BY 4.0.

1.3.2.2 Solar Cell

The bulk semiconductors in the II–VI group have large binding energy and greater light-emitting and transmission coefficients [116]. By integrating semi-material with distinct bandwidth, each section of the heterojunction may preferentially absorb sunlight in a specific spectral region, resulting in more light absorption and better light usage [117]. As a result, heterojunctions have shown great potential in the improvement and advancements of solar cells. CdTe is a viable candidate for solar applications, with a bandgap of 1.45 eV and a greater absorption coefficient [118]. Because a 2 mm CdTe layer absorbs nearly all input direct sunlight, the p-CdTe/n-CdS heterostructures are the least common PV arrangement. Solar cells must be stable to be used in meaningful implementations. Nonetheless, perovskite-based materials, such as $CsPbI_3$, which are widely used in PVs, are unsteady and rapidly transition to solar cell that optimized light absorption by rising the interfacial region as well as illumination entrapment. These results mentioned possibilities for solar absorber material selection. TiO_2–SiO_2 is the cubic perovskite phase in the atmosphere [118]. Wu et al. created solar systems made of CdS, including Ga nanoribbons and Si heterojunctons. During UV activation, the transistors showed PV activity, exhibiting open-circuit photovoltage and short-circuit current of 0.45 V and 3.49 nA, respectively, resulting in a throughput of 44.1% and an energy transfer effectiveness of 1.2% [119].

Zhang and coworkers presented a type II ZnO/ZnSe core–shell nanostructure antireflection materials, which may increase the refractive indices duration via a scattered phenomenon or by producing an optical properties variation in Cu(In, Ga)Se_2 PV [120]. Since using the TiO_2–SiO_2 core–shell nanostructures to reduce reflectance the efficiency of power conversion increased from 6.32% to 7.00%. CdS/Cu_2S CSNW solar cells were fabricated by Zhang et al. which had greater open-circuit voltage and fill factor than comparable planar cells and also a 5.4% energy conversion efficiency which is equivalent to their counterpart planar cells when light absorption levels are low. They also used many cells on single nanostructures including both equivalent and consecutive topology to get high emission voltages and currents (Figure 1.7a–f) [102]. A reduced solution-based covalent bond approach, which might also establish a nanocrystalline interface within a single-crystalline CdS core and single-crystalline Cu_2S shell, is thought to be responsible for the remarkable photocatalytic efficiency of CdS/Cu_2S core–shell nanostructures [121].

1.3.2.3 Light-Emitting Diode

In a perfect PV material, the Shockley–Queisser limit asserts that radioactive decay is the only mechanism for charge recombination [122]. Owing to the recent significant growth in PV efficiency, it has been discovered that hybrid perovskites have extremely high PL quantum yields, which are near 70% at room temperature and nearing 100% at 195 K. This justifies the remarkable PV performance and also actively supports light-emitting device applicability [123]. Huang et al. have made significant change in building electronically driven electroluminescent diode, for example micro-LED, using a variety of semiconductor nanostructures [124]. Despite utilizing nanostructured transistors' growth to create p–n junctions, they employed
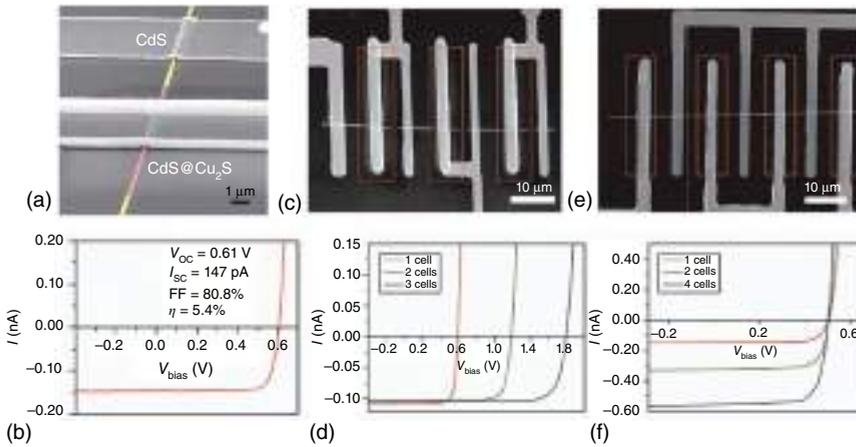
Figure 1.7 (a) SEM picture of a PV unit with yellow and brown artificial dyes highlighting CdS and Cu_2S, accordingly; (b) $I-V$ property of a fundamental nanowire exposed with (AM1.5G); (c) SEM picture of triple PV units in a sequence of a separate nanowire, showing the brown shapes indicating the core–shell areas; (d) the $I-V$ properties of the parallel devices within one sunlight irradiation (AM1.5G) demonstrate that the voltages add and the current remains unchanged; (e) SEM view shows four PV units off the single nanowire simultaneously, with brown boxes indicating the core–shell areas; and (f) during irradiation (AM1.5G), the $I-V$ property of the four perpendicular devices shows that the currents accumulate and the voltage remains constant. Source: Zhang et al. [102], MDPI, CC BY 4.0.

a linked p- and n-type NW technique. Additional NW processes have now been connected to the InP NWs electrode, such as p-Si/n-GaN, p-GaN/n-GaN, p-Si/n-CdS, and p-Si/n-CdSe [124, 125]. Ye et al. produced short-chain organic linker attached $CsPbBr_3$ NCs at room temperature in an ambient atmosphere [126]. They eventually succeeded in fabricating $CsPbBr_3$ NCs-based LED with a brightness of 5033 Cd/m^{-2}, an external quantum efficiency (EQE) of 5.4%, and excellent thermal resilience [126]. Yassitepe and coworkers developed an alkaline production approach for nanocrystalline QDs, which resulted in coatings with low chemical composition and improved durability. Additionally, inversion QD-based red, green, and blue LEDs with EQE of 0.05%, 0.325%, and 0.075, respectively, were developed [127]. Demchyshyn and coworkers developed a new method for stabilizing perovskite materials. They enclosed perovskite NCs in an anodic aluminum oxide (AAO) thin film that served as an encapsulation scaffold, and the newly generated perovskite NCs' luminescence stability increased considerably. The photoluminescence quantum yield (PLQY) of these perovskite NCs was up to 90%, but only 0.03% EQE was attained, indicating that additional optimization of this design was required [128]. Duan et al. demonstrated infrared illumination from CdS NWs by attaining a large charge injecting frequency along the width of a CdS cavity that used a hybridized structure. The device's reduced temperature testing demonstrated a tendency for numerous extraction methods. The bandgap of the main emission line at 493 is 0.8 nm, which can be compared to the sensor resolution [129]. Tan and Friend et al. used perovskites to exhibit high electroluminescence. The color of the emission may

be altered by adjusting the perovskite layer's constitution. The wavelength of light emitted by MAPbI$_3$ is 780 nm. The use of Br$^-$ instead of I$^-$ induces the emissive band to change to red and green hues. A sandwich arrangement was used to limit charge recombination inside the emissive layer, and quantum well structures give a high EL EQE of 0.8% [130].

Organic LED (OLED), inorganic quantum dots (QLEDs), and metal halide perovskites (PeLED)-based LED are leading in a new era of solid-state lighting where light can be modified as required [131]. OLEDs have offered up a range of unique options with exceptional flexibility over color, high contrast, and also reduced production procedures, while OLEDs also demonstrate an increasing position in the visual sectors [132, 133]. The adoption of defined techniques by the LED community to evaluate the performance of innovative materials and designs has resulted in various LED advancements and the self-sufficiency that this area requires to develop [134, 135]. LEDs, which are focused on a variety of transmitters including 3D, 2D, 1D, and 0D or double perovskites, have attracted a lot of interest in the illumination or display sectors. However, owing to a range of unique occurrences in these advanced technologies, which includes temporary impacts, these experimental results are often not explained in a cohesive and coherent method [131, 135, 136].

1.4 Conclusions

This book chapter explains the current achievements in fabrication, characterizations, and device implementation of 1D nanostructures. Either of the bottom-up and top-down techniques can be used to create 1D hybrid nanomaterials. The narrow shape and huge surface area of these nanomaterials allow them to be used in gas sensors and optoelectronic devices. However, despite the large amount of investigation being conducted in the field of 1D nanostructures, there seems to be a long way to go before they can be commercialized due to the challenges of scaling up manufacturing and maintaining characteristics throughout mass production.

Acknowledgment

References

1 Liu, X. and Li, Y. (2009). One-dimensional hybrid nanostructures with light-controlled properties. *Dalton Trans.* 33: 6447–6457.

2 Murray, C.B., Norris, D.J., and Bawendi, M.G. (1993). Synthesis and characterization of nearly monodisperse CdE (sulfur, selenium, tellurium) semiconductor nanocrystallites. *J. Am. Chem. Soc.* 115 (19): 8706–8715.

3 Fu, N., Li, Z., Myalitsin, A. et al. (2010). One-dimensional heterostructures of single walled carbon nanotubes and CdSe nanowires. *Small* 6 (3): 376–380.

4 Cui, Y. and Lieber, C.M. (2001). Functional nanoscale electronic devices assembled using silicon nanowire building blocks. *Science* 291 (5505): 851–853.

5 Peng, X., Chen, J., Misewich, J.A., and Wong, S.S. (2009). Carbon nanotube–nanocrystal heterostructures. *Chem. Soc. Rev.* 38 (4): 1076–1098.

6 Tan, C., Chen, J., Wu, X.J., and Zhang, H. (2018). Epitaxial growth of hybrid nanostructures. *Nat. Rev. Mater.* 3 (2): 17089.

7 Huang, X., Tan, C., Yin, Z., and Zhang, H. (2014). 25th anniversary article: hybrid nanostructures based on two dimensional nanomaterials. *Adv. Mater.* 26 (14): 2185–2204.

8 Tan, C. and Zhang, H. (2015). Two-dimensional transition metal dichalcogenide nanosheet-based composites. *Chem. Soc. Rev.* 44 (9): 2713–2731.

9 Fateixa, S., Nogueira, H.I.S., and Trindade, T. (2015). Hybrid nanostructures for SERS: materials development and chemical detection. *Phys. Chem. Chem. Phys.* 17 (33): 21046–21071.

10 Reddy, K.R., Hassan, M., and Gomes, V.G. (2015). Hybrid nanostructures based on titanium dioxide for enhanced photo catalysis. *Appl. Catal., A* 489: 1–16.

11 Du, N., Zhang, H., and Yang, D. (2012). One-dimensional hybrid nanostructures: synthesis via layer-by-layer assembly and applications. *Nanoscale* 4 (18): 5517–5526.

12 Wang, X., Song, J., Li, P. et al. (2005). Growth of uniformly aligned ZnO nanowire heterojunction arrays on GaN, AlN, and $Al_{0.5}Ga_{0.5}N$ substrates. *J. Am. Chem. Soc.* 127 (21): 7920–7923.

13 Kovtyukhova, N.I., Kelley, B.K., and Mallouk, T.E. (2004). Coaxially gated in-wire thin-film transistors made by template assembly. *J. Am. Chem. Soc.* 126 (40): 12738–12739.

14 Vila-Fungueirino, J.M., Bachelet, R., Saint-Girons, G. et al. (2015). Integration of functional complex oxide nanomaterials on silicon. *Front. Phys.* 3: 38.

15 Peng, L., Zhang, Z., Wang, S., and Liang, X. (2012). A doping-free approach to carbon nanotube electronics and optoelectronics. *AIP Adv.* 2 (4): 041403.

16 Fu, Y., Zhu, H., Chen, J. et al. (2019). Metal halide perovskite nanostructures for optoelectronic applications and the study of physical properties. *Nat. Rev. Mater.* 4 (3): 169–188.

17 Zhao, Y.S., Fu, H., Peng, A. et al. (2010). Construction and optoelectronic properties of organic one-dimensional nanostructures. *Acc. Chem. Res.* 43 (3): 409–418.

18 Razeghi, M., Haddadi, A., Hoang, A.M. et al. (2014). Antimonide-based type II superlattices: a superior candidate for the third generation of infrared imaging systems. *J. Electron. Mater.* 43 (8): 2802–2807.

19 Tan, C.L. and Mohseni, H. (2018). Emerging technologies for high performance infrared detectors. *Nanophotonics* 7 (1): 169–197.

20 Sotiropoulou, S., Sierra-Sastre, Y., Mark, S.S., and Batt, C.A. (2008). Biotemplated nanostructured materials. *Chem. Mater.* 20 (3): 821–834.

21 Arole, V.M. and Munde, S.V. (2014). Fabrication of nanomaterials by top-down and bottom-up approaches-an overview. *JAAST Mater. Sci.* 1 (2): 89–93.

22 Chen, Y., Chadderton, L.T., Gerald, J.F., and Williams, J.S. (1999). A solid-state process for formation of boron nitride nanotubes. *Appl. Phys. Lett.* 74 (20): 2960–2962.

23 Fernandez, A., Reddy, E.P., Rojas, T.C., and Sanchez-Lopez, J.C. (1999). Application of the gas phase condensation to the preparation of nanoparticles. *Vaccum* 52 (1-2): 83–88.

24 Chepkasov, I.V., Gafner, Y.Y., Gafner, S.L., and Bardahanov, S.P. (2016). Condensation of Cu nanoparticles from the gas phase. *Phys. Met. Metall.* 117 (10): 1003–1012.

25 Colson, P., Henrist, C., and Cloots, R. (2013). Nanosphere lithography: a powerful method for the controlled manufacturing of nanomaterial. *J. Nanomater.* 2013: 948510.

26 Manouras, T. and Argitis, P. (2020). High sensitivity resists for EUV lithography: a review of material design strategies and performance results. *Nanomaterials* 10 (8): 1593.

27 Dhawan, A., Du, Y., Batchelor, D. et al. (2011). Hybrid top-down and bottom-up fabrication approach for wafer-scale plasmonic nanoplatforms. *Small* 7 (6): 727–731.

28 Shen, G. and Chen, D. (2009). One-dimensional nanostructure and device of II-V group semiconductor. *Nanoscale Res. Lett.* 4 (8): 779–788.

29 Kumar, S., Bhushan, P., and Bhattacharya, S. (2018). Fabrication of nanostructures with bottom-up approach and their utility in diagnostics, therapeutics, and others. In: *Environmental* (ed. S. Bhattacharya, A.A. Kumar, N. Chanda, et al.), 167–198. Singapore: Chemical and Medical Sensors.

30 Ploog, K. (1980). Molecular beam epitaxy of III–V compounds. In: III–V Semiconductors. In: *Crystals (Growth, Properties, and Applications)* (ed. H.C. Freyhardt), 73–162. Berlin Heidelberg: Springer-Verlag.

31 Cho, A.Y. and Arthur, J. (1975). Molecular beam epitaxy. *Prog. Solid State Chem.* 10 (3): 157–191.

32 Rothemund, P.W.K. (2005). Design of DNA origami. ICCAD-2005. In: *IEEE/ACM International Conference on Computer Aided Design*, vol. 2005, 471–448. IEEE.

33 Whitesides, G.M., Mathias, J.P., and Seto, C.T. (1991). Molecular self-assembly and nanochemistry: a chemical strategy for the synthesis of nanostructures. *Science* 254 (5036): 1312–1319.

34 Chen, Y., Xu, P., Xu, T. et al. (2017). ZnO-nanowire size effect induced ultra-high sensing response to ppb-level H_2S. *Sens. Actuators, B* 240: 264–272.

35 Sharma, B., Sharma, A., and Myung, J.H. (2021). Selective ppb-level NO_2 gas sensor based on SnO_2-boron nitride nanotubes. *Sens. Actuators, B* 331: 129464.

36 Bhowmik, B., Dutta, K., and Bhattacharyya, P. (2019). An efficient room temperature ethanol sensor device based on p-n homojunction of TiO_2 nanostructures. *IEEE Trans. Electron Devices* 66 (2): 1063–1068.

37 Li, X., Wang, Y., Le, Y., and Gu, Z. (2012). Highly sensitive H_2S sensor based on template-synthesized CuO nanowires. *RSC Adv.* 2 (6): 2302–2307.

38 Wang, J.X., Sun, X.W., Yang, Y., and Wu, C.M.L. (2009). N–P transition sensing behaviors of ZnO nanotubes exposed to NO_2 gas. *Nanotechnology* 20 (46): 465501.

39 Lupan, O., Postica, V., Wolf, N. et al. (2017). Localized synthesis of iron oxide nanowires and fabrication of high performance nanosensors based on a single Fe_2O_3 nanowire. *Small Methods* 13 (16): 1602868.

40 Navale, S.T., Yang, Z.B., Liu, C. et al. (2018). Enhanced acetone sensing properties of titanium dioxide nanoparticles with a sub-ppm detection limit. *Sens. Actuators, B* 255: 1701–1710.

41 Yan, S., Li, Z., Li, H. et al. (2018). Ultra-sensitive room-temperature H_2S sensor using Ag–In_2O_3 nanorod composites. *J. Mater. Sci.* 53 (24): 16331–16344.

42 Andre, R.S., Mercante, L.A., Facure, M.H.M. et al. (2019). Enhanced and selective ammonia detection using In_2O_3/reduced graphene oxide hybrid nanofibers. *Appl. Surf. Sci.* 473: 133–140.

43 Wang, X., Li, Z., Shi, J., and Yu, Y. (2014). One-dimensional titanium dioxide nanomaterials: nanowires, nanorods, and nanobelts. *Chem. Rev.* 114 (19): 9346–9384.

44 Hench, L.L. and West, J.K. (1990). The sol-gel process. *Chem. Rev.* 90 (1): 33–72.

45 Choi, K.S. and Chang, S.P. (2018). Effect of structure morphologies on hydrogen gas sensing by ZnO nanotubes. *Mater. Lett.* 230 (1): 48–52.

46 Sen, R., Govindaraj, A., and Rao, C.N. (1997). Carbon nanotubes by the metallocene route. *Chem. Phys. Lett.* 267 (3-4): 276–280.

47 Soares, O.S.G.P., Rocha, R.P., Gonçalves, A.G. et al. (2015). Easy method toprepare N-doped carbon nanotubes by ball milling. *Carbon* 91: 114–121.

48 Popov, V.N. (2004). Carbon nanotubes: properties and applications. *Mater. Sci. Eng., R* 43: 61–102.

49 Singh, N., Buddharaju, K.D., Manhas, S.K. et al. (2008). Si, SiGe nanowire devices by top–down technology and their applications. *IEEE Trans. Electron Devices* 55 (11): 3107–3118.

50 Hobbs, R.G., Petkov, N., and Holmes, J.D. (2012). Semiconductor nanowire fabrication by bottom-up and top-down paradigms. *Chem. Mater.* 24 (11): 1975–1991.

51 Shakthivel, D., Ahmad, M., Alenezi, M.R. et al. (2019). *1D Semiconducting Nanostructures for Flexible and Large-Area Electronics: Growth Mechanisms and Suitability*, Elements in Flexible and Large Area Electronics (ed. R. Dahiya and L. Occhipinti), 1–98. Cambridge University Press.

52 Wu, Y., Yan, H., Huang, M. et al. (2002). Inorganic semiconductor nanowires: rational growth, assembly and novel properties. *Chem. Eur. J.* 8 (6): 1260–1268.

53 Wagner, R.S. and Ooherty, C.J. (1968). Mechanism of branching and kinking during VLS crystal growth. *J. Electrochem. Soc.* 115 (1): 93.

54 He, R., Gao, D., Fan, R. et al. (2005). Si nanowire bridges in microtrenches: integration of growth into device fabrication. *Adv. Mater.* 17 (17): 2098–2102.

55 Panda, D. and Tseng, T.Y. (2013). One-dimensional ZnO nanostructures: fabrication, optoelectronic properties, and device applications. *J. Mater. Sci.* 48 (20): 6849–6877.

56 Pauzauskie, P.J. and Yang, P. (2006). Nanowire photonics. *Mater. Today* 9 (10): 36–45.

57 Huang, M.H., Mao, S., Feick, H. et al. (2001). Room-temperature ultraviolet nanowire nanolasers. *Science* 292 (5523): 1897–1899.

58 Wagner, R.S. and Ellis, W.C. (1964). Vapor-liquid-solid mechanism of single crystal growth. *Appl. Phys. Lett.* 4 (5): 89–90.

59 Ghassan, A.A., Mijan, N.A., and Taufiq-Yap, Y.H. (2019). Nanomaterials: an overview of nanorods synthesis andoptimization. In: *Nanorods and Nanocomposites* (ed. M.S. Ghamsari and S. Dhara), 1–24. London: Intech Open.

60 Li, L.S. and Alivisatos, A.P. (2003). Origin and scaling of the permanent dipole moment in CdSe nanorods. *Phys. Rev. Lett.* 90 (9): 097402.

61 Liu, J., Tanaka, T., Sivula, K. et al. (2004). Employing end-functional polythiophene to control the morphology of nanocrystal-polymer composites in hybrid solar cells. *J. Am. Chem. Soc.* 126 (21): 6550–6551.

62 Mutiso, R.M., Sherrott, M.C., Rathmell, A.R. et al. (2013). Integrating simulations and experiments to predict sheet resistance and optical transmittance in nanowire films fortransparent conductors. *ACS Nano* 7 (9): 7654–7663.

63 Rao, M.V., Amareshwari, K., Viditha, V. et al. (2013). Flame synthesis of carbon nanorods with/without catalyst. *Int. J. Innov. Appl. Stud.* 3 (1): 1–5.

64 Yuan, Z., Li, R., Meng, F. et al. (2019). Approaches to enhancing gas sensing properties: a review. *Sensors* 19 (7): 1495.

65 Oh, E., Choi, H.Y., Jung, S.H. et al. (2009). High-performance NO_2 gas sensor based on ZnO nanorod grown by ultrasonic irradiation. *Sens. Actuators, B* 141 (1): 239–243.

66 Fine, G.F., Cavanagh, L.M., Afonja, A., and Binions, R. (2010). Metal oxide semi-conductor gas sensors in environmental monitoring. *Sensors* 10 (6): 5469–5502.

67 Nikolic, M.V., Milovanovic, V., Vasiljevic, Z.Z., and Stamenkovic, Z. (2020). Semiconductor gas sensors: materials, technology, design and application. *Sensors* 20 (22): 6694.

68 Rosty, R., Kebbekus, B., and Zaitsev, V. (2005). The testing of a semiconductor-based adsorption modified photosensitive sensor for its response to a volatile organic compound, oxygen, humidity and temperature. *Sens. Actuators, B* 107 (1): 347–352.

69 Huang, B., Lei, C., Wei, C., and Zen, G. (2014). Chlorinated volatile organic compounds (Cl-VOCs) in environment-sources, potential human impacts, and current remediation technologies. *Environ. Int.* 71: 118–138.

70 Wen, X., Fang, Y., Pang, Q. et al. (2005). ZnO nanobelt arrays grown directly from and on Zinc substrates: Synthesis, characterization, and applications. *J. Phys. Chem. B.* 109 (32): 15303–15308.

71 Fang, X., Hu, L., Ye, C., and Zhang, L. (2010). One-dimensional inorganic semiconductor nanostructures: a new carrier for nanosensors. *Pure Appl. Chem.* 82 (11): 2185–2198.

72 Velasco, G. and Schnell, J.P. (1983). Gas sensors and their applications in the automotive industry. *J. Phys. E: Sci. Instrum.* 16 (10): 973–977.

73 Leelakumar, M. (2020). Design of Electronic Control for Diesel Engines. In: *Design and Development of Heavy Duty Diesel Engines* (ed. P.A. Laxminarayanan and A.A. Kumar), 795–830. Singapore.

74 Masikini, M., Chowdhury, M., and Nemraoui, O. (2020). Metal oxides: application in exhaled breath acetone chemiresistive sensors. *J. Electrochem. Soc.* 167 (3): 037537.

75 Eddy, D.S. and Sparks, D.R. (1998). Application of MEMS technology in automotive sensors and actuators. *Proc. IEEE* 86 (8): 1747–1755.

76 Sun, P., Bisschop, R., Niu, H., and Huang, X. (2020). A review of battery fires in electric vehicles. *Fire Technol.* 56 (4): 1361–1410.

77 Nunes, D., Pimentel, A., Gonçalves, A. et al. (2019). Metal oxide nanostructures for sensor applications. *Semicond. Sci. Technol.* 34 (4): 043001.

78 Pavelko, R.G., Vasiliev, A.A., Llobet, E. et al. (2009). Comparative study of nanocrystalline SnO_2 materials for gas sensor application: thermal stability and catalytic activity. *Sens. Actuators, B* 137 (2): 637–643.

79 Padvi, M.N., Moholkar, A.V., Prasad, S.R., and Prasad, N.R. (2021). A critical review on design and development of gas sensing materials. *Eng. Sci.* 15: 20–37.

80 Kumar, R., Jaiswal, M., Singh, O. et al. (2019). Selective and reversible sensing of low concentration of carbon monoxide gas using Nb-doped OMS-2 nanofibers at room temperature. *IEEE Sens. J.* 19 (17): 7201–7206.

81 Wang, Z., Zhu, L., Sun, S. et al. (2021). One dimensional nanomaterial in resistive gas sensor: from material design to application. *Chemosensors* 9 (8): 198–200.

82 Raza, M.H., Kaur, N., Comini, E., and Pinna, N. (2020). Toward optimized radial modulation of the space-charge region in one-dimensional SnO_2-NiO core-shell nanowires for hydrogen sensing. *ACS Appl. Mater. Interfaces* 12 (4): 4594–4606.

83 Nikfarjam, A., Hosseini, S., and Salehifar, N. (2017). Fabrication of a highly sensitive single aligned TiO_2 and gold nanoparticle embedded TiO_2 nano-fiber gas sensor. *ACS Appl. Mater. Interfaces* 9 (18): 15662–15671.

84 Spetz, A.L., Unéus, L., Svenningstorp, H. et al. (2001). SiC based field effect gas sensors for industrial applications. *Phys. Stat. Sol.* 185 (1): 15–25.

85 Shimizu, Y., Matsunaga, N., Hyodo, T., and Egashira, M. (2001). Improvement of SO_2 sensing properties of WO_3 by noble metal loading. *Sens. Actuators, B* 77 (2): 35–40.

86 Sowmya, B., John, A., and Panda, P.K. (2021). A review on metal-oxide based p-n and n-n hetero structured nanomaterials for gas sensing applications. *Sens. Int.* 2 (3): 100085.

87 Tao, W.H. and Tsai, C.H. (2002). H_2S sensing properties of noble metal doped WO_3 thin film sensor fabricatedby micromachining. *Sens. Actuators, B* 81 (2-3): 237–247.

88 Kuswandi, B., Wicaksono, Y., Jayus, A.A. et al. (2011). Smart packaging: sensors for monitoring of food quality and safety. *Sens. Instrum. Food Qual. Saf.* 5 (3): 137–146.

89 Kim, N.H., Choi, S.J., Yang, D.J. et al. (2014). Highly sensitive and selective hydrogen sulfide and toluene sensors using Pd functionalized WO_3 nanofibers for potential diagnosis of halitosis and lung cancer. *Sens. Actuators, B* 193 (193): 574–581.

90 Ama, O., Sadiq, M., Johnson, M. et al. (2020). Novel 1D/2D KWO/$Ti_3C_2T_x$ nanocomposite-based acetone sensor for diabetes prevention and monitoring. *Chemosensors* 8 (4): 102.

91 Wang, X., Li, Y., Pionteck, J. et al. (2018). Flexible poly(styrene-butadiene-styrene)/carbon nanotube fiber based vapor sensors with high sensitivity, wide detection range and fast response. *Sens. Actuators, B* 256: 896–904.

92 Gong, H., Zhao, C., Niu, G. et al. (2020). Construction of 1D/2D α-Fe_2O_3/SnO_2 hybridnanoarrays for sub-ppm acetone detection. *Res. Sci. Partner J.* 2020: 2196063.

93 Moon, S.E., Choi, N.J., Lee, H.K. et al. (2013). Semiconductor-type MEMS gas sensor for real-time environmental monitoring applications. *ETRI J.* 35 (4): 617–624.

94 Tomchenko, A.A., Harmer, G.P., Marquis, B.T., and Allen, J.W. (2003). Semiconducting metal oxide sensor array for the selective detection of combustion gases. *Sens. Actuators, B* 93 (1-3): 126–134.

95 Ibrahim, R.K., Hayyan, M., AlSaadi, M.A. et al. (2016). Environmental application of nanotechnology: air, soil, and water. *Environ. Sci. Pollut. Res.* 23 (14): 13754–13788.

96 Yamazoe, N. and Miura, N. (1994). Environmental gas sensing. *Sens. Actuators, B* 20 (2-3): 95–102.

97 Suh, J.M., Kwon, K.C., Lee, T.H. et al. (2021). Edge-exposed WS_2 on 1D nanostructures for highly selective NO_2 sensor at room temperature. *Sens. Actuators, B* 333: 129566.

98 Dai, W., Yu, J., Luo, S. et al. (2020). WS_2 quantum dots seeding in Bi_2S_3 nanotubes: a novel Vis-NIR light sensitive photocatalyst with low-resistance junction interface for CO_2 reduction. *Chem. Eng. J.* 389: 123430.

99 Lim, K., Jo, Y.M., Yoon, J.W. et al. (2021). A transparent nanopatterned chemiresistor: visible light plasmonics sensor for trace level NO_2 detection at room temperature. *Small* 17 (20): 2100438.

100 Cui, S., Pu, H., Lu, G. et al. (2012). Fast and selective room-temperature ammonia sensors using silver nanocrystal-functionalized carbon nanotubes. *ACS Appl. Mater. Interfaces* 4 (9): 4898–4904.

101 Pescaglini, A. and Iacopino, D. (2015). Metal nanoparticle–semiconductor nanowire hybrid nanostructures for plasmon-enhanced optoelectronics and sensing. *J. Mater. Chem. C.* 3 (45): 11785–11800.

102 Zhang, X., Wu, D., and Geng, H. (2017). Heterojunctions based on II-VI compound semiconductor one dimensional nanostructures and their optoelectronic applications. *Crystals* 7 (10): 307.

103 Jeon, N.J., Noh, J.H., Yang, W.S. et al. (2015). Compositional engineering of perovskite materials for high-performance solar cells. *Nature* 517 (7535): 476–480.

104 Liu, J., Yang, Z., Ye, B. et al. (2019). A review of stability-enhanced luminescent materials: fabrication and optoelectronic applications. *J. Mater. Chem. C.* 7 (17): 4934–4955.

105 Hyun, J.K. and Lauhon, L.J. (2011). Spatially resolved plasmonically enhanced photocurrent from Au nanoparticles on a Si nanowire. *Nanoletters* 11 (7): 2731–2734.

106 Grinblat, G., Rahmani, M., Cortés, E. et al. (2014). High efficiency second harmonic generation from a single hybrid ZnO nanowire/Au plasmonic nano-oligomer. *Nano Lett.* 14 (11): 6660–6665.

107 Knight, M.W., Sobhani, H., Nordlander, P., and Halas, N.J. (2011). Photodetection with active optical antennas. *Science* 332 (6030): 702–704.

108 Kawawaki, T., Wang, H., Kubo, T. et al. (2015). Efficiency enhancement of PbS quantum dot/ZnO nanowire bulk-heterojunction solar cells by plasmonic silver nanocubes. *ACS Nano* 9 (4): 4165–4172.

109 Chen, W., Hao, J., Hu, W. et al. (2017). Enhanced stability and tunable photoluminescence in perovskite $CsPbX_3$/ZnS quantum dot heterostructure. *Small* 13 (21): 1604085.

110 Jie, J., Zhang, W., Bello, I. et al. (2010). One-dimensional II–VI nanostructures: synthesis, properties and optoelectronic applications. *Nanotoday* 5 (4): 313–336.

111 Chen, Q., De Marco, N., Yang, Y.M. et al. (2015). Under the spotlight: the organic-inorganic hybrid halide perovskite for optoelectronic applications. *Nanotoday* 10 (3): 355–338.

112 Luo, L.B., Xie, W.J., Zou, Y.F. et al. (2015). Surface plasmon propelled high-performance CdSe nanoribbons photodetector. *Opt. Express* 23 (10): 12979–12988.

113 Dong, R., Fang, Y., Chae, J. et al. (2015). High-gain and low-driving-voltage photodetectors based on organolead triiodide perovskites. *Adv. Mater.* 27 (11): 1912–1918.

114 Wang, L., Chen, R., Ren, Z.F. et al. (2016). Plasmonic silver nanosphere enhanced ZnSe nanoribbon/Si heterojunction optoelectronic devices. *Nanotechnology* 27 (21): 215202.

115 Dou, L., Yang, Y.M., You, J. et al. (2014). Solution-processed hybrid perovskite photodetectors with high detectivity. *Nat. Commun.* 5 (1): 5404.

116 Afzaal, M. and Brien, P. (2006). Recent developments in II–VI and III–VI semiconductors and their applications in solar cells. *J. Mater. Chem.* 16 (17): 1597–1602.

117 Ferekides, C.S., Balasubramanian, U., Mamazza, R. et al. (2004). CdTe thin film solar cells: device and technology issues. *Sol. Energy* 77 (6): 823–830.

118 Bamola, P., Rana, S., Singh, B. et al. (2021). Nanostructured oxide based ceramic materials for light and mechanical energy harvesting applications. In: *Advanced Ceramics for Energy and Environmental Applications*, vol. 11 (ed. A. Kumar), 116–135. Boca Raton.

119 Wu, D., Jiang, Y., Li, S. et al. (2011). Construction of highquality CdS: Ga nanoribbon/silicon heterojunctions and their nano-optoelectronic applications. *Nanotechnology* 22: 405201.

120 Zhang, X., Zhang, X., Wang, L. et al. (2013). ZnSe nanowire/Si p heterojunctions: device construction and optoelectronic applications. *Nanotechnology* 24 (39): 395201.

121 Wong, A.B., Brittman, S., Yu, Y. et al. (2015). Core–shell CdS–Cu$_2$S nanorod array solar cells. *Nano Lett.* 15 (6): 4096–4101.

122 Tvingstedt, K., Malinkiewicz, O., Baumann, A. et al. (2014). Radiative efficiency of lead iodide based perovskite solar cells. *Sci. Rep.* 4: 6071.

123 Duan, X., Huang, Y., Cui, Y. et al. (2001). Indium phosphide nanowires as building blocks for nanoscale electronic and optoelectronic devices. *Nature* 409 (6816): 66–69.

124 Huang, Y., Duan, X., and Lieber, C.M. (2005). Nanowires for integrated multicolor nanophotonics. *Small* 1 (1): 142–147.

125 Li, Y., Qian, F., Xiang, J., and Lieber, M. (2006). Nanowire electronic and optoelectronic devices. *Mater. Today* 9 (10): 18–27.

126 Ye, F., Zhang, H., Li, W. et al. (2019). Ligand-exchange of low-temperature synthesized CsPbBr$_3$ perovskite toward high efficiency light emitting diodes. *Small Methods* 3 (3): 1800489.

127 Yassitepe, E.Y., Yang, Z., Voznyy, O. et al. (2016). Amine-free synthesis of cesium lead halide perovskite quantum dots for efficient light emitting diodes. *Adv. Funct. Mater.* 26 (47): 8757–8763.

128 Demchyshyan, S., Roemer, J.M., Groib, H. et al. (2017). Confining metal-halide perovskites in nanoporous thin films. *Sci. Adv.* 3 (8): 1700738.

129 Duan, X., Huang, Y., Agarwal, R., and Lieber, C.M. (2003). Single-nanowire electrically driven lasers. *Nature* 421: 241–245.

130 Tan, Z.K., Moghaddam, R.S., Lai, M.L. et al. (2014). Bright light-emitting diodes based on organometal halide perovskite. *Nat. Nanotechnol.* 9 (9): 687–692.

131 Anaya, M., Rand, B.P., Holmes, R.J. et al. (2019). Best practices for measuring emerging light-emitting diode technologies. *Nat. Photonics* 13 (12): 818–821.

132 Greenham, N.C., Friend, R.H., and Bradley, D.D.C. (1994). Angular dependence of the emission from a conjugated polymer light-emitting diode: implications for efficiency calculations. *Adv. Mater.* 6 (6): 491–494.

133 Chen, H.W., Lee, J.H., Lin, B.Y. et al. (2018). Liquid crystal display and organic light-emitting diode display: present status and future perspectives. *Light Sci. Appl.* 7 (3): 17168.

134 Long, X., He, J., Zhou, J. et al. (2015). A review on light-emitting diode based automotive headlamps. *Renewable Sustainable Energy Rev.* 41: 29–41.

135 Zhao, B., Bai, S., Kim, V. et al. (2018). High-efficiency perovskite–polymer bulk heterostructure light-emitting diodes. *Nat. Photonics* 12 (12): 783–789.

136 Lin, K., Xing, J., Quan, L.N. et al. (2018). Perovskite light-emitting diodes with external quantum efficiency exceeding 20 per cent. *Nature* 562 (7726): 245–248.

2

Synthesis and Gas-Sensing Application of 1D Semiconducting Hybrid Nanostructures

Nguyen D. Cuong[1,2] and Nguyen Van Hieu[3]

[1] *Hue University, University of Sciences, Faculty of Chemistry, 77 Nguyen Hue, Phu Nhuan Ward, Hue 530000, Vietnam*
[2] *Hue University, School of Hospitality and Tourism, 22 Lam Hoang, Vy Da Ward, Hue 530000, Vietnam*
[3] *Phenikaa University, Faculty of Electrical and Electronic Engineering, Yen Nghia Ward, Ha Dong District, Hanoi 100000, Vietnam*

2.1 Introduction

The significant increase of toxic and flammable gas emissions from various fields such as industrial, agricultural processes, and transportation has greatly influenced environmental issues such as global warming and climate change and harmfully affected human health [1, 2]. Since Seiyama et al. found the significant change of electrical conductivity of ZnO in air and reactive gases in 1962, the semiconductor gas sensors have been attracted interest. Especially, today, with the fast spread of internet of things, gas sensors play an important role to precisely environmental monitoring, security, and healthcare diagnostics [3–5]. Significant efforts have been devoted to develop gas sensors of perfect performance, which covers some aspects including theories, techniques, and sensing materials, to continuously improve gas-sensing features such as excellent selectivity, high sensitivity, rapid response–recovery times, durability and stability, mini-size device, and low energy consumption [6, 7].

Nanomaterials, which were first envisaged by Feynman [8], possess various advantages such as small size, large surface area, boundaries, and quantum effects [9–12], and they provide new opportunities to explore remarkable chemical, physical, and optical properties of materials at nanoscopic scale for many important applications. The nanostructures can be classified as zero dimension (0D), one dimension (1D), two dimensions (2D), and three dimensions (3D) [5]. Therein, 1D nanostructures, as an important class of nanomaterials, have attracted considerable attention because they offer benefits such as well-defined crystal orientations, high-aspect-ratio structural feature, high electron mobility along the growth direction of one dimension, and potential as building blocks for designing nanodevices [13]. The development of

1D-nanostructured sensors have been focused a lot on metal oxide semiconductors and carbon nanotubes. These are the two most important materials of gas sensor, which have created huge potential to design extremely high sensitivity sensors [14]. In spite of the significant progress in fabrication of gas sensors based on pure 1D nanostructures such as carbon nanotube [15, 16], metal oxide semiconductor nanorods (NRs) [17, 18], nanowires (NWs) [19–22], nanotube [23], and nanofibers [24], it is still a major scientific challenge to enhance the sensing ability of single-phase-based gas sensors.

Various strategies have been implemented with the focus of doping other elements in sensing materials, surface functionalization with metallic nanoparticle catalysts, and fabrication of hybrid nanostructures to find the novel gas-sensing properties of the 1D nanostructures [25]. In particular, 1D hybrid nanomaterials, which are 1D nanostructures that composed of two or more different components with multiple functions [26], have opened new opportunities to ever more sensitive sensors and overcome the weaknesses of single-component-based sensors. The gas-sensing properties of a 1D hybrid nanostructure depend not only its intrinsic structures, available from the individual component, but also on its synergistic effect caused multicomponent.

Wang et al. [27] have successfully fabricated novel-sensing hybrid Au NPs-functionalized ZnO NWs by a two-stage solution route. The ZnO NWs functionalization by Au nanoparticle exhibited not only faster response and recovery times but also higher sensitivity toward benzene and toluene compared with pristine ZnO sensors due to the strong catalytic effect of the Au NPs and the increase of Schottky barriers caused by the electronic interaction between ZnO and Au. The formaldehyde sensitivity of core–shell α-Fe_2O_3@NiO hollow nanofiber sensors increased by almost 10 and 7 times compared with respective pure NiO and α-Fe_2O_3 because of its synergy between the heterojunctions [28]. Gong et al. reported the formation of p–n heterojunction between TiO_2 microfibers and polyaniline (PANI) nanoparticle displayed a vital role in gas-sensing properties of TiO_2/PANI nanocomposites. This sensors was 1000 times more sensitive toward NH_3 gas (50 ppt) than the best pure PANI sensors reported in previous literature [29]. The single-walled carbon nanotubes (SWCNT)/polypyrrole (PPy) core–shell sensor exhibited an enhancement in sensitivity to NH_3 gas more than 10 times compared with those of SWCNTs and PPy because of the formation of n–p junctions that modified the electronic structure of PPy. This is a synergistic effect in gas-sensing feature [30]. Therefore, the 1D semiconducting hybrid nanostructures are active candidates for exploring the novel-sensing materials.

Until now, the 1D nanostructures have been thrived in gas-sensing area. There are a few reviews on the development of gas sensor based on 1D nanostructures. Choi and Jang [31] have reported gas sensor application of the individual 1D- and self-assembled 1D nanostructures of metal oxides. Kaur et al. of Sensor Laboratory (University of Brescia) [25] have presented an overview of the remarkable performance of metal oxide nanowire-based gas sensors. The authors particularly emphasized the major role of the nanowire heterostructures as promising materials to further improve sensing performance of metal oxide-based gas sensors. The overviews of the design, fabrication, and working principles of unique 1D carbon nanotubes for gas sensors have been systematically reported [14, 32]. Recently, Yang et al. [33] have especially emphasized the vital role of the construction of heterojunction based on metal oxide to improve

Figure 2.1 The overview of this chapter.

gas-sensing performance. However, the overview of the development of 1D hybrid nanostructures-based gas sensors still gets little attention. In this chapter, we summarized recent research progress in the development of 1D hybrid conducting nanostructure sensors based on metal oxide semiconductors and carbon nanotubes that are the two most important sensing materials. Some typical 1D hybrid nanostructures of metal oxide semiconductors and carbon nanotubes for gas sensors have been presented in this chapter, which include noble metal-functionalized metal oxide, metal oxide/metal oxide heterojunction nanostructures, conducting polymer/1D metal oxide nanocomposites, and polymer/carbon nanotubes nanocomposite (Figure 2.1). Additionally, the synergistic effects of hybrid nanostructure that play an important role in the enhancement of gas-sensing performance have discussed clearly, which is expected to encourage further progress in this field. Some perspectives on the future development and directions of the 1D hybrid nanostructures in gas-sensing area will be introduced.

2.2 Noble Metal-Functionalized 1D Metal Oxide Semiconductors for Gas Sensors

Semiconducting metal oxides are widely used in gas sensor, which usually work at temperature range of 100–500 °C [34]. At this range of temperature, the oxygen molecules adsorb onto the surface of metal oxide semiconductors to form either an electron depletion layer or a hole accumulation surface charge layer, according to n-type

or p-type metal oxide semiconductors, respectively [35]. By controlling metal oxide semiconductor parameter, which include morphology, size, shape, surface area, synthetic methods, doping level, composition, humidity, and operating temperature, their sensing parameters such as sensitivity, selectivity, response–recovery speed, and stability can be tuned [10, 11, 36, 37]. Although promising results of gas-sensing properties of pristine metal oxide semiconductors have been investigated, the pure metal oxide semiconductor-based sensors usually exhibit poor selectivity and work at high temperature.

One popular and novel hybrid nanostructure for improving gas-sensing properties is 1D metal oxide nanostructure functionalized with noble metal NPs. The strong spillover effect of the excellent catalytic noble metals (mainly Pt, Pd, Au, and Ag) and the synergistic electronic interaction between the noble metal and metal oxide can enhance the surface depletion layer, thus altering the height of the Schottky barrier. These effects are called the electric sensitization and the chemical sensitization that play an important role to promote sensing feature of 1D hybrid noble metal–metal oxide nanostructures. As shown in Table 2.1, noble metal NPs-loaded 1D metal oxide sensors showed a dramatic improvement of gas-sensing parameters in comparison with pristine metal oxide-based sensors.

Many synthetic strategies have been developed to prepare noble metal nanoparticles-decorated surface of 1D metal oxide nanostructures such as wet chemical method, electrospinning route, and thermal vaporization [47]. The typical synthesis of hybrid noble metal NPs-decorated 1D metal oxide nanostructures usually possesses two stages, in which, the 1D metal oxide semiconductor was first prepared, and then that was used as support to load noble metal NPs. This process can both maintain well the 1D structures of metal oxides and decorate uniformly noble metal NPs on the surface of metal oxide. We have synthesized successfully SnO_2 NWs by the *in situ* growth of SnO_2 NWs on the sensors chips (Figure 2.2a). Afterward, the decoration of Pd NPs on the surface of SnO_2 NWs was carried out by the reduction of the palladium complex using Pluronic 123 as surfactant and reducing agent. Our developed Pd NPs-functionalized SnO_2 NWs sensors showed that ultrafast response–recovery speeds to CO gas due to the accelerating adsorption and desorption rates of CO molecules caused the catalytic activity of Pd NPs. In addition, the Pd-decorated SnO_2 NWs strongly enhanced the CO-sensing performance compared with pristine SnO_2 NWs sensors. The enhancement was due to the strong spillover of Pd NPs and the formation of electron depletion region or Schottky barrier between SnO_2 NWs and Pd NPs originated from the electron flow from SnO_2 to Pd [48]. Some notable similar strategies, Kolmakov et al. [50] fabricated hybrid sensors based on SnO_2 NWs and nanobelts functionalized with Pd NPs by *in situ* deposition of Pd on individual SnO_2 nanostructures. The sensors based on hybrid Pd–SnO_2 nanostructures showed a significant improvement in sensitivity to O_2 and H_2 compared to pristine SnO_2 sensors because of the enhanced catalytic dissociation of molecular adsorbate-originated Pd NPs. Singh et al. [51] synthesized the high-coverage gold NPs onto In_2O_3 NWs by a selective solution self-assembly route using monolayer of *p*-aminophenyl trimethoxysilane-functionalized In_2O_3 NWs. The high coverage of Au NPs on the surface of In_2O_3 NWs exhibited high response toward low concentration of CO gas in

Table 2.1 The gas-sensing properties of noble metal NPs-functionalized 1D nanostructures compared with bare metal oxide nanostructure counterpart.

Sensors	Synthesis method	Target gas	Response–recovery times (s)	Optimal working temperature	Response	References
ZnO NWs	Vapor–liquid–solid growth	H_2 (100 ppm)	——	300	$2.63^{a)}$	[38]
Pd-ZnO NWs				350	87.17	
SnO_2 NWs	Vapor–liquid–solid growth	H_2 (100 ppm)	104/314	300	$55.72^{a)}$	[39]
Pd-SnO_2 NWs			22/164		4.34	
ZnO NWs	Hydrothermal method	H_2S (5 ppm)	—/860	25	$15.9^{b)}$	[40]
Au-ZnO NWs			—/170		79.4	
ZnO NRs	Hydrothermal method	H_2S (100 ppb)	430/—	260	$3.4^{a)}$	[41]
Pt-ZnO NRs			174/—		23.1	
			(20 ppb)			
TiO_2 NRs	Hydrothermal method	Acetone (3.8 ppm)	——	200	$6.58^{a)}$	[42]
Ag-TiO_2 NRs			23.03–38.05 (min)		7.31	
In_2O_3 NRs	Co-precipitation method	Ethanol (50 ppm)	8/16	250	$12.6^{a)}$	[43]
Au-In_2O_3 NRs			7/14		42.1	
			(10 ppm)			
α-Fe_2O_3 NRs	Hydrothermal method	Triethylamine (50 ppm)	9/16	40	$8.6^{a)}$	[44]
Au-α-Fe_2O_3 NRs			12/8		17.5	
WO_3 NRs	Thermal evaporation	NO_2 (100 ppm)	450/380	300	$2.97^{a)}$	[45]
Pt-WO_3 NRs			500/300		11.34	
WO_3	Hydrothermal method	H2 (50 ppm)	—8/10	290	$1.6^{a)}$	[46]
Au-WO_3					6.6	
ZnO NWs	Hydrothermal method	Ethanol (100 ppm)	5/6	380	$3.7^{a)}$	[13]
Au-ZnO NWs			3/1		33.6	

a) R_{gas}/R_{air}.
b) I_{gas}/I_{air}.
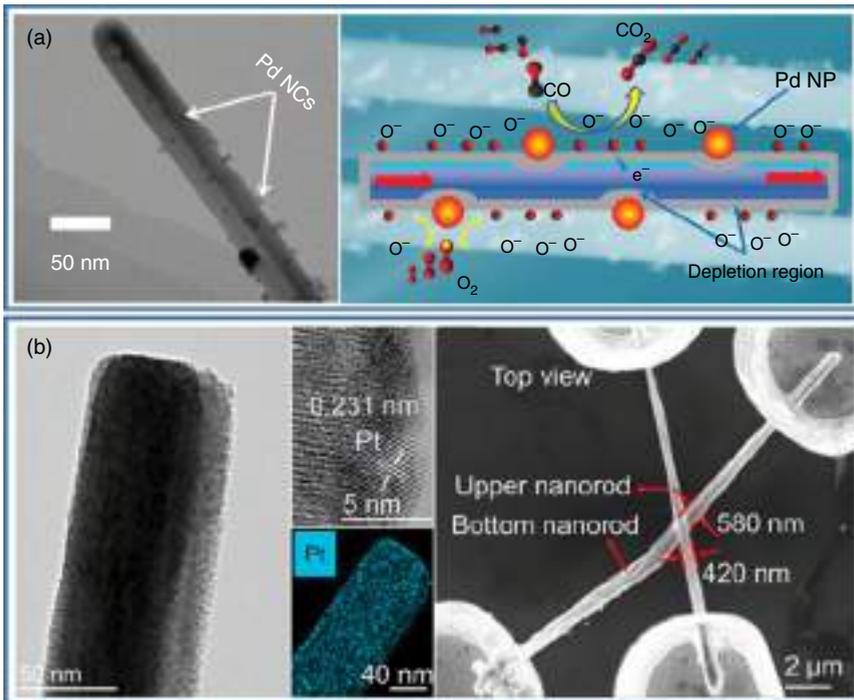
Figure 2.2 The promising gas sensors based on noble metal-functionalized 1D metal oxide: (a) Pd NPs-functionalized SnO_2 NWs sensor. Source: Trung et al. [48], Elsevier.; (b) and cross-stacked Pt-coated WO_3 NRs sensor. Source: Fan et al. [49], Elsevier.

comparison with those of pure In_2O_3 NWs or low coverage of Au NPs-loaded NWs at room temperature. The gas-sensing results were due to the unique catalytic properties of Au NPs for the CO oxidation. Besides two-stage synthetic approach, the noble metal NPs-functionalized 1D metal oxide nanostructures can fabricate a one-step method, in which the staring reaction mixture contains both salts of precious noble and metal oxide. Yang et al. [52] presented a new route to prepare Pd-loaded SnO_2 nanofiber by electrospinning followed by hot-pressing at 80 °C and calcining at high temperature. The porous SnO_2 nanofibers functionalized with Pd NPs have been formed by the decomposing organic components and oxidizing and crystallizing inorganic precursor. The Pd-loaded SnO_2 nanofiber sensors with the outstanding catalytic effect of PdO NPs as well as the increase of electron depletion layer on SnO_2 surface caused the Pd–SnO_2 heterojunctions that showed a significant enhancement to H_2 gas-sensing performance compared with that of pure SnO_2.

One of the important features of gas sensors is operating temperature. The sensor that operates at low working temperature has simple design, low power consumption, and increasing security and stability as well as easy practical application [53], so this is a mandatory requirement for the development of new-generation gas sensors. Hybrid noble metal/1D metal oxide-based sensors can not only enhance the sensitivity and response–recovery times but also dramatically decrease working

temperature compared to pure metal oxide-based sensors. These nanosensors possess spillover effect that originates the facile adsorption and ionization of oxygen molecules on noble metal surface and then the oxygen species spill onto the surface of metal oxide, leading to an increase of oxygen ions on the sensing surface. The high concentration of oxygen ions on the sensing surface plays a major role in the enhancement of the oxidation reaction of analytic gases at low temperature [54–56]. In addition, the excellent catalytic feature of noble metal NPs can promote the dissociation of target gas molecules into atoms, which is beneficial for the reaction oxidation of molecular gas at low temperature. The Pt and Pd NPs can make H_2 molecules dissociate easily into H atoms, thereby improving the detection of H_2 at very low working temperature with ultrahigh sensitivity and fast response time [57, 58]. Choi et al. [59] suggested that there are two effects that influence the sensitivity of Pd nanodots-decorated ZnO NWs, which included the electron transport between Pd and ZnO NWs, and catalytic activity of Pd nanodots for the dissociation of CO molecules. Specifically, the nano-Schottky-type junction barriers result at noble metal–metal oxide interface, which was suggested as an important factor to improve sensing performance at room temperature. Ramgir et al. have demonstrated that the Au NPs in Au/ZnO NWs not only enhanced sensitivity but also lead to faster recovery time at room temperature than that of pure ZnO NWs due to the formation of nano-Schottky-type junction barriers at Au–ZnO interface [40]. Tu et al. also reported that the formation of Schottky diode between ZnO NRs and Au NPs-based sensors had responsivity and selectivity toward NH_3 gas at room temperature [60].

Some novel approaches have recently been developed to continuously explore interesting gas-sensing properties based on 1D hybrid noble metal–metal oxide nanostructures. One approach is the use of noble bimetallic nanoparticles-decorated 1D metal oxide nanostructures, which can combine the unique advantages of two metals, that is, higher sensitivity and faster response and recovery times in comparison with sensors functionalized with individual noble metal NPs. Choi et al. [61] reported that the SnO_2 NWs loaded with bimetallic Pd/Pt NPs revealed faster response and recovery speeds compared to SnO_2 NW functionalized with individual Pd or Pt, relating the synergistic effect of Pd and Pt NPs. The Pt/Pd bimetallic core–shell NPs-functionalized ZnO NRs showed accelerated H_2 gas detection due to the atomic arrangements and chemical potentials of the core–shell interfacial region [62]. The PdAu alloy NPs with less than 25% Au in alloy NPs were loaded on the surface of TiO_2 NWs that have higher sensitivity and faster response time than that of Pd NPs-functionalized TiO_2 NWs [63]. The PdPt-functionalized α-Fe_2O_3 hollow NRs showed faster response–recovery times and higher response to trimethylamine compared with α-Fe_2O_3, Pd/α-Fe_2O_3, and Pt/α-Fe_2O_3 hollow NRs due to the synergistic effect of PdPt [64]. Vahl et al. [65] have developed the new chemical sensors by functionalizing the ZnO:Ag columnar with AgAu or AgPt bimetallic alloy NPs. By both theoretical calculation and experiment, the authors demonstrated that the Ag_5Au_5 alloy NPs-functionalized ZnO:Ag columnar was the most sensing material for the detection of volatile organic compounds (VOCs), while the Ag_9Pt/ZnO:Ag nanocomposites were is in line with the high selectivity toward H_2.

On the other hand, noble metal NPs-decorated metal oxide nanostructures that were assembled from several individual 1D metal oxide nanostructures have considered as fantastic route to achieve an effective sensing material because they possess both the chemical sensitization and electronic sensitization promoters. Fan et al. [49] have synthesized the novel nanojunction sensor by constructing a cross-stacked Pt-coated WO_3 NRs. There are two important factors in the novel sensors that include the excellent catalytic Pt NPs for dissociation reaction of H_2 molecules and the change in electrical transport of nanojunctions, which attributed the improved sensor performance. The Pt-functionalized WO_3 NRs showed rapid response toward H_2 gas with millisecond response time, a lower power consumption of $<6\,\mu W$ at the working temperature of $30\,°C$, and outstanding performance (Figure 2.2b).

2.3 1D Metal Oxide/Metal Oxide Heterojunctions-Based Gas Sensors

The hybrid metal oxide/metal oxide nanostructures, which consist of two or more different metal oxides, have been expected to improve remarkably physical and chemical properties in comparison with pristine metal oxide, because they provide ultrahigh-specific surface area and unique electronic interactions at the heterojunction interface [66]. Therein, the 1D metal oxide nanostructures have been considered as fantastic backbone to decorate, cover, or grow an other metal oxide on their surface to form novel heterojunction nanostructures. The synthetic process of 1D hybrid metal oxide–metal oxide nanostructures usually consists of two steps. The first step is that the 1D metal oxide-nanostructured substrate is synthesized by several approaches such as hydrothermal method, electrospinning technique, and thermal evaporation process [67–69]. The second step is that the as-synthesized 1D metal oxide nanostructures were used as backbone that is decorated, covered, or grown with other metal oxide to form heterostructures. Based on the synthetic strategy, a large number of hetero-architectures of 1D metal oxide–metal oxide nanostructures such as $ZnO–Fe_2O_3$ [67, 70, 71], $ZnO–NiO$ [72, 73], $Co_3O_4–TiO_2$ [74], and $CuO–NiO$ [75] have been fabricated successfully for many important applications. In particular, the metal oxide–metal oxide heterojunction nanostructures are gaining increasing attention and are actively being pursued for gas sensors due to the extraordinary electronic effect at n–n, p–p, and n–p heterojunctions, leading to the enhancement of sensing capacities [67, 74, 76].

We have proposed the ideal of designing SnO_2/ZnO hierarchical nanostructures by a facile and scalable route involving two steps. The SnO_2 NWs have been fabricated by thermal evaporation process, which was used as backbone in hierarchical heterostructure. Subsequently, after spray-coating with ZnO seed NPS, ZnO NRs branches were grown directly to the SnO_2 NW backbones via hydrothermal route. We recognized that the SnO_2/ZnO hierarchical nanostructured sensors showed an increase significantly in ethanol-sensing performance compared with that of SnO_2 NWs sensors. Furthermore, the ZnO growth time affected their ethanol-sensing

properties, which may be contributed to the formation of SnO_2/ZnO heterojunction [77]. Lou et al. [78] have introduced a novel hierarchical heterostructure of α-Fe_2O_3 NRs/TiO_2 nanofiber sensors by using a facile two-step way that combined both the electrospinning route and hydrothermal method. The TiO_2 nanofibers of backbone with about 200 nm in diameter were synthesized by electrospinning technique. Subsequently, α-Fe_2O_3 NRs have uniformly grown on TiO_2 nanofiber substrates through hydrothermal process to form the hierarchical heterostructure of α-Fe_2O_3 NR/TiO_2 nanofibers. This sensor markedly enhanced TMA-sensing performance in comparison with pure α-Fe_2O_3 NRs and TiO_2 nanofibers, which may be due to the formation of the synergistic effect of TiO_2 nanofiber and α-Fe_2O_3 NRs that originated from Schottky barrier and additional depletion layer at interface.

Until now, many efforts have demonstrated the 1D hybrid metal oxide/metal oxide nanostructures-based sensors that showed a dramatically response in comparison to that of 1D bare metal oxide nanostructure counterpart. The ZnO-decorated Fe_2O_3 NRs presented outstanding *n*-butanol-sensing properties, which showed both better sensitivity and faster response time compared with pure Fe_2O_3 NRs and ZnO NRs sensors [67]. The hybrid CuO NPs-decorated porous ZnO NRs can detect H_2S gas at low operating temperature of 100 °C with high sensitivity, reversible response, and good selectivity, which had a much higher H_2S response compared with that of ZnO NRs sensor [79]. The nano-coaxial Co_3O_4/TiO_2 heterojunction exhibited an increase of response and shorten response–recovery times and lower operating temperature in comparison with pristine TiO_2 sensors [74]. The enhanced performance for 1D hybrid metal oxide-oxide-nanostructured sensors may be due to the energy band structure of heterojunction, which lead to the transformation of charge carriers between their conduction bands as well as valence bands. For example, at the CuO–ZnO interface, the electron will flow from conducting band of Cu to that of ZnO, whereas the holes will transfer the opposite direction from valance band of ZnO to that of CuO [79]. This phenomenon makes a substantial addition of the electron depletion layer or hole accumulation layer at the interface. It is known that the concentration of charge carrier is a key parameter for tuning the gas-sensing properties of metal oxide, which is referred to as electronic sensitization [80]. Therefore, this is a very suitable mechanism that has been used to explain the enhanced gas-sensing performance for various 1D metal oxide/metal oxide heterojunctions such as NiO–WO_3 NRs [81], $SnO_2@Co_3O_4$ p–n heterostructure nanotubes, and n–SnO_2–p–Co_3O_4 composite nanofiber [82]. Furthermore, the catalytic effect of metal oxide also promotes gas-sensing performance. For example, the catalytic activity of NiO NPs for the hydrogenation of benzene may assign the enhancement and selective detection of C_6H_6 of the NiO-decorated Co_3O_4 NRs sensors [83]. The chemical affinity between CuO with H_2S molecules was vital role for enhancing H_2S gas-sensing properties of CuO-functionalized ZnO nanofibers [69]. The catalytic effect of Co_3O_4 for oxidation reaction of target gas can contribute to the significant improvement of gas-sensing performance in n–SnO_2–p–Co_3O_4 composite nanofiber sensors [82].

By combining the strong advantageous of precious metal, NPs and 1D hybrid of metal oxides can provide the great sensing materials with excellent performance. As shown in Figure 2.3, Ju et al. [84] indicated that the Au-loaded hybrid ZnO/SnO_2
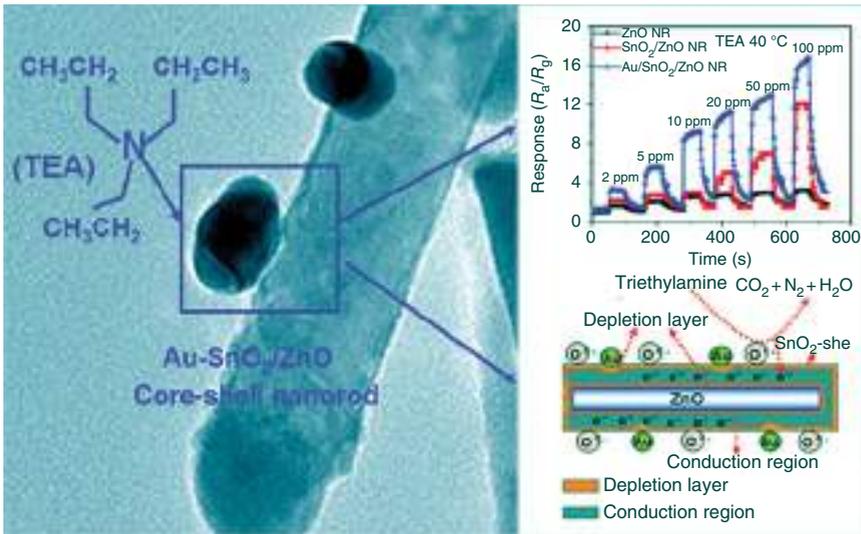
Figure 2.3 The gas-sensing feature of Au-loaded ZnO/SnO$_2$ core–shell NRs. Source: Ju et al. [84], Reproduced with permission from American Chemical Society.

core–shell NRs sensors exhibited a remarkably high-sensing performance, fast response time, and impressive selective trimethylamine at near room temperature of 40 °C. This sensor was higher-sensing performance in comparison with that of pristine ZnO NR, SnO$_2$/ZnO NR. The enhanced sensor properties may be due to several reasons: (i) the electrons transfer from SnO$_2$ to ZnO until the Fermi levels equalize, increasing the electron depletion layer on the surface of SnO$_2$; (ii) the electrons also flow from SnO$_2$ to Au NPs, leading to the formation of Au–SnO$_2$ Schottky contact and increase the depletion layer on the SnO$_2$; and (iii) the excellent catalytic activity of Au NPs may accelerate the dissociation of O$_2$. Recently, research results also indicated that this is a potential nanostructure to create ultrasensitive gas sensors. The Au/Fe$_2$O$_3$/ZnO NWs sensor has achieved a giant response as high as 74 500 to NO$_2$ gas. Its NO$_2$ response was much higher than that of Au-functionalized ZnO NWs sensors (about 42 times) [85]. The porous Au@Cr$_2$O$_3$–In$_2$O$_3$ NR sensor displayed reliable detection ability of typical VOCs biomarkers at low concentration (ppb) with excellent selectivity and long-term stability and works at high humidity, which originated from the heterojunction effect between Cr$_2$O$_3$ and In$_2$O$_3$ as well as the electron sensitization of Au [86].

2.4 Conducting Polymer/1D Metal Oxide Nanocomposites for Gas Sensors

Conducting polymers have been recognized as new type of gas-sensing materials since early 1980s [87] because the sensors based on conducting polymer can work at room temperature with fast response–recovery times. However, the poor stability of

conducting polymer hinders their use in practical applications [88]. The combination of the 1D metal oxide nanostructures and conducting polymers has been particularly interesting for gas sensor due to the formation a synergic effect between conducting polymer and metal oxide such as chemical and electronic effects [89], which provide a great opportunity to design new sensors that can work at room temperature with rapid response and good stability.

Ja et al. [90] have found that the PANI shell can protect well the oxygen surface vacancies of SnO_2 nanotubes, whereas the rich and stable oxygen vacancies of SnO_2 nanotubes can accelerate the PANI to generate more protons and lead to an enhancement of the gas sensor toward NH_3 gas at room temperature. The synergistic oxidation of CeO_2 promotes the protonation degrees of PANI in the PANI–CeO_2 nanocomposites. This is an important effect for the excellent NH_3-sensing properties of PANI–CeO_2 nanocomposite sensors at room temperature [91]. The formation of the p–n heterojunction interface between metal oxide nanostructures and conducting polymer such as Fe_2O_3 nanosheets/PANI [92], WO_3 nanoflowers/PANI [93], and SnO_2 nanosheets/PPy [94] presented a vital role in the highly desirable gas-sensing performance of hybrid conducting polymer/metal oxide nanocomposite sensors due to the increase of depletion region at interfaces. As a result, synergistic between conducting polymer and metal oxide semiconductor improves the interactive performance of the analytic gas molecules with conducting polymer [95], conducting enhanced gas sensitivity. Therefore, some research efforts have used typical conducting polymers with extraordinary electrical properties, cost-effectiveness, good environmental stability, and relatively high conductivity [96] such as PPy and PANI to cover metal oxide nanostructures to form new hybrid-sensing sensors that can excellently detect various target gas such as NH_3, CO, NO_2, H_2S, and LPG at room temperature [97–104].

Among various synthetic strategies, the conducting polymer is grown on the surface of the 1D metal oxide nanostructure that has been considered as an excellent route to fabricate 1D hybrid conducting polymer/metal oxide nanostructures. Zhu et al. [105] have introduced a facile strategy to synthesize PANI/ZnO nanograss, which involved two steps. The ZnO nanograss was first prepared by a hydrothermal method, and then this nanostructure was dipped in the PANI solution for 24 hours to form the chemical interaction between PANI molecules and ZnO surface. The approach did not alter the ZnO morphology after coating PANI onto ZnO surface. Jun et al. [106] have presented an effective approach to synthesizing PPy-coated 1D SnO_2 complex tubular nanostructures for future gas-sensing technology (Figure 2.4). The smooth electrospun nanofibers were synthesized by electrospinning method using a two-solvent polymer solution (poly(vinylpyrrolidone) in *N,N*-dimethylformamide mixed with $SnCl_2{\cdot}2H_2O$ in ethanol). The as-synthesized electrospun nanofibers were calcined at 600 °C to obtain unique SnO_2 hollow tubular structure consisted of a large number of nanograins, and its inner tube and outer shell are about 100 and 350 nm, respectively. The c. 10 nm PPy layer coated onto the surface of SnO_2 complex tubular nanostructures was fabricated by vapor deposition polymerization without any structural deformation. The PPy-coated SnO_2 tube-in-tube nanostructures-based sensors displayed an excellent detecting capability for dimethyl
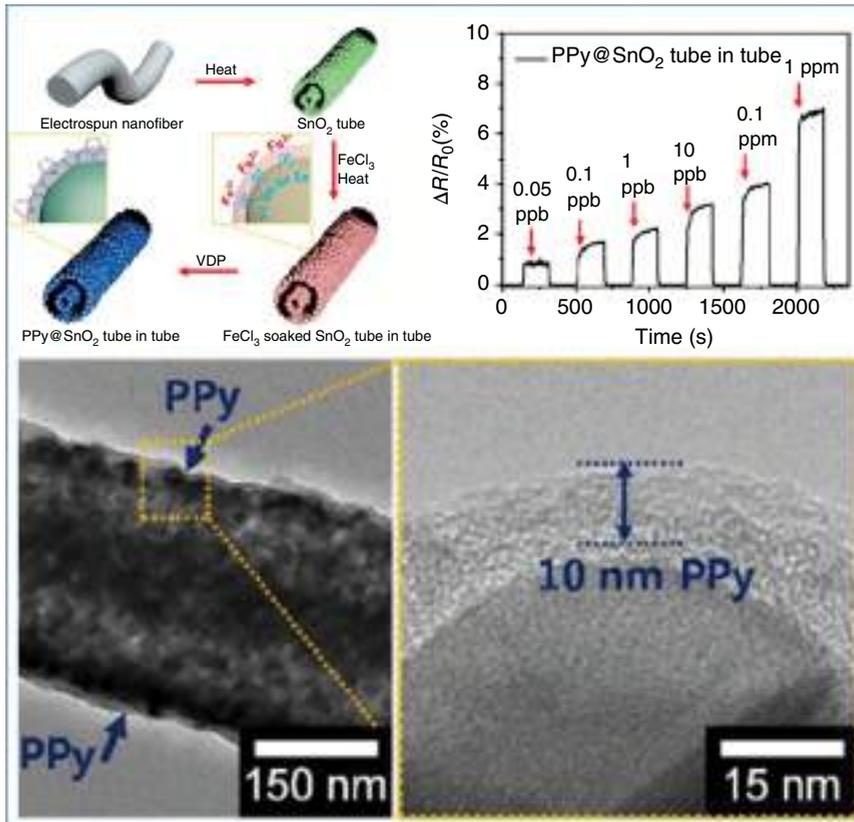
Figure 2.4 The synthetic strategy and gas-sensing feature of PPy-coated 1D SnO_2 complex tubular nanostructures. Source: Jun et al. [106], Royal Society of Chemistry.

methylphosphonate with outstanding sensitivity of 0.05 ppb, highly selectivity, good stability, and fast response–recovery times at room temperature. The excellent gas-sensing properties of PPy-coated SnO_2 sensors were due to the structural effect of 1D complex tubular structure and synergistic effect between PPy and SnO_2. Likewise, Gong et al. developed novel-sensing material based on the TiO_2 nanofiber enchased with PANI. The TiO_2 nanofibers were fabricated by calcining process of electrospun polyvinylpyrrolidone/Tin(IV)-isopropoxide nanofiber precursor at 600 °C for three hours. After that, the TiO_2 nanofibers were immersed in a solution of aniline for polymerization. The sensing device based on TiO_2 nanofiber enchased with PANI exhibited a superior reversibility to NH_3 gas at ppt level concentration, which may originate from the formation of p–n junction between PANI and TiO_2 [29]. The PANI/TiO_2 nanofibers have been also found to be promising sensing material for the detection of CO_2 at room temperature because of the formation of a positively charged depletion layer on the surface of TiO_2, which could be the electron migration from TiO_2 to PANI at the heterojunction. This phenomenon leads to the reduction of the activation energy of an enthalpy of physisorption for CO_2 [107].

2.5 Hybrid Conducting Polymer/Carbon Nanotube-Based Gas Sensors

The concept of carbon nanotube was taken place around 1950s [108] and 1970s [109] before it was first explored by Iijima in 1991 [110]. The material consists of rolling graphene layers with a sp^2-hybridized hexagonal array of carbon atoms with the ends of tubes capped with half of fullerene molecules [111]. Carbon nanotubes (CNTs) can be classified into SWCNTs and multi-walled carbon nanotubes (MWCNTs), which possess excellent strength-to-weight ratio, high flexibility (typically 1–5 TPa), low mass density, and large length-to-diameter aspect ratio (~300–1000) [112], originating its extraordinary electrical, mechanical, optical, and thermal properties. CNTs dispersion in solution can be agglomerated into large bundles caused by some factors including (i) van der Waals forces interaction between the bare tubes, (ii) the length of CNTs, and (iii) high polarizability of CNTs [113]. The agglomerate could damage the unique electrical and mechanical properties of CNTs. Thus, many efforts have been attracted to find the novel route to overcome this issue.

The fabrication of CNTs/polymer composites is a key strategy, because the uniqueness of CNTs and polymers has significant improvement in these materials such as stiffness, strength, toughness as well as electrical, optical, and thermal properties [114]. The first CNTs/polymer nanocomposites were explored by Ajayan et al. in 1994 [115]. In the reports, the authors have dispersed randomly purified nanotubes in a liquid epoxide-based resin through mechanical mixing process. After that, various routes have been proposed to prepare CNTs/polymer nanocomposites, because the property of nanocomposites was extremely depended on the dispersion of CNTs, interfacial adhesion between nanotubes and polymers, and the alignment and control of the CNTs in polymer [116]. In general, the interaction of CNTs and polymer was classified into noncovalent interaction such as π–π interactions, electrostatic interactions, hydrogen bonding, hydrophobic interaction, and covalent interaction that is the formation of strong chemical bonds between polymer and nanotubes [111]. Based on the origin of interaction between CNTs and polymer, the main objective is to obtain their uniform dispersion of CNTs in the polymer matrix, and several approaches have been used for the preparation of CNTs/polymer nanocomposites including solution mixing, melt bending, and *in situ* polymerization (Figure 2.5).

The CNTs with outstanding 1D nanostructure, exception electrical properties, ultra-large-specific surface area, and high charge carrier mobility are ideal candidates for the design of novel gas sensors working at room temperature, reducing power consumption and easy processing [117, 118]. The first report by Kong et al. [119] in 2000 have been indicated that the chemical resistance of CNTs significantly change when gas molecules adsorbed on their surface as well as CNTs based-sensors showed fast response and better sensitivity than that of existing other sensors at room temperature. There are two gas-sensing mechanisms based on bare CNTs sensors that include physisorption and chemisorption [120]. Kumar
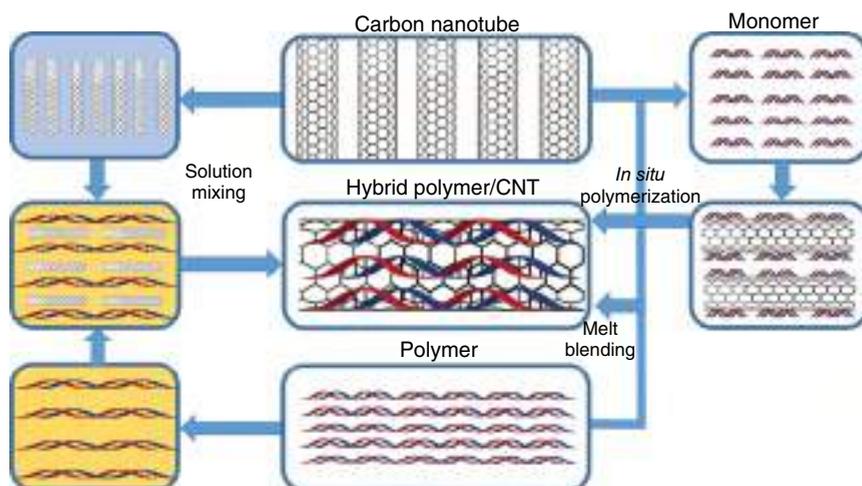
Figure 2.5 The typical approach to fabricate hybrid polymer/carbon nanotubes composites.

et al. reported a general model that was developed using coupled differential equations, which were suitable for the adsorption kinetics of NO_2 gas on SWCNT sensors [121]. Although CNTs have been proven to be good sensing materials, pure CNTs exhibit no response to several target gases such as H_2 because of their weak binding energy [122]. The gas-sensing properties of pure CNTs often have low sensitivity and difficulty to recover to initial state [123, 124]. Combination of these carbon materials with functional materials such as metal oxide [125, 126], noble metal [127], and polymer is an effective way for improving their gas-sensing properties [128]. In particular, the combination of CNT and polymers is creating a new class of material for developing novel gas sensors because of synergistic effects arising from the excellent properties of polymer matrix and nanofillers. We have synthesized PPy/SCCNTs nanocomposite by facile and straightforward *in situ* chemical polymerization of pyrrole monomer mixed with SWCNTs. The SWCNTs were well embedded within the matrix of PPy. The PPy/SCCNTs nanocomposite-based sensors showed fast response–recovery times of 22–38 seconds toward NH_3 gas at room temperature. The enhanced gas sensor was due to several factors: (i) the site defects on the sidewall of CNTs as physisorption and chemical sorption of NH_3, which were formed through the synthesis and purification process, were functionalized with PPy; (ii) the formation the permanent nanochannels in nanocomposite caused the hollow-core SWCNTs that lead to the easy diffusion of NH_3 molecules on sensor surface. Additionally, the PPy/SWCNTs nanocomposite sensors can detect NH_3 with a wide range of concentration, and their responses are good linear with NH_3 gas concentration, which is effective for practical applications [129]. Many research groups have been published studies on polymer/CNTs nanocomposites as shown in Table 2.2.

Among various conducting polymers, PANI and PPy with outstanding advantages have been focused on designing novel 1D polymer/CNTs core–shell-sensing

Table 2.2 Gas sensors based on CNTs/polymer nanocomposites.

Sensing materials	Method	Target gases	Response (%)	Working temperature (°C)	References
MWCNTs/PANI	Chemical oxidation polymerization	NH$_3$	2.3 (10 ppm) (R_g/R_a)	RT.	[130]
MWCNTs/PANI	*In situ* polymerization	CHCl$_3$	31.3 (100 ppm)	RT.	[131]
MWCNTs/PANI	*In situ* polymerization	NH$_3$	15.5 (2 ppm)	RT.	[132]
MWCNTs/PANI	Polymerization	NH$_3$	6.1 (10 ppm)	RT.	[133]
MWCNTs/PANI	Polymerization	NH$_3$	40 (30 ppm)	RT.	[134]
MWCNTs/PANI	Polymerization	NH$_3$, NO$_2$	65.9 (50 ppm)	RT.	[135]
MWCNTs/PPy	*In situ* polymerization	NH$_3$	3.07 (200 ppm)	RT.	[136]
MWCNTs/PPy	Sonochemical polymerization	NH$_3$	525 (0.1 ppm)	RT.	[137]
SWCNTs/PPy	*In situ* chemical polymerization	NO$_2$	90 (3000 ppm)	RT.	[138]
SWCNTs/PTh	Wet chemical	Methylphenethylamine	0.008 (32 ppb)	RT.	[139]
SWCNTs/PTh	Chemical-oxidative polymerization	NH$_3$	—	RT.	[140]
MWCNTs/PTh	Chemical-oxidative polymerization	NH$_3$	27.66 (0.1 ppm)	RT.	[141]
MWCNTs/PMMA	Ultrasonication	CH$_2$Cl$_2$	809 (−)	RT.	[142]

nanomaterials. The MWCNTs-doped PANI (MP) nanopowders were synthesized by chemical oxidation polymerization [130]. Then, MP was modified by plasma for 30 minutes at radio frequency. The modified MP NRs sensor exhibited high response amplitudes of 35.6–150 ppm ammonia at room temperature. At the same year, in another report, Kar et al. synthesized polyaniline (PANI) nanocomposites doped with carboxylic acid-functionalized multi-walled carbon nanotube (c-MWCNT) [131]. The formation of PANI layer on the exterior walls of the c-MWCNTs was clearly observed in the TEM images. The carboxyl-functionalized MWCNTs favorably interact with the conjugated PANI chains and create a pathway for strong dipole interaction with the analytic molecules, which leads to facilitate electron delocalization and charge transport through the polymer chain and consequently decrease the resistance of the exposed nanocomposite sensor. Abdulla et al. prepared PANI-functionalized MWCNTs (PANI/MWCNTs)-based nanocomposite for trace-level detection of ammonia (NH_3) gas [132]. Enhancement in the response of the PANI/MWCNTs-based sensor was attributed to the thin PANI layer wrapped around the c-MWCNT with large specific area for the adsorption of the NH_3 molecules. A hierarchical PANI/CNTs nanocomposite network film was deposited on polyethylene terephthalate (PET) substrate for NH_3 detection [133]. It exhibited highly sensitive NH_3 sensing from 200 ppb to 50 ppm, fast response–recovery time (85/20 seconds), room-temperature operation without external aid, reliable flexibility, and excellent selectivity to NH_3 compared to other VOCs. Eising et al. [134] doped carbon nanotubes and polyaniline nanocomposites using three distinct approaches (sulfuric acid, camphorsulfonic acid, and *m*-cresol). The sensor in which the doping was conducted by camphorsulfonic acid showed the best response to ammonia of 418%. The 1D core–shell PANI/CNT composite with p–n heterojunctions for NO_2 and NH_3 was investigated [135]. It was found that 1D hierarchical structures and the deeper charge depletion layer enhanced by structural changes of PANI contributed to the sensitive and fast responses to NH_3 and NO_2.

The nanocomposite of PPy and carboxylated MWCNTs was synthesized for NH_3 detection [136]. In this study, Bachhav et al. utilized HCl as a dopant and ammonium persulphate (APS) as an oxidant. The most sensitive PPy-MWCNT nanocomposites sensor to NH_3 gas obtained 4 wt% MWCNT content and found to be stable in operation against the variation in operating temperature and humidity. Hamouma et al. fabricated paper strips coated with PPy-wrapped CNTs composites for ammonia investigation [137]. The procedure was done in three steps: (i) anchor –NH_2 groups on CNT sidewalls; (ii) coat modified CNTs on paper strips, and (iii) deposit PPy top coating. Comparative gas-sensing properties analysis of the nanocomposite-based gas sensors synthesized with different ratio molar CNT/amine revealed excellent sensor performance for paper strip@CNT-$N_{1/1}$@PPy nanocomposite in the concentration range of 0.005–0.05 ppm of NH_3 with high sensitivity and low DL of 0.04 ppb. While, An et al. fabricated nanocomposite based on PANI and SWCNTs [138], which presented n-type characteristics in which resistance increased with NO_2 adsorption.

Besides PANI and PPy, several polymers have also been used to cover CNTs for exploring new gas-sensing properties. A gas sensor based on nanocomposite

composed of poly[3-(6-carboxyhexyl)thiophene-2,5-diyl] (P3CT) and MWCNTs was fabricated to detect *n*-methylphenethylamine (NMPEA) vapor [139]. The carboxylic acid group in the polymer acts as a binder of organic amines via acid–base interaction. NMPEA was detected at concentrations as low as 4 ppb. The acid–base interaction between the amine compounds of the gas and the carboxylic acid groups in the polymer is attributed to the extraordinary sensitivity of the sensor. Husain et al. developed a gas sensor based on polythiophene/SWCNTs nanocomposite (PTh/SWCNT) for NH_3 detection [140]. The good sensitivity of the sensor was attributed to the association of polarons of the composite in an electronic interaction with lone pairs of ammonia during adsorption and desorption. Parallelly Husain et al. prepared a nanocomposite made of PTh and MWCNTs [141]. The results reveal that
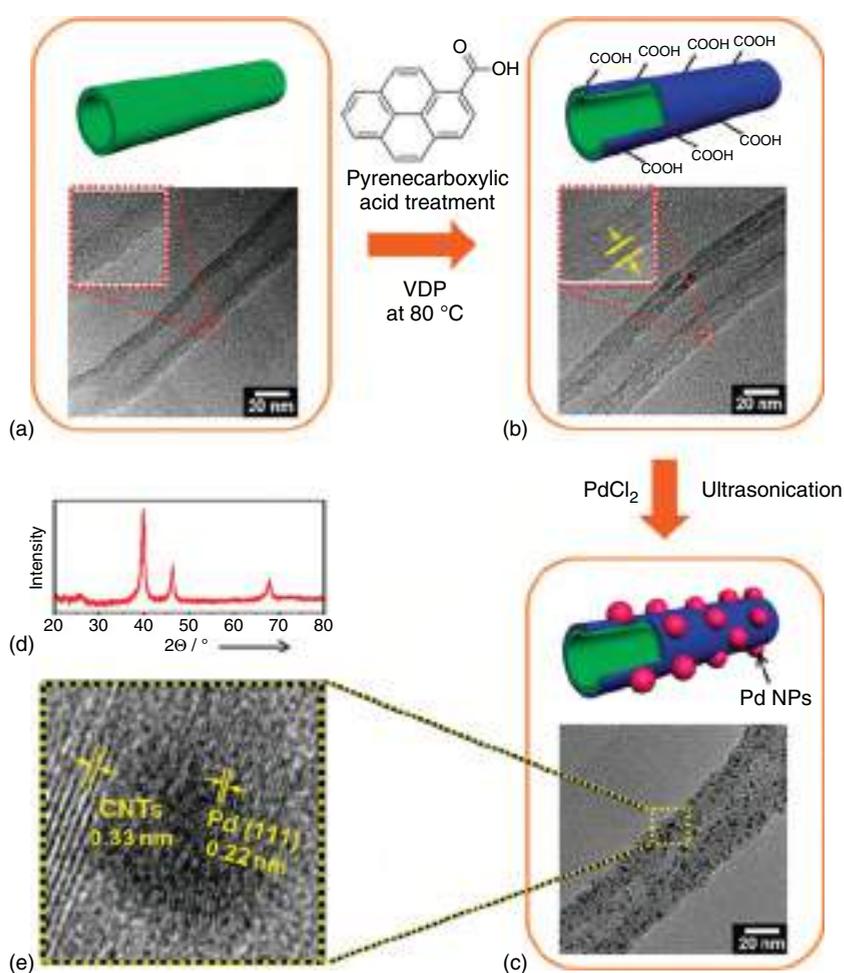
Figure 2.6 The synthetic process hybrid carboxylated polypyrrole (CPPy) skin-coated CNTs loaded with uniform Pd NPs sensor: (a) bare CNTs, (b) ultrathin CPPy skin-coated CNTs, (c) ultrathin CPPy skin-coated CNTs loaded with uniform Pd NPs, and (d, e) XRD and HRTEM of Pd NPs. Source: Park et al. [143], Royal Society of Chemistry.

the relative humidity had only a small effect on ammonia-sensing performance of the composite sensor. Philip et al. designed and developed composite thin films of polymethylmethacrylate (PMMA) with MWCNTs for dichloromethane, chloroform, acetone, methanol, ethyl acetate, toluene, and hexane investigation [142]. The sensing mechanism of the composite may be due to the basis of volume expansion and polar interaction of various vapors on the CNT surface.

Park et al. [143] have reported a novel route for synthesizing hybrid carboxylated polypyrrole (CPPy) skin-coated CNTs loaded with uniform Pd NPs (Figure 2.6). The synthesis strategy of Pd NPs-decorated CPPy-CNTs included three steps. First, the CNTs were functionalized their surface by 1-pyrenecarboxylic acid and then were coated with ultrathin PPy skins of 5 nm by vapor deposition polymerization. The sonochemical reduction method was used to decorate Pd NPs on the CPPy-CNTs. The CPPy ultra-layers were suitable matrices to immobilize highly uniform and monodisperse Pd NPs. With suitable amount of Pd NPs, the Pd NPs-functionalized CPPy-CNTs nanohybrids sensors showed excellent detection of H_2 with very fast response time (<1 seconds), low detection limit, and reproducible and reversible response at room temperature. The sensing behavior of Pd-CPPy-CNTs nanohybids may be due to the interaction between Pd NPs that generated electron transfer from Pd to CPPy-CNTs. The ultrathin CPPy skin may enable facile flow of electronic charges for enhanced sensing capability. By combining the outstanding properties of CNTs, conducting polymer, and noble metal, the noble metal NPs-decorated 1D CTNs@conducting polymer nanohybrids may generate new class of sensing materials with extraordinary performance.

2.6 Conclusion and Future Perspectives

As novel and promising materials, 1D hybrid semiconducting nanostructures are expected as potential candidates that could contribute to many fields of applications, particularly gas sensor. Although there have been significant advances in gas-sensing capability of single-phase-based sensors such as metal oxide semiconductor, CNTs and conducting polymer, the shortcomings of these materials such as poor stability, low sensitivity, and high operating temperature still need to be handled. The functionalization of 1D metal oxide nanostructures and CNTs with noble metal, metal oxide, and conducting polymer has been suggested as a potential strategy to generate novel-sensing device with excellent performance for new technological time. The 1D hybrid nanostructures such as noble metal-functionalized metal oxide, metal oxide/metal oxide, conducting polymer/metal oxide, and conducting polymer/CNTs possess interfacial junctions functioned as building bridges for either charge transfer or synergistic interaction to result in enhancing sensing response. In addition, the great catalytic activity of noble metal and metal oxide as well as the chemical interaction between conducting polymer with analysis gas molecules play an important role to dramatically improve gas-sensing properties. These effects are called electric sensitization and chemical sensitization, which form the basis for the development of new sensing strategies both theoretically and experimentally.

Therefore, the new synthesis strategy based on the synergistic effect of heterojunction and the outstanding catalytic of precious metal NPs will be the future trends in gas-sensing filed.

Acknowledgment

References

1 Cuong, N.D., Hoa, T.T., Khieu, D.Q. et al. (2012). Gas sensor based on nanoporous hematite nanoparticles: effect of synthesis pathways on morphology and gas sensing properties. *Curr. Appl. Phys.* 12: 1355–1360.

2 Dai, J., Ogbeide, O., Macadam, N. et al. (2020). Printed gas sensors. *Chem. Soc. Rev.* 49: 1756–1789. https://doi.org/10.1039/C9CS00459A.

3 Bales, E., Nikzad, N., Quick, N. et al. (2019). Personal pollution monitoring: mobile real-time air quality in daily life. *Pers. Ubiquitous Comput.* 23: 309–328. https://doi.org/10.1007/s00779-019-01206-3.

4 Di Natale, C., Paolesse, R., Martinelli, E., and Capuano, R. (2014). Solid-state gas sensors for breath analysis: a review. *Anal. Chim. Acta* 824: 1–17. https://doi.org/10.1016/j.aca.2014.03.014.

5 Nunes, D., Pimentel, A., Gonçalves, A. et al. (2019). Metal oxide nanostructures for sensor applications. *Semicond. Sci. Technol.* 34: 043001. https://doi.org/10.1088/1361-6641/ab011e.

6 Li, J., Lu, Y., Ye, Q. et al. (2003). Carbon nanotube sensors for gas and organic vapor detection. *Nano Lett.* 3: 929–933. https://doi.org/10.1021/nl034220x.

7 Han, S.T., Peng, H., Sun, Q. et al. (2017). An overview of the development of flexible sensors. *Adv. Mater.* 29: 1–22. https://doi.org/10.1002/adma.201700375.

8 Feynman, R.P. (1992). There's plenty of room at the bottom [data storage]. *J. Microelectromech. Syst.* 1: 60–66. https://doi.org/10.1109/84.128057.

9 Quang, P.L., Cuong, N.D., Hoa, T.T. et al. (2018). Simple post-synthesis of mesoporous p-type Co_3O_4 nanochains for enhanced H_2S gas sensing performance. *Sens. Actuators, B* 270: 158–166. https://doi.org/10.1016/j.snb.2018.05.026.

10 Trung, D.D., Cuong, N.D., Trung, K.Q. et al. (2018). Controlled synthesis of manganese tungstate nanorods for highly selective NH_3 gas sensor. *J. Alloys Compd.* 735: 787–794.

11 Thu, N.T.A., Cuong, N.D., Nguyen, L.C. et al. (2017). Fe_2O_3 nanoporous network fabricated from Fe_3O_4/reduced graphene oxide for high-performance ethanol gas sensor. *Sens. Actuators, B* 255: 3275–3283.

12 Huang, C., Chen, X., Xue, Z., and Wang, T. (2020). Effect of structure: a new insight into nanoparticle assemblies from inanimate to animate. *Sci. Adv.* 6: https://doi.org/10.1126/sciadv.aba1321.

13 Guo, J., Zhang, J., Zhu, M. et al. (2014). High-performance gas sensor based on ZnO nanowires functionalized by Au nanoparticles. *Sens. Actuators, B* 199: 339–345. https://doi.org/10.1016/j.snb.2014.04.010.

14 Wang, Y. and Yeow, J.T.W. (2009). A review of carbon nanotubes-based gas sensors. *J. Sens.* 2009: 1–24. https://doi.org/10.1155/2009/493904.

15 Chen, G., Paronyan, T.M., Pigos, E.M., and Harutyunyan, A.R. (2012). Enhanced gas sensing in pristine carbon nanotubes under continuous ultraviolet light illumination. *Sci. Rep.* 2: 343. https://doi.org/10.1038/srep00343.

16 Mittal, M. and Kumar, A. (2014). Carbon nanotube (CNT) gas sensors for emissions from fossil fuel burning. *Sens. Actuators, B* 203: 349–362. https://doi.org/10.1016/j.snb.2014.05.080.

17 Hu, Q., Zhang, W., Wang, X. et al. (2021). Binder-free CuO nanoneedle arrays based tube-type sensor for H_2S gas sensing. *Sens. Actuators, B* 326: 128993. https://doi.org/10.1016/j.snb.2020.128993.

18 Xu, S., Zhao, H., Xu, Y. et al. (2018). Carrier mobility-dominated gas sensing: a room-temperature gas-sensing mode for SnO_2 nanorod array sensors. *ACS Appl. Mater. Interfaces* 10: 13895–13902. https://doi.org/10.1021/acsami.8b03953.

19 Vomiero, A., Comini, E., and Sberveglieri, G. (2012). Oxide nanowires for new chemical sensor devices. In: *Oxide Ultrathin Film* (ed. G. Pacchioni and S. Valeri), 329–343. https://doi.org/10.1002/9783527640171.ch14. KGaA, Weinheim, Germany: Wiley-VCH Verlag GmbH & Co.

20 Comini, E. (2020). Metal oxides nanowires chemical/gas sensors: recent advances. *Mater. Today Adv.* 7: 100099. https://doi.org/10.1016/j.mtadv.2020.100099.

21 Thong, L.V., Loan, L.T.N., and Van Hieu, N. (2010). Comparative study of gas sensor performance of SnO_2 nanowires and their hierarchical nanostructures. *Sens. Actuators, B* https://doi.org/10.1016/j.snb.2010.07.033.

22 Wang, B., Zhu, L.F., Yang, Y.H. et al. (2008). Fabrication of a SnO_2 nanowire gas sensor and sensor performance for hydrogen. *J. Phys. Chem. C* 112: 6643–6647. https://doi.org/10.1021/jp8003147.

23 Zhang, J., Guo, J., Xu, H., and Cao, B. (2013). Reactive-template fabrication of porous SnO_2 nanotubes and their remarkable gas-sensing performance. *ACS Appl. Mater. Interfaces* 5: 7893–7898. https://doi.org/10.1021/am4019884.

24 Kim, J.H., Mirzaei, A., Woo Kim, H. et al. (2019). Design of supersensitive and selective ZnO-nanofiber-based sensors for H_2 gas sensing by electron-beam irradiation. *Sens. Actuators, B* 293: 210–223. https://doi.org/10.1016/j.snb.2019.04.113.

25 Kaur, N., Singh, M., and Comini, E. (2020). One-dimensional nanostructured oxide chemoresistive sensors. *Langmuir* 36: 6326–6344. https://doi.org/10.1021/acs.langmuir.0c00701.

26 Tan, C., Chen, J., Wu, X.-J., and Zhang, H. (2018). Epitaxial growth of hybrid nanostructures. *Nat. Rev. Mater.* 3: 17089. https://doi.org/10.1038/natrevmats.2017.89.

27 Wang, L., Wang, S., Xu, M. et al. (2013). A Au-functionalized ZnO nanowire gas sensor for detection of benzene and toluene. *Phys. Chem. Chem. Phys.* 15: 17179. https://doi.org/10.1039/c3cp52392f.

28 Cao, J., Wang, Z., Wang, R. et al. (2015). Synthesis of core–shell α-Fe$_2$O$_3$@NiO nanofibers with hollow structures and their enhanced HCHO sensing properties. *J. Mater. Chem. A* 3: 5635–5641. https://doi.org/10.1039/C4TA06892K.

29 Gong, J., Li, Y., Hu, Z. et al. (2010). Ultrasensitive NH$_3$ gas sensor from polyaniline nanograin enchased TiO$_2$ fibers. *J. Phys. Chem. C* 114: 9970–9974. https://doi.org/10.1021/jp100685r.

30 Huyen, D.N., Tung, N.T., Vinh, T.D., and Thien, N.D. (2012). Synergistic effects in the gas sensitivity of polypyrrole/single wall carbon nanotube composites. *Sensors* 12: 7965–7974. https://doi.org/10.3390/s120607965.

31 Choi, K.J. and Jang, H.W. (2010). One-dimensional oxide nanostructures as gas-sensing materials: review and issues. *Sensors* 10: 4083–4099. https://doi.org/10.3390/s100404083.

32 Zaporotskova, I.V., Boroznina, N.P., Parkhomenko, Y.N., and Kozhitov, L.V. (2016). Carbon nanotubes: sensor properties. A review. *Mod. Electron. Mater.* 2: 95–105. https://doi.org/10.1016/j.moem.2017.02.002.

33 Yang, S., Lei, G., Xu, H. et al. (2021). Metal oxide based heterojunctions for gas sensors: a review. *Nanomaterials* 11: 1026. https://doi.org/10.3390/nano11041026.

34 Zhang, J., Liu, X., Neri, G., and Pinna, N. (2016). Nanostructured materials for room-temperature gas sensors. *Adv. Mater.* 28: 795–831. https://doi.org/10.1002/adma.201503825.

35 Lee, J.-H. (2009). Gas sensors using hierarchical and hollow oxide nanostructures: overview. *Sens. Actuators, B* 140: 319–336. https://doi.org/10.1016/j.snb.2009.04.026.

36 Cuong, N.D., Hoa, T.T., Khieu, D.Q. et al. (2012). Synthesis, characterization, and comparative gas-sensing properties of Fe$_2$O$_3$ prepared from Fe$_3$O$_4$ and Fe$_3$O$_4$-chitosan. *J. Alloys Compd.* 523: 120–126.

37 Broza, Y.Y., Vishinkin, R., Barash, O. et al. (2018). Synergy between nanomaterials and volatile organic compounds for non-invasive medical evaluation. *Chem. Soc. Rev.* 47: 4781–4859. https://doi.org/10.1039/C8CS00317C.

38 Kim, J.-H., Mirzaei, A., Kim, H.W., and Kim, S.S. (2019). Pd functionalization on ZnO nanowires for enhanced sensitivity and selectivity to hydrogen gas. *Sens. Actuators, B* 297: 126693. https://doi.org/10.1016/j.snb.2019.126693.

39 Cai, Z. and Park, S. (2020). Synthesis of Pd nanoparticle-decorated SnO$_2$ nanowires and determination of the optimum quantity of Pd nanoparticles for highly sensitive and selective hydrogen gas sensor. *Sens. Actuators, B* 322: 128651. https://doi.org/10.1016/j.snb.2020.128651.

40 Ramgir, N.S., Sharma, P.K., Datta, N. et al. (2013). Room temperature H$_2$S sensor based on Au modified ZnO nanowires. *Sens. Actuators, B* 186: 718–726. https://doi.org/10.1016/j.snb.2013.06.070.

41 Yu, A., Li, Z., and Yi, J. (2021). Selective detection of parts-per-billion H$_2$S with Pt-decorated ZnO nanorods. *Sens. Actuators, B* 333: 129545. https://doi.org/10.1016/j.snb.2021.129545.

42 Kılıç, A., Alev, O., Özdemir, O. et al. (2021). The effect of Ag loading on gas sensor properties of TiO$_2$ nanorods. *Thin Solid Films* 726: 138662. https://doi.org/10.1016/j.tsf.2021.138662.

43 Xing, R., Xu, L., Song, J. et al. (2015). Wei Song, preparation and gas sensing properties of In_2O_3/Au nanorods for detection of volatile organic compounds in exhaled breath. *Sci. Rep.* 5: 10717. https://doi.org/10.1038/srep10717.

44 Song, X., Xu, Q., Zhang, T. et al. (2018). Room-temperature, high selectivity and low-ppm-level triethylamine sensor assembled with Au decahedrons-decorated porous α-Fe_2O_3 nanorods directly grown on flat substrate. *Sens. Actuators, B* 268: 170–181. https://doi.org/10.1016/j.snb.2018.04.096.

45 Park, S., Kim, H., Jin, C. et al. (2012). Enhanced CO gas sensing properties of Pt-functionalized WO_3 nanorods. *Thermochim. Acta* 542: 69–73. https://doi.org/10.1016/j.tca.2011.12.002.

46 Xiang, Q., Meng, G.F., Zhao, H.B. et al. (2010). Au nanoparticle modified WO_3 nanorods with their enhanced properties for photocatalysis and gas sensing. *J. Phys. Chem. C* 114: 2049–2055. https://doi.org/10.1021/jp909742d.

47 Li, Z., Li, H., Wu, Z. et al. (2019). Advances in designs and mechanisms of semiconducting metal oxide nanostructures for high-precision gas sensors operated at room temperature. *Mater. Horiz.* 6: 470–506. https://doi.org/10.1039/C8MH01365A.

48 Trung, D.D., Hoa, N.D., Van Tong, P. et al. (2014). Effective decoration of Pd nanoparticles on the surface of SnO_2 nanowires for enhancement of CO gas-sensing performance. *J. Hazard. Mater.* 265: 124–132. https://doi.org/10.1016/j.jhazmat.2013.11.054.

49 Fan, L., Xu, N., Chen, H. et al. (2021). A millisecond response and microwatt power-consumption gas sensor: realization based on cross-stacked individual Pt-coated WO_3 nanorods. *Sens. Actuators, B* 346: 130545. https://doi.org/10.1016/j.snb.2021.130545.

50 Kolmakov, A., Klenov, D.O., Lilach, Y. et al. (2005). Enhanced gas sensing by individual SnO_2 nanowires and nanobelts functionalized with Pd catalyst particles. *Nano Lett.* 5: 667–673. https://doi.org/10.1021/nl050082v.

51 Singh, N., Gupta, R.K., and Lee, P.S. (2011). Gold-nanoparticle-functionalized In_2O_3 nanowires as CO gas sensors with a significant enhancement in response. *ACS Appl. Mater. Interfaces* 3: 2246–2252. https://doi.org/10.1021/am101259t.

52 Yang, D.-J., Kamienchick, I., Youn, D.Y. et al. (2010). Ultrasensitive and highly selective gas sensors based on electrospun SnO_2 nanofibers modified by Pd loading. *Adv. Funct. Mater.* 20: 4258–4264. https://doi.org/10.1002/adfm.201001251.

53 Lai, H.-Y. and Chen, C.-H. (2012). Highly sensitive room-temperature CO gas sensors: Pt and Pd nanoparticle-decorated In_2O_3 flower-like nanobundles. *J. Mater. Chem.* 22: 13204. https://doi.org/10.1039/c2jm31180a.

54 Yan, S., Li, Z., Li, H. et al. (2018). Ultra-sensitive room-temperature H_2S sensor using Ag–In_2O_3 nanorod composites. *J. Mater. Sci.* 53: 16331–16344. https://doi.org/10.1007/s10853-018-2789-z.

55 Chen, X., Shen, Y., Zhou, P. et al. (2019). NO_2 sensing properties of one-pot-synthesized ZnO nanowires with Pd functionalization. *Sens. Actuators, B* 280: 151–161. https://doi.org/10.1016/j.snb.2018.10.063.

56 Shingange, K., Tshabalala, Z.P., Ntwaeaborwa, O.M. et al. (2016). Highly selective NH_3 gas sensor based on Au loaded ZnO nanostructures prepared using

microwave-assisted method. *J. Colloid Interface Sci.* 479: 127–138. https://doi.org/10.1016/j.jcis.2016.06.046.

57 Lee, J.M., Park, J., Kim, S. et al. (2010). Ultra-sensitive hydrogen gas sensors based on Pd-decorated tin dioxide nanostructures: room temperature operating sensors. *Int. J. Hydrogen Energy* 35: 12568–12573. https://doi.org/10.1016/j.ijhydene.2010.08.026.

58 Kim, S.S., Park, J.Y., Choi, S.-W. et al. (2010). Significant enhancement of the sensing characteristics of In_2O_3 nanowires by functionalization with Pt nanoparticles. *Nanotechnology* 21: 415502. https://doi.org/10.1088/0957-4484/21/41/415502.

59 Choi, S.-W. and Kim, S.S. (2012). Room temperature CO sensing of selectively grown networked ZnO nanowires by Pd nanodot functionalization. *Sens. Actuators, B* 168: 8–13. https://doi.org/10.1016/j.snb.2011.12.100.

60 Tu, Y., Kyle, C., Luo, H. et al. (2020). Ammonia gas sensor response of a vertical zinc oxide nanorod-gold junction diode at room temperature. *ACS Sens.* 5: 3568–3575. https://doi.org/10.1021/acssensors.0c01769.

61 Choi, S.-W., Katoch, A., Sun, G.-J., and Kim, S.S. (2013). Bimetallic Pd/Pt nanoparticle-functionalized SnO_2 nanowires for fast response and recovery to NO_2. *Sens. Actuators, B* 181: 446–453. https://doi.org/10.1016/j.snb.2013.02.007.

62 Hassan, K. and Chung, G.-S. (2017). Catalytically activated quantum-size Pt/Pd bimetallic core–shell nanoparticles decorated on ZnO nanorod clusters for accelerated hydrogen gas detection. *Sens. Actuators, B* 239: 824–833. https://doi.org/10.1016/j.snb.2016.08.084.

63 Ren, S. and Liu, W. (2016). One-step photochemical deposition of PdAu alloyed nanoparticles on TiO_2 nanowires for ultra-sensitive H_2 detection. *J. Mater. Chem. A* 4: 2236–2245. https://doi.org/10.1039/C5TA06917C.

64 Li, G., Ma, Z., Hu, Q. et al. (2021). PdPt nanoparticle-functionalized α-Fe_2O_3 hollow nanorods for triethylamine sensing. *ACS Appl. Nano Mater.* 4: 10921–10930. https://doi.org/10.1021/acsanm.1c02377.

65 Vahl, A., Lupan, O., Santos-Carballal, D. et al. (2020). Surface functionalization of ZnO:Ag columnar thin films with AgAu and AgPt bimetallic alloy nanoparticles as an efficient pathway for highly sensitive gas discrimination and early hazard detection in batteries. *J. Mater. Chem. A* 8: 16246–16264. https://doi.org/10.1039/D0TA03224G.

66 Zhu, L., Hong, M., and Ho, G.W. (2015). Hierarchical assembly of SnO_2/ZnO nanostructures for enhanced photocatalytic performance. *Sci. Rep.* 5: 11609. https://doi.org/10.1038/srep11609.

67 Kaneti, Y.V., Zakaria, Q.M.D., Zhang, Z. et al. (2014). Solvothermal synthesis of ZnO-decorated α-Fe_2O_3 nanorods with highly enhanced gas-sensing performance toward *n*-butanol. *J. Mater. Chem. A* 2: 13283–13292. https://doi.org/10.1039/C4TA01837K.

68 Xue, X., Xing, L., Chen, Y. et al. (2008). Synthesis and H_2S sensing properties of $CuO-SnO_2$ core/shell PN-junction nanorods. *J. Phys. Chem. C* 112: 12157–12160. https://doi.org/10.1021/jp8037818.

69 Vuong, N.M., Chinh, N.D., Huy, B.T., and Lee, Y.-I. (2016). CuO-decorated ZnO hierarchical nanostructures as efficient and established sensing materials for H_2S gas sensors. *Sci. Rep.* 6: 26736. https://doi.org/10.1038/srep26736.

70 Chakraborty, M., Roy, D., Biswas, A. et al. (2016). Structural, optical and photo-electrochemical properties of hydrothermally grown ZnO nanorods arrays covered with α-Fe$_2$O$_3$ nanoparticles. *RSC Adv.* 6: 75063–75072. https://doi.org/10.1039/C6RA15752A.

71 Gandha, K., Mohapatra, J., Hossain, M.K. et al. (2016). Mesoporous iron oxide nanowires: synthesis, magnetic and photocatalytic properties. *RSC Adv.* 6: 90537–90546. https://doi.org/10.1039/C6RA18530D.

72 Mao, Y., Cheng, Y., Wang, J. et al. (2016). Amorphous NiO electrocatalyst overcoated ZnO nanorod photoanodes for enhanced photoelectrochemical performance. *New J. Chem.* 40: 107–112. https://doi.org/10.1039/C5NJ01815C.

73 Wei, C., Xu, J., Shi, S. et al. (2019). Self-powered visible-blind UV photodetectors based on p-NiO nanoflakes/n-ZnO nanorod arrays with an MgO interfacial layer. *J. Mater. Chem. C* 7: 9369–9379. https://doi.org/10.1039/C9TC01179J.

74 Liang, Y.Q., Cui, Z.D., Zhu, S.L. et al. (2013). Design of a highly sensitive ethanol sensor using a nano-coaxial p-Co$_3$O$_4$/n-TiO$_2$ heterojunction synthesized at low temperature. *Nanoscale* 5: 10916. https://doi.org/10.1039/c3nr03616b.

75 Xu, Y., Ding, Y., Zhang, L., and Zhang, X. (2021). Highly sensitive enzyme-free glucose sensor based on CuO–NiO nanocomposites by electrospinning. *Compos. Commun.* 25: 100687. https://doi.org/10.1016/j.coco.2021.100687.

76 Li, D., Zhang, Y., Liu, D. et al. (2016). Hierarchical core/shell ZnO/NiO nanoheterojunctions synthesized by ultrasonic spray pyrolysis and their gas-sensing performance. *CrystEngComm* 18: 8101–8107. https://doi.org/10.1039/C6CE01621A.

77 Khoang, N.D., Trung, D.D., Van Duy, N. et al. (2012). Design of SnO$_2$/ZnO hierarchical nanostructures for enhanced ethanol gas-sensing performance. *Sens. Actuators, B* 174: 594–601. https://doi.org/10.1016/j.snb.2012.07.118.

78 Lou, Z., Li, F., Deng, J. et al. (2013). Branch-like hierarchical heterostructure (α-Fe$_2$O$_3$/TiO$_2$): a novel sensing material for trimethylamine gas sensor. *ACS Appl. Mater. Interfaces* 5: 12310–12316. https://doi.org/10.1021/am402532v.

79 Wang, L., Kang, Y., Wang, Y. et al. (2012). CuO nanoparticle decorated ZnO nanorod sensor for low-temperature H$_2$S detection. *Mater. Sci. Eng., C* 32: 2079–2085. https://doi.org/10.1016/j.msec.2012.05.042.

80 Kim, H.J. and Lee, J.H. (2014). Highly sensitive and selective gas sensors using p-type oxide semiconductors: overview. *Sens. Actuators, B* https://doi.org/10.1016/j.snb.2013.11.005.

81 Nakate, U.T., Yu, Y.T., and Park, S. (2021). High performance acetaldehyde gas sensor based on p-n heterojunction interface of NiO nanosheets and WO$_3$ nanorods. *Sens. Actuators, B* 344: 130264. https://doi.org/10.1016/j.snb.2021.130264.

82 Kim, J.-H., Lee, J.-H., Mirzaei, A. et al. (2017). Optimization and gas sensing mechanism of n-SnO$_2$-p-Co$_3$O$_4$ composite nanofibers. *Sens. Actuators, B* 248: 500–511. https://doi.org/10.1016/j.snb.2017.04.029.

83 Suh, J.M., Sohn, W., Shim, Y.-S. et al. (2018). p–p Heterojunction of nickel oxide-decorated cobalt oxide nanorods for enhanced sensitivity and selectivity toward volatile organic compounds. *ACS Appl. Mater. Interfaces* 10: 1050–1058. https://doi.org/10.1021/acsami.7b14545.

84 Ju, D.-X., Xu, H.-Y., Qiu, Z.-W. et al. (2015). Near room temperature, fast-response, and highly sensitive triethylamine sensor assembled with Au-loaded ZnO/SnO$_2$ core–shell nanorods on flat alumina substrates. *ACS Appl. Mater. Interfaces* 7: 19163–19171. https://doi.org/10.1021/acsami.5b04904.

85 Zhang, B., Huang, Y., Vinluan, R. et al. (2020). Enhancing ZnO nanowire gas sensors using Au/Fe$_2$O$_3$ hybrid nanoparticle decoration. *Nanotechnology* 31: 325505. https://doi.org/10.1088/1361-6528/ab89cf.

86 Wu, X., Wang, H., Wang, J. et al. (2022). VOCs gas sensor based on MOFs derived porous Au@Cr$_2$O$_3$-In$_2$O$_3$ nanorods for breath analysis. *Colloids Surf., A* 632: 127752. https://doi.org/10.1016/j.colsurfa.2021.127752.

87 Nylabder, C., Armgrath, M., and Lundstrom, I. (1983). An ammonia detector based on a conducting polymer. In: *Proceedings of the International Meeting on Chemical Sensors*; Fukuoka, Japan, 203–207.

88 Kaushik, A., Kumar, R., Arya, S.K. et al. (2015). Organic–inorganic hybrid nanocomposite-based gas sensors for environmental monitoring. *Chem. Rev.* 115: 4571–4606. https://doi.org/10.1021/cr400659h.

89 Yan, Y., Yang, G., Xu, J.-L. et al. (2020). Conducting polymer-inorganic nanocomposite-based gas sensors: a review. *Sci. Technol. Adv. Mater.* 21: 768–786. https://doi.org/10.1080/14686996.2020.1820845.

90 Jia, A., Liu, B., Liu, H. et al. (2020). Interface design of SnO$_2$@PANI nanotube with enhanced sensing performance for ammonia detection at room temperature. *Front. Chem.* 8: https://doi.org/10.3389/fchem.2020.00383.

91 Liu, C., Tai, H., Zhang, P. et al. (2018). A high-performance flexible gas sensor based on self-assembled PANI-CeO$_2$ nanocomposite thin film for trace-level NH$_3$ detection at room temperature. *Sens. Actuators, B* 261: 587–597. https://doi.org/10.1016/j.snb.2017.12.022.

92 Li, Y., Zhao, H., Ban, H., and Yang, M. (2017). Composites of Fe$_2$O$_3$ nanosheets with polyaniline: preparation, gas sensing properties and sensing mechanism. *Sens. Actuators, B* 245: 34–43. https://doi.org/10.1016/j.snb.2017.01.103.

93 Li, S., Lin, P., Zhao, L. et al. (2018). The room temperature gas sensor based on Polyaniline@flower-like WO$_3$ nanocomposites and flexible PET substrate for NH$_3$ detection. *Sens. Actuators, B* 259: 505–513. https://doi.org/10.1016/j.snb.2017.11.081.

94 Li, Y., Ban, H., and Yang, M. (2016). Highly sensitive NH$_3$ gas sensors based on novel polypyrrole-coated SnO$_2$ nanosheet nanocomposites. *Sens. Actuators, B* 224: 449–457. https://doi.org/10.1016/j.snb.2015.10.078.

95 Bandgar, D.K., Navale, S.T., Naushad, M. et al. (2015). Ultra-sensitive polyaniline–iron oxide nanocomposite room temperature flexible ammonia sensor. *RSC Adv.* 5: 68964–68971. https://doi.org/10.1039/C5RA11512D.

96 Shahmoradi, A., Hosseini, A., Akbarinejad, A., and Alizadeh, N. (2021). Noninvasive detection of ammonia in the breath of hemodialysis patients using a highly sensitive ammonia sensor based on a polypyrrole/sulfonated graphene nanocomposite. *Anal. Chem.* 93: 6706–6714. https://doi.org/10.1021/acs.analchem.1c00171.

97 Dhawale, D.S., Salunkhe, R.R., Patil, U.M. et al. (2008). Room temperature liquefied petroleum gas (LPG) sensor based on p-polyaniline/n-TiO$_2$ heterojunction. *Sens. Actuators, B* 134: 988–992. https://doi.org/10.1016/j.snb.2008.07.003.

98 Zhang, J., Wang, S., Xu, M. et al. (2009). Polypyrrole-coated SnO_2 hollow spheres and their application for ammonia sensor. *J. Phys. Chem. C* 113: 1662–1665. https://doi.org/10.1021/jp8096633.

99 Hosono, K., Matsubara, I., Murayama, N. et al. (2005). Synthesis of polypyrrole/ MoO_3 hybrid thin films and their volatile organic compound gas-sensing properties. *Chem. Mater.* 17: 349–354. https://doi.org/10.1021/cm0492641.

100 Yenorkar, S.M., Zade, R.N., Mude, B.M. et al. (2021). Polymer-metal oxide composite ($PPy–MoO_3$) for ammonia and ethanol gas sensor. *Macromol. Symp.* 400: 2100049. https://doi.org/10.1002/masy.202100049.

101 Geng, L. (2009). Gas sensitivity of polyaniline/SnO_2 hybrids to volatile organic compounds. *Trans. Nonferrous Met. Soc. China* 19: s678–s683. https://doi.org/10.1016/S1003-6326(10)60131-8.

102 Arora, R., Mandal, U., Sharma, P., and Srivastav, A. (2017). Nano composite film based on conducting polymer, SnO_2 and PVA. *Mater. Today Proc.* 4: 2733–2738. https://doi.org/10.1016/j.matpr.2017.02.150.

103 Liu, A., Lv, S., Jiang, L. et al. (2021). The gas sensor utilizing polyaniline/MoS_2 nanosheets/SnO_2 nanotubes for the room temperature detection of ammonia. *Sens. Actuators, B* 332: 129444. https://doi.org/10.1016/j.snb.2021.129444.

104 Ram, M.K., Yavuz, O., and Aldissi, M. (2005). NO_2 gas sensing based on ordered ultrathin films of conducting polymer and its nanocomposite. *Synth. Met.* 151: 77–84. https://doi.org/10.1016/j.synthmet.2005.03.021.

105 Zhu, S., Wei, W., Chen, X. et al. (2012). Hybrid structure of polyaniline/ZnO nanograss and its application in dye-sensitized solar cell with performance improvement. *J. Solid State Chem.* 190: 174–179. https://doi.org/10.1016/j.jssc.2012.02.028.

106 Jun, J., Lee, J.S., Shin, D.H. et al. (2017). Fabrication of a one-dimensional tube-in-tube polypyrrole/tin oxide structure for highly sensitive DMMP sensor applications. *J. Mater. Chem. A* 5: 17335–17340. https://doi.org/10.1039/C7TA02725G.

107 Nimkar, S.H., Agrawal, S.P., and Kondawar, S.B. (2015). Fabrication of electrospun nanofibers of titanium dioxide intercalated polyaniline nanocomposites for CO_2 gas sensor. *Procedia Mater. Sci.* 10: 572–579. https://doi.org/10.1016/j.mspro.2015.06.008.

108 Ebbesen, T.W. and Ajayan, P.M. (1992). Large-scale synthesis of carbon nanotubes. *Nature* 358: 220–222. https://doi.org/10.1038/358220a0.

109 Oberlin, A., Endo, M., and Koyama, T. (1976). Filamentous growth of carbon through benzene decomposition. *J. Cryst. Growth* 32: 335–349. https://doi.org/10.1016/0022-0248(76)90115-9.

110 Iijima, S. (1991). Helical microtubules of graphitic carbon. *Nature* 354: 56–58. https://doi.org/10.1038/354056a0.

111 Basheer, B.V., George, J.J., Siengchin, S., and Parameswaranpillai, J. (2020). Polymer grafted carbon nanotubes—synthesis, properties, and applications: a

review. *Nano-Struct. Nano-Objects* 22: 100429. https://doi.org/10.1016/j. nanoso.2020.100429.

112 Ma, P.-C., Siddiqui, N.A., Marom, G., and Kim, J.-K. (2010). Dispersion and functionalization of carbon nanotubes for polymer-based nanocomposites: a review. *Compos. Part A Appl. Sci. Manuf.* 41: 1345–1367. https://doi.org/10.1016/j. compositesa.2010.07.003.

113 Banerjee, J. and Dutta, K. (2019). Melt-mixed carbon nanotubes/polymer nanocomposites. *Polym. Compos.* 40: 4473–4488. https://doi.org/10.1002/pc.25334.

114 Spitalsky, Z., Tasis, D., Papagelis, K., and Galiotis, C. (2010). Carbon nanotube–polymer composites: chemistry, processing, mechanical and electrical properties. *Prog. Polym. Sci.* 35: 357–401. https://doi.org/10.1016/j.progpolymsci.2009.09.003.

115 Ajayan, P.M., Stephan, O., Colliex, C., and Trauth, D. Aligned carbon nanotube arrays formed by cutting a polymer resin–nanotube composite. *Science (80-.)* 265 (1994): 1212–1214. https://doi.org/10.1126/science.265.5176.1212.

116 Chen, J., Liu, B., Gao, X., and Xu, D. (2018). A review of the interfacial characteristics of polymer nanocomposites containing carbon nanotubes. *RSC Adv.* 8: 28048–28085. https://doi.org/10.1039/c8ra04205e.

117 Salavagione, H.J., Díez-Pascual, A.M., Lázaro, E. et al. (2014). Chemical sensors based on polymer composites with carbon nanotubes and graphene: the role of the polymer. *J. Mater. Chem. A* 2: 14289–14328. https://doi.org/10.1039/c4ta02159b.

118 Norizan, M.N., Moklis, M.H., Ngah Demon, S.Z. et al. (2020). Carbon nanotubes: functionalisation and their application in chemical sensors. *RSC Adv.* 10: 43704–43732. https://doi.org/10.1039/D0RA09438B.

119 Kong, J., Franklin, N.R., Zhou, C. et al. Nanotube molecular wires as chemical sensors. *Science (80-.)* 287 (2000): 622–625. https://doi.org/10.1126/science.287.5453.622.

120 Han, T., Nag, A., Chandra Mukhopadhyay, S., and Xu, Y. (2019). Carbon nanotubes and its gas-sensing applications: a review. *Sens. Actuators, A* 291: 107–143. https://doi.org/10.1016/j.sna.2019.03.053.

121 Kumar, D., Kumar, I., Chaturvedi, P. et al. (2016). Study of simultaneous reversible and irreversible adsorption on single-walled carbon nanotube gas sensor. *Mater. Chem. Phys.* 177: 276–282. https://doi.org/10.1016/j.matchemphys.2016.04.028.

122 Dag, S., Ozturk, Y., Ciraci, S., and Yildirim, T. (2005). Adsorption and dissociation of hydrogen molecules on bare and functionalized carbon nanotubes. *Phys. Rev. B – Condens. Matter Mater. Phys.* 72: 1–8. https://doi.org/10.1103/PhysRevB.72.155404.

123 Schedin, F., Geim, A.K., Morozov, S.V. et al. (2007). Detection of individual gas molecules adsorbed on graphene. *Nat. Mater.* 6: 652–655. https://doi.org/10.1038/nmat1967.

124 Dan, Y., Lu, Y., Kybert, N.J. et al. (2009). Intrinsic response of graphene vapor sensors. *Nano Lett.* 9: 1472–1475. https://doi.org/10.1021/nl8033637.

125 Kwon, Y.J., Mirzaei, A., Kang, S.Y. et al. (2017). Synthesis, characterization and gas sensing properties of ZnO-decorated MWCNTs. *Appl. Surf. Sci.* 413: 242–252. https://doi.org/10.1016/j.apsusc.2017.03.290.

126 Van Hieu, N., Thuy, L.T.B., and Chien, N.D. (2008). Highly sensitive thin film NH_3 gas sensor operating at room temperature based on SnO_2/MWCNTs composite. *Sens. Actuators, B* 129: 888–895. https://doi.org/10.1016/j.snb.2007.09.088.

127 Zanolli, Z., Leghrib, R., Felten, A. et al. (2011). Gas sensing with Au-decorated carbon nanotubes. *ACS Nano.* 5: 4592–4599. https://doi.org/10.1021/nn200294h.

128 Chen, N., Li, X., Wang, X. et al. (2013). Enhanced room temperature sensing of Co_3O_4-intercalated reduced graphene oxide based gas sensors. *Sens. Actuators, B* 188: 902–908. https://doi.org/10.1016/j.snb.2013.08.004.

129 Van Hieu, N., Dung, N.Q., Tam, P.D. et al. (2009). Thin film polypyrrole/SWCNTs nanocomposites-based NH_3 sensor operated at room temperature. *Sens. Actuators, B* 140: 500–507. https://doi.org/10.1016/j.snb.2009.04.061.

130 Du, H.Y., Wang, J., Yao, P.J. et al. (2013). Preparation of modified MWCNTs-doped PANI nanorods by oxygen plasma and their ammonia-sensing properties. *J. Mater. Sci.* 48: 3597–3604. https://doi.org/10.1007/s10853-013-7157-4.

131 Kar, P. and Choudhury, A. (2013). Carboxylic acid functionalized multi-walled carbon nanotube doped polyaniline for chloroform sensors. *Sens. Actuators, B* 183: 25–33. https://doi.org/10.1016/j.snb.2013.03.093.

132 Abdulla, S., Mathew, T.L., and Pullithadathil, B. (2015). Highly sensitive, room temperature gas sensor based on polyaniline-multiwalled carbon nanotubes (PANI/MWCNTs) nanocomposite for trace-level ammonia detection. *Sens. Actuators, B* 221: 1523–1534. https://doi.org/10.1016/j.snb.2015.08.002.

133 Xue, L., Wang, W., Guo, Y. et al. (2017). Flexible polyaniline/carbon nanotube nanocomposite film-based electronic gas sensors. *Sens. Actuators, B* 244: 47–53. https://doi.org/10.1016/j.snb.2016.12.064.

134 Eising, M., Cava, C.E., Salvatierra, R.V. et al. (2017). Doping effect on self-assembled films of polyaniline and carbon nanotube applied as ammonia gas sensor. *Sens. Actuators, B* 245: 25–33. https://doi.org/10.1016/j.snb.2017.01.132.

135 Zhang, W., Cao, S., Wu, Z. et al. (2019). High-performance gas sensor of polyaniline/carbon nanotube composites promoted by Interface Engineering. *Sensors* 20.

136 Bachhav, S.G. and Patil, D.R. (2015). Study of polypyrrole-coated MWCNT nanocomposites for ammonia sensing at room temperature. *J. Mater. Sci. Chem. Eng.* 03: 30–44. https://doi.org/10.4236/msce.2015.310005.

137 Hamouma, O., Kaur, N., Oukil, D. et al. (2019). Paper strips coated with polypyrrole-wrapped carbon nanotube composites for chemi-resistive gas sensing. *Synth. Met.* 258: 116223. https://doi.org/10.1016/j.synthmet.2019.116223.

138 An, K.H., Jeong, S.Y., Hwang, H.R., and Lee, Y.H. (2004). Enhanced sensitivity of a gas sensor incorporating single-walled carbon nanotube-polypyrrole nanocomposites. *Adv. Mater.* 16: 1005–1009. https://doi.org/10.1002/adma.200306176.

139 Zhang, Y., Bunes, B.R., Wu, N. et al. (2018). Sensing methamphetamine with chemiresistive sensors based on polythiophene-blended single-walled carbon

nanotubes. *Sens. Actuators, B* 255: 1814–1818. https://doi.org/10.1016/j. snb.2017.08.201.

140 Husain, A., Ahmad, S., Shariq, M.U., and Khan, M.M.A. (2020). Ultra-sensitive, highly selective and completely reversible ammonia sensor based on polythiophene/SWCNT nanocomposite. *Materialia* 10: 100704. https://doi. org/10.1016/j.mtla.2020.100704.

141 Husain, A., Ahmad, S., and Mohammad, F. (2020). Electrical conductivity and ammonia sensing studies on polythiophene/MWCNTs nanocomposites. *Materialia* 14: https://doi.org/10.1016/j.mtla.2020.100868.

142 Philip, B., Abraham, J.K., Chandrasekhar, A., and Varadan, V.K. (2003). Carbon nanotube/PMMA composite thin films for gas-sensing applications. *Smart Mater. Struct.* 12: 935–939. https://doi.org/10.1088/0964-1726/12/6/010.

143 Park, S.J., Kwon, O.S., and Jang, J. (2013). A high-performance hydrogen gas sensor using ultrathin polypyrrole-coated CNT nanohybrids. *Chem. Commun.* 49: 4673. https://doi.org/10.1039/c3cc41020j.

Z

3

Room-Temperature Gas-Sensing Properties of Metal Oxide Nanowire/Graphene Hybrid Structures

Pooja Devi[1], Sandeep Sharma[2], and Rajan Saini[3]

[1] *Department of Physics, Maharaja Ranjit Singh Punjab Technical University, Bathinda, Punjab, 151001, India*
[2] *Department of Physics, Guru Nanak Dev University, Amritsar, Punjab, 143005, India*
[3] *Department of Physics, Akal University, Talwandi Sabo, Punjab, 151302, India*

3.1 Introduction

Graphene, a monolayer of sp^2-hybridized carbon atoms assembled in a honeycomb lattice with exceptional structural, mechanical, and electrical properties, was discovered by Geim and Novoselov in 2004 for which they shared the Noble Prize in 2010 [1, 2]. Soon after its discovery, in 2007, Schedin et al. [3] demonstrated the application of pristine graphene toward the sensing of a single NO_2 molecule, and it has also been reported that pristine graphene responds to NH_3, H_2O, and CO as well. After this breakthrough work, graphene-based gas sensors have been widely explored for the detection of various oxidizing/reducing gases as well as volatile organic compounds (VOCs), and to date, graphene-based gas sensors have been the center of attraction for academic as well as research purposes [4–6]. Some of the prominent reasons for graphene being a promising candidate for gas-sensing applications are (i) graphene is a single-atom-thick two-dimensional conjugate layer in which all the atoms behave as surface atoms for the test gas molecules, providing the largest surface-to-area ratio (theoretical specific surface area $\sim 2630\,m^2/g$), (ii) weak van der Waals interactions between graphene surface and gas molecules resulting in reversible sensing characteristics, (iii) due to unique electronic band structure, the charge carriers behave like relativistic massless particles near the Dirac point, thus exhibiting high mobility $2\times10^6\,cm^2/Vs$, and combined with regular honeycomb conjugate structure provides low electrical noise to the sensor signal, and (iv) flexible nature with good mechanical strength (Young's modulus $\sim0.05\,TPa$) [4–6]. Apart from these, the derivative of graphene, reduced graphene

oxide (RGO), could be produced at a large scale using various techniques and has been widely used for the detection of various toxic gases.

3.2 Synthesis of Graphene and Graphene Oxide

The synthesis methods of graphene can be broadly divided into two categories: the top-down approach and the bottom-up approach. The former pertains to breaking apart the stacked layers of graphite to produce single graphene layers, whereas the latter includes the synthesis of graphene from carbon sources. The top-down approach normally suffers the limitation of low yield and re-agglomeration of the exfoliated sheets, whereas the bottom-up approach could be used to produce large-area graphene sheets. The top-down approach includes methods like mechanical exfoliation, electrochemical exfoliation, graphite intercalation, nanotube slicing, pyrolysis, sonication, and ball milling [7]. On the other hand, the bottom-up approach includes the techniques like chemical vapor deposition (CVD), epitaxial growth on silicon carbide (SiC), and growth from metal–carbon melts. Some of these techniques are discussed briefly as follows.

3.2.1 Mechanical Exfoliation

This is one of the oldest and most widely used methods to synthesize graphene from graphite. In the year 2004, Geim and Novoselov from Manchester University employed the scotch tape method to repeatedly peel off mono-, bi-, and few-layered graphene from graphite [1]. The scotch tape holding optically transparent flakes was then dissolved in acetone, and the flakes containing both multi-layer and monolayer graphene were obtained, so were sedimented on a Si wafer and investigated for the structural analysis. The problem with this method is its low yield, so although it has been widely used for research purposes, it was not used for commercial purposes [8].

3.2.2 Electrochemical Method

In this method, graphene is obtained by electrochemical exfoliation of graphite using an electrolyte mixture of H_2SO_4 and KOH. The graphite flake and platinum are employed as anode and cathode materials. H_2SO_4 exfoliates the graphite by intercalating sulfate ions into the layers, while KOH controls the extent of oxidation in the process. Finally, few-layered graphene is obtained by centrifugation of dissolved flakes at the end of the process [8].

3.2.3 Sonication

This is also one of the traditional methods to produce high-quality few-layered graphene in which ultrasonic energy is used to exfoliate the layers by injecting thermal shock into the bulk graphite which is further assisted by intercalating different

precursors into the layers. Such exfoliation has been achieved by intercalation of lithium salts to produced graphite intercalation compounds. The yield of this method depends on the type of solvents used in the sonication of lithium salt inter-calated graphite. The large energy required for sonication and removal of impurities in this process poses limits on the commercial application of this process.

Apart from this, the exfoliation of natural graphite flakes by sonicating in more than 40 different solvents has also been reported by several research groups. Based on the different parameters and experimental investigations, *N*-methyl-2-pyrrolidone (NMP) is reported to be the best choice with a higher concentration of monolayer graphene dispersed in it, while cyclopentanone pertains to the highest percentage of few- to mono-layer graphene dispersion. The problem with this method is that the solvents pertaining to higher graphene concentrations (for example, NMP) exhibit a higher boiling point ~202 °C which makes it problematic to remove the solvent, and the film samples could retain the NMP residue in them and affects the film proper-ties. Keeping it in consideration, aqueous surfactant solutions have also been used where the surfactants reduce the re-aggregation of graphene. Besides this, increas-ing sonication time is also found helpful in increasing the graphene concentration. The prolonged sonication time increases the graphene dispersibility but also could lead to higher defect concentration [7, 8].

3.2.4 Exfoliation of Graphite Oxide

Graphene has also been synthesized by exfoliation and reduction of graphite oxide using concentrated oxidizing acids. In this category, Hummer's method is widely used for the production of RGO. The exfoliation of graphite oxide produces gra-phene oxide which is further reduced to obtain graphene. The resulting product is known as RGO or functionalized graphene. However, reduction of graphene oxide tends to aggregate the graphene oxide sheets, so the complete reduction of graphene oxide has not been attained so far. The graphene oxide is reported to be an insula-tor-type material, and the reduction of graphene oxide is an important step to tailor its electrical properties, making it suitable for various device applications [7, 8].

3.2.5 Unzipping Carbon Nanotubes

Few-layered graphene has also been obtained by unzipping the single- and multi-walled carbon nanotubes by chemical (using strong oxidizing reagents) and physi-cal (for example laser irradiation) techniques. Such unzipping generally produces graphene nanoribbons with the width depending on the diameter of carbon nano-tubes used. The physical and optoelectronic properties of these graphene nanorib-bons are further governed by their width and edge type (armchair/zigzag) [7, 8].

3.2.6 Epitaxial Growth on Silicon Carbide (SiC)

The formation of graphene over SiC surface is obtained by the sublimation of Si at high temperature (~1100 °C) under high vacuum conditions or pulsed electron

irradiation. The size, thickness, mobility, and charge carrier density of so-obtained graphene are governed by the surface of the SiC wafer. Both hexagonal and cubic phase Sic wafers have been used for this purpose. The structure of graphene exhibits differences pertaining to the Si-rich and carbon-rich phases of hexagonal SiC wafer where the growth of graphene in Si-rich phase is in single orientation, while in case of carbon-rich phase, the graphene exhibits rotational stacking. However, the high cost of SiC poses a limit on the commercialization of this method [7, 8].

3.2.7 Chemical Vapor Deposition

CVD has been widely used to deposit graphene thin films onto the metallic substrate by the high-temperature pyrolysis of carbon-based gases. The graphene growth occurs by two methods: surface-catalyzed and segregation methods. In the surface-catalyzed method, the dissociation of carbon-based gases and subsequently graphene growth occurs at the surface of the metal. In the segregation method, a carbon source (for example graphite powder) is kept in contact with a transition metal and heated at such a high temperature to melt the metal. The carbon starts dissolving into the molten metal, and the temperature is lowered subsequently to reduce the solubility of carbon, resulting in excessive carbon precipitation. The precipitate can be ripped off to produce few- to mono-layered graphene. Many transition metals and alloys have been used for this purpose. Since the interaction of graphene at the metal interface is different for different metals, the quality, yield, and physical properties of the so-produced graphene depend on the type of metal/alloy and the experimental conditions. In this regard, copper and nickel appeared to be promising candidates to produce graphene films with a diagonal dimension of ~30 in. [7, 8].

3.3 Graphene/Metal Oxide Nanowires Hybrid-Based Sensors

In general, the mechanism of graphene-based sensors to detect test gases is based on the interaction of the test gas molecules with the sensing layer which results in the change in conductance/resistance of the sensor. Graphene is a p-type semiconductor that exhibits different sensor response toward the various oxidizing and reducing test gases. For example, when a graphene sensor is exposed to oxidizing gas like Cl_2, the concentrations of holes in the sensing layer increases which increases sensor resistance. On the other hand, when a graphene-based sensor is exposed to a reducing gas like NH_3, the number of holes and hence the sensor conductance decreases. This change in the sensor conductance (or resistance) appears as the output signal of the sensing device.

Yavari et al. [9] have demonstrated the simultaneous sensing of NO_2 and NH_3 at parts-per-billion (ppb) level using CVD graphene with the detection limits as 100 and 500 ppb for NO_2 and NH_3, respectively. However, these sensors need to be heated at 200 °C for a full recovery. Some other researchers predicted the insensitivity of

pristine graphene toward NH_3 at room temperature [10]. These studies suggest the need for the functionalization of graphene-based sensors for improved sensing characteristics. The sensitivity, selectivity, and response kinetics of graphene-based sensors can be tailored by functionalizing the sensing layer with a different type of materials (organic, noble metal nanoparticles, metal oxides, etc.). The purpose of functionalization is to increase the effective surface area and to catalyze the reaction between the gas molecules and graphene-based material. For example, Li et al. [11] demonstrated the highly sensitive and reproducible NO gas-sensing characteristics of graphene-based sensors fabricated by alternating current dielectrophoresis (ac-DEP) of bulk Pd-RGO nanosheets with CVD-grown graphene electrodes with a detection limit up to 2 ppb. The improved sensing kinetics of these sensors have been attributed to work function matching between Pd-RGO nanosheets and the CVD-grown graphene contacts. These studies indicate that functionalization of graphene/RGO results to enhance the sensing kinetics of the graphene-based sensor. In the following subsections, we shall discuss some gas sensors based on graphene functionalized with metal oxide nanowires (NWs).

3.3.1 ZnO Nanowires Reduced Graphene Oxide-Based Hybrids for NH₃ Detection

Right after the discovery of graphene [1], owing to its layered structure, exceptionally large electronic mobility, lower spin–orbit coupling, various applications including in the areas of nanoelectronics, spintronics, and gas sensing have emerged. Exceptionally large electronic mobility coupled with layered structure giving rise to a higher specific surface area and the fact that absorption and desorption of the gas molecules strongly affect the electronic properties, and graphene have been considered as a promising candidate for manufacturing chemiresistor-type gas sensors. Various studies have shown that graphene-based sensors could be used for room-temperature detection of NH_3. From a sensing point of view, it is not only the higher response a device must possess but a few other conditions, for instance, selectivity and faster response–recovery transients are also among the prime concerns. The graphene-based sensors have shown very poor sensitivity and sluggish recovery after exposure to NH_3 at room temperature. Chemically derived graphene, also known as RGO, is considered an excellent building block for making hybrid functional materials. Various strategies, for instance, grain size reduction, elemental doping, and making composites with dissimilar materials but having complementary properties have been used for improving the sensing performance of two-dimensional materials. The synergistic effects arising from composite formation give rise to significant enhancement in the sensing properties of the devices. For making composites with RGO, various metal oxide semiconductors have been explored. Among these, the most widely explored ZnO system has shown promising results either as an individual host material or as a composite with other low-dimensional semiconducting materials. For instance, ZnO NWs have been used extensively for making field effect transistors, photoluminescence, and other light-sensitive devices such as solar cells. The larger bandgap (3.37 eV)

and accompanied enhancement in nanostructured form further make it difficult to use them directly as a gas sensor for room-temperature operation. Several previous studies have revealed that ZnO NWs prepared via the carbothermal method displayed poor conductivity, making it difficult to have a gas sensor with the room-temperature operation. Here, the role of the second host material becomes important. When combining the graphene with its direct E versus k relationship and exceptionally large electronic mobility [1] with such metal oxide semiconductor-based NWs, the composite obtained possesses superior properties as compared to both host materials. For instance, Wang et al. [12] have prepared a nanocomposite of ZnO NWs and graphene oxide sheets via mechanical mixing followed by a low-temperature thermal reduction process. In a typical synthesis procedure, they mixed 1.0 g ZnO powder and 1.0 g graphite and put them into a quartz tube furnace. Then the furnace was heated to 1150 °C in an N_2 atmosphere (4.5 l/min) and air (0.1 l/min) as carrier gas and reactive gas, respectively. Following this procedure, they obtained approximately 0.8 g of ZnO NWs. Graphene oxide was prepared through a modified Hummer's method [13]. Followed by this, graphene oxide powder was sonicated in DI water, and in a separate step, a small amount of ZnO NWs along with 0.1 g PVP were also mixed in DI water and then sonicated for 15 minutes. Subsequently, these two solutions were mixed and stirred for an hour. This was accompanied by centrifugation, removal of impurities, final drying of the composite, and thermal reduction at 300 °C to form ZnO–NW composites. The morphological studies on these samples indicated that ZnO NWs arrange themselves uniformly over the RGO sheets and interconnect with each other, therefore allowing electron transfer between these two materials. Following an identical synthesis procedure, Sun et al. [14] have also reported the synthesis of ZnO–NW–RGO hybrid. Coincidently, almost identical results have been obtained in these two different investigations. This will become clearer from the discussion in the following section.

As reported by Sun et al. [14], the ZnO–NW–RGO composites-based sensor devices, when exposed to NH_3, display an increase in sensor resistance. After a while, the resistance saturates and reduces further when ammonia is removed from the test chamber. The well-known reducing character of NH_3 and accompanying increase in device resistance implies p-type conduction in ZnO–RGO composite. In their detailed analysis with variable ammonia concentrations in the range 500 ppb to 5000 ppm, a linear variation of the sensing response was observed. They have obtained a relative response of $\approx 7.2\%$ for 1 ppm of NH_3 with a response (recovery) time of 50 seconds (200 seconds) at room temperature [14]. These results indicate the highly sensitive nature of ZnO–NW/RGO composite toward room-temperature NH_3 sensing. These devices can detect NH_3 over a wider range of concentration, ranging from 500 ppb (with the relative response of 3%) to 5000 ppm. They also emphasized that relatively higher concentrations the response saturates, which they attributed to saturated absorption of ammonia gas molecules on the composite surface. But in all cases, reversible response characteristics were obtained.

3.3.1.1 Influence of Weight Percentage on Ammonia-Sensing Characteristics

Wang et al. [12] also made use of the same composite and have shown significant improvement in ammonia sensing. They did not limit their investigations to a single composite. Rather, they extended their investigations by employing ZnO–NW/RGO composites with variable weight ratios. This makes sense in a way that the process of making a composite between two different materials involves the formation of an intimate contact which in turn depends on available specific surface area and various other material parameters such as surface energies and defects. Similar effects have been observed with composites of other two-dimensional materials with metal oxide semiconductors [15–17]. In their study, Wang et al. [12] have given a detailed investigation about individual host material, i.e. ZnO–NW, RGO, and ZnO–NW/ RGO composites with 10, 25, and 50 wt% ZnO-NW, respectively. They didn't limit their investigations to composites with variable weight ratios but also studied the influence of annealing temperature on gas-sensing characteristics of ZnO–NW– RGO composites. In their initial investigations, the electrical resistance of as-obtained device was quite large (2.8 MΩ). The device resistance was found to be 2.2 MΩ, 0.18 MΩ, 900 Ω, and 90 Ω for ZnO–NW–RGO composites that were annealed at temperatures 100, 200, 300, and 400 °C, respectively. They associated two reasons for resistance change after thermal annealing. First, the downward movement of Fermi level is away from Dirac point [18], and second the annealing at a higher temperature may give rise to better contact formation between RGO and ZnO-NWs, thereby improving electrical conductance of the composites [19, 20]. The measured resistance values for as-obtained composite and the one annealed at 100 °C were quite large, and no such sensing data were obtained. Indeed, this is true with other systems also, where device resistance plays an important decisive role in obtaining a better sensing response [21]. Similarly, a drastic difference in response transients was obtained from the devices made from sample annealed at 200 and 400 °C. The sample annealed at 200 °C with a base resistance of 1200 kΩ displayed superior response transients compared with the one obtained at 400 °C with a base resistance of 0.257 kΩ [12].

The data shown in Figure 3.1 correspond to samples that were annealed at 300 °C. In Figure 3.1a for pure ZnO-NW-based devices, the response is quite fast, but delayed recovery (larger than 5000 seconds) limits its use. Similarly, RGO-based device also displayed a very low response with 50 ppm of NH_3 (Figure 3.1b). A quick look at response transients obtained on devices with 10 and 50 wt% ZnO-NW indicates that recovery is quite sluggish in both cases (Figure 3.1c,d). Where the former exhibits a faster response, the latter possesses delayed response as well as recovery. The device with 25 wt% ZnO-NW displays a response transient with faster response and recovery times as shown in Figure 3.1e. As shown in Figure 3.1e, the best response transients were obtained for the 25 wt% ZnO–NW/RGO sample annealed at 300 °C. These results highlighted the importance of composites, where individual materials with complementary properties may turn out to be inferior but when they are combined, the interfacial interactions may give rise to superior
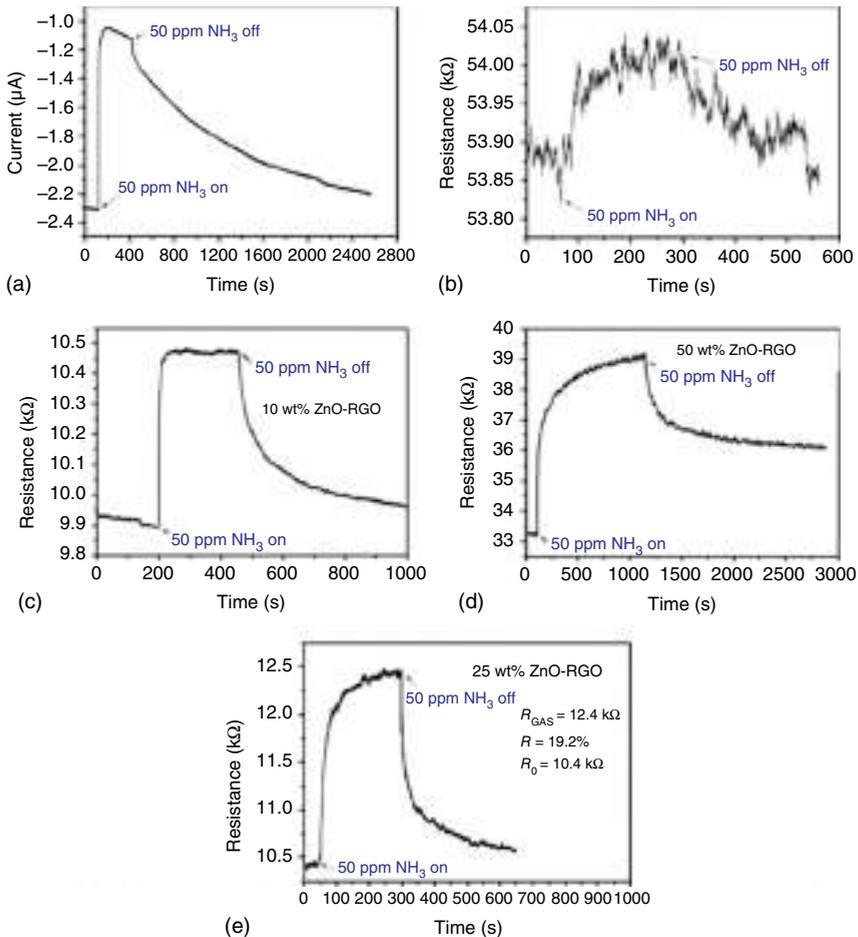
Figure 3.1 Response transients for (a) ZnO NWs, (b) pure RGO, (c) 10 wt% ZnO-RGO, (d) 50 wt% ZnO-RGO, and (e) 25 wt% ZnO-RGO exposed to 50 ppm NH_3 at room temperature. Source: Wang et al. [12]/with permission of Elsevier.

sensing characteristics. This is indeed clear from the present discussion. Therefore, the devices with 10 and 50 wt% ZnO NWs were discarded, and only one with 25 wt% was investigated in detail [12].

This device displayed superior sensing response to ammonia concentration ranging from 50 ppb to 5000 ppm with a linear response. The sensing response increased from 5.1% at 50 ppb to nearly 47.6% at 5000 ppm. Detailed analysis with increased relative humidity levels of 10%, 30%, 50%, and 70% indicated a gradual increase of sensing response from 8% to 13%, thus emphasizing the influence of RH level on sensing performance of the devices. Further, excellent repeatability and long-term durability along with a slight reduction in sensing response was observed [12].

In an entirely different synthesis routine, Anasthasiya et al. [22] have also shown room-temperature ammonia detection using ZnO-NW-functionalized RGO. In their

synthesis method, ZnO NWs were grown on a glass substrate by successive ionic layer adsorption and reaction (SILAR) method. The functionalization of ZnO NW with RGO was performed in a separate step involving a cleaned glass substrate. The obtained composite displayed p-type conduction with room-temperature ammonia detection down to 0.5 ppm

3.3.2 NO_2 Detection Using Metal Oxide Nanowires Hybrids with Reduced Graphene Oxide

NO_2 is the decomposition product of various explosive formulations and improvised explosive devices. Detection of NO_2 gas is important in such cases. Various industrial and recycling processes involve the emission of NO_2, and its monitoring becomes essential to avoid any accidental situation. Various 2D materials-based sensing channels have been used in this regard, and here, we will discuss only examples utilizing either Cu_2O- or SnO_2-based composites with RGO for the detection of NO_2. We shall start our discussion with the work by Deng et al. [23].

3.3.2.1 Cu_2O Nanowires/RGO-Based Hybrid

The cuprous oxide, a p-type semiconductor, due to its intriguing optical and electrical properties has been successfully integrated into solar energy devices, sensors, and photocatalytic degradation. The controlled synthesis of cuprous oxide crystals with variable morphology, including nanocubes, NWs, polyhedrons, solid and hollow spheres, has been achieved via various synthesis routes, for instance, electrodeposition, vacuum evaporation, and liquid-phase reduction of a metal salt. In a few recent examples, the complex 3D structure of Cu_2O such as NW polyhedra and multipod frameworks has also been reported. Such types of structures with a larger surface-to-volume ratio may prove beneficial for gas sensing. Here, we shall continue our discussion with such an example that involves the synthesis of Cu_2O/RGO composites where Cu_2O acquires octahedron morphologies [23]. In their synthesis, Deng et al. made use of modified Hummer's method for preparing RGO [23, 24]. Thereafter, a composite of Cu_2O/RGO was obtained via hydrothermal method. They obtained Cu_2O mesocrystals with octahedron morphologies with the size in the range of 10–100 μm. Figure 3.2 compares the dynamic response of the sensor devices made from RGO, Cu_2O–NW, and Cu_2O–NW/RGO composites. Owing to their p-type nature, the sensitivities of all three sets of devices displayed an increase with increasing concentration. With 2.0 ppm of NO_2, these devices have shown a sensitivity of 22.5%, 44.5%, and 67.7%, respectively (Figure 3.2). The corresponding calculated limits of detection (LOD) were found to be 82, 81, and 64 ppb, respectively. It is to be noted that all these measurements were performed at room temperature.

A separate study by Huang et al. [25] also made use of Cu_2O–NW/RGO composite for the detection of NO_2. In their study, they obtained Cu_2O–NW in a slightly different method. They prepared polypyrrole-coated Cu_2O NWs via the single-step hydrothermal method. The RGO was obtained via a similar modified Hummer's method. The composite so obtained was used for NO_2 sensing at room temperature, and corresponding results are displayed in Figure 3.3 for varying NO_2 concentrations
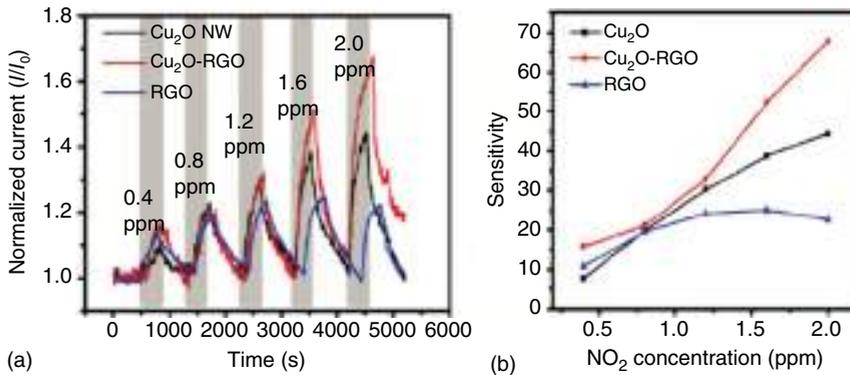
Figure 3.2 (a) Dynamic response of Cu₂O-NW, RGO-Cu₂O, and RGO devices for increasing NO₂ concentrations. (b) The sensitivities of the three sensors. Source: Deng et al. [23]/with permission of American Chemical Society.
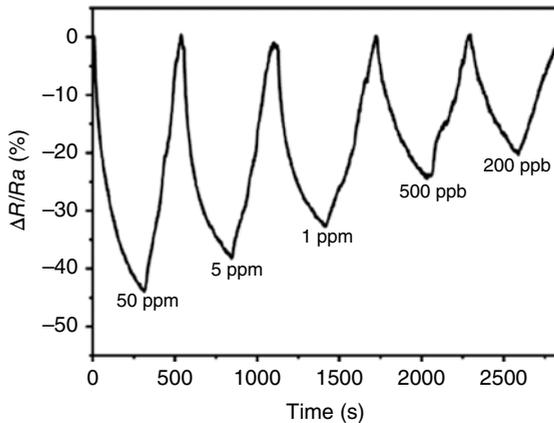
Figure 3.3 The sensing response curves for the device under different NO_2 concentrations. Source: Huang et al. [25]/MDPI/Public Domain CC BY.

(200 ppb to 50 ppm). These results indicate a significant improvement over the previous one obtained by Deng et al. [23].

3.3.2.2 SnO₂ Nanowires/RGO-Based Hybrid

It is to be noted that NO_2 detection was not only limited to Cu_2O, but another metal oxide semiconductor namely SnO_2 also deserves equal importance. Quang et al. [26] have shown successful integration of SnO_2 NWs with graphene, thereby making SnO_2/graphene Schottky junctions. The results so obtained are shown in Figure 3.4. At a temperature of 100 °C and 10 ppb of NO_2, the sensor displayed a longer response/recovery time of 116 seconds and 114 seconds, respectively.

With increased working temperature, however, a decrease in response–recovery time was observed. The device also exhibited a linear and maximum response at an
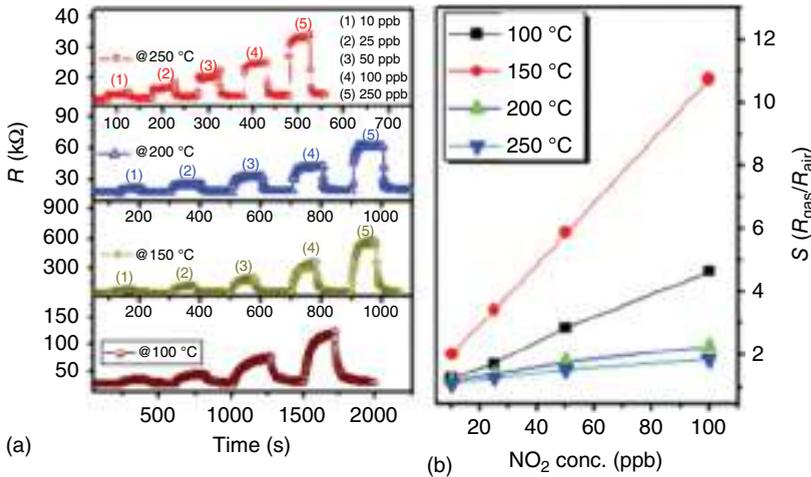
Figure 3.4 The sensing response curves for SnO_2 nanowires/RGO-based sensing device under different NO_2 concentrations. Source: Van Quang et al. [26]/with permission of AIP Publishing.

optimum temperature of 150 °C. They attributed the enhanced device performance for nano-junction formation between SnO_2 NWs and graphene oxide.

3.3.3 H$_2$S Detection Using SnO$_2$ Quantum Wire/RGO-Based Hybrid

The use of SnO_2/RGO-based composites is not only limited to NO_2 detection, but as shown by Song et al. [27] they are also useful in the room-temperature detection of H_2S. They obtained RGO via the well-known modified Hummer's method. Thereafter, SnO_2 quantum wires were obtained in a single-step hydrothermal synthesis by using $SnCl_4 \cdot 5H_2O$, oleic acid, and oleylamine [27]. Following this procedure, a SnO_2 quantum wire/RGO composite was obtained for different reaction times of 3, 6, and 8 hours. The reaction time plays an important role in determining the size of quantum wires. Later, when used as a sensing device, they noticed that the smaller diameter of SnO_2 quantum wires did not necessarily ensure superior sensing properties. Rather, for the sample synthesized with 8 hours' reaction time, an optimum H_2S-sensing response of 33 was obtained (see Figure 3.5a). These results further suggest that quantum wire length and their networking on RGO nanosheets might play an important role in deciding the sensing characteristics and require further investigations [27]. More detailed investigations with variable H_2S concentration (10–100 ppm) are shown in Figure 3.5b.

3.3.4 ZnO Nanowires-Graphene-Based H$_2$ Sensor

Liu et al. [28] have fabricated room-temperature H_2 gas sensor using ZnO NWs and graphene-based nanocomposite. H_2 is the potential material for clean and renewable energy. H_2 sensing is typically challenging due to its small molecular size. In
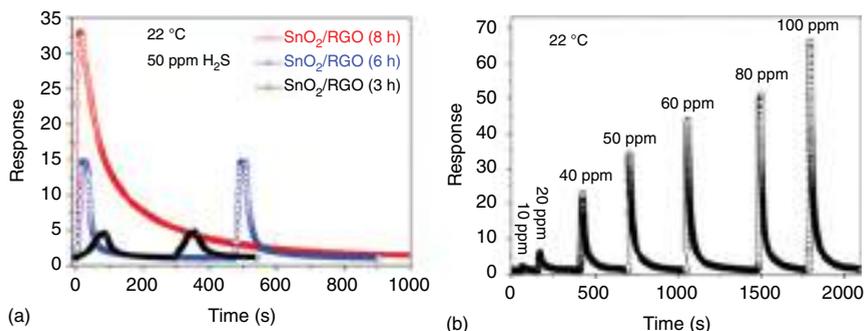
Figure 3.5 (a) Response transients for SnO_2/RGO nanocomposite-based gas sensors. The composites were synthesized at 180 °C for different reaction times. (b) Response transients for different H_2S concentrations. Source: [27]/with permission of American Chemical Society.

this work, the ZnO–NWs–graphene composite has been prepared by a cost-effective and novel seedless growth technique. This work emphasized the synergic combination between high-quality single-crystalline NWs and single-layer CVD graphene. The high surface-to-volume ratio of ZnO NWs provided more adsorption sites for H_2 molecules, while the superior quality of graphene provided high charge mobility and thus short response and recovery time of the sensor. The graphene layer has been synthesized onto the 25 μm Cu foil in a CVD system using CH_4 and H_2 gases as precursors. Polymethyl methacrylate (PMMA) layer has been coated onto the top side of CVD-synthesized graphene, and then it was immersed into 0.1 g/ml $FeCl_3$ solution to etch the Cu foil. After the removal of Cu foil, the cleaned graphene film was immersed into $Zn(NO_3)_2$ and NH_4OH solution at 80 °C for 12 hours to grow ZnO micro-wire/NWs on the graphene layer. Due to the lower density of PMMA/graphene composite than that of the solution, the sample was floating onto the solution surface during the ZnO nanostructure growth process. The defects present onto the surface of the CVD-grown graphene layer interacted with the OH groups from the solution and reacted with Zn^{2+} ions, resulting in the fast nucleation of ZnO which ultimately led to the formation of nanostructures onto the graphene film due to lateral physical confinement. After this, ZnO/graphene nanostructures have been transferred to the substrate with predeposited Au electrodes for H_2-sensing studies. Formation of hexagonal-shaped ZnO NWs with a diameter range of 500–1500 nm has been reported. The single crystalline nature of NWs is confirmed by HRTEM pertaining to ZnO growth along [0001] direction with an average spacing of 0.26 nm between the ZnO planes. The dynamic response of the sensor is investigated for different concentrations of H_2 concentration 0.06–1% balanced in synthetic air using a mass flow controller. The sensor response is reported to increase with increasing H_2 concentration. These preliminary investigations indicate that the demonstrated low-cost and non-vacuum growth process could be used for large area deposition onto the flexible substrate for the fabrication of metal oxide NWs/graphene hybrid-based H_2 sensors.

3.3.5 ZnO Nanowires on Laser-Scribed Graphene-Based Devices for NO Gas Detection

Chou et al. [29] have demonstrated a facile and low-cost hydrothermal technique to fabricate ZnO NWs on laser-scribed graphene-based sensor for NO detection. Graphene film of thickness ~13 μm has been obtained by spin-coating the graphene ink over the glass substrate and drying it at 280 °C for 2 hours. The V-shaped grooves have been scribed on the graphene film/glass substrate by using a 532-nm picosecond laser. The dimensions of the grooves have been optimized by varying the laser fluence, scanning speed, and the number of scribing cycles. A groove as wide as 32.38 μm has been obtained by varying the laser parameters. ZnO NWs have been fabricated onto the walls of the V-shaped grooves by employing a facile hydrothermal procedure. The graphene/glass substrates containing V-shaped grooves have been dipped into a solution of 0.08 M $Zn(CH_3COO)_2 \cdot 2H_2O$ blended with C_3H_8O and $C_6H_{15}N$ and heated in the temperature range 150–350 °C for 20 minutes in an autoclave. Subsequently, these samples have been immersed in a solution of $Zn(NO_3)_2 \cdot 6H_2O$, hexamethylenetetramie (0.05 M each) mixed in DI water at room temperature. During the growth stage of NWs, this solution has been heated at 85 °C for 8 hours in the autoclave. Further, the surface tension of grooves has been minimized using the methanol surfactant solution.

Ultimately, the gas sensor of NWs-coated graphene has been fabricated after the drying process. ZnO NWs grown without and with using surfactant solution have been deposited onto the V-shaped groove with width nearly 10.9 and 4.46 μm, respectively. The electrical resistance of ZnO NWs grown with surfactant solution was found to be less than that grown without using surfactant solution.

The gas sensor has been fabricated using V-shaped grooves pertaining to laser parameters 300 kHz, 100 mm/s, 1.81 J/cm^2 for three times. The morphology of NWs is shown in Figure 3.6a–d. The sensor was placed in the test chamber filled with dry N_2 at 70 °C before the NO measurement. When the sensor was exposed to NO, the NO molecules got absorbed onto the surface of NWs and take electrons. In addition to it, the absorbed gas molecules reacted with the adsorbed oxygen species. Since ZnO is an N-type material, exposure of NWs to NO molecules reduced the electron concentration, and hence the sensor resistance increases with each NO exposure. For every exposure cycle, N_2 was purged after the sensor attained a stable equilibrium resistance (Figure 3.6e). The sensor was exposed to three NO concentrations of 50, 150, and 300 ppm, respectively. The sensitivity (S) of the sensor was calculated as $S = (|R_0 - R_a|/R_0) \times 100\%$, R_0 and R_a being the sensor resistance under N_2 and NO. The sensor sensitivity of 14.7%, 21.2%, and 40.2% has been reported for NO concentrations of 50, 150, and 300 ppm, respectively (Figure 3.6f).

3.3.6 UV Light-Activated NO$_2$- and SO$_2$-Gas-Sensing Using RGO/ Hollow SnO$_2$ Nanofibers

Li et al. [30] have reported room-temperature selective detection of NO$_2$ and SO$_2$ gases by UV light-activated RGO/hollow SnO$_2$ nanofibers (NFs) sensor where the
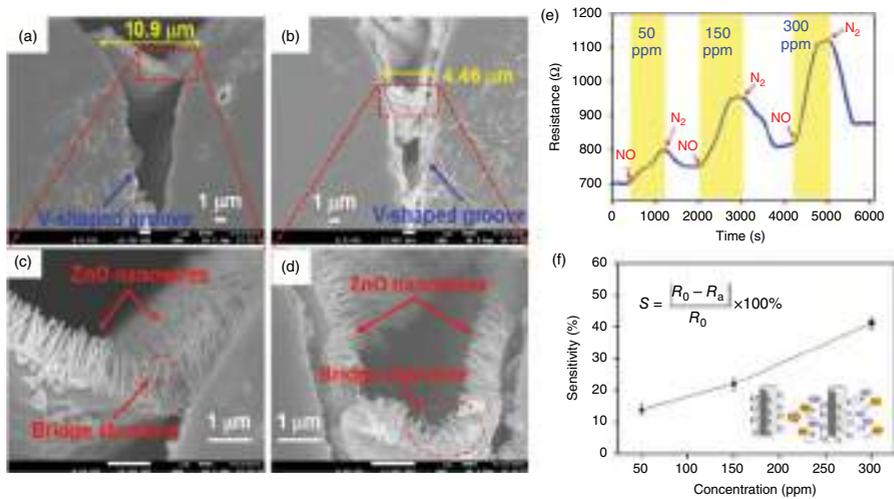
Figure 3.6 SEM images of ZnO-NWs grown (a) with and (b) without using surfactant solution. (c) and (d) The zoomed versions of (a) and (b). Source: Chou et al. [29], Elsevier.

NO_2 and SO_2 gases have been governed by the intensity of UV light and the different concentrations of NFs. The NFs have been synthesized by using electrospinning technique, followed by annealing at 600 °C for 3 hours. Graphene oxide has been prepared by Hummer's method which was further chemically reduced to get RGO. RGO/NFs have been prepared by magnetic stirring of different concentrations of RGO and NFs in ethanol. Three samples with different RGO/NFs mass ratio of 1:38, 1:40, and 1:43 have been prepared. The formation of RGO/NFs composite has been confirmed by X-ray photoelectron spectroscopy (XPS) investigations. The scanning electron microscopy (SEM) and high-resolution transmission electron microscopy (HRTEM) images of hollow NFs indicated lattice spacings of 0.33 and 0.26 nm pertaining to the (110) and (101) lattice planes in NFs as depicted in Figure 3.7a. The gas sensors have been fabricated by dip-coating the RGO/NFs hybrids onto the Si/SiO_2 substrates containing gold electrodes and subsequently dried at 60 °C for 30 minutes. A 25-W UV lamp with 365 nm wavelength has been employed for UV irradiation during the sensing measurements. The sensor response has been calculated as $S(\%) = (R_g - R_a)/R_a \times 100\%$, R_g and R_a being the equilibrium sensor resistance in the test gas and dry air, respectively. Three UV light intensities of 80, 97, and 103 mW/cm^2 have been tested for sensing measurements, and 97 mW/cm^2 was found to be optimum UV intensity which is used for the further NO_2- and SO_2-sensing investigations. It has been observed that among the three mass ratio RGO/NFs samples, the sample with 1:40 (termed as RGO/SnO$_2$-2) exhibited best NO_2- and SO_2-sensing kinetics. The NO_2 response curves of sensor are shown in Figure 3.7b
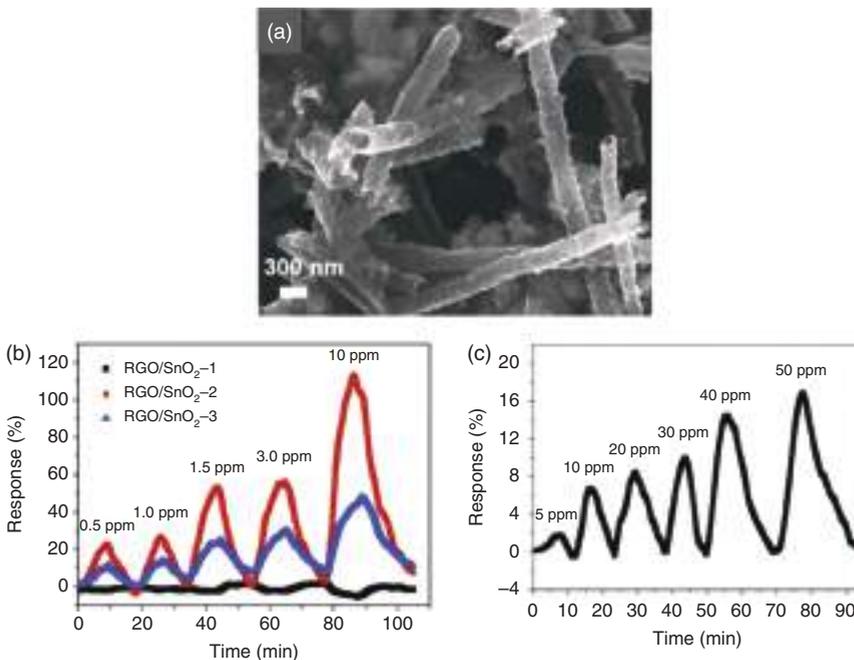
Figure 3.7 (a) SEM of RGO/NFs hybrid. Room-temperature (b) NO_2 and (c) SO_2 response curves of RGO/NFs-based sensor. Source: Weiwei et al. (2019), Elsevier.

for the NO_2 concentration of 0.5–10 ppm. The maximum response for 113% has been reported for 10 ppm of NO_2. The SO_2 response curves for the concentration range 5–50 ppm (Figure 3.7c). The response and recovery time of 4.3 and 2.5 minutes have been observed for 5 ppm of SO_2. A sensor response of >16% has been observed for 50 ppm of SO_2.

For both the gases, sensor resistance increased with gas exposure and then decreased on the flow of dry air which indicated that electrons have been captured from the sensor surface by the test gases. The gas-sensing mechanism of the sensor is correlated to the electron–hole pairs caused by the built-in electric fields with UV radiations, thus resulting into the UV-governed sensor action. Overall, these investigations emphasize toward the significance of UV radiations for enhancing the response kinetics of RGO-based room-temperature gas sensors.

3.4 Conclusion

The application of graphene/metal oxide NWs-based sensors for the detection of various gases typically NH_3, NO_2, H_2S, NO, and H_2 has been discussed in this chapter. The synergic combination of metal oxide nanowires having high surface-to-volume ratio and graphene exhibiting high charge mobility appeared to be beneficial in the detection of these gases.

References

1 Geim, A.K. and Novoselov, K.S. (2007). The rise of graphene. *Nat. Mater.* 6: 183–191.
2 Choi, W., Lahiri, I., Seelaboyina, R., and Kang, Y.S. (2010). Synthesis of graphene and its applications: a review. *Crit. Rev. Solid State Mater. Sci.* 35: 52–71.
3 Schedin, F., Geim, A.K., Morozov, S.V. et al. (2007). Detection of individual gas molecules adsorbed on graphene. *Nature* 6: 652–655.
4 Yuan, W. and Gaoquan, S. (2013). Graphene-based gas sensors. *J. Mater. Chem. A* 1: 10078–10091.
5 Basu, S. and Bhattacharyya, P. (2012). Recent developments on graphene and graphene oxide based solid state gas sensors. *Sens. Actuators, B* 173: 1–21.
6 Chatterjee, S.G., Chatterjee, S., Ray, A.K., and Chakraborty, A.K. (2015). Graphene-metal oxide nanohybrids for toxic gas sensor: a review. *Sens. Actuators, B* 221: 1170–1181.
7 Saqib Shams, S., Zhang, R., and Zhu, J. (2015). Graphene synthesis: a review. *Mater. Sci. Poland* 33: 566–578.
8 Edwards, R.S. and Coleman, K.S. (2013). Graphene synthesis: relationship to applications. *Nanoscale* 5: 38–51.
9 Yavari, F., Castillo, E., Gullapalli, H. et al. (2012). High sensitivity detection of NO_2 and NH_3 in air using chemical vapor deposition grown graphene. *Appl. Phys. Lett.* 100: 203120.

10 Dan, Y., Lu, Y., Kybert, N.J. et al. (2009). Intrinsic response of graphene vapor sensors. *Nano Lett.* 9: 1472–1475.

11 Li, W., Geng, X., Guo, Y. et al. (2011). Reduced graphene oxide electrically contacted graphene sensor for highly sensitive nitric oxide detection. *ACS Nano* 5: 6955–6961.

12 Wang, T., Sun, Z., Huang, D. et al. (2017). Studies on NH_3 gas sensing by zinc oxide nanowire-reduced graphene oxide nanocomposites. *Sens. Actuators, B* 252: 284–294.

13 Hu, N., Wang, Y., Chai, J. et al. (2012). Gas sensor based on p-phenylenediamine reduced graphene oxide. *Sens. Actuators, B* 163: 107–114.

14 Sun, Z., Huang, D., Yang, Z. et al. (2015). ZnO nanowire-reduced graphene oxide hybrid based portable NH_3 gas sensing electron device. *IEEE Electron Device Lett.* 36: 1376–1379.

15 Singh, S. and Sharma, S. (2022). Temperature dependent selective detection of ethanol and methanol using MoS_2/TiO_2 composite. *Sens. Actuators, B* 350: 130798.

16 Singh, S., Deb, J., Sarkar, U., and Sharma, S. (2021). MoS_2/WO_3 nanosheets for detection of ammonia. *ACS Appl. Nano Mater.* 4: 2594–2605.

17 Singh, S. and Sharma, S. (2022). Temperature-based selective detection of hydrogen Sulfide and ethanol with MoS_2/WO_3 composite. *ACS Omega*.

18 Kim, S., Lee, J.M., Lee, D.H., and Park, W.I. (2012). The effect of thermal annealing of graphene under ammonia atmosphere on its electrical properties and contact to p-GaN. Thin Solid Films 2013, 546, 246–249. *The proceedings of International Union of the Materials Research Society-International Conference in Asia 2012- IUMRS-ICA 2012*.

19 Cui, S., Pu, H., Mattson, E.C. et al. (2014). Ultrasensitive chemical sensing through facile tuning defects and functional groups in reduced graphene oxide. *Anal. Chem.* 86: 7516–7522.

20 Yi, J., Lee, J.M., and Park, W.I. (2011). Vertically aligned ZnO nanorods and graphene hybrid architectures for high-sensitive flexible gas sensors. *Sens. Actuators, B* 155: 264–269.

21 Singh, S., Sharma, S., Singh, R.C., and Sharma, S. (2020). Hydrothermally synthesized MoS_2-multiwalled carbon nanotube composite as a novel room-temperature ammonia sensing platform. *Appl. Surf. Sci.* 532: 147373.

22 Anasthasiya, A.N.A., Kishore, K.R., Rai, P.K., and Jeyaprakash, B.G. (2018). Highly sensitive graphene oxide functionalized ZnO nanowires for ammonia vapour detection at ambient temperature. *Sens. Actuators, B* 255: 1064–1071.

23 Deng, S., Tjoa, V., Fan, H.M. et al. (2012). Reduced graphene oxide conjugated Cu_2O nanowire mesocrystals for high-performance NO_2 gas sensor. *J. Am. Chem. Soc.* 134: 4905–4917.

24 Zaaba, N.; Foo, K.; Hashim, U.; Tan, S.; Liu, W.-W.; Voon, C. (2017). Synthesis of Graphene Oxide using Modified Hummers Method: Solvent Influence. Procedia Engineering 2017, 184, 469–477, *Advances in Material Processing Technologies Conference*.

25 Huang, M., Wang, Y., Ying, S. et al. (2021). Synthesis of Cu_2O modified reduced graphene oxide for NO_2 sensors. *Sensors* 21.

26 Van Quang, V., Van Dung, N., Sy Trong, N. et al. (2014). Outstanding gas-sensing performance of graphene/SnO_2 nanowire Schottky junctions. *Appl. Phys. Lett.* 105: 013107.

27 Song, Z., Wei, Z., Wang, B. et al. (2016). Sensitive room-temperature H_2S gas sensors employing SnO_2 quantum wire/reduced graphene oxide nanocomposites. *Chem. Mater.* 28: 1205–1212.

28 Liu, J.W., Wu, J., Ahmad, M.Z., and Wlodarski, W. (2013). Hybrid aligned zinc oxide array on CVD graphene for hydrogen sensing. In: *In 2013 Transducers & Eurosensors XXVII: The 17th International Conference on Solid-State Sensors, Actuators and Microsystems* (Transducers & Eurosensors XXVII) 2013 Jun 16, 194–197. IEEE.

29 Chou, C.-Y., Tseng, S.-F., Chanh, T.-L. et al. (2020). Controlled bridge growth of ZnO nanowires on laser-scribed graphene-based devices for NO gas detection. *Appl. Surf. Sci.* 508: 145204.

30 Li, W., Guo, J., Cai, L. et al. (2019). UV light irradiation enhanced gas sensor selectivity of NO_2 and SO_2 using rGO functionalized with hollow SnO_2 nanofibers. *Sens. Actuators B.* 290: 443–452.

4

Highly Sensitive Room-Temperature Gas Sensors Based on Organic–Inorganic Nanofibers

Bhagyashri Bhangare[1], Sinjumol K. Rajan[1,2], Niranjan S. Ramgir[1,2], Dinesh Kumar Aswal[2,3], and Anil Krishna Debnath[1,2]

[1] *Bhabha Atomic Research Centre, Technical Physics Division, Anushaktinagar, Mumbai, 400085, India*
[2] *Homi Bhabha National Institute, Anushaktinagar, Mumbai, 400094, India*
[3] *Bhabha Atomic Research Centre, Health Safety and Environment Group, Mumbai, 400085, India*

4.1 Introduction

The gas sensors are made to detect the gaseous entities having concentrations well below the human olfaction limit. They serve as a building block for electronic nose (E-nose), electronic skin (E-skin), and electronic tongue (E-tongue). The employment of various low-dimensional nanostructures namely 0D, 1D, 2D, and 3D, in these electronic configurations with interfacing machine learning (ML) and artificial intelligence (AI), has gained prime importance in environmental and health valuation. In day-to-day life, the real-time monitoring of different gaseous entities requires sensor devices exhibiting good stability, higher sensor response (SR), fast response–recovery time, lower limit of detection (LOD), and lowered operating temperature (OT) for less power consumption. It is observed that the lowering of OT can be achieved by making the composites, nanohybrids, and heterostructures and incorporating the noble metal sensitizers in the single- or multiple-host materials. The OT of the gas sensors is important parameter for deciding the sensor casing size, power consumption, and stability of sensor layers. The sensor operational at higher temperature needs additional electronic heater circuitry, and hence size of the sensor devices faces limitations during miniaturization. This is being overcome by using the nanomaterials which are sensitive at room temperature. Recently, polymers such as polyvinyl aniline (PVA), cellulose, polyaniline (PANI), polyvinyl pyrrolidine (PVP) have been used as a matrix with incorporation of metal and semiconductor nanostructures and being studied for room-temperature gas-sensing application [1–3]. The inorganic nanomaterials such as tin oxide (SnO_2), zinc oxide

(ZnO), titanium oxide (TiO_2), copper oxide (CuO), and nickel oxide (NiO) exhibited enhanced catalytic activity by incorporation of noble metals (Au, Pt, and Pd) [4, 5]. In addition, the carbon alloy structures such as graphene and chemically derived graphene/reduced graphene oxide (RGO) are also being employed in high-performance gas sensors [6]. The nanomaterials such as fullerenes, single- or multi-walled carbon nanotubes (CNTs) [7], graphene [8], MoS_2 [9], and MXenes [10] are the emerging nanostructures for highly sensitive gas sensors. Although, the pristine nanostructures of metal oxide semiconductor (MOS), polymers, and metals are sensitive to various analytes but have inherent limitation of poor selectivity due to cross sensitivity. The nanohybrids are realized by mixing of two or more individual organic and inorganic nanomaterials during *in situ* or *ex situ* synthesis and have been proven to be one of the efficient tools to engineer the gas sensor performance [11, 12]. The nanohybrids-sensing performance can be improved by chemical and electronic sensitization. The approaches help to enhance surface properties such as adsorption–desorption kinetics, SR, lowering of OT, and improved long-term stability.

The use of different nanostructures such as nanorods (NRs), nanofibers (NFs), nanowires (NWs), nanosheets (NSs), and quantum dots (QDs) has also contributed to enhance gas sensor characteristics. Among them, NFs are being studied for gas-sensing applications due its intrinsic properties such as maximum surface area per unit mass, high aspect ratio, and enhanced charge transport. As crystallinity considered, the NFs do not have similar nature as NWs, NRs, and NTs which mostly show monocrystalline structures. Contrary, NFs exhibit polycrystalline and amorphous structures. Moreover, they can be achieved in composites, heterostructures, and core–shell forms. Accordingly, different configuration of NFs-based gas sensors is being studied in order to achieve the desired optical, electrochemical, chemiresistive, and capacitive gas sensors. Recently, the development of single-NF-based gas sensors has gained attention due to the rapid response and recovery. The sensitization of the single NF with noble metals additionally improved the response kinetics during the gas sensing.

The various nanohybrids have been studied for gas-sensing applications. Even though some of them work at elevated OTs, they show good sensor characteristics [13, 14]. Most of the nanohybrids demonstrate the enhanced surface reactivity at higher OTs due to accelerated charge transport in presence of adsorbed gas molecules. However, the use of these sensor devices also demands power consumption. The higher OT often leads to fusion of the grain boundaries in MOS nanostructures and hence affects the lifetime of the sensors by destroying the stability of nanostructures. To overcome these drawbacks, the research has been focused on the development of the nanostructures which can be operated at room temperature. The present book chapter reviews most of the possible NFs-based gas sensors and their various possible configurations. The main emphasis is given to summarize the gas-sensing mechanism of the gas sensors [15, 16]. The synthesis of NFs mainly consists the polymers and hence the also contributes majorly for achieving low-temperature gas sensors. The use of conducting polymers and noble metal sensitizers also plays major role by lowering the activation energy of the

nanohybrid of MOS and metal–organic frameworks (MOFs) These hybrid NFs also facilitate the physicochemical properties such as electrical conductivity and adsorption–desorption ability [17].

4.2 Classification of Nanofibers for Gas-Sensing Application

During NFs synthesis, the morphology can be changed in the form of core–shell, surface-coated, and bulk doping. The classification of the NFs can be done according to chemical composition of the materials. Accordingly, the NFs can be classified as organic, inorganic, and organic–inorganic heterostructures/nanohybrids. Some of the various architectures of NFs used for gas sensing are summarized in Table 4.1.

4.2.1 Organic Nanofibers

The organic nanomaterials such as conducting polymers, CNTs, graphene, RGO, and fullerenes are being studied thoroughly and proven to be potential candidates for gas-sensing applications. Their ability to work at room temperature along with tunable structural and chemical properties is made possible using wet chemistry approach. The organic materials not only decrease the OT but also provide flexibility to derive different types of NFs such as core–shell, composites, and surface modified. The organic core–shell NFs, made up from poly(3,3′′′-didodecyl quarter thiophene) (PQT-12) and poly(ethylene oxide) (PEO), have been studied for NH_3 sensing at room temperature [32].

4.2.2 Inorganic Nanofibers

The inorganic materials such as MOS have shown prominent contribution in gas sensors due to high porosity, large surface area-to-volume ratio and wide range of sensitivity. The nanohybrids and different nanostructures of SnO_2, ZnO, In_2O_3, NiO, and CuO have been used for NO_2, H_2, H_2S, ethanol, acetone, volatile organic compounds (VOCs), and NH_3-sensing applications. It has proven that the use of noble metal sensitizers and their binary or ternary composites with MOS enhances the sensing properties. In nanohybrids, the Janus NFs are able to maintain the good stability along with fast response and recovery in ethanol gas sensor [33].

4.2.3 Heterostructure-Based Organic–Inorganic Nanofibers

The use of organic–inorganic hybrid NFs has shown unique sensing properties. It is an approach to derive different gas-sensing patterns. The organic–inorganic NFs can be achieved during electrospinning, by tuning the compositions of the source spray solutions. This is a key point over the available synthesis techniques and hence proved to be promising candidates for high-performance gas sensors by achieving the various heterostructures. The organic–inorganic 1D structures have proven

Table 4.1 Survey of NFs-based nanohybrids for gas-sensing application.

Sr. No.	NFs materials	Operating temperature (°C)	Analytes	Sensor response	LOD (ppm)	References
		Organic NFs				
1	Cobalt phthalocyanine	25 °C	NO_2	5.2 (50 ppm)	0.05	[18]
2	Polyaniline (PANI)-coated polyamide	RT.	NH_3	1.5 (250 ppm)	50	[19]
3	Amino-functionalized graphene/PANI	RT.	CO_2	95% (100 ppm)	20	[20]
4	Polyaniline–graphene/polystyrene nanocomposites	RT.	CO_2	70%	—	[21]
5	RGO nanosheets and electrospun nylon-6 NFs	RT.	NO_2	13.6% (1 ppm)	1	[22]
		Inorganic NFs				
6	$NiO–WO_3$	375	Acetone	22.5 (100 ppm)	20	[23]
7	SnO_2-Ru	200	Acetone	118.8 (100 ppm)	0.5	[24]
8	Zeolitic imidazolate framework-8 (ZIF-8)-coated In_2O_3 nanofibers	140	NO_2	16.4 (1 ppm)	0.010	[25]
9	SnO_2/ZnO	RT.	NO_2	336% (0.5 ppm)	0.5	[26]
10	In_2O_3@CuO multifunction's NFs	RT.	NH_3, H_2S	157% (100 ppm), 223% (100 ppm)	0.3, 1	[27]
		Organic–inorganic NFs				
11	PANI/TiO_2 core–shell NFs	RT.	NH_3	109.87% (1 ppm)	0.050	[28]
12	PANI/TiO_2	RT.	NH_3	467% (10 ppm)	0.5	[29]
13	Pd//polyurethane acrylate (PUA)	RT.	H_2	65% transmittance, (4 vol% H_2 in N_2), 1 atm.	0.1%	[30]
14	Cellulose acetate-WO_3	20	H_2S	31.2%	1	[16]
15	TiO_2-SiO_2/PANI	RT.	NH_3	—	10	[31]

potential contribution in various fields. The hybrids such as core–shell and Janus NFs can be synthesized by electrospinning method by using two parallel nozzles containing independent source of precursors. Further, it is also possible to incorporate two or more materials to achieve the synergistic effect to enhance the gas sensor characteristics.

Previous studies have shown that incorporating two or more metal oxides to form a heterojunction interface can have drastic effects on gas sensor performance, especially the selectivity. Recently, these effects have been amplified by designing heterojunctions on the nanoscale. These designs have evolved from mixed commercial powders and bilayer films to finely tuned core–shell and hierarchical brush-like nanocomposites. The uses of conducting polymers in organic–inorganic heterostructures generates the free standing and flexible sensing layers and is important in wearable electronics for health safety.

4.3 Different Configurations of Gas Sensors

The gas sensors are classified on the basis of working principles using change in the physicochemical properties due to exposure of gases and are measured as output signal. Accordingly, the gas sensors are divided into chemiresistive, amperometric, capacitive, colorimetric, impedance, and quartz crystal microbalance (QCM), etc., where resistance, current, capacitance, color change, impedance, and vibrational frequency are monitored as the output signal, respectively. Nowadays, self-powered gas sensor such as piezoelectric and triboelectric nanogenerator-based gas sensors are also being employed as a new-generation gas sensor and studied widely [34]. Figure 4.1 summarizes the classification of the different configurations of the gas sensors being used.

Among these configurations, chemiresistive gas sensors are being used widely due to their simple and small device semblance. The contribution of conducting polymers in chemiresistive gas sensors is most favorable due to their room-temperature
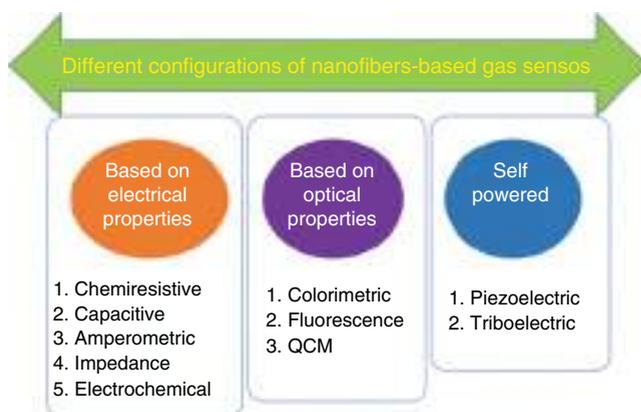
Figure 4.1 Classification of gas sensors based on physicochemical properties.

operation [35]. This ultimately proven to be an opportunity for NFs synthesis and its major contribution for gas sensing. In addition, the changes in the electrical properties and its corresponding signals in gas sensors are easy and more suitable for quantitative analysis. On the other hand, optical gas sensors are more suitable in medical and forensic fields to detect the dissolved VOCs and chemical traces. However, their bulky instrumentation limits its use as handheld devices. Some of the paper-based colorimetric strips are used for single-time clinical testing, limiting their reusability owing to contaminations and hygiene. So, the development of sustainable colorimetric reagents will be a prominent way for single-step and instant visual detection of multiple analytes [36, 37]. During the last decades, the self-powered generated gas sensors are being investigated, where the used triboelectric and piezoelectric materials are gaining the most prime importance [38].

4.4 Synthesis of NFs

The synthesis of NFs is done by conventional wet chemistry routes such as self-catalyst growth, template synthesis, self-assembly, sonochemical synthesis, polymerization, and electrospinning. Additionally, some of the emerging routes includes electrohydrodynamic direct writing, centrifugal jet spinning, plasma-induced synthesis, solution blow spinning, and CO_2 laser drawing [39]. Among these, electrospinning, coaxial electrospinning, and direct writing of NFs on desired substrate are the most suitable techniques for mass production, composite formation of NFs, and on-chip sensor fabrication, respectively.

4.4.1 Electrospinning and Coaxial Electrospinning Techniques

Electrospinning is a simple and low-cost technique used to produce NFs with diameters ranging from nm to μm. The electrospinning setup consists of high-voltage power supply (~10–70 kV), syringe pump, spinneret with nozzle needle, and a collector (e.g. metal foil and any desired substrate) connected to grounded voltage. For electrospinning, the source solution of the desired materials made up with polymers is being used. Use of polymers is attributed to maintain the viscosity for droplet formation at the tip of the needle nozzle. The high voltage is applied to the viscous solution with spinneret and needle. Once the surface tension of the liquid and the repulsive force induced due to the charge distribution on the surface of droplets become equal, the liquid droplets start to distort into conical shape. When repulsive force exceeds the surface tension, charged jet of liquid is ejected from the needle tip and displaced toward the grounded collector plate and deposition of NFs takes place in spiral manner. To lower the humidity interference, the setup can be boxed.

For successful deposition of the NFs, the volatility, conductivity, and surface tension of the polymer solution should be suitable and carefully balanced. The increase in conductivity of the solution helps to decrease the diameter of the NFs. The conventional electrospinning modified to coaxial electrospinning where two-layer nozzle is being used. For NFs-based gas sensors, the metal contacts are mostly deposited

at the top of the sensing layer. Further, the increase in resistance of the sensor films due to deposited contacts by traditional method is a drawback.

4.4.2 On-Chip Fabrication and Direct Writing of NFs-Based Gas Sensors

The alignment and ordering of the NFs are the most challenging tasks for controlled architecture developments. Therefore, the direct patterning of the NFs is essential in novel material configurations. The direct patterning of NFs on a desired substrate chip is being explored for designing the nanodevice sensors. The direct patterning of NFs using near-filed electrospinning [40] and electrohydrodynamic [41] is being used to design the sensor arrays on a single or multiple chip, and hence it is becoming a most popular technique for nano-E-nose fabrication. K. Kang et al. demonstrated the use of near-filed electrospinning and electrohydrodynamic for direct patterning of NFs on sensor chip for patterning array.

4.5 Role of Physicochemical Properties of Nanofibers in Gas Sensing

To study the gas-sensing mechanisms, theories of electron depletion layer (EDL), hole accumulation layer (HAL), grain control, gas diffusion control, and adsorption desorption models were used [42]. The gas-sensing mechanism can be understood with microscopic and macroscopic approaches. Further, to study the gas-sensing mechanism, the ionosorption model and oxygen vacancy model have been explained by Gurlo and Riedel [43, 44].

 (i) The first approach includes monitoring of microscopic perspectives which include changes in electrical properties: Fermi level control, grain boundary control, EDL, and HAL. The study of these microscopic entities leads us to understand the gas-sensing mechanisms in many materials as these properties are the function of changes in physical properties.
(ii) The second approach includes monitoring of macroscopic properties such as adsorption–desorption kinetics of gas molecules, gas diffusion study, and bulk resistance control.

These theories prove to be efficient approach to study the gas-sensing mechanisms using various analytical and spectroscopic techniques such as Kelvin probe (surface band bending) [45], X-ray photoelectron spectroscopy (XPS) (chemisorption) [46], fluorescence spectroscopy [47], and various mathematical models to study the adsorption–desorption kinetics [48]. The physicochemical properties such as bandgap, aspect ratio, surface area, particle size, sensor film thickness, and conductivity play an important role in gas sensing. Depending on the nature of nanostructures, these properties vary and also affects the sensor characteristics. In 2D nanomaterials, the high surface area plays an important role to provide the reaction sites to the adsorbent gas molecules. It also provides flexibility for surface

modifications using noble metals to improve the surface activities and adsorption–desorption kinetics. The surface modifiers also help to lower the OT of the gas sensors. Interestingly, the use of different 1D nanostructures helps to increase the charge carrier transport and increased SR. Among them, NFs play important role to improve the gas sensor characteristics due to high aspect ratio, pore structures, flexible surface modulation, large stacking density, and improved sensitivity.

4.5.1 Surface-Dependent Properties

The use of 1D nanostructures boost the charge transport in the sensor layers due to high aspect ratio. Most importantly, the surface-dependent properties of the materials affect due to the change in surface depletion layer and work function. In gas sensors, the chemisorption of oxygen species plays initial role to govern the sensing mechanism. The presence of the oxygen molecules in the air atmosphere extracts the free electrons from the conduction band of MOS and ionized to adsorbed ions $(O_x\delta: O_2^-, O^-, \text{or } O^{2-})$. At the same time, EDL forming on the surface of the MOS increases the potential barrier and leads to increase in resistance. After exposing the gas molecules, change in surface depletion layer occurs depending on the nature of gas (oxidizing/reducing). For reducing gases, the depletion layer decreases, while oxidizing gas molecules causes increase in width of depletion layer. The NFs shows enhanced surface reactivity after modifying their surface with metal and metal oxide sensitizers. Use of catalytically active metal sensitizers such as Pt, Au, Pd, and Ag as a co-dopant or bimetallic dopant plays an important role to improve the sensor performance [49, 50]. The detection of explosive gases offers the use of room-temperature gas sensors. Further, the bimetallic doping introduces the synergistic effect and improves the surface properties and selectivity of the sensor.

4.5.2 Interface-Dependent Properties

In organic–inorganic nanohybrids, the gas molecules may interact with one component (organic or inorganic) and transfers the changes to second. The formation of heterojunctions at the interface of two dissimilar components modulates the band bending and alters the SR. The phenomenon is referred as synergistic effect. The synergistic reactions at the interfaces of the nanohybrids governs the band bending and collective change in the work function of the both individual materials. Hence, in order to study the interface properties, the nanohybrids, work function analysis is a crucial [51].

To study the band bending at the interfaces of heterojunctions, the Kelvin probe spectroscopy and ambient photoelectron spectroscopy (APS) are used widely. The extent of band bending can be visualized before and after the gas exposure, by arresting the gas molecules on the surface of sensor layer by quenching. The formation of heterojunctions such as p–p, n–n, and p–n in the nanohybrids helps to enhance the gas-sensing properties. In p–n heterojunctions, the p-type materials are used as sensitizers or in hybrid formations with the n-type materials or vice versa.

Similarly, the p-type and n-type materials are assembled in p–p and n–n heterojunction formations. In NFs, the different configurations such as surface-decorated NFs, core–shell NFs, and Janus NFs have been used to modulate the interface properties thereby improving the sensor performance.

4.5.3 Morphology-Controlled Properties

The MOS are excellent candidates to engineer their structures, morphology, charge carrier density, and activation energy and hence used in the high-performance gas sensor devices. The various 1D structures of MOS such as NWs, NTs, and NFs help to improve the sensor characteristics such as OT, stability, selectivity, and sensitivity [52]. In addition to morphology, Debye length and the size of nanostructures have major contribution in sensor performance [53]. Debye length is a region or depth of surface depletion region which can be engineered by tuning the OT, charge carrier density, and gas concentration. In core–shell NFs, it is observed that, if the thickness of the shell is comparable or twice of the Debye length, the sensor exhibits stronger response [54]. The hierarchical nanostructures of metal oxides over the single semiconductors exhibited highest performance, if the growth of secondary component is controlled toward the radial direction of the base or primary NF component. The effect of morphology in hollow aluminum-doped zinc oxide (AZO) core–shell NFs on NO_2 gas-sensing properties is shown in Figure 4.2. The modulation of these heterojunctions in core–shell NFs is responsible for the enhanced sensor performance.

4.5.4 Adsorption–Desorption Kinetics

The physisorption of gas molecules is governed by Coulomb force, week Vander Waal forces, intermolecular forces, and hydrogen bonding without any chemical changes in the materials. However, the change in electrical signal outputs due to physisorption is very negligible and cannot be used to explain the sensing mechanism. On the other hand, chemisorption is the process, where the gas molecules interact with surface of the materials by affecting the electrical properties; thereby it can be used directly to study adsorption/desorption kinetics and sensing mechanism. The change in output signal is a function of adsorption/desorption of gas molecules and amount of gas concentration. The adsorption rate is a function of the reactive sites available on the solid surface, electronegativity, and OT of the sensor. As the OT of the sensor remains higher, adsorption–desorption also accelerates and reflects to the quick response/recovery time. The mathematical models such as oxygen adsorption model, Elovich model, pseudo-first-order equation, pseudo-second-order equation, Ritchie's equations, N_2 adsorption–desorption, and diffusion control have been used to study the kinetics of the interaction of the gas molecules with sensor surface [48, 55]. Further, it is possible to increase the adsorption energy of the solid surfaces by appropriate doping of metals. Using the density function theory (DFT), A. Farzaneh et al. has observed the sizeable increase in the adsorption energy of Ru-doped TiO_2 NFs toward the water molecules [56].
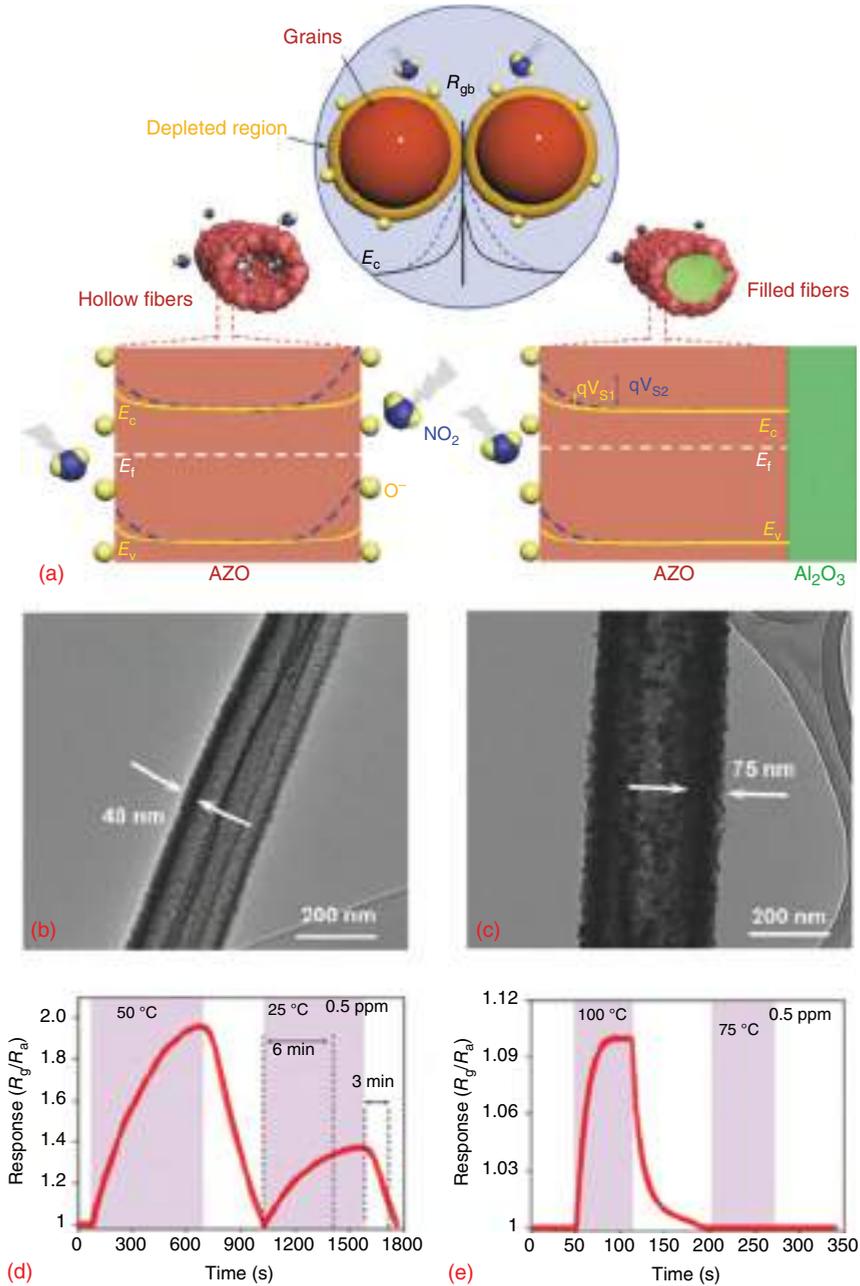
Figure 4.2 Effect of morphology on (a) energy band bending of hollow and filled NFs, (b, c) TEM micrographs shown clear variation of shell thickness, and (d, e) sensor response enhancement in hollow NFs. Source: Sanger et al. [52], John Wiley & Sons, CC BY 4.0.

4.6 Enhancement of Characteristics of Nanofibers-Based Sensor Performance

The gas sensors are considered for commercial deployment if they are able to fulfill the 4-S selection criteria or the "Ramgir-criterion" (4S: Sensitivity, Suitability, Selectivity, and Stability). To enhance physicochemical properties and sensor characteristics, several processes are being implemented during and after the synthesis of nanohybrids for gas sensing. The enhanced performance of the gas-sensing materials is mainly the contribution of electronic sensitization, catalytic reactions, spillover effect, synergistic effect, and oxygen deficiencies. This is further achieved by using sensitizers, hybrid architectures, and nanohybrids of two or more elements. It also includes the nanostructure formation, noble metal doping, organic–inorganic heterostructure formation, ion and light irradiation, and laser irradiation on the sensing layers surface before or during the gas exposure.

4.6.1 UV Light/High-Energy Beam Irradiation

The use of UV illumination during the exposure of gas analytes have been studied using the wide bandgap semiconductors such as ZnO, TiO_2, and SnO_2 for photoreactive gas sensors [57]. As an effect of UV illumination, the generation of electron–hole pair takes place, thereby modulating conductivity of the sensors. The photodesorption of oxygen ions and chemical redox reactions in between the target molecules are able to take place even at lower or room temperature [58]. The operation of gas sensors at higher temperature leads to grain growth and performance degradation. To overcome this, the illumination of UV light is also one of the alternatives along with conducting polymers to achieve the low-temperature gas sensing [59]. It also accelerates the response and recovery of the gas molecules. W. Li et al. have studied the NO_2-sensing properties of SnO_2/RGO NFs in presence of UV light, where it is found that response enhanced from response ratio (NO_2/SO_2) of 1.0 in dark to 9.3 using $97\,mW/cm^2$ of UV light illumination [60].

   In addition to UV illumination, the irradiation of high-energy e-beam causes the structure defects such as interstitials, surface dangling bonds, and oxygen vacancies. These defects increase the surface adsorption sites and thereby enhances the gas molecule adsorption [61]. Among several irradiation techniques, e-beam irradiation is found to be more suitable due to its room-temperature operation and flexible tuning of surface properties of the materials as a function of degree of dose and irradiation energy (Figure 4.3).

4.6.2 Noble Metal Sensitizers

The use of noble metal sensitizers plays an important role by improving the sensor performance as they promote the chemisorption with gas molecules dissociation by accelerating the catalytic reactions at the surface sites. Most effectively, the noble metals such as Pt, Pd, Au, and Ag are being used in gas sensor application [62]. The
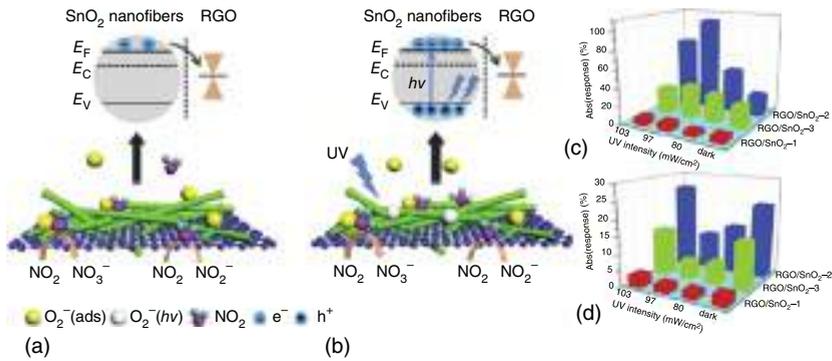
Figure 4.3 Schematic of sensing mechanism of RGO/SnO$_2$ NFs for NO$_2$ (a) in dark, and (b) under UV light, and (c, d) the sensor response of RGO/SnO$_2$ NFs at different UV intensity. Source: Reproduced with permission from Li et al. [60]/Elsevier.

use of noble sensitizers helps to increase the oxygen ions by increasing the adsorption sites, which helps to reduce the activation energy of the material. Y. Liu et al. has reported loading of Pt NPs, and they attribute improved performance to chemical sensitization. The formation of heterostructures helped to decrease the OT from 180 °C to room temperature as effect of porosity and chemical sensitization in In$_2$O$_3$ mesoporous NFs. R. Vishnuraj et al. have reported the modification of ZnO NFs using Au nanograins for NO$_2$ sensing [63].

The detailed investigation of the induced spillover zone and aided charge transfers have been studied using electrical measurements and operando photoluminescence (PL) studies. The PL spectroscopy is proved to be an efficient approach to study the recombination dynamics of charge carriers and involvement of defect states to enhance the gas adsorption. The recombination of charge combination leads to defect emission in the materials. K. G. Nair et al. has reported the well-defined core–shell structure of carbon NFs as the core and AuNPs–PtNPs/NiNPs–PtNPs as the surface-anchored heterojunctions. These chemical sensitizers help to trigger the dissociation of H$_2$ through the spillover H$^+$ effect, thereby causing successive diffusion of charge carriers into the carbon NFs surface. Au doping helps to form the nano-Schottky junctions with the other elements present in the nanohybrids and modulates the surface and interface properties [64]. The Pd doping helps to chemisorb the H$_2$ molecules even at room temperature and often being used in H$_2$ gas sensors with lowered OT. Table 4.2 summarizes some of the recent attempts to improve the gas SR using the noble metal sensitizers.

4.7 Recent Trends

The NF-based heterojunctions are being employed in the commercial gas sensors. The synthesis of these heterojunctions often includes the multiple-step processes. The crescent trends in the NFs are focused on the on-chip fabrication and one-step synthesis for advanced device integration, due to which the NFs held

Table 4.2 Noble metal sensitizers-doped NFs for gas-sensing application.

Sr. No.	NFs materials	Analytes	OT (°C)	LOD	SR	References
1.	Coaxially aligned CFs@Ni NPs–PtNPs nanosystem	H_2	RT.	0.1%	124% (4%)	[65]
2.	Pt-loaded In_2O_3 mesoporous NFs	NO_2	RT.	10 ppb	23.9 (1 ppm)	[66]
3.	Ag: WO_3	NO_2	225	0.5 ppm	90.3 (5 ppm)	[67]
4.	Au: In_2O_3	NH_3	175 20	1 ppm	116.13 11.12 (100 ppm)	[68]
5.	Pd/ZnO-SnO_2 hollow NFs	H_2	240	0.25 ppm	104 (200 ppm)	[69]

crucial attention by overcoming the inconsistency and integration drawbacks over the MOS nanostructure-based gas sensors. Beyond the single nozzle, the use of coaxial electrospinning in synthesis of nanohybrids NFs in single step is achieved [70].

4.7.1 Single-Nanofiber-based Gas Sensors Synthesized by Electrospinning

Recently, the development of sensors using aligned single NF, NW, NS, and NRs are attracting more attention for field effect transistors (FETs) devices. However, it also faces difficulties to generate, align, and trap these single nanostructures in device configuration. An aligning and ordering of the NFs can be done by magnetic field-assisted electrospinning. Here, the strong external field between the spinneret and collector substrate helps to align the NFs, whereas the internal repulsion between the NFs avoids the mixing and interlinking. The similar method is helpful for the deposition of the single NF. Sometimes, the secondary field could be applied between the interdigited electrode (IDE) finger pair and subject to on-chip fabrication of gas sensors (Figure 4.4).

4.7.2 E-Noses and Nano-e-Noses Using NFs

E-noses are the devices that are able to detect and discriminate the two or more gases into characteristic patterns. They are being used in several domains such as environmental safety, health care, food quality and aroma testing, industrial and military applications [73]. The challenges being occurring in e-nose devices are miniaturization freedom due to high OT of the gas sensors. To overcome these limitations, several nanoengineering platforms such as surface modifications and processing, low-dimensional nanostructures, and nanohybrids are being studied widely. The use of room-temperature gas sensors in E-nose is demanded due to flexibility in miniaturization of the devices. The use of conducting polymers is proved to have a major
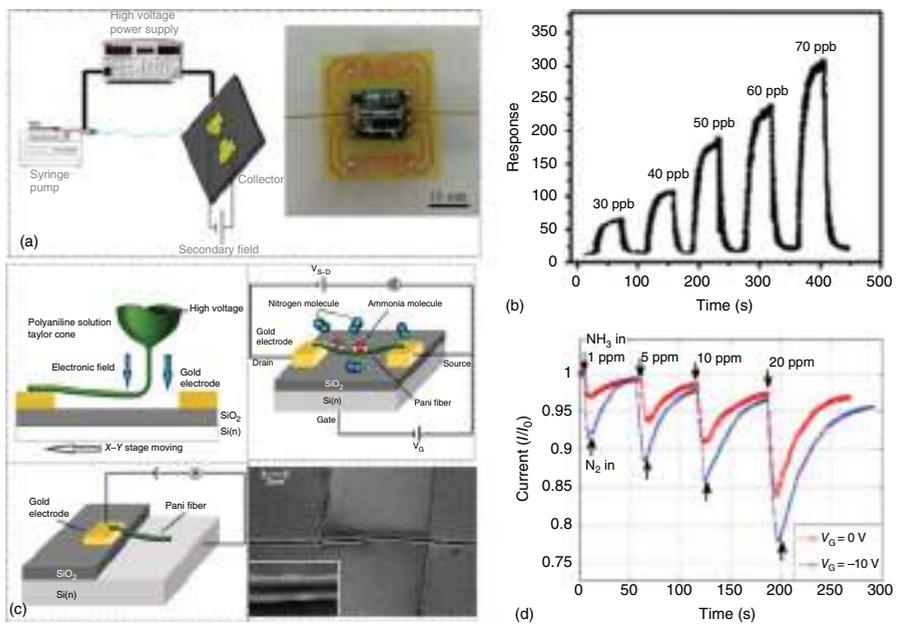
Figure 4.4 Single-aligned NF-based gas sensors, (a, b) TiO_2: Au NF highly sensitive CO gas sensor operating at 250 °C, Source: Nikfarjam et al. [71], Reproduced with permission from American Chemical Society. (c, d) Single PANI NF-based FET, NH_3 gas sensor operating at RT, Source: Chen et al. [72], MDPI, CC BY 3.0.

role in NFs synthesis and also contributes toward achieving room-temperature operating gas sensors. Hence, the employment of NFs study in gas sensing and E-nose miniaturization is more focused recently to fabricate nano-E-noses.

4.7.3 On-Chip Fabrication of Aligned NFs Heterostructures

Recently, on-chip fabrication of aligned NFs and their heterostructures has become possible using the coaxial electrospinning technique, and the technique is proved to be a milestone. It avoids the multiple-step processes during the fabrications allowing the on-chip-fabricated devices that act as best candidates for commercial use. It not only allows the core–shell NFs but also bimetallic doping in the shell of the NFs which helps to improve the surface properties. The use of coaxial electrospinning enables engineering of NFs chemistries and geometries using multiple components and their nanoforms. The schematic representing the coaxial electrospinning is shown in Figure 4.5. R. Vishnuraj et al. has reported the MEMS-compatible, Au:ZnO NFs for NO_2-sensing application [63].
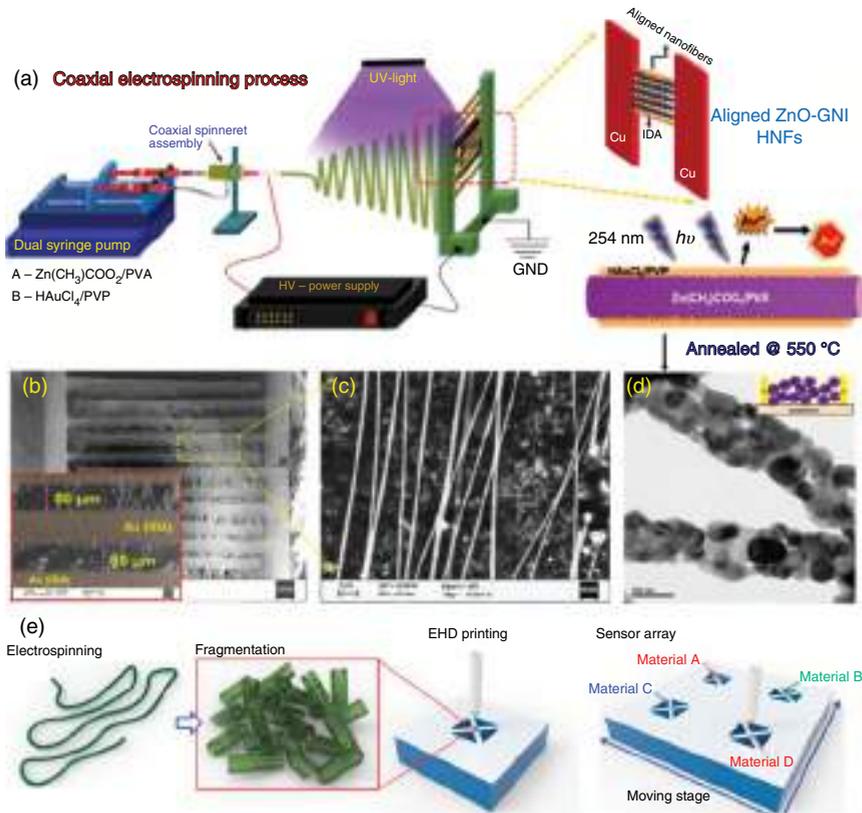
Figure 4.5 (a–d) Schematic of coaxial electrospinning used for on-chip fabrication of aligned ZnO–Au nano-islands of hybrid NFs with *in situ* photoreduction, (b, c) SEM image of aligned NFs deposited on Au IDEs, and (e and d) TEM micrographs of annealed ZnO–Au nano-islands of hybrid NFs. Source: Vishnuraj et al. [63], Royal Society of Chemistry, CC BY 3.0.
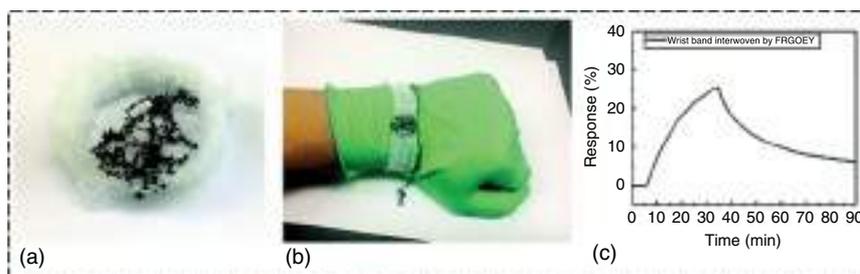
Figure 4.6 (a–c) Trends in the NFs-based wearable electronics, showing use of reduced graphene oxide (RGO)-based e-fibers have been carried out for stretchable and wearable reduced graphene oxide yarn for highly sensitive wearable gas sensors detecting NO_2. Source: Reproduced with permission from Yun et al. [77]/Royal Society of Chemistry.

4.7.4 Wearable Devices

Advancements in flexible and portable electronic devices are growing rapidly due to their near future use in human life [74]. The flexible device configurations in solar cell, flexible E-noses/multifunctional sensors [1], E-skins [75], and electronic smart contact lens [76] are being employed in energy harvesting, health safety, military applications, environment, and agriculture fields. The stretchable electronics has been used as an alternative to flexible devices by overcoming the environmental deformations to achieve the stable device performance. These stretchable materials include the ionogel, liquid metals, and stretchable electronic fibers (e-fibers). These lightweight e-fibers are made available by woven and knitted form with cost-effectiveness. As per the recent findings by Yong Ju Yun et al., [77] the use of RGO-based e-fibers have been carried out for stretchable and wearable RGO yarn for highly sensitive wearable gas sensors detecting NO_2. These RGO e-NFs have demonstrated good stability and repeatability toward the NO_2 detection (Figure 4.6).

4.8 Conclusion and Future Perspectives

The morphology of the nanostructures plays an important role to define the physico-chemical properties and have direct impact on sensor characteristics. Most importantly, the various configurations such as 0D, 1D, and 2D nanostructures have been precisely concluded in order to define their use in specific applications. Among 1D nanostructures, the NFs are looked upon for room-temperature and high-performance sensor devices configurations. By controlling the surface morphology, stoichiometry, and use of multicomponent systems in NFs, the sensor characteristics have shown drastic enhancement and stability over the sensor performance. Hence, it becomes important to study and review the present trends, challenges, scopes, and attempts being made till date. The present chapter highlights the recent trends and development of gas sensors using NFs heterostructures

for gas-sensing application. It is also organized to focus the electrospinning approaches and direct patterning of the NFs for on-chip fabrication of the nanosensors and arrays. It is well understood that the 0D and 1D nanostructures maximize the charge transport due to maximum surface area. Harnessing the benefit of small nanograins in 0D materials as a surface modifier on the outer surface of NFs helps to enhance the sensor performance. The lowered OT in NFs-based gas sensors is proven to be essential characteristics for the deployment of nanosensors and nano-E-noses.

To enhance the performance of NFs-based gas sensors, the heterostructures are subjected to tune the surface properties. It is made possible using the noble metal sensitizers, making nanohybrids and surface modification by means of irradiation with e-beams, lasers, and UV rays. Further, the conducting polymers such as PANI, PPy, PEDOT, and PSS are being studied for NFs-based gas sensors application. The recent trends and fortunate opportunities in the analysis techniques make possible to think upon following opportunities:

(1) The efforts should be made to develop the sensors which operates at temperature scale ranging from <0 to $<50\,°C$. The patterning of NFs in a hydrophobic matrix polymer will be a quest and needs to be studied.
(2) The recent achievements in the NFs heterostructures are good candidates for commercial high-performance solid-state devices, which also includes human sensory systems such as nano-E-noses, E-tongue, E-eye, and E-skin. Furthest evolutionary analysis techniques are being used to understand the basic mechanisms in gas sensors and others devices.
(3) The applicability of various fabrication techniques for single-step possible on-chip fabrications has given new platform for mass-scale production of miniaturized devices. The techniques further help to generate the multiple sensors arrays and best candidates for micro or nano-E-noses, hence becoming useful in day-to-day life wearable devices for military, health, and environmental safety.
(4) Most interesting achievement in the 1D NFs is the ordering and alignment of single-NF-based gas sensors and is not explored widely giving an opportunity to study rigorously.

To fulfill the commercial requirements, the fulfillment of "Ramgir criterion" of 4S parameters, i.e. sensitivity, selectivity, long-term stability, and suitability, is essential. Among them, suitability expresses more concern over the room-temperature gas sensors, as they are required to work over the wide range temperature ($0–50\,°C$) as per the geographical and geospatial conditions. Thus, the present chapter will be valuable addition in the NFs-based gas sensors for the further reference to academics, research, and scientific community.

Acknowledgment

References

1 Park, T., Kim, N., Kim, D. et al. (2019). An organic/inorganic nanocomposite of cellulose nanofibers and ZnO nanorods for highly sensitive, reliable, wireless, and wearable multifunctional sensor applications. *ACS Appl. Mater. Interfaces* 11: 48239–48248.

2 Wang, F., Wu, Y., Huang, Y., and Liu, L. (2018). Strong, transparent and flexible aramid nanofiber/POSS hybrid organic/inorganic nanocomposite membranes. *Compos. Sci. Technol.* 156: 269–275.

3 Hittini, W., Greish, Y.E., Qamhieh, N.N. et al. (2020). Ultrasensitive and low temperature gas sensor based on electrospun organic-inorganic nanofibers. *Org. Electron.* 81: 105659.

4 Lahlou, H., Claramunt, S., Monereo, O. et al. (2021). Preparation of palladium oxide nanoparticles supported on tin oxide nanofibers via modified electrospinning for ultra-low ppb NO_2 detection. *Mater. Today Proc.* 36: 1–9.

5 D'Arienzo, M., Armelao, L., Cacciamani, A. et al. (2010). One-step preparation of SnO_2 and Pt-doped SnO_2 As inverse opal thin films for gas sensing. *Chem. Mater.* 22 (13): 4083–4089.

6 Bhangare, B., Ramgir, N.S., Sinju, K.R. et al. (2020). *Reduced Graphene Oxide (rGO)-Based Nanohybrids as Gas Sensors: State of the Art, Functional Nanomaterials*, 189–217. Springer.

7 Ansari, N., Lone, M.Y., Shumaila, J. et al. (2020). Trace level toxic ammonia gas sensing of single-walled carbon nanotubes wrapped polyaniline nanofibers. *J. Appl. Phys.* 127: 044902.

8 Zhu, J., Cho, M., Li, Y. et al. (2021). Machine learning-enabled textile-based graphene gas sensing with energy harvesting-assisted IoT application. *Nano Energy* 86: 106035.

9 Burman, D., Raha, H., Manna, B. et al. (2021). Substitutional doping of MoS_2 for superior gas-sensing applications: a proof of concept. *ACS Sens.* 6 (9): 3398–3408.

10 Chen, W.Y., Jiang, X., Lai, S.-N. et al. (2020). Nanohybrids of a MXene and transition metal dichalcogenide for selective detection of volatile organic compounds. *Nat. Comm.* 11: 1302.

11 Pang, Z., Nie, Q., Lv, P. et al. (2017). Design of flexible PANI-coated CuO-TiO_2-SiO_2 heterostructure nanofibers with high ammonia sensing response values. *Nanotechnology* 28: 225501 (10pp).

12 Nie, Q., Pang, Z., Li, D. et al. (2018). Facile fabrication of flexible SiO_2/PANI nanofibers for ammonia gas sensing at room temperature. *Colloids Surf. A* 537: 532–539.

13 Hoang, N.V., Hung, C.M., Hoa, N.D. et al. (2019). Excellent detection of H_2S gas at ppb concentrations using $ZnFe_2O_4$ nanofibers loaded with reduced graphene oxide. *Sens. Actuators, B* 282: 876–884.

14 Dang, T.K., Son, N.T., Lanh, N.T. et al. (2021). Extraordinary H_2S gas sensing performance of ZnO/rGO external and internal heterojunctions. *Alloys Comp.* 879: 160457.

15 Nami-Ana, S.F., Nasresfahani, S., Tashkhourian, J. et al. (2021). Nanofibers of polyaniline and Cu(II)–l-aspartic acid for a room-temperature carbon monoxide gas sensor. *ACS Appl. Mater. Interfaces* 13 (33): 39791–39805.

16 Abdel Rahman, N.S., Greish, Y.E., Mahmoud, S.T. et al. (2021). Fabrication and characterization of cellulose acetate-based nanofibers and nanofilms for H_2S gas sensing application. *Carbohydr. Polym.* 258: 117643.

17 Feng, Q., Zeng, Y., Xu, P. et al. (2019). Tuning the electrical conductivity of amorphous carbon/reduced graphene oxide wrapped-Co_3O_4 ternary nanofibers for highly sensitive chemical sensors. *J. Mater. Chem. A* 7: 27522–27534.

18 Jiang, W., Wang, T., Chen, X. et al. (2020). Enhancing room-temperature NO_2 detection of cobalt phthalocyanine based gas sensor at an ultralow laser exposure. *Phys. Chem. Chem. Phys.* 22: 18499–18506.

19 Pang, Z., Yildirim, E., Pasquinelli, M.A., and Wei, Q. (2021). Ammonia sensing performance of polyaniline-coated polyamide 6 nanofibers. *ACS Omega* 6: 8950–8957.

20 Abdali, H., Heli, B., and Ajji, A. (2019). Stable and sensitive amino-functionalized graphene/polyaniline nanofiber composites for room-temperature carbon dioxide sensing. *RSC Adv.* 9: 41240.

21 Bhadra, J., Popelka, A., Abdulkareem, A. et al. (2019). Fabrication of polyaniline–graphene/polystyrene nanocomposites for flexible gas sensors. *RSC Adv.* 9: 12496.

22 Park, H.J., Kim, W.-J., Lee, H.-K. et al. (2018). Highly flexible, mechanically stable, and sensitive NO_2 gas sensors based on reduced graphene oxide nanofibrous mesh fabric for flexible electronics. *Sens. Actuators, B* 257: 846–852.

23 Zhang, J., Lu, H., Liu, C. et al. (2017). Porous $NiO–WO_3$ heterojunction nanofibers fabricated by electrospinning with enhanced gas sensing properties. *RSC Adv.* 7: 40499.

24 Kou, X., Meng, F., Chen, K. et al. (2020). High-performance acetone gas sensor based on Ru-doped SnO_2 nanofibers. *Sens. Actuators, B* 320: 128292.

25 Liu, Y., Wang, R., Zhang, T. et al. (2019). Zeolitic imidazolate framework-8 (ZIF-8)-coated In_2O_3 nanofibers as an efficient sensing material for ppb-level NO_2 detection. *J. Colloids Interface Sci.* 541: 249–257.

26 Guo, J., Li, W., Zhao, X. et al. (2021). Highly sensitive, selective, flexible and scalable room-temperature NO_2 gas sensor based on hollow SnO_2/ZnO nanofibers. *Molecules* 26: 6475.

27 Zhou, J., Ikram, M., Rehman, A.U. et al. (2018). Highly selective detection of NH_3 and H_2S using the pristine CuO and mesoporous $In_2O_3@CuO$ multijunctions nanofibers at room temperature. *Sens. Actuators, B* 255: 1819–1830.

28 Seif, A.M., Nikfarjam, A., and Hajghassem, H. (2019). UV enhanced ammonia gas sensing properties of $PANI/TiO_2$ core-shell nanofibers. *Sens. Actuators B* 298: 126906.

29 Xiong, Y., Li, H., Li, X. et al. (2019). Layer-by-layer self-assembly of polyaniline nanofibers/TiO_2 nanotubes heterojunction thin film for ammonia detection at room temperature. *Nanotechnology* 30: 135501.

30 Han, H., Baik, S., Xu, B. et al. (2017). Bioinspired geometry-switchable Janus nanofibers for eye-readable H_2 sensors. *Adv. Funct. Mater.* 27: 1701618.

31 Pang, Z., Yu, J., Li, D. et al. (2018). Free-standing $TiO_2–SiO_2/PANI$ composite nanofibers for ammonia sensors. *J. Mater. Sci. Mater. Electron.* 29: 3576–3583.

32 Liu, D., Shi, Q., Jin, S. et al. (2019). Self-assembled core-shell structured organic nanofibers fabricated by single-nozzle electrospinning for highly sensitive ammonia sensors. *InfoMat* 1: 525–532.

33 Li, F., Song, H., Yu, W. et al. (2020). Electrospun TiO_2//SnO_2 Janus nanofibers and its application in ethanol sensing. *Mater. Lett.* 262: 127070.

34 Meng, J., Li, H., Zhao, L. et al. (2020). Triboelectric nanogenerator enhanced Schottky nanowire sensor for highly sensitive ethanol detection. *Nano Lett.* 20 (7): 4968–4974.

35 Wong, Y.C., Ang, B.C., Haseeb, A.S.M.A. et al. (2019). Review—conducting polymers as chemiresistive gas sensing materials: a review. *J. Electrochem. Soc.* 167: 037503.

36 Liu, Y., Li, J., Wang, G. et al. (2020). One-step instantaneous detection of multiple military and improvised explosives facilitated by colorimetric reagent design. *Anal. Chem.* 92 (20): 13980–13988.

37 Khachornsakkul, K., Hung, K.-H., Chang, J.-J. et al. (2021). A rapid and highly sensitive paper-based colorimetric device for the on-site screening of ammonia gas. *Analyst* 146: 2919–2927.

38 Kim, D.W., Lee, J.H., Kim, J.K., and Jeong, U. (2020). Material aspects of triboelectric energy generation and sensors. *NPG Asia Mater.* 12: 6.

39 Kenry and Lim, C.T. (2017). Nanofiber technology: current status and emerging developments. *Prog. Polym. Sci.* 70: 1–17.

40 Lim, K., Jo, Y.-M., Yoon, J.-W., and Lee, J.-H. (2019). Metal oxide patterns of one-dimensional nanofibers: on-demand, direct-write fabrication, and application as a novel platform for gas detection. *J. Mater. Chem. A* 7: 24919–24928.

41 Kang, K., Yang, D., Park, J. et al. (2017). Micropatterning of metal oxide nanofibers by electrohydrodynamic (EHD) printing towards highly integrated and multiplexed gas sensor applications. *Sens. Actuators, B* 250: 574–583.

42 Ji, H., Zeng, W., and Li, Y. (2019). Gas sensing mechanisms of metal oxide semiconductors: a focus review. *Nanoscale* 11: 22664.

43 Gurlo, A. and Riedel, R. (2007). In situ and operando spectroscopy for assessing mechanisms of gas sensing. *Angew. Chem. Int. Ed.* 46: 3826–3848.

44 Sinju, K.R., Bhangare, B., Pathak, A. et al. (2022). ZnO nanowires based e-nose for the detection of H_2S and NO_2 toxic gases. *Mater. Sci. Semicond. Process.* 137: 106235.

45 Ramgir, N.S., Bhusari, R., Rawat, N.S. et al. (2020). TiO_2/ZnO heterostructure nanowire based NO_2 sensor. *Mater. Sci. Semicond. Process.* 106: 104770.

46 Kaur, M., Kailasaganapathi, S., Ramgir, N.S. et al. (2017). Gas dependent sensing mechanism in ZnO nanobelt sensor. *Appl. Surf. Sci.* 394: 258–266.

47 Tian, J., Chen, X., Wang, T. et al. (2021). Modification of indium oxide nanofibers by polyoxometalate electron acceptor doping for enhancement of gas sensing at room temperature. *Sens. Actuators, B* 344: 130227.

48 Bhangare, B., Jagtap, S., Ramgir, N.S. et al. (2017). Evaluation of humidity sensor based on PVP-RGO nanocomposites. *IEEE Sensors* 18: 9097–9104.

49 Nair, K.G., Ramakrishnan, V., Unnathpadi, R. et al. (2020). Unraveling hydrogen adsorption kinetics of bimetallic Au−Pt nanoisland-functionalized carbon nanofibers for room temperature gas sensor applications. *J. Phys. Chem. C* 124: 7144–7155.

50 Bhangare, B., Ramgir, N.S., Pathak, A. et al. (2020). Role of sensitizers in imparting the selective response of SnO_2/RGO based nanohybrids towards H_2S, NO_2 and H_2. *Mater. Sci. Semicond. Process.* 105: 104726.

51 Bhangare, B., Ramgir, N.S., Jagtap, S. et al. (2019). XPS and Kelvin probe studies of SnO_2/RGO nanohybrids based NO_2 sensors. *Appl. Surf. Sci.* 487: 918–929.

52 Sanger, A., Kang, S.B., Jeong, M.H. et al. (2018). *Adv. Sci.* 5: 1800816.

53 Tian, X., Yao, L., Cui, X. et al. (2022). Novel Al-doped $CdIn_2O_4$ nanofibers-based gas sensor for enhanced low-concentration n-butanol sensing. *Sens. Actuators, B* 351: 130946.

54 Zhang, M., Sui, N., Wang, R., and Zhang, T. (2021). The effect of shell thickness on gas sensing properties of core-shell fibres. *Sens. Actuators, B* 332: 129456.

55 Ömür, B.C. (2019). Humidity effect on adsorption kinetics of ammonia onto electrospun SnO_2 nanofibers. *Mater. Res. Express* 6: 045043.

56 Farzaneh, A., Esrafili, M.D., and Mermer, O. (2020). Development of TiO_2 nanofibers based semiconducting humidity sensor: adsorption kinetics and DFT computations. *Mater. Chem. Phys.* 239: 121981.

57 Hashemi, M.M., Nikfarjam, A., Hajghassem, H., and Salehifar, N. (2020). Hierarchical dense array of ZnO nanowires spatially grown on ZnO/TiO_2 nanofibers and their ultraviolet activated gas sensing properties. *J. Phys. Chem. C* 124: 322–335.

58 Li, J., Gu, D., Yang, Y. et al. (2019). UV light activated SnO_2/ZnO nanofibers for gas sensing at room temperature. *Front. Mater.* 6: 158.

59 Seif, A.M., Nikfarjam, A., and Hajghassem, H. (2019). UV enhanced ammonia gas sensing properties of PANI/TiO_2 core-shell nanofibers. *Sens. Actuators, B* 298: 126906.

60 Li, W., Guo, J., Cai, L. et al. (2019). UV light irradiation enhanced gas sensor selectivity of NO_2 and SO_2 using rGO functionalized with hollow SnO_2 nanofibers. *Sens. Actuators, B* 290: 443–452.

61 Kim, J.-H., Mirzaei, A., Kim, H.W. et al. (2019). Design of supersensitive and selective ZnO-nanofiber-based sensors for H_2 gas sensing by electron-beam irradiation. *Sens. Actuators, B* 293: 210–223.

62 Chen, Q., Wang, Y., Wang, M. et al. (2019). Enhanced acetone sensor based on Au functionalized In-doped $ZnSnO_3$ nanofibers synthesized by electrospinning method. *J. Colloid. Interface. Sci.* 543: 285–299.

63 Vishnuraj, R., Dhakshinamoorthy, J., Nair, K.G. et al. (2021). MEMS-compatible, gold nano island anchored 1D aligned ZnO heterojunction nanofibers: unveiling the NO_2 sensing mechanism with operando photoluminescence studies. *Mater. Adv.* 2: 3000–3013.

64 Huang, B., Zhang, Z., Zhao, C. et al. (2018). Enhanced gas-sensing performance of ZnO@In_2O_3core@shellnanofibers prepared by coaxial electrospinning. *Sens. Actuators, B* 255: 2248–2257.

65 Nair, K.G., Vishnuraj, R., and Pullithadathil, B. (2021). Integrated co-axial electrospinning for a singlestep production of 1D aligned bimetallic carbon fibers@ AuNPs–PtNPs/NiNPs–PtNPs towards H_2 detection. *Mater. Adv.*, Advance Article.

66 Liu, Y., Gao, X., Li, F. et al. (2018). Pt-In_2O_3 mesoporous nanofibers with enhanced gas sensing performance towards ppb-level NO_2 at room temperature. *Sens. Actuators, B* 260: 927–936.

67 Jaroenapibal, P., Boonma, P., Saksilaporn, N. et al. (2018). Improved NO_2 sensing performance of electrospun WO_3 nanofibers with silver doping. *Sens. Actuators, B* 255: 1831–1840.

68 Huang, B., Wang, Y., Hu, Q. et al. (2018). *J. Mater. Chem. C* 6: 10935–10943.

69 Hu, K., Wang, F., Shen, Z. et al. (2021). Ternary heterojunctions synthesis and sensing mechanism of Pd/ZnO–SnO_2 hollow nanofibers with enhanced H_2 gas sensing properties. *Alloys Comp.* 850: 156663.

70 Rathore, P. and Schiffman, J.D. (2021). Beyond the single-nozzle: coaxial electrospinning enables innovative nanofiber chemistries, geometries, and applications. *ACS Appl. Mater. Interfaces* 13 (1): 48–66.

71 Nikfarjam, A., Hosseini, S., and Salehifar, N. (2017). Fabrication of a highly sensitive single aligned TiO_2 and gold nanoparticle embedded TiO_2 nano-fiber gas sensor. *ACS Appl. Mater. Interfaces* 9: 15662–15671.

72 Chen, D., Lei, S., and Chen, Y. (2011). A single polyaniline nanofiber field effect transistor and its gas sensing mechanisms. *Sensors* 11: 6509–6516.

73 Behera, B., Joshi, R., Anil Vishnu, G.K. et al. (2019). Electronic nose: a non-invasive technology for breath analysis of diabetes and lung cancer patients. *Breath Res.* 13: 024001.

74 Wang, Y., Yokota, T., and Someya, T. (2021). Electrospun nanofiber-based soft electronics. *NPG Asia Mater.* 13: 22.

75 Peng, X., Dong, K., Ye, C. et al. (2020). A breathable, biodegradable, antibacterial, and self-powered electronic skin based on all-nanofiber triboelectric nanogenerators. *Sci. Adv.* 6: 1–10.

76 Wei, S., Yin, R., Tang, T. et al. (2019). Gas-permeable, irritation-free, transparent hydrogel contact lens devices with metal coated nanofiber mesh for eye interfacing. *ACS Nano* 13: 7920–7929.

77 Yun, Y.J., Kim, D.Y., Hong, W.G. et al. (2018). Highly stretchable, mechanically stable, and weavable reduced graphene oxide yarn with high NO_2 sensitivity for wearable gas sensors. *RSC Adv.* 8: 7615–7621.

5

1D Hybrid Tin Oxide Nanostructures: Synthesis and Applications

Pedro H. Suman[1], Alexandre O. Jorgetto[1], Fernanda C. Romeiro[1], Anderson A. Felix[1], Paulo V. Morais[1], Miécio O. Melquíades[1,2], and Marcelo O. Orlandi[1]

[1] *São Paulo State University (UNESP), Institute of Chemistry, Department of Engineering, Physics and Mathematics, Rua Prof. Francisco Degni, 55, Araraquara, 14800-060, Brazil*
[2] *Federal University of Amazonas (UFAM), Institute of Exact Sciences, Department of Physics, Av. General Rodrigo Octávio, 6200, Manaus, 69077-000, Brazil*

5.1 Main Features of 1D Materials

Currently, nanoscience and nanotechnology have significantly contributed to redefining and developing new research paths. These are fields where bottom-up methodologies meet conventional top-down processes. Nanomaterials provide the necessary bridge between atomistic processes and usable macroscale devices. The focus has been mainly on synthesis methods, with specific interests in controlling fundamental properties and architectures. Since the inextricable link between size, geometry, and properties of nanomaterials, it reveals a wide variety of promising applications.

Nanostructures can be classified into some categories based on their dimensionality. In this context, the so-called one-dimensional (1D) nanostructures are usually reported as those whose lateral dimensions are in the nanoscale (1–100 nm). However, the material's properties are considered more important than just dimension limitations. So, the 1D materials can also be defined as the elongated structures presenting different than the same material in bulk form due to the reduced dimensions of materials. Examples include nanorods, nanowires, nanotubes, nanobelts, nanofibers, and nanofilaments [1]. Due to the quantum confinement effects and the long length, these structures are useful for investigating the dependence of electrical/thermal transport in low-dimensionality systems. The narrow width of these materials confines electrons in two dimensions. Consequently,

electronic energy levels are different from those of bulk materials. This characteristic makes 1D materials promising as interconnects and functional units for the fabrication of electronic, optoelectronic, electrochemical, and electromechanical devices with nanoscale dimensions. Among inorganic semiconductor nanomaterials, 1D metal oxide nanostructures are the focus of current research efforts in nanotechnology [2].

Several efforts have been made to develop new synthesis routes and applications for 1D structures. A recent work [3] has demonstrated an approach to explain the effects of low dimensionality on the optical and photocatalytic properties of direct and indirect bandgap materials, using ZnO and α-Fe_2O_3 as a reference. The work demonstrates how the quantum confinement effect can be used for emerging photocatalytic applications. Cho et al. [4] reported a new one-step process for fabricating patterns of hierarchical structures, consisting of 1D microstructures and nanostructures, using a sacrificial layer. Through this method, it is possible to manufacture patterns to control the shape and the density of nanostructures. Zhai et al. [2] provided a comprehensive review of the state of the art of research activities in the field of photodetectors, focusing on 1D metal oxide structures based on ZnO, SnO_2, Cu_2O, Ga_2O_3, Fe_2O_3, In_2O_3, CdO, and CeO_2. Machín et al. [5] demonstrated that 1D TiO_2 and ZnO are being implemented for solar cells applications using a core–shell structure. This structure is composed of a fiber electrode core, another electrode covering the entire system, and an active material sandwiched between them, that is, TiO_2 and/or ZnO. Such devices are being called fiber solar cells (FSCs) [5]. Chen et al. [6], reported a system in which carbon nanotube (CNT) fibers doped with TiO_2 nanoparticles (NPs) are used as the working electrode, while another CNT fiber is used as the counter-electrode. This device had an efficiency of 2.94%. These fibers exhibit efficient energy conversion regardless of incident light angle and cell length, which is an interesting result. Yang et al. [7] presented an approach to produce elastic conductive fibers based on graphene/platinum that were inserted in a long Ti wire, similar to a spring, obtaining an efficiency of up to 7.13%.

Another interesting potential application for 1D structures is their use in flexible electronic devices. The high aspect ratio and the better mechanical elasticity of these materials, when compared to bulk materials or nanoparticles, enabled the development of electronic materials that do not crack and/or delaminate when bent. Lee et al. [8] and Gong et al. [9] have demonstrated the progress of 1D materials based on carbon, metal, metal oxides, polymer, and their hybrid structures, as soft wearable electronics. In particular, extensible conductors, wearable strain and pressure sensors, wearable energy storage devices, wearable heating devices, and 1D material-based extensible LED devices are discussed in detail. 1D nanostructures have also demonstrated advantages for the development of miniaturized, sensitive, and energy-efficient gas sensors. In addition to the high surface-to-volume ratio, effective transport of charge carriers, and high surface energy, 1D nanostructures have a diameter that can reach the Debye length. All of these factors allow for a high variation in the electrical resistance of the sensitive layer after adsorption of gas molecules, enabling the development of high-performance sensors [10].

Hu et al. [11] have reviewed the performance improvements based on materials, morphologies, and subsequent treatments as well as the detection mechanisms of 1D materials for hydrogen gas sensors. The revision made by Yang et al. [12] addressed the main mechanisms of nanoengineering to improve the gas detection performance of 1D metal oxide materials. The integration of these materials into sensor devices is discussed from the perspective of different chemoresistive sensor architectures and fabrication methods.

In most of the works previously mentioned, tin dioxide stands out, with wide application possibilities [13, 14]. This is due to the unique electrical, optical, and electrochemical properties of the SnO_2, in addition to its high thermal stability, biocompatibility, wide bandgap ($E_g = 3.6$ eV at 300 K), and abundant availability [13]. These factors make tin dioxide and the tin oxide-related materials highly relevant from a technological and economic point of view [14–16].

Among the various applications of 1D tin oxides, gas sensing has been one of the most used in commercial devices [17]. This is due to the surface of SnO_2 nanostructures naturally have a certain concentration of defects, such as oxygen vacancies, which are electronically and chemically actives, causing its transport and electrical properties to be significantly affected by the interaction with analyte gases. Some works dedicated exclusively to overview the studies of 1D SnO_2 nanostructures for chemical detection [18]. The main focus is on materials with surface and aspect changes, such as morphology, size, and functionality. The work also discusses the relationship between the properties of the SnO_2 surface and the performance of the sensor from a thermodynamic point of view. Barbosa et al. [19] investigated the effects of decorating SnO nanobelts with platinum (Pt) and palladium (Pd) nanoparticles for the detection of reducing (H_2 and CO) gases. Overall, the decoration improved the performance of the devices, resulting in greater sensitivity at different working temperatures. This was attributed to strong chemical sensitization effects promoted by the Pt and the Pd. The pinning effects of the Fermi level on SnO band structure was also discussed. Several other research works on 1D tin oxides in the field of sensors are interesting to be visited [15, 20–22].

5.2 Synthesis of 1D SnO, Sn₃O₄, and SnO₂ Materials

5.2.1 Hydrothermal Method

The hydrothermal method is an inexpensive approach that provides stability to the synthesis of several materials by using a closed system with pressure and temperature controlled and nontoxic solvents. This method involves heating the precursor solution inside a sealed reactor, increasing its pressure as the temperature exceeds the boiling point of the solution. In this case, the precursors' solubility and reactivity increase [23]. When using the hydrothermal synthesis, the mechanism involved in the nucleation of materials is the dissolution–reprecipitation process. In this process, the dissolution of precursors in the chemical solution, diffusion of dissolved precursor species, and the precipitation of the desired materials take place [23].

One-dimensional (1D) tin oxide nanoarchitectures, such as nanowires and nanorods, have been obtained and attracted attention in the scientific community [24–26]. The growth of 1D materials occurs along one crystallographic direction, and some aspects need to be considered, such as the anisotropic structural feature of the solid, the use of 1D precursors, and the addition of surfactants. Therefore, an extensive study on the synthesis parameters is necessary to determine the crystal growth process of 1D tin oxide structures.

The morphology dimensions and aspect ratio of the SnO_2 nanowires are dependent on the synthesis conditions, including the synthesis time, temperature, and the ratio of Sn^{4+}/OH^- ions in the reaction medium [24]. For instance, by decreasing the $SnCl_4$ precursor concentration in the solution, thinner SnO_2 nanowires can be synthesized, and the formation of nanowires is null by decreasing Sn^{4+} ion concentration and concomitantly increasing OH^- concentration. These results indicate that the growth of SnO_2 nanowires depends on the supersaturation degree of Sn^{4+} ions under hydrothermal conditions [24]. In addition, the length and diameter of 1D SnO_2 nanorods can be influenced by the synthesis parameters [27]. The length of the nanorod was found as 120 nm with a diameter of 45 nm when synthesized for 24 hours, while the nanorods are 150 nm long and 60 nm wide when obtained after 48 hours, and longer length (200 nm) and width (70 nm) when obtained after 72 hours. Moreover, the average length and diameter of SnO_2 nanorods increase with the temperature, showing a dependent relationship between these parameters [27]. Sn-based heterostructures can be also synthesized using the hydrothermal method, like Sn_3O_4/TiO_2 nanobelts [28], $SnO_2–In_2O_3$ nano-heterostructures [29], and $CuO@SnO_2$ nanobelts [30]. In some cases, the heterojunctions are formed by assembling tin oxide nanoparticles on as-prepared 1D structures. As an example, the synthesis of $SnO_2–In_2O_3$ heterojunction is driven by the presence of Sn^{4+} cations, followed by the formation of $Sn(OH)_6^{2-}$ in alkaline conditions and, finally, the SnO_2 nucleation on the surface of In_2O_3 nanowires [29].

5.2.2 Electrospinning Method

The electrospinning technique has demonstrated great potential in designing 1D metal oxide materials for gas-sensing devices, favoring the formation of fine and long fibers with control of both composition and diameter. Additionally, this is a simple and low-cost synthesis method that allows easy tuning of morphological parameters of fibers. Several 1D hybrid materials including $ZnO–SnO_2$ [31], $SnO_2@Co_3O_4$ [32], SnO_2/Fe_2O_3 [33], or $SnO_2–CuO$ [34] can be prepared by the incorporation of different metallic precursors in the polymeric solution or by the surface functionalization of the fiber after the electrospinning process.

This synthesis strategy is based on three main parts: the high-voltage power source, the spinneret, and the conducting collector [35]. Figure 5.1 shows a schematic representation of the synthesis process of the nanofibers using the electrospinning method. In a typical procedure, the solution is injected into a syringe equipped with a stainless needle. A high-voltage power supply is connected between the collector
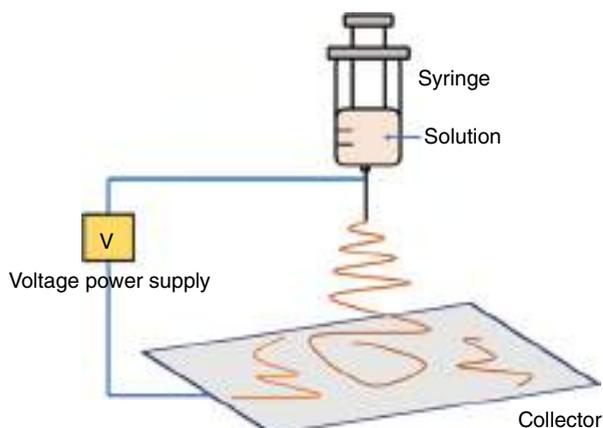
Figure 5.1 Schematic representation of synthesis by the electrospinning method. Source: The authors.

and the needle, creating an electric field [36]. The solution is electrically charged when passing through the tip of the needle and ejected toward an oppositely charged conducting collector, placed at a certain distance from the needle tip. The solvent slowly evaporates while the precursor is released and, consequently, charged fibers are formed on the collector.

The size of the 1D structures can be controlled by several parameters including solution viscosity, concentration, applied voltage, flow rate, humidity, and distance between the tip of the needle to the collector [33, 36, 37]. The use of a polymeric solution to disperse metallic precursors can provide optimal viscosity, and therefore, prevent rapid hydrolysis. On the other hand, the jet needs to reach the collector as stable fibers, which depends on the distance between the tip and the collector and the solvent volatility [36, 37]. Using a higher voltage, improved solution stretching and a stronger electric field are obtained, reducing the fiber diameter [38]. Another important ambient parameter to be considered on the electrospinning methodology is the ambient humidity, which can influence the evaporation of the solvents and thus the solidification rate of the jet containing the precursor solution. At high humidity, the water can condense on the fibers, causing morphological changes to the nanofibers, while at low humidity the formation of thinner fibers with a more dried surface is favored [39].

5.2.3 Chemical Vapor Deposition (CVD)

The chemical vapor deposition (CVD) is a largely used process for 1D nanomaterials synthesis, in which the gas-phase precursors react on a heated substrate via a chemical reaction. A standard CVD equipment consists of a gas delivery system, a sealed reaction chamber (usually a quartz tube), a vacuum system to provide the necessary pressure to transport the reactants, and an exhaust gas treatment system [40].

High-quality products can be obtained using this method as follows: the precursor gases are transported into the reactor and diffuse on the substrate surface. At the gas–solid interface and at high temperature, subsequent reactions promote the desired thin film formation via nucleation, growth, and coalescence. In the final part of the synthesis, gaseous and non-reactant compounds are released from the substrate surface and carried away from the chamber reaction region. The processing parameters of CVD, such as the substrate temperature, atmosphere composition, reaction rate, and pressure, are important to obtain high-quality Sn-based materials [41]. For instance, the temperature in CVD can influence the diameter of SnS nanowires, in which at 650 °C SnS nanowires have grown along the axial direction, presenting a short diameter of the fiber because of the lower nucleation barrier at the top facet of the SnS nanowires. At higher temperatures, the diameter of the nanowires becomes wider due to the growth on the sidewalls of the nanowires [42]. For the synthesis of SnO_2 nanowires, the temperature parameter can positively influence the efficiency of the materials obtainment, when the amount of material is directly proportional to the synthesis temperature [41]. Different nitrogen gas flow in the CVD process was investigated (10, 20, 40, 80, 160, and 240 sccm), and minor efficiency difference was observed for all these parameters, indicating that the gas flow has lower influence on the synthesis yield [41]. In another experiment, oxygen was used as the reaction gas to obtain SnO_2/ZnO heterostructure using the plasma-enhanced chemical vapor deposition (PECVD) [43]. The deposition time necessary to obtain SnO_2 nanorods was studied from 20 to 120 minutes. After 20 minutes of synthesis, only a seed layer of SnO_2 grains was formed, while the growth of short nanorods was observed after 40 minutes. In addition, longer well-aligned SnO_2 nanorods were obtained using 120 minutes of synthesis [43]. Therefore, besides the temperature, atmospheric, reaction rate, and the 1D Sn-based structures length can be also affected by the deposition time of precursors.

5.2.4 Reactive Sputtering Method

The sputtering methodology is one of the most used techniques for surface coating with metal and metal oxide thin films. It presents advantages, such as versatility, high quality, and excellent adhesion of the films. This process involves an evacuated system wherein the source of coating material (target) is converted into plasma by energetic ions bombardment; the plasma is created by ionization of an inert gas (usually argon). The plasma consisted of Ar^+ ions is moved around the target material due to the presence of a magnetic field and then the ionized plasma transfers its energy by hitting the target atoms, which is sputtered and finally can be condensed on the substrate [44].

With controlled parameters, this method allows the direct formation of 1D nanostructures from the deposition of the precursor target over a substrate or device and also can be used for the physical deposition of nanoparticles (decoration) on as-prepared nanomaterials [45, 46]. SnO_2 nanowires have been grown directly onto a

sensing device for formaldehyde detection using reactive sputtering. In this case, the tin film deposition over the Al_2O_3 substrate was the first step, followed by the gold film deposition over the tin film and a thermal treatment. A great advantage of this method is the *in situ* growth of SnO_2 nanowires on the electrodes, making them appropriate for direct applications [45]. The combination of sputtering with other techniques to obtain modified SnO_2/Pt core–shell nanowires was investigated. SnO_2 nanowires can be fabricated in a tube furnace and then Pt decorated using the sputtering method. In this case, the morphology, distribution, and density of Pt nanoparticles can be affected by the Pt shell thickness adjustment [46]. This can be achieved when the sputtering deposition conditions, such as the pressure in the chamber, the applied bias voltage, the deposition time, the target current, and also the temperature of annealing are optimized [47].

5.3 Tin-Based Hybrid Nanostructures

In the last 10 years, tin-based hybrid nanostructures have also attracted great attention of researchers due to its multifunctional properties. Beyond the SnO_2-based hybrid nanostructures widely investigated, it has grown the interest for hybrid nanostructures based on SnO and Sn_3O_4 phases. This section introduces recent research progress over the synthesis and applications of hybrid tin-based nanostructures, indicating it as an effective and promising approach to the development of a new generation of high-performance devices.

5.3.1 SnO₂-Based Hybrid Nanostructures

SnO_2 is the most thermodynamic stable phase of the tin-based oxides showing high chemical and thermal stability and physical properties that are required characteristics for practical applications [16]. SnO_2 hybrid nanostructures, mainly the oxide-based ones, have been investigated aiming the enhancement of material's properties. For instance, for the gas-sensing application, the preparation of hybrid SnO_2 with n-type or p-type semiconductor oxides or catalytic metals has been studied as an effective approach to improve the sensitivity and selectivity of the gas sensor devices [48, 49]. Similar approaches have been investigated in order to enhance the photoelectrochemical activity of SnO_2 hybrid nanostructures for environmental monitoring [50].

More recently, the hybridization process of SnO_2 with inorganic and organic materials has been a promising research field to design and manufacture new hybrid nanostructures and, consequently, high-performance devices [51–53]. Hierarchical SnO_2@rGO nanostructures composed of rGO nanosheets and SnO_2 nanoparticles have been synthesized using a microwave-assisted route [54]. This hierarchical morphology with ultrahigh surface area and a synergistic effect of SnO_2 and rGO phases led to improved gas-sensing response at room temperature. Two-dimensional (2D) SnS_2/SnO_2 nanoflakes were grown by a CVD route with fine control on the phase

composition [55]. These hybrid nanoflakes showed a considerable improvement in photodegradation of methyl blue dyes demonstrating superior performance compared to the standard P25 TiO_2 material.

Nitrogen-doped SnO_2 nanoparticles coated with carbon were produced using metal–organic framework (MOF) template process [56]. These $SnO_2@C$ nanoparticles prevented volume expansion during discharge and charge processes exhibiting excellent performance as lithium-ion batteries (LIBs) anode. $SnO_2/BiOBr$ films were synthesized via one-step hydrothermal method showing excellent photoactive performance and demonstrating a huge potential for detecting biomarkers in bioanalysis [57]. $SnO_2/CH_3NH_3PbI_3$ photodetector was manufactured using conventional ultrasonic-assisted method. SnO_2 nanosheets were dispersed in the $CH_3NH_3PbI_3$ matrix resulting in a very flexible device with excellent mechanical stability [58]. The combination of SnO_2 with emerging organic and carbon-based materials will be a hot research topic in the next years due to of its great potential in biological and energy storage applications.

5.3.2 Sn_3O_4-Based Hybrid Nanostructures

The mixed-valence Sn_3O_4 phase has exhibited outstanding multifunctional properties [16]. However, its hybridization with other materials has slowly emerged in the last years. Well-aligned TiO_2 nanowires coated with Sn_3O_4 nanoflakes were grown on flexible carbon paper via two-step hydrothermal route and used as photoanodes under visible light [59]. These hybrid arrays contributed to increase the separation of photogenerated electrons and holes due to the good band alignment enhancing its photoelectrochemical performance. Hierarchical hybrid Si/Sn_3O_4 arrays were similarly synthesized and reported as promising high-efficient photoanode for hydrogen production [60]. Hierarchical 2D/2D nitrogen-doped $Sn_3O_4/g\text{-}C_3N_4$ nanostructures were prepared by hydrothermal method showing significant enhancement of the photocatalytic performance [61].

Hybrid Sn_3O_4/carbon-based nanostructures, such as CNTs, graphene nanosheets, and reduced graphene oxide (rGO) nanosheets, have been reported using different hydrothermal routes. Sun et al. have reported the growth of Sn_3O_4 nanoflakes over multi-walled carbon nanotubes (MWCNTs) using one-step hydrothermal method obtaining 3D hierarchical Sn_3O_4–CNTs nanostructures [62], as shown in Figure 5.2, which have exhibited extraordinary photocatalytic activity, promoting the decomposition of organic contaminants under visible and/or solar light. Hierarchical $Sn_3O_4/CNTs/graphene$ hybrid nanostructures were synthesized by Xie et al. using a multiple-step hydrothermal route showing enhanced energy storage capability for LIBs [63].

However, hybrid Sn_3O_4 with organic materials have barely been reported, as well as its biosensing properties [64]. Yang et al. synthesized hybrid $Sn_3O_4/PDINH$ hybrid nanostructures by the hydrothermal and the recrystallization routes [65]. These hybrid nanostructures were applied to treat wound infection in a mice
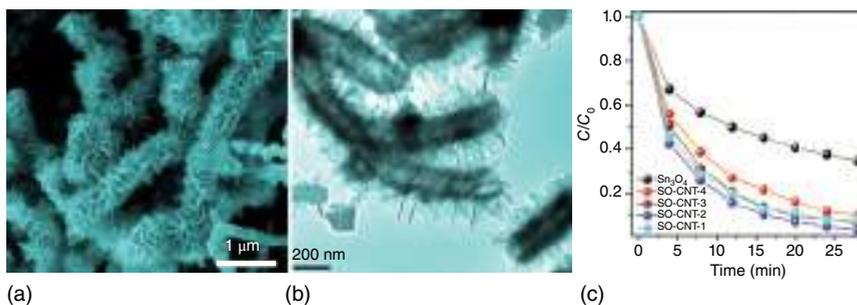
Figure 5.2 (a) Scanning electron microscope (SEM) and (b) Transmission electron microscope (TEM) images and (c) the photocatalytic degradation activity of the CNTs@ Sn_3O_4 hybrid nanostructures prepared by hydrothermal method. Source: Sun et al. [62], Reproduced with permission from Elsevier.

showing to be a nontoxic, stable, and easily tunable material. This result gives new ideas and indicates that Sn_3O_4 hybrid nanostructures have great potential for biological, and perhaps, biosensing applications.

5.3.3 SnO-Based Hybrid Nanostructures

Stoichiometric SnO is a metastable phase with thermodynamic stability up to 400 °C. It has a narrow bandgap (0.7 eV) and is commonly reported as a p-type semiconductor, while SnO_2 and Sn_3O_4 materials presents n-type semiconducting behavior [16]. SnO hybridization with other materials has not been deeply studied, and the exiting works are usually limited to low-temperature applications. Hybrid SnO/ZnO nanowires were prepared using a CVD route via the vapor–liquid–solid (VLS) mechanism [66], as shown in Figure 5.3. These biaxial hybrid nanowires showed a p-type semiconducting behavior, good selectivity to NO_2 as well, and low detection limit at room temperature. Wang et al. reported the electrical, photovoltaic, photosensing, and thermal-sensing properties of hybrid 2D SnO/MoS_2 van der Waals
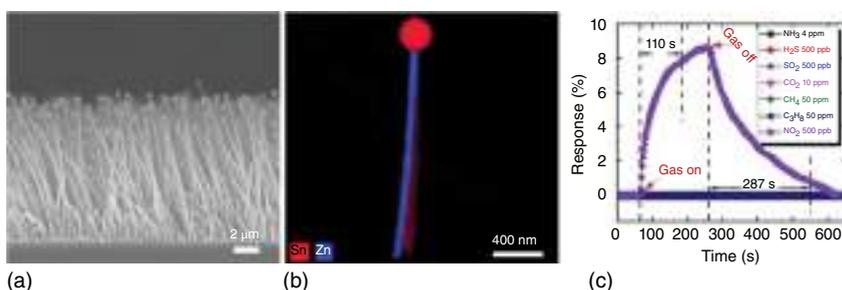

Figure 5.3 (a) SEM, (b) X-ray energy dispersive spectroscopy (EDS)/TEM mapping, and (c) transient response to different gases at room temperature of the biaxial SnO/ZnO hybrid nanowires. Source: Hung et al. [66], American Chemical Society.

heterojunctions produced using complementary nanomanufacturing tools. This 2D hybrid nanostructure rises as a promising multifunctional system for application in nanoelectronic-based devices [67].

Ultrasonic reaction method was employed to prepare hierarchical SnO/ nanographite microspheres composed of well-dispersed graphite nanoparticles inserted in SnO nanosheets. These hybrid nanostructures showed excellent photocatalytic activity on the degradation of methyl orange (MO) pollutant [68]. Volatile organic compounds (VOCs)-sensing response of SnO/rGO nanocomposites synthesized by hydrothermal method were investigated at low operating temperatures displaying good sensitivity and selectivity for ethanol detection in ppb level [69]. Hybrid Au/SnO/Ag nanostructured films were produced using chemical dealloying and electroless plating techniques as SERS-active substrates for resonant and non-resonant molecule detections down to single-molecule levels [70]. The use of SnO hybrid nanostructures in biological and biosensing applications is still a road to be paved.

5.4 Gas-Sensing Performance of 1D Tin Oxide-Based Hybrid Nanostructures

5.4.1 Pristine 1D Tin Oxide Nanostructures

1D materials are attractive building blocks for assembling gas sensor devices taking advantage of the quantum confinement of electrons in two dimensions and the high surface-to-volume ratio. Among the available source materials, 1D nanostructures from semiconducting metal oxides (SMOx) have been interesting architectures, given their structural, morphological, chemical, and electronic properties [71–73]. Since Taguchi's findings [74], stannic oxide (SnO_2) remains the most used SMOx material in commercial solid-state chemoresistors. However, the first investigations on gas sensors based on 1D tin oxide materials were reported in the early 2000s. Comini et al. showed the sensing properties of single-crystalline SnO_2 nanobelts toward NO_2, CO, and C_2H_6O analytes [75]. The possibility of manufacturing nanosensors using individual single-crystalline SnO_2 nanobelt was also demonstrated, although these devices required the aid of UV light exposure to achieve reversible responses at room temperature [76–78]. Wang et al. analyzed the ability of polycrystalline SnO_2 nanowires to detect CO, H_2, and C_2H_6O at room temperature [79]. The porous structure of the sensing layer provided high sensitivity and reversibility of the signals without the need for UV light exposure.

From these studies, the growing interest in a series of 1D SnO_2 nanomaterials and other stoichiometries of tin oxides as active layers in chemoresistors opened up new opportunities for sensing applications in the last two decades. Our group has reported a well-controlled synthesis to prepare SnO and Sn_3O_4 nanobelts using the carbothermal reduction method [22, 41, 80, 81]. These structures presented remarkable sensor response to NO_2 and excellent selectivity to H_2, CO, and CH_4 at 200 °C

compared to SnO_2 when using sensing layers based on multiple randomly oriented nanobelts [20]. Besides, devices fabricated using an individual nanobelt were also sensitive to NO_2 [82].

Despite the excellent sensing performance of pristine tin oxide-based gas sensors toward a wide range of harmful and toxic gaseous compounds, the introduction of additives in the host material has been a strategic alternative to suppress the typical working limitations of SMOx gas sensors, such as the cross-sensitivity in multiple-gas environments (low selectivity), high response time, and the demand for elevated operating temperatures. Surface chemistry engineering has been the primary procedure used to solve those specific requirements. This process is usually achieved from different approaches, including doping, loading, and surface functionalization with noble metal nanoparticles and fabrication of heterostructures and composites materials, which will be addressed in the following sections.

5.4.2 Doping, Loading, and Surface Functionalization with Noble Metals

Doping involves the insertion of impurities (metal ions) into the crystalline lattice of the host material. The incorporation of metallic nanoparticles (secondary phase) in the bulk and surface of the oxide compound refers to the metal loading. Functionalized metal oxides are associated with the covering of the SMOx surface with metallic nanoparticles, generally obtained through impregnation processes. Due to the higher stability and catalytic activity, noble metals (Pt, Pd, Ag, Au, etc.) have been mainly used for these purposes instead of common transition metals (Cu, In, Al, Ga, etc.) aiming to tune the sensitivity, selectivity, and stability of chemoresistive gas sensors [83].

The effect of the metallic additives on the SMOx gas sensor response is understood in terms of two fundamental mechanisms proposed by Yamazoe et al. [84]: chemical sensitization (spillover mechanism) and electronic sensitization (Fermi-level pinning mechanism). In the chemical sensitization, the catalytic metal clusters act as preferred additional adsorption and activation sites for the target molecules, promoting the spillover of reactive species onto the SMOx surface for following interaction with ionosorbed oxygen species. In the electronic sensitization, the electronic coupling of the metal nanoparticles and the host SMOx, resulting from the Fermi levels' pinning, induces an electron-depleted space-charge layer at the metal–SMOx interface. Consequently, the sensor performance can be modulated as a function of the metallic nanoparticles' characteristics, such as size, shape, chemical composition, concentration, coverage distribution, and reactivity.

As mentioned before, the catalytic effects of Pt/PtO and Pd/PdO nanoparticles on the gas-sensing performance of SnO nanobelts were already examined [19]. While pristine SnO exhibited a strong response to NO_2 [19, 20], the noble metal functionalization induced enhanced chemical and/or electronic sensitization effects, resulting in increased sensitivity to H_2 and CO analytes. The combination of the interesting 1D structures with strategic metal decoration led to selective SnO-based gas sensors. Lee et al. investigated the relationship between surface coverage with
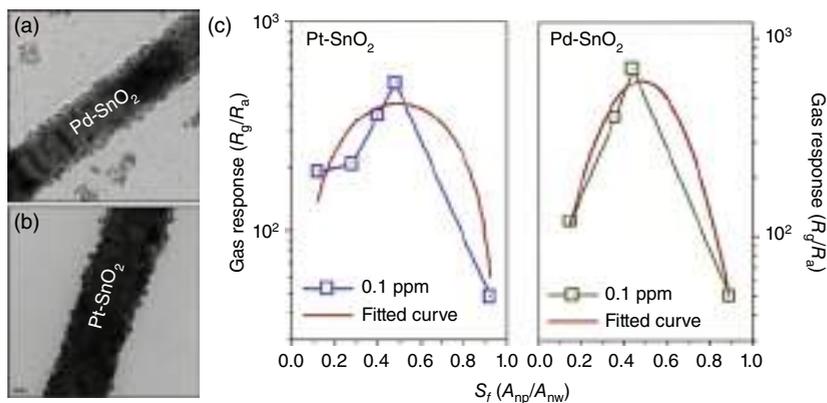
Figure 5.4 TEM images of (a) Pd- and (b) Pt-functionalized SnO_2 nanowires. (c) Sensor response of Pt-SnO_2 and Pd-SnO_2 nanowire sensors to 0.1 ppm NO_2 as a function of the surface coverage (S_f), defined as the ratio of the average surface area of the metallic nanoparticles (A_{np}) to the surface area of SnO_2 nanowires (A_{nw}). Source: Lee et al. [85], Reproduced with permission from Elsevier.

metal nanoparticles on the sensing performance of SnO_2 nanowires [85]. In this study, the surface of the nanowires was functionalized with different amounts of Pt and Pd catalysts. It was revealed the essential role of optimizing the nanoparticles' distribution to maximize the sensing response to NO_2 (Figure 5.4).

5.4.3 Heterostructures and the Effect of Heterojunctions in Gas-Sensing Performance

The combination of n-type and p-type SMOx materials to prepare heterostructures (n–p, n–n, and p–p junctions) has been another strategic approach to produce highly sensitive and selectivity hybrid sensors [48, 86]. The physical-chemistry properties at the interface of the composite materials (heterojunction) differ from the single-compound junctions. Then, the engineering of the interface can play a key role in optimizing the sensor's performance when a p–n junction is established. In p–n junctions, electrons flow across the interface from higher energy levels to unoccupied lower energy states, leading to the bending of the conduction and valence bands to equilibrate the Fermi level. It results in a charge depletion layer at the interface, favoring the oxygen ionosorption and improving the sensing response [87].

1D n-SnO_2/p-NiO core–shell nanowires were synthesized by a two-step process combining VLS and atomic layer deposition (ALD) [21]. The sensing performance to H_2 detection followed the NiO shell layer thickness and reached the higher response using a 4.1 nm layer, where the space-charge region was increased. Kim et al. carried out a similar study using n–n heterojunctions by producing a series of ZnO–SnO_2 core–shell nanowires with the SnO_2 shell thickness ranging from 0 to 120 nm [88]. The highest responses to CO, C_6H_6, and C_7H_8 were achieved in the
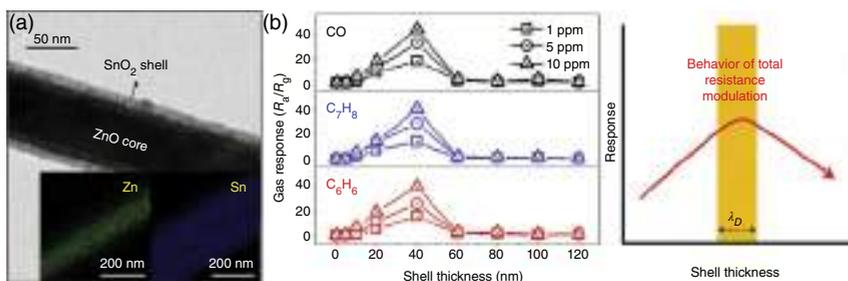
Figure 5.5 (a) TEM image and elemental mapping from EDS analysis (inset) of a ZnO–SnO$_2$ core–shell nanowire. (b) Gas-sensing response of ZnO–SnO$_2$ nanowires with different shell thicknesses toward 1, 5, and 10 ppm of C$_6$H$_6$, C$_7$H$_8$, and CO target gases. Profile of the sensor response as a function of the SnO$_2$ shell thickness, where λ_D is the Debye length of the shell material. Source: Kim et al. [88], Reproduced with permission from Elsevier.

optimized shell thickness of 40 nm (Figure 5.5). The gas-sensing mechanism was proposed based on the contributions from the radial modulation effect and the fraction of volume of the shell layer.

5.4.4 Composites with Carbon-Based Materials

Among multiple possible atomic arrangements of carbon atoms, graphene and CNT are the most exciting allotropes. CNTs are assembled from the roiling up of one or more graphite sheets in a 1D hollow tubular structure (single-walled nanotube [SWNTs] or multi-walled nanotubes [MWNTs], respectively) [89, 90]. In contrast, graphene (and its derivate graphene oxide [GO] and rGO) is a 2D material composed of a single layer of graphite where carbon atoms are arranged into a planar structure [91]. Both materials exhibit extraordinary p-type electrical conductivity and high specific surface area, allowing chemical sensors to operate at room temperature [92].

Inaba et al. prepared n-SnO$_2$/p-CNT composites using dielectrophoretic assembly and investigated the influence of SnO$_2$ and CNTs ratio on the NO$_2$-sensing response [93]. The devices reached sensor signals of 80 and 20 to 1 ppm of NO$_2$ in N$_2$ and O$_2$ atmospheres, respectively. The number of p–n heterojunction formed at the SnO$_2$/CNT interface was related to the observed enhanced signals. The role of GO incorporation on the sensing performance of SnO$_2$ nanotubes to ethanol was analyzed by Reddy et al. [94]. The presence of GO on the SnO$_2$ structures induced a fast sensor response (9 seconds) coupled with a high signal of 85 to 100 ppm ethanol at 300 °C, which was higher compared to pristine SnO$_2$ nanotubes. Li et al. produced a UV-light-activated gas sensor using rGO functionalized with hollow SnO$_2$ nanofibers as the sensing layer [95]. rGO/SnO$_2$ nanocomposites showed selective and reversible responses to NO$_2$ and SO$_2$ at room temperature under UV light illumination. The improved sensing performance of the composites was attributed to the modulation effect of UV light assistance on the gas detection and the synergistic effect of the rGO and SnO$_2$ materials to the p–n heterojunction formation.

5.4.5 Composites with Conducting Polymers

Chemoresistive gas sensors typically operate in the temperature range from 200 to 400 °C to favor the reactions between the target gases molecules and the chemosorbed oxygen species on the surface of the sensing layers [96]. At room temperature, the gaseous species interacts with the SMOx surface by physisorption, and then the transduction of the electronic signals is compromised, resulting in typical low sensitivity. Conducting polymers, such as polyaniline (PANI), polypyrrole (PPy), and polyacetylene (PA), present intrinsically high conductivity in both undoped and doped states due to the highly delocalized, polarized, and electron-dense π-bonds on their backbone [97]. Thus, they are suitable alternatives for flexible and high-performance composite sensors operating at room temperature [97, 98].

Liu et al. described the fabrication of flexible room-temperature NH_3 sensors onto a polyethylene terephthalate (PET) platform using PANI-coated Rh-doped SnO_2 hollow nanotubes as the sensitive layer [99]. High selectivity against more than 15 gaseous species was found due to the particular deprotonation/protonation process to NH_3 by PANI. Undoped and doped (Ni and Pd) SnO_2/PANI/P3HB biodegradable nanocomposite fibers demonstrated high sensor responses to ethanol at 80 °C [100]. This performance was attributed to the p–n heterojunction between SnO_2 and PANI, the large surface-to-volume ratio of the 1D structure, and the presence of the catalyst nanoparticles. Jun et al. reported the fabrication of a complex PPy-coated SnO_2 tube-in-tube structure [101]. The material was highly sensitive to dimethyl methylphosphonate (DMMP) at room temperature, even for concentrations lower than 0.05 ppb.

5.5 Photo(Electro)Catalytic Application of 1D Tin Oxide-Based Heterostructures and Doped Materials

In this section, we address 1D tin oxide-based heterostructures and doped materials applied in photo(electro)catalysis, including photodegradation of organic compounds and gases, photo(electro)catalytic water splitting, and the photocatalytic oxidation of benzyl alcohol.

5.5.1 Photocatalytic Degradation of Organic Pollutants and NO Gas and Photocatalytic Conversion of Benzyl Alcohol into Benzaldehyde Using 1D Tin Oxide-Based Materials

The combination of SnO_2 with TiO_2 has been the main strategy to develop 1D tin oxide-based composite photocatalysts to decompose organic contaminants or NO gas. The production of such materials has been noted to involve the formation of conjugated, interspersed, or decorated phases in a heterostructure. These different approaches are addressed in this section.

Liu et al. [102] prepared side-by-side conjugated SnO_2/TiO_2 nanofibers, which were tested for the photodegradation of Rhodamine B (RB). The produced SnO_2/

TiO_2 nanofibers were able to mineralize all RB content in ~80 minutes under ultraviolet (UV) light irradiation. Concerning the formation of interspersed phases, Shi et al. [103] prepared highly porous interspersed SnO_2/TiO_2 nanofibers. These heterostructures were also employed in the decomposition of RB under UV–visible light irradiation, providing a photodegradation efficiency of 99% in 30 minutes. Another approach employed to obtain 1D tin-oxide/TiO_2-based photocatalysts is the production of heterostructures via decoration of 1D SnO_2 nanostructures with TiO_2, or vice versa, which may lead to the formation of core–shell nanostructures in some cases. For the TiO_2-coated SnO_2 1D heterostructures, Cheng et al. [104] performed the deposition of a TiO_2 layer on the surface of SnO_2 nanotubes. These heterostructures were applied in the photodegradation of methylene blue (MB) under UV light irradiation, exhibiting a photodegradation rate constant of $0.263 h^{-1}$. Pan et al. [105] synthesized $TiO_2@SnO_2$ core–shell nanowires. The efficiency of the produced material in the decomposition of methyl violet under UV light irradiation was tested, reaching a decay constant of $0.87 h^{-1}$.

Nirmala et al. [106] decorated the surface of TiO_2 nanofibers with SnO_2 nanoparticles for the photodegradation of MB and MO. Their photocatalytic experiments indicated that the material decomposed nearly all MB content in 60 minutes and 87.5% of MO in 80 minutes. Huy et al. [107] applied the SnO_2-coated TiO_2 nanotubes for the gas–solid photocatalytic degradation of NO gas under visible light irradiation, obtaining a decomposition efficiency of 59.5% for NO concentration in 30 minutes; the photocatalytic activity of SnO_2-coated TiO_2 nanotubes synthesized by Hou et al. [108] was determined in terms of the photodegradation of MB under UV light illumination, resulting in a decomposition of all MB content in 20 minutes.

The combination of SnO_2 with CNTs (or related materials) is another common strategy attempted to obtain high-efficiency photocatalysts. In Kim et al.'s investigation [109], CNTs heterostructures decorated with SnO_2 nanoparticles were tested for the photodegradation of MB and MO under UV–visible light irradiation. Results showed a MB decomposition of 93% after 180 minutes of light irradiation, whereas the decomposition of MO by the CNTs/SnO_2 composite reached 79% for the same time interval. Ahmaruzzaman et al. [110] employed CNTs decorated with SnO_2 nanoparticles to carry out the photodegradation of alizarin red S (*ARS*) and metronidazole (*MN*). The authors verified that the CNTs/SnO_2 heterostructures were able to photodegrade ~97% and 82% of ARS and MN, respectively, in 45 minutes under UV light illumination. Wu et al. [111] obtained a RB photodegradation efficiency of 95.6% in 150 minutes with CNTs decorated with SnO_2 nanoparticles. The literature shows many other works on heterostructures based on carbon and tin oxide, like SnO_2-decorated multi-walled CNTs [112], SnO_2-decorated N-doped CNTs [113], and carbon quantum dots [114, 115].

1D heterostructures combining SnO_2 and ZnO for the photodegradation of organic compounds have also attracted the attention of the research groups. Concerning interspersed 1D tin oxide/ZnO heterostructures, Zhang et al. [116] demonstrated the complete decolorization of a RB solution within 30 minutes under UV light irradiation, while Pascariu et al. [117]. obtained a RB photodegradation efficiency of 49% in 360 minutes under visible light irradiation using ZnO/SnO_2

nanofibers. In Chen et al.'s work [118], a similar material was applied in the photodegradation of MB, MO, congo red (*CR*), and eosin red (*ER*) under UV light irradiation. Their photocatalytic experiments demonstrated that the ZnO/SnO$_2$ nanofibers decomposed 97.3% of MB in 35 minutes, 98.8% of CR in 20 minutes, 97.7% of MO in 100 minutes, and 98.9% of ER in 70 minutes. With respect to decorated 1D tin oxide/ZnO heterostructures, Sehar et al. [119] synthesized heterostructures consisting of arrays of SnO$_2$-coated ZnO nanorods, which were employed in the photodegradation of MB and MO, decomposing ~80% of MO and 55% of MB in 125 minutes under UV light irradiation. Concerning the use of another tin oxide phase to decorate ZnO 1D nanostructures to undertake the photodegradation of organic contaminants, Harish et al. [120] synthesized SnO-decorated ZnO nanorods to photodegradate MB under visible light irradiation, and total decomposition of MB was reached after 28 minutes. The decoration of 1D SnO$_2$ nanostructures with ZnO has also been reported. Lan et al. [121] developed a photocatalyst consisting of core–shell SnO$_2$-coated ZnO nanowires sensitized with Ag$_2$S quantum dots. They evaluated its photocatalytic activity with basis on its ability to decompose MB under either UV or visible light. Their results demonstrated that the Ag$_2$S-sensitized ZnO/SnO$_2$ nanowires reached a MB photodegradation efficiency of 71.6% under visible light in 60 minutes, whereas that obtained under UV was 57.58%.

Besides the fabrication of 1D tin oxide-based composites with TiO$_2$, C-based materials and ZnO, the combination of SnO$_2$ with BaTiO$_3$, V$_2$O$_5$, ZnS, Ag, and SrO to undertake the photocatalytic decomposition of organic contaminants has also been reported. In this respect, Selvarajan et al. [122] fabricated SnO$_2$ nanorods decorated with BaTiO$_3$, which were applied in the photodegradation of *o*-chloroaniline (*CA*) and MB. Their results demonstrated that the material was able to decompose ~91% of CA and ~84% of MB within 180 minutes under UV–visible light irradiation. Shahid et al. [123] fabricated V$_2$O$_5$ nanowires coated with SnO$_2$ nanoparticles. The resulting V$_2$O$_5$/SnO$_2$ nanowires were tested for the photocatalytic degradation of toluidine blue O dye under UV light irradiation, obtaining a decomposition of nearly 100% of the dye content in ~35 minutes. Lee et al. [124] produced ZnS nanorods and deposited SnO$_2$ quantum dots on its surface. They evaluated the photocatalytic activity of these heterostructures in terms of the photodegradation of RB and phenol in water, observing that nearly all RB content was decomposed within 50 minutes. With respect to the photodegradation of phenol, the rate constant was determined as 0.0074 min^{-1}. Liu et al. [125] produced Ag nanowires and coated these nanostructures with a SnO$_2$ layer. As these heterostructures were tested for the photodegradation of RB under UV or visible light irradiation, it was verified that 93% of RB was degraded in 35 minutes and 80% in 200 minutes, under UV and visible light illumination, respectively. Sultana et al. [126] fabricated SnO$_2$/SrO nanowires, subsequently using these materials to phodegrade acid red 88 (*AR*), metalaxyl (*ML*), and tinidazole (*TN*). Their photocatalytic experiments were performed under UV light irradiation and provided rate constants of 3.00, 2.40, and 1.60 s^{-1} for the degradation of AR, ML, and TN, respectively.

In an alternative photocatalytic application, Liu et al. [127] developed a photocatalyst consisting of CdS nanorods decorated with SnO$_2$ nanoparticles for the

photocatalytic and selective oxidation of benzyl alcohol (*BA*) into benzaldehyde (*BAD*) under visible light irradiation. Their results demonstrated that these heterostructures yielded 80% of BAD conversion after eight hours of irradiation.

5.5.2 Photo(Electro)Catalytic Water Splitting with 1D Tin Oxide-Based Materials

The combination of SnO_2 with TiO_2 is a common approach to carry out water splitting. Radecka et al. [128] produced interspersed TiO_2/SnO_2 nanotubes arrays and determined their theoretical water splitting performances with basis on photoelectrochemical catalysis (PEC) measurements collected under simulated sunlight. The conversion efficiencies reported for these TiO_2/SnO_2 nanotubes arrays reached 2.72%. An example involving SnO_2-coated TiO_2 nanorods was provided by Sun et al. [129]. By decorating interspersed rutile-anatase TiO_2 nanorods arrays with SnO_2 quantum dots, they developed a photocatalyst to carry out water splitting, generating 1100 µmol of H_2 and 500 µmol of O_2 in a 5-hour photocatalytic run, under simulated solar light irradiation. The employment of doped SnO_2 varieties in 1D TiO_2 materials has also been demonstrated. Park et al. [130] carried out the decoration of Sb-doped SnO_2 (ATO) nanowires arrays with spherical anatase TiO_2 nanoparticles, yielding a theoretical maximum H_2 production of 0.41% under simulated solar light.

Other 1D tin oxide-based heterostructures employed in H_2 evolution involve the combination of SnO_2 with SiC, In_2O_3, SnS_2, ZnO, and Au. In this aspect, Liao et al. [131] prepared SiC/SnO_2 nanowires by the decoration of SiC nanowires with SnO_2 nanoparticles. The material was employed under simulated sunlight irradiation, and their results demonstrated a H_2 generation rate of 274 µmol/g/h. Liu et al. [132] fabricated SnO_{2-x}/In_2O_{3-y} nanowires by means of the deposition of an indium film on the surface of SnO_2 nanowires, followed by their annealing under low or ultrahigh vacuum, leading to the formation of In_2O_3 islands onto the SnO_2 nanowires. They verified that the heterostructures produced under ultrahigh vacuum provided the highest H_2 production of all tested samples. Li et al. [133] performed the sulfurization of SnO_2 nanotubes to obtain SnO_2 nanotubes coated with a SnS_2 layer. The heterostructures yielded a H_2 production rate of 50 µmol/h under visible light irradiation. Li et al. [134] decorated ZnO nanorods with SnO_2-coated Au nanoparticles to fabricate a photoanode to perform photoelectrocatalytic water splitting. Their results on the photoelectrocatalytic activity of the photoanodes were determined with basis on PEC measurements collected under white light illumination and yielded a photoconversion efficiency of 0.55%.

5.6 Other Applications of 1D Tin Oxides

Tin dioxide materials (SnO_2) have also been studied as anode material for LIBs applications, which is used in most advanced devices presenting higher power densities compared to other battery systems. SnO_2 exhibits an excellent electrochemical

behavior and a theoretical capacity of 992 mAh/g [135], faster lithiation/delithiation kinetics, enhanced cyclability, and higher operating voltage than traditional carbonaceous anode [135–137]. This specific capacity is more than twice the conventional graphite capacity [138]. However, the large volume expansion–contraction (around 300%) presented by SnO_2 during the charge–discharge process can jeopardize the cycling life of electrodes [138].

Nanostructured SnO_2 is reported as a partial solution to solve the volume variation observed from bulk SnO_2, since the nano-morphology drastically affects the material properties [135, 139]. In addition, the use of 1D SnO_2 can minimize some negative effects in LIBs, as the LiO_2 formation contributes to Li^+ storage, which induces an initial irreversible capacity and prevents the abrupt loss of the capacity caused by volume variation [135, 137, 140]. In this way, SnO_2 is a promising active anode material for next-generation LIBs.

SnO_2-based anodes assembled from nanowires showed a higher specific capacity for lithium insertion when compared with anodes based on nanoparticles, and this improved capacity is retained even at fast discharge rates (>700 mAh/g) [137, 141, 142]. SnO_2 nanowires are reported to provide more reaction sites on the surface and enhance the charge transfer in electrochemical reactions. In addition, SnO_2 nanowires exhibit an initial Coulombic efficiency of ~46.91% coupled with a reversible specific capacity higher than 300 mAh/g up to the 50th cycle [141].

Electrodes based on SnO_2 nanorods for LIB anode can be produced in a one-pot template-free alkaline hydrothermal process, and this particular geometry can offer direct channels for efficient electron transport [135]. It is reported that this electrode array provides the capacity retention value of 580 mAh/g (after 100 cycles) at 0.1 C and rate capability (stable 350 mAh/g at 5 C) [143].

Jiao et al. reported the synthesis of SnO_2 nanorods by controlling the state of $SnCl_2 \cdot 2H_2O$ precursor on SBA-15, which was used as a hard template [138]. Electrochemical measurements on SnO_2 nanorods, SnO_2 mesoporous, and nanoparticles revealed that the morphology did not affect significantly the materials initial Coulombic efficiencies. However, the capacitance during the cycles decreased for mesoporous and nanoparticles structures, which is differently from nanorods that presented a higher life cycle due to the effect of the insignificant expansion volume of rods upon the cycling process. Also, the interspace between the nanorods attenuates the voltage associated with lithium uptake [138].

For application in dye-sensitized solar cells (DSSC), SnO_2 material is attractive due to the wide bandgap (3.6 eV) that results in a fewer number of oxidative holes in the valence band under UV illumination providing long-term stability, and the high electron mobility, which is between 100 and 200 cm^2/V s [144–146]. The mobility can be enhanced using 1D nanofibers and nanorods once these morphologies offer direct electron pathways. SnO_2 have been reported with an efficiency of 4.67% for nanorods morphology [144], 4.06% for porous hollow fibers [146], 5.11% for nanotubes [147], 6.17% for SnO_2 nanofibers/TiO_2 composite [147], and 8.61% for SnO_2 nanorods-TiO_2 [144].

Sintering of SnO_2-based materials can produce high-density devices to be employed as varistors. For this application, doping with ions in oxidation states

lower than Sn^{+4} is used to create oxygen vacancies, favoring the densification, and the addition of ions with oxidation state +5 improve the electronic conductivity of material. In this way, the SnO_2–MnO_2–Nb_2O_5 system can present a nonlinear coefficient (α) of 11 with a breakdown electric field (E_b) of 8786 V/cm, while the composition 98.90% SnO_2–1.00% CoO−0.05% Cr_2O_3–0.05% Nb_2O_5 is reported presenting a nonlinear coefficient of 41 and a breakdown electric field of 3990 V/cm [148, 149].

To decrease the high breakdown electric field shown by conventional varistors, it is possible to add 1D SnO_2 nanobelts in the SnO_2 varistor composition, making the tin dioxide applicable in medium- and low-voltage networks. The varistors containing nanobelts exhibited a reduction of up to 75% in the breakdown electric field (270 V/cm) in comparison with varistors without the belts. It is directly related to the long length of the nanobelts and its three-dimensional growth during the sintering, causing the elimination of the grain boundaries, and consequently potential barriers, which creates numerous low electrical resistance parallel paths inside the device [150].

Another attractive application for 1D SnO_2 materials application is in active photonic devices, including light-emitting diodes (LEDs), lasers, and detectors.

The development of nanophotonic systems fully integrated containing nanoscale sources and detector blocks are advantageous for applications ranging from biodetection to information processing. SnO_2 nanowires exhibit properties such as extreme mechanical flexibility and chemical stability that can be interesting in the nanophotonic field. The dimensions of SnO_2 nanowires, between 100 and 400 nm, are optimal for efficiently guide visible and UV wavelengths, which is related with the high index of refraction ($n > 2$). Also, a side-by-side stepped configuration can be formed through optical linkages between active nanowires (GaN and ZnO) and passive nanowires (SnO_2) in which the active and passive elements interact over a few microns, outperform bridged, or direct end-to-end coupling. In this way, it should be possible the development of more functional geometries for optical modulators [135]. Also, the effectively transducing and routing packets of optimal information within an optical computer or communication device can be improved in the future by the integration of high-frequency electrically driven lasers with passive nanowire waveguides [151].

5.7   Final Considerations and Future Outlook

This chapter reviewed the state-of-art synthesis and application of 1D tin oxide hybrid nanostructures, especially on gas sensing and photoelectrocatalysis. SnO_2-based materials have established themselves as semiconductor oxides that remain attractive to modern industry. In addition, the exciting properties of unusual stoichiometries of tin oxide, such as SnO and Sn_3O_4, represent new possibilities for several applications. However, precise stoichiometry control is still required for technological developments of 1D mixed-valence tin oxide materials. Finally, in the next decades, it will be possible to simulate the application of a variety of 1D

materials in practical devices, supporting the decision of researchers. Moreover, the use of big data and machine learning will facilitate the data comparison of different materials, allowing a better understanding of each component in the device response.

Acknowledgments

References

1 Castillo-Blas, C., Montoro, C., Platero-Prats, A.E. et al. (2020). The role of defects in the properties of functional coordination polymers. *Adv. Inorg. Chem.* 76: 73–119.

2 Zhai, T., Fang, X., Liao, M. et al. (2009). A comprehensive review of one-dimensional metal-oxide nanostructure photodetectors. *Sensors* 9 (8): 6504–6529.

3 Edvinsson, T. (2018). Optical quantum confinement and photocatalytic properties in two-, one- and zerodimensional nanostructures. *R. Soc. Open Sci.* 5 (9): 180387.

4 Cho, S.J., Seok, S.Y., Kim, J.Y. et al. (2013). One-step fabrication of hierarchically structured silicon surfaces and modification of their morphologies using sacrificial layers. *J. Nanomater.* 2013: 289256.

5 Machín, A., Fontánez, K., Arango, J.C. et al. (2021). One-dimensional (1d) nanostructured materials for energy applications. *Materials* 14 (10): 2609.

6 Chen, T., Qiu, L., Cai, Z. et al. (2012). Intertwined aligned carbon nanotube fiber based dye-sensitized solar cells. *Nano Lett.* 12 (5): 2568–2572.

7 Yang, Z. (2016). High performance fiber-shaped solar cells. *Pure Appl. Chem.* 88 (1–2): 113–117.

8 Lee, J., Llerena Zambrano, B., Woo, J. et al. (2020). Recent advances in 1D stretchable electrodes and devices for textile and wearable electronics: materials, fabrications, and applications. *Adv. Mater.* 32 (5): 1902532.

9 Gong, S. and Cheng, W. (2017). One-dimensional nanomaterials for soft electronics. *Adv. Electron. Mater.* 3 (3): 1600314.

10 Gupta, V.K., Alharbie, N.S., Agarwal, S., and Grachev, V.A. (2018). New emerging one dimensional nanostructure materials for gas sensing application: a mini review. *Curr. Anal. Chem.* 15 (2): 131–135.

11 Hu, K., Wang, F., Shen, Z. et al. (2021). Enhancement methods of hydrogen sensing for one-dimensional nanomaterials: a review. *Int. J. Hydrogen Energy* 46 (38): 20119–20138.

12 Yang, B., Myung, N.V., and Tran, T.T. (2021). 1D metal oxide semiconductor materials for chemiresistive gas sensors: a review. *Adv. Electron. Mater.* 7 (9): 2100271.

13 Sharma, A., Ahmed, A., Singh, A. et al. (2021). Review—recent advances in tin oxide nanomaterials as electrochemical/Chemiresistive sensors. *J. Electrochem. Soc.* 168 (2): 027505.

14 Chen, Z., Pan, D., Li, Z. et al. (2014). Recent advances in tin dioxide materials: some developments in thin films, nanowires, and nanorods. *Chem. Rev.* 114 (15): 7442–7486.

15 Chen, D., Xu, J., Xie, Z., and Shen, G. (2011). Nanowires assembled SnO_2 nanopolyhedrons with enhanced gas sensing properties. *ACS Appl. Mater. Interfaces* 3 (6): 2112–2117.

16 Orlandi, M.O. (2020). Tin oxide materials. *Tin Oxide Mater.*

17 Choi, K.J. and Jang, H.W. (2010). One-dimensional oxide nanostructures as gas-sensing materials: review and issues. *Sensors* 10 (4): 4083–4099.

18 Ma, Y., Qu, Y., and Zhou, W. (2013). Surface engineering of one-dimensional tin oxide nanostructures for chemical sensors. *Microchim. Acta* 180 (13–14): 1181–1200.

19 Barbosa, M.S., Suman, P.H., Kim, J.J. et al. (2019). Investigation of electronic and chemical sensitization effects promoted by Pt and Pd nanoparticles on single-crystalline SnO nanobelt-based gas sensors. *Sens. Actuators, B* 301: 127055.

20 Suman, P.H., Felix, A.A., Tuller, H.L. et al. (2015). Comparative gas sensor response of SnO_2, SnO and Sn_3O_4 nanobelts to NO_2 and potential interferents. *Sens. Actuators, B* 208: 122–127.

21 Raza, M.H., Kaur, N., Comini, E., and Pinna, N. (2020). Toward optimized radial modulation of the space-charge region in one-dimensional SnO_2-NiO core-shell nanowires for hydrogen sensing. *ACS Appl. Mater. Interfaces* 12 (4): 4594–4606.

22 Suman, P.H., Longo, E., Varela, J.A., and Orlandi, M.O. (2014). Controlled synthesis of layered Sn_3O_4 nanobelts by carbothermal reduction method and their gas sensor properties. *J. Nanosci. Nanotechnol.* 14 (9): 6662–6668.

23 Einarsrud, M.A. and Grande, T. (2014). 1D oxide nanostructures from chemical solutions. *Chem. Soc. Rev.* 43 (7): 2187–2199.

24 Lupan, O., Chow, L., Chai, G. et al. (2009). A rapid hydrothermal synthesis of rutile SnO_2 nanowires. *Mater. Sci. Eng. B Solid-State Mater. Adv. Technol.* 157 (1–3): 101–104.

25 Hou, L.R., Lian, L., Zhou, L. et al. (2014). Interfacial hydrothermal synthesis of SnO_2 nanorods towards photocatalytic degradation of methyl orange. *Mater. Res. Bull.* 60: 1–4.

26 Matysiak, W., Tański, T., Smok, W., and Polishchuk, O. (2020). Synthesis of hybrid amorphous/crystalline SnO_2 1D nanostructures: investigation of morphology, structure and optical properties. *Sci. Rep.* 10 (1): 14802.

27 Lv, Y., Wang, P., Cai, B. et al. (2018). Facile fabrication of SnO_2 nanorod arrays films as electron transporting layer for perovskite solar cells. *Sol. RRL* 2 (9): 1800133.

28 Chen, G., Ji, S., Sang, Y. et al. (2015). Synthesis of scaly Sn_3O_4/TiO_2 nanobelt heterostructures for enhanced UV-visible light photocatalytic activity. *Nanoscale* 7 (7): 3117–3125.

29 Shen, H., Li, L., and Xu, D. (2017). Preparation of one-dimensional SnO_2-In_2O_3 nano-heterostructures and their gas-sensing property. *RSC Adv.* 7 (53): 33098–33105.

30 Zhu, X., Shi, H., Yin, J. et al. (2014). Facile preparation of $CuO@SnO_2$ nanobelts as a high-capacity and long-life anode for lithium-ion batteries. *RSC Adv.* 4 (65): 34417–34420.

31 Du, H., Li, X., Yao, P. et al. (2018). Zinc oxide coated tin oxide nanofibers for improved selective acetone sensing. *Nanomaterials* 8 (7): 509.

32 Bai, S., Liu, H., Luo, R. et al. (2014). $SnO_2@Co_3O_4$ p-n heterostructures fabricated by electrospinning and mechanism analysis enhanced acetone sensing. *RSC Adv.* 4 (108): 62862–62868.

33 Zhu, C., Li, Y., Su, Q. et al. (2013). Electrospinning direct preparation of $SnO_2/$ Fe_2O_3 heterojunction nanotubes as an efficient visible-light photocatalyst. *J. Alloys Compd.* 575: 333–338.

34 Bai, S., Guo, W., Sun, J. et al. (2016). Synthesis of SnO_2-CuO heterojunction using electrospinning and application in detecting of CO. *Sens. Actuators, B* 226: 96–103.

35 Patil, J.V., Mali, S.S., Kamble, A.S. et al. (2017). Electrospinning: a versatile technique for making of 1D growth of nanostructured nanofibers and its applications: an experimental approach. *Appl. Surf. Sci.* 423: 641–674.

36 Bhardwaj, N. and Kundu, S.C. (2010). Electrospinning: a fascinating fiber fabrication technique. *Biotechnol. Adv.* 28 (3): 325–347.

37 Mercante, L.A., Andre, R.S., Mattoso, L.H.C., and Correa, D.S. (2019). Electrospun ceramic nanofibers and hybrid-nanofiber composites for gas sensing. *ACS Appl. Nano Mater.* 2 (7): 4026–4042.

38 Zhang, C., Yuan, X., Wu, L. et al. (2005). Study on morphology of electrospun poly(vinyl alcohol) mats. *Eur. Polym. J.* 41 (3): 423–432.

39 Xue, J., Wu, T., Dai, Y., and Xia, Y. (2019). Electrospinning and electrospun nanofibers: methods, materials, and applications. *Chem. Rev.* 119 (8): 5298–5415.

40 Sun, L., Yuan, G., Gao, L. et al. (2021). Chemical vapour deposition. *Nat. Rev. Methods Prim.* 1 (1): 5. https://doi.org/10.1038/s43586-020-00005-y.

41 Suman, P.H. and Orlandi, M.O. (2011). Influence of processing parameters on nanomaterials synthesis efficiency by a carbothermal reduction process. *J. Nanopart. Res.* 13 (5): 2081–2088.

42 Mudusu, D., Nandanapalli, K.R., Dugasani, S.R. et al. (2017). Growth of single-crystalline cubic structured tin(II) sulfide (SnS) nanowires by chemical vapor deposition. *RSC Adv.* 7 (66): 41452–41459.

43 Huang, H., Gong, H., Chow, C.L. et al. (2011). Low-temperature growth of SnO_2 nanorod arrays and tunable n-p-n sensing response of a ZnO/SnO_2 heterojunction for exclusive hydrogen sensors. *Adv. Funct. Mater.* 21 (14): 2680–2686.

44 Simon, A.H. (2018). Sputter processing. In: *Handbook of Thin Film Deposition*, 4e (ed. K. Seshan and D. Schepis), 195–230. Elsevier.

45 Castro-Hurtado, I., Herrán, J., Mandayo, G., and Castaño, E. (2012). SnO_2-nanowires grown by catalytic oxidation of tin sputtered thin films for formaldehyde detection. *Thin Solid Films* 520: 4792–4796.

46 Na, H.G., Yang, J.C., Kwak, D.S. et al. (2013). Drastic improvement of sensing characteristics in SnO_2 nanowires by functionalizing with Pt. *J. Nanosci. Nanotechnol.* 13 (9): 6216–6221.

47 van Dijk, K., Schaeken, H.G., Wolke, J.C.G. et al. (1995). Influence of discharge power level on the properties of hydroxyapatite films deposited on Ti6A14V with RF magnetron sputtering. *J. Biomed. Mater. Res. Part A* 29 (2): 269–276.

48 Zappa, D., Galstyan, V., Kaur, N. et al. (2018). Metal oxide-based heterostructures for gas sensors – a review. *Anal. Chim. Acta* 1039: 1–23.

49 Li, T., Zeng, W., and Wang, Z. (2015). Quasi-one-dimensional metal-oxide-based heterostructural gas-sensing materials: a review. *Sens. Actuators, B* 221: 1570–1585.

50 Shi, L., Yin, Y., Zhang, L.C. et al. (2019). Design and engineering heterojunctions for the photoelectrochemical monitoring of environmental pollutants: a review. *Appl. Catal., B* 248: 405–422.

51 Xu, M., Zhang, J., Wang, S. et al. (2010). Gas sensing properties of SnO_2 hollow spheres/polythiophene inorganic-organic hybrids. *Sens. Actuators, B* 146 (1): 8–13.

52 Zhang, D., Sun, Y., Li, P., and Zhang, Y. (2016). Facile fabrication of MoS_2-modified SnO_2 hybrid nanocomposite for ultrasensitive humidity sensing. *ACS Appl. Mater. Interfaces* 8 (22): 14142–14149.

53 Xiong, P., Zhu, J., Zhang, L., and Wang, X. (2016). Recent advances in graphene-based hybrid nanostructures for electrochemical energy storage. *Nanoscale Horiz.* 1 (5): 340–374.

54 Yin, L., Chen, D., Cui, X. et al. (2014). Normal-pressure microwave rapid synthesis of hierarchical SnO_2@rGO nanostructures with superhigh surface areas as high-quality gas-sensing and electrochemical active materials. *Nanoscale* 6 (22): 13690–13700.

55 Wang, C.Y., Wu, Y.K., Tsai, L.F. et al. (2021). Visible light photocatalytic properties of one-step SnO_2-templated grown SnO_2/SnS_2 heterostructure and SnS_2 nanoflakes. *Nanotechnology* 32 (30): 305706.

56 Li, F., Du, J., Yang, H. et al. (2017). Nitrogen-doped-carbon-coated SnO_2 nanoparticles derived from a SnO_2@MOF composite as a lithium ion battery anode material. *RSC Adv.* 7 (32): 20062–20067.

57 Long, D., Tu, Y., Chai, Y., and Yuan, R. (2021). Photoelectrochemical assay based on SnO_2/BiOBr p-n heterojunction for ultrasensitive DNA detection. *Anal. Chem.* 93 (38): 12995–13000.

58 He, J., Wu, J., Hu, S. et al. (2019). A low-cost flexible broadband photodetector based on SnO_2/$CH_3NH_3PbI_3$ hybrid structure. *Opt. Mater. (Amst).* 88: 689–694.

59 Xia, W., Qian, H., Zeng, X. et al. (2019). TiO_2@Sn_3O_4 nanorods vertically aligned on carbon fiber papers for enhanced photoelectrochemical performance. *RSC Adv.* 9 (40): 23334–23342.

60 Yang, R., Ji, Y., Li, Q. et al. (2019). Ultrafine Si nanowires/Sn_3O_4 nanosheets 3D hierarchical heterostructured array as a photoanode with high-efficient photoelectrocatalytic performance. *Appl. Catal., B* 256: 117798.

61 Wen, Y., Wang, D., Li, H. et al. (2021). Enhanced photocatalytic hydrogen evolution of 2D/2D N-Sn_3O_4/g-C_3N_4 S-scheme heterojunction under visible light irradiation. *Appl. Surf. Sci.* 567: 150903.

62 Sun, M., Yan, T., Tingting, W. et al. (2018). Self-assembled hierarchical Sn_3O_4-multi-wall carbon nanotubes: facile fabrication, promoted charge separation, and enhanced photocatalytic performances. *Mater. Res. Bull.* 103: 104–113.

63 Xie, Q., Zhu, Y., Zhao, P., and Yang, C. (2021). A strategic co-assembly of carbon nanotubes and graphene on hierarchical flower-like Sn_3O_4 clusters aimed to enhance lithium storage capability. *J. Electroanal. Chem.* 880: 114898.

64 Lv, M., Yang, L., Wang, X. et al. (2019). Visible-light photocatalytic capability and the mechanism investigation of a novel PANI/Sn_3O_4 p-n heterostructure. *RSC Adv.* 9 (69): 40694–40707.

65 Yang, R., Song, G., Wang, L. et al. (2021). Full solar-Spectrum-driven antibacterial therapy over hierarchical Sn_3O_4/PDINH with enhanced photocatalytic activity. *Small* 17 (39): 2102744.

66 Hung, P.T., Hoat, P.D., Hien, V.X. et al. (2020). Growth and NO_2-sensing properties of biaxial p-SnO/n-ZnO Heterostructured nanowires. *ACS Appl. Mater. Interfaces* 12 (30): 34274–34282.

67 Wang, Z., He, X., Zhang, X.X., and Alshareef, H.N. (2017). Hybrid van der Waals SnO/MoS_2 heterojunctions for thermal and optical sensing applications. *Adv. Electron. Mater.* 3 (12): 1700396.

68 Liang, B., Zhang, W., and Zhang, Y. (2019). Facile fabrication of SnO/nano-graphite composite microspheres with excellent visible photocatalytic performance. *J. Inorg. Organomet. Polym. Mater.* 29 (1): 17–21.

69 Gengzang, D.J., Chen, W.J., Chen, Q. et al. (2021). Down to ppb level ethanol detection based on heterostructured SnO/rGO composites. *Mater. Lett.* 284: 128987.

70 Fu, H.Y., Lang, X.Y., Hou, C. et al. (2014). Nanoporous Au/SnO/Ag heterogeneous films for ultrahigh and uniform surface-enhanced Raman scattering. *J. Mater. Chem. C.* 2 (35): 7216–7222.

71 Wang, Z., Zhu, L., Sun, S. et al. (2021). One-dimensional nanomaterials in resistive gas sensor: from material design to application. *Chemosensors* 9 (8): 198.

72 Kaur, N., Singh, M., and Comini, E. (2020). One-dimensional nanostructured oxide chemoresistive sensors. *Langmuir* 36 (23): 6326–6344.

73 Korotcenkov, G. (2020). Current trends in nanomaterials for metal oxide-based conductometric gas sensors: advantages and limitations. Part 1: 1D and 2D nanostructures. *Nanomaterials* 10 (7): 1–62.

74 Taguchi, N. (1971). Gas detecting device . Vol. 3, US patent. p. 436. https://patents.google.com/patent/US3695848A/en.

75 Comini, E., Faglia, G., Sberveglieri, G. et al. (2002). Stable and highly sensitive gas sensors based on semiconducting oxide nanobelts. *Appl. Phys. Lett.* 81 (10): 1869–1871.

76 Law, M., Kind, H., Messer, B. et al. (2002). Photochemical sensing of NO_2 with SnO_2 nanoribbon nanosensors at room temperature. *Angew. Chem. Int. Ed.* 41 (13): 2405–2408.

77 Kolmakov, A., Zhang, Y., Cheng, G., and Moskovits, M. (2003). Detection of CO and O_2 using tin oxide nanowire sensors. *Adv. Mater.* 15 (12): 997–1000.

78 Arnold, M.S., Avouris, P., Pan, Z.W., and Wang, Z.L. (2003). Field-effect transistors based on single semiconducting oxide nanobelts. *J. Phys. Chem. B.* 107 (3): 659–663.

79 Wang, Y., Jiang, X., and Xia, Y. (2003). A solution-phase, precursor route to polycrystalline SnO_2 nanowires that can be used for gas sensing under ambient conditions. *J. Am. Chem. Soc.* 125 (52): 16176–16177.

80 Orlandi, M.O., Leite, E.R., Aguiar, R. et al. (2006). Growth of SnO nanobelts and dendrites by a self-catalytic VLS process. *J. Phys. Chem. B.* 110 (13): 6621–6625.

81 Orlandi, M.O., Suman, P.H., Silva, R.A., and Arlindo, E.P.S. (2017). Carbothermal reduction synthesis: an alternative approach to obtain single-crystalline metal oxide nanostructures. In: *Recent Advances in Complex Functional Materials: From Design to Application* (ed. E. Longo and F. de Almeida La Porta), 43–67. Springer.

82 Masteghin, M.G., Silva, R.A., Cox, D.C. et al. (2021). The role of surface stoichiometry in NO_2 gas sensing using single and multiple nanobelts of tin oxide. *Phys. Chem. Chem. Phys.* 23 (16): 9733–9742.

83 Rai, P., Majhi, S.M., Yu, Y.T., and Lee, J.H. (2015). Noble metal@metal oxide semiconductor core@shell nano-architectures as a new platform for gas sensor applications. *RSC Adv.* 5 (93): 76229–76248.

84 Yamazoe, N., Kurokawa, Y., and Seiyama, T. (1983). Effects of additives on semiconductor gas sensors. *Sens. Actuators* 4 (C): 283–289.

85 Lee, J.H., Mirzaei, A., Kim, J.Y. et al. (2020). Optimization of the surface coverage of metal nanoparticles on nanowires gas sensors to achieve the optimal sensing performance. *Sens. Actuators, B* 302: 127196.

86 Walker, J.M., Akbar, S.A., and Morris, P.A. (2019). Synergistic effects in gas sensing semiconducting oxide nano-heterostructures: a review. *Sens. Actuators, B* 286: 624–640.

87 Karnati, P., Akbar, S., and Morris, P.A. (2019). Conduction mechanisms in one dimensional core-shell nanostructures for gas sensing: a review. *Sens. Actuators, B* 295: 127–143.

88 Kim, J.H., Mirzaei, A., Kim, H.W., and Kim, S.S. (2020). Variation of shell thickness in ZnO-SnO_2 core-shell nanowires for optimizing sensing behaviors to CO, C_6H_6, and C_7H_8 gases. *Sens. Actuators, B* 302: 127150.

89 Iijima, S. (1991). Helical microtubules of graphitic carbon. *Nature* 354 (6348): 56–58.

90 Iijima, S. and Ichihashi, T. (1993). Single-shell carbon nanotubes of 1-nm diameter. *Nature* 363 (6430): 603–605.

91 Novoselov, K.S., Geim, A.K., Morozov, S.V. et al. (2004). Electric field in atomically thin carbon films. *Science (80-)* 306 (5696): 666–669.

92 Malik, R., Tomer, V.K., Mishra, Y.K., and Lin, L. (2020). Functional gas sensing nanomaterials: a panoramic view. *Appl. Phys. Rev.* 7 (2): 021301.

93 Inaba, M., Oda, T., Kono, M. et al. (2021). Effect of mixing ratio on NO_2 gas sensor response with SnO_2-decorated carbon nanotube channels fabricated by one-step dielectrophoretic assembly. *Sens. Actuators, B* 344: 130257.

94 Reddy, C.S., Murali, G., Reddy, A.S. et al. (2020). GO incorporated SnO_2 nanotubes as fast response sensors for ethanol vapor in different atmospheres. *J. Alloys Compd.* 813: 152251.

95 Li, W., Guo, J., Cai, L. et al. (2019). UV light irradiation enhanced gas sensor selectivity of NO_2 and SO_2 using rGO functionalized with hollow SnO_2 nanofibers. *Sens. Actuators, B* 290: 443–452.

96 Barsan, N. and Weimar, U. (2001). Conduction model of metal oxide gas sensors. *J. Electroceram.* 7 (3): 143–167.

97 Namsheer, K. and Rout, C.S. (2021). Conducting polymers: a comprehensive review on recent advances in synthesis, properties and applications. *RSC Adv.* 11: 5659–5697.

98 Yan, Y., Yang, G., Xu, J.L. et al. (2020). Conducting polymer-inorganic nanocomposite-based gas sensors: a review. *Sci. Technol. Adv. Mater.* 21 (1): 768–786.

99 Liu, A., Lv, S., Zhao, L. et al. (2021). Room temperature flexible NH_3 sensor based on polyaniline coated Rh-doped SnO_2 hollow nanotubes. *Sens. Actuators, B* 330: 129313.

100 Inderan, V., Arafat, M.M., Haseeb, A.S.M.A. et al. (2020). Electrospun (nickel and palladium) tin(IV) oxide/polyaniline/polyhydroxy-3-butyrate biodegradable nanocomposite fibers for low temperature ethanol gas sensing. *Nanotechnology* 31 (42): 425503.

101 Jun, J., Lee, J.S., Shin, D.H. et al. (2017). Fabrication of a one-dimensional tube-in-tube polypyrrole/tin oxide structure for highly sensitive DMMP sensor applications. *J. Mater. Chem. A.* 5 (33): 17335–17340.

102 Liu, Z., Sun, D.D., Guo, P., and Leckie, J.O. (2007). An efficient bicomponent TiO_2/SnO_2 nanofiber photocatalyst fabricated by electrospinning with a side-by-side dual spinneret method. *Nano Lett.* 7 (4): 1081–1085.

103 Shi, H., Zhou, M., Song, D. et al. (2014). Highly porous SnO_2/TiO_2 electrospun nanofibers with high photocatalytic activities. *Ceram. Int.* 40 (7 PART B): 10383–10393.

104 Cheng, H.E., Lin, C.Y., and Hsu, C.M. (2017). Fabrication of SnO_2-TiO_2 core-shell nanopillar-array films for enhanced photocatalytic activity. *Appl. Surf. Sci.* 396: 393–399. https://www.sciencedirect.com/science/article/pii/S0169433216322917.

105 Pan, J., Hühne, S.M., Shen, H. et al. (2011). SnO_2-TiO_2 Core-shell nanowire structures: investigations on solid state reactivity and photocatalytic behavior. *J. Phys. Chem. C* 115 (35): 17265–17269.

106 Nirmala, R., Kim, H.Y., Navamathavan, R. et al. (2012). Photocatalytic activities of electrospun tin oxide doped titanium dioxide nanofibers. *Ceram. Int.* 38 (6): 4533–4540.

107 Huy, T.H., Bui, D.P., Kang, F. et al. (2019). SnO_2/TiO_2 nanotube heterojunction: the first investigation of NO degradation by visible light-driven photocatalysis. *Chemosphere* 215: 323–332.

108 Hou, L.R., Yuan, C.Z., and Peng, Y. (2007). Synthesis and photocatalytic property of SnO_2/TiO_2 nanotubes composites. *J. Hazard Mater.* 139 (2): 310–315.

109 Kim, S.P., Choi, M.Y., and Choi, H.C. (2015). Characterization and photocatalytic performance of SnO_2-CNT nanocomposites. *Appl. Surf. Sci.* 357: 302–308. https://www.sciencedirect.com/science/article/pii/S0169433215021388.

110 Ahmaruzzaman, M., Mohanta, D., and Nath, A. (2019). Environmentally benign fabrication of SnO_2-CNT nanohybrids and their multifunctional efficiency as an adsorbent, catalyst and antimicrobial agent for water decontamination. *Sci. Rep.* 9 (1): 12935.

111 Wu, S. and Dai, W. (2017). Microwave-hydrothermal synthesis of SnO_2-CNTs hybrid nanocomposites with visible light photocatalytic activity. *Nanomaterials* 7 (3): 54.

112 Wang, N., Xu, J., and Guan, L. (2011). Synthesis and enhanced photocatalytic activity of tin oxide nanoparticles coated on multi-walled carbon nanotube. *Mater. Res. Bull.* 46 (9): 1372–1376.

113 Wang, L., Wang, L., Shen, L. et al. (2012). Preparation and photocatalytic properties of SnO_2 coated on nitrogen-doped carbon nanotubes. *J. Nanomater.* 2012: 794625.

114 Pan, J., Zhou, Y., Cao, J. et al. (2016). Fabrication of carbon quantum dots modified granular SnO_2 nanotubes for visible light photocatalysis. *Mater. Lett.* 170: 187–191.

115 Quan, B., Liu, W., Liu, Y. et al. (2016). Quasi-noble-metal graphene quantum dots deposited stannic oxide with oxygen vacancies: synthesis and enhanced photocatalytic properties. *J. Colloid Interface Sci.* 481: 13–19.

116 Zhang, Z., Shao, C., Li, X. et al. (2010). Electrospun nanofibers of ZnO-SnO_2 heterojunction with high photocatalytic activity. *J. Phys. Chem. C* 114 (17): 7920–7925.

117 Pascariu, P., Airinei, A., Olaru, N. et al. (2016). Photocatalytic degradation of rhodamine B dye using ZnO-SnO_2 electrospun ceramic nanofibers. *Ceram. Int.* 42 (6): 6775–6781. https://www.sciencedirect.com/science/article/pii/S0272884216000857.

118 Chen, X., Zhang, F., Wang, Q. et al. (2015). The synthesis of ZnO/SnO_2 porous nanofibers for dye adsorption and degradation. *Dalton Trans.* 44 (7): 3034–3042.

119 Sehar, S., Naz, I., Perveen, I., and Ahmed, S. (2019). Superior dye degradation using SnO_2-ZnO hybrid heterostructure catalysts. *Korean J. Chem. Eng.* 36 (1): 56–62.

120 Harish, S., Silambarasan, A., Navaneethan, M. et al. (2015). ZnO:SnO nanorods and nanosheets and their enhanced photocatalytic activity under visible light irradiation. *AIP Conf. Proc.* 050135.

121 Lan, J., Gao, M., Haw, C. et al. (2020). Layer-by-layer assembly of Ag_2S quantum dots-sensitized ZnO/SnO_2 core-shell nanowire arrays for enhanced photocatalytic activity. *Phys. Lett. Sect. A Gen. Solid State Phys.* 384 (26): 126708.

122 Selvarajan, S., Malathy, P., Suganthi, A., and Rajarajan, M. (2017). Fabrication of mesoporous $BaTiO_3$/SnO_2 nanorods with highly enhanced photocatalytic degradation of organic pollutants. *J. Ind. Eng. Chem.* 53: 201–212.

123 Shahid, M., Shakir, I., Yang, S.J., and Kang, D.J. (2010). Facile synthesis of core-shell SnO_2/V_2O_5 nanowires and their efficient photocatalytic property. *Mater. Chem. Phys.* 124 (1): 619–622.

124 Lee, J., Kim, Y., Kim, J.K. et al. (2017). Highly efficient photocatalytic performances of SnO_2-deposited ZnS nanorods based on interfacial charge transfer. *Appl. Catal., B* 205: 433–442.

125 Liu, H., Liu, T., Dong, X. et al. (2014). Preparation and enhanced photocatalytic activity of Ag-nanowires@SnO_2 core-shell heterogeneous structures. *Ceram. Int.* 40 (PB): 16671–16675.

126 Sultana, S., Rafiuddin, Khan, M.Z. et al. (2015). SnO_2-SrO based nanocomposites and their photocatalytic activity for the treatment of organic pollutants. *J. Mol. Struct.* 1098: 393–399.

127 Liu, Y., Zhang, P., Tian, B., and Zhang, J. (2015). Core-shell structural CdS@SnO$_2$ nanorods with excellent visible-light photocatalytic activity for the selective oxidation of benzyl alcohol to benzaldehyde. *ACS Appl. Mater. Interfaces* 7 (25): 13849–13858.

128 Radecka, M., Wnuk, A., Trenczek-Zajac, A. et al. (2015). TiO$_2$/SnO$_2$ nanotubes for hydrogen generation by photoelectrochemical water splitting. *Int. J. Hydrogen Energy* 40 (1): 841–851.

129 Sun, B., Chen, Y., Tao, L. et al. (2019). Nanorod array of SnO$_2$ quantum dot interspersed multiphase TiO$_2$ heterojunctions with highly photocatalytic water splitting and self-rechargeable battery-like applications. *ACS Appl. Mater. Interfaces* [Internet] 11 (2): 2071–2081. https://doi.org/10.1021/acsami.8b18884.

130 Park, S., Lee, C.W., Cho, I.S. et al. (2014). Growth of anatase and rutile TiO$_2$@ Sb:SnO$_2$ heterostructures and their application in photoelectrochemical water splitting. *Int. J. Hydrogen Energy* 17508–17516.

131 Liao, X., Chen, J., Wang, M. et al. (2016). Enhanced photocatalytic and photoelectrochemical activities of SnO$_2$/SiC nanowire heterostructure photocatalysts. *J. Alloys Compd.* 658: 642–648.

132 Liu, W.T., Wu, B.H., Lai, Y.T. et al. (2018). Enhancement of water splitting by controlling the amount of vacancies with varying vacuum level in the synthesis system of SnO$_{2-x}$/In$_2$O$_{3-y}$ heterostructure as photocatalyst. *Nano Energy* 47: 18–25.

133 Li, Y.Y., Wang, J.G., Sun, H.H. et al. (2018). Heterostructured SnS$_2$/SnO$_2$ nanotubes with enhanced charge separation and excellent photocatalytic hydrogen production. *Int. J. Hydrogen Energy* 43 (31): 14121–14129.

134 Li, J.M., Cheng, H.Y., Chiu, Y.H., and Hsu, Y.J. (2016). ZnO-Au-SnO$_2$ Z-scheme photoanodes for remarkable photoelectrochemical water splitting. *Nanoscale* 8 (34): 15720–15729.

135 Pan, J., Shen, H., and Mathur, S. (2012). One-dimensional SnO**$_2$** nanostructures: synthesis and applications. Shen, G., editor. *J. Nanotechnol.* 2012: 917320.

136 Paek, S.M., Yoo, E.J., and Honma, I. (2009). Enhanced cyclic performance and lithium storage capacity of SnO$_2$/graphene nanoporous electrodes with three-dimensionally delaminated flexible structure. *Nano Lett.* 9 (1): 72–75.

137 Hochbaum, A.I. and Yang, P. (2010). Semiconductor nanowires for energy conversion. *Chem. Rev.* 110 (1): 527–546.

138 Jiao, Z., Chen, D., Jiang, Y. et al. (2014). Synthesis of nanoparticles, nanorods, and mesoporous SnO$_2$ as anode materials for lithium-ion batteries. *J. Mater. Res.* 29 (5): 609–616.

139 Zoller, F., Böhm, D., Bein, T., and Fattakhova-Rohlfing, D. (2019). Tin oxide based nanomaterials and their application as anodes in lithium-ion batteries and beyond. *ChemSusChem* 12: 4140–4159.

140 Hassoun, J., Panero, S., Simon, P. et al. (2007). High-rate, long-life Ni-Sn nanostructured electrodes for lithium-ion batteries. *Adv. Mater.* 19 (12): 1632–1635.

141 Park, M.S., Wang, G.X., Kang, Y.M. et al. (2007). Preparation and electrochemical properties of SnO$_2$ nanowires for application in lithium-ion batteries. *Angew. Chem. Int. Ed.* 46 (5): 750–753.

142 Li, N. and Martin, C.R. (2001). A high-rate, high-capacity, nanostructured Sn-based anode prepared using sol-gel template synthesis. *J. Electrochem. Soc.* 148 (2): A164.

143 Liu, J., Li, Y., Huang, X. et al. (2009). Direct growth of SnO_2 nanorod array electrodes for lithium-ion batteries. *J. Mater. Chem.* 19 (13): 1859–1864.

144 Shang, G., Wu, J., Tang, S. et al. (2013). Enhancement of photovoltaic performance of dye-sensitized solar cells by modifying tin oxide nanorods with titanium oxide layer. *J. Phys. Chem. C* 117 (9): 4345–4350.

145 Niu, H., Zhang, S., Wang, R. et al. (2014). Dye-sensitized solar cells employing a multifunctionalized hierarchical SnO_2 nanoflower structure passivated by TiO_2 Nanogranulum. *J. Phys. Chem. C* 118 (7): 3504–3513.

146 Sigdel, S., Elbohy, H., Gong, J. et al. (2015). Dye-sensitized solar cells based on porous hollow tin oxide nanofibers. *IEEE Trans. Electron Devices* 62 (6): 2027–2032.

147 Gao, C., Li, X., Lu, B. et al. (2012). A facile method to prepare SnO_2 nanotubes for use in efficient SnO_2-TiO_2 core-shell dye-sensitized solar cells. *Nanoscale* 4 (11): 3475–3481.

148 Orlandi, M.O., Bomio, M.R.D., Longo, E., and Bueno, P.R. (2004 Sep). Nonohmic behavior of SnO_2-MnO polycrystalline ceramics. II. Analysis of admittance and dielectric spectroscopy. *J. Appl. Phys.* 96 (7): 3811–3817.

149 Masteghin, M.G. and Orlandi, M.O. (2016). Grain-boundary resistance and nonlinear coefficient correlation for SnO_2-based varistors. *Mater. Res.* 19 (6): 1286–1291.

150 Masteghin, M.G., Bertinotti, R.C., and Orlandi, M.O. (2017). High-performance and low-voltage SnO_2-based varistors. *Ceram. Int.* 43 (16): 13759–13764.

151 Pauzauskie, P.J. and Yang, P. (2006). Nanowire photonics. *Mater. Today* 9 (10): 36–45.

Z

6

Recent Advances in Semiconducting Nanowires-Based Hybrid Structures for Solar Cell Application

Jaydip Bhaliya[1], Meera R. Popaliya[2], Gautam M. Patel[1], Arvnabh Mishra[2], and Vraj Shah[1]

[1] *ITM SLS Baroda University, Department of Chemistry, School of Science, Vadodara, Gujarat 391510, India*
[2] *CVM University, Institute of Science & Technology for Advanced Studies & Research (ISTAR), Department of Industrial Chemistry, V.V. Nagar, Gujarat 388120, India*

6.1 Introduction

During the last decade, research on clean and renewable energy sources has exploded due to the fast rise in global energy necessity and the environmental effect of traditional energy supplies [1]. Humans rely on the environment (as an energy source) to satisfy their daily needs. Solar cells (which convert solar energy to electrical energy) were critical in the transition from fossil fuels to renewable and sustainable energy sources in the twenty-first century. Cutting down the size and cost of the solar cell at the same time as boosting the power conversion efficiency (PCE) would make it even more suitable [2]. The solar cell is also available on the market with other names as a photovoltaic (PV) cell, since it converts photon energy to a usable electrical energy source using predominantly materials of semiconductor [1]. Several materials are neither good conductors (metals) nor good insulators (insulators) (glass). Semiconductor materials exist in crystalline forms and have a tiny amount of free electrons at normal temperatures. At room temperature, it works as an insulator. It possesses resistance that is half that of a conductor and half that of an insulator. Controlled conductivity is achieved by adding sufficient impurities to semiconductors. Semiconductors such as silicon, carbon, germanium, and other elements are commonly utilized in solar cells. Semiconductors, which include solar cells, sensors, biosensors, transistors, light-emitting diodes (LEDs), and digital and analog-integrated circuits, are the fundamental building blocks of today's electronic applications [2–18].

The number of charge carriers in a semiconducting material is greatly increased by doping it with impurity atoms. When a doped semiconductor has largely free

holes, it is called "p-type," and when it contains mostly free electrons, it is called "n-type." Semiconductor materials used in electrical devices are doped under precise conditions to control the distribution and concentration of p- and n-type dopants. In a single crystal of semiconductor, several p-and n-type areas may occur; the beneficial electrical behavior is due to the p–n junctions that interconnect these regions [19]. However, inner engineering of semiconductor materials improves the PCE of solar cells [20]. In the beginning, solar cells were generally manufactured using simple p–n-type semiconductor materials. A solar cell is an advanced tool in PV energy conversion because it converts the energy source of light into usable electrical energy. The bulk of solar cell materials includes semiconductors. When light energy is absorbed, electron–hole pairs and charge carriers separate in a semiconductor. A p–n junction is used to separate carriers of charge in most applications [21]. Understanding the new type of solar cell requires an understanding of the basic properties of semiconductors as well as the principle of conventional p–n-type solar cells. Understanding the P–N junction-type solar cell will provide you with tips on how to enhance solar cells in terms of cost of manufacturing, efficiency, and fabrication energy consumption, among other things [21]. However, as the world's population continues to grow, conventional solar cells cannot provide enough electricity because they are inefficient in terms of manufacturing cost, electrical energy generation, and high electron/ion transfer [22]. Furthermore, the Shockley–Queisser limit sets a PCE limit for single-junction solar cells at 33.7% [23].

Over the past decade, various nanostructures have been dynamically researched and manufactured for the advanced management of photons to enhance the absorption in thin film silicon solar cells [24–26] like, photonic crystals [25], grating couplers [25], randomly surface texture [26], plasmonic [26], and nanowires (NWs) [26, 27]. Recently, semiconductor nanowires have gained a lot of attention as a way to improve PCE, especially for materials having a shorter diffusion length compared to their optical thickness [28, 29] Because NWS structures have a high aspect ratio (e.g. surface-to-volume ratio) and are small, they can be used in solar cells [30, 31]. The performance of nanowire solar cells is expected to improve as they get closer to planar options and the Shockley–Queisser limit [30, 31] by enhancing their structure and size. The introduction of third-generation PVs, in particular, which reduces the amount of material used and hence lowers the cost, will make solar cells more efficient and cheaper than they are now [32, 33]. The usage of nanowire materials in solar applications will grow in the future years as their qualities improve. Moreover, the number of research projects that have been conducted in the last 15 years is shown in the publication graph on the topic of nanowire materials for solar cell applications, which has been demonstrated in Figure 6.1.

The main flaw of planar solar cells, large losses in reflection, may be overcome by the use of nanowire-based solar cells, in which sunlight penetrates the NW surface and then reflects on the neighboring NW surface. NWs-based solar cells have better photovoltage and photocurrent than planar solar cells, making them excellent. Silicon (Si), the second most plentiful material in the earth's crust, has outstanding electrical and optical properties, and a broad range of bandgaps may be created by
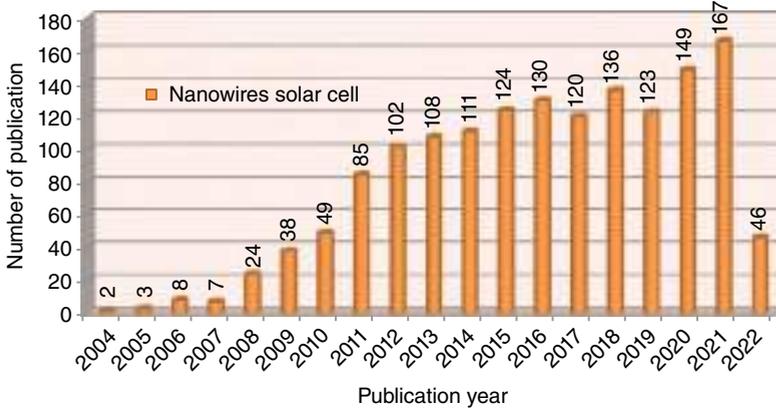
Figure 6.1 Total number of publications in the last 15 years on nanowire as a solar cell application (Web of science accessed on 15th April 2022).

altering the physical parameters. Due to their widespread purpose in the energy segment, silicon nanowires (Si-NWs) are essential one-dimensional (1D) semiconductors. Si-NWs are now gaining a lot of attention due to their improved electrical and optical capabilities compared to parent bulk Si. Due to their morphology-dependent characteristics [34–39], Si-NWs are used in a wide range of applications, including biosensors [40–43], transistors [40, 41, 44–47], lithium-ion battery [48–51], data-saving memory [52], and solar cells [53–57]. Several other materials in the NWs geometry are investigated and incorporated with solar cell include CdS/CdTe [58], CdS/CuS$_2$ [59], GaAs [60], and InP [61–63]. Moreover, the arrangement of the NWs in the solar cell for the generation of electricity is presented in Figure 6.2 [30]. For better understanding, this chapter describes the application of the nanowire structure in the solar cell as well as the state of the art of the 1D nanowire syntheses along with application-related energy.

6.2 Semiconductor Materials

Semiconductor materials can transmit electric current, are readily controlled, and can function as insulators and conductors. Semiconductors have been essential in the electronics area since their inception due to their properties. Temperature, light, magnetic forces, and a small number of impurity atoms all alter a semiconductor's conductivity. One of the most significant materials for electronic applications is the semiconductor because of its sensitivity to conductivity. We live in a world full of semiconductor devices. From the automotive sector to pocket calculators, they are in almost every commercial item we come across. Semiconductors are used in a variety of sectors today, including computing, telecommunication, aircraft, healthcare, manufacturing, and agriculture. Electronic devices such as CD players, HDTVs or TVs, MP3 players, mobile phones, and laptops have grown smaller, inexpensive, faster, and more trustworthy due to semiconductors [64–68].
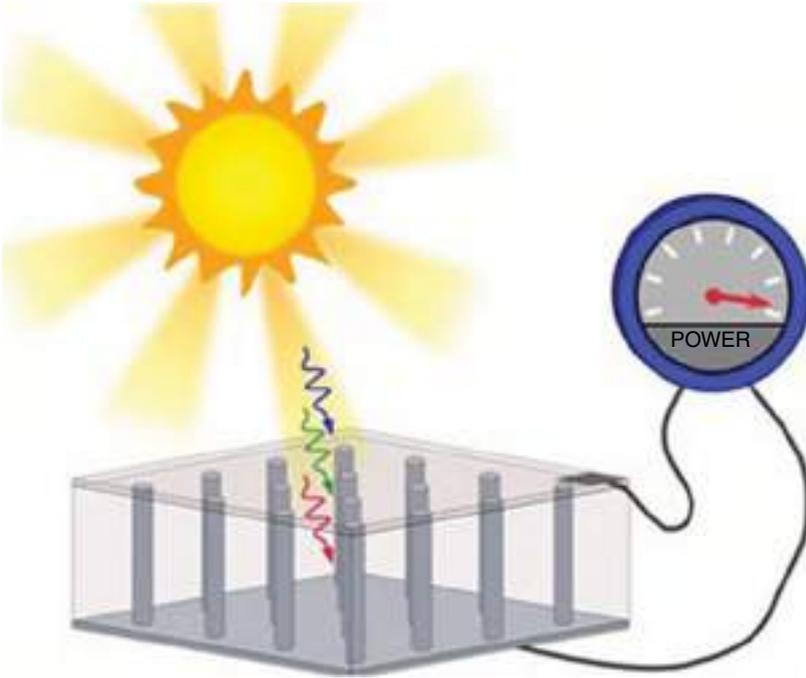
Figure 6.2 Nanowires for solar cell application. Source: Otnes and Borgström [30]/with permission of Elsevier.

Semiconductor devices play a significant role in research and industry as well. These devices are used to conduct testing, measuring, and a range of other experiments on a variety of electronic equipment at research institutions [69–79]. Automated telephone exchanges and industrial control systems both employ semiconductors (such as those used in automobile manufacture). Heavy-duty solid-state rectifier diodes are still used in electric trains today to convert enormous quantities of electricity. Solid-state technology has a wide range of applications, including spacecraft, computers, and data processing devices [80].

6.2.1 Classification Semiconductors

A semiconductor is a solid chemical element or compound that can conduct electricity under some circumstances but not others, making it an excellent medium for regulating electrical current flow. A semiconductor is a crystalline substance that lies midway between a conductor and an insulator in terms of electrical conductivity. Semiconductors may be found in a variety of forms and sizes. Semiconductors are divided into two categories: Extrinsic and intrinsic semiconductors are the two kinds of semiconductors.

6.2.1.1 Intrinsic Semiconductor
There are two approaches to characterization of an intrinsic semiconductor. An intrinsic semiconductor, in layman's terms, is a semiconductor made completely of

exceptionally pure semiconductor material. An intrinsic semiconductor, in more scientific terms, is one in which the number of holes in the conduction band equals the number of electrons. The forbidden energy gap in such semiconductors is quite tiny, and the valence electrons have enough energy to jump into the conduction band even at room temperature. Another distinguishing property of intrinsic semiconductors is the Fermi level, which is located halfway between the valence band and the conduction band. This can be demonstrated in theory, but that is outside the scope of this study. If you are unfamiliar with the term "Fermi level," it refers to the energy level where the chances of discovering an electron are half as likely (remember, probability is measured on a scale of 0 to 1). When there is a big difference in voltage across an intrinsic semiconductor, electrons go to the positive side and holes go to the negative side. The total current inside the semiconductor is the sum of the currents generated by free electrons and holes. The number of hole–electron pairs grows as the temperature of the semiconductor rises, and current across the semiconductor climbs with it. As the temperature lowers, the reverse is true [80].

6.2.1.2 Extrinsic Semiconductor

These are some semiconductors that have a small amount of impurities added to dilute the pure state of the semiconductor material. Impurities are referred to as dopants, or doping agents, to be more exact. It is critical to remember that such contaminants are introduced in minute quantities, with average dopant concentrations of 1 part in 100 million parts, or 0.01 ppm The valence band of doping materials is purposely engineered to contain either five or three electrons. As a consequence, they are referred to as trivalent or pentavalent dopants. Based on the type of dopant utilized in extrinsic semiconductors, they are classified as n-type or p-type. Antimony and other donor impurities are pentavalent dopants that contribute an additional electron to the crystal structure that is not necessary for bonding of covalent and may be relocated to the conduction band. The term "n-type intrinsic semiconductors" derives from the fact that when a base material, like germanium, is doped with such a substance, the base material carries more electrons than holes. When boron, known as trivalent dopant, is introduced into germanium, the process is completely reversed, resulting in extra or additional holes. As a result, a p-type semiconductor is produced by this dopant, also known as an acceptor. As a consequence, in the n-type, electrons make up the majority (of current) carriers, while holes make up the minority. p-type semiconductors are the polar opposites of semiconductors of the n-type. An additional distinction is that, in intrinsic semiconductors, the Fermi level is half the distance between the conduction and valence bands. For obvious reasons, it grows higher in n-type semiconductors than in p-type semiconductors [80]. Figure 6.3a depicts a p-type semiconductor, whereas Figure 6.3b depicts an n-type semiconductor.

6.2.2 Solar Photovoltaic Systems

The most widely used renewable energy source is solar energy. A PV system converts solar or light energy into electrical energy. The solar cell is a PV system's most essential component. A single solar cell may provide around 5 V of power. A solar
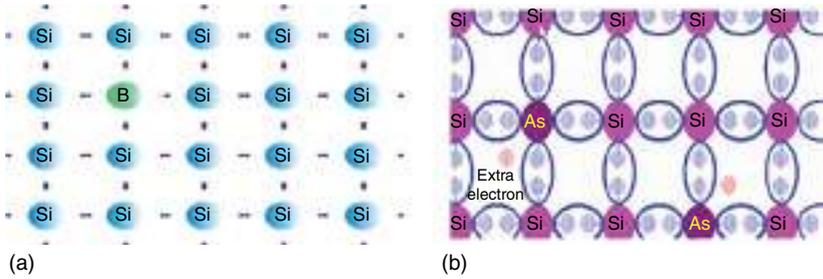
Figure 6.3 (a) p-Type and (b) n-type semiconductors. Source: Atikur Rahman [80].

panel is a collection of solar cells that are linked in series to provide useable electricity. The number of solar cells in a solar panel may be increased to enhance the voltage. For example, 30 solar cells placed in series will yield 15 V. A combination of these is known as a solar array and can be used to achieve the required current and voltage. The PV effect is the creation of energy when exposed to sunshine. Solar cells, as seen in Figures 6.4, employ this concept to generate power. Solar cells are built up of three layers of semiconductor materials, mostly silicon. The top layer, called the n-type layer, is relatively thin and contains a high concentration of electrons. While in the p-type layer, present at the bottom, there is a huge concentration of holes. When p-type and n-type semiconductors are joined, a p–n junction is produced. The electrons of n-type materials strive to reach the p-type area and form a negatively charged layer. p-type materials' holes also strive to reach the n-type area, forming a positively charged layer (Figure 6.4). The depletion zone of the
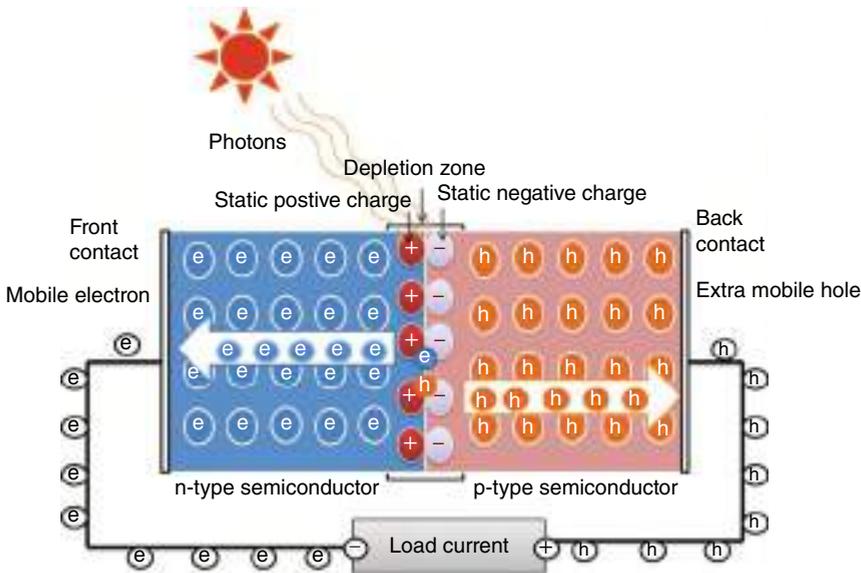
Figure 6.4 Schematic representation of a simple photovoltaic cell. Source: Simya et al. [81]/with permission of Elsevier.

semiconductors is the area between the two layers. Sunlight quickly passes through the top thin layer and enters the depletion zone. It comprises neutral atoms due to the lack of charge in the depletion area. When photons from the sun reach the depletion layer, they break these neutral atoms. The electrons from the neutral atom dwelling behind the hole are nocked by them, resulting in carriers of free charge. After that, the electrons migrate to the n-type layer and the holes to the p-type layer. Because of the electric field existing in the depletion layer on the associated electron circuit, the electron flow generates power for electrical devices such as lights, fans, motors, and batteries [81].

6.2.3 Nanomaterials as Semiconductors

New opportunities for increasing hybrid solar cell (HSC) performance have emerged as a result of scientific advances in semiconductor nanostructuring. To begin, quantum confinement alters the optoelectronic features of nanostructured semiconductors, resulting in a tunable bandgap, increased light absorption, and changed electrical conductivity, all of which are dependent on the nanoscale characteristic size. In such instances, a new parameter (nanoscale tunability) is introduced to provide the best possible compatibility between the inorganic and organic components, resulting in heterojunctions with better PV performance. Because heterojunctions have a bigger interfacial area and a shorter average distance between two sites, their construction is very important. Exciton dissociation induces charge carrier separation at surfaces, which is aided by such structures, resulting in a boost in photocurrent. Figure 6.6 illustrates the advantages of a nanostructured organic–inorganic interface over flat heterojunctions. The figure of merit for the organic layer efficiency in a flat heterojunction is F Lex/Lab, where Lex is the length of the exciton diffusion and Lab $= 1/k$ is the length of the light penetration (k is the absorption coefficient). As a result, a thin organic layer with d Lex and d Lab thicknesses provides high charge separation (all excitons reach the interface) but low absorbance (Figure 6.5a). A relatively thick organic layer absorbs more light energy, yet only a small percentage of excitons dissolve at the interface (Lab $d >$ Lex) (Figure 6.5b). Even if a nanostructured semiconductor infiltrated with organics has a typical
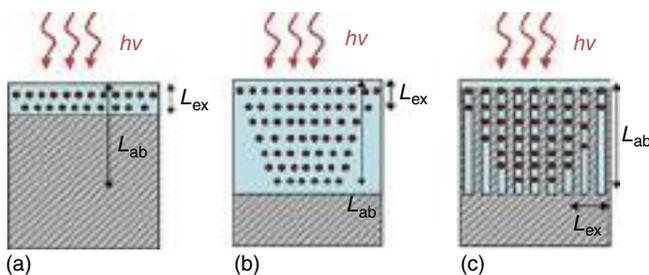
Figure 6.5 (a, b) In flat hybrid devices, the formation of exciton (dots), and (c) the formation of exciton in heterojunctions nanostructured. Source: Patel et al. [46]/with permission of Elsevier.

length (normal distance between pillars or pore diameter) near to the exciton diffusion length, the nanostructured layer may be thick enough to absorb considerable light energy (Figure 6.5c). Large contact, on the other hand, promotes interfacial recombination. Lex (many tens of nanometers for singlet excitons) is frequently smaller than Lab (several hundred nanometers) for many polymers and tiny compounds. As a consequence, an ideal nanostructured semiconductor design might include axial nanostructures having a length of 500–1000 nm or greater, with an average spacing of 5–20 nm, such as pillars or pores (highly organized) [82].

6.2.4 Effect of Nanomaterial Morphology in Semiconductors Applications

Nanomaterials include nanotubes, nanorods, nanotips, nanowires, nanospindles, hexagonal nanoplates, nanofibers, and many others (shown in Figure 6.6). Here, we briefly discussed nanowire HSCs.

Thin sheet silicon solar cells are substantially less effective due to the poor absorption of sunlight [84]. Organic photovoltaics (OPVs), which are made up of polymers or small molecules, have gained a lot of interest in addition to inorganic solar cells because of benefits such as inexpensive material prices [85], solution processability [86], and mechanical flexibility [87]. HSCs are organic–inorganic HSCs that integrate the benefits of organic and inorganic materials. To replace the expensive p–n junction, hybrid heterojunctions are synthesized at low temperatures using a solution-processable approach. The inorganic semiconductor materials with correct bandgaps will absorb the majority of the incoming light. Thus, with proper design, hybrid inorganic–organic solar cells (OSCs) should be able to compete in terms of
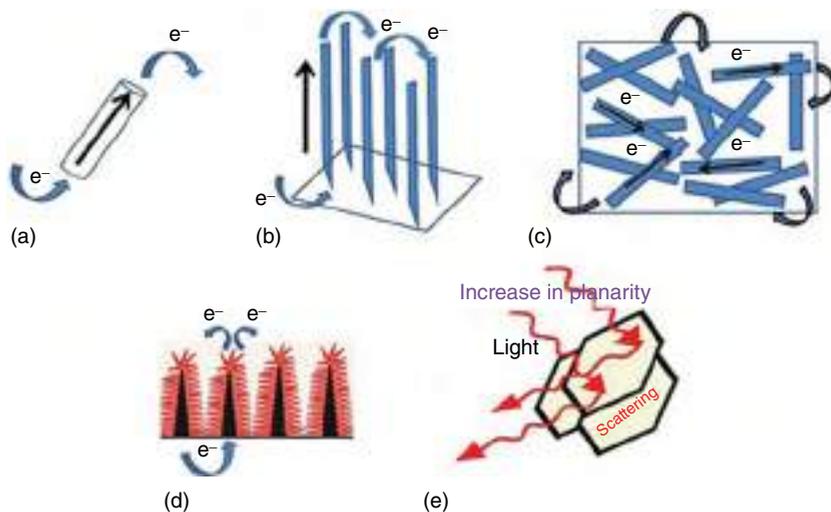
Figure 6.6 Electron transport channels and light propagation paths in various nanostructures used as photoanodes: (a) nanotubes, (b) nanowires, (c) nanorods, (d) nanotips, and (e) hexagonal plates. Source: Sengupta et al. [83]/with permission of Elsevier.

efficiency with ordinary inorganic solar cells [88]. Because of their low manufacturing cost, HSCs-based nanowire propose a better future for very much efficient and cheaper solution for solar cell. To date, the GaAs NWs/polymer HSCs with the greatest PCE received 9.2% [89]. Inorganic semiconductor NWs-based HSCs with high performance and cheap cost are difficult to come by. As a substitute for the current HSC design, novel low-cost NWs-based HSCs are urgently required.

As a result, HSCs based on inorganic semiconductor NWs are being developed with the objective of improving PCE by combining the benefits of both inorganic and organic materials. The main difference between [6,6]-phenyl-C_{61}-butyric acid methyl ester (PCBM) (or any other fullerene analogue) and OPVs is that PCBM uses an inorganic NW rather than an organic electron-accepting material. This design has many benefits, including light harvest, dissociation of exciton, and conveyance, as well as reliability of devices. Unlike in a traditional polymer system of fullerene, where the fullerene plays a minor role in photocurrent generation, both components have the potential to absorb light energy from renewable sources [90].

The fundamental structure of a nanowire-based HSC for an inorganic semiconductor is a sandwich-type photoactive layer between the two electrodes. The photoactive layer is made up of organic polymers and inorganic NWs semiconductors. Bottom-up or top-down approaches can be used to synthesize NWs. Thermal evaporation is commonly used to put the other electrode on the active layer [91]. There are two forms of heterojunctions in HSCs based on NWs: bulk heterojunctions in Figure 6.7a,b demonstrated interdigital heterojunctions [93]. The nanowires are peeled off their growing substrates and uniformly mixed with the organic substances for the bulk heterojunctions. To form a photoactive layer, the mixture is placed around on a substrate. Although the simple structure of the nanowires in the mixture tends to agglomerate around, preventing the establishment of an effective donor–acceptor (DA) interface. The dissociation of exciton will be delayed [94]. Vertically aligned NWs may stand on inorganic substrates with organic material spin-coated on top of them at the same time. Ordered heterojunctions, as shown in Figure 6.7b, are widely accepted as the best configuration for efficient charge transfer and exciton dissociation [91, 95]. The distance between exciton generating sites in the donor material and the DA interface may be adjusted in such a system. After
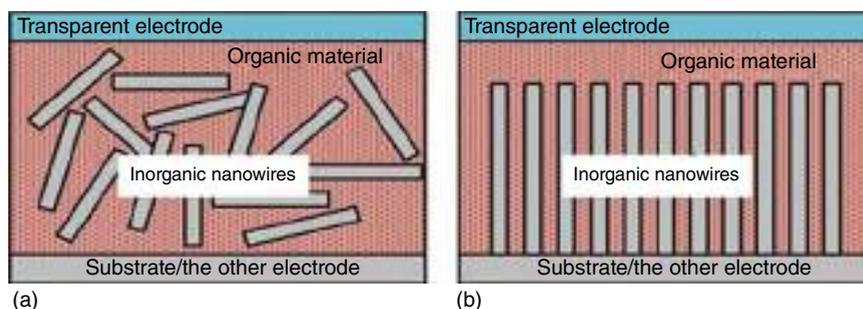

Figure 6.7 Schematics of the fundamental architectures of HSCs based on inorganic semiconductor nanowires with (a) bulk and (b) interdigital heterojunctions [92].

the exciton splits, both electrons and holes are sent to their respective electrodes through separate paths.

6.3 Semiconductor Nanowires Synthesis

These are nanowire structures having a diameter of a nanometer and an unconstrained length. Nanowires are considerably longer than their diameters, and they are also known as quantum wires since they exhibit unusual quantum mechanical effects at this size. Nanowires come in a variety of shapes and sizes. Carbon nanowires, molecular nanowires, metallic nanowires, and so on are examples. Wu et al. created long hierarchical TiO_2 nanowires for application in DSSC using a one-step hydrothermal process [96]. The cell has a 7.34% PCE due to its large surface area for adsorbing larger dye molecules and enhanced light-scattering abilities. The use of ultra-long anatase TiO_2 nanowire arrays in DSSC results in a higher efficiency (9.40%) than the previous method. More studies on TiO_2 nanowires are being done in order to come up with new ways to increase their efficiency [97, 98]. Sun et al. recently reported how to develop a DSSC using a bilayer TiO_2 photoanode with a nanowire–nanoparticle bottom layer and a spherical void-scattering layer with a nanowire–nanoparticle bottom layer [99]. The cell has a 4.07% average photoconversion efficiency, and this may be attributed to optimal dye loading, effective light scattering for sufficient light harvesting, and quick charge transfer for efficient charge collecting.

Using hydrothermal procedures, Ko et al. created a "nanoforest" of high density, long branching "treelike" hierarchical ZnO nanowire (NW) and used it to make photoanodes [100]. Two types of growth modes, lengthwise growth (LG) and branching growth (BG) NWs, are created according to the hydrothermal treatment. Longer ZnO nanowires are produced by LG, while many branched ZnO NWs are produced by BG. The researcher designed six distinct ZnO nanostructures, each with its own hierarchy and surface area, ranging from standing NWs (LG1, LG2, and LG3) to nanoforests (BG1, BG2, and BG3). A scanning electron microscope (SEM) picture of the ZnO nanoforest at higher magnifications and its inset are shown in Figure 6.8a. The JSC–V graphs for BG- and LG-type ZnO used in the fabrication of solar cells are shown in Figure 6.8b. These DSSCs' estimated photovoltaic properties are summarized. As expected, the photo-conversion efficiency of the BG3 ZnO-based DSSC with the most hierarchical branching has been the greatest. The BG3 structure is most effective because of its wide surface area, allowing for more dye loading and photon absorption. The branching NWs of crystalline ZnO in a network have the ability to increase the length and speed of electron transport.

Barpuzary et al. utilized a hydrothermal process to make a 1D nanorod of ZnO for usage as a DSSC photoanode material. In this investigation, a novel metal-free carbazole dye (SK1) was employed as a sensitizer [101]. The 5.7% photoconversion efficiency determines the manufactured cell. Fan et al. explored annealing environment that affects the performance of DSSCs produced from ZnO nanowires that were hydrothermally synthesized [102]. Due to the increased
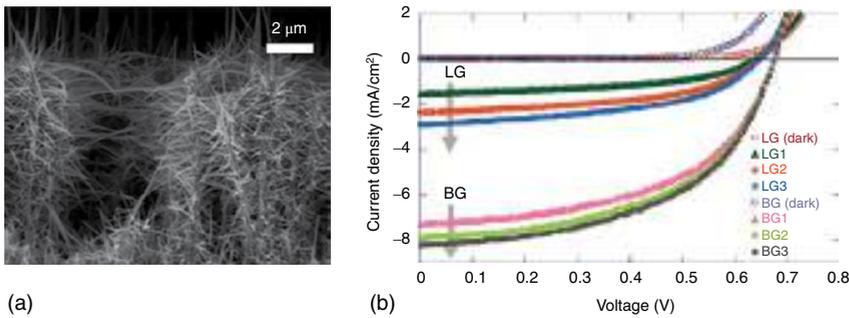
Figure 6.8 (a) SEM images of the ZnO NW nanoforest with a slanted perspective (inset shows the higher magnification) and (b) JSC–V curve using ZnO nanoforest and nanowire for dye-sensitized solar cells. Source: Ko et al. [100], Elsevier.

electrical conductivities in the inert atmosphere, the photo-conversion efficiency of argon ($\eta\frac{1}{4}1.62\%$) exceeded that of air ($\eta\frac{1}{4}1.26\%$). The conductivity of ZnO is increased by a higher oxygen vacancies and lower density of negative charge surface species. Wang et al. [67] built flexible, double-sided, transparent, and ITO-free DSSCs using ZnONWs array synthesized on stainless steel, Cu, Ag, and Au microwires. With a 0.35% photo-conversion efficiency, a 20-minute dye loading period provides the greatest device performance.

6.3.1 Advantages of Nanowire Morphology

There are different causes of loss in every solar cell that must be resolved. The stages essential to translating light to electricity consist of absorption of photons, generation of exciton, separation of exciton into free carriers, and charge carrier collection with the help of electrodes. At each level, nanowires rather than thin films or wafers allow for reduced costs and losses. Lower the impurities required and the amount of semiconductor material necessary to achieve higher efficiency, increase defect tolerance, and permit the use of novel single-crystalline materials without the necessity of expensive, lattice-matched substrates, all prospective cost savings [103].

Semiconductor nanowires have a high aspect ratio, which means that the ratio of length to diameter is quite high. This opens up a significant range of possibilities [22]. Because of their small size, nanowires offer a variety of features that make them appealing for solar cell applications. To begin with, nanowires are formed from natural silicon, have low toxicity, and are compatible with integrated circuit manufacturing technology. Second, silicon nanowires that are vertically oriented have limited reflection and good broadband absorption [30, 32]. These structures can also be employed as antireflection coatings on top of the SC active layer [32]. Emerging technology and novel materials, such as nanowires and organic dyes, are used to manufacture solar cells. They prefer to improve efficiency while lowering costs. Because of their high light-trapping capabilities, inorganic semiconductor NWs are especially suitable for PV applications. Inorganic materials have extinction

coefficients that are orders of magnitude higher than biological materials. As a result, inorganic components play a vital part in the solar energy harvesting via the hybrid active layer. One of the requirements for ensuring excellent performance of NW-based HSCs is to maximize the light absorption of the arrays. The most appealing aspect of NWs is that their light-absorbing cross section has been many times larger than their physical cross-sectional dimensions, allowing for substantial light absorption. The geometrical dimensions of NW arrays play a key role in this advantageous quality. In the frequently used cylindrical nanowire, the arrangement, periodicity, diameter, and length all play essential roles [22].

Some benefits of NW-based solar cells have been examined to demonstrate their superiority to planar PV systems (based on thin films and wafers). Better electrical and optical properties, low semiconductor material, different mechanisms of separation for charges and effects of strain relaxation, low demand for purity of crystal, and low cost with flexible substrates are just a few of the benefits of solar cell devices based on nanowires. ZnO, TiO_2, SnO_2, CdSe, CdTe, ZnS, Si, InAs, Ge, CuO, InGaN, GaAs, GaN, and many other materials were used to make nanowire-based solar cells. The process of converting light to energy involves several processes. It is critical to reduce losses at each phase if you want to improve the efficiency. These stages are as follows: (i) incoming light absorption; (ii) electron–hole pairs created by light (excitons); (iii) the separation of excitons is assisted by an electric potential gradient generated inside the structure; and (iv) the collection of charge carriers at the electrodes [104]. It is worth noting that, when properly designed, NWs are incredibly good at trapping light and forming exciton. Furthermore, the size of NWs falls within the range of carrier diffusion length, resulting in better free carrier collection during the separation process. NWs are ideal candidates for solar energy conversion because of these two properties.

6.3.2 Nanowire Synthesis

Nanowire synthesis currently has a large body of literature, and comprehensive studies detail the growth processes [104–107]. Chemical vapor deposition (CVD) and programmed chemical etching are the two most popular processes utilized in NWs semiconductor-based solar cells. CVD forms nanowires by passing chemical vapors through it with a furnace's hot zone, where they react on a substrate, usually with the help of a metal catalyst nanoparticle. A vapor source might be a gas, a liquid, or a heated solid. A chemically inert gas, which is commonly mixed with other gas reactants, transports the precursor vapors to the substrate. The substrate is put in the furnace's deposition zone, which promotes chemical breakdown. A number of mechanisms support nanowire formation rather than homogenous thin film deposition. The vapor–liquid–solid (VLS) process is the most generally referenced approach, which utilizes metal-based catalysts to create an eutectic of the liquid with the required NWs material [106, 108]. The solution becomes supersaturated and overcomes the nucleation barrier during chemical-phase separation into the liquid eutectic droplet, prompting precipitation to initiate. More precipitation and nanowire development result from increased dissolved species flow. With the

correct precursor, substrate, catalyst, temperature, and concentration, the growth could be possible of vertical nanowires [109], it is beneficial for solar cells. Catalyst patterning methods may be used to create ordered nanowire arrays [58]. Dopants can be added throughout the development process or separately during the diffusion stage [110, 111]. In situ doping has been essential because it is possible at very low temperatures, since it cannot totally depend on diffusion, which also occurs with incorporation by the catalysts [110]. Doping *ex situ*, in contrast to *in situ* doping, has no effect on the kinetics of the formation of nanowires or thin films, and separates the growth and doping periods and temperatures [111–113]. Nanowire devices are far more difficult to measure dopant concentration and dispersion than bulk wafers or thin films. Other methods like vapor–solid (VS), vapor–solid–solid (VSS), and dislocation-mediated formation are also feasible in CVD nanowires [105, 114–117]. The VSS process is the same as the VLS process, but instead of creating an eutectic liquid, the catalyst remains solid. This phase difference indicates that in the VSS process, concentration of substance and precipitation are not primary factors for the development of 1D materials; rather, the catalyst speeds precursor decomposition. To promote 1D development, a catalyst cannot be used in the VS process, which depends on the surface energy differential between the crystal and the nanowire. The dislocation-mediated growth method incorporated atoms along a screw dislocation using high-energy defect sites, which is responsible for 1D material formation in the same manner as the upward spiral of a spiral staircase. A lithography stage has been followed by an etch step in the etching of pattered chemicals. That is a top-down or combined approach, like the bottom-up/top-down technique. Top-down lithography includes nanoimprint and e-beam, whereas spontaneous bottom-up lithography includes anodic alumina, nanosphere assembly, and block copolymer creation [58, 118–121].

A guided etching by the selective substrate, such as deep reactive ion etching (DRIE) or etching based on chemical metal-assisted, was used to destroy the patterned substrate [121–124]. The nanosphere assembly patterning technique is very beneficial, since it allows for independent control of the diameter and pitch of nanowire prior to the substrate etch phase by altering sphere diameter and etch duration [123]. Langmuir–Blodgett, roll-coating, and dip-coating processes may be used to synthesize and assemble silica and polymer spheres in a broad range of diameter in general 100–1000 nm [123, 125–127]. Templates of block copolymer and anodic alumina may reach even smaller dimension sizes normally 10–100 nm and have been used to make less than 10 nm diameter of nanowires [120, 124]. The advantage of the patterned chemical etching process is that the doping level and material composition of the starting wafer or thin film are already set. This allows for more precise control of material characteristics and easier material characterization.

6.3.2.1   ZnO Nanowire

To make the ZnO NWs array to have a large area, in the tube furnace, thin zinc foil was used to produce vapor of zinc at high pressure. Before being carried to the center of a 2-in. (about 5 cm) furnace of quartz tube, the Zn foil and TCO substrate

were gradually arranged in a ceramic boat at a distance of 5 mm. Before getting a 40 sccm (standard cubic centimeters per minute) flow of argon and being heated, the tube of quartz was evacuated to 10 mTorr (1 Torr ¼ 133 Pa). When the temperature of the quartz tube approached 70 °C, a 70-sccm flow of air was likewise injected (the melting point of Zn). After the temperature hit 600 °C, the reaction kept going for 30 minutes. The pressure has been maintained at 8 Torr during the NWs production by adjusting the rate of pumping. At room temperature, the furnace tube was kept far too cool. Then, a layer of yellowish-white color was generated on the substrate of TCO.

Nanowire arrays of ZnO/ZnSe synthesis: The ZnO NWs were then transported to the pulse laser deposition (PLD) chamber and used as a template for the coating of ZnSe. The pulse frequency, energy density, and laser wavelength were 2 Hz, 130 mJ/cm^2, and 266 nm, respectively. The system vacuum was initially evacuated to 1×10^{-3} Torr before the deposition. After being deposited for 20 minutes at 400 °C, for 1 hour, the sample was annealed at a temperature of 500 °C. The same procedure was utilized to achieve room temperature for the ZnSe shell coating of PLD at 27 °C for 20 minutes without any additional annealing using the same method [128].

6.3.2.2 SiNWs Preparation

The electroless etching technique that is associated with aqueous metal ion is used for the generation of Si-NWs on the substrate of planar silicon [129]. Cleaned substrates of n-type Si were submerged for 15 minutes at room temperature with 0.02 M AgNO$_3$ and 4.8 M HF aqueous solutions. To remove any remaining silver, the substrate was washed in a 30% W/W HNO$_3$ solution and then washed with deionized water (DI). In 5 M HF aqueous, moderate shaking for 10 minutes removed silicon oxide by wet chemical etching. Then, they were submerged in deionized water and, under the steam of nitrogen gas, they dried. This method produces hydrogen-terminated silicon (H–Si), and then it is immediately put in the glovebox [130, 131].

6.3.2.3 NaNbO$_3$ Nanowire

The synthesis included the use of Nb$_2$O$_5$ and NaOH. Nb$_2$O$_5$ and NaOH are typically dissolved in deionized water during a typical procedure. The resulting hydrothermal reaction mixture was autoclaved for two hours at 180 °C to yield a solid white niobate after one hour of magnetic stirring. The residues were removed from the white precipitate by washing it many times with DI and CH$_3$COOH (ethanol) and then drying it overnight. Figure 6.9 shows the final calcination of the product [132].

6.3.2.4 TiO$_2$ Nanowires

Two hydrothermal processes were used to generate regular TiO$_2$ nanowires (RN). Hydrogen titanate nanowires were originally made using a comparable technique based on a hydrothermal process described in the literature [133]. A hydrothermal technique was used to transfer hydrogen titanate NWs into conventional TiO$_2$ NWs.
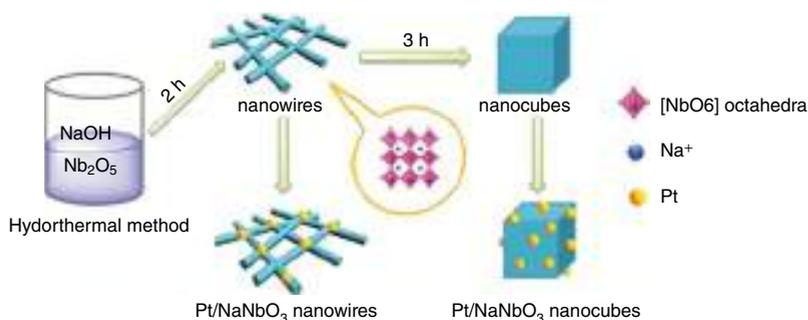
Figure 6.9 The catalysts' formation paths, which include a network of corner-shared octahedral units of [NbO₆]. Source: Liu et al. [132]/with permission of Elsevier.

A 1 mg powder of TiO_2 (99%, Alfa Aesar, Anatase) was placed in a Teflon-lined stainless steel autoclave, which was then filled with an aqueous solution of 80% NaOH. The autoclave was preheated before being allowed to cool naturally to the ambient temperature. Before drying, the precipitate of hydrogen titanate NWs was washed many times by the solution of water and mild HCl. The hydrogen titanate NWs were then placed in a Teflon-lined autoclave that had been previously filled to 80% capacity with deionized water (pH 7). The autoclave was preheated before being allowed to cool normally at room temperature. The resulting normal TiO_2 NWs were collected and dried at room temperature [134].

6.3.2.5 ZnS Nanowire
All activities were carried out in the presence of a steady supply of dry argon. In a three-necked flask, zinc stearate and octadecylamine (ODA) were combined in a conventional synthesis. The mixture was heated at a constant temperature until it produced a solution that was homogeneous. Similarly, to the zinc precursor, the sulfur precursor was created in the same method. Thiourea and ODA were combined in a three-necked flack, heated, and kept at that temperature until the solution was homogeneous. The solution of zinc as a precursor was then added once the sulfur precursor solution had cooled. The reaction was kept at 150 °C for one hour. The mixture of crude reactions is cooled at room temperature before being dissolved in chloroform (1 equiv). Before being dissolved in 1 equiv chloroform volume, the crude reaction mixture was refrigerated to room temperature. Methanol was used to precipitate the ZnS nanoparticles, which were then centrifuged three times, The ZnS NPs were washed using methanol and chloroform. In a vacuum oven, the NPs were finally dried [132].

6.3.2.6 CdS Nanowires
The CdS NWs film was made by employing the chemical bath deposition (CBD) technique to deposite a film of $Cd(OH)_2$ nanowire onto a flat film of CdS at room temperature [135]. Aqueous ammonia (pH ~ 11) was used to make the aqueous bath containing $CdCl_2$ more complicated. The flat substrate of CdS was vertically dipped in the solution for 9 hours, and nucleation and growth occurred as a result

coagulation at surface by the adsorbed $Cd(OH)_2$ NPs [136]. Equation (6.1)–(6.3) depicts the reaction that occurs as a result of cluster-by-cluster deposition [137]:

$$Cd_2 + +2OH- \rightarrow Cd(OH)_2 \tag{6.1}$$

$$Cd(OH)_2 + 4(NH_4)^+ \rightarrow Cd(NH_3)_4^{2+} + 2H_2O + 2H^+ \tag{6.2}$$

$$Cd(NH_3)_4^{2+} + 4H_2O \rightarrow Cd(OH)_2 + 4NH^+ + 2OH^- \tag{6.3}$$
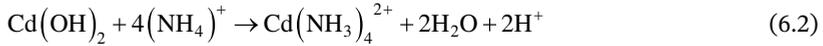
As time passes, present product in the solution in the form of ionic surpasses the solubility of the product inside the bath solution. The ion exchange method was used to convert $Cd(OH)_2$ to CdS, with the film of $Cd(OH)_2$ nanowire submerged in a 0.02 M solution of sodium sulfide flakes (Na_2S). Because the solubility of CdS (1028) is lower than that of $Cd(OH)_2$ (1014), CdS has been synthesized by replacing hydroxyl ions with sulfide ions from Na_2S. The following generalized reaction Eq. (6.4) helps for the better understanding [138].

$$Cd(OH)_2 + mS^{2-} \rightarrow mCdS + 2m(OH)^- \tag{6.4}$$
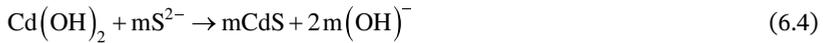
where (m ¼ 1, 2, 3 . . . n), resulting in film that was washed with double distilled water (DDW) and annealed at temperature of 250 °C in air up to one hour for the elimination of content of hydroxyl as well as to improve crystallinity, resulting in CdS NW film.

6.3.3 Characterization

Figure 6.10 show FE-SEM images of TiO_2 nanowire-coated with electrodes of a photoanode. Once the process time was less than 72 hours, two subsequent hydrothermal procedures yielded usual TiO_2 NWs with a length of some meters and a diameter of 80–140 nm, as illustrated in Figure 6.10a–c. The TiO_2 nanowires have a similar structure to corm and are comparable in diameter and length to normal nanowires. They are produced when the treatment time is increased by up to 72 hours. The synthesized nanowires showed similar behavior after a single-step hydrothermal operation, with a procedure time increase of up to 160 hours. After the dispersion agent and solvents were removed, all of the electrodes produced had a porous structure [134].

The ZnS NWs were made using a straightforward hot injection method using just solvent with high boiling and acted as surfactant and reducing agent, ODA, at the same time. TEM, EDX, and XRD investigations were used to explore the shape and crystalline structure of ZnS nanowire for application in solar cells. The TEM and electrostatic discharge (ESD) analysis of the ZnS NWs are shown in Figure 6.11. The as-prepared product can be observed in the TEM image to be made up of numerous one-dimensional-like ZnS nanocrystals. As shown in the high magnification image (Figure 6.11a–d), these agglomerations are made up of multi-well-defined, extremely homogeneous ZnO NWs structures with diameters
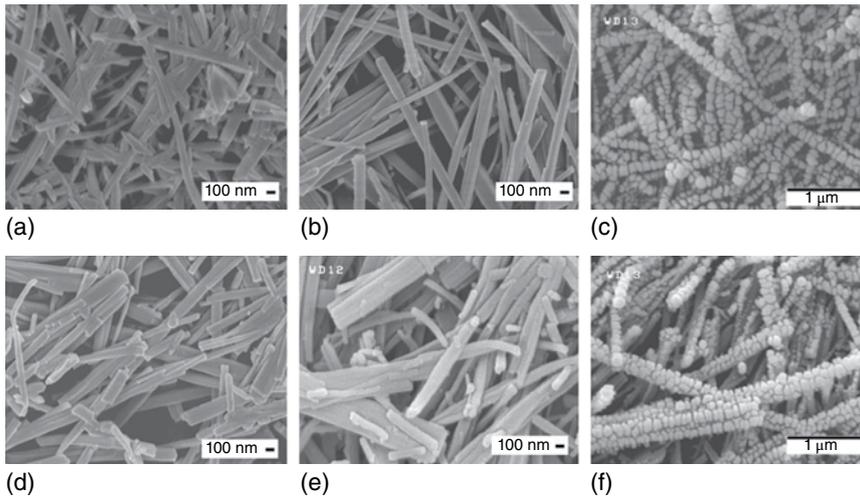
Figure 6.10 FE-SEM image of the TiO_2 NWs fabricated by the process of two hydrothermal, the first at temperature of 180 °C and the second at 180 °C with changes in times: (a) 12 hours, (b) 48 hours (c) 72 hours, (d) 120 hours, (e) 140 hours, and (f) 160 hours. Source: Bakhshayesh et al. [134], Elsevier.
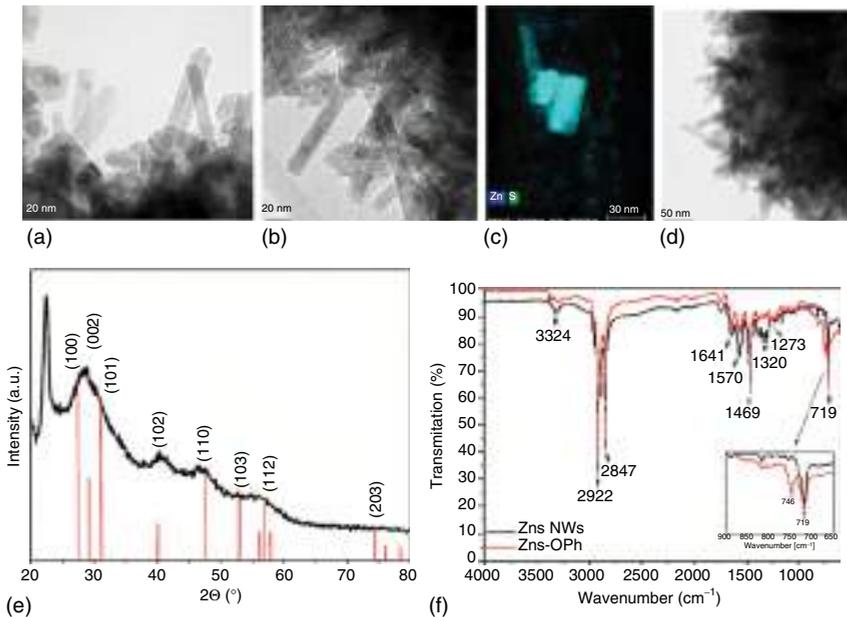

Figure 6.11 (a–d) TEM morphological image of the ZnS nanowire, and (e, f) EDS analysis of the ZnS nanowire. Source: Matras-Postołek et al. [139], Elsevier.

of 10–20 nm and lengths of up to 100–150 nm. According to the energy dispersive spectroscopy (EDS) analysis (Figure 6.11e), the ZnS NWs included zinc and sulfur in an atomic ratio of about 1 : 1 for S to Zn, which was close to the ZnS stoichiometry. The exchange of ligand process with the help of o-phenylenediamine had no

significant influence on the ZnS nanowire's morphology and size, as illustrated in Figure 6.11f [139].

To acquire a thorough knowledge of the PbS nanoparticles coated as a shell over the CdS NWs, FE-SEM morphological images on scale 200 nm have been observed as exhibited in Figure 6.12 for CdS nanowire as well as encapsulated by PbS in 5, 10, 15, and 20 successive ionic layer adsorption and reaction (SILAR) cycles, respectively. Figure 6.12a shows the CdS NWs with a bigger surface area and an interconnected nanonetwork. For 10 cycles (Figure 6.12c), the size increase can be seen, but for 5 cycles (Figure 6.12b), the small growth of PbS particles can be seen. Overgrowth of the PbS layer occurs in the region of the pre-adsorbed PbS nucleation sites where embryo centers originate. Furthermore, repeated immersion and cleaning cycles beyond a certain threshold induce the PbS layer to densify over the CdS NWs, increasing the nanowire diameter by filling the empty space between them. Figure 6.12d shows the design of a device with the configuration FTO/CdS flat/CdS NWs/PbS/polysulfide/CuS, where the photoanode is CdS NWs/PbS and the counter electrode is CuS-coated FTO, separated by a 50-mm thick scotch spacer [140].

The shape of the $NaNbO_3$ and $Pt/NaNbO_3$ NWs was investigated using high-resolution transmission electron microscopy (HRTEM), transmission electron microscopy (TEM), and SEM. Figures 6.13a,b show a significant number of $NaNbO_3$ NWs with diameters of 100 nm and lengths of micrometers [132].
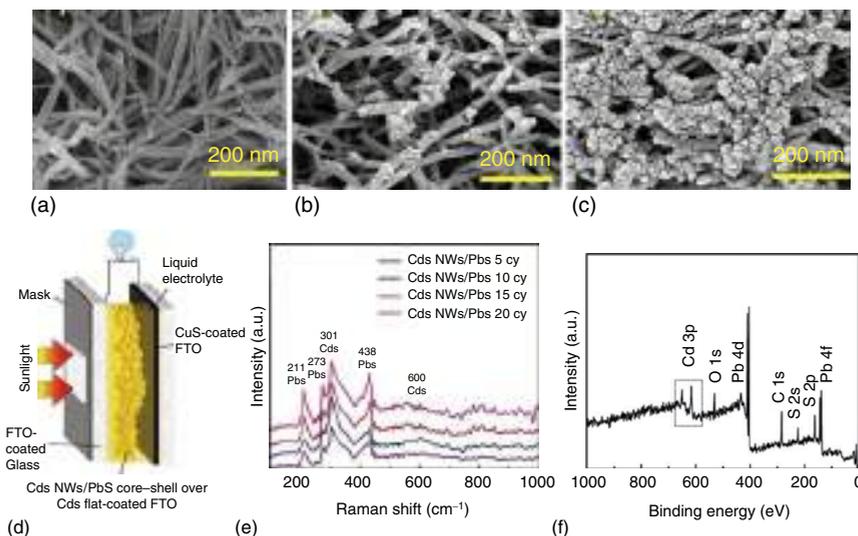
Figure 6.12 (a) FE-SEM image of CdS NWs, (b, c) SEM image of the structure of CdS NWs/PbS core–shell over PbS layer with 5 and 20 cycles, respectively, (d) the schematic representation of the photoelectrochemical cell of the CdS NWs/PbS core–shell, (e) Raman spectra of CdS NWs/PbS, and (f) X-ray photoelectron spectroscopy (XPS) image of PbS conformal growth over the CdS NWs. Source: Majumder et al. [140], Elsevier.

(a)　　　　　　　　　　　　　　　(b)
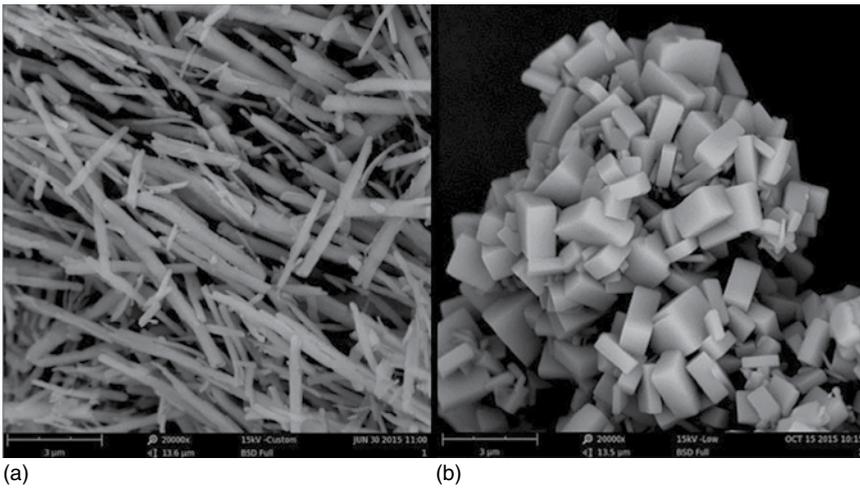
Figure 6.13 (a) SEM images of NaNbO$_3$ nanowires and (b) SEM images of Pt/NaNbO$_3$ nanowires. Source: Liu et al. [132], Elsevier.

6.4 Applications of Semiconductors in Solar Cells

6.4.1 Si-NWs for Solar Cells

The creation of charge carriers in semiconductor materials and the subsequent separation of the charge carriers generated by photons are the foundations of most conventional solar cells [141]. As a result, the semiconductor layers are the most important components of the solar cell, accounting for the vast majority of the device. A variety of semiconductor materials are suitable for converting photon energy to electrical energy. The solar cell based on crystalline structure silicon (c-Si), which today dominates the industry sector by PV, is an excellent example of a traditional solar cell structure because of its simple construction. The key properties of c-Si solar cells are shown in Figure 6.14. A square wafer of p-type doped with a thickness of about 300 m and 10×10 or $12.5 \times 12.5 \, cm^2$ area is commonly used as an absorber material. A highly doped layer is generated on the wafer of c-Si top and back sides, n$^+$-type and p$^+$-type, respectively. The charge carriers generated by photons are separated through a highly doped layer of wafers of c-Si. The solar industry is moving toward wafers with a thickness and area of up to 250 m and $20 \times 20 \, cm^2$, respectively [80].

Solar cells have a bottom and top grid of metallic as well as additional contacts of electrical, which capture the charge carriers that are separated and link them to the load of the cell, in addition to semiconductor layers. A thin layer of antireflective coating is frequently applied to the cell's topside to reduce light reflection. A transparent encapsulant or glass sheet is applied to the cell's sides to protect it from the effects of the outside environment while it is working. The layer that makes up thin film cells is deposited on the carrier of the substrate in thin film solar cells. The cheaper substrates, like foil of polymer, metal, or glass sheet, are utilized at low

Figure 6.14 A schematic of c-Si solar cell structure. Source: Atikur Rahman et al. [80], ASRJETS, Public domain.

temperatures during the processing of layer deposition. c-Si was the first practical solar cell, and it is now the most extensively used PV material. As a result, we may use c-Si to describe semiconductor characteristics that are important for solar cell operations. This offers us a fundamental grasp of how other semiconductor materials-based solar cells function [80]. A solar cell's performance and design can be affected by a lot of different things:

(i) doping atom concentration, which may be either donor atoms that supply free electrons (ND) or acceptor atoms that accept electrons (NA). The width of a junction's space-charge zone is determined by the concentrations.

(ii) the charge carrier mobility parameter and the diffusion coefficient, D, are two parameters that define how charge carriers move as a result of diffusion and drift, respectively.

(iii) the lifespan of surplus carriers, τ, and the diffusion length, L, that defines generation-recombination processes.

(iv) The bandgap energy, e.g. the absorption coefficient, α and the refractive index, n, all describe a semiconductor's ability to absorb visible and non-visible light.

6.4.2 ZnO Nanowires for Solar Cell

Nanostructured materials of metal oxide are a hot topic in science right now, with a lot of potential applications [142–144]. Solar cells are particularly interested in dye-sensitized nanoporous materials. ZnO NWs' ultra-thin absorber ZnO/CdSe/CuSCN (eta)-solar cells were able to make a lot of electricity with simple electrochemical and solution deposition processes [145]. The layer of ZnO/CdSe NWs showed a substantial effect of light trapping in the spectrum of the sun in the region of 400–800 nm, with an effective 8% reflectance and 89.6% absorbance. The nanotube ZnO arrays were created by the usage of simple ZnO nanorods that are generated

electrochemically [146]. For solar cell applications, cadmium selenide nanoparticle sensitizers were placed on the nanorods and nanotubes of ZnO arrays. The solar cell based on the nanotube of CdSe/ZnO could exhibit a conversion efficiency of 0.44% when illuminated with white light at $85\,mW/cm^2$ intensity. The photocurrent density of nanorods and nanotubes of CdSe/ZnO solar cells was enhanced by 8%, resulting in an 8% improvement in conversion efficiency. This technology for making PV electrodes might point the way forward in the realm of multifunction solar cell materials. The DSSC is a good option for a new renewable energy technology due to its low cost and immense efficiency. Several attempts to employ ZnO in DSSC have been made [147]. ZnO NWs were employed as the photo-electrode in DSSCs. The overall efficiencies, photovoltage, photocurrent, and fill factor of a typical solar cell were 0.3%, 0.7V, $1.3\,mA/cm^2$, and 0.35–0.40, respectively. The nanowires' sizes have no impact on electron transit inside them.

OSCs, with their cheap price, light weight, and capabilities of solution processing, have sparked a lot of attention. A conjugated polymer with a low bandgap is combined with fullerene to make bulk heterojunction devices. The review evaluated the compound of polymer with a low bandgap and its use in OPVs [148, 149]. A complete roll-to-roll (R2R) solar cell polymer module was manufactured in the ambient environment with processing of solution and no vacuum stages. The finished modules (Figure 6.15) were adaptable and durable. They have shown how to transition P3CT/ZnO technology in ways that allow for complete compatibility of R2R in the ambient environment, with vacuum coating phases not necessary throughout the modules' five layers of manufacturing.

Nadarajah et al. reported a unique solar cell structure made up of ZnO NWs It is an n-type, undoped layer of CdSe generated from precursors of quantum dots and a layer of p-type polymer. During the manufacturing process, the layer of quantum dot is transformed into a polycrystalline film that is 30 nm thick. While both MEH-PPV and P3HT have been tested for this contact, P3HT provided the greatest results. The cell is created at temperatures below 100 °C in lab air. The energy conversion efficiency is increased by roughly 1% after many phases of intermittent annealing [150].

Figure 6.15 One of the completed modules in front of the R2R coater. Source: Krebs et al. [149], Elsevier.

6.4.3 Ag-NWs for Solar Cells

Because of their low resistance and high transparency, metallic nanowire electrodes are appealing candidates for assembly in many existing solar cells. The randomly stacked nanowires always have a high haze because of the random stacking of nanowires. A high haze factor indicates that there is a lot of light scattering into the device, which means the PV system's effective absorption cross section is higher. As a consequence, Ag-NWs have been employed as front electrodes in solar cells by a number of organizations [151–158]. In many PV modules, increasing the conductivity of electrode to improve PCE is a typical problem. Singh et al. [159] discovered an all-printing approach for making copper indium gallium selenide (CIGS) solar cell using an Ag-NW/ZnO front electrode by 16/sq. resistance and 94% transparency. The high conductivity front electrode has a higher PCE than the sprayed electrode of ZnO/ITO. A solution process Ag-NW/poly(3,4-ethylenedioxy-thiophene (PEDOT): electrode of PSS transparent also achieved a 3.6% PCE, which is almost as high as a silver electrode [160]. Furthermore, metallic nanowire networks have inherent haze factors that can be used to improve PCE [128, 129]. These haze factors can range from 1% to 30% depending on the manufacturing conditions. For example, spin coating and spray deposition may provide haze factors of less than 2%. A haze factor of roughly 30% was obtained using standard vacuum filtering and transfer processes. In a polymer solar cell, Gaynor et al. [152] achieved a 10% improvement in conversion efficiency by substituting the ITO standard with an Ag–NW composite electrode. Furthermore, visible range of semi-transparent solar cell might be produced utilizing the IR spectrum by the network of metal nanowire [156]. This kind of solar cell might be used to make tinted windows that produce energy while lowering glare, perhaps addressing the issue of a hot island in a major city.

Metallic nanowires' flexibility, in addition to their high transparency and conductivity, provides a fantastic opportunity to create free bendable solar cells, particularly flexible organic solar cells (FOSCs), which have received a lot of interest as a potential next-generation cost-efficient and energy-harvesting device due to their low manufacturing cost, lighter weight, great flexibility, and short processing time based on printing [86, 161]. Because of their low resistance, higher specular transmittance, effect of surface plasmon resonance, and good flexibility, metallic nanowire are the materials as electrode for great performance of FOSCs. The great performance OSCs employing an Ag-NW sheet as an electrode were reported by Lee et al. [162]. Because of its higher optical transmittance, considerable absorption owing to scattering of light, and improved roughness of surface, the Ag-nanowire film acquired a higher short-circuit current than the electrode based on the ITO device. Although substantial roughness boosted solar cell light absorption, it resulted in a superior dark current and a lower voltage of open circuit. As a consequence, new methods for lowering the roughness of the surface of metallic nanowire films have been reported lately. Choi et al. [163] used a simple brush painting approach to embed the network of Ag-NWs between the thin films of ITO, resulting in flexible multilayer electrode of ITO/Ag-NW/ITO with high transmittance, low

sheet, and significant mechanical flexibility. To overcome the roughness of the Ag-NW electrode, Tokuno et al. [151] adopted the pressure approach to achieve the same PCE in the FOSCs as the electrode of ITO. According to Noh et al. [164], the surface of electrode of Ag-nanowires were becoming smooth using an additional PEDOT spray-coated layer, resulting to improve the efficiency of cell. A simple and scaled-up solution strategy was also employed to create a less expensive Cu-NW integrating electrode of PEDOT: PSS with a low roughness of surface of approximately 70 nm, high oxidation flexibility, and stability. It is used to build an OSC with a highly PCE coating [165]. These findings suggest that raising conductivity, transmittance, and roughness to ideal fabrication conditions may boost the performance of solar cells produced from solution-processed nanowires of metallic material. The manufacturing technology in particular might be expanded into a high-throughput, R2R low-cost process, possibly decreasing the expensive cost of flexible FOSCs and opening up a new market in the future.

6.4.4 III-V NWs

Due to the structure, there are two techniques for applying devices made of III–V nanowires. The first is to employ epitaxial heterostructures in cutting-edge electronics like single-photon emitters [166]. The second process is the fabrication of the structure of the core–shell for sources of light and detectors. In an application based on III–V NW, the use of a core–shell structure would be critical in terms of surface passivation. In addition, research on PV devices and optical applications that exploit the geometric properties of nanowires has been developing applications based on the latter method, which has recently become extremely popular. Also, they used radial p–n junction to make GaAs/AlGaAs CMS NW-based near-infrared (NIR) LEDs [167] and solar cell based on core–shell InP NWs [133].

6.4.5 Cu-NWs for Solar Cell

Cu-NW-based TCFs have demonstrated strong optoelectronic performance as well as mechanical flexibility. As a result, they might be used in touch screens [168, 169], solar cells [170–173], OLEDs [174–176], and sensors [177, 178], along with many other optoelectronic devices. Stewart et al. demonstrated that OSCs using nanowire of Cu core–Ni shell films as anodes may reach a device 4.9% efficiency, which is substantially comparable to the efficiency of 5% attained by OSCs with anodes of Ag-NW [170]. Won et al. also obtained a PCE of 7.1% by merging transparent electrodes based on Cu-NW with Cu(In1x,Gax)(S,Se)2 thin film solar cells [172]. Song et al. stated that Cu@Cu–Ni NWs were employed as conductors in devices of OLED that were stable under severe stretching and bending circumstances [174]. Because of their superior electron transport and great mechanical strength, Cu-NWs have been extensively explored in the production of electrochemical-based biosensors for sensing applications. Stortini et al. designed a series of Cu-NWs electrodes with various shapes. At concentrations as low as a few micromoles, the electrodes displayed excellent nitrate detection performance [177].

6.5 Conclusion and Future Perspectives

The sun generates solar energy, which is a mix of heat and light. This energy travels from the sun to the ground, where it is collected by solar collectors and converted into whatever kind of energy it desired. According to one estimate, this renewable energy source is strong enough to replace the 650 barrels of oil we use each year for electricity. Thanks to a newly found structure of nanotube capable of transmitting charges of electricity 100 million times higher than previously observed, next-generation solar cells might be vastly more helpful. Silicon is now used to absorb light in the majority of solar cells. Scientists have developed nanotubes of carbon material that may be used to improve the absorption of light capacities of present cells due to inefficiencies in the material. However, since nanotubes are difficult to organize, they have been arbitrarily inserted into solar cells in poor configurations until recently. According to research from Britain's Exeter University, modern solar panels constructed from a perovskite mineral have a high potential for converting solar energy into domestic power more cheaply than ever before. Senthilarasu Sundaram, one of the study's authors, told the Thomson Reuters Foundation that super-thin, custom-colored panels affixed to a building's windows might become a "holy grail" for Indian and African nations. These sorts of materials will be like the holy grail in such countries: they can shade windows while also producing power. Solar panels made of perovskite minerals will be up to 40% cheaper and 50% more efficient than those currently on the market, with a thickness estimated to be billionths of a meter. Perovskite solar panels, unlike other solar panels, can absorb the majority of the solar spectrum and operate in a variety of air circumstances. This form of solar cell material works many times better under dispersed settings than any other type of solar cell. The material has previously been tested throughout the Middle East, Europe, Asia, and the Americas by researchers. According to the Exeter research, existing commercial products of solar power, such as thin film or silicon-based technologies, are costly due to the process carried out under the vacuum-based condition. According to the report, the manufacturing procedure for panels of perovskite material is simple, but researchers must test the material under various situations to better understand its features before corporations begin production at industrial scale. Because of government objectives for the production of renewable energy and as much as possible reduction of CO_2 emissions, the PV energy sector has been rising, and the International Energy Agency has predicted that solar energy will be the world's largest source of power by 2050.

Solar cells must become low in cost and consume fewer natural resources to offer clean energy to a large portion of the world's population. The amount and grade of material that can be utilized to make solar cells much more efficient is limited by current planar technology. The nanowire design relaxes these criteria, particularly when it features a radial junction, enabling the use of a small quantity of plentiful, nontoxic materials. The cost of materials is very low to build solar cells with performance comparable to present planar technology. The capacity to create nanowires on low-cost substrates like aluminum foil, as well as the ability to relax strain in succeeding epitaxial layers, eliminates two additional important cost barriers in high-efficiency

planar solar cells. Despite the enormous potential of solar cells based on nanowires, a number of significant obstacles must be overcome before the advantages can be realized economically. Mechanical and chemical stability, fine morphology and doping control, nanowire array homogeneity, surface roughness, surface and interface recombination, and synthetic scalability are some of the issues that need to be addressed. Significant progress has been achieved in most of these domains, but much more effort is required, particularly in the field of understanding surfaces and interfaces. Even though nanowire devices may achieve efficiency equivalent to planar devices at substantially lower prices, practical concerns like quick scaling, module integration, and packaging of devices must be addressed. Nanowire solar cells should get more attention because of the huge improvements in efficiency over the last five years, as well as the possibility of cost reductions well below planar constraints.

References

1 Thony, P. (2015). Semiconductor nanowires for solar cells. In: *Semiconductor Nanowires: Materials, Synthesis, Characterization and Applications*, Woodhead Publishing Series in Electronic and Optical Materials (ed. J. Arbiol and Q. Xiong), 411–439.

2 Semiconductor|Definition, Examples, Types, Uses, Materials, Devices, & Facts|Britannica. https://www.britannica.com/science/semiconductor.

3 Materon, E.M., Ibáñez-Redín, G., Joshi, N. et al. (2020). Analytical detection of pesticides, pollutants, and pharmaceutical waste in the environment. In: *Nanosensors for Environmental Applications. Environmental Chemistry for a Sustainable World*, vol. 43 (ed. S. Kumar Tuteja, D. Arora, N. Dilbaghi and E. Lichtfouse), 87–129. Cham. https://doi.org/10.1007/978-3-030-38101-1_3: Springer.

4 Singh, A., Salmi, Z., Joshi, N. et al. (2013). Photo-induced synthesis of polypyrrole-silver nanocomposite films on N-(3-trimethoxysilylpropyl)pyrrole-modified biaxially oriented polyethylene terephthalate flexible substrates. *RSC Adv.* 3 (16): 5506.

5 Singh, A., Salmi, Z., Jha, P. et al. (2013). One step synthesis of highly ordered free standing flexible polypyrrole-silver nanocomposite films at air–water interface by photopolymerization. *RSC Adv.* 3 (32): 13329.

6 Singh, A., Salmi, Z., Joshi, N. et al. (2013). Electrochemical investigation of free-standing polypyrrole–silver nanocomposite films: a substrate free electrode material for supercapacitors. *RSC Adv.* 3 (46): 24567.

7 Singh, A., Kumar, A., Kumar, A. et al. (2013). Bending stress induced improved chemiresistive gas sensing characteristics of flexible cobalt-phthalocyanine thin films. *Appl. Phys. Lett.* 102 (13): 132107.

8 Mekki, A., Joshi, N., Singh, A. et al. (2014). H_2S sensing using in situ photo-polymerized polyaniline–silver nanocomposite films on flexible substrates. *Org. Electron.* 15 (1): 71–81.

9 Joshi, N., Saxena, V., Singh, A. et al. (2014). Flexible H_2S sensor based on gold modified polycarbazole films. *Sens. Actuators, B* 200: 227–234.

10 Kumar, A., Joshi, N., Samanta, S. et al. (2015). Room temperature detection of H_2S by flexible gold–cobalt phthalocyanine heterojunction thin films. *Sens. Actuators, B* 206: 653–662.

11 Joshi, N., da Silva, L.F., Jadhav, H. et al. (2016). One-step approach for preparing ozone gas sensors based on hierarchical $NiCo_2O_4$ structures. *RSC Adv.* 6 (95): 92655–92662.

12 Gusain, A., Joshi, N.J., Varde, P.V., and Aswal, D.K. (2017). Flexible NO gas sensor based on conducting polymer poly[N-9′-heptadecanyl-2,7-carbazole-alt-5,5-(4′,7′-di-2-thienyl-2′,1′,3′-benzothiadiazole)] (PCDTBT). *Sens. Actuators, B* 239: 734–745.

13 Bishnoi, A., Kumar, S., and Joshi, N. (2017). Wide-Angle X-ray Diffraction (WXRD). In: *Microscopy Methods in Nanomaterials Characterization* (ed. S. Thomas, R. Thomas, A.K. Zachariah and R.K. Mishra), 313–337. Elsevier.

14 Joshi, N., Hayasaka, T., Liu, Y. et al. (2018). A review on chemiresistive room temperature gas sensors based on metal oxide nanostructures, graphene and 2D transition metal dichalcogenides. *Microchim. Acta* 185 (4): 213.

15 Liu, H., Chu, Y., Liu, Y. et al. (2018). Selective sensing of chemical vapors using phase spectra detection on CVD graphene fet. In: *2018 IEEE Micro Electro Mechanical Systems (MEMS)*, 210–213.

16 Joshi, N., da Silva, L.F., Jadhav, H.S. et al. (2018). Yolk-shelled $ZnCo_2O_4$ microspheres: surface properties and gas sensing application. *Sens. Actuators, B* 257: 906–915.

17 Liu, H., Liu, Y., Chu, Y. et al. (2018). AC phase sensing of graphene FETs for chemical vapors with fast recovery and minimal baseline drift. *Sens. Actuators, B* 263: 94–102.

18 Nie, J., Wu, Y., Huang, Q. et al. (2019). Dew point measurement using a carbon-based capacitive sensor with active temperature control. *ACS Appl. Mater. Interfaces* 11 (1): 1699–1705.

19 Salzmann, I., Heimel, G., Oehzelt, M. et al. (2016). Molecular electrical doping of organic semiconductors: fundamental mechanisms and emerging dopant design rules. *Acc. Chem. Res.* 49 (3): 370–378.

20 Sahoo, M.K. and Kale, P. (2019). Integration of silicon nanowires in solar cell structure for efficiency enhancement: a review. *J. Mater.* 5 (1): 34–48.

21 Soga, T. (2006). Fundamentals of solar cell. *Nanostruct. Mater. Solar Energy Convers.* 3–43.

22 Nehra, M., Dilbaghi, N., Marrazza, G. et al. (2020). 1D semiconductor nanowires for energy conversion, harvesting and storage applications. *Nano Energy* 76 (104): 991.

23 Shockley, W. and Queisser, H.J. (1961). Detailed balance limit of efficiency of p-n junction solar cells. *J. Appl. Phys.* 32 (3): 510–519.

24 Li, H.M., Lee, D.Y., and Yoo, W.J. (2012). Optoelectronic performance of radial-junction Si nanopillar and nanohole solar cells. *IEEE Trans. Electron Devices* 59 (9): 2368–2374.

25 Wang, B. and Leu, P.W. (2012). Enhanced absorption in silicon nanocone arrays for photovoltaics. *Nanotechnology* 23 (19): 194003.

26 Zhou, L., Yu, X., and Zhu, J. (2014). Metal-core/semiconductor-shell nanocones for broadband solar absorption enhancement. *Nano Lett.* 14 (2): 1093–1098.

27 Xie, C., Nie, B., Zeng, L. et al. (2014). Core-shell heterojunction of silicon nanowire arrays and carbon quantum dots for photovoltaic devices and self-driven photodetectors. *ACS Nano* 8 (4): 4015–4022.

28 Ali, N.M. and Rafat, N.H. (2017). Modeling and simulation of nanorods photovoltaic solar cells: a review. *Renewable Sustainable Energy Rev.* 68: 212–220.

29 Shah, V., Bhaliya, J., Patel, G.M., and Joshi, P. (2022). Room-temperature chemiresistive gas sensing of SnO_2 nanowires: a review. *J. Inorg. Organomet. Polym. Mater.* 32 (3): 741–772.

30 Otnes, G. and Borgström, M.T. (2017). Toward high efficiency nanowire solar cells. *Nano Today* 12: 31–45.

31 Shah, V., Bhaliya, J., Patel, G.M., and Joshi, P. (2022). Recent advancement in Pd-decorated nanostructures for its catalytic and chemiresistive gas sensing applications: a review. *Topics Catal.*

32 Krogstrup, P., Jørgensen, H.I., Heiss, M. et al. (2013). Single-nanowire solar cells beyond the Shockley–Queisser limit. *Nat. Photonics* 7 (4): 306–310.

33 Patel, G., Pillai, V., and Vora, M. (2019). Liquid phase exfoliation of two-dimensional materials for sensors and photocatalysis – a review. *J. Nanosci. Nanotechnol.* 19 (8): 5054–5073.

34 Singh, N., Sahoo, M.K., and Kale, P.G. (2018). Effect of MACE parameters on length of porous silicon nanowires (PSiNWs). *J. Cryst. Growth* 496–497: 10–14.

35 Amri, C., Ouertani, R., Hamdi, A., and Ezzaouia, H. (2017). Effect of silver-assisted chemical vapor etching on morphological properties and silicon solar cell performance. *Mater. Sci. Semicond. Process.* 63: 176–183.

36 Kurokawa, Y., Yano, M., Miyajima, S., and Yamada, A. (2017). Bandgap tuning of silicon nanowire arrays for application to all-silicon tandem solar cells. *Jpn J. Appl. Phys.* 56 (4S): 04CS03.

37 Zhang, X., Zeng, X., Zhang, S., and Liu, F. (2016). Improving the performance of radial n-i-p junction Si nanowire solar cells by catalyst residue removal. *Mater. Sci. Semicond. Process.* 41: 457–461.

38 Nafie, N., Lachiheb, M.A., and Bouaicha, M. (2012). Effect of etching time on morphological, optical, and electronic properties of silicon nanowires. *Nanoscale Res. Lett.* 7 (1): 393.

39 Al-Taay, H.F., Mahdi, M.A., Parlevliet, D., and Jennings, P. (2017). Fabrication and characterization of solar cells based on silicon nanowire homojunctions. *Silicon* 9 (1): 17–23.

40 Vu, X.T., GhoshMoulick, R., Eschermann, J.F. et al. (2010). Fabrication and application of silicon nanowire transistor arrays for biomolecular detection. *Sens. Actuators, B* 144 (2): 354–360.

41 Zhang, G.-J. and Ning, Y. (2012). Silicon nanowire biosensor and its applications in disease diagnostics: a review. *Anal. Chim. Acta* 749: 1–15.

42 Choi, J.-H., Kim, H., Kim, H.-S. et al. (2013). MMP-2 detective silicon nanowire biosensor using enzymatic cleavage reaction. *J. Biomed. Nanotechnol.* 9 (4): 732–735.

43 Biswas, P., Karn, A.K., Balasubramanian, P., and Kale, P.G. (2017). Biosensor for detection of dissolved chromium in potable water: A review. *Biosens. Bioelectron.* 94: 589–604.

44 Gao, A., Lu, N., Dai, P. et al. (2011). Silicon-nanowire-based CMOS-compatible field-effect transistor nanosensors for ultrasensitive electrical detection of nucleic acids. *Nano Lett.* 11 (9): 3974–3978.

45 Tomioka, K., Yoshimura, M., and Fukui, T. (2012). A III–V nanowire channel on silicon for high-performance vertical transistors. *Nature* 488 (7410): 189–192.

46 Patel, G., Pillai, V., Bhatt, P., and Mohammad, S. (2020). Application of nanosensors in the food industry. In: *Nanosensors for Smart Cities*, 355–368. Elsevier.

47 Patel, G.M., Shah, V.R., Bhatt, G.J., and Deota, P.T. (2021). Humidity nanosensors for smart manufacturing. In: *Nanosensors for Smart Manufacturing* (ed. S. Thomas, T.A. Nguyen, M. Ahmadi, et al.), 555–580. Elsevier.

48 Ge, M., Rong, J., Fang, X., and Zhou, C. (2012). Porous doped silicon nanowires for lithium ion battery anode with long cycle life. *Nano Lett.* 12 (5): 2318–2323.

49 Yang, Y., Ren, J.-G., Wang, X. et al. (2013). Graphene encapsulated and SiC reinforced silicon nanowires as an anode material for lithium ion batteries. *Nanoscale* 5 (18): 8689.

50 McSweeney, W., Geaney, H., and O'Dwyer, C. (2015). Metal-assisted chemical etching of silicon and the behavior of nanoscale silicon materials as Li-ion battery anodes. *Nano Res.* 8 (5): 1395–1442.

51 Baek, S.-H., Park, J.-S., Jeong, Y.-M., and Kim, J.H. (2016). Facile synthesis of Ag-coated silicon nanowires as anode materials for high-performance rechargeable lithium battery. *J. Alloys Compd.* 660: 387–391.

52 Yu, H., Sun, Y., Singh, N. et al. (2012). Perspective of flash memory realized on vertical Si nanowires. *Microelectron. Reliab.* 52 (4): 651–661.

53 Kayes, B.M., Atwater, H.A., and Lewis, N.S. (2005). Comparison of the device physics principles of planar and radial p-n junction nanorod solar cells. *J. Appl. Phys.* 97 (11): 114 302.

54 Perraud, S., Poncet, S., Noël, S. et al. (2009). Full process for integrating silicon nanowire arrays into solar cells. *Sol. Energy Mater. Sol. Cells* 93 (9): 1568–1571.

55 Kale, P.G., Pratibha, S., and Solanki, C.S. (2012). Synthesis and characterization of Si nanoparticles obtained on sonication of porous silicon multilayer films. *J. Nano Res.* 17: 13–25.

56 Kim, J., Lim, J., Kim, M. et al. (2014). Fabrication of carbon-coated silicon nanowires and their application in dye-sensitized solar cells. *ACS Appl. Mater. Interfaces* 6 (21): 18788–18794.

57 Chehata, N., Ltaief, A., Beyou, E. et al. (2015). Functionalized silicon nanowires/ conjugated polymer hybrid solar cells: optical, electrical and morphological characterizations. *J. Lumin.* 168: 315–324.

58 Fan, Z., Razavi, H., Do, J. et al. (2009). Three-dimensional nanopillar-array photovoltaics on low-cost and flexible substrates. *Nat. Mater.* 8 (8): 648–653.

59 Tang, J., Huo, Z., Brittman, S. et al. (2011). Solution-processed core–shell nanowires for efficient photovoltaic cells. *Nat. Nanotechnol.* 6 (9): 568–572.

60 Aberg, I., Vescovi, G., Asoli, D. et al. (2016). A GaAs nanowire array solar cell with 15.3% efficiency at 1 sun. *IEEE J. Photovoltaics* 6 (1): 185–190.

61 Mann, S.A., Oener, S.Z., Cavalli, A. et al. (2016). Quantifying losses and thermodynamic limits in nanophotonic solar cells. *Nat. Nanotechnol.* 11 (12): 1071–1075.

62 Wallentin, J., Anttu, N., Asoli, D. et al. (2013). InP nanowire array solar cells achieving 13.8% efficiency by exceeding the ray optics limit. *Science (1979)* 339 (6123): 1057–1060.

63 van Dam, D., van Hoof, N.J.J., Cui, Y. et al. (2016). High-efficiency nanowire solar cells with omnidirectionally enhanced absorption due to self-aligned indium–tin–oxide Mie scatterers. *ACS Nano* 10 (12): 11414–11419.

64 Ibáñez-Redín, G., Joshi, N., do Nascimento, G.F. et al. (2020). Determination of p53 biomarker using an electrochemical immunoassay based on layer-by-layer films with $NiFe_2O_4$ nanoparticles. *Microchim. Acta* 187 (11): 619.

65 Wu, Y., Joshi, N., Zhao, S. et al. (2020). NO_2 gas sensors based on CVD tungsten diselenide monolayer. *Appl. Surf. Sci.* 529 (147): 110.

66 Joshi, N., Braunger, M.L., Shimizu, F.M. et al. (2020). Two-dimensional transition metal dichalcogenides for gas sensing applications. In: *Nanosensors for Environmental Applications. Environmental Chemistry for a Sustainable World*, vol. 43 (ed. S. Kumar Tuteja, D. Arora, N. Dilbaghi and E. Lichtfouse), 131–155. Cham. https://doi.org/10.1007/978-3-030-38101-1_4: Springer.

67 Wu, Y., Huang, Q., Nie, J. et al. (2019). All-carbon based flexible humidity sensor. *J. Nanosci. Nanotechnol.* 19 (8): 5310–5316.

68 Liu, H., Chu, Y., Liu, Y. et al. (2019). Label-free AC sensing by a graphene transistor for 100-ppb formaldehyde in air. In: *2019 IEEE 32nd International Conference on Micro Electro Mechanical Systems (MEMS)*, 488–491.

69 Subramani, I.G., Perumal, V., Gopinath, S.C.B. et al. (2020). 3D nanoporous hybrid nanoflower for enhanced non-faradaic redox-free electrochemical impedimetric biodetermination. *J. Taiwan Inst. Chem. Eng.* 116: 26–35.

70 Kumar, A. and Joshi, N. (2021). Self-powered environmental monitoring gas sensors: piezoelectric and triboelectric approaches. In: *Nanobatteries and Nanogenerators* (ed. H. Song, R. Venkatachalam, T.A. Nguyen, et al.), 463–489. Elsevier.

71 Vasudevan, M., Tai, M.J.Y., Perumal, V. et al. (2021). Cellulose acetate-MoS_2 nanopetal hybrid: a highly sensitive and selective electrochemical aptasensor of Troponin I for the early diagnosis of Acute Myocardial Infarction. *J. Taiwan Inst. Chem. Eng.* 118: 245–253.

72 Materon, E.M., Joshi, N., Shimizu, F.M. et al. (2021). Electrochemical sensors based on metal oxide-boron nitride nanocomposites in the detection of biomolecules and toxic chemicals. In: *Metal Oxides in Nanocomposite-Based Electrochemical Sensors for Toxic Chemicals* (ed. A. Pandikumar and P. Rameshkumar), 293–311. Elsevier.

73 Materon, E.M., Wong, A., Gomes, L.M. et al. (2021). Combining 3D printing and screen-printing in miniaturized, disposable sensors with carbon paste electrodes. *J. Mater. Chem. C* 9 (17): 5633–5642.

74 Miyazaki, C.M., Joshi, N., Oliveira, O.N., and Shimizu, F.M. (2021). Metal oxides and sulfide-based biosensors for monitoring and health control. In: *Metal, Metal-Oxides and Metal Sulfides for Batteries, Fuel Cells, Solar Cells, Photocatalysis and Health Sensors. Environmental Chemistry for a Sustainable World*, vol. 62 (ed. S. Rajendran, H. Karimi-Maleh, J. Qin and E. Lichtfouse), 169–208. Cham. https://doi.org/10.1007/978-3-030-63791-0_6: Springer.

75 Materon, E.M., Gómez, F.R., Joshi, N. et al. (2021). Smart materials for electrochemical flexible nanosensors: advances and applications. In: *Nanosensors for Smart Manufacturing* (ed. S. Thomas, T.A. Nguyen, M. Ahmadi, et al.), 347–371. Elsevier.

76 Joshi, N., Braunger, M.L., Shimizu, F.M. et al. (2021). Insights into nano-heterostructured materials for gas sensing: a review. *Multifunct. Mater.* 4 (3): 032002.

77 Vasudevan, M., Tai, M.J.Y., Perumal, V. et al. (2020). Highly sensitive and selective acute myocardial infarction detection using aptamer-tethered MoS_2 nanoflower and screen-printed electrodes. *Biotechnol. Appl. Biochem.* https://doi.org/10.1002/bab.2060.

78 Materón, E.M., Miyazaki, C.M., Carr, O. et al. (2021). Magnetic nanoparticles in biomedical applications: a review. *Appl. Surf. Sci. Adv.* 6 (100): 163.

79 Lu, Y.-W., Wang, C., Joshi, N., and Liu, H. (2022). MoS_2 nanoflowers-activated peroxydisulfate oxidation for rapid and efficient water disinfection. *Water Cycle* 3: 44–49.

80 Atikur Rahman, M. (2014). A review on semiconductors including applications and temperature effects in semiconductors. *Am. Sci. Res. J. Eng. Technol. Sci.ences* 7 (1): 50–70.

81 Simya, O.K., Radhakrishnan, P., Ashok, A. et al. (2018). Engineered nanomaterials for energy applications. In: *Handbook of Nanomaterials for Industrial Applications* (ed. C.M. Hussain), 751–767. Elsevier.

82 Ong, P.-L. and Levitsky, I. (2010). Organic/IV, III-V semiconductor hybrid solar cells. *Energies (Basel)* 3 (3): 313–334.

83 Sengupta, D., Das, P., Mondal, B., and Mukherjee, K. (2016). Effects of doping, morphology and film-thickness of photo-anode materials for dye sensitized solar cell application – a review. *Renewable Sustainable Energy Rev.* 60: 356–376.

84 Kupec, J., Witzigmann, B., Choi, S. et al. (2009). Dispersion, wave propagation and efficiency analysis of nanowire solar cells. *Opt. Express* 17 (12): 10399–10410.

85 Kalowekamo, J. and Baker, E. (2009). Estimating the manufacturing cost of purely organic solar cells. *Sol. Energy* 83 (8): 1224–1231.

86 Li, G., Zhu, R., and Yang, Y. (2012). Polymer solar cells. *Nat. Photonics* 6 (3): 153–161.

87 Kaltenbrunner, M., White, M.S., Głowacki, E.D. et al. (2012, 2012). Ultrathin and lightweight organic solar cells with high flexibility. *Nat. Commun.* 3 (1): 1–7.

88 Huynh, W.U., Dittmer, J.J., and Alivisatos, A.P. (2002). Hybrid nanorod-polymer solar cells. *Science (1979)* 295 (5564): 2425–2427.

89 Chao, J.J., Shiu, S.C., and Lin, C.F. (2012). GaAs nanowire/poly(3,4-ethylenedioxythiophene):poly(styrenesulfonate) hybrid solar cells with incorporating electron blocking poly(3-hexylthiophene) layer. *Sol. Energy Mater. Sol. Cells* 105: 40–45.

90 Diener, M.D. and Alford, J.M. (1998). Isolation and properties of small-bandgap fullerenes. *Nature* 393 (6686): 668–671.

91 Wright, M. and Uddin, A. (2012). Organic – inorganic hybrid solar cells: a comparative review. *Sol. Energy Mater. Sol. Cells* 107: 87–111.

92 Wu, D. (2017) Compound semiconductor nanowires based organic-inorganic hybrid solar cell. PhD Thesis. Nanyang Technological University, Singapore.

93 Heeger, A.J. (2014). 25th anniversary article: bulk heterojunction solar cells: understanding the mechanism of operation. *Adv. Mater.* 26 (1): 10–28.

94 Bouclé, J., Chyla, S., Shaffer, M.S.P. et al. (2008). Hybrid solar cells from a blend of poly(3-hexylthiophene) and ligand-capped TiO_2 nanorods. *Adv. Funct. Mater.* 18 (4): 622–633.

95 Xu, T. and Qiao, Q. (2011). Conjugated polymer–inorganic semiconductor hybrid solar cells. *Energy Environ. Sci.* 4 (8): 2700–2720.

96 Wu, W.-Q., Lei, B.-X., Rao, H.-S. et al. (2013). Hydrothermal fabrication of hierarchically anatase TiO_2 nanowire arrays on FTO glass for dye-sensitized solar cells. *Sci. Rep.* 3 (1): 1352.

97 Fan, J., Fàbrega, C., Zamani, R.R. et al. (2013). Enhanced photovoltaic performance of nanowire dye-sensitized solar cells based on coaxial TiO_2@TiO Heterostructures with a cobalt(II/III) redox electrolyte. *ACS Appl. Mater. Interfaces* 5 (20): 9872–9877.

98 Lee, D., Rho, Y., Allen, F.I. et al. (2013). Synthesis of hierarchical TiO_2 nanowires with densely-packed and omnidirectional branches. *Nanoscale* 5 (22): 11 147.

99 Sun, P., Zhang, X., Wang, L. et al. (2015). Bilayer TiO_2 photoanode consisting of a nanowire–nanoparticle bottom layer and a spherical voids scattering layer for dye-sensitized solar cells. *New J. Chem.* 39 (6): 4845–4851.

100 Ko, S.H., Lee, D., Kang, H.W. et al. (2011). Nanoforest of hydrothermally grown hierarchical ZnO nanowires for a high efficiency dye-sensitized solar cell. *Nano Lett.* 11 (2): 666–671.

101 Barpuzary, D. and Qureshi, M. (2013). Enhanced photovoltaic performance of semiconductor-sensitized ZnO-CdS coupled with graphene oxide as a novel photoactive material. *ACS Appl. Mater. Interfaces* 5 (22): 11673–11682.

102 Fan, J., Hao, Y., Munuera, C. et al. (2013). Influence of the annealing atmosphere on the performance of ZnO nanowire dye-sensitized solar cells. *J. Phys. Chem. C* 117 (32): 16349–16356.

103 Garnett, E.C., Brongersma, M.L., Cui, Y., and McGehee, M.D. (2011). Nanowire solar cells. *Ann. Rev. Mater. Res.* 41: 269–295.

104 Hochbaum, A.I. and Yang, P. (2010). Semiconductor nanowires for energy conversion. *Chem. Rev.* 110 (1): 527–546.

105 Law, M., Goldberger, J., and Yang, P. (2004). Semiconductor nanowires and nanotubes. *Annu. Rev. Mater. Res* 34: 83–122.

106 Schmidt, V. and W.J.G.U. (2010). Growth, thermodynamics, and electrical properties of silicon nanowires. *Chem. Rev.* 110 (1): 361–388.

107 Fan, H.J., Werner, P., and Zacharias, M. (2006). Semiconductor nanowires: from self-organization to patterned growth. *Small* 2 (6): 700–717.

108 Wacaser, B.A., Dick, K.A., Johansson, J. et al. (2009). Preferential interface nucleation: an expansion of the VLS growth mechanism for nanowires. *Adv. Mater.* 21 (2): 153–165.

109 Hochbaum, A.I., Fan, R., He, R., and Yang, P. (2005). Controlled growth of Si nanowire arrays for device integration. *Nano Lett.* 5 (3): 457–460.

110 Perea, D.E., Hemesath, E.R., Schwalbach, E.J., and Lensch-Falk, J.L. (2009). Direct measurement of dopant distribution in an individual vapor-liquid-solid nanowire. *Nat. Nanotechnol.* 4 (5): 315–319.

111 Garnett, E.C., Tseng, Y.-C., Khanal, D.R. et al. (2009). Dopant profiling and surface analysis of silicon nanowires using capacitance-voltage measurements. *Nat. Nanotechnol.* 4 (5): 311–314.

112 Whang, S.J., Lee, S., Chi, D.Z. et al. (2007). B-doping of vapor–liquid–solid grown Au-catalyzed and Al-catalyzed Si nanowires: effects of B_2H_6 gas during Si nanowire growth and B-doping by a post-synthesis in situ plasma process. *Nanotechnology* 18 (27): 275302.

113 Pan, L., Lew, K.K., Redwing, J.M., and Dickey, E.C. (2005). Effect of diborane on the microstructure of boron-doped silicon nanowires. *J. Cryst. Growth* 277 (1–4): 428–436.

114 Dick, K.A., Deppert, K., Karlsson, L.S. et al. (2005). A new understanding of Au-assisted growth of III–V semiconductor nanowires. *Adv. Funct. Mater.* 15 (10): 1603–1610.

115 Persson, A.I., Larsson, M.W., Stenström, S. et al. (2004). Solid-phase diffusion mechanism for GaAs nanowire growth. *Nat. Mater.* 3 (10): 677–681.

116 Bierman, M.J., Lau, Y.K.A., Kvit, A.V. et al. (2008). Dislocation-driven nanowire growth and Eshelby twist. *Science (1979)* 320 (5879): 1060–1063.

117 Zhu, J., Peng, H., Marshall, A.F. et al. (2008). Formation of chiral branched nanowires by the Eshelby Twist. *Nat. Nanotechnol.* 3 (8): 477–481.

118 Schmid, H., Björk, M.T., Knoch, J. et al. (2008). Patterned epitaxial vapor-liquid-solid growth of silicon nanowires on Si(111) using silane. *J. Appl. Phys.* 103 (2): 024304.

119 Mårtensson, T., Carlberg, P., Borgstrom, M. et al. (2004). Nanowire arrays defined by nanoimprint lithography. *Nano Lett.* 4 (4): 699–702.

120 Zschech, D., Kim, D.H., Milenin, A.P. et al. (2007). Ordered arrays of <100>−oriented silicon nanorods by CMOS-compatible block copolymer lithography. *Nano Lett.* 7 (6): 1516–1520.

121 Huang, Z., Fang, H., and Zhu, J. (2007). Fabrication of silicon nanowire arrays with controlled diameter, length, and density. *Adv. Mater.* 19 (5): 744–748.

122 Garnett, E.C. and Yang, P. (2008). Silicon nanowire radial p-n junction solar cells. *J. Am. Chem. Soc.* 130 (29): 9224–9225.

123 Hsu, C.-M., Connor, S.T., Tang, M.X., and Cui, Y. (2008). Wafer-scale silicon nanopillars and nanocones by Langmuir-Blodgett assembly and etching. *Appl. Phys. Lett.* 93 (13): 133109.

124 Huang, Z., Zhang, X., Reiche, M. et al. (2008). Extended arrays of vertically aligned sub-10 nm diameter [100] Si nanowires by metal-assisted chemical etching. *Nano Lett.* 8 (9): 3046–3051.

125 Garnett, E. and Yang, P. (2010). Light trapping in silicon nanowire solar cells. *Nano Lett.* 10 (3): 1082–1087.

126 Bogush, G.H., Tracy, M.A., and Zukoski, C.F. IV (1988). Preparation of monodisperse silica particles: control of size and mass fraction. *J. Non-Cryst. Solids* 104 (1): 95–106.

127 Jeong, S., Hu, L., Lee, H.R. et al. (2010). Fast and scalable printing of large area monolayer nanoparticles for nanotexturing applications. *Nano Lett.* 10 (8): 2989–2994.

128 Wang, K., Chen, J., Zhou, W. et al. (2008). Direct growth of highly mismatched type II ZnO/ZnSe core/shell nanowire arrays on transparent conducting oxide substrates for solar cell applications. *Adv. Mater.* 20 (17): 3248–3253.

129 Peng, K., Xu, Y., Wu, Y. et al. (2005). Aligned single-crystalline Si nanowire arrays for photovoltaic applications. *Small* 1 (11): 1062–1067.

130 Shen, X., Sun, B., Liu, D., and Lee, S.-T. (2011). Hybrid heterojunction solar cell based on organic–inorganic silicon nanowire array architecture. *J. Am. Chem. Soc.* 133 (48): 19408–19415.

131 Patel, G.M., Bhatt, G.J., and Deota, P.T. (2022). Synthesis and characterization of silicon-based hybrid nanoparticles. In: *Silicon-Based Hybrid Nanoparticles* (ed. S. Thomas, T.A. Nguyen, M. Ahmadi, et al.), 11–43. Elsevier.

132 Liu, Q., Chai, Y., Zhang, L. et al. (2017). Highly efficient Pt/NaNbO$_3$ nanowire photocatalyst: its morphology effect and application in water purification and H$_2$ production. *Appl. Catal., B* 205: 505–513.

133 Kasuga, T., Hiramatsu, M., Hoson, A. et al. (1999). Titania nanotubes prepared by chemical processing. *Adv. Mater.* 11 (15): 1307–1311.

134 Bakhshayesh, A.M., Mohammadi, M.R., Dadar, H., and Fray, D.J. (2013). Improved efficiency of dye-sensitized solar cells aided by corn-like TiO$_2$ nanowires as the light scattering layer. *Electrochim. Acta* 90: 302–308.

135 Majumder, S., Baviskar, P.K., and Sankapal, B.R. (2016). Straightening of chemically deposited CdS nanowires through annealing toward improved PV device performance. *Ceram. Int.* 42 (6): 6682–6691.

136 Bouroushian, M. (2010). Chalcogens and metal chalcogenides. In: *Electrochemistry of Metal Chalcogenides. Monographs in Electrochemistry*. Berlin, Heidelberg: Springer https://doi.org/10.1007/978-3-642-03967-6_1.

137 Hodes, G. (2002). *Chemical Solution Deposition Of Semiconductor Films*. CRC Press.

138 Nair, N. and Sankapal, B.R. (2016). Cationic-exchange approach for conversion of two dimensional CdS to two dimensional Ag$_2$S nanowires with an intermediate core–shell nanostructure toward supercapacitor application. *New J. Chem.* 40 (12): 10144–10152.

139 Matras-Postołek, K., Żaba, A., Nowak, E.M. et al. (2018). Formation and characterization of one-dimensional ZnS nanowires for ZnS/P$_3$HT hybrid polymer solar cells with improved efficiency. *Appl. Surf. Sci.* 451: 180–190.

140 Majumder, S., Mendhe, A.C., and Sankapal, B.R. (2019). Nanoheterojunction through PbS nanoparticles anchored CdS nanowires toward solar cell application. *Int. J. Hydrogen Energy* 44 (14): 7095–7107.

141 Cagnani, G.R., Joshi, N., and Shimizu, F.M. (2019). Carbon nanotubes-based nanocomposite as photoanode. In: *Interfacial Engineering in Functional Materials for Dye-Sensitized Solar Cells* (ed. A. Pandikumar, K. Jothivenkatachalam and K. Bhojanaa), 213–229. Wiley.

142 Joshi, N., Shimizu, F.M., Awan, I.T. et al. (2016). Ozone sensing properties of nickel phthalocyanine:ZnO nanorod heterostructures. *IEEE Sens.* 2016: 1–3.

143 Gonçalves, R.A., Toledo, R.P., Joshi, N., and Berengue, O.M. (2021). Green synthesis and applications of ZnO and TiO$_2$ nanostructures. *Molecules* 26 (8): 2236.

144 Joshi, N., da Silva, L.F., Shimizu, F.M. et al. (2019). UV-assisted chemiresistors made with gold-modified ZnO nanorods to detect ozone gas at room temperature. *Microchim. Acta* 186 (7): 418.

145 Peng, Q. and Qi, Y. (2011). ZnO nanowires and their application for solar cells. In: *Nanowires - Implementations and Applications* (ed. A.A. Hashim), 157–178. InTech.

146 Luo, L., Lv, G., Li, B. et al. (2010). Formation of aligned ZnO nanotube arrays by chemical etching and coupling with CdSe for photovoltaic application. *Thin Solid Films* 518 (18): 5146–5152.

147 Baxter, J.B., Walker, A.M., van Ommering, K., and Aydil, E.S. (2006). Synthesis and characterization of ZnO nanowires and their integration into dye-sensitized solar cells. *Nanotechnology* 17 (11): S304–S312.

148 Bundgaard, E. and Krebs, F. (2007). Low band gap polymers for organic photovoltaics. *Sol. Energy Mater. Sol. Cells* 91 (11): 954–985.

149 Krebs, F.C. (2009). Polymer solar cell modules prepared using roll-to-roll methods: knife-over-edge coating, slot-die coating and screen printing. *Sol. Energy Mater. Sol. Cells* 93 (4): 465–475.

150 Nadarajah, A., Word, R.C., VanSant, K., and Könenkamp, R. (2008). Nanowire–quantum-dot–polymer solar cell. *Phys. Status Solidi (b)* 245 (9): 1834–1837.

151 Tokuno, T., Nogi, M., Karakawa, M. et al. (2011). Fabrication of silver nanowire transparent electrodes at room temperature. *Nano Res.* 4 (12): 1215–1222.

152 Gaynor, W., Lee, J.Y., and Peumans, P. (2010). Fully solution-processed inverted polymer solar cells with laminated nanowire electrodes. *ACS Nano* 23 (26): 30–34.

153 Morgenstern, F.S.F., Kabra, D., Massip, S. et al. (2011). Ag-nanowire films coated with ZnO nanoparticles as a transparent electrode for solar cells. *Appl. Phys. Lett.* 99 (18): 183307.

154 Lim, J.-W., Cho, D.Y., Eun, K. et al. (2012). Mechanical integrity of flexible Ag nanowire network electrodes coated on colorless PI substrates for flexible organic solar cells. *Sol. Energy Mater. Sol. Cells* 105: 69–76.

155 Yang, L., Zhang, T., Zhou, H. et al. (2011). Solution-processed flexible polymer solar cells with silver nanowire electrodes. *ACS Appl. Mater. Interfaces* 3 (10): 4075–4084.

156 Chen, C.C., Dou, L., Zhu, R. et al. (2012). Visibly transparent polymer solar cells produced by solution processing. *ACS Nano* 6 (8): 7185–7190.

157 Ajuria, J., Ugarte, I., Cambarau, W. et al. (2012). Insights on the working principles of flexible and efficient ITO-free organic solar cells based on solution processed Ag nanowire electrodes. *Sol. Energy Mater. Sol. Cells* 102: 148–152.

158 Stubhan, T., Krantz, J., Li, N. et al. (2012). High fill factor polymer solar cells comprising a transparent, low temperature solution processed doped metal oxide/metal nanowire composite electrode. *Sol. Energy Mater. Sol. Cells* 107: 248–251.

159 Singh, M., Jiu, J., Sugahara, T., and Suganuma, K. (2014). Thin-film copper indium gallium selenide solar cell based on low-temperature all-printing process. *ACS Appl. Mater. Interfaces* 6 (18): 16297–16303.

160 Margulis, G.Y., Greyson Christoforo, M., Lam, D. et al. (2013). Spray deposition of silver nanowire electrodes for semitransparent solid-state dye-sensitized solar cells. *Adv. Energy Mat.* 3 (12): 1657–1663.

161 Brabec, C.J. and Durrant, J.R. (2008). Solution-processed organic solar cell. *MRS Bull.* 33 (7): 670–675.

162 Lee, J.-Y., Connor, S.T., Cui, Y., and Peumans, P. (2008). Solution-processed metal nanowire mesh transparent electrodes. *Nano Lett.* 8 (2): 689–692.

163 Choi, K.-H., Kim, J., Noh, Y.-J. et al. (2013). Ag nanowire-embedded ITO films as a near-infrared transparent and flexible anode for flexible organic solar cells. *Sol. Energy Mater. Sol. Cells* 110: 147–153.

164 Noh, Y.-J., Kim, S.-S., Kim, T.-W., and Na, S.-I. (2014). Cost-effective ITO-free organic solar cells with silver nanowire–PEDOT:PSS composite electrodes via a one-step spray deposition method. *Sol. Energy Mater. Sol. Cells* 120: 226–230.

165 Chen, J., Zhou, W., Chen, J. et al. (2015). Solution-processed copper nanowire flexible transparent electrodes with PEDOT:PSS as binder, protector and oxide-layer scavenger for polymer solar cells. *Nano Res.* 8 (3): 1017–1025.

166 Borgstrom, M.T., Zwiller, V., Muller, E., and Imamoglu, A. (2005). Optically bright quantum dots in single nanowire. *Nano Lett.* 5: 1439.

167 Dorenbos, S.N., Sasakura, H., van Kouwen, M.P. et al. (2010). Position controlled nanowires for infrared single photon emission. *Appl. Phys. Lett.* 97 (171): 106.

168 Han, S., Hong, S., Ham, J. et al. (2014). Fast plasmonic laser nanowelding for a Cu-nanowire percolation network for flexible transparent conductors and stretchable electronics. *Adv. Mater.* 26 (33): 5808–5814.

169 Bao, C., Yang, J., Gao, H. et al. (2015). In situ fabrication of highly conductive metal nanowire networks with high transmittance from deep-ultraviolet to near-infrared. *ACS Nano* 9 (3): 2502–2509.

170 Stewart, I.E., Rathmell, A.R., Yan, L. et al. (2014). Solution-processed copper-nickel nanowire anodes for organic solar cells. *Nanoscale* 6 (11): 5980–5988.

171 Ahn, Y., Jeong, Y., Lee, D., and Lee, Y. (2015). Copper nanowire-graphene core-shell nanostructure for highly stable transparent conducting electrodes. *ACS Nano* 9 (3): 3125–3133.

172 Won, Y., Kim, A., Lee, D. et al. (2014). Annealing-free fabrication of highly oxidation-resistant copper nanowire composite conductors for photovoltaics. *NPG Asia Mater.* 6 (6): e105–e105.

173 Ko, S.H. (2014). Review of the multi-scale nano-structure approach to the development of high efficiency solar cells. *Smart Sci.* 2 (2): 54–62.

174 Song, J., Li, J., Xu, J., and Zeng, H. (2014). Superstable transparent conductive Cu@Cu$_4$Ni nanowire elastomer composites against oxidation, bending, stretching, and twisting for flexible and stretchable optoelectronics. *Nano Lett.* 14 (11): 6298–6305.

175 Won, Y., Kim, A., Yang, W. et al. (2014). A highly stretchable, helical copper nanowire conductor exhibiting a stretchability of 700%. *NPG Asia Mater.* 6 (9): e132–e132.

176 Im, H.G., Jung, S.H., Jin, J. et al. (2014). Flexible transparent conducting hybrid film using a surface-embedded copper nanowire network: a highly oxidation-resistant copper nanowire electrode for flexible optoelectronics. *ACS Nano* 8 (10): 10973–10979.

177 Stortini, A.M., Moretto, L.M., Mardegan, A. et al. (2015). Arrays of copper nanowire electrodes: preparation, characterization and application as nitrate sensor. *Sens. Actuators, B* 207 (Part A): 186–192.

178 Zhao, Y., Fan, L., Zhang, Y. et al. (2015). Hyper-branched Cu@Cu$_2$O coaxial nanowires mesh electrode for ultra-sensitive glucose detection. *ACS Appl. Mater. Interfaces* 7 (30): 16802–16812.

7

Introduction and Types of Semiconducting Hybrid Nanostructures for Optoelectronic Devices

Byrappanapalya S. Ravikumar[1] and Baishali Garai[2]

[1] M. S. Ramaiah University of Applied Sciences, Department of Physics, Faculty of Mathematical and Physical Sciences, Peenya 4th Phase, Bengaluru, 560058, India
[2] Dayananda Sagar University, Department of Physics, Bengaluru, 560068, India

7.1 Introduction

During the past few decades, increase in the innovation of high-performance materials and integration technologies have created more demand in a wide range. Applications, including environmental monitoring, optical communication, security and motion detection, and photodetectors with high "5S" (sensitivity, excellent selectivity, speed, great stability, and signal to noise ratio) characteristics have gained intensive attention of scientists worldwide [1–5]. Photodetectors made from nanostructured materials have been showing superior properties pertaining to detector responsivity and response enrichment, compared with bulk and traditional thin film-based photodetectors due to their condensed dimension and enriched surface-to-volume ratio. The nanostructures large surface-to-volume ratio leads to enhanced photodetector properties [6–10].

Over the past few years, various nanostructures have been made the stimulating growth in the applications of photodetector. There have numerous articles merely related to ZnO-nanostructured photodetectors [11–13]. On the other hand, main limitation of 1D ZnO-based photodetectors is low quantum competence because of generated electron–hole pairs that get recombined at faster rate on nanorod (NR)/nanowire (NW) surfaces. Furthermore, nanostructured ZnO limiting its application in broadband detection of light due to its wide bandgap that makes ZnO more responsive to UV light. Worldwide advanced hybrid nanostructures open up innovative wings and challenges for the creation of better response devices in optoelectronics to overcome the failure of devices which have been built by single component [14–21].

Broad materials, built from metals, metal oxides, carbonaceous materials, chalcogenides, etc., can be sensibly combined with tunable composition and merged to custom various composite structures. Also, composite shapes are inventive, for example three-dimensional, two-dimensional, one-dimensional, and zero-dimensional arrangements [22–33]. From the past few years, wide range of nanohybrid structure has been constructed using various effective synthesis techniques and integrated into photodetectors for understanding novel properties. According to diverse combination, a variety of hybrid nanostructures have been highlighted; in the present work, we have given in-depth information on 1D/2D hybrid nanostructure. Figure 7.1a shows that the isolated atomic planes might get reunited into heterostructures design through sheet by sheet in a specifically chosen order. Research on atomic planes is liable to continue important topic in the science of materials. Figure 7.1b gives an outline of the chemical vapor deposition (CVD) technique of two-dimensional materials, from single crystals to heterostructures and further to their device applications.

In this work, we have highlighted the advanced, scalable, and low-cost synthesis methods and compared the photo-detecting ability of photodetectors, based on hybrid nanostructure 1D semiconducting nanostructures composed of 2D materials, and deliberated their assembly process. We have debated the light-sensing properties of the 1D ZnO materials decorated with graphene and/or reduced graphene oxide (RGO), and MoS_2 2D materials. The synthesized method to build the 1D ZnO NW/NR on 2D layer-like material is discussed and summarized. The extensive choice of stimulating properties and probable use of growing technologies recommend hybrid structure composed of 1D ZnO and 2D transition metal chalcogenides (TMC: MoS_2, WS_2), and RGO material play an important role in the next few years. At the end, our viewpoints on upcoming challenges and openings in optoelectronics fields are discussed.

7.2 Synthesis of Nanostructured Materials

The synthetic approach to construct 1D, 2D, and 1D/2D nanostructures can be categorized into bottom-up and top-down methodology. To obtain nanosized
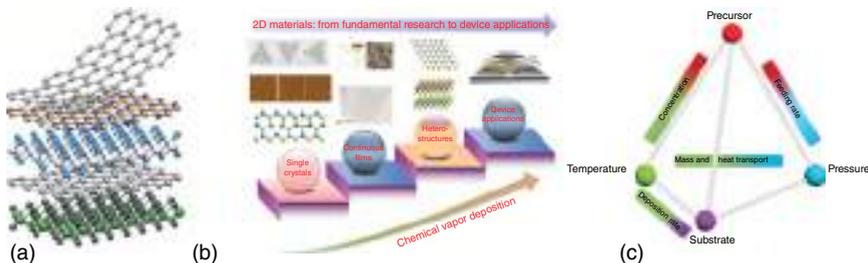
Figure 7.1 (a) Van der Waals hybrid structures. Source: Geim et al. [32]/Macmillan Publishers Limited. (b) Overview of the 2D materials using CVD growth, from single crystal to 2D material-based hybrid structures and their applications. (c) Schematic showing how various parameters affect the kinetics in the growth of 2D materials. Source: Reprinted with permission from Cai et al. [33]/American Chemical Society.

structures, the top-down method requires lateral planning of bulk materials using either additive or subtractive procedures [34]. Several techniques, such as ball milling and gas-phase condensation, are employed to produce nanostructures using a top-down method [35]. The production of nanostructures using top-down technique has several drawbacks, including high costs, the necessity for high surface finished materials, longer etching periods, and the development of defects in treated materials. Nanostructures are also built from molecules or an atom in a bottom-up technique. Organized separation of molecules or atoms happens during the assembly of desired nanostructures in this method [36]. Molecular beam epitaxy, laser pyrolysis, sol–gel technique, CVD, metal–organic decomposition, wet chemical synthesis, and self-assembly processes are some of the approaches employed in the bottom-up technique [37].

The 2D materials are most widely applied to decorate different metal oxides to improve their light-sensing performances. A series of methods are possible to construct the hybrid structure of 2D materials with 1D semiconducting nanostructures. The introduction of 2D material might efficiently upsurge the surface area and offer more active sites in the composite material, a positive parameter for boosting the light-sensing response of 1D semiconducting materials. In this study, we reviewed some of the common 2D materials such as RGO and MoS_2.

7.2.1 1D ZnO Nanostructures (Nanowires/Nanorods)

Solution-phase method has many benefits when compared to other synthetic methods. The hydrothermal method has gained extensive attention due to its advantages, including low temperature, low cost, high yield, good expansibility, and ease of handling. Normally, solution-phase techniques occur at relatively low temperatures (160–200 °C) compared to vapor-phase technique. Therefore, a solution synthesis method offers a better choice of precursors, additives, and substrates [38–40]. Due to the various benefits, solution-phase methods have paying attention in synthesizing different kinds of nanomaterials. In solution-phase method, the growth procedure could be carried out in organic or aqueous solution and also in combination of the two [41, 42].

7.2.1.1 Hydrothermal Method: Experimental Steps for ZnO

Hydrothermal method employ special closed containers called autoclaves that used for reactions and maintaining a particular temperature and creating a high-pressure setting in the reaction medium containing water, organic solvents, or mixtures solvents [43, 44]. It is a highly effective synthesis technique for nanomaterial preparation, particularly for those insoluble chemicals under atmospheric pressure. Compared with other synthesis methods via wet chemistry, the hydrothermal/solvothermal technique has several noticeable benefits:

- Nanomaterials can be synthesized in Teflon-coated autoclave at relatively lower temperatures.
- It is possible to obtain some nanomaterials at metastable state and is difficult to get by other methods.

- It is easy to control the shape, size, good crystal shape, and purity.
- Particle size distribution is done by simply changing the parameters of the reaction such as time, temperature, concentrations, solvent medium, variation of pH, and surfactants.

The properties and shape of ZnO NWs can be well ordered by changing the growth factors [45, 46]. Normally, NWs aspect ratio increases gradually by increasing the growth time attributes to the point that the axial growing rate is higher than the lateral growing rate [47, 48]. Hydrothermal synthesis techniques have given a lot of consideration and have been extensively used for the preparation of one-dimensional nanostructured materials. For example, ZnO was used as a photodetector and was synthesized using low-temperature hydrothermal method [49]. Additional metal oxides like titanium oxide, TiO_2 [50], Nb_2O_5 [51], and many other materials were also prepared by a hydrothermal technique.

The following examples show the common method for ZnO NWs grown vertically on a silica substrate using hydrothermal technique:

- A definite (SiO_2/Si) substrate promotes the nucleation of the seeds for the ZnO NW growth [52].
- Solvents such as sodium hydroxide (NaOH)/hexamethylenetetramine (HMTA) and precursors of zinc salt aqueous solution mixture are used as growth precursors.
- The nucleated substrate placed in the growth precursor solution for certain period at fixed temperature.
- The seeded growth layer and the substrate washed multiple times and dried. After choosing precursors such as HTMA and zinc salt. The summarized chemical reaction is given as follows [53]:

ZnO growth reaction:

$$\left(CH_2\right)_6 N_4 + 6H_2O \rightarrow 6HCHO + 4NH_3 \tag{7.1}$$

$$NH_3 + H_2O \rightarrow NH_4^+ + OH^- \tag{7.2}$$

$$2OH^- + Zn^{2+} \rightarrow Zn\left(OH\right)_2 \tag{7.3}$$

$$Zn\left(OH\right)_2 \rightarrow ZnO + H_2O \tag{7.4}$$
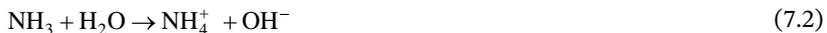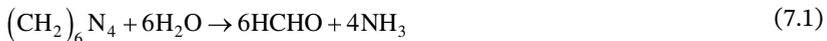
Change in the concentration of growth solution leads to the change in diameter and length of the NWs, and a higher concentration produces a greater length and diameter [54]. Muchuweni et al. [55] witnessed enhanced crystallinity and unwell-aligned NWs with increasing growth rate. Also, Gerbreders et al. [56] proposed that the concentrations lower than the minimum concentration value of 25 mM would lead to incomplete NR. Study with the result of solution concentration increased temperatures to develop the dynamic force of the chemical reaction, giving rise to more length-to-width ratio of ZnO NWs [47]. The pH value is one more significant parameter in the growth mechanism. When the solution of pH value reduced, the acidic background may etch the growing seed layer and thus shrink the density of

the ZnO NWs [56, 57], whereas on the other side, more Zn^{2+} results in the growth of NWs with larger diameters and lengths [45, 46]. However, the growth of ZnO NWs is not witnessed at pH less than 4.6 values [46]. This performance is certainly attributable to the lack of hydroxide complexes $(Zn(OH)_n)$, which are more essential for the progress of ZnO NWs [58].

7.2.2 Chemical Vapor Deposition: MoS$_2$ Few Layer Structures

In recent few years, due to the uniqueness of MoS$_2$ few layer structures and remarkable semiconducting performance have paying a great deal of attentions. An aforementioned extraordinary property finds potential applications in chemical sensors [59], flexible electrons [60], nanoelectronic [61], and optoelectronic [62–64]. Numerous synthesis techniques for few layers of MoS$_2$ have been implemented extensively during the past few years, such as numerous categories of exfoliation [65–67], hydrothermal synthesis [68], CVD [69–74], and magnetron sputtering [75]. Hydrothermal and CVD routes are among the best routes for synthesizing large area and high-quality MoS$_2$ film with desired morphologies. Since the hydrothermal method is simple and cheap, it is focused mainly to get MoS$_2$. Figure 7.1c representation shows how different various factors like precursor and substrate affect pressure, and temperature on the kinematics and the thermodynamics in the growth of 2D materials.

Generally, MoS$_2$ nanosheets of different structures and properties are significant to the domain size [76], morphology [77], dopants or defects [78], and the number of layers [79] and properties and structure of MoS$_2$ can be tunable by varying growth factors, such as flow rate of the carrier gas [80, 81], distance between source and substrate [82], growth temperature [83, 84] and also the ingredients ratio [85, 86]. Zusong Zhu et al. [87] results shows that amount of ingredients is crucial for tuning morphology and properties of MoS$_2$ grown by CVD technique. Also, Najmaei et al. [88] witnessed the MoS$_2$ transformation nature from flakes to triangles and hexagonal after decreasing the precursor S quantity. Furthermore, Wang et al. [70] planned for the morphology transformation from nanosheet by varying the precursor ratio. Additionally, Shuming Han et al. [89] successfully synthesized MoS$_2$ NRs with different thickness and length by using CVD technique, and they observed the regular morphology evolution of CVD-grown MoS$_2$ NRs on the SiO$_2$/Si substrate along the gas flow direction. MoS$_2$ nanomaterials with different shapes like nanotubes (NTs) and NRs MoS$_2$ have been reported earlier using hydrothermal methods under a 180 °C temperature [90]. Ye Tian et al. have given an explanation on crucial parameters which played major role in the morphology of MoS$_2$ and its mechanism.

7.2.2.1 CVD: Experimental Steps for MoS$_2$

Zusong Zhu et al. [87] used the precursors MoO$_3$ and S powder as reaction precursor to synthesize MoS$_2$ nanolayers on SiO$_2$/Si substrate using CVD experimental technique. Figure 7.2h shows a diagram of the CVD experimental technique for the growth of MoS$_2$. The experimental CVD set includes furnace having single temperature area and attached heating ring to monitor precursor's temperature

independently. Two separate quartz cruisers with calculated amount of MoO_3 and S powder were placed in the center of furnace and heating ring, and two quartz cruiser distances maintained for the sake of ignoring the vapor concentration gradient of S on the Si/SiO_2 substrates.

At the beginning, the tube of the furnace was expelled for 20–30 minutes by pure N_2 or Ar/O_2 in sccm. Then, MoO_3 powder heated to some fixed temperature of 100 °C temperature for five minutes and maintained constant at same temperature of about 30 minutes to bow hosting gases and water out of the tube. Later, MoO_3 precursor was heated to 700 °C with a 15 °C min^{-1} heating rate and maintained for 30 minutes in the N_2 atmosphere. After reaching the MoO_3 precursor to temperature of 700 °C, the S precursor was heated by a heating ring to a temperature 200 °C for 5 minutes. At the end, the furnace was adjusted to room temperature by following cooling steps in the meantime and the heating ring was taken out. N_2 gas was introduced in the course of cooling to prevent obtained MoS_2 samples from contamination/oxidation:

$$MoO_3\left(Solid\right) + S\left(gas\right) \rightarrow MoO_{3-x}\left(Sub\,oxide\right) + SO_x\left(gas\right)$$

$$MoO_{3-x}\left(Solid\right) + S\left(gas\right) \rightarrow MoS_2\left(Solid\right)$$
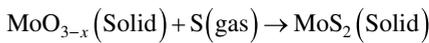
7.2.2.2 CVD: Experimental Steps for ZnO

Similar to MoS_2 synthesis, ZnO NWs fabrication was carried out using CVD in a tubular furnace, as shown in Figure 7.2g. The Zn source taken in a quartz cruiser
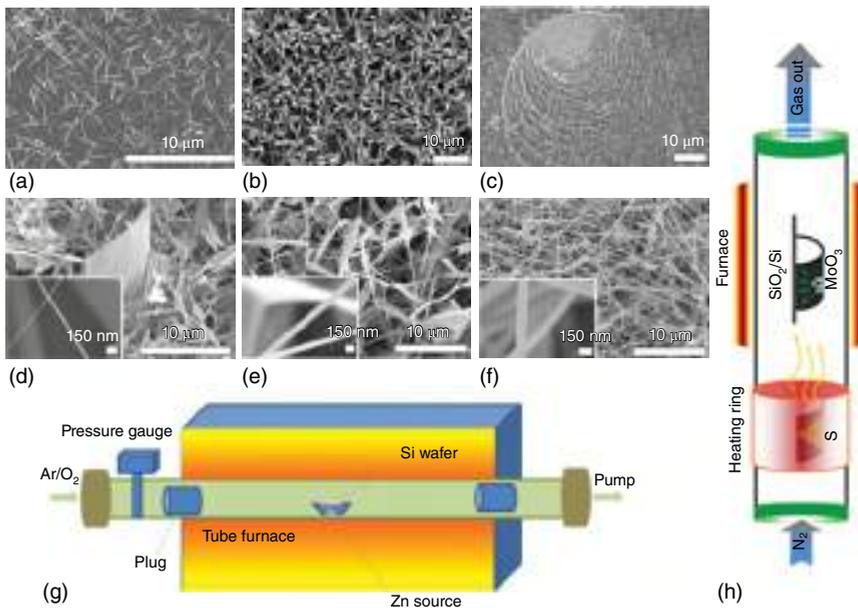
Figure 7.2 (a–f) SEM images of ZnO nanowires/nanorods grown by CVD system. (g) Schematic sketch of CVD system for growing ZnO nanowires [91]. Source: Nannan Bi et al. [91]/with permission of Elsevier. (h) Schematic experimental system of CVD for MOS$_2$ few layer growth. Source: Zhu et al. [87]/IOP Science/Public Domain CC BY.

and Si substrate was placed at the center of quartz tube, and the whole system was placed inside a furnace tube [91]. Commonly, the synthesis of different lengths and diameters can be attained by adjusting the flow rate of the Ar/O_2 as a carrier gas and the pressure during the nucleation of ZnO. In an experiment, the diameter and length of the ZnO NWs increase with the increase of oxygen supply. An additional increase in the flow rate of carrier gas causes turbulent flow in the mixing process of zinc vapor, and the carrier gas tends to irregular results [91].

Figure 7.2a–h shows the SEM images of ZnO obtained by CVD method with different flow rates of Ar/O_2. Bhutto et al. [92] proposed that the obtained product was short-length ZnO NWs, while ZnO NWs were grown with good alignment and uniform density at a suitable vapor pressure. Li et al. [93] showed that the increased NWs density and the degree of vertical organization enhanced with the growth in the seed layer thickness. Further, other studies have also shown that the different deposition methods and temperature affect the ZnO seed layer morphology orientation and crystal quality of ZnO NWs prepared by vapor deposition [93, 94].

7.2.3 Reduced Graphene Oxide (RGO)

Mainly, carbonaceous nanomaterials, including carbon NTs, fullerenes, graphene, and graphene oxides, have directed preparation of nanocomposites with semiconductors. These hybrid structures open up new era in the photodetectors applications because of its extraordinary surface area, high chemical and thermal stability, and greater conductivity. The main focus of this work is graphene. Since its discovery, graphene has been one of the maximum deliberated nanocarbons. A graphene material is made up of carbon atoms with single-layer hexagons and is reflected as the fundamental structure of other nanocarbons also [95]. Materials with conjugated long-array configuration result in better thermal and electrical conductivity. Graphene derivatives, namely graphene oxide and RGO, are largely used in their original as well as hybrid form. Derivatives of graphene such as graphene oxide (GO) and RGO are widely used both in their original and hybrid forms. Chemical configuration and properties of RGO differ from graphene material [95].

7.2.3.1 Experimental Steps for RGO

Preparation of RGO by the Tour method has been presented previously [96]. In this technique, calculated amount of graphite flakes were taken in a volumetric flask along with the volumetric measurement of sulfuric acid and kept in an ice bath. The whole systems kept on a magnetic stirrer for about 15 minutes, and the temperature was maintained in the range of about 5 °C. Calculated quantity of potassium permanganate was added to the mixture taken in a volumetric flask by maintaining the magnetic stirring for about 10–12 mins and retaining the temperature less than 30 °C. Also, the solution was then maintained a constant magnetic stirring by keeping whole system at the temperature of 35 °C for three hours. Further, 100 ml of distilled water was transferred cautiously to the solution with stirring and maintaining the temperature less than 90 °C in the next 15–20 minutes. The calculated

quantity of hydrogen peroxide was added directly to the solution under magnetic stirring and then followed by HCl addition to the mixture. The obtained solution washed multiple times and filtered using distilled water.

The obtained remainder was then dried at 40–50 °C in an oven for 5 hours, and the obtained product is a graphene oxide (GO). Thereafter, GO was then discharged into deionized water with magnetic stirring continuously by keeping temperature of about 35 °C for 30 minutes. Then measured quantity of hydrazine hydrate was distributed in water under stirring for four hours and poured to the GO colloidal suspension. The achieved mixture was then filtered, and obtained remainder is RGO. The achieved filtrate was dried to a temperature of 40 °C for 20 hours in an oven.

7.2.3.2 Experimental Steps for ZnO/RGO Hybrid Structure

The execution of effective ways to synthesize and improve nanocomposites for the real-world application has turned out to be very significant. Yield and performance of the photodetectors mainly depend on different syntheses and their reaction parameters such as morphology, particle size, and preparation time. Worldwide researchers are using different methods for the fabrication of ZnO–graphene hybrid structure. Compared to all other methods, sol–gel, solvothermal, co-precipitation, and hydrothermal methods are commonly described methods. Among different methods, the most commonly described techniques are the sol–gel, solvothermal, co-precipitation, and hydrothermal. These techniques denote more than 75% of all synthesis routes. The solution technique will remain to be the better choice on all other synthesis methods.

Despite the fact, a precise concentration toward solid-state method due to its simplicity and attention in solid-state method is also growing due to its simplicity and openness. Furthermore, other important techniques like spin coating [97], sonochemical [98], pulsed laser [99], ultrasonication [100], self-assembly [101], template method [102], and ionothermal precipitation [103] are used very less during the past few years. In favor of green chemistry, for scalability, and for better performance, people have been using progressively simple techniques such as hydrothermal and solvothermal methods. Figure 7.3e shows clear information on different methods for hybrid structure conducted during 2016–2020.

Both the synthetic methods are most adaptable to prepare nanomaterials and their heterostructures [106]. Depending on the solvent utilized, the hydrothermal/solvothermal route is established. Water and organic solvents are utilized as solvents in the process of hydrothermal and solvothermal, respectively. Aforementioned reactions taken place at above the boiling point temperature and one bar above pressure [107, 108]. On this occasion, zinc precursor was first reduced using hydroxide to get a zinc hydroxide precursor, and the precursor is heated to 120–300 °C temperature at different times from 8 to 24 hours in Teflon-layered autoclave. Furthermore, in many works, researchers are used surfactants during synthesis of ZnO–graphene hybrid structure to control the shape of ZnO nanoparticles.

ZnO nanoparticles morphology can be tuned during the process, and the preparation is mainly based on temperature and pressure of the system, type of precursors,
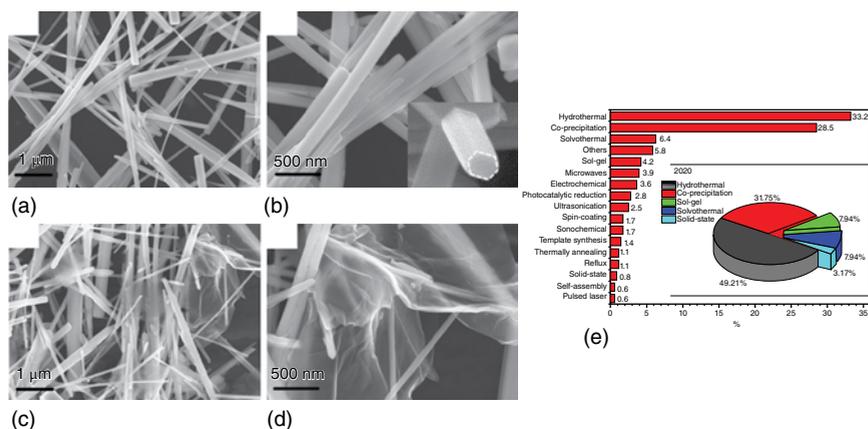
Figure 7.3 (a, b) 1D ZnO nanowires. (c, d) Enlarged FESEM images of ZnO/RGO composites. Source: Chen et al. [104], MDPI, CC BY 4.0. (e) Different methods for ZnO–graphene hybrid materials during 2016–2020. Source: Albiter et al. [105]/MDPI/Public Domain CC BY.

and its concentrations and pH of solution mixture. ZnO and carbon heterostructures with different morphology have been obtained using hydrothermal/solvothermal route [109–113]. The ZnO NWs obtained by hydrothermal method are shown in Figure 7.3a,b.

Various shapes are synthesized by changing a few parameters in synthesis method. Kumaresan et al described ZnO NRs and nanospheres on ZnO/RGO composites. The flexible tuning of morphology from 1D to 0D ZnO is done by varying the amount of RGO. Concurrently, GO is transformed to RGO by means of different quantities of RGO in a hydrothermal synthesis [114]. Figure 7.3c,d highlights the morphology of ZnO/RGO composites.

7.2.4   Experimental Steps for ZnO/MoS$_2$ Hybrid Structure

Before fabricating the ZnO–MoS$_2$ heterostructure, ZnO NWs/NRs were first synthesized by the hydrothermal method [115]. To obtain ZnO NRs, a solution was prepared using zinc acetate and was dissolved in 35 ml of ethanol. Sodium hydroxide was added dropwise to the mixture and stirred for 30 minutes at room temperature. After the solution was poured to 100 ml, Teflon-coated stainless steel autoclave maintained the reaction temperature at 160 °C for 24 hours. Then, the reaction mixture was cooled down to room temperature, collected by centrifugation, washed three times with water and two times with ethanol, and dried at 60 °C for a day.

Hui Wu et al. proposed the fabrication of ZnO–MoS$_2$ through simple hydrothermal method [116]. The calculated quantity of precursors such as sodium molybdate and thiourea were scaled using digital balance. Precursors in measured amount of aqueous solution were placed for the signification to dissolve completely. The dissolved solution was poured to autoclave and the calculated quantity of ZnO NRs was added into the solution and stirred to form a heterogeneous mixture. After, the
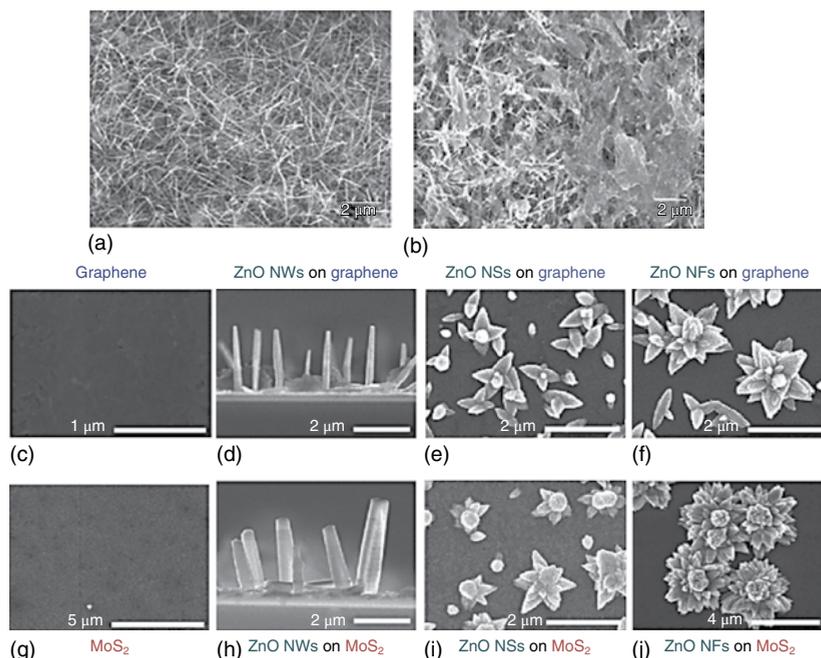
Figure 7.4 (a, b) Typical SEM picture of ZnO and ZnO–MoS$_2$. Source: Aldalbahi [117], Hindawi, CC BY 4.0. (c, j) pH-mediated hydrothermal growth of hybrid structure of 2D materials with ZnO nanostructures. Source: Lee et al. [118], Reproduced with permission from American Chemical Society.

reaction container system is closed, maintained the temperature of 210 °C for 21 hours, and later cooled down to room temperature. The precipitate solution was centrifuged and washed many times with deionized water, and the resultant was dispersed in water using sonication and fully dried by lyophilization. At the end, obtained powder product was collected and heated at 350 °C in air for four hours. The corresponding SEM images are shown in Figure 7.4.

7.3 Applications of ZnO–Graphene Heterostructure for Photon Detection

One-dimensional nanostructures like NWs and NTs when added to 2D atomic sheets like graphene/MOS$_2$ exhibit excellent electronic, optoelectronic, and mechanical properties which make them a promising material for optoelectronic devices [119]. The presence of heterojunction interfaces plays a critical role in the functionality and performance of the nanohybrids-based devices. One very significant application of hybridized one-dimensional and two-dimensional nanomaterial is in flexible electronics. In the heterostructure, the inorganic 1D nanostructures exhibit

excellent electrical and optical characteristics, including high carrier mobility, radiative recombination rate, and long-term stability. Consequently, the 1D semiconductor nanostructures, such as NWs, NRs, nanopillars, nanocolumns (NCs), and NTs, offer potential opportunities for the fabrication of high-performance optoelectronic and electronic devices

Among the various one-dimensional semiconducting structures, zinc oxide (ZnO) is one of the best material for optoelectronic devices. ZnO is a promising semiconducting material due to its unique optical and electrical properties. ZnO has a wide direct bandgap of 3.37 eV and also exhibits large exciton binding energy of 60 meV which is much larger than the room-temperature thermal energy (26 meV). Hence, ZnO material is broadly employed in various applications such as electronic and optoelectronic devices. ZnO NWs are highly used in ultraviolet (UV) photodetectors due to large surface-to-volume ratio. Moreover, UV photodetectors based on different ZnO heterostructure are used to improve the device parameters like response time, recovery time, responsivity, and external quantum efficiency.

Two-dimensional nanomaterials like graphene, which is a monolayer of carbon, has attracted much attention in the recent years in electronics and optoelectronic devices because of excellent carriers transport mobility, high electrical conductivity, and mechanical flexibility. In addition to graphene, other 2D-layered materials, like hexagonal boron nitride (hBN), transition metal dichalcogenides (TMDCs), and their hybrids with other nanomaterials, are flexible, stretchable, and mechanically strong and also have interesting and excellent physical properties and hence find application in optoelectronic devices [120].

Graphene is prominently used with semiconducting oxide materials to improve the performance of optoelectronic devices [121]. Monolayer of graphene or a three-dimensional microstructure of graphene in the form of graphene foam (GF) could be an excellent choice in conjunction with highly dense ZnO NWs for optoelectronic devices, for example UV photodetector. In the following section, we will see how ZnO NWs and GF heterostructure can be used for fabricating UV photon detector.

7.3.1 ZnO Nanowire/Graphene-Based Photodetector

One-dimensional semiconducting zinc oxide NWs grown on graphene layer is used as the photosensitive layer in photodetectors. Figure 7.5a shows the structure of such a device [122]. The device is made on a glass substrate. The photosensitive layer is present between two metal electrodes. In the absence of UV illumination, a low-conductivity depletion layer forms on the surface of photosensitive layer due to adsorption of oxygen molecules from the ambient air that captures free electrons from n-type ZnO NWs.

When UV light falls on it, electron–hole pairs are generated with energy greater or equal to the bandgap of ZnO and causes desorption of oxygen molecules due to the trapping of generated free holes by oxygen ions present onto the surface. A decrease in the depletion layer results in an increase in free charge carrier concentrations,
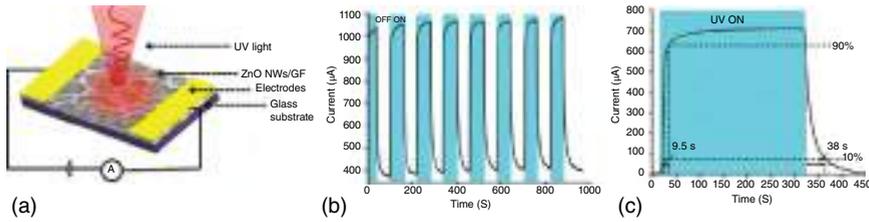
Figure 7.5 (a) ZnO NW/graphene foam-based UV photon detector. (b) Cyclic photoresponse of the device. (c) Saturation response of the device to find response time and recovery time. Source: Reproduced with permission from Boruah et al. [122]/American Chemical Society.

which enhance the conductivity of the device. In ZnO NWs/GF device, conduction of charge carriers takes place mainly through ZnO NWs-GF-ZnO NWs due to highly dense growth of ZnO NWs on GF. However, conduction through graphene layer mainly contributes to the generation of dark current. Hence, upon UV exposure, the photogenerated free charge carriers are transferred from ZnO NWs to graphene layers of the foam, and higher charge carrier mobility of graphene induces a faster collection of the charge carriers at the electrode with longer lifetime by reducing the charge recombination rate.

7.3.2 Figure of Merits of a Photodetector

There are different figures of merits of a photodetector like responsivity, response time, recovery time, and external quantum efficiency of the detector.

a. The responsivity of the photodetector is defined as:

$$R = \text{Photocurrent} - \text{Dark current} / \text{Power*Area of illumination}$$

b. Response time of a photodetector is defined as the time required for the current to reach from 10% to 90% of its maximum value.
c. Recovery time is defined as the time required by the current to fall from 90% to 10% from the maximum value.
d. External quantum efficiency of a photodetector is defined as the number of charge carriers generated per number of incident photons on the device.

Figure 7.5b shows the *I–V* response of ZnO NWs/GF device both in the absence and presence of UV illumination up to eight cycles of turning ON and OFF. The UV ON−OFF cycle is measured at an appropriate bias voltage [122].

The plot clearly reveals the dark current, i.e. the current flowing through the device is much lesser than the photocurrent, i.e. the current flowing through the device under illumination [121]. Literature reports that the responsivity of the detector showed a dependency on the applied bias voltage.

Figure 7.5c shows the response and recovery time of the photon detector. The response time and recovery time of the device are estimated to be 9.5 and

38 seconds, respectively. This is significantly better than the response and recovery time of only ZnO-based photodetectors which usually range between 50 and 500 seconds [123, 124].

The reason for longer recovery time is explained as follows.

In ZnO nanostructure-based UV photodetectors, the response and recovery times of device are mainly determined by oxygen desorption and absorption processes. Upon UV illumination in ZnO NWs/GF device, when oxygen desorption takes place, the generated free charge carriers are transferred to graphene and quickly get saturated. After switching off the UV illumination, until the oxygen molecules capture all the photogenerated free charge carriers, they continue to contribute to the current in the device. The process of absorption of oxygen molecules from air takes longer time as compared to the desorption process. Therefore, observed recovery time is longer than response time [122]. The external quantum efficiency of the device also showed a dependence on the bias applied.

In the next section, the authors discuss about the application of one-dimensional chalcogenides for optoelectronic applications.

7.3.3 One-Dimensional Chalcogenide Material for Optoelectronic Applications

Chalcogenide materials are chemical compounds consisting of at least one chalcogen ion, i.e. a chemical element in column VI of the periodic table. Chalcogenide refers to the sulfides, selenides, and tellurides. Chalcogenide semiconductors possess unique electronic and optical properties, and one-dimensional chalcogenide materials like chalcogenide NWs find application in optical gain materials and high-performance wave guides [125]. The key component of photonic and electronic devices is the heterostructure constructed by different semiconductors. Unique properties of chalcogenide-heterostructured NRs made them attractive for optoelectronic applications.

NW is a kind of 1D structure with a radial restriction of less than 100 nm. Semiconductor NWs have been found to have the potential to be considered as versatile building blocks for future generation integrated photonic and optoelectronic devices, such as nanolasers, transistors, and optical sensors. While semiconductor heterostructures are considered to be crucial components for various traditional electrical and optoelectronic device applications, 1D semiconductor NWs are suitable for realizing miniaturized semiconductor heterostructures. This is because defect-free lattice-mismatched axial semiconductor heterostructures can be formed by them due to their highly efficient strain relaxation property. This is crucially important for high-performance optical and optoelectronic devices [125].

Semiconductor axial NW heterostructures, due to their one-dimensional structure, can confine light and carriers in one dimension. This results in the possibility of realization of photon detectors, light emitting diodes (LEDs), multicolor nanolasers LEDs, etc. In the next section, the authors discuss the fabrication and performance study of a ZnO NW/2D MoS_2-based solar cell.

7.3.4 Heterostructure-Based Solar Cell

Heterostructured solar cells and self-powered photodetectors are fabricated by coupling ZnO NW and 2D MoS_2 nanosheets. While fabricating the device, initially the ZnO NWs are synthesized by sputtering, and then MoS_2 nanosheets are deposited on ZnO NW using spin coating. The fabrication process is easy and cost-effective. The fabricated device is an n-ZnO NW/p-MoS_2 nanosheet heterostructure. Imperfections and impurities that are present in the defect sites of MOS_2 are corrected by the presence of ZnO [117].

The photovoltaic mode of operation was demonstrated by impinging white light on the device. An increase in photocurrent was observed without the application of any external bias which proves the photovoltaic effect. The device showed a maximum photocurrent of 120 nA when it was illuminated by light of wavelength 420 nm. The responsivity of the device was estimated to be 2.1 mA/W.

A comparison between a binary MoS_2-based device and a heterostructure-based device shows that when the heterostructure was made with ZnO NWs, the photoresponse improves significantly. This is because, when ZnO NWs are present in the heterostructure, the recombination rate is reduced which significantly improves the photoresponse of the detector [117].

7.4 Conclusion and Summary

One-dimensional heterostructures like ZnO/graphene nanohybrids are used largely in photonic and optoelectronic devices. The main advantage of these nanohybrids over the only ZnO counterpart is that in the nanohybrids, the charge transport occurs majorly through graphene. As graphene has extraordinarily high charge mobility, this leads to the realization of high-performing devices. The compatibility of growth mechanism of ZnO on graphene enables a layer-by-layer growth of ZnO with controlled morphology and orientation. This results in having a good quality ZnO/graphene interface which plays a crucial role in the performance of nanohybrid devices. Another major advantage of ZnO/graphene heterostructure is that when the substrate is flexible, sample can be directly used for fabricating flexible electronics. However, there is a challenge as well in ZnO/graphene heterostructure-based device fabrication. The defects at the ZnO/graphene interface can lead to reduction in responsivity and response speed of the device. Hence, special care needs to be taken while synthesizing this heterostructure so that defects at the interface can be eliminated [121]. As ZnO has a wide bandgap and demonstrates ferroelectric and piezoelectric properties, ZnO/graphene heterostructures will definitely prompt scientist and researchers to explore new areas of research where ambipolar gating effect of graphene can be used together with the properties of ZnO for developing flexible, self-powered optoelectronic devices [121].

Many researchers have been doing lot of work to satisfy the "5S" parameters as we have highlighted in Introduction part. In the past few years, people have covered the way to the fabrication of 1D/2D hybrid material-based photodetectors.

Hybrid material devices have been used, not fully exploited, for reliability, low cost, and other applications. Surface engineering by chemical modification increases the movement of charge carriers required for the better performance of devices. Heterostructures made up of n-ZnO NW and p-type 2D MoS$_2$ nanosheets also demonstrated promising result for the application in optoelectronic devices operating in photovoltaic mode. The cost-effective fabrication technique together with good performance in terms of fast response, high photocurrent, repeatability, and very good signal-to-noise ratio make it a strong candidate for solar cell applications.

References

1 Razeghi et al. (1996). Semiconductor ultraviolet detectors. *J. Appl. Phys.* 79 (10): 7433–7473.

2 Taniyasu et al. (2006). An aluminium nitride light-emitting diode with a wavelength of 210 nanometres. *Nature* 441 (7091): 325–328.

3 Wang, L.K. et al. (2009). Single-crystalline cubic Mg-ZnO films and their application in deep-ultraviolet optoelectronic devices. *Appl. Phys. Lett.* 95 (13): 131113.

4 Tian et al. (2015). Nanoscale ultraviolet photodetectors based on one dimensional metal oxide nanostructures. *Nano Res.* 8 (2): 382–405.

5 Monroy et al. (2003). Wide-bandgap semiconductor ultraviolet photodetectors. *Semicond. Sci. Technol.* 18 (4): R33.

6 Kind et al. (2002). Nanowire ultraviolet photodetectors and optical switches. *Adv. Mater.* 14 (2): 158–160.

7 McDonald et al. (2005). Solution-processed PbS quantum dot infrared photodetectors and photovoltaics. *Nat. Mater.* 4 (2): 138–142.

8 Fang et al. (2009). Single-crystalline ZnS nanobelts as ultraviolet-light sensors. *Adv. Mater.* 21 (20): 2034–2039.

9 Soci et al. (2007). ZnO nanowire UV photodetectors with high internal gain. *Nano Lett.* 7 (4): 1003–1009.

10 Huang et al. (2012). Assembly of three-dimensional hetero-epitaxial ZnO/ZnS core/shell nanorod and single crystalline hollow ZnS nanotube arrays. *ACS Nano.* 6 (8): 7333–7339.

11 Wu et al. (2012). Lead zirconate titanate nanowire textile nanogenerator for wearable energy-harvesting and self-powered devices. *ACS Nano.* 6 (7): 6231–6235.

12 Zhou et al. (2009). Gigantic enhancement in response and reset time of ZnO UV nanosensor by utilizing Schottky contact and surface functionalization. *Appl. Phys. Lett.* 94 (19): 191103.

13 Gedamu et al. (2014). Rapid fabrication technique for interpenetrated ZnO nanotetrapod networks for fast UV sensors. *Adv. Mater.* 26 (10): 1541–1550.

14 Hou et al. (2013). SnO$_2$-microtube-assembled cloth for fully flexible self-powered photodetector nanosystems. *Nanoscale* 5 (17): 7831–7837.

15 Pescaglini et al. (2014). Hot-electron injection in Au nanorod–ZnO nanowire hybrid device for near-infrared photodetection. *Nano Lett.* 14 (11): 6202–6209.

16 Lee et al. (2012). Graphene–nanowire hybrid structures for high-performance photoconductive devices. *J. Mater. Chem.* 22 (17): 8372–8376.

17 Hong et al. (2014). Self-powered ultrafast broadband photodetector based on p–n heterojunctions of CuO/Si nanowire array. *ACS Appl. Mater. Interfaces* 6 (23): 20887–20894.

18 Zhou et al. (2014). Ultrahigh sensitivity and gain white light photodetector based on GaTe/Sn: CdS nanoflake/nanowire heterostructures. *Nanotechnology* 25 (44): 445202.

19 Chen et al. (2010). ZnS branched architectures as optoelectronic devices and field emitters. *Adv. Mater.* 22 (21): 2376–2380.

20 Yang et al. (2007). Single-crystalline branched zinc phosphide nanostructures: synthesis, properties and optoelectronic devices. *Nano Lett.* 7 (2): 269–275.

21 Wu et al. (2004). Single-crystal metallic nanowires and metal/semiconductor nanowire heterostructures. *Nature* 430 (6995): 61–65.

22 Perera et al. (2012). Hydrothermal synthesis of graphene-TiO_2 nanotube composites with enhanced photocatalytic activity. *ACS Catal.* 2 (6): 949–956.

23 Lu et al. (2010). Nanoelectronics from the bottom up. In: *Nanoscience and Technology: A Collection of Reviews from Nature Journals* (ed. V. Dusastre), 137–146. Nature Publishing Group.

24 Park et al. (2013). Graphene cathode-based ZnO nanowire hybrid solar cells. *Nano Lett.* 13 (1): 233–239.

25 Wang et al. (2015). Simultaneous electrochemical reduction and delamination of graphene oxide films. *ACS Nano.* 9 (9): 8737–8743.

26 Li et al. (2011). MoS_2 nanoparticles grown on graphene: an advanced catalyst for the hydrogen evolution reaction. *J. Am. Chem. Soc.* 133 (19): 7296–7299.

27 Reddy et al. (2012). Hybrid nanostructures for energy storage applications. *Adv. Mater.* 24 (37): 5045–5064.

28 Tian et al. (2007). Coaxial silicon nanowires as solar cells and nanoelectronic power sources. *Nature* 449 (7164): 885–889.

29 Han et al. (2015). Hierarchically CdS decorated 1D ZnO nanorods-2D graphene hybrids: low temperature synthesis and enhanced photocatalytic performance. *Adv. Funct. Mater.* 25 (2): 221–229.

30 Wang et al. (2014). Liquid-phase growth of platinum nanoparticles on molybdenum trioxide nanosheets: an enhanced catalyst with intrinsic peroxidase-like catalytic activity. *Nanoscale* 6 (21): 12340–12344.

31 Bao et al. (2011). Flexible Zn_2SnO_4/MnO_2 core/shell nanocable carbon microfiber hybrid composites for high-performance supercapacitor electrodes. *Nano Lett.* 11 (3): 1215–1220.

32 Geim, K. et al. (2013). Van der Waals heterostructures, PERSPECTIVE. *Nature* 499: 419 Macmillan Publishers Limited.

33 Cai et al. (2018). Chemical vapor deposition growth and applications of two-dimensional materials and their heterostructures. *Chem. Rev.* 118 (13): 6091–6133.

34 Du, N. et al. (2012). One-dimensional hybrid nanostructures: synthesis via layer-by-layer assembly and applications. *Nanoscale* 18: 5517–5526.

35 Wang, X., Song, P.L., Ryou, J.H. et al. (2005). Growth of uniformly aligned ZnO nanowire heterojunction arrays on GaN, AlN, and $Al_{0.5}Ga_{0.5}N$ substrates. *J. Am. Chem. Soc.* 21: 7920–7923.

36 Kovtyukhova, N.I. et al. (2004). Coaxially gated in-wire thin-film transistors made by template assembly. *J. Am. Chem. Soc.* 40: 1273–1279.

37 Chen, J.S. et al. (2018). 0D–2D and 1D–2D semiconductor hybrids composed of all inorganic perovskite nanocrystals and single layer graphene with improved light harvesting. *Part. Part. Syst. Char.* 2: 1700–1310.

38 Zhu, R. et al. (2018). Growth of uniform nanowires with orientation control. In: *Synthesis and Characterization of Piezotronic Materials for Application in Strain/Stress Sensing; Mechanical Engineering Series* (ed. F.A. Kulacki). Cham, Switzerland: Springer.

39 Hu, H. et al. (2007). Hydrothermal synthesis of ZnO nanowires and nanobelts on a large scale. *Mater. Chem. Phys.* 106: 58–62.

40 Podrezova, L.V. et al. (2013). Comparison between ZnO nanowires grown by chemical vapor deposition and hydrothermal synthesis. *Appl. Phys. A Mater. Sci. Process.* 113: 623–632.

41 Liu, B. et al. (2003). Hydrothermal synthesis of ZnO nanorods in the diameter regime of 50 nm. *J. Am. Chem. Soc.* 125 (15): 4430–4431.

42 An, G. et al. (2011). CO_2-mediated synthesis of ZnO nanorods and their application in sensing ethanol vapor. *J. Nanosci. Nanotechnol.* 11: 1252–1258.

43 Kim, J.Y. et al. (2011). The characteristic of the ZnO nanowire morphology grown by the hydrothermal method on various surface-treated seed layers. *Mater. Lett.* 65 (8): 1161–1164.

44 Song, J., S. et al. (2009). Selective growth of vertical ZnO nanowires with the control of hydrothermal synthesis and nano-imprint technology. *J. Nanosci. Nanotechnol.* 9 (6): 3909–3913.

45 Chevalier-César, C. et al. (2014). Growth mechanism studies of ZnO nanowire arrays via hydrothermal method. *Appl. Phys. A Mater. Sci. Process.* 115: 953–960.

46 Amin, G. et al. (2011). Influence of PH, precursor concentration, growth time, and temperature on the morphology of ZnO nanostructures grown by the hydrothermal method. *J. Nanomater.* 2011.

47 Akgun, M.C. et al. (2012). Hydrothermal zinc oxide nanowire growth using zinc acetate dihydrate salt. *J. Mater. Res.* 27: 1445–1451.

48 Yang, W. et al. (2011). Effect of growth time on morphology and photovoltaic properties of ZnO nanowire Array films. *Rare Met.* 30: 676–680.

49 Tian, W. et al. (2014). *Adv. Mater.* 26: 3088–3093.

50 Zhang, H.F. et al. (2012). *IEEE Elec. Device Lett.* 33: 83–85.

51 Fang, X.S., Hu, L.F., Huo, K.F. et al. (2011). *Adv. Funct. Mater.* 21: 3907–3915.

52 Sugunan, A., H. C. et al. (2006). Zinc oxide nanowires in chemical bath on seeded substrates: role of hexamine. *J. Sol-Gel Sci. Technol.* 39 (1): 49–56.

53 Ladanov, M. et al. (2011). Structure and opto-electrochemical properties of ZnO nanowires grown on n-Si substrate. *Langmuir* 27 (14): 9012–9017.

54 Yu, J. et al. (2012). Size-selected growth of transparent well-aligned ZnO nanowire arrays. *Nanoscale Res. Lett.* 7: 1–6.

55 Muchuweni, E. et al. (2017). Hydrothermal synthesis of ZnO nanowires on Rf sputtered Ga and Al Co-doped ZnO thin films for solar cell application. *J. Alloys Compd.* 721: 45–54.

56 Gerbreders, V. et al. (2020). Hydrothermal synthesis of ZnO nanostructures with controllable morphology change. *Cryst. Eng. Comm.* 22: 1346–1358.

57 Cao, B. et al. (2008). From ZnO nanorods to nanoplates: chemical Bath deposition growth and surface-related emissions. *J. Phys. Chem. C* 112: 680–685.

58 Rakhsha et al. (2019). Ag and Cu doped ZnO nanowires: a PH-controlled synthesis via chemical bath deposition. *Materialia* 5: 100212.

59 Lee, D. et al. (2020). Phase-dependent gas sensitivity of MoS_2 chemical sensors investigated with phase-locked MoS_2. *Nanotechnology* 31 225504.

60 Singh, E. et al. (2019). Flexible molybdenum disulfide (MoS_2) atomic layers for wearable electronics and optoelectronics. *ACS Appl. Mater. Interfaces* 11: 11061–11105.

61 Romanov, R.I. et al. (2019). Synthesis of large area two-dimensional MoS_2 films by sulfurization of atomic layer deposited MoO_3 thin film for nanoelectronic applications. *ACS Appl. Nano Mater.* 2: 7521–7531.

62 Yang, P. et al. (2019). Thickness tunable wedding-cake-like MoS_2 flakes for high-performance optoelectronics. *ACS Nano.* 13: 3649–3658.

63 Li, F. et al. (2020). High-performance optoelectronic devices based on van der Waals vertical MoS_2/$MoSe_2$ heterostructures. *Nano Res.* 13: 1053–1059.

64 Sarma, S. et al. (2019). Layer-by-layer MoS_2: GO composite thin films for optoelectronics device applications. *Appl. Surf. Sci.* 479: 1118–1123.

65 Santhosh, A.L. et al. (2019). Exfoliated MoS_2 as electrode for all-solid-state rechargeable lithium-ion batteries. *J. Phys. Chem. C* 123: 12126–12134.

66 Palleschi, S. et al. (2020). On the role of nano-confined water at the 2D/SiO_2 interface in layer number engineering of exfoliated MoS_2 via thermal annealing. *2D Mater.* 7: 025001.

67 Nguyen, V.T. et al. (2020). Plasma-induced exfoliation provides onion-like graphene-surrounded MoS_2 nanosheets for a highly efficient hydrogen evolution reaction. *ACS Appl. Mater. Interfaces* 12: 11533–11542.

68 Zheng, X. et al. (2018). Hydrothermal synthesis of MoS_2 with different morphology and its performance in thermal battery. *J. Power Sources* 395: 318–327.

69 Najmaei, S. et al. (2013). Vapor phase growth and grain boundary structure of molybdenum disulphide atomic layers. *Nat. Mater.* 12: 754–759.

70 Wang, S. et al. (2014). Shape evolution of monolayer MoS_2 crystals grown by chemical vapor deposition. *Chem. Mater.* 26: 6371–6379.

71 Zafar, A. et al. Probing the intrinsic optical quality of CVD grown MoS_2. *Nano Res.* 10: 1608–1617.

72 Jeon, J. et al. (2015, 2017). Layer-controlled CVD growth of large-area two-dimensional MoS_2 films. *Nanoscale* 7: 1688–1695.

73 Yu, H. et al. (2017). Wafer-scale growth and transfer of highly-oriented monolayer MoS_2 continuous films. *ACS nano* 11: 12001–12007.

74 Ling et al. (2014). Role of the seeding promoter in MoS_2 growth by chemical vapor deposition. *Nano Lett.* 14 (2): 464–472.

75 Sirota, B. et al. (2019). Room temperature magnetron sputtering and laser annealing of ultrathin MoS$_2$ for flexible transistors. *Vacuum* 160: 133–138.

76 Zhan, L. et al. (2017). Centimeter-scale nearly single-crystal monolayer MoS$_2$ via self-limiting vapor deposition epitaxy. *J. Phys. Chem. C* 121: 4703–4707.

77 Ji, Q. et al. (2016). Morphological engineering of CVD-grown transition metal dichalcogenides for efficient electrochemical hydrogen evolution. *Adv. Mater.* 28: 6207–6212.

78 Ye, G. et al. (2016). Defects engineered monolayer MoS$_2$ for improved hydrogen evolution reaction. *Nano Lett.* 16: 1097–1103.

79 Bhattacharyya, S. et al. (2014). Effect of strain on electronic and thermoelectric properties of few layers to bulk MoS$_2$. *Nanotechnology* 25: 465701.

80 Liu, H. et al. (2017). Role of the carrier gas flow rate in monolayer MoS2 growth by modified chemical vapor deposition. *Nano Res.* 10: 643–651.

81 Cao, Y. et al. (2015). Influences of carrier gas flow rate on the morphologies of MoS$_2$ flakes. *Chem. Phys. Lett.* 631-632: 30–33.

82 Kumar, N. et al. (2018). Growth of highly crystalline and large scale monolayer MoS$_2$ by CVD: the role of substrate position. *Cryst. Res. Technol.* 53: 1800002.

83 Cunningham et al. (2016). Charge trapping and exciton dynamics in large-area CVD grown MoS$_2$. *J. Phys. Chem. C* 120 (10): 5819–5826.

84 Chen, F. et al. (2017). Temperature-dependent two-dimensional transition metal dichalcogenide heterostructures: controlled synthesis and their properties. *ACS Appl. Mater. Interfaces* 9: 30821–30831.

85 Chen, F. et al. (2018). The effect of the experimental parameters on the growth of MoS$_2$ flakes. *Cryst. Eng. Comm.* 20: 4823–4830.

86 Rajan, G. et al. (2016). Generalized mechanistic model for the chemical vapor deposition of 2D transition metal dichalcogenide monolayers. *ACS Nano.* 10 (4): 4330–4344.

87 Zhu et al. (2021). Effect of precursor ratio on the morphological and optical properties of CVD-grown monolayer MoS$_2$ nanosheets. *Mater. Res. Express* 8 (4): 045008.

88 Der Zande, V. et al. (2013). Grains and grain boundaries in highly crystalline monolayer molybdenum disulphide. *Nat. Mater.* 12 (6): 554–561.

89 Han, S. et al. (2015). Morphology evolution of MoS$_2$ nanorods grown by chemical vapor deposition. *J. Cryst. Growth* 430 (15): 1–6.

90 Tian, Y. et al. (2004). Low temperature synthesis and characterization of molybdenum disulfide nanotubes and nanorods. *Mater. Chem. Phys.* 87: 87–90.

91 Bi, N. et al. (2017). Control of ZnO nanowire growth and optical properties in a vapor deposition process. *J. Mater. Sci. Technol.* 33: 850–855.

92 Bhutto, W.A. et al. (2019). Controlled growth of zinc oxide nanowire arrays by chemical vapor deposition (CVD) method. *Int. J. Comput. Sci. Netw. Secur.* 19: 135–141.

93 Li, C. et al. (2008). Effect of seed layer on structural properties of ZnO nanorod arrays grown by vapor-phase transport. *J. Phys. Chem. C* 112: 990–995.

94 Serrano et al. (2017). Effect of the seed layer on the growth and orientation of the ZnO nanowires: consequence on structural and optical properties. *Vacuum* 146: 509516.

95 Li, D. et al. (2020). Application of graphene-based materials for detection of nitrate and nitrite in water-a review. *Sensors* 20: 54.

96 Gómez, E. et al. (2013). *Rev. Colomb. Mater.* 5: 177–184.

97 Kindalkar et al. (2019). Sol-gel synthesized spin coated GO: ZnO composite thin films: optical, structural and electrical studies. *Mater. Res. Express* 6: 096435.

98 Yein et al. (2018). Enhancement of photocatalytic performance in sonochemical synthesized ZnO–rGO nanocomposites owing to effective interfacial interaction. *Environ. Chem. Lett.* 16: 251–264.

99 Moqbel, R.A. et al. (2018). Pulsed laser synthesis in liquid of efficient visible-light-active ZnO/rGO nanocomposites for improved photo-catalytic activity. *Mater. Res. Express* 5: 035050.

100 Adam, R.E. et al. (2019). Graphene based plasmonic nanocomposites for highly enhanced solar-driven photocatalytic activities. *RSC Adv.* 9: 30585–30598.

101 Yu, W. et al. (2017). Photocatalytic and electrochemical performance of three-dimensional reduced graphene oxide/WS_2/Mg-doped ZnO composites. *Appl. Surf. Sci.* 400: 129–138.

102 Samal, A. et al. (2018). Transfiguring UV light active "metal oxides" to visible light active photocatayst by reduced graphene oxide hypostatization. *Catal. Today* 300: 124–135.

103 Jin, X. et al. (2020). In-situ ionothermal precipitation of well-dispersed ZnO nanoparticles onto 2-dimension neat graphene sheets with excellent photocatalytic activity. *J. Environ. Chem. Eng.* 8: 104030.

104 Chen et al. (2018). UV-assisted photochemical synthesis of reduced graphene oxide/ZnO nanowires composite for photoresponse enhancement in UV photodetectors. *Nanomaterials* 8 (1): 26.

105 Albiter et al. (2021). Synthesis, characterization, and photocatalytic performance of ZnO–graphene nanocomposites: a review. *J. Compos. Sci.* 5 (1): 4.

106 Shwetharani, R. et al. (2020). Photocatalytic semiconductor thin films for hydrogen production and environmental applications. *Int. J. Hydrogen Energy* 45: 18289–18308.

107 Wojnarowicz, J. et al. (2020). A review of microwave synthesis of zinc oxide nanomaterials: reactants process parameters and morphologies. *Nanomaterials* 10: 1086.

108 Gautam, S. et al. (2020). Metal oxides and metal organic frameworks for the photocatalytic degradation: a review. *J. Environ. Chem. Eng.* 8: 103726.

109 Neelgund et al. (2020). ZnO conjugated graphene: an efficient sunlight driven photocatalyst for degradation of organic dyes. *Mater. Res. Bull.* 129: 110911.

110 Tuan, V. et al. (2020). In-situ hydrothermal fabrication and photocatalytic behavior of ZnO/reduced graphene oxide nanocomposites with varying graphene oxide concentrations. *Mater. Sci. Semicond. Process.* 115: 105114.

111 Boukhoubza et al. (2020). Graphene oxide coated flower-shaped ZnO nanorods: optoelectronic properties. *J. Alloys Compd.* 831: 154874.

112 Mahmud, R.A. et al. (2020). Graphene nanoplatelets with low defect density as a synergetic adsorbent and electron sink for ZnO in the photocatalytic degradation of methylene blue under UV–vis irradiation. *Mater. Res. Bull.* 128: 110876.

113 Lee, K.S. et al. (2020). Inhibition of photoconversion activity in self-assembled ZnO-graphene quantum dots aggregated by 4-aminophenol used as a linker. *Molecules* 25: 2802.

114 Kumaresan, N. et al. (2020). Synthesis of ZnO/RGO nanocomposites by wet impregnation method for photocatalytic performance against RhB dye and 4-chlorophenol under UV light irradiation. *J. Mater. Sci. - Mater. Electron.* 31: 3361–3374.

115 Moussa, H. et al. (2016). ZnO rods/reduced graphene oxide composites prepared via a solvothermal reaction for efficient sunlight-driven photocatalysis. *Appl. Catal., B* 185: 11–21.

116 Wu, H. et al. (2020). Fabrication of ZnO-MoS$_2$ nanocomposite heterojunction arrays and their photoelectric properties. *Micromachines* 11 (2): 189.

117 Aldalbahi, A. et al. (2021). Two-step facile preparation of 2D MoS$_2$/ZnO nanocomposite-junctions with enhanced photoelectric performance. *Int. J. Photoenergy*.

118 Lee et al. (2017). Dimensional-hybrid structures of 2D materials with ZnO nanostructures via pH-mediated hydrothermal growth for flexible UV photodetectors. *ACS Appl. Mater. Interfaces* 9 (17): 15031–15037.

119 Wu, J.Z. et al. (2021). Nanohybrid photodetectors. *Adv. Photonics Res.* 2: 2100015.

120 Joon, Y. et al. (2021). One-dimensional semiconductor nanostructures grown on two-dimensional nanomaterials for flexible device applications. *APL Mater.* 9: 060907.

121 Wua, J. et al. (2021). ZnO/graphene heterostructure nanohybrids for optoelectronics and sensors. *J. Appl. Phys.* 130: 070905.

122 Boruah, B.D. et al. (2015). Highly dense ZnO nanowires grown on graphene foam for ultraviolet photodetection. *ACS Appl. Mater. Interfaces* 7 (19): 10606–10611.

123 Manekkathodi, A., Lu, M-Y., Wang, C.W et al. (2010). Direct growth of aligned zinc oxide nanorods on paper substrates for low-cost flexible electronics. *Adv. Mater.* 22: 4059–4063.

124 Liu, K. et al. (2010). Giant improvement of the performance of ZnO nanowire photodetectors by Au nanoparticles. *J. Phys. Chem. C* 114: 19835.

125 Li, H., Wang, X., Zhu, X. et al. (2018). Composition modulation in one-dimensional and two-dimensional chalcogenide semiconductor nanostructures. *Chem. Soc. Rev.* 47 (20).

Z

8

One-Dimensional Si Nanostructure-Based Hybrid Systems: Surface-Enhanced Raman Spectroscopy and Photodetector Applications

Prajith Karadan[1] and Arvind Kumar[2]

[1] *Paul Scherrer Institute, Laboratory for X-ray Nanoscience and Technologies, Forschungsstrasse 111, 5232 Villigen PSI, Switzerland*
[2] *Chaman Lal Mahavidyalaya, Department of Physics, Haridwar 247664, India*

8.1 Introduction

Hybrid nanomaterials consisting of two or more components are getting lot of research attention because of the possibility of tuning the properties of individual components at nanoscale [1]. Hybrid nanomaterials show superior properties over the individual components, and their properties depend on the structure, composition, interface, distribution of each materials, etc. [2]. On the other hand, 1D semiconductor nanostructures including nanowires (NWs), nanopillars, nanorods, nanofibers, and nanocones have emerged as promising materials due to their unique and additional functional properties for various device applications [3, 4]. 1D semiconductor nanomaterials-based hybrids have received significant research interest owing to their exceptional optical, electronic, and mechanical properties [5–7].

Among various semiconducting hybrid nanosystems, Si nanostructure-based hybrids have gained significant attention, since the 1D Si nanostructures play central role in current semiconducting industry [8, 9]. 1D Si nanostructures-based hybrid systems have been widely studied for their applications in photovoltaics, chemical and biosensing, nanoelectronics, surface-enhanced Raman spectroscopy (SERS), and photodetectors [5, 10–12]. The electronic and photonic applications of these structures are particularly important due to their advantages such as compatibility with currently existing semiconductor technology, the ability of miniaturization in microelectronics, and enhanced light matter interaction [13, 14]. In addition to the existing advantages such as well-established fabrication techniques, availability, and stability over wide range of processing conditions,

the structural one dimensionality of Si NWs/pillars provides unique properties such as superior light trapping, increased surface-to-volume ratio, and quantum confinement effect. [15–17]. These properties can further be tuned toward specific applications by transforming them to a 1D Si nanostructure-based hybrid system [18, 19]. 1D Si nanostructures-based hybrids possess unique electrical and optical properties, which lead to wide range of applications in diverse fields [20, 21].

The fabrication methods of the 1D Si nanostructures include both top-down and bottom up approaches [22–25]. In top-down process, Si substrates are patterned using photolithography, E-beam lithography, nanoimprint or nanosphere lithography, and nanostructures are realized by dry or chemical etching processes. Top down approaches are very effective to scale down the structures to sub-nanometer regime [26]. On the other hand, using bottom-up methods, Si nanostructures are produced with excellent quality using facile methods such as vapor–liquid–solid (VLS) or vapor–solid–solid (VSS) growth techniques. According to this method, the nanostructures can be grown on various substrates and possible to transfer as grown nanostructures to any substrates [27, 28].

This chapter discusses the fabrication methods of 1D Si nanostructure-based hybrid systems and their applications in SERS and photodetectors. This chapter also describes how efficiently the structure and morphology of the Si nanostructure-based hybrids can be tuned toward SERS and photodetector applications.

8.2 Si Nanostructures

Various Si nanostructures such as Si nanocrystals, nanowires, nanopillars, nanocones, nanodomes, and nanoholes have been developed to meet increasing demands of Si nanostructures for the variety of applications. Silicon nanocrystals are quasi-zero-dimensional (0D) Si nanostructures, which received extensive interest after the report on the efficient photoluminescence from porous Si by Canham [29]. He has reported a very strong light emission from the porous SiNWs fabricated by the combined procedure of electrochemical etching and chemical dissolution. The room-temperature photoluminescence originated from the quantum confinement effect of the porous Si nanocrystallites, which can produce photoluminescence well above the bandgap of crystalline Si. These new findings led the researchers to think about the manipulation of matter in the nanometer scale to achieve suitable optoelectronic systems for various potential applications. Later, the mechanism of the visible light emission from the Si nanocrystals was thoroughly investigated by many other researchers [30–32]. Silicon nanoholes have gained research attention due to their mechanical stability and the possibility to tune the optical and electrical by controlling the structural parameters. Silicon nanoholes are extensively utilized for various applications such as solar cells, chemical and gas sensors, and photodetectors [33]. Silicon nanohole arrays showed superior light trapping owing to their effective optical coupling between the incident light and nanohole arrays [34, 35]. Periodic arrays of Si nanodomes are another class of Si nanostructures, which are effectively utilized for photovoltaic and photonic crystal applications [36, 37]. Silicon nano/micropyramids have been extensively studied

for photovoltaics and SERS applications because of their high surface area and light-trapping capabilities [38–40]. In general, Si pyramids are fabricated by wet chemical etching process using KOH or NaOH solution. Si-inverted pyramids are also fabricated using Cu-assisted growth in the solution of HF/H_2O_2 and H_2O [41]. 1D silicon nanostructures including nanowires, nanopillars, nanocones, and nanofibers are one of the most popular nanostructures due to their intensive applications in various fields ranging from optoelectronics to biosensing. SiNWs/pillars are important class of 1D nanostructures used for wide applications such as solar cell, SERS, biosensing, field-effect transistor (FET), gas sensing, and Li-ion batteries. [42–44]. SiNWs are considered as the inevitable components in nanoelectronics because of their exceptional electrical properties. Commonly used fabrication methods of SiNWs are chemical vapor deposition (CVD), metal-assisted chemical etching (MACE), laser ablation, etc. [45, 46]. Si nanocones exhibit unique properties such as superior antireflection and angle-insensitive light absorption. These excellent optical properties of Si nanocones have been utilized for their potential applications in SERS, solar cells, etc. [18, 47–49].

Hereafter, this chapter extensively focuses on the fabrication, SERS, and photo-detector applications of 1D Si nanostructures.

8.3 Fabrication of 1D Si Nanostructures

8.3.1 Vapor–Liquid–Solid Growth

VLS growth is one of the most commonly used methods for the fabrication of SiNWs. Wagner and Ellis are reported the VLS method in the mid-1960s for the first time [27]. In this process, the vapor phase precursor of the nanowire material gets adsorbed on Au–Si alloy in liquid phase from which the growth of nanowire takes place [27]. Since the Si is highly sensitive to oxidation, the main challenge in the VLS growth is the selection of suitable precursor material. Generally, the monosilanes, disilanes, and chlorosilanes are the oxygen-free precursors used for the VLS growth of SiNWs. Highly protective, strict, and safe procedures are required for the safe operation due to the pyrophoric nature of the silanes. The chlorosilanes produce hydrochloric acid in presence of H_2, which cause the random etching of the substrate. Moreover, high temperatures (>800 °C) are required for the decomposition of chlorosilanes [50, 51]. CVD is one of the bottom-up fabrication techniques, which utilize VLS growth mechanism for producing high-aspect-ratio Si nanostructures [52–54]. Picraux et al. have reported the VLS mechanism in a CVD reactor with a clear explanation. According to this mechanism, the silane molecules react at the Au surface through the hydrogen decomposition and introduce atomic Si to the seed material. Si–Au liquid alloy is formed at a particular eutectic temperature and concentration.

On further addition of Si, the Au–Si alloy becomes supersaturated with atomic Si, and the crystallization occurs beneath the liquid droplet [45]. The VLS growth of SiNWs is shown in Figure 8.1 [55]. Gaseous reactants such as SiH_2Cl_2, $SiCl_4$, and Si_2H_6 with different reaction temperature have been used for the CVD growth of the
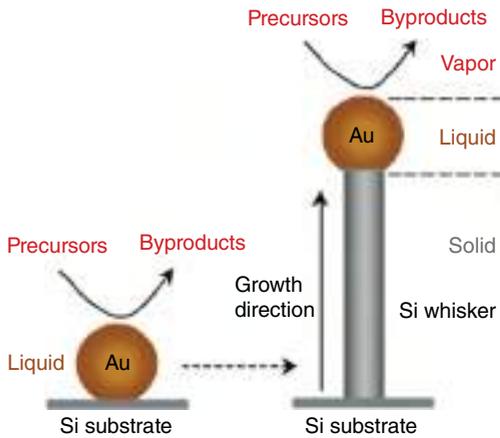
Figure 8.1 (a) VLS mechanism for the growth of SiNWs proposed by Wagner and Ellis. Source: Wang et al. [55]/with permission of American Chemical Society.

Si nanostructures. The CVD process is aimed at for the deposition of high-quality films. In 2004, Wu et al. have demonstrated growth of SiNWs with molecular-scale dimension of ~3 nm using gold clusters catalyzed CVD growth [54]. Yang's research group has reported the controlled growth of SiNWs (i.e. diameter, density, and position are precisely controlled) through direct seeding in VLS–CVD growth [28]. The colloidal seeds of gold are adequate to determine the position and size of the SiNWs. The decomposition of the precursor material $SiCl_4$ in H_2 produces HCl, which removes the unwanted oxide layer on the Si substrate and ensures the growth of pure SiNWs.

8.3.2 Dry Etching

Reactive ion etching (RIE) is the most common dry etching method, which utilizes the plasma of reactive gases such as SF_6, O_2, and C_4F_8 for the removal of masked pattern of semiconductor material from the exposed surface. Generally, RIE is performed in two ways: (i) cryogenic plasma etching and (ii) Bosch process [22]. In cryogenic plasma etching, the sidewall etching and the evaporation rates of halogens are affected, since the substrate is kept at low temperature. The substrate temperature has less effect on the reaction rate at ion-bombarded surfaces because of the local increase in energy density by the high energy ions [23]. In Bosch process, the etching and passivating gases are introduced simultaneously on the masked substrate. The process undergoes through many cycles until the desired structure has been achieved. The main disadvantage of the RIE method is the undercutting, which arises from the radical-induced sidewall etching reactions. The electron shadowing effect is also observed for high-aspect-ratio structures because of the nonuniformly charged etching surfaces. High-cost lithographic techniques such as interference lithography and deep ultraviolet lithography have been used with the RIE for producing desired patterns on the Si substrate [56].

8.3.3 Metal-Assisted Chemical Etching

MACE is a wet chemical fabrication method for producing high-aspect-ratio nanostructures at low cost. Dimova et al. have demonstrated the MACE of silicon for the first time in 1997 [57]. An aluminum-coated Si substrate was immersed in etching solution composed of HF, HNO$_3$, and H$_2$O for producing porous silicon. In the early 2000, Li et al. have reported the most acceptable form of MACE by utilizing noble metal (Au, Pt, Ag, or Au/Pd alloy) catalyzed Si substrates in an etching solution consists of HF, H$_2$O$_2$, and ethanol. MACE is extensively used for the fabrication of various 1D nanostructures including random and periodic SiNWs and Si nanocones. Mainly, two types of MACE are employed for the fabrication of SiNWs: one-step MACE and two-step MACE [58]. In one-step process, etching solution is prepared by dissolving metal salts like AgNO$_3$ and HAuCl$_4$ in HF and solvents such as water and ethanol. When Si substrate is placed in etching solution, metal ions are reduced on the Si surfaces leading to the formation of nanoscale metallic islands, which in turn promote the formation of SiNWs. Reaction rate can be increased by adding oxidizing agents such as HNO$_3$ and H$_2$O$_2$ [59]. In two-step MACE, metallic film is deposited on Si using physical vapor deposition, which acts as a metal catalyst for the Si etching in HF and H$_2$O$_2$ solution. In this method, SiNWs with different morphologies tilted or zigzag NWs can be formed by tuning the parameters such as oxidizer concentration and crystal orientation. [60] Notably, periodic arrays of SiNWs/pillars can also be fabricated by the combination of nanosphere lithography, or standard lithography and MACE. Peng et al. have achieved periodic array of SiNWs for the first time using colloidal silica monolayer as a shadow mask followed by MACE using HF/H$_2$O$_2$. Recently, Karadan et al. have reported the fabrication of Si nanopillars (SiNPLs) by using polystyrene nanosphere lithography and MACE [61]. SEM images are presented in Figure 8.2. The diameter, distance between the pillars, packing density, etc., can be controlled by this method.

For the MACE with HF/H$_2$O$_2$ solution, H$_2$O$_2$ acts as a reducing agent and the noble metal acts as cathode. Initially, H$_2$O$_2$ is reduced at the metal surface (cathodic reaction) by the following reaction [24]:

$$H_2O_2 + 2H^+ \rightarrow 2H_2O + 2h^+$$
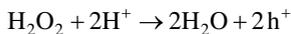
Noble metal catalyzes the reduction of H$_2$O$_2$ at the metal surface. The protons get reduced into hydrogen in another cathodic reaction:

$$2H^+ \rightarrow H_2 + 2h^+$$
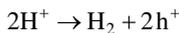
At the anode, the Si substrate gets oxidized and finally dissolved in HF. There are three possible mechanisms for the anodic process.

Direct dissolution of tetravalent state Si in solution [62, 63]:

$$Si + 4h^+ + 4HF \rightarrow SiF_4 + 4H^+$$

$$SiF_4 + 2HF \rightarrow H_2SiF_6$$
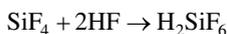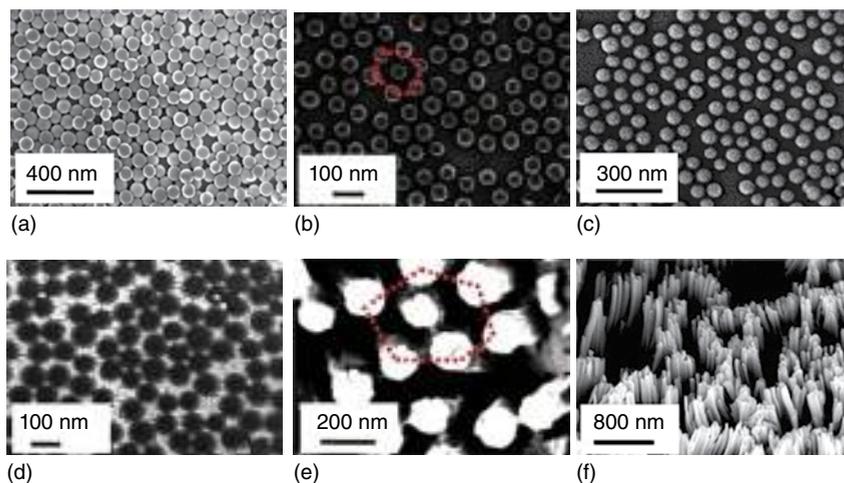
Figure 8.2 (a) SEM images for polystyrene nanosphere lithography (a) monolayer of polystyrene nanospheres on Si substrate. (b) Separated polystyrene nanosphere by O$_2$ plasma etching. (c) Thin film of Au deposited on separated polystyrene nanospheres. (d) Nanoporous Au template on Si after the removal of polystyrene nanospheres. (e and f) Top and 20° tilted view of SiNPLs. Source: Karadan et al. [61], Reproduced with permission from Springer Nature.

8.4 Applications of 1D Si Nanostructures Hybrids in SERS and Photodetectors

8.4.1 SERS Applications of Si Nanostructure Hybrids

SERS is a well-known surface-sensitive technique, which enhances Raman scattering by molecules adsorbed on metal surfaces. The discovery of SERS enabled the exploration of Raman spectroscopy toward the label-free recognition of molecules at single molecule level. SERS enables the enormous enhancement in the Raman intensity, as high as 10^{14}–10^{15}, which could lead to the single-molecule detection. SERS involves mainly two types of enhancement mechanisms, i.e. electromagnetic enhancement and chemical enhancement. When the light strikes on the metal nanoparticles, the hot electrons are getting excited, which results in the formation of surface plasmons, schematically represented in Figure 8.3 [64]. Surface plasmons are electromagnetic waves that propagate along the surface parallel to the metal/dielectric interface [65, 66]. When a molecule is near to metal nanoparticle, it experiences an enhanced electromagnetic field leading to the detection of various molecules. Chemical enhancement involves charge transfer between the chemisorbed species and the metal surface. This enhancement is generally less than a factor of 10 [67].

Good SERS substrates provides strong plasmon resonance leading to high electromagnetic enhancement. For an ideal SERS substrate, the requirements are as follows [68, 69]:

Metal sphere   Electric field   Molecule
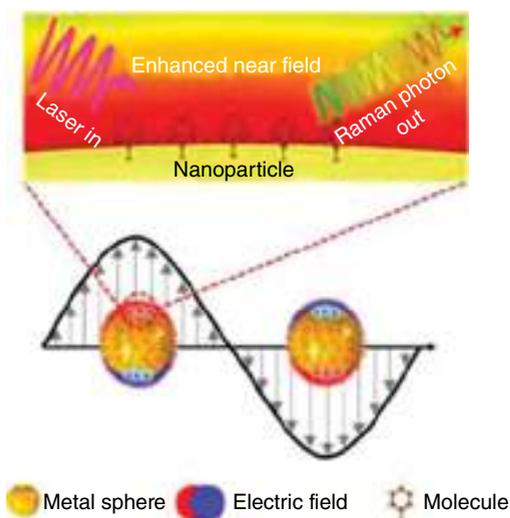
Figure 8.3 Schematic diagram illustrating localized surface plasmon at Au/air interface. Source: Li et al. [64]/with permission of American Chemical Society.

(1) small metal features, i.e. metallic nanostructures with nanoscale separation;
(2) Large surface area, which can accommodate plenty of metal nanoparticles with nanogaps;
(3) Reusability and reproducibility of the substrates.

There are several metal deposition strategies in order to fabricate Si nanostructure-based hybrid nanosystem for SERS applications. Plasmonic nanostructures can be incorporated on the Si nanostructures by colloidal deposition, sputtering, evaporation, physical vapor deposition, etc. [70–72]. Si nanostructure-based hybrid nanosystems have been extensively studied for SERS applications over the past decade [73–76]. Porous silicon/metal nanoparticle-based hybrids have been demonstrated as efficient SERS substrates since 2003 [74, 75, 77]. SERS performance on the porous silicon is found to be improved by tuning the morphology of the porous Si, using combination of porous silicon with Bragg structures, controlling the size and position of the plasmonic nanoparticles on the porous Si [70, 73]. Later, 1D Si nanostructure-based hybrid systems are introduced and emerged as the most promising candidates for SERS detection of various molecules [78–80].

SERS performance of 1D Si nanostructure-based hybrids depends on several factors such as size and shape of metal nanoparticles, surface roughness, surface area, and gap between metal nanoparticles. Metal nanoparticles are incorporated in to 1D Si nanostructures in several ways.

Kanipe and coworkers have reported SiNPLs hybrids (Figure 8.4a,b), where metal nanoparticles are capped on the top of SiNPLs enabling uniform Raman enhancement by a factor of $\sim 10^7$ [81]. Lin et al. have demonstrated large-area SERS using Si nanorods in conjugation with AuNPs. The conjugation of AuNPs on the Si nanorods is achieved by "grafting on to" strategy using 3-mercaptopropyltrimethoxysilane as
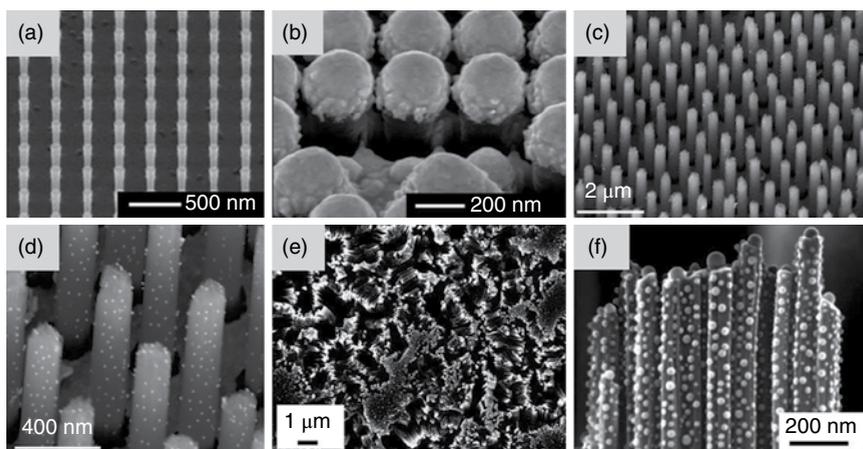
Figure 8.4 Scanning electron micrographs of (a and b) 45° tilted view SiNPLs and Au-capped SiNPLs. Source: Kanipe et al. [81], Adapted with permission from American Chemical Society. (c and d) AuNPs-conjugated Si nanorod arrays. Source: Lin et al. [82], Adapted with permission from American Chemical Society. (e) Top view of SiNPLs fabricated by nanosphere lithography and MACE (f) Cross-sectional view of AgNPs-decorated SiNPLs. Source: Karadan et al. [83], Reproduced with permission from Elsevier.

grafting material, which has no overlap with the Raman signals of analyte molecules (Figure 8.4c,d and Figure 8.5c) [82]. This method helps to overcome the usual challenges such as nonuniformity and aggregation of NPs during the deposition of metal nanoparticles for SERS applications. Highly uniform deposition of AgNPs with a good control over the density and morphology is achieved by Akin et al., in which AgNPs are deposited along the SiNWs through polydopamine coating followed by electroless plating [86].

Karadan et al. have reported a hybrid nanostructure based on SiNPLs, where the AgNPs are decorated on the sidewalls and top of SiNPLs (Figure 8.4e,f) [83]. SiNPLs are fabricated using nanosphere lithography and MACE; later, SiNPLs are converted in to hybrid nanosystem by the decoration of AgNPs by sputtering followed by vacuum annealing at 400 °C. This hybrid nanosystem is utilized as universal SERS substrates for biosensing with enhancement factor of ~10^8. These substrates are employed for the detection of various biomolecules such as BSA, HSA, a-beta, lysozyme, DNA, and E-coli [83], as shown in Figure 8.5a. Hui Wang et al. have reported single-molecule detection utilizing single-SiNW-based SERS sensor, in which, AgNPs are distributed over the single SiNW in a controlled manner [87].

Wide range of SERS substrates are achieved by the deposition of thin metallic layer on whole SiNWs [84, 88]. This hybrid system eliminates the difficulty in the uniform arrangement of molecules in gap-based SERS system by providing wide surface area for the absorption of molecules [84] (Figure 8.6b and Figure 8.5b). Xu et al. have reported a hybrid SERS platform based on a hydrophobic SiNPLs, in which AgNPs are formed uniformly on the top of the SiNPLs by droplets-confined electroless deposition, as shown in Figure 8.6a and Figure 8.5d [85]. Jeon et al. have
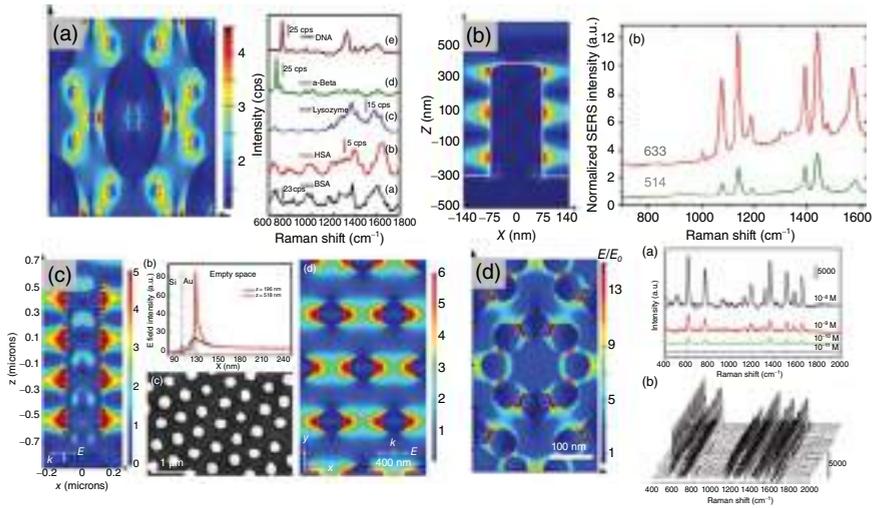
Figure 8.5 (a) Finite difference time domain (FDTD) simulated plasmonic hot spot distributions of SiNPLs SERS sensors. SERS detection of various molecules using SiNPLs-SERS sensor. Source: Karadan et al. [83], Reproduced with permission from Elsevier. (b) FDTD simulated E field intensity of Ag film-coated SiNWs and SERS spectra for 4-aminothiophenol using Ag film-coated SiNWs under 514 and 633 nm lasers. Source: Huang et al. [84], Adapted with permission from American Chemical Society. (c) FDTD simulated plasmonic hot spot distributions of AuNPs functionalized Si nanorod arrays, top view of AuNPs-functionalized Si nanorod arrays. Source: Lin et al. [82], Adapted with permission from American Chemical Society. (d) FDTD simulated electromagnetic field distributions and SERS enhancement R6G molecules adsorbed on superhydrophobic AgNPs/SiNPLs hybrid system. Source: Xu et al. [85], Adapted with permission from American Chemical Society.

presented a novel hybrid structure of noncircular SiNWs coordinated triangularly, where the triangles are arranged in a hexagonal geometry [91]. The unique geometry of the hybrid structure along with the possibility of tuning the optical properties in the near-IR region assure good homogeneity and highly enhanced Raman signals.

The morphology and distribution of Si nanostructures play key role in anchoring the density and distribution of metal nanoparticles that enable the formation of plasmonic hot spots. 1D hierarchical architectures based on Si micropillar arrays have been attained an increasing amount of interest because of their enormous surface area and structural complexity that facilitates the formation of plasmonic hot spots by accommodating large number of metal nanoparticles. Huang and coworkers have reported "wire on pillar" 3D architecture by enabling the lateral growth of gold nanowires on the sidewalls of Si micropillars (Figure 8.6c) [89]. The uniqueness of the "wire on pillar" architecture resulted in the abundance of hotspots between adjacent gold nanowires leading to very high SERS enhancement.

Xuan He et al. have demonstrated biomimetic structure (cicada wing topography) based on Si pillars, where Si pillars are used as a template for the growth of superhydrophobic Ag micro/nanopillar arrays via electrochemical deposition [92]. The corresponding SERS substrates are employed for efficient and reproducible detection
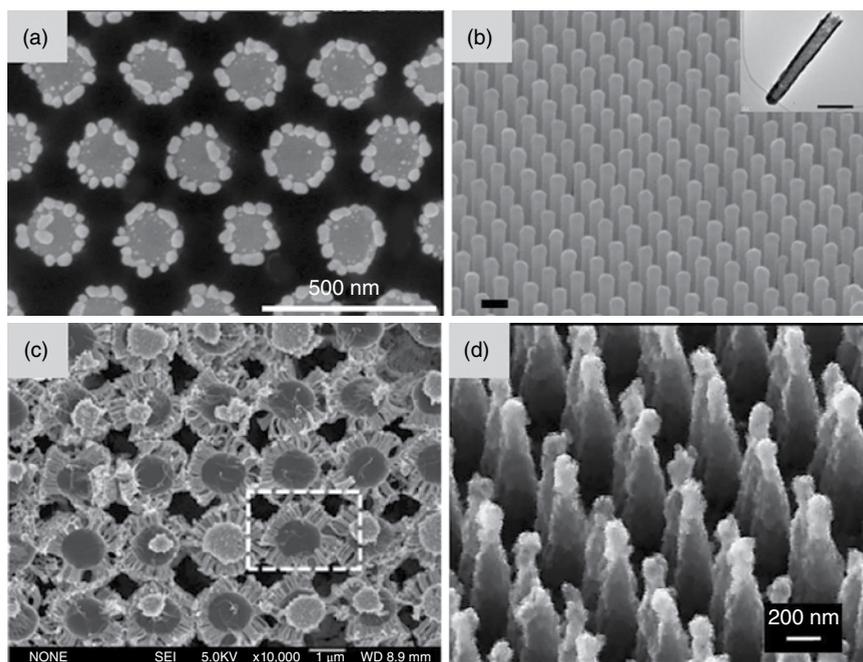
Figure 8.6 (a) Scanning electron micrograph for AgNPs formed on SiNPLs. Source: Xu et al. [85], Adapted with permission from American Chemical Society. (b) SEM image of Ag film-coated SiNWs. Inset is TEM image showing the Ag film was continuous. Source: Huang et al. [84], Adapted with permission from American Chemical Society. (c) Au wire bundles-decorated SiNWs. Source: Huang et al. [89], Adapted with permission from American Chemical Society. (d) SEM image of Si double nanocone arrays. Source: Mehrvar et al. [90], Springer Nature, CC BY 4.0.

of explosives like picric acid and 3-nitro-1,2,3-triazol-5-one. Liu et al. have reported ultrasensitive SERS substrates with high-density 3D hot spots created from AgNPs-decorated Ge nanotapers grafted on Si micropillar arrays [93].

Other 1D Si nanostructures Si nanocones, nanodomes, etc., are also demonstrated for their applications in SERS. For instance, Mehrvar et al. have reported a unique hybrid structure based on Si double nanocone array fabricated by E-beam lithography and plasma etching process. AgNPs are decorated using electroless deposition. These substrates resulted in an enhancement factor of ~10^9 with high density of hot spot distributions (Figure 8.6d) [91]. Split-type gap-induced SERS substrates based on Al_2O_3@Ag@Si nanocone arrays and AgNPs are reported by Wang et al., where an ultrathin layer (2 nm) of Al_2O_3 is deposited between the AgNPs and Ag@Si nanocone by atomic layer deposition (ALD) leading to high-dense gap-induced hot spots [94].

Si pyramids-based nanocermets are reported as efficient SERS substrates with high enhancement factor of 10^7. Si wafers are etched anisotropically to form Si micropyramids, and the Ag:a-Si_3N_4 nanocermets are deposited by direct current unbalanced magnetron sputtering system. Anisotropic etching in Si helps in anchoring the size

of AgNPs as well as the effective light trapping, which in turn facilitates the SERS enhancement. These Si micropyramid-based SERS hybrid sensors are effectively utilized for multi-analytes detection such as thiophenol, R6G, lysozyme, BSA, HSA, and ATP [40]. Recently, Au–Ag alloy film/Si micropillars hybrids which showed better sensitivity and chemical stability than the individual Au/Ag films are explored for SERS detection [95].

8.4.2 Si Nanostructure Hybrids for Photodetector Applications

8.4.2.1 Device Geometries of Photodetectors

The performance of the photodetector relies on the operating principle and device geometries. Photodetectors are mainly configured into three different device geometries such as photoconductors, photodiodes, and phototransistors.

Photoconductive mode: Photoconductive mode is the simplest device geometry, which consists of an active light-absorbing layer and symmetrical ohmic contact. The absorption of the incident light by the semiconducting layer produces electron–hole pairs, and an external power supply is used to drive the charge carriers in opposite electrodes, which accounts for the increase in the conductivity. However, this device configuration has disadvantages such as high dark current and slow response time, which restrict their applications in photoswitching, light communication, etc. [96].

p–n or Schottky diodes: These are p–n photodiodes consisting of semiconductors with opposite conductivity types. The working principle relies on the photovoltaic effect, where the Fermi levels of the two types of semiconductors are being equalized due to the charge transfer between them. p–n photodiodes shows rectifying I–V characteristics in the dark. Upon illumination, the electron–hole pairs are developed in the semiconductor owing to the absorption of photons. The electron–hole pairs within the diffusion length from the junction flow to the depletion region, where the charge carriers are separated due to the built-in potential and drive toward the opposite directions. Schottky photodiodes also work with the similar mechanism, where the semiconductor and a metal with varying work function are in contact instead of semiconductors with different doping types [97].

Phototransistor: Phototransistor is three-terminal device consisting of semiconducting layer with source, drain, and gate contacts. In this geometry, gate voltage is used to modulate the charge transport through semiconducting channel.

8.4.2.2 1D Si Nanostructure Hybrids for Photodetectors

1D Si nanostructures have been emerged as a great platform for the light-detecting devices such as photovoltaics, photodetectors, and metamaterial devices [13, 98–100]. The light-detecting capability of the 1D Si nanostructures has been greatly enhanced by the incorporation of metal nanostructures, graphene, and quantum dots [43, 101–103]. Chen et al. have shown the ability of SiNWs decorated with AuNPs for enhanced Raman scattering, polarization sensitivity, and efficient photodetection owing to strong electromagnetic coupling in hybrid nanostructure. They

have reported an enhancement in photocurrent of SiNWs by 100% by the decoration of plasmonic nanoparticles [11].

Arvind et al. have investigated the photodetector properties of SiNPLs/AgNWs heterojunction along with pristine SiNPLs. To fabricate the heterojunction, AgNWs with diameter 50–80 nm and length ~5–30 μm were deposited on the SiNPLs. It was observed that heterojunction photodetector exhibits ~10 times more sensitivity as compared to SiNPLs-based photodetector as shown in Figure 8.7. The sensitivity is attributed to the enhanced light absorption properties of AgNWs/SiNPLs and modification of work function and charge trapping at the interface [104].

Combination of 1D Si nanostructure and graphene is used to widen the spectrum of detection [105, 106]. Hybrid nanostructures composed of SiNWs and reduced graphene oxide are utilized for the detection of light from visible–terahertz range [106]. Lin Bao et al. have reported highly efficient NIR photodetector using SiNWs-AuNPs-decorated graphene hybrids [43]. In this case, they observed superior light trapping into SiNWs through the surface plasmon excitation and coupling in the AuNPs-decorated graphene [43]. Core–shell SiNWs coated with Cu or Ag films have also been exploited for photodetector applications. Chun Yan Wu et al. have demonstrated ultrasensitive NIR photodetector with high responsivity, detectivity, and fast response speed [101].
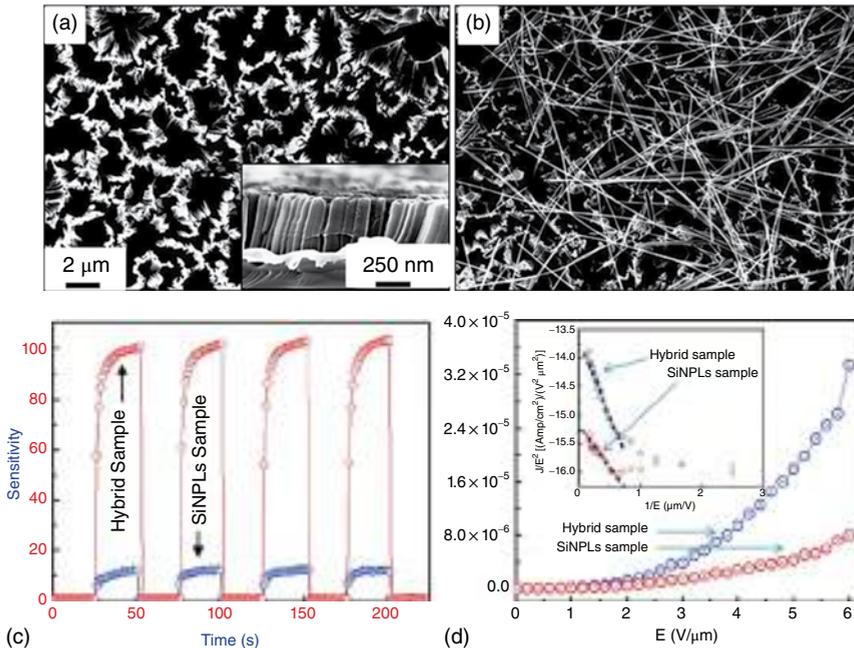
Figure 8.7 (a) SEM images of SiNPLs. Cross-sectional image is shown in inset; (b) AgNWs coated on SiNPLs (c); sensitivity versus time plot showing the performance comparison between SiNPLs and SiNPLs/AgNWs hybrid detector. (d) Current density is plotted against electric field of SiNPLs and AgNWs/SiNPLs hybrids. Source: Kumar et al. [104], Reproduced with permission from Elsevier.

Organic–SiNW hybrid photodetectors are another important class of hybrid photodetectors, which utilize the outstanding photosensitive properties of various organic molecules along with SiNWs [107, 108]. Porphyrin–SiNWs hybrids are getting much research attention since 2007, as porphyrin is an organic molecule that is ubiquitous in biological systems [108]. These hybrids are demonstrated as optical inverters, complementary logic gates, etc. [109]. Recently, Lefler et al. have reported an interesting fluorophore–SiNW hybrid FETs, enabling the detection of specific visible wavelength [110].

8.5 Conclusions

This chapter explains the fabrication of 1D silicon nanostructure-based hybrid systems and their potential applications in SERS and photodetectors. Different approaches for the fabrication of 1D Si nanostructures such as VLS growth, MACE, and dry etching are discussed in detail. SERS is a widely accepted molecular detection technique by utilizing the localized surface plasmon resonance of metal nanoparticles. 1D Si nanostructure–metal nanoparticle hybrids and a brief discussion on the utilization of these hybrids system for highly sensitive detection of various molecules are also included in this chapter. Additionally, the combination of 1D Si nanostructures with Au, graphene, quantum dots, and organic molecules are also discussed for photodetector applications.

References

1 Tan, C., Chen, J., Wu, X.J., and Zhang, H. (2018). Epitaxial growth of hybrid nanostructures. *Nat. Rev. Mater.* 3: 1–13.

2 Huang, X., Tan, C., Yin, Z., and Zhang, H. (2014). 25th anniversary article: hybrid nanostructures based on two-dimensional nanomaterials. *Adv. Mater.* 26 (14): 2185–2204.

3 Garnett, E., Mai, L., and Yang, P. (2019). Introduction: 1D nanomaterials/ nanowires. *Chem. Rev.* 119 (15): 8955–8957.

4 Zhang, Z., Zou, R., Yu, L., and Hu, J. (2011). One-dimensional silicon-based semiconductor nanomaterials: synthesis, structures, properties and applications. *Crit. Rev. Solid State Mater. Sci.* 36 (June 2011): 148–173.

5 Baraban, L., Ibarlucea, B., Baek, E., and Cuniberti, G. (2019). Hybrid silicon nanowire devices and their functional diversity. *Adv. Sci.* 6 (15).

6 Baek, E., Pregl, S., Shaygan, M. et al. (2015). Optoelectronic switching of nanowire-based hybrid organic/oxide/semiconductor field-effect transistors. *Nano Res.* 8 (4): 1229–1240.

7 Jiang, R., Li, B., Fang, C., and Wang, J. (2014). Metal/semiconductor hybrid nanostructures for plasmon-enhanced applications. *Adv. Mater.* 26 (31): 5274–5309.

8 Bashouti, M.Y., Sardashti, K., Schmitt, S.W. et al. (2013). Oxide-free hybrid silicon nanowires: from fundamentals to applied nanotechnology. *Prog. Surf. Sci.* 88 (1): 39–60.

9 Priolo, F., Gregorkiewicz, T., Galli, M., and Krauss, T.F. (2014). Silicon nanostructures for photonics and photovoltaics. *Nat. Nanotechnol.* 9 (1): 19–32.

10 Lee, J., Jang, J., Choi, B. et al. (2015). A highly responsive silicon nanowire/ amplifier MOSFET hybrid biosensor. *Sci. Rep.* 5: 1–6.

11 Chen, R., Li, D., Hu, H. et al. (2012). Tailoring optical properties of silicon nanowires by au nanostructure decorations: enhanced Raman scattering and photodetection. *J. Phys. Chem. C* 116 (7): 4416–4422.

12 Vendamani, V.S., Nageswara Rao, S.V.S., Venugopal Rao, S. et al. (2018). Three-dimensional hybrid silicon nanostructures for surface enhanced Raman spectroscopy based molecular detection. *J. Appl. Phys.* 123 (1).

13 Bae, J., Kim, H., Zhang, X.M. et al. (2010). Si nanowire metal-insulator-semiconductor photodetectors as efficient light harvesters. *Nanotechnology* 21 (9).

14 Karadan, P., Anappara, A.A., Moorthy, V.H.S. et al. (2016). Improved broadband and omnidirectional light absorption in silicon nanopillars achieved through gradient mesoporosity induced leaky waveguide modulation. *RSC Adv.* 6 (110): 109157–109167.

15 Kiraly, B., Yang, S., and Huang, T.J. (2013). Multifunctional porous silicon nanopillar arrays: antireflection, superhydrophobicity, photoluminescence, and surface-enhanced Raman scattering. *Nanotechnology* 24 (24).

16 Hasan, M., Huq, M.F., and Mahmood, Z.H. (2013). A review on electronic and optical properties of silicon nanowire and its different growth techniques. *Springerplus* 2 (1): 1–9.

17 Chan, C.K., Peng, H., Liu, G. et al. (2008). High-performance lithium battery anodes using silicon nanowires. *Nat. Nanotechnol.* 3 (1): 31–35.

18 Jeong, S., Garnett, E.C., Wang, S. et al. (2012). Hybrid silicon nanocone-polymer solar cells. *Nano Lett.* 12 (6): 2971–2976.

19 Almenabawy, S.M. and Swillam, M.A. (2020). Broad-band organic-silicon nanowire hybrid composites for solar energy applications. *ACS Appl. Nano Mater.* 3 (8): 7446–7453.

20 Wu, S.L., Deng, J.H., Zhang, T. et al. (2012). Tunable synthesis of carbon nanosheet/silicon nanowire hybrids for field emission applications. *Diamond Relat. Mater.* 26: 83–88.

21 Reddy, A.L.M., Gowda, S.R., Shaijumon, M.M., and Ajayan, P.M. (2012). Hybrid nanostructures for energy storage applications. *Adv. Mater.* 24 (37): 5045–5064.

22 Elbersen, R., Vijselaar, W., Tiggelaar, R.M. et al. (2015). Fabrication and doping methods for silicon nano- and micropillar arrays for solar-cell applications: a review. *Adv. Mater.* 27 (43): 6781–6796.

23 Fu, Y.Q., Colli, A., Fasoli, A. et al. (2009). Deep reactive ion etching as a tool for nanostructure fabrication. *J. Vac. Sci. Technol. B Microelectron. Nanom. Struct.* 27 (3): 1520.

24 Huang, Z., Geyer, N., Werner, P. et al. (2011). Metal-assisted chemical etching of silicon: a review. *Adv. Mater.* 23 (2): 285–308.

25 Hobbs, R.G., Petkov, N., and Holmes, J.D. (2012). Semiconductor nanowire fabrication by bottom-up and top-down paradigms. *Chem. Mater.* 24 (11): 1975–1991.

26 Sun, M.C., Kim, G., Lee, J.H. et al. (2013). Patterning of Si nanowire array with electron beam lithography for sub-22 nm Si nanoelectronics technology. *Microelectron. Eng.* 110: 141–146.

27 Wagner, R.S. and Ellis, W.C. (1964). Vapor-liquid-solid mechanism of single crystal growth. *Appl. Phys. Lett.* 4 (5): 89–90.

28 Hochbaum, A.I., Fan, R., He, R., and Yang, P. (2005). Controlled growth of Si nanowire arrays for device integration. *Nano Lett.* 5 (3): 457–460.

29 Canham, L.T. (1990). Silicon quantum wire array fabrication by electrochemical and chemical dissolution of wafers. *Appl. Phys. Lett.* 57 (10): 1046–1048.

30 Yu, Y., Fan, G., Fermi, A. et al. (2017). Size-dependent photoluminescence efficiency of silicon nanocrystal quantum dots. *J. Phys. Chem. C* 121 (41): 23240–23248.

31 Limpens, R., Lesage, A., Fujii, M., and Gregorkiewicz, T. (2015). Size confinement of Si nanocrystals in multinanolayer structures. *Sci. Rep.* 5: 1–6.

32 Heitmann, J., Müller, F., Zacharias, M., and Gösele, U. (2005). Silicon nanocrystals: size matters. *Adv. Mater.* 17 (7): 795–803.

33 Peng, K.Q., Wang, X., Li, L. et al. (2010). High-performance silicon nanohole solar cells. *J. Am. Chem. Soc.* 132 (20): 6872–6873.

34 Han, S.E. and Chen, G. (2010). Optical absorption enhancement in silicon nanohole arrays for solar photovoltaics. *Nano Lett.* 10 (3): 1012–1015.

35 Deng, C., Tan, X., Jiang, L. et al. (2018). Efficient light trapping in silicon inclined nanohole arrays for photovoltaic applications. *Opt. Commun.* 407 (August 2017): 199–203.

36 Zhu, J., Hsu, C.M., Yu, Z. et al. (2010). Nanodome solar cells with efficient light management and self-cleaning. *Nano Lett.* 10 (6): 1979–1984.

37 Becker, C., Lockau, D., Sontheimer, T. et al. (2012). Large-area 2D periodic crystalline silicon nanodome arrays on nanoimprinted glass exhibiting photonic band structure effects. *Nanotechnology* 23 (13).

38 Zhong, S., Wang, W., Zhuang, Y. et al. (2016). All-solution-processed random Si nanopyramids for excellent light trapping in ultrathin solar cells. *Adv. Funct. Mater.* 26 (26): 4768–4777.

39 Tang, Q., Shen, H., Gao, K. et al. (2016). Efficient light trapping of quasi-inverted nanopyramids in ultrathin c-Si through a cost-effective wet chemical method. *RSC Adv.* 6 (99): 96686–96692.

40 Gupta, N., Gupta, D., Aggarwal, S. et al. (2014). Thermally stable plasmonic nanocermets grown on microengineered surfaces as versatile surface enhanced Raman spectroscopy sensors for multianalyte detection. *ACS Appl. Mater. Interfaces* 6 (24): 22733–22742.

41 Branham, M.S., Hsu, W.C., Yerci, S. et al. (2015). 15.7% efficient 10-μm-thick crystalline silicon solar cells using periodic nanostructures. *Adv. Mater.* 27 (13): 2182–2188.

42 He, Y., Su, S., Xu, T. et al. (2011). Silicon nanowires-based highly-efficient SERS-active platform for ultrasensitive DNA detection. *Nano Today* 6 (2): 122–130.

43 Luo, L.B., Zeng, L.H., Xie, C. et al. (2014). Light trapping and surface plasmon enhanced high-performance NIR photodetector. *Sci. Rep.* 4: 3914.

44 Cao, L., Fan, P., and Brongersma, M.L. (2011). Optical coupling of deep-subwavelength semiconductor nanowires. *Nano Lett.* 11 (4): 1463–1468.

45 Picraux, S.T., Dayeh, S.A., Manandhar, P. et al. (2010). Silicon and germanium nanowires: growth, properties, and integration. *JOM* 62: 35–44.

46 Chang, S.W., Chuang, V.P., Boles, S.T. et al. (2009). Densely packed arrays of ultra-high-as pect-ratio silicon nanowires fabricated using block-copolymer lithography and metal-assisted etching. *Adv. Funct. Mater.* 19 (15): 2495–2500.

47 Magdi, S., El-Rifai, J., and Swillam, M.A. (2018). One step fabrication of silicon nanocones with wide-angle enhanced light absorption. *Sci. Rep.* 8 (1): 1–10.

48 Li, Y., Li, M., Fu, P. et al. (2015). A comparison of light-harvesting performance of silicon nanocones and nanowires for radial-junction solar cells. *Sci. Rep.* 5 (April): 1–5.

49 Yang, H.J., Yuan, F.W., and Tuan, H.Y. (2010). Vapor-liquid-solid growth of silicon nanowires using organosilane as precursor. *Chem. Commun.* 46 (33): 6105–6107.

50 Tuan, H.Y. and Korgel, B.A. (2008). Importance of solvent-mediated phenylsilane decomposition kinetics for high-yield solution-phase silicon nanowire synthesis. *Chem. Mater.* 20 (4): 1239–1241.

51 Arbiol, J., Kalache, B., Cabarrocas, P.R.I. et al. (2007). Influence of Cu as a catalyst on the properties of silicon nanowires synthesized by the vapour-solid-solid mechanism. *Nanotechnology* 18 (30).

52 Stelzner, T., Andrä, G., Wendler, E. et al. (2006). Growth of silicon nanowires by chemical vapour deposition on gold implanted silicon substrates. *Nanotechnology* 17 (12): 2895–2898.

53 Lee, D.C., Hanrath, T., and Korgel, B.A. (2005). The role of precursor-decomposition kinetics in silicon-nanowire synthesis in organic solvents. *Angew. Chem. Int. Ed.* 44 (23): 3573–3577.

54 Wu, Y., Cui, Y., Huynh, L. et al. (2004). Controlled growth and structures of molecular-scale silicon nanowires. *Nano Lett.* 4 (3): 433–436.

55 Wang, F., Dong, A., Sun, J. et al. (2006). Solution-liquid-solid growth of semiconductor nanowires. *Inorg. Chem.* 45 (19): 7511–7521.

56 Rangelow, I.W. (2003). Critical tasks in high aspect ratio silicon dry etching for microelectromechanical systems. *J. Vac. Sci. Technol. A Vacuum, Surfaces, Film.* 21 (4): 1550–1562.

57 Dimova-Malinovska, D., Sendova-Vassileva, M., Tzenov, N., and Kamenova, M. (1997). Preparation of thin porous silicon layers by stain etching. *Thin Solid Films* 297 (1–2): 9–12.

58 Alhmoud, H., Brodoceanu, D., Elnathan, R. et al. (2021). A MACEing silicon: towards single-step etching of defined porous nanostructures for biomedicine. *Prog. Mater Sci.* 116 (June 2019): 100636.

59 Smith, Z.R., Smith, R.L., and Collins, S.D. (2013). Mechanism of nanowire formation in metal assisted chemical etching. *Electrochim. Acta* 92: 139–147.

60 Chen, H., Wang, H., Zhang, X.H. et al. (2010). Wafer-scale synthesis of single-crystal zigzag silicon nanowire arrays with controlled turning angles. *Nano Lett.* 10 (3): 864–868.

61 Karadan, P., John, S., Anappara, A.A. et al. (2016). Evolution mechanism of mesoporous silicon nanopillars grown by metal-assisted chemical etching and

nanosphere lithography: correlation of Raman spectra and red photoluminescence. *Appl. Phys. A Mater. Sci. Process* 122 (7): 1–10.

62 Li, X. and Bonn, P.W. (2000). Metal-assisted chemical etching in HF/H$_2$O$_2$ produces porous silicon. *Appl. Phys. Lett.* 77 (16): 2572–2574.

63 Geng, X., Li, M., Zhao, L., and Bohn, P.W. (2011). Metal-assisted chemical etching using Tollen's reagent to deposit silver nanoparticle catalysts for fabrication of quasi-ordered silicon micro/nanostructures. *J. Electron. Mater.* 40 (12): 2480–2485.

64 Li, J.F., Zhang, Y.J., Ding, S.Y. et al. (2017). Core-shell nanoparticle-enhanced Raman spectroscopy. *Chem. Rev.* 117 (7): 5002–5069.

65 Le Ru, E.C. and Etchegoin, P.G. (2009). *Principles of Surface-Enhanced Raman Spectroscopy*. Elsevier.

66 Willets, K.A. and Van Duyne, R.P. (2007). Localized surface plasmon resonance spectroscopy and sensing. *Annu. Rev. Phys. Chem.* 58: 267–297.

67 Schlücker, S. (2014). Surface-enhanced Raman spectroscopy: concepts and chemical applications. *Angew. Chem. Int. Ed.* 53 (19): 4756–4795.

68 Sharma, B., Fernanda Cardinal, M., Kleinman, S.L. et al. (2013). High-performance SERS substrates: advances and challenges. *MRS Bull.* 38 (8): 615–624.

69 Deng, Y.L. and Juang, Y.J. (2014). Black silicon SERS substrate: effect of surface morphology on SERS detection and application of single algal cell analysis. *Biosens. Bioelectron.* 53: 37–42.

70 Khinevich, N., Bandarenka, H., Zavatski, S. et al. (2021). Porous silicon – a versatile platform for mass-production of ultrasensitive SERS-active substrates. *Microporous Mesoporous Mater.* 323 (May).

71 Siddhanta, S., Thakur, V., Narayana, C., and Shivaprasad, S.M. (2012). Substrate for biosensing. *ACS Appl. Mater. Interfaces* 4 (11): 5807–5812.

72 Chen, X., Wen, J., Zhou, J. et al. (2018). Superhydrophobic SERS substrates based on silicon hierarchical nanostructures. *J. Opt.* 20 (2).

73 Kosovic, M., Balarin, M., Ivanda, M. et al. (2015). Porous silicon covered with silver nanoparticles as surface-enhanced Raman scattering (SERS) substrate for ultra-low concentration detection. *Appl. Spectrosc.* 69 (12): 1417–1424.

74 Tsao, C.W., Zheng, Y.S., Sun, Y.S., and Cheng, Y.C. (2021). Surface-enhanced Raman scattering (SERS) spectroscopy on localized silver nanoparticle-decorated porous silicon substrate. *Analyst* 146 (24): 7645–7652.

75 Ouhibi, A., Raouafi, A., Lorrain, N. et al. (2021). Functionalized SERS substrate based on silicon nanowires for rapid detection of prostate specific antigen. *Sens. Actuators, B* 330 (December 2020): 129352.

76 Li, H., Yang, B., Yu, B. et al. (2021). Graphene-coated Si nanowires as substrates for surface-enhanced Raman scattering. *Appl. Surf. Sci.* 541 (July 2020): 148486.

77 Vo, V.T., Gwon, Y., Phung, V.D. et al. (2021). Ag-deposited porous silicon as a SERS-active substrate for the sensitive detection of catecholamine neurotransmitters. *Electron. Mater. Lett.* 17 (3): 292–298.

78 Schmidt, M.S., Hübner, J., and Boisen, A. (2012). Large area fabrication of leaning silicon nanopillars for surface enhanced Raman spectroscopy. *Adv. Mater.* 24 (10): 11–18.

79 Magno, G., Bélier, B., and Barbillon, G. (2018). Al/Si nanopillars as very sensitive SERS substrates. *Materials* 11 (9): 1–9.

80 Seol, M.L., Choi, S.J., Baek, D.J. et al. (2012). A nanoforest structure for practical surface-enhanced Raman scattering substrates. *Nanotechnology* 23 (9).

81 Kanipe, K.N., Chidester, P.P.F., Stucky, G.D., and Moskovits, M. (2016). Large format surface-enhanced Raman spectroscopy substrate optimized for enhancement and uniformity. *ACS Nano* 10 (8): 7566–7571.

82 Lin, D., Wu, Z., Li, S. et al. (2017). Large-area Au-nanoparticle-functionalized Si nanorod arrays for spatially uniform surface-enhanced Raman spectroscopy. *ACS Nano* 11 (2): 1478–1487.

83 Karadan, P., Aggarwal, S., Anappara, A.A. et al. (2018). Tailored periodic Si nanopillar based architectures as highly sensitive universal SERS biosensing platform. *Sens. Actuators, B* 254: 264–271.

84 Huang, J.A., Zhao, Y.Q., Zhang, X.J. et al. (2013). Ordered Ag/Si nanowires array: wide-range surface-enhanced Raman spectroscopy for reproducible biomolecule detection. *Nano Lett.* 13 (11): 5039–5045.

85 Xu, D., Teng, F., Wang, Z., and Lu, N. (2017). Droplet-confined electroless deposition of silver nanoparticles on ordered superhydrophobic structures for high uniform SERS measurements. *ACS Appl. Mater. Interfaces* 9 (25): 21548–21553.

86 Akin, M.S., Yilmaz, M., Babur, E. et al. (2014). Large area uniform deposition of silver nanoparticles through bio-inspired polydopamine coating on silicon nanowire arrays for practical SERS applications. *J. Mater. Chem. B* 2 (30): 4894–4900.

87 Wang, H., Han, X., Ou, X. et al. (2013). Silicon nanowire based single-molecule SERS sensor. *Nanoscale* 5 (17): 8172–8176.

88 Zhao, Y., Huang, J.A., Zhang, Z. et al. (2014). Quantitative analysis of multiplex-components and double stranded DNA by wide-range surface-enhanced Raman spectroscopy based on ordered Ag/Si nanowire arrays. *J. Mater. Chem. A* 2 (26): 10218–10224.

89 Huang, Y., Ferhan, A.R., Cho, S.J. et al. (2015). Gold nanowire bundles grown radially outward from silicon micropillars. *ACS Appl. Mater. Interfaces* 7 (32): 17582–17586.

90 Mehrvar, L., Sadeghipari, M., Tavassoli, S.H. et al. (2017). Optical and surface enhanced Raman scattering properties of Ag modified silicon double nanocone array. *Sci. Rep.* 7 (1): 1–13.

91 Jeon, H.C., Heo, C.J., Lee, S.Y., and Yang, S.M. (2012). Hierarchically ordered arrays of noncircular silicon nanowires featured by holographic lithography toward a high-fidelity sensing platform. *Adv. Funct. Mater.* 22 (20): 4268–4274.

92 He, X., Liu, Y., Xue, X. et al. (2017). Ultrasensitive detection of explosives: via hydrophobic condensation effect on biomimetic SERS platforms. *J. Mater. Chem. C* 5 (47): 12384–12392.

93 Liu, J., Meng, G., Li, Z. et al. (2015). Ag-NP@Ge-nanotaper/Si-micropillar ordered arrays as ultrasensitive and uniform surface enhanced Raman scattering substrates. *Nanoscale* 7 (43): 18218–18224.

94 Wang, Z., Zheng, C., Zhang, P. et al. (2020). A split-type structure of Ag nanoparticles and Al_2O_3@Ag@Si nanocone arrays: An ingenious strategy for SERS-based detection. *Nanoscale* 12 (7): 4359–4365.

95 Shinki, S. and J., and Sarkar, S. (2021). Tuning the topographical parameters of Si pyramids for a better surface enhanced Raman response. *Phys. Chem. Chem. Phys.* 23 (46): 26407–26416.

96 Xie, C., Lu, X.T., Tong, X.W. et al. (2019). Recent progress in solar-blind deep-ultraviolet photodetectors based on inorganic ultrawide bandgap semiconductors. *Adv. Funct. Mater.* 29 (9).

97 Tian, W., Sun, H., Chen, L. et al. (2019). Low-dimensional nanomaterial/Si heterostructure-based photodetectors. *InfoMat* 1 (2): 140–163.

98 Karadan, P., Parida, S., Kumar, A. et al. (2017). Charge transport studies on Si nanopillars for photodetectors fabricated using vapor phase metal-assisted chemical etching. *Appl. Phys. A Mater. Sci. Process* 123 (11): 1–10.

99 Li, X. (2012). Metal assisted chemical etching for high aspect ratio nanostructures: a review of characteristics and applications in photovoltaics. *Curr. Opin. Solid State Mater. Sci.* 16 (2): 71–81.

100 Xie, C., Nie, B., Zeng, L. et al. (2014). Core À shell heterojunction of silicon nanowire arrays and carbon quantum dots for photovoltaic devices and self driven photodetectors. *ACS Nano* 8 (4): 4015–4022.

101 Wu, C.Y., Pan, Z.Q., Wang, Y.Y. et al. (2016). Core-shell silicon nanowire array-Cu nanofilm Schottky junction for a sensitive self-powered near-infrared photodetector. *J. Mater. Chem. C* 4 (46): 10804–10811.

102 Fan, P., Huang, K.C.Y., Cao, L., and Brongersma, M.L. (2013). Redesigning photodetector electrodes as an optical antenna. *Nano Lett.* 13 (2): 392–396.

103 Fan, P., Chettiar, U.K., Cao, L. et al. (2012). An invisible metal-semiconductor photodetector. *Nat. Photonics* 6 (6): 380–385.

104 Kumar, A., Karadan, P., and Barshilia, H.C. (2018). Synthesis of silver nanowires towards the development the ultrasensitive AgNWs/SiNPLs hybrid photodetector and flexible transparent conductor. *Mater. Sci. Semicond. Process.* 75 (November 2017): 239–246.

105 Luongo, G., Grillo, A., Giubileo, F. et al. (2019). Graphene Schottky junction on pillar patterned silicon substrate. *Nanomaterials* 9 (5): 1–10.

106 Cao, Y., Zhu, J., Xu, J. et al. (2014). Ultra-broadband photodetector for the visible to terahertz range by self-assembling reduced graphene oxide-silicon nanowire array heterojunctions. *Small* 10 (12): 2345–2351.

107 Seol, M.L., Ahn, J.H., Choi, J.M. et al. (2012). Self-aligned nanoforest in silicon nanowire for sensitive conductance modulation. *Nano Lett.* 12 (11): 5603–5608.

108 Winkelmann, C.B., Ionica, I., Chevalier, X. et al. (2007). Optical switching of porphyrin-coated silicon nanowire field effect transistors. *Nano Lett.* 7 (6): 1454–1458.

109 Choi, S.J., Lee, Y.C., Seol, M.L. et al. (2011). Bio-inspired complementary photoconductor by porphyrin-coated silicon nanowires. *Adv. Mater.* 23 (34): 3979–3983.

110 Lefler, S., Vizel, R., Yeor, E. et al. (2018). Multicolor spectral-specific silicon nanodetectors based on molecularly embedded nanowires. *Nano Lett.* 18 (1): 190–201.

9

Hybrid 1D Semiconducting ZnO and GaN Nanostructures for Light-Emitting Devices

Vinod Kumar[1], Habtamu F. Etefa[1], Mulugeta T. Efa[2], and Leta T. Jule[1]

[1] *Dambi Dollo University, College of Natural and Computational Science, Department of Physics, Dambi Dollo, P.O. Box 260, Ethiopia*
[2] *Dambi Dollo University, College of Natural and Computational Science, Department of Chemistry, Dambi Dollo, P.O. Box 260, Ethiopia*

9.1 Introduction About 1D Nanostructures

Nanomaterials play a great attention due to their outstanding device performance in the field of photonics and electronics. These nanomaterials are usually divided into three different categories: zero-dimensional (0D), one-dimensional (1D), and two-dimensional (2D) nanostructures. Zero-dimensional nanostructures are referred as nanoparticles (NPs) and quantum dots with the aspect ratio of approximately unity. It has been comprehensively used in different kinds of applications in the field bio-medical [1, 2]. While, the 1D nanostructures, such as nanorods (NRs), nanotubes (NTs), nanowires (NWs), nanofibers (NFs), and nanobelts (NBs), have been of extreme interest in the academic research as well as in industrial applications due to their potential in the building blocks for the other kinds of structures [3]. The 1D nanostructures are constructive materials to investigate the dependence of electrical transport as well as the mechanical properties with reduction of size, which is called quantum confinement phenomena [4]. They also play a significant role for inter-connects as well as functional units in the preparation of electronic and optoelec-tronic devices [5]. The 2D nanostructures have also been broadly used as a semiconductor thin film devices and optical coating [6]. Among these three kinds of nanostructures, 1D nanostructures are one of the largely significant nanomaterials for the development of today's nanotechnology-based research and its implementa-tion in technological growth [7].

Recently, oxide semiconductors (ZnO, TiO_2, and SnO_2) have been attracting to the researcher because of the short wavelength photonic devices growing requirement and high-power with a high-frequency electronic devices. ZnO is a potential

semiconductor used as light-emitting diodes (LEDs) in UV range compared to the other oxide semiconductors. It is due to their high exciton binding energy (60 meV) and direct wide bandgap [8–14]. The UV LEDs have numerous applications, such as photoelectrochemical hydrogen generation, solid-state lighting, sensing, photopolymerization, and sterilization, and are used for the treatment of different diseases, including skin disorders as well as cancer [15, 16]. Generally, the 1D nanostructures (NTs and NWs) with high quality are excellent candidates for lasers, UV LEDs as well as other different kinds of applications (photodetectors) [17, 18]. Therefore, 1D nanostructures (ZnO) such as NRs are paying significant attention due to their good crystal quality, large surface area, increased effect quantum confinement, and unique photonic properties. So, 1D ZnO nanostructure is an optional material for UV LEDs, and it can tackle all of the aforementioned problems associated with UV LEDs. Other than this, 1D ZnO structures have excellent electrical and optical properties because of their good crystalline quality, high aspect ratio, strong quantum confinement effect, and easy synthesis process [18, 19]. In addition, a lattice-matched substrate is also not necessary for growing dislocation-free high-quality 1D nanostructure. It is noticed by the available evidence that the 1D ZnO nanostructure is a capable material for self-powered nanogenerator which converts mechanical into electric energy [20]. It can be an extremely important quality for self-powered UV LEDs. Therefore, the results of 1D-based ZnO nanostructures are in the form of more cost-effective and high-efficient LEDs. Although, lot of work has been reported in the field of ZnO thin films-based LEDs with low efficiency because of the low quality of ZnO film. The 1D ZnO nanostructures fabricated by using metal seed are also showing poor device efficiency [21–26]. It is also well known that the introduction of metal seeding provides the metal contamination, which absorbs the UV emission and results in an inefficient UV emission [27].

Thus, there is a requirement for high-quality structural and optical 1D semiconductor materials. It must be achieved with different synthesis routes, which is a favored approach for different kinds of optoelectronic UV devices including LEDs. Although, the production of highly efficient and low-cost UV LEDs, in particular, 1D nanostructure based n-ZnO/p-GaN heterostructure, is challenging due to such kind of 1D devices have not yet been commercialized.

9.2 Synthesis Methods for the Growth of 1D Nanostructure

ZnO has highest range of reported semiconductor nanostructures. The NWs, NRs, NBs, and NTs have generally four types of 1D ZnO nanostructures [28–35]. Different kinds of synthesis method have been utilized for the growth of 1D ZnO nanostructures, such as chemical vapor deposition (CVD), hydrothermal method, pulse laser deposition (PLD) technique, electrochemical deposition technique, metal–organic chemical vapor deposition (MOCVD), and magnetron sputtering method [28–38]. Some of the synthesis methods for 1D nanostructure are discussed in the following sections.

9.2.1   Hydrothermal Method for the Synthesis of 1D ZnO Nanorods

Hydrothermal method for the fabrication of 1D ZnO nanostructures is a very powerful process, which is involved in the chemical reaction of substances in solution at a particular pressure and temperature for the formulation of 1D nanostructure. This method is enabled to fabricate most materials with the essential chemical and physical properties. Hydrothermal method has many advantages compared to other conventional preparation methods, such as ease of synthesis, low-cost, low pollution, good nucleation with control manner of shape, and low temperature for the growth of nanostructure. Apart from that, the distribution of shape and size observed using hydrothermal method is homogeneous and found less aggregation. The shape and size of synthesized nanomaterials are affected by the different synthesis parameters, such as concentration of the reactant, molar ratio, temperature, and time of reaction. Park et al. reported the growth of low-temperature undoped and In-doped 1D ZnO NRs by hydrothermal method on GaN/Al$_2$O$_3$ (001) substrates [30]. The Mg-doped GaN films were developed by MOCVD technique on GaN buffer layer/c-Al$_2$O$_3$ substrates. The hole concentration and thickness of the p-GaN layer were ~7.5×10^{18} cm^{-3} and 0.36 μm, respectively. The first step is to grow the 1D ZnO NRs on p-GaN substrate of p-GaN. Spin coating technique is used for the preparation of seed layer on substrate. A solution of 0.05 M was made by dissolving zinc acetate dihydrate into 2-methoxyethanol. Spin coating technique is used for coating of this solution with 3000 rpm for 30 seconds on the substrate. Then, these seed layer-coated p-GaN substrates were immersed in an aqueous solution (mixture of 0.025 M zinc nitrate hexahydrate and equivalent molar hexamethylenetetramine) at 95 °C for four hours. Indium nitrate hydrate was also added into the aqueous solution at different concentrations (2 and 5 mol%) for In-doped ZnO sample. In electrodes were prepared onto the p-GaN films and ZnO NRs by thermal evaporation technique for the measurement of LEDs. This schematic diagram of LEDs is shown in Figure 9.1.
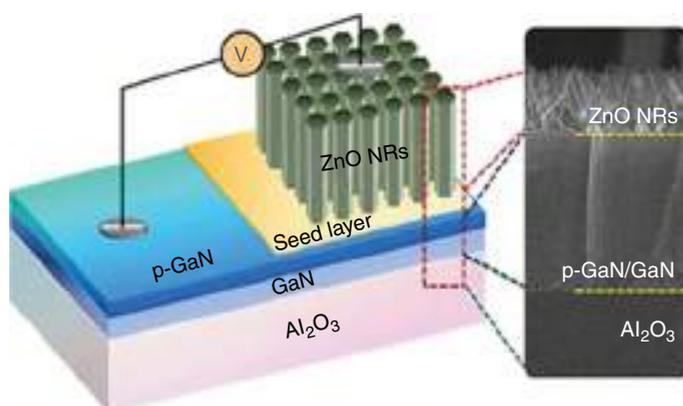
Figure 9.1   Schematic diagram of LEDs fabricated by hydrothermal method based on ZnO NRs/p-GaN/heterojunction. Source: Park et al. [30], Springer Nature, CC BY 4.0.

9.2.2 Pulsed Laser Deposition Method

Alwadai et al. [36] have also reported the fabrication of LED using vertically aligned 1D NT arrays. These devices were based on n-type Gd-doped ZnO, which were fabricated on the commercial high-quality p-type (0001) GaN substrate using PLD technique. They did not use any catalyst or pre-prepared textured layer for the growth of NTs. The p-GaN layer with the thickness of 0.5 μm was developed on c-plane (0001) sapphire by using MOCVD technique. ZnO target with 2 wt% doping is used for the growth of ZnO NTs. The krypton fluoride (KrF) excimer laser system with the wavelength of 248 nm was used for target ablation in the PLD system. The vertical distance between the substrate and target substrate was ~9 cm with 10^{-6} Torr vacuum during the deposition by PLD. The growth condition such as temperature, partial pressure, laser pulses, and fluence are set 660 °C, 150 mTorr, 30 000, and ~5 J/cm^2, respectively. The thickness of poly(methylmethacrylate) (PMMA) layer was optimized ~200 nm by adjusting the speed of spin coater 3500 rpm for 45 seconds and 180 °C bake temperature with the 60 seconds baking time. A 100 nm thick indium tin oxide film was prepared for spreading current on the NTs using radio-frequency (RF) magnetron sputtering. Finally, the contact of Ni/Au was deposited by thermal evaporation technique onto the p-GaN substrate and on tips of ZnO NTs. The schematic diagram of this kind of LEDs device fabricated by PLD is shown in Figure 9.2.

9.2.3 Chemical Vapor Deposition Method

CVD method is the one of the most usually used synthesis techniques for the synthesis of 1D nanostructure. In this synthesis method, Zn powder, ZnO powder, or another compound of Zn were used as raw materials for the fabrication of 1D ZnO. A horizontal tube furnace was usually used for the growth process. It consisted of a horizontal quartz/alumina tube, heater for tube, gas supply system, and control arrangement. The 1D ZnO nanostructures fabrications using CVD technique were usually dependent on different fabrication parameters, like distance between substrate and source, growth temperatures between source and substrate,
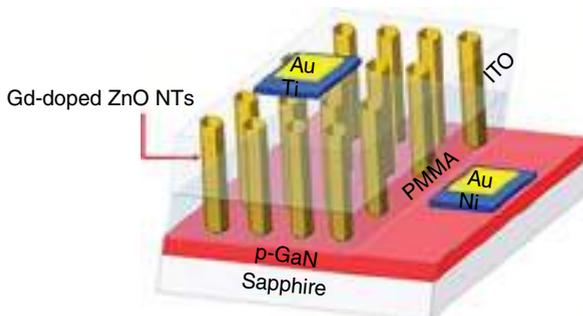
Figure 9.2 Schematic representation of LED device (Gd-doped ZnO NTs/p-GaN) prepared by PLD. Source: Alwadai et al. [36]/with permission of American Chemical Society.

diameter of the tube, heating rate, pressure, carrier gas, and growth atmosphere. Generally, the vapor–liquid–solid (VLS) route was applied for the growth of 1D ZnO nanostructure via CVD technique. The droplet of liquid was serving as a favored site for the absorption of gas-phase reactant until the droplet was saturated and after that the nucleation sites become crystallized. The droplet of the catalyst regulates the direction of the growth and controls the diameter of NWs during the growth process. The variation in the thickness of Au layer can also change the diameter of NWs. Other than this, Zn itself can also act as a catalyst under some conditions using external catalysts to fabricate the 1D ZnO nanostructures [37]. The morphology of ZnO was also varied with the influence of different catalyst thin films. The different catalysts used for the fabrication of ZnO recorded differences in size as well as in length-to-diameter ratio. Other than this, a change was noticed in the atomic composition ratio of Zn to O. Therefore, the relative intensity of defects-dependent emission in photoluminescence (PL) curve due to the oxygen vacancy was varied in different nanostructures.

9.2.4 Metal Organic Chemical Vapor Deposition

The UV LEDs based on 1D nanostructure were grown on p-GaN layers by a MOCVD technique [38]. There is not used any metal catalysts for the growth of the ZnO 1D nanostructures by MOCVD. In the first step, the p-GaN layer with the thickness of 2.5 mm was deposited on substrate (c-plane sapphire) by MOCVD technique with a nucleation layer grown at low temperature. In the next step, vertically well-aligned n-type ZnO NRs arrays were fabricated on the p-type GaN substrate by the catalyst-free MOCVD process. Diethylzinc (DEZn) and high-purity oxygen were used as staring precursors of zinc and oxygen, respectively. Substrate temperature is maintained at 260–380 °C, and chamber pressure should be ~1 Torr throughout the growth process of the ZnO nanostructure. The precursor of Zn was directly flowed into the chamber of MOCVD with the carrier gas of Ar. The flow rates of the carrier gas and precursor were monitored by a mass flow controller and electrical pressure controller, respectively. Growth temperature can be controlled by the dimensional growth of nanostructure from 1D to 2D.

9.3 Application of ZnO- and GaN-Based Hybrid 1D Nanostructure for Light-Emitting Devices

Outstanding light transmission quality makes 1D ZnO nanomaterials more attractive for utilizing highly efficient LEDs and laser devices. The UV LEDs have practical applications in UV photolithography, solid-state lighting, biomedical, and high-density data storage [39]. p–n Junction is used for the construction of the basis of LED devices. Unintentionally doped ZnO typically has shown an n-type conductivity. It was difficult to achieve a p-type conductivity in ZnO because of its deep acceptor level, low dopant solubility, and effect of self-compensation. Thus, the initial ZnO LEDs were developed by using other p-type semiconductors for the

formation of p–n heterojunctions that shown in electroluminescence (EL). In the early stages, LEDs based on ZnO were generally fabricated by thin films. After the thin film LEDs were realized, many researchers were shifted their attention into the study on 1D ZnO nanostructure-based LEDs.

Liu et al. have reported the construction of LEDs based on ZnO NRs array/p-GaN film heterojunction embedded in an Ag NPs/ PMMA composite [40]. They have established ZnO NRs-based LEDs device embedded in the Ag-NPs/PMMA composite. The UV EL data from ZnO NRs-based device was selectively improved, and the spatial distribution of EL output intensity was extended with the Ag NPs. A typical image of cross-sectional SEM of ZnO NRs/p-GaN film heterostructure is shown in Figure 9.3a. The UV emission due to ZnO exciton was observed to enhance more than 13-fold in EL spectra, which is shown in Figure 9.3b. It was also recorded that the intensity of near-UV emission was improved with increased concentration of Ag NPs in PMMA from 0 to 4C0. A blue shift was observed in the peak position from 403 to 390 nm. The whole spectral line shape is transformed slightly due to shifting. The curve could be de-convoluted in to three Gaussian peaks, which was centered at 387, 405, and 439 nm. These peaks were attributed to the excitonic emission of ZnO, interfacial radiative recombination, and emission from p-GaN-related acceptor, respectively [14, 41–43]. Later, Lu et al. have also reported that the Al NPs decorated in n-ZnO NRs/p-GaN for efficient LEDs [44]. An EL enhancement was obtained 30-fold compared to the device without Al NPS. This enhancement in EL is due to the effect of Al localized surface plasmons (LSPs). It was indicated that due to Al decoration, additional efficient recombination of the excited carriers was observed. Corresponding to the improvement of the PL spectra under the electrically driven, the efficient resonant coupling occurred between excitons of ZnO and surface plasmons (SPs) of Al NPs.

Alwadai et al. reported the fabrication vertical ZnO NTs array (without using any catalyst) on p-GaN for the application in the field of UV LED [36]. The current–voltage (I–V) characteristic of these LEDs (Gd-doped ZnO NTs/GaN) is shown in Figure 9.4a. PMMA thin layer was used to fill the free space between the individual
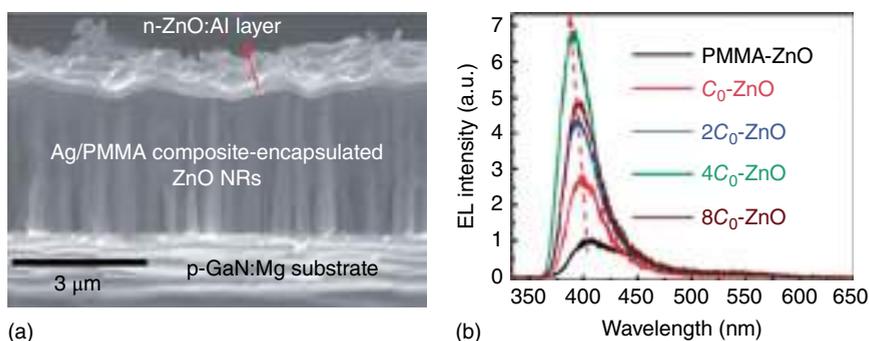
Figure 9.3 (a) The cross-sectional SEM image of ZnO NRs/p-GaN film heterostructure. (b) The EL intensity curve of ZnO/GaN based LEDs with different concentration of Ag NPs in PMMA with an injection current of 5 mA. Source: Liu et al. [40], Reproduced with permission from Royal Society of Chemistry.
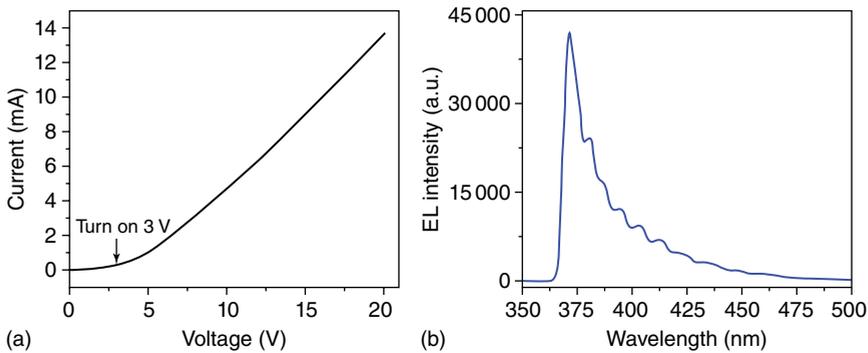
Figure 9.4 (a) Current–voltage characteristics of Gd-doped ZnO NTs/p-GaN heterojunction. (b) The room-temperature EL curve of Gd-doped ZnO NTs/p-GaN heterojunctions-based LED. Source: Alwadai et al. [36]/with permission of American Chemical Society.

NTs to extract the emission only from NTs. So, it was getting emission from the p–n junction (n-ZnO NTs/ p-GaN). The forward bias current was observed nonlinear, and it was indicating reasonable quality of the p–n junction. The device junction exhibited the diode properties with a turn-on forward bias voltage well above 3 V. A low leakage current value of 5.6×10^{-9} A was measured at the junction under the reverse bias above 10 V. It was representative of a well-fabricated junction between Gd-doped ZnO NTs and the metal electrode. The EL curve of LEDs based on Gd-doped ZnO NTs/p-GaN under forward bias current (120 mA) is represented in Figure 9.4b. The EL spectrum at RT exhibited a strong UV emission at 371 nm (without observing a defect-related emission). These results displayed that 1D NTs structures-based highly efficient LED devices can be achieved. The broad emission peak in the region of the EL spectra of device was attributed to the emission-related donor–acceptor pair, while the oscillations in the EL spectrum were recognized as the interference fringes between the reflections from the sapphire/ GaN/ZnO wetting interface. The p-GaN films have high density of acceptors, while the donors are introduced in ZnO NTs by the doping of Gd element.

Recently, researcher have more attention in graphene-based hybrid 1D ZnO/GaN LED, because graphene has shown unique properties, such as high mobility, high conductivity, low optical absorption rate, good chemical stability, and high mechanical elasticity [45–48]. In contrast to indium tin oxide electrodes and opaque metal electrodes, graphene sheets are appropriate for the applications as transparent window layer and good quality electrodes in the fields of nanoelectronics [45–50]. So, vertical junction and flexible transparent electrodes of graphene were enfold on the upper surface of 1D ZnO nanostructures, which enhanced the carrier injection area reported by different researcher. Zhang et al. reported an improvement in the near-UV EL curve of ZnO NRs array/p-GaN LEDs by the combination of graphene plasmon layer. A schematic illustration of graphene-inserted LEDs based on ZnO NR array/p-GaN heterostructure is shown in Figure 9.5a. The layer of graphene plasmon incorporated in device without changing the original heterostructure. It is indicated that the layer of graphene plasmon did not appreciably degrade
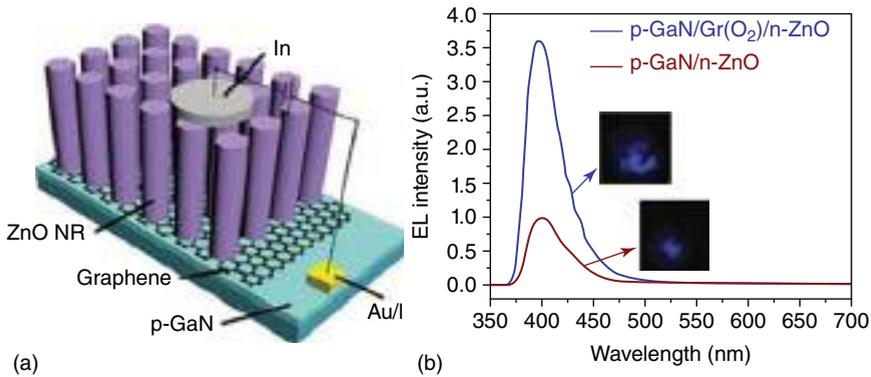
Figure 9.5 (a) Schematic diagram of graphene-decorated LED device based on ZnO NR array/p-GaN heterostructure. (b) EL characteristic curve of LEDs with and without graphene plasmon layer recorded at an applied current of 1 mA (the insets of figure shows instant EL photographs). Source: Zhang et al. [50]/Reproduced with permission from Royal Society of Chemistry.

longitudinal electrical transport. The graphene-inserted LEDs have recorded low forward injection and reverse leakage currents at a particular value of voltage, which was shown as the result from the increased series resistance. In Figure 9.5b, the main difference is that the intensity of the graphene-inserted heterostructure LED device is recorded more than ~4 times with respect to the primitive ZnO NR array/p-GaN device, which was displayed in EL results. However, there is no shifted observed in the peak position of UV emission of EL spectra.

Lin et al. also reported ZnO/p-GaN junction-based high-performance hybrid LED [51]. These graphene included LEDs were fabricated with ZnO NWs/p-GaN heterojunctions, which shows an intense emission of UV EL at 397 nm. The room-temperature EL curve of LEDs based on NWs of n-ZnO /p-GaN heterojunction is observed with different forward biases. The EL curve shows a broad peak near-UV emission peak, which was centered at ~400 nm at different values of forward bias (20–100 V). The emission band of EL curve extends unsymmetrically up to 470 nm. The analysis of EL spectrum indicated that emission band has recorded three different electron–hole recombination processes. A strong UV emission band (393 nm) was attributed to NBE emission in the ZnO NWs, while a relatively weak radiative recombination was observed at the interface of n-ZnO/p-GaN and obtained a very weak emission peak due to the p-GaN film. This work observed the physical mechanism as well as light output process of near-UV EL in the vertical graphene/ZnO NWs/p-GaN thin film heterojunction. The established nanoscale high-performance light source should be useful for the future integration technology of the optoelectronic device (Figure 9.6).
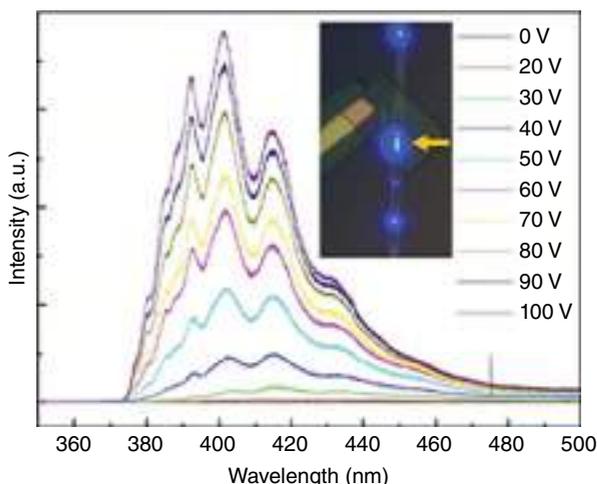
Figure 9.6 The EL curve of the graphene-incorporated n-ZnO NWs/p-GaN vertical hetrojunctions at different values of forward biases (inset of the figure shows the data collection area, which is denoted by the yellow arrow). Source: Lin et al. [51], Reproduced with permission from American Chemical Society.

9.4 Conclusion

One-dimensional (1D) nanomaterials could be appropriate for use in LEDs because of their favorable properties. This chapter is dedicated to different methods of fabrication used for the growth of 1D nanostructure and parameters of growth that control the properties of 1D nanostructure. The fabricated 1D nanostructure could be used to build novel devices with enhanced efficiency for different kinds of applications. The basic properties and applications of 1D ZnO nanostructure materials are widely explored to optimize their advantages and provide a path to meet realistic desires in nanoscience and nanotechnology. In the recent year, the applications of 1D ZnO nanostructure materials were expanded greatly. Other than this, the performance of different devices has been enhanced continuously. Novel highly efficient LEDs devices based on 1D nanostructure of ZnO and GaN nanomaterials will definitely be a significant focus of research in the twenty-first century for nanotechnology industry. At current, 1D nanostructure-based LEDs are paid much attention, and more research in interdisciplinary field has been conducted, such as biomedical applications. So, 1D nanomaterial will play an increasingly significant role in the fields of energy, biomedicine, information science technology, environmental protection, security as well as national defense. It can be recorded by the improvement of preparation technology, constant progress of device efficiency, and development of nanotechnology industrialization. It is concluded that the research on 1D ZnO and GaN nanostructure-based LEDs will yield further progress.

References

1 Liu, W., Greytak, A.B., and Lee, J. (2010). Compact biocompatible quantum dots via RAFT-mediated synthesis of imidazole based random copolymer ligand. *J. Am. Chem. Soc.* 132 (2): 472–483.

2 Hoshino, A., Fujioka, K., and Oku, T. (2004). Quantum dots targeted to the assigned organelle in living cells. *Microbiol. Immunol.* 48 (12): 985–994.

3 Weintraub, B., Zhou, Z., Li, Y., and Deng, Y. (2010). Solution synthesis of one-dimensional ZnO nanomaterials and their applications. *Nanoscale* 2 (9): 1573–1587.

4 Xia, Y., Yang, P., Sun, Y. et al. (2003). One-dimensional nanostructures: synthesis, characterization, and applications. *Adv. Mater.* 15 (5): 353–389.

5 Yi, G.C., Wang, C., and Park, W.I. (2005). ZnO nanorods: synthesis, characterization and applications. *Semicond. Sci. Technol.* 20: S22–S34.

6 Zhang, Y., Ram, M.K., Stefanakos, E.K., and Goswami, D.Y. (2012). Synthesis, characterization, and applications of ZnO nanowires. *J. Nanomater.* 624520, 22 pages, doi:https://doi.org/10.1155/2012/624520.

7 Wang, Z.L. (2009). Ten years' venturing in ZnO nanostructures: from discovery to scientific understanding and to technology applications. *Chin. Sci. Bull.* 54 (22): 4021–4034.

8 ÖzgÜr, Ü., Alivov, Y.I., Liu, C. et al. (2005). A comprehensive review of ZnO materials and devices. *J. Appl. Phys.* 98: 041301.

9 Venkatesh, S., Franklin, J., Ryan, M. et al. (2015). Defect band mediated ferromagnetism in Gd-doped ZnO thin films. *J. Appl. Phys.* 117: 013913.

10 Aravindh, S.A., Schwingenschloegl, U., and Roqan, I.S. (2014). Ferromagnetism in Gd doped ZnO nanowires: a first principles study. *J. Appl. Phys.* 116: 233906.

11 Flemban, T.H., Sequeira, M., Zhang, Z. et al. (2016). Identifying the influence of the intrinsic defects in Gd doped ZnO thin-films. *J. Appl. Phys.* 119: 065301.

12 Bantounas, I., Singaravelu, V., Roqan, I.S., and SchwingenschlÖgl, U. (2014). Structural and magnetic properties of Gd doped ZnO. *J. Mater. Chem. C* 2: 10331–10336.

13 Zhang, Z., SchwingenschlÖgl, U., and Roqan, I.S. (2014). Possible mechanism for d0 ferromagnetism mediated by intrinsic defects. *RSC Adv.* 4: 50759–50764.

14 Vinod Kumar, O.M., Ntwaeaborwa, T., Soga, V.D., and Swart, H.C. (2017). Rare earth doped zinc oxide nanophosphor powder: a future material for solid state lighting and solar cell. *ACS Photonics* 4 (11): 2613–2637.

15 Kurin, S.Y., Usikov, A.S., Papchenko, B.P. et al. (2016). The efficiency of GaN/AlGaN p-n heterostructures in UV spectral range. *J. Phys. Conf. Ser.* 741: 012107.

16 Hirayama, H., Fujikawa, S., and Kamata, N. (2015). Recent progress in AlGaN based deep UV LEDs. *Electron. Commun. Jpn.* 98: 1–8.

17 Alwadai, N., Haque, M.A., Mitra, S. et al. (2017). Roqan high performance ultraviolet to infrared broadband perovskite photodetectors achieved via inter−/intraband transitions. *ACS Appl. Mater. Interfaces* 9: 37832–37838.

18 Flemban, T.H., Haque, M.A., Ajia, I. et al. (2017). A photodetector based on p-Si/n-ZnO nanotube heterojunctions with high ultraviolet responsivity. *ACS Appl. Mater. Interfaces* 9: 37120–37127.

19 Flemban, T.H., Singaravelu, V., Devi, A.A.S., and Roqan, I.S. (2015). Homogeneous vertical ZnO nanorod arrays with high conductivity on an in situ Gd nanolayer. *RSC Adv.* 5: 94670–94678.

20 Rahman, W., Garain, S., Sultana, A. et al. (2018). Self powered piezoelectric nanogenerator based on wurtzite ZnO nanoparticles for energy harvesting application. *Mater. Today Proc.* 5: 9826–9830.

21 Jha, S., Qian, J.C., Kutsay, O. et al. (2011). Violet blue LEDs based on p-GaN/n-ZnO nanorods and their stability. *Nanotechnology* 22: 245202.

22 Sadaf, J., Israr, M., Kishwar, S. et al. (2011). Forward and reverse biased electroluminescence behavior of chemically fabricated ZnO nanotubes/GaN interface. *Semicond. Sci. Technol.* 26: 075003.

23 Zhang, L., Li, Q., Shang, L. et al. (2012). Electroluminescence from n-ZnO:Ga/p-GaN heterojunction light emitting diodes with different interfacial layers. *J. Phys. D: Appl. Phys.* 45: 485103.

24 Ren, X., Zhang, X., Liu, N. et al. (2015). White light emitting diode from Sb-doped p-ZnO nanowire arrays/n-GaN film. *Adv. Funct. Mater.* 25: 2182–2188.

25 Zhao, W., Xiong, X., Han, Y. et al. (2017). Fe-doped p-ZnO nanostructures/n-GaN heterojunction for "blue free" orange light emitting diodes. *Adv. Opt. Mater.* 5: 1700146.

26 Zhang, X., Li, L., Su, J. et al. (2014). Bandgap engineering of $Ga_xZn_{1-x}O$ nanowire arrays for wavelength-tunable light-emitting diodes. *Laser Photonics Rev.* 8: 429–435.

27 Gomez, J.L. and Tigli, O. (2013). Zinc oxide nanostructures: from growth to application. *J. Mater. Sci.* 48: 612–624.

28 Soci, C., Zhang, A., Xiang, B. et al. (2007). ZnO nanowire UV photodetectors with high internal gain. *Nano Lett.* 7: 1003–1009.

29 Fang, F., Zhao, D.X., Zhang, J.Y. et al. (2007). Growth of well aligned ZnO nanowire arrays on Si substrate. *Nanotechnology* 18: 235604.

30 Park, G.C., Hwang, S.M., Lee, S.M. et al. (2014). Hydrothermally grown in-doped ZnO nanorods on p-GaN films for color tunable heterojunction light emitting diodes. *Sci. Rep.* 5: 10410.

31 Kim, K.S., Jeong, H., Jeong, M.S., and Jung, G.Y. (2010). Polymer templated hydrothermal growth of vertically aligned single crystal ZnO nanorods and morphological transformations using structural polarity. *Adv. Funct. Mater.* 20: 3055–3063.

32 Wang, W.Z., Zeng, B.Q., Yang, J. et al. (2006). Aligned ultralong ZnO nanobelts and their enhanced field emission. *Adv. Mater.* 18: 3275–3278.

33 Yang, J., Liu, G., Lu, J. et al. (2007). Electrochemical route to the synthesis of ultrathin ZnO nanorod/nanobelt arrays on zinc substrate. *Appl. Phys. Lett.* 90: 103109.

34 Wei, A., Sun, X.W., Xu, C.X. et al. (2006). Stable field emission from hydrothermally grown ZnO nanotubes. *Appl. Phys. Lett.* 88: 213102.

35 Xing, Y.J., Xi, Z.H., Xue, Z.Q. et al. (2003). Optical properties of the ZnO nanotubes synthesized via vapor phase growth. *Appl. Phys. Lett.* 83: 1689–1691.

36 Alwadai, N., Ajia, I.A., Janjua, B. et al. (2019). Catalyst free vertical ZnO nanotube array grown on p-GaN for UV light emitting devices. *ACS Appl. Mater. Interfaces* 11: 27989–27996.

37 Ma, S. and Kitai, A.H. (2017). ZnO nanowire growth by chemical vapor deposition with spatially controlled density on Zn_2GeO_4:Mn polycrystalline substrates. *Mater. Res. Express* 4: 065012.

38 Kim, D.C., Han, W.S., Kong, B.H. et al. (2007). Fabrication of the hybrid ZnO LED structure grown on p-type GaN by metal organic chemical vapor deposition. *Physica B* 401-402: 386–390.

39 Sun, X.W., Ling, B., Zhao, J.L. et al. (2009). Ultraviolet emission from a ZnO rod homojunction light emitting diode. *Appl. Phys. Lett.* 95: 133124.

40 Liu, W.Z., Xu, H.Y., Wang, C.L. et al. (2013). Enhanced ultraviolet emission and improved spatial distribution uniformity of ZnO nanorod array light-emitting diodes via Ag nanoparticles decoration. *Nanoscale* 5: 8634–8639.

41 Dai, J., Xu, C.X., and Sun, X.W. (2011). ZnO-microrod/p-GaN heterostructured whispering gallery mode microlaser diodes. *Adv. Mater.* 23: 4115.

42 Vinod Kumar, H.C., Swart, O.M., Ntwaeaborwa, R.E. et al. (2013). Origin of the red emission in zinc oxide nanophosphors. *Mater. Lett.* 101: 57.

43 Dai, J., Ji, Y., Xu, C.X. et al. (2011). White light emission from CdTe quantum dots decorated n-ZnO nanorods/p-GaN light-emitting diodes. *Appl. Phys. Lett.* 99: 063112.

44 Lu, J., Shi, Z., Wang, Y. et al. (2016). Plasmon enhanced electrically light emitting from ZnO nanorod arrays/*p*-GaN heterostructure devices. *Sci. Rep.* 6: 25645.

45 Zhang, Y., Tan, Y.W., Stormer, H.L., and Kim, P. (2005). Experimental observation of the quantum hall effect and berry's phase in graphene. *Nature* 438: 201.

46 Choi, D., Choi, M.Y., Choi, W.M. et al. (2010). Fully rollable transparent nanogenerators based on graphene electrodes. *Adv. Mater.* 22: 2187–2192.

47 Nair, R.R., Blake, P., Grigorenko, A.N. et al. (2008). Fine structure constant defines visual transparency of graphene. *Science* 320: 1308.

48 Lee, C., Wei, X., Kysar, J.W., and Hone, J. (2008). Measurement of the elastic properties and intrinsic strength of monolayer graphene. *Science* 321: 385–388.

49 Pang, S., Hernandez, Y., Feng, X., and MÜllen, K. (2011). Graphene as transparent electrode material for organic electronics. *Adv. Mater.* 23: 2779–2795.

50 Zhang, C., Qiu, Y., Liu, W. et al. (2019). Improved near-UV electroluminescence of ZnO nanorod array LEDs by coupling with a graphene plasmon layer. *Nanophotonics* 8 (12): 2203–2213.

51 Lin, F., Liao, X., Liu, C.P. et al. (2020). Graphene/ZnO nanowire/p-GaN vertical junction for a high performance nanoscale light source, ACS. *Omega* 5: 4133–4138.

10

Optoelectronic Properties of TiO$_2$ Nanorods/Au Nanoparticles Heterostructure

Dhyey Raval[1], Abhijit Ray[1], and Brijesh Tripathi[2]

[1] *Pandit Deendayal Energy University, School of Technology, Department of Solar Energy, Raisan, Gandhinagar, 382426, India*
[2] *Pandit Deendayal Energy University, School of Technology, Department of Physics, Gandhinagar, 382426, India*

10.1 Introduction

The optoelectronic properties of hydrothermally synthesized titanium dioxide nanorods (TiO$_2$NRs) with the gold nanoparticles (AuNPs) as a heterostructure on the transparent substrate are attracting wide attention. The heterostructure studied here consists of titanium dioxide (TiO$_2$) semiconductor layer with noble metal (gold) nanostructures [1–3] to increase light incident radiation in the visible wavelength and enhance the charge separation and conversion capabilities for photoelectrocatalysis micro-optical devices [4]. In comparison with the single-phase TiO$_2$ photocatalyst, these unique heterostructures integrate diverse electrical characteristics of the component materials and increase photocatalytic efficiency [5–7]. In comparison with the TiO$_2$NP-based mesoporous layer, the TiO$_2$NR had improved charge transport capabilities [8]. On the surface of TiO$_2$NR, noble metal NPs can boost photocatalytic capabilities through following manner: (i) the noble metal NPs coated over the semiconductor layer improves quantum yield by enhancing electron–hole separation [7, 9, 10]; (ii) the surface plasmon resonance (SPR) effect, which is caused by collective oscillations of the electrons on the AuNPs in coherence when exposed to visible light. These effects can increase the localized electric field around AuNPs, which aids in the interaction of the localized electrical field with TiO$_2$NR which facilitates the formation of electron hole (e$^-$–h$^+$) pair in the near surface area of the TiO$_2$NR/AuNP interfaces [11–14]. AuNP and other metal nanostructures have recently been explored for their potential application in micro-optical [15–17] and photocatalytic devices, and the localized surface plasmon resonance (LSPR) effects of AuNP and photocatalytic devices due to the localized SPR

effects to increase photoelectrochemical characteristics [4, 18, 19]. Multicenter flat fiber-shaped SPR device is validated by Rifat et al. [20], indicates an opportunity for real-time diagnosis as a lab-on-a-chip. Awazu and Linic have used the plasmon-improved photocatalytic mechanism through Ag-NP used with SiO_2 and polyvinylpyrrolidone (PVP) as a shell [11, 12]. Liu et al. [21] proposed a powerful method as plasmon-attached photocatalyst for the splitting of molecules of water in the presence of light irradiation with doped TiO_2-NT/AuNP systems. The literature suggests that the plasmon resonance wavelength and intensity strongly rely upon the dimensions and shape of NPs, dielectric property of the encompassing medium, and interparticle spacing [22–26]. Hydrothermally grown 1D TiO_2NR with a thin layer of TiO_2 as surface passivation layer was used to prepare a perovskite-based solar cell with an efficiency of 13.45% [27].

In current literature, noble metal nanoparticles, such as Pt [28, 29], Pd [30, 31], Ag [32, 33], and Au [34, 35], reveal better catalytic efficiency for the electro-oxidation and are the usual catalysts [36]. To improve its efficiency along with stability for such noble metal nanoparticles, a specific surface structure scheme is explored [31, 37, 38]. Also, different alloying structure are used for better applicability [39–42]. Further, a photoelectrocatalyst has been studied because of its better localized SPR characteristics and can enhance the catalytic efficiency of noble metal nanoparticles [43]. The recombination of photons-generated hot electron and hole decreases the phenomenon of localized SPR [44, 45]. This recombination phenomenon is decreased by attaching semiconductor to the noble metal nanoparticle which provides a pathway to the generated hot electrons in the conduction band (CB) defined as plasmonic-induced charge separation [46, 47] beneficial for catalytic activity [46, 48, 49]. A light radiation improves the catalytic activity in a nanostructure having noble metal particles to improve the incoming photon to energy conversion ways [50]. Titania nanorods (TiO_2NRs) with a vertical align structures are more useful for plasmon-induced photocatalytic conversion to its 1D facile charge conversion [51]. Few reports found for describing the phenomenon of metal nanostructure which improves plasmon resonance energy and to boost the photocatalysis efficiency of the semiconductors family [52, 53].

In this chapter, a method to develop TiO_2 nanorods using hydrothermal process route is explained and corresponding structural, morphological, and optoelectronic properties are discussed, and its reports are not found in the previous literature [5, 10, 13, 20]. Further, this chapter describes the hydrothermally synthesized TiO_2NR and effect of AuNPs on their surface. Deposited layer were characterized by field emission scanning electron microscopy (FESEM), X-ray diffraction (XRD), and optical (UV–vis) and amperometric (current–time) measurements. It is seen that the AuNP enhances photocatalytic performance of TiO_2NR, which is studied by a quantum mechanical approach. A theoretical estimation is carried out to quantify the results of electrical measurements of the AuNP on TiO_2NR.

10.2 Theory of Electron Transfer

10.2.1 Description of Band Diagram

Figure 10.1 describes the localized SPR under visible light irradiation. The charge carriers are transferred to the CB of TiO$_2$ from the gold NP at Au/TiO$_2$ interface. It is realized that the AuNP mostly appears as a sensitizer and absorbs incident photons due to the process of the localized SPR excitation which generates the highly strenuous hot electrons. These hot electrons gets added into the CB of the attached TiO$_2$NR [55]. It is observed that under illumination, the AuNP exhibits the optically induced oscillating electrostatic potential with the wavelength of incident light [56]. This excess electron density in the CB of TiO$_2$NR acts as photoreceptor of the TiO$_2$NR/AuNP system [57]. The probability of transmission of converted hot electrons in AuNPs through the potential barrier of TiO$_2$NR can be calculated using Eqs. (10.1)–(10.6) [58] under following assumptions: (i) a junction is existing between AuNP and TiO$_2$NR interface and serves as a barrier for charge transport, and (ii) the Fermi level of AuNP and TiO$_2$NR stays aligned when photon interacts with potential barrier:

$$\frac{\partial^2 \Psi_1(x)}{\partial x^2} + k_1^2 \Psi_1(x) = 0, \ x < 0 \text{ marked as region 1 (AuNP)} \tag{10.1}$$

$$\frac{\partial^2 \Psi_2(x)}{\partial x^2} + k_2^2 \Psi_2(x) = 0, \ x > 0 \text{ marked as region 2 (TiO}_2\text{NR)} \tag{10.2}$$
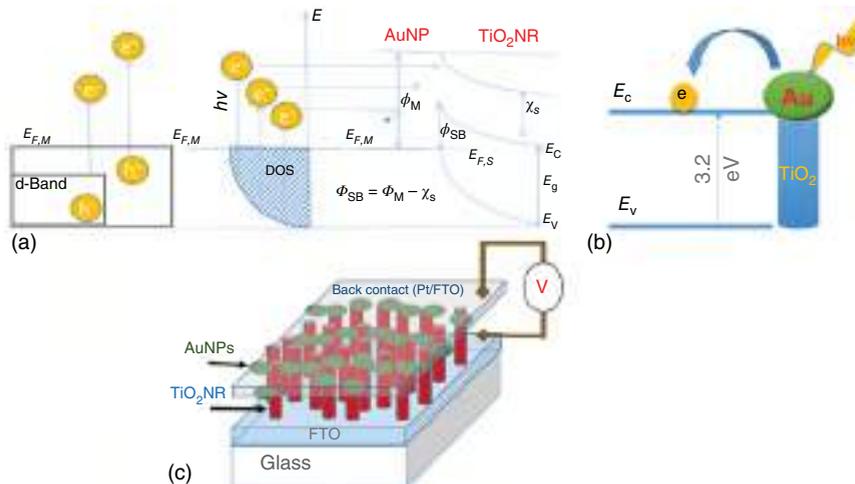
Figure 10.1 (a) Band diagram of TiO$_2$NR/AuNP, (b) schematic electron transfer of TiO$_2$NR/AuNP, and (c) device configuration of TiO$_2$NR/AuNP. Source: Raval et al. [54]/with permission of Springer Nature.

here,

$$k_1^2 = \frac{2mE_0}{\hbar^2}, \, k_2^2 = \frac{2m(E_0 - V)}{\hbar^2}, \, m = 9.1 \times 10^{-31} \, \text{kg}, \, \hbar = \frac{h}{2\pi} = 1.054 \times 10^{-34} \, \text{Js}$$

The wave functions of electron in Eqs. (10.1) and (10.2) on the AuNP and TiO₂-NR side, respectively, is given as follows:

$$\psi_1 = Ae^{-jk_1 x} + Be^{jk_1 x} \tag{10.3}$$

$$\psi_2 = Ce^{-jk_2 x} \tag{10.4}$$

Subjected to the boundary conditions given below:

1. A wave function was continuous at interface, i.e. $\Psi_1(0) = \Psi_2(0)$, and denotes $A + B = C$ from Eq. (10.3).

2. A first derivate of wave function was continuous, i.e. $\frac{\partial}{\partial x}\Psi_1(0) = \frac{\partial}{\partial x}\Psi_2(0)$, and denotes that $A - B = \frac{k_2}{k_1}C$ from Eq. (10.4).

The transmission (T) and reflection (R) probability of the electrons from the AuNP side to TiO₂NR side can be estimated from the following equations:

$$T = \left|\frac{B}{A}\right|^2 = \left|\frac{k_1 - k_2}{k_1 + k_2}\right|^2 \tag{10.5}$$

$$R = \left|\frac{C}{A}\right|\frac{k_2}{k_1} = \frac{4k_1 k_2}{\left|k_1 + k_2\right|^2} \tag{10.6}$$

10.2.2 Extinction Estimation

The particle diameter should be less than the incident light wavelength. The scattering cross section (C_{scat}) and the absorption cross section (C_{abs}) are expressed as [59]:

$$C_{scat} = \frac{1}{6\pi}\left(\frac{2\pi}{\lambda}\right)^4 |\alpha|^2 \tag{10.7}$$

$$C_{abs} = \frac{2\pi}{\lambda} Im[\alpha] \tag{10.8}$$

where $\alpha = 3V\left[\dfrac{\varepsilon_p / \varepsilon_m - 1}{\varepsilon_p / \varepsilon_m + 2}\right]$ shows nanoparticle's polarizability. Where V shows volume of nanoparticle (function of particle radius), ε_p shows the dielectric function of the nanoparticle, and ε_m shows the dielectric function for the medium in which the particle is embedded/attached. These expressions describe that the C_{scat} is governed

by NP size which converts greater amount of light and scatters in a high refractive index medium. As shown in Figure 10.4, it is seen that the absorption of the AuNP attached TiO_2NR layer is high when compared to the TiO_2NR without AuNP. Conversely, with increase in the size of AuNP beyond threshold, phase retardation starts to direct its behavior [60]. An upper order multi-pole excitation mode (octupole and quadrupole) gives decrease in the efficiency of the scattering process [61]. The size of AuNP might be tuned by controlling the gold film thickness during the process of deposition by varying temperature. The efficiency of extinction ($Q_{ext} = C_{scat}/S + C_{abs}/S$, where S acts as nanoparticle's area of scattering) of AuNP is reported using Mie theory [62]. The extinction efficiency changes with the size of AuNP, which is already given in the literatures [63, 64]. The bigger particle size leads to Mie scattering. Q_{sca} indicates radiative loss and Q_{abs} indicates non-radiative loss. Through the radiative and a non-radiative phenomenon, the incident radiation observed the losses from the surface layers of the samples. These losses are included in Q_{ext} for nanoparticles which are much smaller than the wavelength of incident light [59].

10.3 Experimental

10.3.1 TiO$_2$ Nanorods

Stainless steel autoclave with teflon liner having 50 ml capability is used for the preparation of TiO_2 nanorods using hydrothermal process. Thirty-seven percent of hydrochloric acid and deionized water in a quantity of 15 ml each was mixed and sonicated for five minutes in a typical step of synthesis. Nanorods of TiO_2 have been grown on the glass substrate coated with FTO (Sigma-Aldrich, 7 Ω/sq.). Consequently, 0.4 ml of titanium (IV) isopropoxide ($Ti(OCH(CH_3)_2)_4$, 97%, Sigma-Aldrich) was mixed and then sonicated for five minutes. Usually, two pieces of glass substrates as FTO with the size of 1.5×1.5 cm^2 are kept in the Teflon (melting point: 326.8 °C) liner having active layer facing its wall, and then precursor solution is poured in autoclave containing the conducting glass substrates. Temperature is changed in the interval of 200–280 °C and reaction time period is fixed to 2 hours. Nanorods are not obtained after 280 °C. The autoclave is left to cool to its room temperature after the completion of the process. Thereafter, coated samples are taken out from the hydrothermal autoclave and rinsed followed by annealing in air at a temperature of 300 °C before use.

At a time duration of 2 hours and a fix temperature of 230 °C, TiO_2NRs are prepared with change in concentration ($Ti(OCH(CH_3)_2)_4$ precursor from the range of 0.4 to 1.0 ml in the 30-ml dilute HCl (prepared in the previous step). In the experimental procedure, with the increase in the concentration of titanium isopropoxide precursor solution, the nanorod diameter increases and the inter-rod separation decreases with increase in layer thickness. A gold target (99.9%) (2 in. diameter and 3 mm thick) is fixed in the pulsed DC magnetron (10 kHz, with duty cycle: 50%) sputtering system (Millman, India). For preparing gold layer, argon gas was allowed

to enter to the vacuum chamber with the constant flow rate of 50 sccm. The working pressure was maintained at 8×10^{-2} mbar during deposition process. A voltage applied is 350 V during sputtering of Au and current measured is ~40 mA in 1 minute of time interval. Also, temperature was close to 450 °C during this process. Film was prepared during the process, and the samples were annealed for 1 hour in a vacuum chamber. The samples were cooled down naturally in vacuum chamber and then after removed at room-temperature conditions [51].

10.3.2 Structural, Morphological, Elemental, and Optical Measurement

The layer thickness was measured using stylus-based surface profilometer (Dektak 150, Veeco). The structural, morphological, elemental, and optical characterization of TiO₂NR were done by XRD (X'Pert Pro, PANalytical), FESEM (ULTRA55, Zeiss), energy-dispersive spectrometer (Model: X-Max, Make: OXFORD), and UV–visible diffuse reflectance spectroscopy (UV 2600, Shimadzu), respectively.

10.3.3 Amperometric Measurement

A calibrated light-emitting diode source with an intensity of 20 mW/cm² has been used for photocurrent measurement. In order to control ON–OFF mechanism, an optical chopper was kept between the light source and the photoelectrode. From the output signal, photocurrent density was determined by attaching a test cell to the potentiostat (CHI-660D) without any applied voltage. 0.5 M KOH electrolyte solution was used in the test cell consisting of a working electrode (made of TiO₂NR with and without AuNP) and a platinized FTO counter electrode for the amperometric measurements.

10.4 Results and Discussion

10.4.1 Morphology

The TiO₂NR and AuNP morphology has been examined by FESEM, and related observations are shown in Figure 10.2a–c. FESEM observations of AuNP with TiO₂NR are given in Figure 10.2b. Porous morphology was observed in TiO₂NR layer, and its pores are 100s of nanometers wide as seen in the top view through FESEM in Figure 10.2a. The range of diameter of TiO₂NR is around 80 ± 5 nm as per Figure 10.2a. AuNP deposited over TiO₂NR is shown in Figure 10.2b with an observed size of 15 ± 10 nm size. The size distribution of diameter for AuNP is described in the insert of Figure 10.2b for AuNP over TiO₂NR heterostructure. Figure 10.2C shows the cross section of TiO₂NR with AuNP layer. FTO layer thickness is found to be 293 ± 10 nm. The TiO₂ seed layer thickness is observed as 700 ± 10 nm. TiO₂NR layer thickness is found to be 2241 ± 10 nm as shown in Figure 10.2c. A comprehensive profile elemental measurement was observed from
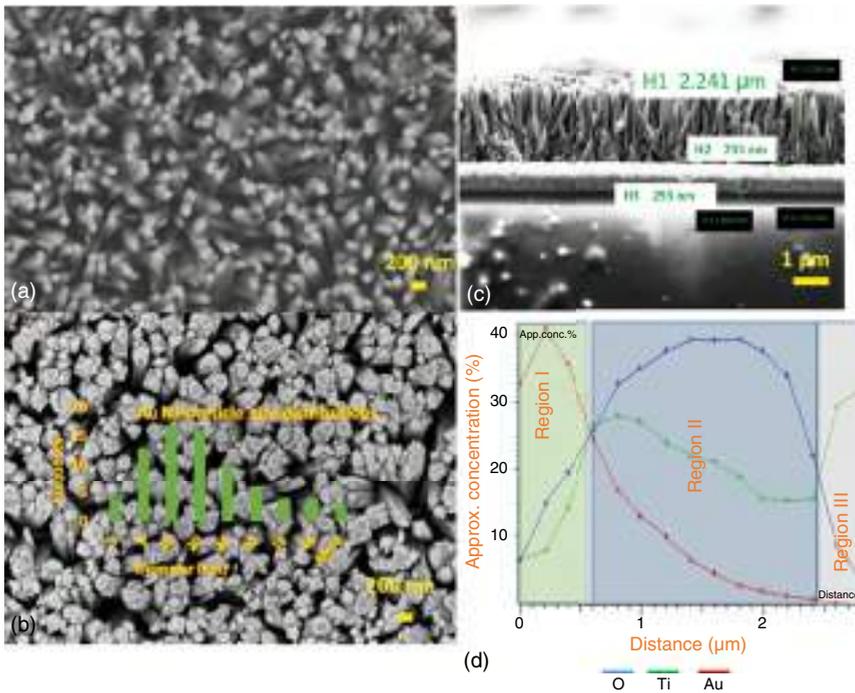
Figure 10.2 (a) FESEM of TiO$_2$NR, (b) FESEM of TiO$_2$NR/AuNP, (c) cross section FESEM of TiO$_2$NR/AuNP, and (d) cross section EDS of TiO$_2$NR/AuNP. Source: Raval et al. [54], Reproduced with permission from Springer Nature.

cross-sectional view of EDS for AuNP/TiO$_2$NR as shown in Figure 10.2d. In Figure 10.2d, the top red curve in region I describes a higher percentage of gold than TiO$_2$ which confirms that the AuNP is on the top of NR. Top blue curve in region II of Figure 10.2d describes approximate concentration (in %) of oxygen with respect to the cross-sectional thickness (distance), the middle green curve in region II describes approximate concentration (%) of titanium, and the bottom red curve in region II describes approximate concentration (%) of gold. Region II shows a higher percentage of TiO$_2$ with respect to gold in its thickness range. Decreasing trend of Au percentage in region II confirms that there is no physical connection of Au with FTO substrate. Region III describes the titanium abundant layer that acts as seed layer.

As shown in Figure 10.2, the nanorods are homogeneously located on the FTO substrate as seen in FESEM pictures. With variation in the temperature range of 170–280 °C, the nanorod dimensions are changed during the autoclaving process. As observed during the process, the length and width are majorly influenced by the temperature for a set time of 2 hours. TiO$_2$ nanorods dimension was estimated to be 0.09–2.1 μm long and 80–200 nm wide for set temperature range and process time. The vertically aligned nanorods and homogeneous nanorods form at relatively higher reaction temperature as compared with reduced degree of order and alignment seen at lower reaction temperature. In a same manner, vertically aligned and

homogeneous nanorods have been seen at higher precursor concentration compared with reduced degree of order and alignment observed at lower reaction temperature as shown in Figure 10.2. The cross-sectional view of TiO$_2$NR in Figure 10.2 confirms the given thickness. The average roughness is measured from the profilometry recorder, and it is observed to vary in the range of 12–519 nm with nanorod diameter in the range of 70–204 nm. Here, it is essential to note that the samples of nanorod utilized for the FESEM characterization and fabrication of device are from the same synthesis batch but deposited on separate substrates; thus, they have minor variation in the length of the nanorod as shown in Figure 10.2. From the experimental process and data, the surface area of nanorod layer does not linearly change with the length because of instantaneous increase in the length and diameter.

10.4.2 Structural

XRD pattern for the hydrothermally grown TiO$_2$ nanorods on FTO glass substrates and TiO$_2$NR/AuNP is given in Figure 10.3. These diffraction peaks are majorly rutile phase of TiO$_2$ as per JCPDS 21-1276. A randomly oriented crystal structure for rutile phase of TiO$_2$ has been observed with a higher (110) diffraction peak as shown in
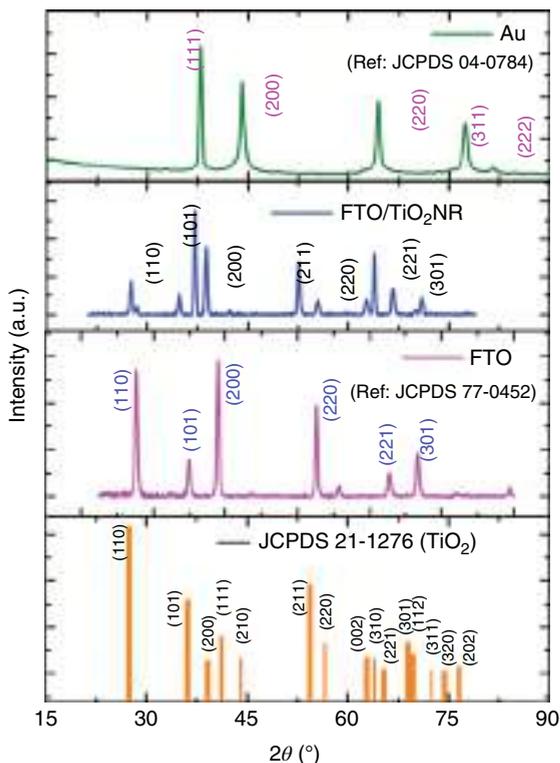
Figure 10.3 X-ray diffraction pattern for TiO$_2$NR and TiO$_2$NR/AuNP. Source: Raval et al. [54]/with permission of Springer Nature.

Figure 10.3 (JCPDS), which matches with described data for the rod-like rutile TiO_2 structure [65]. In the reported data as shown in Figure 10.3, the (101) diffraction peak is highest; on the other side, the (110) peak intensity is comparatively less and (002) peak is comparatively high according to the randomly oriented powder sample as observed by other investigators [8]. For the nanorod layer, an intense (101) peak along with the improved (002) peak are observed which describe the growth of rutile crystal along (101) plane as parallel to the FTO layer and NR are oriented along the (002) plane [8, 66, 67].

Figure 10.3 shows peak intensity related to the (220), (200), and (111) planes of FCC structure of Au, and it is in agreement with the reported data for AuNP (JCPDS 04-0784) [68]. The favored orientation in XRD diagram indicates nano-morphology as observed from FESEM in Figure 10.2. The presence of NP confirmed from the peak intensity (111) plane was higher than the other peaks.

10.4.3 Optical

The UV–vis spectroscopic recorded data are shown in Figure 10.4. The incident energy ($h\nu$) and absorption coefficient (α) relationship are given as [69]:

$$(\alpha h\nu)^p \propto (h\nu - E_g) \tag{10.9}$$

where h signifies Planck's constant, ν signifies the frequency of incident light, the exponent p depends on the type of the transition, and E_g is the bandgap of the material. The p numerical data are given as 2, 1/2, 3, and 3/2 corresponding to the allowed direct, indirect, forbidden direct, and forbidden indirect transition, respectively. The p is taken as 2 due to allowed direct transition in TiO_2 [70].

The absorption coefficient (α) can be estimated using the relation [71]:

$$\alpha = (1/d)\ln(1/T) \tag{10.10}$$

where T and d signify percentage transmission and thickness layer, respectively, and the nanorod distribution over the surface of substrate changes with variation in absorption coefficient (α). The maximum bandgap (E_g) is observed for the sample processed at 230 °C with a precursor amount of 0.6 ml, which is attributed to the improved crystallization in XRD pattern of Figure 10.3. The sample prepared at 200 °C having precursor value of 0.4 ml which is recognized to low crystallization in XRD pattern of Figure 10.3 and nonuniform growth of the nanorod layer in SEM image of Figure 10.2 confirms the minimum bandgap in Figure 10.4. The absorbance spectrum is plotted with wavelength of light for TiO_2NR layer and compared with $TiO_2NR/AuNP$ layer. It is observed that the $TiO_2NR/AuNP$ layer has high absorbance for wavelengths greater than 400 nm compared to TiO_2NR layer. There are generally four ways in a plasmonic photocatalytic system for energy transfer [72] as follows: (i) hot electron transfer, (ii) resonance photon scattering, (iii) electromagnetic augmentation through near-field, and (iv) plasmon-induced heating . The energy associated with plasmonic heating is lower compared to the E_g of TiO_2NR; therefore, this mechanism is not considered for increased charge density in the CB
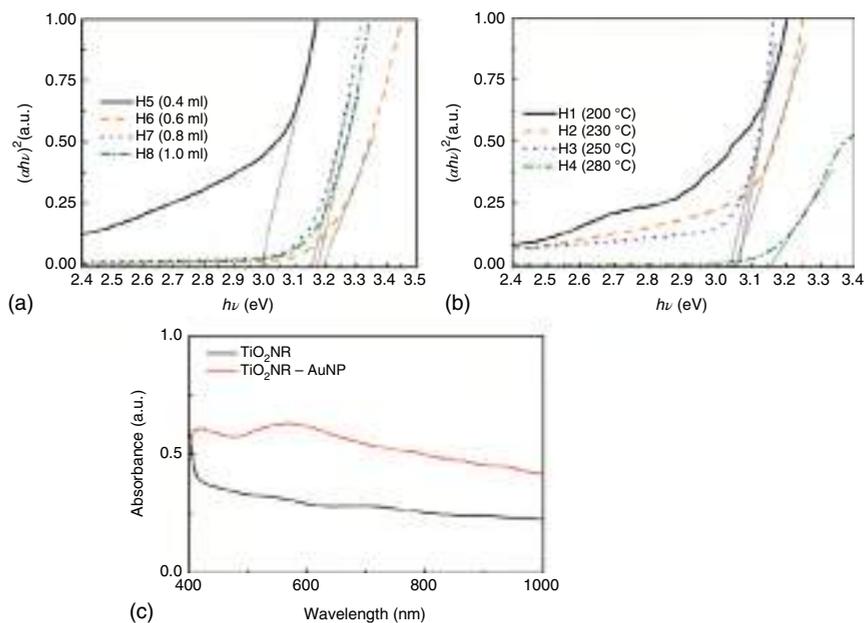
Figure 10.4 (a) Tauc plot for TiO$_2$NR with concentration variation, (b) Tauc plot for TiO$_2$NR with variation in temperature, and (c) absorbance spectra for TiO$_2$NR and TiO$_2$NR/AuNP. Source: Raval et al. [51, 54]/with permission of Springer Nature.

of TiO$_2$NR [21]. The mechanism of photon scattering resonance is not considered as a governing mechanism in case of the AuNP/TiO$_2$NR, because it is applicable for larger plasmonic NP (diameter larger than ∼50 nm) [73, 74]. Further, near-field-based electromagnetic increment is commonly seen for the overlap of semiconductor absorption with plasmon resonance wavelengths; hence, this mechanism is not considered for charge transfer [75]. Therefore, the dominant way of charge transfer is attributed to hot electron-induced absorption increment. So hot electron transfer is a major contributor to increased charge carrier density in the CB of TiO$_2$ in the visible light radiation. This effect improves the performance of the Au/TiO$_2$NR devices. In this case, incident photon energy greater than 0.9 eV is responsible for the generation of hot electrons. The non-homogeneity of AuNP size is responsible for broad absorption spectra in the visible and near-infrared region [47]. Decrease in the absorbance due to lower exposed surface of the TiO$_2$NR in ultraviolet region is covered by AuNP as shown in Figure 10.4.

10.4.4 Electrical

10.4.4.1 Electron Transfer Mechanism from AuNP to TiO₂NR

Electron transfer from AuNP to TiO$_2$NR encounters a potential barrier from CB of TiO$_2$NR at the interface of AuNP/TiO$_2$NR. Potential barrier from CB of TiO$_2$NR at the interface of AuNP/TiO$_2$NR has been described in Figure 10.1a. The height of potential barrier (V) is estimated from AuNP work function (ϕ, varied in the range

of 3.6–5.1 eV [76]), and the TiO$_2$ electron affinity is 4.5 eV [77]. A plasmonic oscillation was accountable for an increased free electron energy of AuNP due to the function of wavelength for incident radiation. Ground-state energy of electron (E_0) is estimated in range of 1.24–3.1 eV for the wavelengths of 400–1000 nm respectively. Transmission probability of electron compared to AuNP size and respective work function are shown in Figure 10.5b. When the diameter of AuNPs increases, then the ϕ increases linearly in agreement with $\phi(eV) = 0.030 \times (nm) + 3.37$ which matches closely to the literature [76]. Figure 10.5b describes transmission probability compared to the wavelength of the light assuming overall transfer of photon energy to electrons in the AuNP. Figure 10.5(b) states that transmission probability of electron increases till 35 nm diameter of AuNP and thereafter starts decreasing due to increase in the barrier height [54]. By further increasing wavelength, the energy related to photons decreases thus decreasing the energy of its electrons in AuNP and decreases its transmission probability.
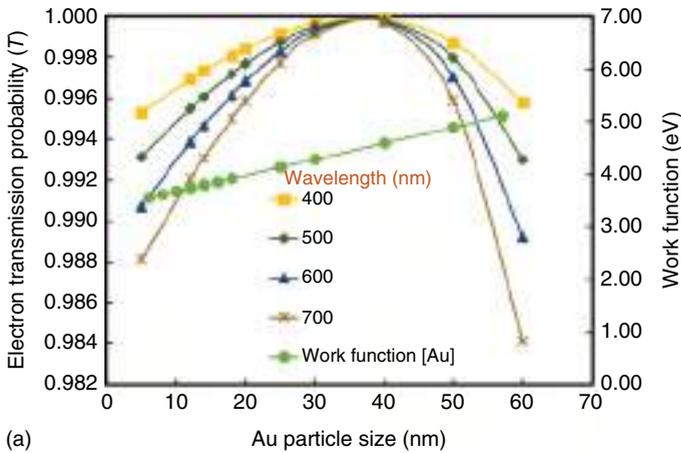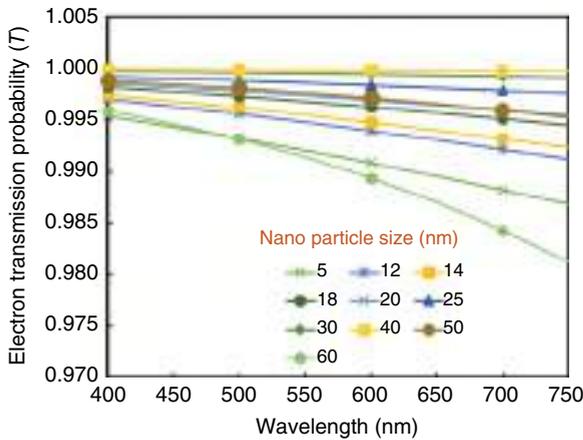
Figure 10.5 Quantum mechanical analysis for (a) TiO$_2$NR and (b) TiO$_2$NR/AuNP interface. Source: Raval et al. [54]/with permission of Springer Nature.

10.4.4.2 Amperometric (Current–Time)

As described in Figure 10.6, an amperometric current–time (*I*–*t*) data curves were plotted for a constant potential of 0 V, and light is turned OFF and turned ON for every single interval of 30 seconds. It is observed that the photocurrent decays in dark and grows due to illumination have been recorded with constant intensity of light during the experimental measurement is 20 mW/cm². Photocurrent starts to grow with dark value and when light is switched ON beyond 30th second, it remains ON till it reaches 60th second. At the highest current value reached, the light is switched OFF (60th second) and the photocurrent starts to fall freely to reach its initial dark current value. To explore the correlations with localized SPR light absorption in TiO₂NR/AuNP system and respective increase photocurrent density, a quantum mechanical approach confirms theoretical analysis and experimental measurements. Evidently, the TiO₂NR/AuNP system revealed clear photocurrent improvement compared to the TiO₂NR without AuNP in the visible range of wavelengths from 400 to 700 nm as described in Figure 10.6. In visible wavelength illumination, a catalytic activity of TiO₂NR is enhanced with AuNP due to plasmon-induced charge separation, and this indicates higher current compared to without AuNP sample. A higher photocurrent density of AuNP/TiO₂NR of ~150 μA/cm² is obtained under prevailing condition, and overall it is 50 times higher compared to TiO₂NR without AuNP which has small photocurrent density of <3 μAcm. The considerable enhanced photocurrent density on the AuNP/TiO₂NR compared to TiO₂NR is described as enhanced electron density in the CB of TiO₂NR due to boost in the catalytic behavior under visible light illumination. This improved photocurrent density possibly attributes to thermodynamic free energy minima of system due to an electrostatic surface potential on a resonating AuNP which is driven by absorption increment as shown in Figure 10.4 and its electrons injection (Figure 10.1) [56]. Higher absorbance does not lead to increase in photocatalytic
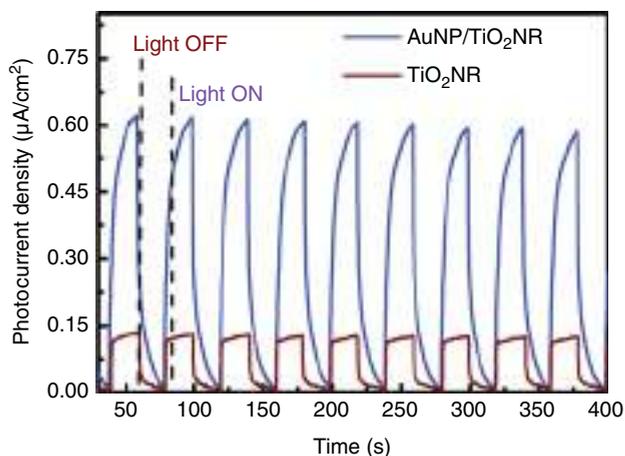
Figure 10.6 Amperometric (current–time) analysis for TiO₂NR and TiO₂NR/AuNP. Source: Raval et al. [54]/with permission of Springer Nature.

efficiency. Kowalska et al. reported a correlation between the quantum efficiency and absorption spectrum of the Au/TiO_2 layers [78, 79]. According to available literature, a convincing report proves that the plasmonic enhancement is coincidence to the absorption peak of localized SPR [80]. The Mie scattering is less compared to the absorption in noble metal nanoparticles <60 nm [47, 81].

10.5 Conclusions

In the present chapter, vertically aligned TiO_2NR with AuNP heterostructure have been grown on FTO substrate using hydrothermal and sputtering process for their optoelectronic application. Localized SPR and electron transfer activity of AuNP attached to TiO_2NR are explored for their optoelectronic device application. TiO_2NR with AuNP revealed a substantial photocurrent improvement compared to TiO_2NR without AuNP. A higher photocurrent in amperometric measurement has been described through the theory of excess electron density in the CB of TiO_2NR because of hot electron transfer from AuNP. The heterostructures grown on the transparent substrates have been used to explain the suitability of $TiO_2NR/AuNP$ for useful optoelectronic applications. A higher photocurrent density of the $\sim150\,\mu A/cm^2$ in the $AuNP/TiO_2NR$ heterostructure is achieved under prevailing conditions, and overall it is 50 times higher compared to TiO_2NR without AuNP, which has small photocurrent density of $<3\,\mu A/cm^2$.

Acknowledgments

Compliance with Ethical Standards

The authors declare that they have no conflict of interest.

References

1 Liu, G., Wang, L., Yang, H.G. et al. (2010). Titania-based photocatalysts-crystal growth, doping and heterostructuring. *J. Mater. Chem.* 20 (5): 831–843.

2 Chen, X. and Mao, S.S. (2007). Titanium dioxide nanomaterials: synthesis, properties, modifications, and applications. *Chem. Rev.* 107 (7): 2891–2959.

3 Wang, H., Bai, Y., Zhang, H. et al. (2010). CdS quantum dots-sensitized TiO$_2$ nanorod array on transparent conductive glass photoelectrodes. *J. Phys. Chem. C* 114 (39): 16451–16455.

4 Lee, C.-H., Liao, S.-C., Lin, T.-R. et al. (2016). Boosted photocatalytic efficiency through plasmonic field confinement with bowtie and diabolo nanostructures under LED irradiation. *Opt. Express* 24 (16): 17541–17552.

5 Tada, H., Mitsui, T., Kiyonaga, T. et al. (2006). All-solid-state Z-scheme in CdS-Au-TiO$_2$ three-component nanojunction system. *Nat. Mater.* 5 (10): 782–786.

6 Baker, D.R. and Kamat, P.V. (2009). Photosensitization of TiO$_2$ nanostructures with CdS quantum dots: particulate versus tubular support architectures. *Adv. Funct. Mater.* 19 (5): 805–811.

7 Zhang, H., Wang, G., Chen, D. et al. (2008). Tuning photoelectrochemical performances of Ag−TiO$_2$ nanocomposites via reduction/oxidation of ag. *Chem. Mater.* 20 (20): 6543–6549.

8 Kim, H.-S., Lee, J.-W., Yantara, N. et al. (2013). High efficiency solid-state sensitized solar cell-based on submicrometer rutile TiO$_2$ nanorod and CH3NH3PbI3 perovskite sensitizer. *Nano Lett.* 13 (6): 2412–2417.

9 Paramasivam, I., Macak, J.M., and Schmuki, P. (2008). Photocatalytic activity of TiO$_2$ nanotube layers loaded with Ag and Au nanoparticles. *Electrochem. Commun.* 10 (1): 71–75.

10 Lidia, A., Davide, B., Gregorio, B. et al. (2007). Photocatalytic and antibacterial activity of TiO$_2$ and Au/TiO$_2$ nanosystems. *Nanotechnology* 18 (37): 375709.

11 Awazu, K., Fujimaki, M., Rockstuhl, C. et al. (2008). A plasmonic photocatalyst consisting of silver nanoparticles embedded in titanium dioxide. *J. Am. Chem. Soc.* 130 (5): 1676–1680.

12 Ingram, D.B. and Linic, S. (2011). Water splitting on composite plasmonic-metal/semiconductor photoelectrodes: evidence for selective plasmon-induced formation of charge carriers near the semiconductor surface. *J. Am. Chem. Soc.* 133 (14): 5202–5205.

13 Thimsen, E., Le Formal, F., Grätzel, M., and Warren, S.C. (2011). Influence of plasmonic Au nanoparticles on the photoactivity of Fe$_2$O$_3$ electrodes for water splitting. *Nano Lett.* 11 (1): 35–43.

14 Xu, Z., Li, C., Kang, X. et al. (2010). Synthesis of a multifunctional nanocomposite with magnetic, mesoporous, and near-IR absorption properties. *J. Phys. Chem. C* 114 (39): 16343–16350.

15 Zhang, M., Hu, D.J.J., Shum, P.P., et al. (2016). High-birefringent microstructured optical fiber based surface plasmon resonance sensor. *Conference on Lasers and Electro-Optics*, 2016/06/05, San Jose, California: Optical Society of America.

16 Sun, X., Dai, D., Thylén, L., and Wosinski, L. (2015). High-sensitivity liquid refractive-index sensor based on a Mach-Zehnder interferometer with a double-slot hybrid plasmonic waveguide. *Opt. Express* 23 (20): 25688–25699.

17 Feng, D., Zhou, W., Qiao, X., and Albert, J. (2016). High resolution fiber optic surface plasmon resonance sensors with single-sided gold coatings. *Opt. Express* 24 (15): 16456–16464.

18 Erwin, W.R., Zarick, H.F., Talbert, E.M., and Bardhan, R. (2016). Light trapping in mesoporous solar cells with plasmonic nanostructures. *Energy Environ. Sci.* 9 (5): 1577–1601.

19 Huang, H.J., Zhen, S.-Y., Li, P.-Y. et al. (2016). Confined migration of induced hot electrons in Ag/graphene/TiO$_2$ composite nanorods for plasmonic photocatalytic reaction. *Opt. Express* 24 (14): 15603–15608.

20 Rifat, A.A., Mahdiraji, G.A., Sua, Y.M. et al. (2016). Highly sensitive multi-core flat fiber surface plasmon resonance refractive index sensor. *Opt. Express* 24 (3): 2485–2495.

21 Liu, Z., Hou, W., Pavaskar, P. et al. (2011). Plasmon resonant enhancement of photocatalytic water splitting under visible illumination. *Nano Lett.* 11 (3): 1111–1116.

22 Feldstein, M.J., Keating, C.D., Liau, Y.-H. et al. (1997). Electronic relaxation dynamics in coupled metal nanoparticles. *J. Am. Chem. Soc.* 119 (28): 6638–6647.

23 El-Sayed, M.A. (2001). Some interesting properties of metals confined in time and nanometer space of different shapes. *Acc. Chem. Res.* 34 (4): 257–264.

24 Lin, S., Li, M., Dujardin, E. et al. (2005). One-dimensional plasmon coupling by facile self-assembly of gold nanoparticles into branched chain networks. *Adv. Mater.* 17 (21): 2553–2559.

25 Feng, X., Ruan, F., Hong, R. et al. (2011). Synthetically directed self-assembly and enhanced surface-enhanced Raman scattering property of twinned crystalline Ag/Ag homojunction nanoparticles. *Langmuir* 27 (6): 2204–2210.

26 Rycenga, M., Cobley, C.M., Zeng, J. et al. (2011). Controlling the synthesis and assembly of silver nanostructures for plasmonic applications. *Chem. Rev.* 111 (6): 3669–3712.

27 Mali, S.S., Shim, C.S., Park, H.K. et al. (2015). Ultrathin atomic layer deposited TiO$_2$ for surface passivation of hydrothermally grown 1D TiO$_2$ nanorod arrays for efficient solid-state perovskite solar cells. *Chem. Mater.* 27 (5): 1541–1551.

28 Zhou, W., Zhou, Z., Song, S. et al. (2003). Pt based anode catalysts for direct ethanol fuel cells. *Appl. Catal., B* 46 (2): 273–285.

29 Xu, C., Pk, S., and Liu, Y. (2007). Ethanol electrooxidation on Pt/C and Pd/C catalysts promoted with oxide. *J. Power Sources* 164 (2): 527–531.

30 Liang, Z.X., Zhao, T.S., Xu, J.B., and Zhu, L.D. (2009). Mechanism study of the ethanol oxidation reaction on palladium in alkaline media. *Electrochim. Acta* 54 (8): 2203–2208.

31 Qi, K., Wang, Q., Zheng, W. et al. (2014). Porous single-crystalline palladium nanoflowers with enriched {100} facets for highly enhanced ethanol oxidation. *Nanoscale* 6 (24): 15090–15097.

32 Fu, S., Zhu, C., Du, D., and Lin, Y. (2015). Facile one-step synthesis of three-dimensional Pd–Ag bimetallic alloy networks and their electrocatalytic activity toward ethanol oxidation. *ACS Appl. Mater. Interfaces* 7 (25): 13842–13848.

33 Liang, Y.Q., Cui, Z.D., Zhu, S.L. et al. (2011). Silver nanoparticles supported on TiO$_2$ nanotubes as active catalysts for ethanol oxidation. *J. Catal.* 278 (2): 276–287.

34 Cherevko, S., Kulyk, N., and Chung, C.-H. (2012). Utilization of surface active sites on gold in preparation of highly reactive interfaces for alcohols electrooxidation in alkaline media. *Electrochim. Acta* 69: 190–196.

35 Chen, J., Cui, X., Wang, Q. et al. (2012). One-pot photochemical synthesis of ultrathin Au nanocrystals on co-reduced graphene oxide and its application. *J. Colloid Interface Sci.* 383 (1): 140–147.

36 Jin, Z., Wang, Q., Zheng, W., and Cui, X. (2016). Highly ordered periodic Au/TiO$_2$ hetero-nanostructures for plasmon-induced enhancement of the activity and stability for ethanol electro-oxidation. *ACS Appl. Mater. Interfaces* 8 (8): 5273–5279.

37 Xu, C.W., Wang, H., Shen, P.K., and Jiang, S.P. (2007). Highly ordered Pd nanowire arrays as effective electrocatalysts for ethanol oxidation in direct alcohol fuel cells. *Adv. Mater.* 19 (23): 4256–4259.

38 Cui, C.-H., Yu, J.-W., Li, H.-H. et al. (2011). Remarkable enhancement of electrocatalytic activity by tuning the Interface of Pd–Au bimetallic nanoparticle tubes. *ACS Nano* 5 (5): 4211–4218.

39 Dutta, A., Mahapatra, S.S., and Datta, J. (2011). High performance PtPdAu nano-catalyst for ethanol oxidation in alkaline media for fuel cell applications. *Int. J. Hydrogen Energy* 36 (22): 14898–14906.

40 Oliveira, M.C., Rego, R., Fernandes, L.S., and Tavares, P.B. (2011). Evaluation of the catalytic activity of Pd–Ag alloys on ethanol oxidation and oxygen reduction reactions in alkaline medium. *J. Power Sources* 196 (15): 6092–6098.

41 Wang, Q., Cui, X., Guan, W. et al. (2014). A nanoflower shaped gold-palladium alloy on graphene oxide nanosheets with exceptional activity for electrochemical oxidation of ethanol. *Microchim. Acta* 181 (3–4): 373–380.

42 Zhu, C., Guo, S., and Dong, S. (2012). PdM (M=Pt, Au) bimetallic alloy nanowires with enhanced electrocatalytic activity for electro-oxidation of small molecules. *Adv. Mater.* 24 (17): 2326–2331.

43 Hutter, E. and Fendler, J.H. (2004). Exploitation of localized surface plasmon resonance. *Adv. Mater.* 16 (19): 1685–1706.

44 Wu, J.-L., Chen, F.-C., Hsiao, Y.-S. et al. (2011). Surface plasmonic effects of metallic nanoparticles on the performance of polymer bulk heterojunction solar cells. *ACS Nano* 5 (2): 959–967.

45 Wang, H., You, T., Shi, W. et al. (2012). Au/TiO$_2$/Au as a plasmonic coupling photocatalyst. *J. Phys. Chem. C* 116 (10): 6490–6494.

46 Tian, Y. and Tatsuma, T. (2005). Mechanisms and applications of plasmon-induced charge separation at TiO$_2$ films loaded with gold nanoparticles. *J. Am. Chem. Soc.* 127 (20): 7632–7637.

47 Bian, Z., Tachikawa, T., Zhang, P. et al. (2013). Au/TiO$_2$ superstructure-based plasmonic photocatalysts exhibiting efficient charge separation and unprecedented activity. *J. Am. Chem. Soc.* 136 (1): 458–465.

48 Xu, Z., Yu, J., and Liu, G. (2011). Enhancement of ethanol electrooxidation on plasmonic Au/TiO$_2$ nanotube arrays. *Electrochem. Commun.* 13 (11): 1260–1263.

49 Murdoch, M., Waterhouse, G., Nadeem, M. et al. (2011). The effect of gold loading and particle size on photocatalytic hydrogen production from ethanol over Au/TiO$_2$ nanoparticles. *Nat. Chem.* 3 (6): 489–492.

50 Kim, K., Thiyagarajan, P., Ahn, H.-J. et al. (2013). Optimization for visible light photocatalytic water splitting: gold-coated and surface-textured TiO$_2$ inverse opal nano-networks. *Nanoscale* 5 (14): 6254–6260.

51 Raval, D., Tripathi, B., and Ray, A. (2016). Titanium dioxide nanorod diameter and layer porosity optimization by estimating electrical performance of dye and perovskite sensitized solar cell. *J. Porous Mater.* 24 (1): 1–15.

52 Yen, Y.C., Chen, J.A., Ou, S. et al. (2017). Plasmon-enhanced photocurrent using gold nanoparticles on a three-dimensional TiO_2 nanowire-web electrode. *Sci. Rep.* 7: 42524.

53 Long, P.D., Chien, D.T., Trung, N.T. et al. (2017). Plasmonic effect enhanced photocurrent in nanostructured TiO_2 films decorated with gold nanoparticles. *J. Electron. Mater.* 46 (7): 4448–4454.

54 Raval, D., Tripathi, B., and Ray, A. (2018). Quantum mechanical investigation of optoelectronic properties of gold nanoparticle attached titanium dioxide nanorods for device applications. *J. Nanopart. Res.* 20 (2).

55 Zhang, Z., Zhang, L., Hedhili, M.N. et al. (2012). Plasmonic gold nanocrystals coupled with photonic crystal seamlessly on TiO_2 nanotube photoelectrodes for efficient visible light photoelectrochemical water splitting. *Nano Lett.* 13 (1): 14–20.

56 Van de Groep, J., Sheldon, M.T., Atwater, H.A., and Polman, A. (2016). Thermodynamic theory of the plasmoelectric effect. *Sci. Rep.* 6.

57 Reineck, P., Brick, D., Mulvaney, P., and Bach, U. (2016). Plasmonic hot electron solar cells: the effect of nanoparticle size on quantum efficiency. *J. Phys. Chem. Lett.* 7 (20): 4137–4141.

58 Ghatak, A. (2010). *Basic Quantum Mechanics*. New Delhi: Macmillan Publishers India Limited.

59 Bohren, C.F. and Huffman, D.R. (2008). *Absorption and Scattering of Light by Small Particles*. Wiley.

60 Westcott, S., Jackson, J., Radloff, C., and Halas, N. (2002). Relative contributions to the plasmon line shape of metal nanoshells. *Phys. Rev. B* 66 (15): 155431.

61 Bing, Z., Dong-Sheng, L., Lue-Lue, X., and De-Ren, Y. (2010). Enhanced optical absorption of amorphous silicon films by Ag nanostructures. *Chin. Phys. Lett.* 27 (3): 037303.

62 Tripathi, B., Yadav, P., and Kumar, M. (2013). Plasmon-enhanced light trapping to improve efficiency of TiO_2 nanorod-based dye-sensitized solar cell. *Plasmonics* 8 (3): 1501–1507.

63 Huang, X. and El-Sayed, M.A. (2010). Gold nanoparticles: optical properties and implementations in cancer diagnosis and photothermal therapy. *J. Adv. Res.* 1 (1): 13–28.

64 Jain, P.K., Lee, K.S., El-Sayed, I.H., and El-Sayed, M.A. (2006). Calculated absorption and scattering properties of gold nanoparticles of different size, shape, and composition: applications in biological imaging and biomedicine. *J. Phys. Chem. B* 110 (14): 7238–7248.

65 Park, N.-G., Schlichthörl, G., van de Lagemaat, J. et al. (1999). Dye-sensitized TiO_2 solar cells: structural and photoelectrochemical characterization of nanocrystalline electrodes formed from the hydrolysis of $TiCl_4$. *J. Phys. Chem. B* 103: 3308–3314.

66 Zhang, F. and Liu, X. (1998). Effect of O_2 pressure on the preferred orientation of TiO_2 films prepared by filtered arc deposition. *Thin Solid Films* 326: 171–174.

67 Nayak, J., Prabakar, K., Park, J.W., and Kim, H. (2012). Effect of synthesis temperature on structure, optical and photovoltaic properties of TiO_2 nanorod thin films. *Electrochim. Acta* 65: 44–49.

68 Zhao, L., Thomas, J.P., Heinig, N.F. et al. (2014). Au–Pt alloy nanocatalysts for electro-oxidation of methanol and their application for fast-response non-enzymatic alcohol sensing. *J. Mater. Chem. C* 2 (15): 2707–2714.

69 Ishikawa, Y., Wada, K., Cannon, D.D. et al. (2003). Strain-induced band gap shrinkage in Ge grown on Si substrate. *Appl. Phys. Lett.* 82: 2044–2046.

70 Kim, H.-S., Lee, C.-R., Im, J.-H. et al. (2012). Lead iodide perovskite sensitized all-solid-state submicron thin film mesoscopic solar cell with efficiency exceeding 9%. *Sci. Rep.* 2: 591.

71 Zhao, Y. and Zhu, K. (2013). Charge transport and recombination in perovskite $(CH_3NH_3)PbI_3$ sensitized TiO_2 solar cells. *J. Phys. Chem. Lett.* 4: 2880–2884.

72 Linic, S., Christopher, P., and Ingram, D.B. (2011). Plasmonic-metal nanostructures for efficient conversion of solar to chemical energy. *Nat. Mater.* 10 (12): 911–921.

73 Burda, C., Chen, X., Narayanan, R., and El-Sayed, M.A. (2005). Chemistry and properties of nanocrystals of different shapes. *Chem. Rev.* 105 (4): 1025–1102.

74 Evanoff, D.D. and Chumanov, G. (2005). Synthesis and optical properties of silver nanoparticles and arrays. *ChemPhysChem* 6 (7): 1221–1231.

75 Warren, S.C. and Thimsen, E. (2012). Plasmonic solar water splitting. *Energy Environ. Sci.* 5 (1): 5133–5146.

76 Zhang, Y., Pluchery, O., Caillard, L. et al. (2015). Sensing the charge state of single gold nanoparticles via work function measurements. *Nano Lett.* 15 (1): 51–55.

77 Sarkar, D., Ghosh, C.K., and Chattopadhyay, K.K. (2012). Morphology control of rutile TiO_2 hierarchical architectures and their excellent field emission properties. *CrystEngComm* 14 (8): 2683–2690.

78 Kowalska, E., Abe, R., and Ohtani, B. (2009). Visible light-induced photocatalytic reaction of gold-modified titanium (IV) oxide particles: action spectrum analysis. *Chem. Commun.* 2: 241–243.

79 Kowalska, E., Mahaney, O.O.P., Abe, R., and Ohtani, B. (2010). Visible-light-induced photocatalysis through surface plasmon excitation of gold on titania surfaces. *Phys. Chem. Chem. Phys.* 12 (10): 2344–2355.

80 Ohtani, B. (2008). Preparing articles on photocatalysis-beyond the illusions, misconceptions, and speculation. *Chem. Lett.* 37 (3): 216–229.

81 Hodak, J.H., Henglein, A., and Hartland, G.V. (2000). Photophysics of nanometer sized metal particles: electron-phonon coupling and coherent excitation of breathing vibrational modes. *J. Phys. Chem. B* 104 (43): 9954–9965.

11

2D Materials with 1D Semiconducting Nanostructures for High-Performance Gas Sensor

Shulin Yang[1,2], Yinghong Liu[1], Gui Lei[1,2], Huoxi Xu[1], Zhigao Lan[1], Zhao Wang[2], and Haoshuang Gu[1,2]

[1] *Huanggang Normal University, Hubei Key Laboratory for Processing and Application of Catalytic Materials, School of Physics and Electronic Information, 146 Xingang 2nd Road, Huanggang, Hubei Province, 438000, China*
[2] *Hubei University, Hubei Key Laboratory of Ferro & Piezoelectric Materials and Devices, Faculty of Physics and Electronic Sciences, 368 Youyi Road, Wuhan, Hubei Province, 430062, China*

11.1 Introduction

Gaseous pollution has been becoming a serious issue in modern society with the rapid development of industry and the increasing popularity of automobiles [1–3]. The high-concentration gas in the air poses serious threats to our health and our security in life [4–6]. It is reported that the colorless/toxic CO would interact strongly with the hemoglobin in our blood and prevent the red blood cells from transferring oxygen in our body, resulting in asthma, cardiovascular disease or cardiac disease, and even death with its concentration being over 5000 ppm [7]. Moreover, there would be a high risk of explosion when the CO concentration reaches 12.5–74.2% in the air [8]. The colorless, odorless, and tasteless H_2 could also cause an explosion with its concentration being in the range of 4–75.6% [9]. The greenhouse gases of CO_2 and CH_4 have been proved to be mainly responsible for global warming, resulting in serious changes in the climate [10]. And the SO_2 or NO_2 is also reported to be a threat gas to cause acid rain and would damage our health with the concentration being extremely low (ppm level) [11–13]. Additionally, the formaldehyde in modern decorative materials and the triethylamine (TEA) released with the decay of fishes and other seafood are potential threat gases, and they are also a danger to our health [14]. Therefore, high-performance gas sensors are of great importance and urgent demand to effectively detect or monitor the gases.

Recently, the one-dimensional (1D) semiconducting nanostructures have been more and more popular sensing materials to show promising sensing properties with their advantages of high surface activity, facile synthesization, small size,

low cost, and good stability [15, 16]. Moreover, the 1D structure could be channels for the transport of carriers in the sensing material [17, 18]. Metal oxide-based gas sensors have attracted lots of attention, since the gas-sensing performance of the ZnO film was reported by Taguchi et al. in 1962 [19]. There are numerous metal oxides assembled to be the gas sensors, including TiO_2, Nb_2O_5, WO_3, In_2O_3, NiO, MoO_3, Fe_2O_3, or SnO_2 [16, 18, 20–26]. The sensor based on the single SnO_2 nanowire with a length of over $3\,\mu m$ was reported to exhibit a sensor response (R_{air}/R_{gas}, R_{air} or R_{gas} presenting the resistance of sensor in air or target gas, respectively) of 6.76 50 ppm ethanol at the working temperature of $350\,°C$ [27]. The work of Liu et al. suggested that the electrospun In_2O_3 nanowires could be a possible sensing material to detect 1 ppm acetone under 100% RH at $320\,°C$ with the response/ recovery time being 11/13 seconds [28]. And the NiO nanowires with average length and diameter being $\sim 20\,\mu m$ and $\sim 120\,nm$, respectively, yield a sensor response (R_{air}/R_{gas}) being ~ 13–100 ppm formaldehyde at $200\,°C$ [29]. Meanwhile, the sensor based on the decorated Si nanowires was found to be a potential substrate to sense 1 mbar CO_2 with the response time or recovery time being 95 or 103 seconds, respectively [30]. Based on these reports, it was reasonable to infer that the sensors based on the pure semiconducting nanostructures could be used to detect various gases but with the relatively low sensor responses or long response/recovery times, a negative factor constraining the promotion of their application in the gas sensor.

The construction of heterojunction is proved to effectively improve the gas-sensing performances of 1D semiconducting nanostructures [20, 31]. The two-dimensional (2D) materials have been also widely used to composite with the 1D metal oxides to assemble high-performance gas sensors with their advantages of high specific surface area and unique chemical and physical properties [32–34]. As it was reported, the gas-sensing performance of metal oxide was mainly attributed to the redox reaction between the chemisorbed oxygen species and the target gas molecules [20, 35]. The sheet-like structure and the abundant active site of the 2D materials would fascinate the adsorptions and diffusions of gas molecules in the composite. The sensor response of the ZnO nanorods composited with reduced graphene oxide (RGO) was reported to be $\sim 70\%$ ($\Delta R/R_{gas}*100\%$, $\Delta R = R_{air} - R_{gas}$) toward 400 ppb NO_2 at the working temperature of $22.4 \pm 0.2\,°C$ [36]. The formaldehyde sensing performance of the SnO_2 nanowires was also improved with decorating with RGO, exhibiting a higher sensor response (R_{air}/R_{gas}) of 5437 to 50 ppm formaldehyde at $50\,°C$ [37]. The investigation of Xu et al. showed that the sensor response (R_{air}/R_{gas}) of the ZnO nanorods toward 100 ppm ethanol at $350\,°C$ was effectively enhanced from the original 15 to 125 via compositing them with sheet-like Co_3O_4 nanostructures [38]. Nowadays, both the typical 2D materials of the graphene or RGO, MoS_2, or WS_2 and the synthesized sheet-like NiO, ZnO, or SnO_2 have been applied to enhance the sensing response of the metal oxides with the establishment of heterojunctions. The sensor response of the composite was higher than that of the pure metal oxide, and the working temperature could also be decreased at the same time. Some reviews have compared the gas-sensing performances of the 1D metal oxides and reported their gas-sensing mechanisms [20, 21, 31, 35].

However, there were few reports focusing on the gas-sensing properties of the 1D semiconducting nanostructures composited with 2D materials.

In this work, we have compared the sensing performances of the sensors based on 1D semiconducting nanostructures composited with 2D materials and discussed their assembly process. We have discussed the gas-sensing properties of the 1D-sensing materials decorating with graphene/RGO, MoS_2, WS_2, NiO nanosheet, ZnO nanosheet, or the other 2D materials. The method to construct the 1D nanomaterial of a nanowire, nanorod, nanoribbon, or nanofiber composited with 2D sheet-like material is discussed and summarized. The sensor response, the response time, and the recovery time are compared in detail, and the improved sensing mechanisms are discussed as well. Additionally, the potential challenges and the possible methods to further improve the sensing based on 2D materials with 1D semiconducting nano-structures are proposed.

11.2 Enhanced Gas-Sensing Performances of 1D-Sensing Materials Composited with Different 2D Materials

The 2D materials have been widely applied to decorate with metal oxides to improve their gas-sensing performances. And a series of methods could be successfully to construct the heterostructure of 2D materials with 1D semiconducting nanostructures, mainly a two-step process. The introduction of 2D material could effectively increase the special surface area and provide more active sites in the composite, a positive factor for improving the gas-sensing response of 1D semiconducting materials. Some of the common 2D materials were reviewed in this study, mainly including graphene-based material, MoS_2, WS_2, NiO, or ZnO.

11.2.1 Graphene or Reduced Graphene Oxide-based Composites

The graphene has attracted lots of attention since it was first synthesized and reported in 2004 [39]. The graphene and the graphene-based materials are widely applied in gas sensors due to their unique layer structures and the special physical/chemical prosperities [40]. The graphene oxide (GO) is one of the typical graphene-based materials and has been popularly used to decorate the metal oxides to enhance their gas-sensing performance with the abundant functions groups on their surfaces [41, 42]. In some work, the RGO was also directly described as graphene because a majority of the functional groups were removed from the surface of the GO during the synthesization of the composite. In this review, the GO-based sheet in the final composite has been uniformly described as RGO.

Roshan et al. suggested that the graphene-decorated ZnO nanowires were reported to be a potential substrate to sense ethanol [43]. The authors firstly prepared a mixture of zinc acetate and 2-methoxyethanol and then further added the monoethanolamine into the obtained mixture to obtain the seed solution. The seed solution was spin-coated on the surface of the electrode covered with a layer

of graphene. The scanning electron microscopy (SEM) image of the used graphene was shown in Figure 11.1a,b. The treated electrode was immersed into a precursor of $Zn(NO_3)_2$ and hexamethylenetetramine. The ZnO nanowires were directly grown on the surface of the graphene covered on the electrode through a hydrothermal method at 70 °C (seen the inset in Figure 11.1f). The average length of the prepared hexagonal ZnO nanowires was ~2 μm with the average diameter being 100–200 nm (Figure 11.1c–e). The sensor based on the graphene-decorated ZnO nanowires exhibited a senor response (R_{air}/R_{gas}) of ~23 at the optimal working temperature of 125 °C, over five times higher than that of the pure ZnO nanowires (~3.5) at a higher working temperature of 200 °C (Figure 11.1f–h). The authors also pointed out that the pure ZnO nanowires exhibited a typical n-type sensing performance to ethanol, while a p-type sensing property of graphene-decorated ZnO nanowires was observed. The sensor response of the decorated ZnO nanowires to 1–50 ppm ethanol was higher than that of the pure ones. And the graphene-decorated ZnO nanowires also presented a higher sensor response to 20 ppm ethanol at 125 °C compared with that to 1000 ppm CH_4, 100 ppm CO, 4000 ppm H_2O, 1000 ppm CO_2, or 1000 ppm CH_2O (Figure 11.1i), indicating the good selectivity of the composite. The different work functions of the ZnO (~4.45 eV) and the graphene (4.9 eV) would result in the bending of their bands and form a potential barrier at the heterojunctions. When the ethanol was introduced on the surface of the sensing material, the released electrons could effectively decrease the height of the potential barrier, leading to a higher sensor response of the composite. On the other hand, the electrons would mainly be transferred through the graphene due to its high mobility and high conductivity, facilitating the transport of carries in the sensing material during the sensing performance. Then, an enhanced sensing performance of the composite was achieved due to the decoration of graphene acting as a high conductive carrier path. This research indicated that the sensing performance of the metal oxide could be improved with the help of graphene. It should be noted that there were only some references reporting the metal oxides decorated with pure graphene. We found that more attention was focused on improving the gas-sensing performances of metal oxides composited with RGO.

The work of Lee's team reported that the sensing performance of vertical zinc oxide nanorods was enhanced through compositing them with RGO [44]. The authors have directly assembled the RGO-decorated ZnO on the surface of AlGaN/GaN layer. The ZnO nanorods array was grown on a prepared substrate without a seed layer at 90 °C for 4 hours. A modified Hummers' method was applied to synthesize the RGO with an average thickness or size of ~3 or ~200 nm, respectively. Then the prepared RGO was adsorbed on the ZnO nanorods modified with poly-(diallydimethylammonium chloride) (PDDA) via a drop-casting method, and the assembled sensor was further annealed at 120 °C for three hours to enhance its stability. The sensor based on the composite showed promising sensing properties to NO_2, SO_2, or HCHO gas with low concentrations of 120–1000 ppb. The composite showed a typical p-type sensing performance toward NO_2 or SO_2 but an n-type sensing response to HCHO. The composite exhibited a sensor response ($\Delta R/R_{air}$, $\Delta R = R_{air} - R_{gas}$) of 1.875 ppm^{-1} toward 120 ppb NO_2 with the response/recovery
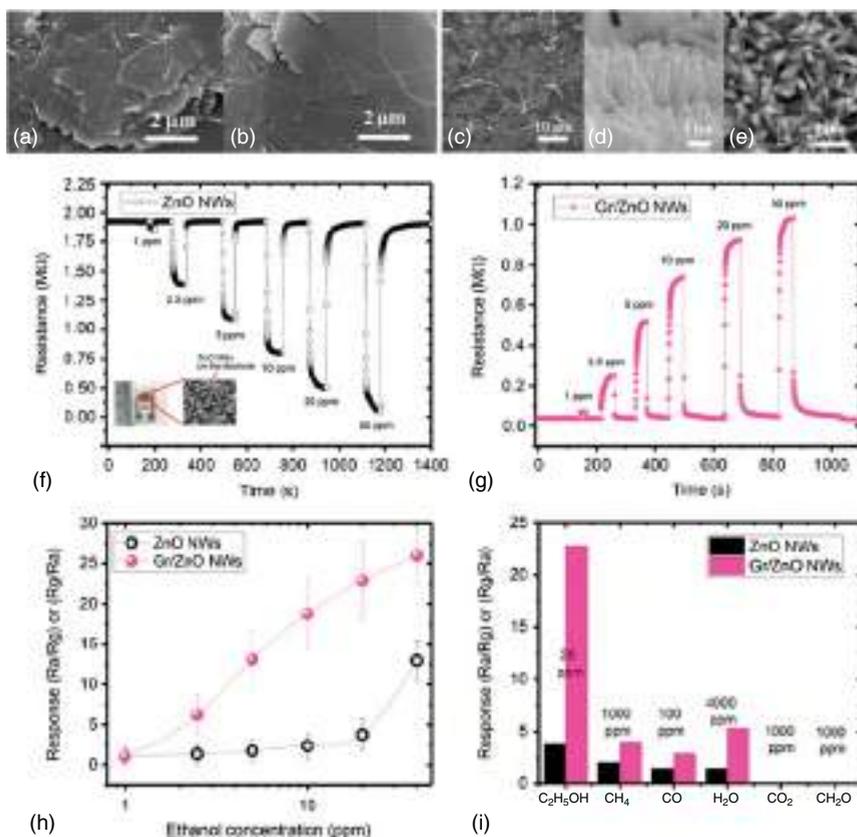
Figure 11.1 SEM images of graphene (a and b) and ZnO nanowires composited with graphene nanowires. (f–h) The gas-sensing performances of pure ZnO nanowires and ones composited with graphene nanowires, the inset in (f) is the digital image of the assembled sensor and the SEM image of the ZnO nanowires on the electrodes. (i) The gas selectivity of ZnO nanowires and the composite toward different gases. Source: Rafiee et al. [43], Reproduced with permission from Elsevier.

time being 120/320 seconds at room temperature (300 ± 1 K). The sensor response of the composite to NO_2 was higher than that to SO_2 (0.933 ppm^{-1}) or HCHO (0.875 ppm^{-1}). This research paved a possible way to design the effective sensing material to show high-sensitive gas-sensing performance with low power consumption, and functionality at a low working temperature. According to the reported results, the sensor based on the RGO-decorated ZnO on AlGaN/GaN layer could be an effective material to detect hazardous gas with a low detection limit. It might be better if the sensing selectivity of the sensor to different gas was improved because the sensor showed a relatively high and close sensor response to NO_2, SO_2, or HCHO gas. And the shift of the baseline of the assembled sensor was also found during the sensing response, which should also be improved to ensure the accuracy and the sensing stability of the composite.

Gu et al. have assembled a sensor based on the MoO_3 nanoribbons decorated with RGOs (directly described as graphene in the work) and studied their hydrogen-sensing performance [45]. The GOs were prepared with a similar modified Hummers' method and then added into the precursor to construct the MoO_3 nano-ribbons/RGO composite via a hydrothermal method. The average length of the MoO_3 was ~10 μm, and the RGO also remained the sheet-like morphology (Figure 11.2a–d). The MoO_3 composited with the 1.5 wt% RGO exhibited optimal hydrogen-sensing performance with the senor response (R_{air}/R_{gas}) being 8.83–500 ppm H_2 in the air at room temperature, as shown in Figure 11.2e,f. The sensor also could be used to effectively detect hydrogen gas with the concentration being 0.5–1000 ppm at room temperature (Figure 11.2g). And the senor based on composited exhibited a high senor response of ~20.5, one time higher than that of the pure MoO_3, with the response/recovery time being ~10/30 section (Figure 11.2h). The higher specific surface area, the formation of heterojunction around the inter-faces, and the improved electronic conductivity were reported to be mainly respon-sible for the enhancement hydrogen gas-sensing performance of the MoO_3 nanoribbons/RGO composite. The remarkable hydrogen selectivity and repeatabil-ity were also reported by the authors, further indicating the potential of the compos-ite in the area of the hydrogen gas sensor.

Kim et al. have assembled a sensor based on the ZnO nanofibers decorated with RGO nanosheets and studied their potential application in hydrogen sensors [46]. The GO was firstly prepared with a modified Hummers' method, and then the RGO was obtained by an oil bath with the hydrazine monohydrate. The solution of the prepared RGO and the zinc acetate was used to synthesize the RGO-decorated ZnO nanofibers through an electrospinning method, and then the prepared composite was annealed at 600 °C in the air for 30 minutes. The RGO-decorated ZnO nano-fibers exhibited an optimal sensor response of 2524 (R_{air}/R_{gas}) to 10 ppm H_2 at the optimal working temperature of 400 °C. Moreover, the composite also exhibited a promising sensor response of 866 to 0.1 ppm H_2 at 400 °C with the response time or recovery time being 3.5 or 3.9 minutes, respectively. The authors also compared the hydrogen-sensing performance of the RGO-loaded ZnO nanofibers with that of the RGO-loaded SnO_2 nanofibers. The sensor response of the former composite to 10 ppm H_2 at 400 °C was approximately 25 times higher than that of the latter one (74.8), inferring the more superior hydrogen-sensing performance of the RGO-loaded ZnO nanofibers. In the H_2 atmosphere, there would be a metallic Zn layer along the junctions between the RGO and the ZnO nanofibers, making the ZnO more n-type. And the released electrons would not be transferred from the ZnO to the RGO during the sensing process, further improving the conductivity of the ZnO and resulting in a lower resistance of the composite. The spillover effect of the RGO would also enhance the sensing response of the RGO-loaded ZnO nanofibers. These three factors should be mainly responsible for the excellent hydrogen-sensing per-formance of the RGO-loaded ZnO nanofibers. Even the working temperature was relatively high, the excellent senor response (865.9) of the composite to H_2 with a low concentration of 0.1 ppm also indicated its great potential in the application of hydrogen gas sensors. This work also provided a possible way to construct the
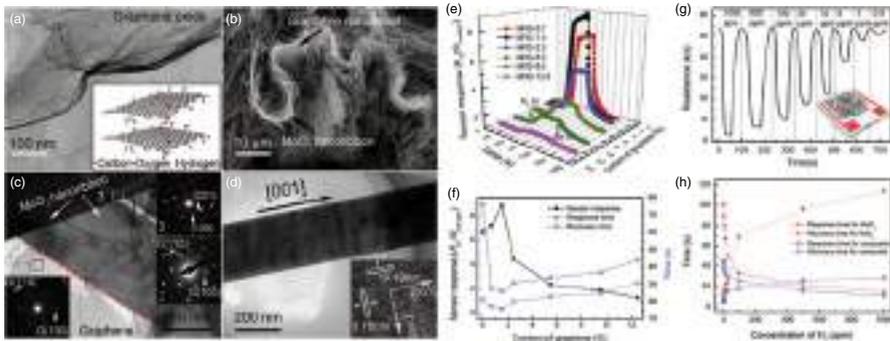
Figure 11.2 SEM image of graphene oxide (a) and the MoO₃ nanoribbons composited with RGO (b). (c) TEM image and the selected area diffraction (SAED) patterns of RGO and MoO₃ nanoribbon in the composite. (d) TEM image of single MoO₃ nanoribbon. (e and f) Hydrogen-sensing performance of composite with different content of RGO. (g and h) Dynamic sensing performance of the composite to 0.5–1000 ppm H_2 at room temperature, the inset in (g) is the sketch of the assembled gas sensor. Source: Yang et al. [45], Reproduced with permission from Elsevier.

promising sensing material to exhibit a high and stable sensor response to low-concentration hydrogen gas.

The RGO-decorated In_2O_3 nanofibers, reported by Gao et al., were found to show improved NO_2-sensing performance at a low working temperature of 50 °C [47]. The In_2O_3 nanofibers decorated with RGO nanosheets were synthesized via a similar process proposed by Kim et al. discussed ahead. In the work of decorated In_2O_3 nanofibers, the GO was also firstly prepared through a modified Hummers' method at a high temperature of 500 °C for two hours. The obtained GO was added into the precursor with raw materials of $In(NO_3)_3 \cdot 4.5H_2O$ and DMF solution to synthesize the decorated In_2O_3 nanofibers. The effects of the concentration of RGO on the NO_2-sensing performance of the In_2O_3 were studied via adding different contents of GO. The results showed that the sensor response (R_{gas}/R_{air}) of the decorated In_2O_3 nanofibers was 20.0, 42.0, and 26.6 to 5 ppm NO_2 at 50 °C for the composites with 1.1 wt%, 2.2 wt%, and 3.6 wt% RGO, respectively. Then the sensor based on the 2.2 wt% RGO-In_2O_3 nanofibers showed optimal NO_2-sensing performance among all the samples. Meanwhile, the sensor response of the composite was approximately 4.4 times higher compared with that of the pure In_2O_3 (9.5). In addition, further research showed that the 2.2 wt% RGO-In_2O_3 nanofibers exhibited a promising sensor response of 1.8 or 10 to the NO_2 with the low concentration of 1 or 2 ppm, respectively. The response time and the recovery time of the optimal composite to 5 ppm NO_2 at 50 °C were 261 and 698 seconds, respectively, also shorter than those of the pure In_2O_3 (316 and 1669 seconds). The enhanced NO_2-sensing performance of the decorated In_2O_3 was reported to be ascribed to the modification of the resistance with the formation of p–n heterojunction between the RGO and the In_2O_3 and the high special surface area of the composite. The special surface area of the decorated In_2O_3 was calculated to be 315.30 m^2/g, approximately 10 times higher compared with pure In_2O_3. The rich defects and the dangling bonds in the RGO provide more adsorption sites for the NO_2 and fascinate the adsorptions of more NO_2, also resulting in the enhanced gas-sensing property of the composite. This research further revealed that the GO could be applied to synthesize RGO-decorated nanofibers via a two-step method to construct effective material with promising gas-sensing performance. It should also be noted that the humidity showed a significant effect on the gas-sensing performance. Both the sensor response and the resistance exhibited a negative relationship with the humidity, which might be a factor that constrains the practical application of the sensor based on RGO-decorated In_2O_3 nanofibers.

The research of Galstyan et al. revealed that the hydrogen-sensing performance of the TiO_2 nanotubes was highly improved via decorating them with RGO nanosheets [48]. The TiO_2 nanotubes were synthesized with a method of electrochemical anodization with the raw material of titanium films with the thickness of 500 nm which was deposited on the substrate of Al. Then the obtained tubular structures were annealed in the O_2/Ar atmosphere at 400 °C for six hours. The GO used in the study was prepared with a widely modified Hummers' method and then dropped on the surface of the obtained TiO_2 nanotubes arrays. Then the GO-decorated TiO_2 nanotubes were further annealed at 400 °C for four hours to reduce

the GO to be RGO. The authors have assembled a series of sensors based on TiO_2 nanotubes loaded by RGO with different contents. The results showed that the TiO_2 nanotubes with 4.5 ng/mm^2 GO exhibited a higher sensor response ($\Delta I/I_{air}$, $\Delta I = I_{air} - I_{gas}$, R_{air} or R_{gas} presenting the current of sensor in air or target gas, respectively) compared with that of the nanotubes composited with 0 ng/mm^2 GO or 40.5 ng/mm^2 GO. The sensor response of the RGO-decorated TiO_2 nanotubes was ~37.6 to 480 ppm H_2 at the working temperature of 200 °C. But the corresponding response time or recovery time was reported to be 1110 or $\leq$ 300 seconds, respectively, too long to meet the practical requirements of the hydrogen gas sensor.

Yang et al. suggested that the RGO-decorated ZnO nanowires could be used to detect NH_3 with promising sensing performance [49]. The ZnO nanowires were synthesized with a modified carbothermal reduction and the GO was prepared via a modified Hummers' method. The RGO-decorated ZnO nanowires were obtained by mixing the prepared ZnO nanowires and the collected GO, and then the mixture was annealed at 300 °C. The ZnO nanowires with an average length of 1.5 μm were well dispersed on both sides of the RGO. The electrodes were fabricated with a standard micro-electromechanical systems (MEMS) process, and the sensing material was deposited on the center zone of the obtained Au electrodes to assemble the gas sensor. Moreover, the authors also designed an operating system and peripheral circuits to assemble a portable gas-sensing device with five separated parts of power supplies, signal modulating circuits, analog-to-digital (A/D) conversion circuits, microprogrammed control unit (MCU), and hosting computer. The assembled sensor presented a good sensing performance to NH_3 with the concentration in the range of 500 ppb to 5000 ppm The sensor response showed a positive relationship with the concentration of NH_3. The sensor response ($\Delta R/R_{air}*100\%$, $\Delta R = R_{gas} - R_{air}$) of the composite was 7.2% or 3% to 1 ppm or 500 ppb NH_3, respectively. The wire-like morphology of the ZnO in the composite could be channels for electrons transfer and provided more active sites for more O_2 molecules or NH_3, resulting in the enhancement of the NH_3-sensing performance of RGO-decorated ZnO.

Similar improvement was also reported in the study on gas-sensing performance of Cu_2O nanorods modified by RGO nanosheets, graphene–WO_3 composite, MoO_3–RGO hybrids, ultrathin ZnO nanorods–RGO mesoporous nanocomposites, ZnO nanowire–RGO nanocomposite, In_2O_3 nanorod-decorated RGO composite, RGO-decorated GaN nanorod or vanadium-doped cerium oxide nanorods wrapped RGO toward NH_3, acetaldehyde, H_2S, NO_2, NO_x, or H_2 [50–57].

11.2.2 MoS$_2$-based Composites

The MoS$_2$ is also one of the typical 2D materials and has attracted more and more attention in recent years, which was widely to decorate the metal oxides to improve their gas-sensing properties [58]. The ZnO nanorods decorated with MoS$_2$ nanosheets were reported to be successfully assembled via a typical two-step process. The array of the uniform ZnO nanorods with an average diameter of 100 nm was firstly prepared by immersing a patterned Si substrate covered with ZnO seeds in the nutrition solution consisting of zinc nitrate hexahydrate and

hexamethylenetetramine at 95 °C for seven hours (Figure 11.3a–d). The MoS_2 nanosheets were synthesized with the ultrasonication of MoS_2 powder in ethanol for 90 minutes and then collected by centrifugation. Then the obtained MoS_2 nanosheets were dropped on the surface of the ZnO nanorods and were further heated at 90 °C to prepare the MoS_2-decorated ZnO nanorods (Figure 11.3e–k). The assembled sensor was reported to be limited in a small size with a compact structure, as shown in Figure 11.3a. The sensor response ($\Delta R/R_{air}$*100%, $\Delta R = R_{gas} - R_{air}$) of the pure ZnO nanorods was calculated to be 184% toward NO_2 with the concentration being as low as 100 ppb. With the decoration of MoS_2 on ZnO, the sensor response was highly improved to be 1280% (Figure 11.3l,m), which was over seven times higher than that of the pure ZnO. The response time of the sensor to 200 ppb NO_2 was 118 seconds, and the recovery time of the sensor was short toward 500 ppb NO_2, being 32 seconds. Meanwhile, there was also a linear relationship between the sensor response and the concentration of NO_2 in the range of 5–100 ppb (Figure 11.3n). The outstanding NO_2-sensing performance of the composite was mainly attributed to the abundant adsorption sites in the composite and the fast charge carrier migration between the heterojunction. The lowest detection limit of the sensor based on the ZnO nanorods decorated with MoS_2 nanosheets was estimated to be as low as approximately 0.2 ppb. The lowest detection limit was so low that also revealed the advantages of the prepared composite. This investigation paves a possible way to improve the NO_2-sensing performance of the sensor based on metal oxides.

More recently, the SO_2-sensing performance of the SnO_2 nanofibers was also reported to be highly enhanced via decorating them with 2D MoS_2 nanosheets [59]. The MoS_2 nanosheets-decorated SnO_2 nanofibers were prepared through a two-step method that was similar to the way in ref. [58]. The uniform SnO_2 nanofibers were synthesized via one-chip electrospinning, and the MoS_2 nanosheets were prepared through a treatment of exfoliation of bulk MoS_2 with a high-power ultrasonic probe. The composite was then assembled by dropping the dispersed solution of the MoS_2 nanosheets on the surface of the SnO_2 nanofibers. The sensor based on the MoS_2 nanosheets-decorated SnO_2 nanofibers exhibited an enhanced SO_2-sensing performance at 150 °C with a sensor response (R_{gas}/R_{air}) being 10 times higher than that of the pure SnO_2 nanofibers. Meanwhile, the composite also could be operated at a lower working temperature (150 °C) compared with the pure SnO_2 nanofibers (300 °C). The authors pointed out that the decorated SnO_2 nanofibers were the potential to sense SO_2 with a low gas concentration of 1 ppm due to the high carrier mobility and low electrical noise of the MoS_2 nanosheets. This is a typical advantage of the senor based on the MoS_2 nanosheets-decorated SnO_2 nanofibers, making the composite be promisingly applied to detect SO_2 with outstanding performance. The chemical sensitization of MoS_2 nanosheets and the heterojunction between the MoS_2 and the SnO_2 were mainly responsible for the enhanced gas-sensing performance of the composite. We should note that the MoS_2 nanosheets were dispersed on the SnO_2 nanofibers, making the heterojunctions be formed via physical interaction between the MoS_2 and the SnO_2. Then the sensor response of the composite was not very high, being 11.1 to 10 ppm SO_2
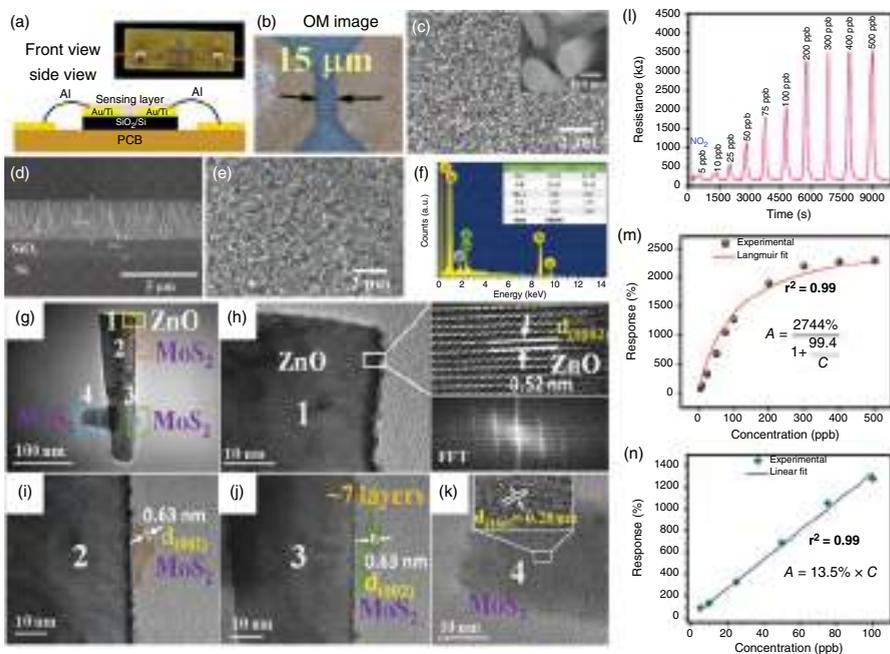
Figure 11.3 The sketch (a) and the optical micrograph image (b) of the assembled gas sensor. Low-resolution SEM image of top view (c) and the cross-sectional view of (d) the ZnO nanorods. (e) SEM image and (f) EDS spectrum of ZnO nanorods decorated with MoS$_2$ nanosheets. TEM image and the HRTEM image of the ZnO nanorods and the MoS$_2$ nanosheets in the composites (g–k). (l) Dynamic gas-sensing performance of the decorated ZnO nanorods to 5–500 ppb NO$_2$. (m and n) The relationship between the NO$_2$ concentration and the sensor response of the composite. Source: Kumar et al. [58], Reproduced with permission from Elsevier.

150 °C. If the MoS$_2$ nanosheets were directly synthesized on the surface of the SnO$_2$ nanofibers, the sensor based on the composite might exhibit a more promising sensing performance to SO$_2$ compared with the results reported by the authors.

The study of Lin et al. also revealed that the gas-sensing performance of the SnO$_2$ nanotubes could be enhanced through decorating them with MoS$_2$ nanosheet and polyaniline [60]. The SnO$_2$ nanotubes were synthesized through an electrospinning process with the working voltage being 21 kV followed by annealing at a high temperature of 500 °C in the air for two hours. The MoS$_2$ nanosheets were then decorated on the surface of the prepared SnO$_2$ nanotubes via a hydrothermal method with the raw materials of $(NH_4)_2MoS_4$ and $N_2H_4 \cdot H_2O$ at 210 °C. An in situ polymerization was applied to construct the MoS$_2$ nanosheets/SnO$_2$ nanotubes decorated with polyaniline (PMS). The results showed the specific surface area of the PMS (49.2 m^2/g) was almost the same as that of the MoS$_2$ nanosheets/SnO$_2$ nanotubes, a positive factor facilitating the adsorption and the diffusion of the gas molecules reported by the authors. The NH$_3$-sensing performance of the MoS$_2$ nanosheets/SnO$_2$ nanotubes was found to be further enhanced with the decoration of polyaniline. The sensor response (R_{gas}/R_{air}) of the MoS$_2$ nanosheets/SnO$_2$ nanotubes was just slightly higher than 1–100 ppm NH$_3$ at ~24 °C. Then the sensor response of the PMD was effectively improved to be 10.9 with a short response/recovery time being 21/130 seconds. Moreover, the sensor based on the PMS exhibited promising sensing performance to 0.5–100 ppm NH$_3$ with the detection limit being as low as 200 ppb. It was reported that the high humidity always showed negative effects on the gas-sensing performance gas sensor based on metal oxide. Interestingly, the gas-sensing response of the prepared PMS was found to have a positive relationship with the humidity in the experiment. The sensor was reported to smoothly detect 50 ppm NH$_3$ under the humidity in the range of 20–80% with the sensor response increasing from ~5 under 20% RH to ~10 under 80% RH. This was possibly attributed to the reaction between the NH$_3$ and the water molecule and the greater deprotonation rate of the reaction product than NH$_3$ on the surface of the PMS. This work also revealed that the gas-sensing performance of the 1D material/2D material composite could be further enhanced with modification of the third-phase material, which would be applied to explore new gas-sensing materials with promising material for reference.

The study of Wang et al. also showed the SnO$_2$ nanotubes decorated with MoS$_2$ nanosheets exhibited outstanding NO$_2$-sensing performance at room temperature [61]. The authors also synthesized the SnO$_2$ nanotubes via a method of electrospinning with the raw material of $SnCl_2 \cdot 2H_2O$ and the constant voltage being 15 kV combined with an annealing treatment at 500 °C. And the MoS$_2$ nanosheets were vertically grown on the surface of the SnO$_2$ nanotubes through a hydrothermal method with the $C(NH_2)_2S$ and $Na_2MoO_4 \cdot 2H_2O$ at 200 °C for 12 hours. The resistance of the obtained SnO$_2$ nanotubes decorated with MoS$_2$ nanosheets decreased quickly when the NO$_2$ was injected, indicating the n-type sensing response of the obtained composite. The sensor response (R_{air}/R_{gas}) of the decorated SnO$_2$ nanotubes was found to be 34.67–100 ppm NO$_2$, ~26.5 times higher than that of the pure SnO$_2$. And the response time was also calculated to be as short as 2.2 seconds with

the recovery time being 10.54 seconds. The low detection limit of the SnO_2 nanotubes decorated with MoS_2 nanosheets was only 10 ppb, revealing the potential application in the area of hydrogen sensors. Additionally, the composite also showed excellent sensing repeatability and long-term stability to NO_2 with promising selectivity. The enhanced chemisorbed oxygen on the surface of the composite was reported to be one factor for the improvement in their NO_2 gas-sensing performance. The formation of p–n heterojunction further provided more active sites for the gas molecules and accelerated the charge transfer between the adsorbed gas molecules and the decorated SnO_2 nanotubes, another positive factor for the enhanced NO_2-sensing response. This research further inferred that the 2D MoS_2 nanosheets could be effectively decorated on the 1D semiconducting materials with rough surfaces and improved their interactions with the gas molecules, resulting in the improved gas-sensing performances of metal oxides.

The nanocomposite film composed of MoS_2 nanosheets-decorated Co_3O_4 nanorods was reported by Zhang et al. to be the potential to detect NH_3 with high performance [62]. Both the MoS_2 nanosheets and the Co_3O_4 nanorods were synthesized through a hydrothermal method with the temperature of 200 and 180 °C, respectively. Then the sensor based on the nanocomposite film was prepared via typical layer-by-layer (LBL) self-assembly. The prepared Co_3O_4 showed typical rod-like morphology with the measured average diameter being 98.15 nm. And the average size of the MoS_2 nanosheets was found to be 197.43 nm with good distribution. The sensor response ($\Delta R/R_{air}$*100%, $\Delta R = R_{air} - R_{gas}$) of nanocomposite film showed a close relationship with the number of self-assembled MoS_2/Co_3O_4 layers. The study showed that the sensor based on the five MoS_2/Co_3O_4 layers exhibited a more promising NH_3-sensing performance compared with the one with 1, 3, or 7 layers. The value of the sensor response of the five MoS_2/Co_3O_4 layers was 8.74% toward 0.1 ppm NH_3. Meanwhile, the nanocomposite film also showed good response performance to 1–6 ppm NH_3 with an excellent recovery property in the air atmosphere. The formation of the p–n heterojunction, the build of the potential barrier, and the bending of the energy bands would take place with the MoS_2 contacting with the Co_3O_4. The release of the free electrons and the recombination of holes in the Co_3O_4 in the nanocomposite modified the concentration of carries and the height of the potential barrier, which would be responsible for the superior NH_3-sensing property of the self-assembled MoS_2/Co_3O_4. The strategy and the method used in their work might also be applied to assemble metal oxides with other 2D nanomaterials with different layers to construct promising sensing material.

A sensor based on the MoS_2 nanosheets-decorated ZnO nanowires array was reported to effectively detect NO_2 at 200 °C [63]. A simple hydrothermal method was applied to prepare the ZnO nanowires array with a smooth surface. Then a layer of Mo was deposited on the surface of ZnO via a direct current (DC) magnetic sputtering. The Mo seed layers with different thicknesses were prepared via the magnetic sputtering with controlling the sputtering time, which was the source material that would be further used to synthesize MoS_2. The MoS_2 was grown with a chemical vapor deposition process at 770 °C. The authors investigated the effects of the working temperature on the NO_2-sensing performance. The sensor response

($\Delta R/R_{N2}*100\%$, $\Delta R = R_{gas} - R_{N2}$) of the composite at 200 °C was found to be ~30%, approximately five times higher than that at room temperature (~6%). Meanwhile, the sensor response of the composite was highly dependent on the thickness of the MoS_2 nanosheets. The research showed that the composite with the magnetic sputtering time being five minutes exhibited a more outstanding NO_2-sensing performance compared with the other samples, showing a promising sensor response that was three times higher than that of the one with the sputtering time being one minute. As it was pointed out in the study, the thin MoS_2 layer persisted the conductive layer in the sensing material under the effect of interface depletion, which would result in poor sensitivity to NO_2. The too thick MoS_2 layer that made the depletion layers formed in the composite little effect the resistance of the MoS_2/ZnO nanowires. The enhanced sensing performance of the composite was attributed to the recombination of the electrons and the holes in the sensing material and the modification of the width of the depletion layer between the MoS_2 nanosheet and the ZnO nanowires. The uniform ZnO nanowires arrays were also a positive factor for the outstanding NO_2-sensing performance due to their role of channel for the transfer of carries, which could be a possible structure applied to improve the gas-sensing properties of metal oxides decorated with 2D nanosheets. The resistance of the sensor based on the prepared composited in their work was found to be unable to recover to the original level during the sensing process, which might indicate that the stability of the assembly sensor should be further explored and improved.

The 1D TiO_2 nanotubes decorated by 2D MoS_2 nanosheets, reported by Liang et al., were found to be sensing material to detect alcohol [64]. The TiO_2 nanotubes arrays were synthesized through anodization of untreated titanium foils with the water/ethylene glycol and NH_4F. The applied anodization voltage was 60 V with a time of two hours. The synthesized TiO_2 nanotubes were clearly in order with the average diameter and the average wall thickness of 120 and 20 nm, respectively. Then the small-size MoS_2 nanosheets were modified on the surface of the uniform TiO_2 nanotubes with the source materials being $MoCl_5$ and $Na_2S \cdot 9H_2O$ through a hydrothermal method at 180 °C. The synthesized MoS_2 nanosheets increased the wall thickness of the nanotubes to be 90 nm. And the specific surface area of the TiO_2 nanotubes was also increased from the original value of 26.8–47.4 m^2/g when they were decorated with MoS_2 nanosheets, indicating the positive effects of MoS_2 on the TiO_2 nanotubes. The pure TiO_2 nanotubes exhibited n-type sensing performance to alcohol, while the ones decorated with MoS_2 nanosheets showed a contrary p-type sensing property. The n-type sensor response (R_{air}/R_{gas}) of the TiO_2 nanotubes was found to be only 1.3–100 ppm alcohol at 150 °C, so low that the TiO_2 nanotubes could not be effective to sense alcohol. When the TiO_2 nanotubes were decorated with MoS_2 nanosheets, the p-type sensor response (R_{gas}/R_{air}) was successfully improved to be as high as 14.2, further indicating the positive effects of MoS_2 on the sensing performance of TiO_2 nanotubes. It was reported the high surface area of the MoS_2 nanosheets, the fast transportation of electrons through vertical tube walls of TiO_2, and the formation of heterojunctions between them were the main factors to enhance the alcohol sensing of the composite. This research revealed that

the nanotubes array were effective channels for the carriers, and their gas-sensing performance could be positively improved via decorating with 2D nanomaterials.

The study of Li et al. also revealed that the MoS_2 nanosheets could be applied to effectively enhance the sensing response of Si nanowires to NO_2 at room temperature [65]. The silicon wafer was firstly cut and cleaned and then treated with 5% HF to remove the layer of silicon oxide layer on its surface. A layer of Ag nanoparticles was prepared on the surface of the treated silicon wafer. The Si nanowires array was obtained with a further chemical etching in the solution of HF and H_2O_2 at 30 °C. The results showed that the average length of the prepared Si nanowire was approximately 6 μm with a rough surface and clustered tip. To obtain the MoS_2-decorated Si nanowire, a layer of Mo was deposited on the surface of the Si nanowires via a DC magnetic sputtering and then was sulfurized through a method of the chemical vapor deposition with the temperature of 770 °C. The deposition rate of the MoS_2 nanosheets on the surface of Si nanowires was measured to be approximately 20 nm/min. It was reported that the gas-sensing performance of MoS_2-decorated Si nanowire with the deposition time being three minutes was superior compared with that of the one being deposited with the time of one or five minutes. The obtained MoS_2-decorated Si nanowires with the optimal deposition time exhibited promising sensing performance to NO_2 with different concentrations of 1–50 ppm It should be noted that the recovery process was found to be not fully completed during the sensing circle. The sensor response ($\Delta R/R_{N2}$*100%, $\Delta R = R_{gas} - R_{N2}$) of the Si nanowires was extremely improved through decorating with MoS_2 nanosheets. The sensor response of the composite was 28.4% toward 50 ppm NO_2, ~2.5 times higher than that of the pure Si nanowires (~10%). The MoS_2 nanosheets decorated on the Si nanowires introduced more active sites for the gas molecules, and the abundant S vacancies also facilitated the adsorptions of more NO_2 molecules on the composite. Furthermore, there would be a band bending taking place when the Si nanowires were composited with MoS_2, resulting in the formation of a potential barrier between their surfaces. The adsorption of NO_2 during the sensing process would capture the charges from the MoS_2 and then modify the height of the potential barrier in the composite, improving the sensing response of the composite. The authors have systematically studied the NO_2-sensing performance of the MoS_2-decorated Si nanowires and indicated that the MoS_2 could also be used to enhance the gas-sensing property of the semiconductor (not metal oxides).

11.2.3 WS$_2$-based Composite

The structure of the WS_2 was similar to that of the MoS_2 discussed ahead, which has been used to enhance the gas-sensing property of metal oxide. The sheet-like WS_2 was also applied to decorate metal oxide to effectively modify their gas-sensing property [66]. The gas-sensing performance of the ZnO nanorods was successfully enhanced via decorating them with uniform WS_2 nanosheets, which was reported by Fauzia and his group. In their work, a seed layer was prepared through a method of ultrasonic spray pyrolysis with the source material being Zn acetate dihydrate on the glass substrate. Then, a facile hydrothermal method was applied to grow the

uniform ZnO nanorods array with the raw materials being Zn nitrate tetrahydrate and hexamethylenetetramine at a low temperature of 95 °C for six hours. The WS_2 nanosheets were prepared via a probe sonication technique to exfoliate the nanosheets from the bulk WS_2. The obtained WS_2 was then spin-coated on the ZnO nanorods to assemble the composite (Figure 11.4a–f). Then the prepared composite was dried in air to obtain the stable gas sensor, as shown in Figure 11.4g. Meanwhile, the content of the WS_2 nanosheets was adjusted by modifying the deposition circles. There were two different composites assembled with the deposition circle being 1 or 3, named as ZnO/WS_2 1× or ZnO/WS_2 3×, respectively. The sensor response was defined as $(C_x - C_{18})/C_x*100\%$, in which the C_x and the C_{18} represented the capacitance of the sensor in target humidity or 18% RH, respectively. The sensor response of the sensor based on pure ZnO or WS_2 to the humidity of 85% RH was 73.10 or 30.51, respectively. This sensor response was effectively improved to be 87.28 or 378.05 for ZnO/WS_2 1× or ZnO/WS_2 3×, respectively. The recovery time of the composite was almost the same as that of the pure ZnO or MoS_2, being in the range of 25.67–27.69 seconds (Figure 11.4h,i). While, the response times for ZnO/WS_2 1× or ZnO/WS_2 3× were calculated to be 41.38 or 74.51 seconds (Figure 11.4j,k), respectively. The humidity-sensing performance of the WS_2-decorated ZnO nanorods was reported to be attributed to the adsorption of water molecules on their surface. In the prepared composite, the WS_2 nanosheets also provided adsorption sites for the water molecules and made more gas molecules interact with the composite during the sensing process. And the authors also reported that the n–n heterojunction between the ZnO and WS_2 induced the establishment of an accumulation layer on one side of the ZnO/WS_2 interfaces, which would effectively increase the water dissociation rate. These two factors were mainly responsible for the improvement of the humidity-sensing property of the WS_2-decorated ZnO nanorods. This research indicated that the 2D WS_2 could also be the potential to enhance the gas-sensing performance of metal oxides.

Furthermore, the WS_2 nanosheets were found to be effective to enhance the NO_2-sensing performance of highly porous SiO_2 nanorods at room temperature (25 °C) [67]. The 1D SiO_2 nanorods were synthesized via a method of glancing angle deposition with an e-beam evaporator. The authors have deposited a series of SiO_2 nanorods with the same thickness of approximately 500 nm but different glancing angles of 75°, 77.5°, 80°, 82.5°, or 85°. The prepared SiO_2 nanorods were then treated with UV-O_3 cleaner and were further spin-coated with a solution of WCl_6. The WS_2 was decorated on the surface of the SiO_2 nanorods through a CVD system with two separated furnaces for sulfur and pretreated nanorods. The result showed that the WS_2 deposited at 85° presented a highly porous morphology. And the glancing angles also had significant effects on the NO_2-sensing performance of the SiO_2 nanorods at room temperature. The WS_2 deposited at 82.5° exhibited an optimal sensor response ($\Delta R/R_{gas}*100\%$, $\Delta R = R_{air} - R_{gas}$) of 151.24% to 5 ppm NO_2 at room temperature, which was over six times higher than the bare WS_2 thin film (22.96%). Moreover, the sensor based on the WS_2 deposited at 82.5° also exhibited a promising sensing property to 400 ppb NO_2 with the theatrical detection limit being as low as 13.726 ppb. The enhanced NO_2 gas-sensing performance of the composite could be
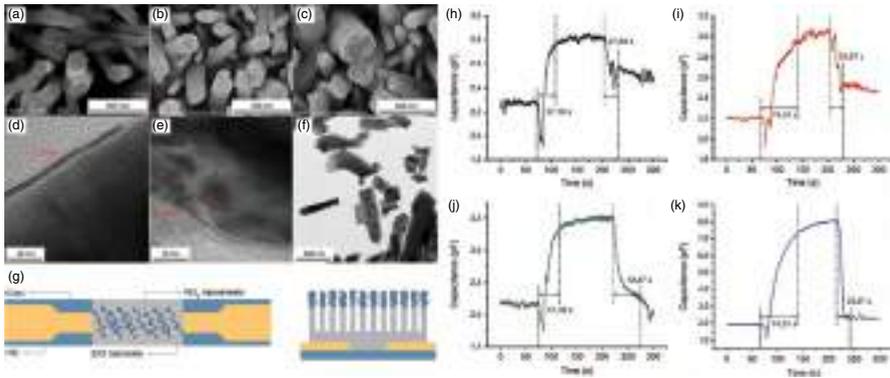
Figure 11.4 FESEM and TEM images of (a) ZnO, (b, d) ZnO/WS$_2$ 1×, (c, e) ZnO/WS$_2$ 3×, (g) the sketch of the assembled sensor, humidity sensing performance of sensor based on (h) WS$_2$, (i) ZnO, (j) ZnO/WS$_2$ 1×, or (k) ZnO/WS$_2$ 3×. Source: Dwiputra et al. [66], Reproduced with permission from Elsevier.

attributed to the highly porous structure of the vertically aligned SiO_2 nanorods decorated with WS_2 and the exposed edge sites of the WS_2. The porous structure and the high specific surface area of the composite facilitated more gas molecules diffused into the sensing material and adsorbed on its surface. And more edge sites of the WS_2 also enhanced the interaction between the gas molecule and the sensing substrate, further improving the NO_2-sensing performance of the SiO_2 nanorods decorated with WS_2. But only a few reports were focusing on this promising nanosheet up to now. More potential sensing materials could be constructed via decorating metal oxides with WS_2 nanosheets.

11.2.4 ZnO-based Composite

The ZnO nanosheet was also one of the popular 2D materials and has also been proved to be effective to improve the gas-sensing performance of 1D material. The investigation of Wang et al. revealed that the hydrogen-sensing performance of the Zn_2SnO_4 nanowires was effectively enhanced by decorating them with ZnO nanosheets [68]. In their work, the ZnO nanosheets decorated with Zn_2SnO_4 were prepared with a method of the metallic catalyst-assisted thermal evaporation of ZnO, SnO_2, and active carbon. A layer of Au with a thickness of 5 nm was firstly deposited on the surface of the substrate of the Si wafer via a sputtering method. Then a mixture of active carbon, ZnO, and SnO_2 powders was thermally evaporated to prepare the Zn_2SnO_4 decorated with ZnO at 800 °C with the pressure of 300 Torr in N_2, as shown in Figure 11.5a–c. Then a thin layer of Pd was also sputtered on the synthesized decorated Zn_2SnO_4 nanowires to assemble the gas sensor (Figure 11.5d–f). The result showed that the sensor based on the composite exhibited promising sensing performance toward 2–1000 ppm H_2 at the working temperature being 120, 200, 255, 270, or 300 °C (Figure 11.5g–j). The sensor response ($\Delta R/R_{air}*100\%$, $\Delta R = R_{air} - R_{gas}$) of the sensor based on the ZnO-decorated Zn_2SnO_4 was 46% at the working temperature of 270 °C. With the sputtering of the Pd layer, the sensor response was further improved to be 74% and the working temperature was decreased to be 255 °C. The response time of the Pd-coated composite was 28 seconds to 1000 ppm H_2, also shorter compared to that of the bare ZnO-decorated Zn_2SnO_4 (41 seconds). And the Pd-coated composite exhibited excellent repeatability, selectivity, and long-term stability toward H_2, further indicating the potential of the composite in the area of hydrogen sensor. It should be noted that the sensor response of the composite was not high, which might be further improved to better meet the demands of practical application.

Meanwhile, Tian et al. have also synthesized a similar composite of ZnO-decorated Zn_2SnO_4 nanowire through a different method of a hydrothermal process combined with calcination [69]. The ZnO-decorated Zn_2SnO_4 nanowire in their research was reported to show outstanding sensing response to TEA at 200 °C. The raw materials of ZnO powder, $SnCl_4 \cdot 5H_2O$, and ZnOH were used to prepare the precipitates via a hydrothermal method at 200 °C for 20 hours. Then ZnO-decorated Zn_2SnO_4 nanowires were synthesized through annealing the obtained precipitates at 450 °C for two hours. The result showed there were numerous nanosheets contacted on the surface of the nanowires with an average diameter of 36.6 nm. And the
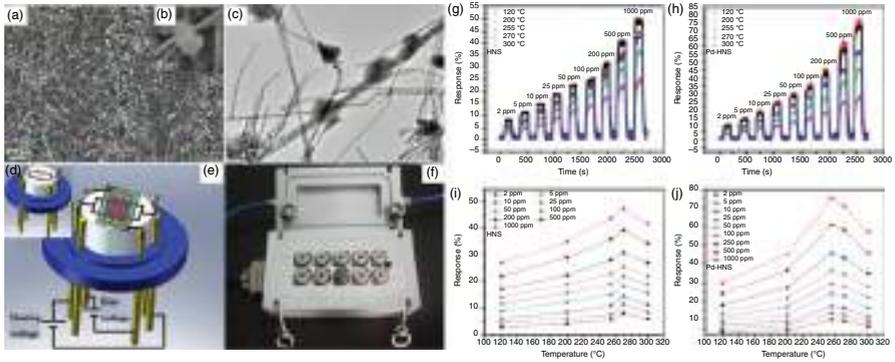
Figure 11.5 SEM images (a and b) and TEM image (c) of the ZnO-decorated Zn_2SnO_4 nanowires. The 3D schematic diagram of the heater (d) and the sensor (e), test gas chamber (f). The dynamic sensing performances of the sensor based on the ZnO-decorated Zn_2SnO_4 nanowires (g) and the Pd-decorated composite to 2–1000 ppm H_2 at various working temperatures (h). The relationship between the operating working temperature and the sensor response of the ZnO-decorated Zn_2SnO_4 nanowires (i) and the Pd-decorated composite (j). Source: Wang et al. [68], Reproduced with permission from Elsevier.

XRD pattern confirmed that the nanosheet and the nanowire in the composite were ZnO and Zn_2SnO_4 with the phase being hexagonal wurtzite and cubic spinel, respectively. The sensing response of the sensor based on the ZnO-decorated Zn_2SnO_4 was found to be effectively improved. The sensor response (R_{air}/R_{gas}) of the pure ZnO or Zn_2SnO_4 was 5.7 or 3.7, respectively, to 100 ppm TEA at 200 °C. Then the sensor response was improved to be 175.5 for the ZnO-decorated Zn_2SnO_4 nanowires. Moreover, the composite also exhibited promising sensing properties to 10–200 ppm TEA at 200 °C. The sensor response of the composite was 292.4–200 ppm TEA at 200 °C, so high indicating its great potential in the TEA sensor. And the sensor based on the composite also exhibited a short response time or recovery time to 100 ppm TEA, being 13 or 189 seconds, respectively. The special surface area of the composite was 19.11 m²/g, over 1.5 times higher than that of the pure ZnO (12.49 m²/g). The high special surface area would make more gas molecules adsorbed on the surface of the composite. The unique hierarchical structure of the composite also resulted in the establishment of a space charge layer and electron depletion layer, another factor being responsible for the improvement of the TEA sensing response. In addition, the building of heterojunction between the ZnO and the Zn_2SnO_4 would form an accumulation layer in the side of ZnO, making more oxygen molecules adsorbed and more charges captured. Therefore, the sensor based on the composite exhibited enhanced TEA sensing property.

Cho et al. have also constructed a novel sensor based on the heterojunctions of p-CuO nanowire and n-ZnO nanosheets [70]. The sensor based on the heterojunctions1 was found to show promising near-UV-sensing performance. According to the study of ZnO-decorated Zn_2SnO_4, the sensor based on the heterojunctions of p-CuO nanowire and n-ZnO nanosheets might also be the potential to exhibit outstanding gas-sensing performance under the UV.

Up to now, only a few researches were focusing on the improved gas-sensing performances of 1D nanostructures decorated with ZnO nanosheets. More attention should also be paid to this sheet-like metal oxide, because the ZnO has been proved to be effective to detect various gases. There would be more effective gas-sensing material assembled by decorating the metal oxides with 2D ZnO nanosheets.

11.2.5 NiO-based Composites

The NiO sheets with porous structures were reported to be positive to improve the gas-sensing performance of the ZnO nanorods [71]. The ZnO nanorods were synthesized with a hydrothermal method with source material of $Zn(CH_3COO)_2·2H_2O$ and the PH of 10 at 180 °C for 14 hours. The NiO nanosheets were decorated on the surface of the prepared ZnO nanorods via a hydrothermal route with the source material being $NiCl_2·6H_2O$ at a low temperature of 140 °C for 10 hours. The ZnO nanorods with a length of 1–3 μm were uniformly decorated with porous NiO nanosheets. The sensor was assembled via coating the paste composed of the prepared powders and deionized water on a ceramic tube. The sensor response of the pure ZnO (or NiO) was obtained to be 34.67 (or 85.88) to 100 ppm acetone at 200 °C (or 320 °C). Then the sensing performance of the NiO/ZnO composite was

significantly improved compared with the pure NiO or ZnO. The sensor based on the composite exhibited a high sensor response (R_{air}/R_{gas}) of 205.14–100 ppm acetone at the working temperature of 240 °C, which was two or six times higher than that of the pure ZnO or NiO, respectively. Moreover, the NiO/ZnO composite also showed a short response time or recovery time of 7 or 20 seconds, respectively, to 100 ppm acetone. In addition, the composite presented outstanding sensing selectivity toward acetone with sensing stability over 60 days. The larger specific surface area of the composite with more active sites facilitated the adsorptions of gas molecules on the sensing material compared with the pure ZnO or NiO. And the porous structure of the composite was also a positive factor improving the diffusion of gas molecules into the sensing materials. The formation of p–n heterojunction and the modulation of the width of the depletion layer between the interfaces between the NiO and ZnO made the resistance be changed more effectively, further resulting in the enhancement of the sensing response of the composite. The authors prepared a potential sensing material of NiO-decorated ZnO nanorods with promising acetone-sensing performance via a simple hydrothermal method. The working temperature was over 200 °C, which might be negative to full its application. There would have to be a heater in the sensor, increasing the power dissipation and the volume of the sensor. More attention should be paid to decreasing the working temperature of the composite, an issue to be overcome to further improve the comprehensive performances of sensors based on metal oxides.

The vertically aligned ZnO nanorods arrays decorated with 2D NiO nanosheets were, reported by Hur et al., effective to sense NO_2 [72]. The ZnO nanorods were synthesized with a hydrothermal method with the raw materials of diethanolamine, zinc acetate dehydrate, 2-methoxyethanol, zinc nitrate hexahydrate, and hexamethylenetetramine. A seed layer was firstly prepared on SiO_2/Si wafer, and then a hydrothermal process was conducted at a low temperature of 90 °C for five hours to synthesize the uniform ZnO nanorods array with the average diameter of ~800 nm. Then a layer of Ni seed was also preprepared on the surface of the ZnO nanorods and was further exposed to a mixed aqueous solution of nickel acetate tetrahydrate. Finally, the prepared composite was annealed in air at 400 °C to obtain the stable NiO-decorated ZnO. The growth time of the NiO showed a significant effect on the morphology of the composite, and there was also a close relationship between the content of NiO and the decorated ZnO nanorods. The sensor based on the decorated ZnO nanorods with the growth time of the NiO being 30 min exhibited the highest sensor response toward NO_2 among all the studied composites. The sensor response ($\Delta R/R_{gas}$*100%, $\Delta R = R_{gas} - R_{air}$) of the composites was calculated to be ~350%, which was three times or ~six times higher than that of the pure ZnO nanorods or NiO nanosheets, respectively. Meanwhile, the response time of the composite was also shorter compared with that of the NiO nanosheets. The surface area of the ZnO nanorods was effectively improved with the decoration of 2D NiO nanosheets, which was a positive factor that made more NO_2 molecules adsorbed on the surface of the composite. And there would be heterojunctions formed between ZnO and NiO, the electron depletion regions around which also adsorbing more NO_2 in the composite. In addition, the authors pointed out that the transfer of electrons and

holes between NiO and ZnO could maintain the adsorption of NO_2 on the surface of the composite, another factor being responsible for the enhanced NO_2-sensing performance of the ZnO nanorods decorated with NiO nanosheets. The method of preparing seed layers to synthesize the ZnO nanorods or the NiO nanosheets was an interesting and possible way to obtain uniform nanomaterials at low temperatures. The synthesizing temperature of the ZnO nanorods or the NiO nanosheets was 90 °C, paving a possible method to prepare the metal oxide and the 2D nanosheets at low temperatures.

Park et al. have fabricated a novel sensing material of WO_3 nanorods decorated with 2D NiO nanosheets and studied their potential sensing response toward acetaldehyde [73]. Their work revealed that the decorated NiO nanosheets could also be applied to decorate the WO_3 nanorods to improve their acetaldehyde sensing performance at 250 °C. A simple hydrothermal chemical route was applied to synthesize the composite. In their study, the NiO nanosheets were prepared via a hydrothermal process at 200 °C for 10 hours with the raw materials of $Ni(NO_3)_2 \cdot 6H_2O$ and NaOH. Then the WO_3 was synthesized with the $Na_2WO_4 \cdot 2H_2O$ and could be obtained with the hydrothermal method at 180 °C for 24 hours. The thickness of the prepared NiO was approximately 6 nm, and the average length and width of the WO_3 were reported to be 3.5 μm and 56 nm, respectively (Figure 11.6a,b). The composite was prepared by just mixing the obtained NiO nanosheets and the WO_3 nanorods. The composite with proportions of NiO nanosheets and WO_3 nanorods being 15 : 85 (NW2) exhibited a higher response to acetaldehyde compare the pure WO_3 and other composites with different proportions (Figure 11.6c,d). The decorated WO_3 with optimal proportion showed a promising sensing response to 20–100 ppm acetaldehyde at 250 °C with outstanding repeatability to 100 ppm acetaldehyde (Figure 11.6e–f). The sensor response ($\Delta R/R_{air}$*100%, $\Delta R = R_{gas} - R_{air}$) of the composite was 2184% to 100 ppm acetaldehyde at 250 °C with the response/recovery time being 1177/632 seconds. There would be n–p heterojunctions forming between the n-type WO_3 and the p-type NiO. The transfer of holes and electrons across their surfaces would form the depletion regions around heterojunctions and facilitate the adsorptions of oxygen gas molecules in the air and the target acetaldehyde molecules and improve their reactions. Then the released electrons recombined with the holes in the NiO, decreasing the net concentration of holes. The depletion region would also be widened with the migration of conduction electrons from WO_3. Then the sensing property of the sensor based on the NiO was effectively improved by decorating with WO_3. The WO_3 nanorods decorated with NiO nanosheets could be potential to effectively detect acetaldehyde with a relatively high sensor response. It would be better for the composite to decrease the sensor response time and recovery time, which should be overcome and be of great importance to further improve the application of sensors based on the metal oxides decorated with 2D NiO nanosheets.

11.2.6 Other 2D material-decorated 1D nanomaterial

The research of Zhang et al. revealed the ZnO nanoflowers, consisting of rod-like ZnO, decorated with Sb-doped SnO_2 nanosheets were effectively to detect NO_2 with
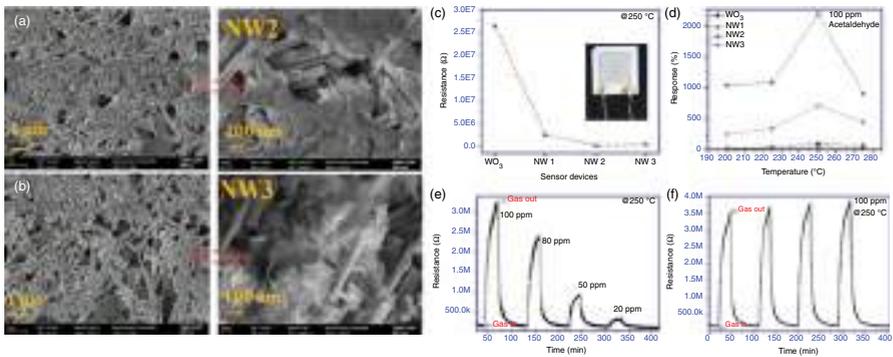
Figure 11.6 SEM images of NiO-decorated WO$_3$ with their proportions (wt%) being 15:85 (NW2, a) or 25:75 (NW3, b). (c) The resistance of the pure WO$_3$ or the composite with different proportions, the inset is the digital image of the assembled sensor. (d) The sensor response of the pure WO$_3$ or the composite under different working temperatures. (e) The dynamic sensing performance of NW2 sensor to 20–100 ppm acetaldehyde at 250 °C. (f) The sensing repeatability of NW2 to 100 ppm acetaldehyde at 250 °C. Source: Nakate et al. [73], Reproduced with permission from Elsevier.

low concentrations of 100–1000 ppb [74]. In the study, the ZnO nanorods were prepared with a microwaved hydrothermal method via raw materials being NaOH and $Zn(CH_3COO)_2·2H_2O$ at 200 °C for 15 minutes. The obtained ZnO nanorods showed average length and diameter being ~6 μm and 500 nm, respectively. The Sb-doped SnO_2 nanosheets were then synthesized via a microwaved hydrothermal method. The morphology of the Sn-doped SnO_2 was significantly affected by the concentration of the doped Sn. The undoped SnO_2 exhibited typical nanowire-like morphology, but the morphology of the doped SnO_2 gradually changed to be nanosheets. It was observed that there were uniform SnO_2 nanosheets decorated on the surface of ZnO nanorods when the concentration of doped Sn was elevated to be 3%. The sensor response ($\Delta R/R_{N2}$, $\Delta R = R_{gas} - R_{N2}$) of the composites consisting of the Sb-doped SnO_2/ZnO heterojunctions increased with the increase of the doped Sb. The sensor response of the SnO_2/ZnO heterojunctions with the concentration of doped Sb being 7% was ~9.5 to 1000 ppb NO_2, one time higher than that of the one with the Sb being 1% (5.7). The response time of the composites of Sb being 7% was calculated to be only 16 seconds toward 1000 ppb NO_2, also shorter than that of the one with Sb of 1% (100 seconds). The sheet-like Sb-doped SnO_2 provided more active sites for the gas adsorption compared with the nanowire-like SnO_2. And more NO_2 was also adsorbed on the surface of the doped SnO_2 when the Sn^{4+} was replaced by Sb^{5+} or Sb^{3+}. Therefore, there would be more gas molecules adsorbed on the surface of the ZnO nanorods decorated with Sb-doped SnO_2 nanosheets during the response and recovery process, resulting in the enhanced gas-sensing performance of the heterojunctions. This study provided a possible and fast way to synthesize the 1D metal oxides decorated with 2D metal oxides, which would be promising to design novel sensing materials with heterostructure to exhibit outstanding sensing material.

Vertically ultrathin SnO_2 nanosheets were also grown *in situ* on the quasi-1D SiC nanofibers to form hierarchical architecture by a two-step method [75]. The SiC nanofibers were firstly prepared and then was immersed into the precursor with the raw material of $SnCl_2·2H_2O$ to synthesize the SnO_2 nanosheet-decorated SiC via a simple hydrothermal process at 100–180 °C for six hours. Finally, the samples were calcined at 600 °C for two hours to obtain the SnO_2 nanosheet-decorated SiC nanofibers. The sensor based on the composited showed a sensor response (R_{air}/R_{gas}) of ~23 toward 100 ppm ethanol at 350 °C with the response time and the recovery time being four and six seconds, respectively. Furthermore, the hierarchical composite also exhibited a superior gas-sensing performance including high sensor response, excellent repeatability, and outstanding selectivity toward ethanol among the target gases. This work highlighted the possibility to develop a novel high-performance gas sensor based on 1D/2D hybrids used in harsh environments.

Wang et al. have reported a sensor based on Pt single atoms-decorated SnO_2 nanorods-loaded on SiC nanosheets with excellent C_2H_5OH-sensing property at 350 °C [76]. The SiC nanosheets were synthesized with a method of carbothermal reduction with the raw materials of Si powder and GO. Then the prepared SiC nanosheets were further treated by a hydrothermal reaction at 150 °C for the loading of abundant active sites (–OH). The functional SiC nanosheets could be a possible substrate for anchoring SnO_2 nanorods on their surfaces via a one-step colloidal

synthesis. The formed SnO_2 nanorods showed an average length and diameter of 8 and 2 nm, respectively (Figure 11.7a,b). Finally, the Pt single atoms were decorated on the SnO_2-loaded SiC nanosheets through a wet impregnation method combined with carefully controlling the concentration of H_2PtCl_6 in the prepared precursor. An aberration-corrected high-angle annular dark-field scanning transmission electron microscopy (HAADF-STEM) clearly illustrated that the dispersed Pt was 0.1–0.2 nm (Figure 11.7c), reasonably indicating that the single-atom Pt was successfully synthesized in the composite. The exquisite structure and the highly active Pt composite (Figure 11.7d) showed excellent gas-sensing performance at 350 °C with a high sensor response (R_{air}/R_{gas}) of 119.75 ± 3.90 toward 500 ppm ethanol (Figure 11.7e). Meanwhile, the Pt-decorated SnO_2-loaded SiC nanosheets also exhibited a promising sensor response of ~1.4 to 500 ppb ethanol with the response time and recovery time of ~14 and ~20 s (Figure 11.7f,g), respectively, further inferring the potential application of the composite to detect ethanol. Additionally, the sensor based on the prepared composite also exhibited outstanding sensing repeatability, long stability, and selectivity to ethanol at 350 °C (Figure 11.7h–j). The enhanced ethanol sensing property of the composite was mainly attributed to the formation of heterojunctions, the high-catalytic single-atom Pt for facilitating the generation of negative oxygen species, the large specific surface area, and the abundant active sites in the composite. This research revealed that the gas-sensing property of the SnO_2-based materials could be enhanced with the help of single-atom Pt. In addition, the facile method to efficiently synthesize the single-atom Pt and the design of novel ternary sensing material is also a possible way to assemble gas sensors with exciting sensing properties.

Xu and his workmates have synthesized the MoO_3 nanorods and then decorated them with porous $NiCO_2O_4$ nanosheets to improve their ethanol sensing performance [77]. The uniform MoO_3 nanorods were prepared via a hydrothermal method with the source material of Mo powder and H_2O_2 at 180 °C for 24 hours. The obtained MoO_3 exhibited typical rod-like morphology with a clean surface. The average length or width of the MoO_3 nanorods was reported to be approximately 20 μm or 200 nm, respectively. The uniform MoO_3 nanorods were then decorated with porous $NiCO_2O_4$ nanosheets through a route of chemical deposition with the $Ni(NO_3)_2 \cdot 6H_2O$, 2 mmol $Co(NO_3)_2 \cdot 6H_2O$, and 15 mmol $CO(NH_2)_2$ at 95 °C for two hours. The decoration of $NiCO_2O_4$ nanosheets increased the width of the MoO_3 nanorod to be 500 nm, and the composite was well dispersed with porous surfaces (Figure 11.8a–h). The sensor based on the composite exhibited a typical p-type sensing performance toward ethanol with the concentration of 50–1000 ppb at 350 °C (Figure 11.8i). However, the pure MoO_3 nanorods or the bare $NiCO_2O_4$ nanosheets exhibited no obvious sensing response to the ethanol vapor, indicating their poor sensing property. The sensor response (R_{gas}/R_{air}) of the composite to 50 ppb ethanol was 2.7, and the sensor response was increased to be 20 when the concentration of ethanol was increased to be 1000 ppb (Figure 11.8j). Moreover, the composite also showed excellent sensing repeatability and stability to ethanol with high selectivity. The special surface area of the MoO_3 nanorods was effectively increased when they were decorated with $NiCO_2O_4$ nanosheets, which would fascinate more oxygen molecules chemically adsorbed on their surfaces. And the porous structure of the composite
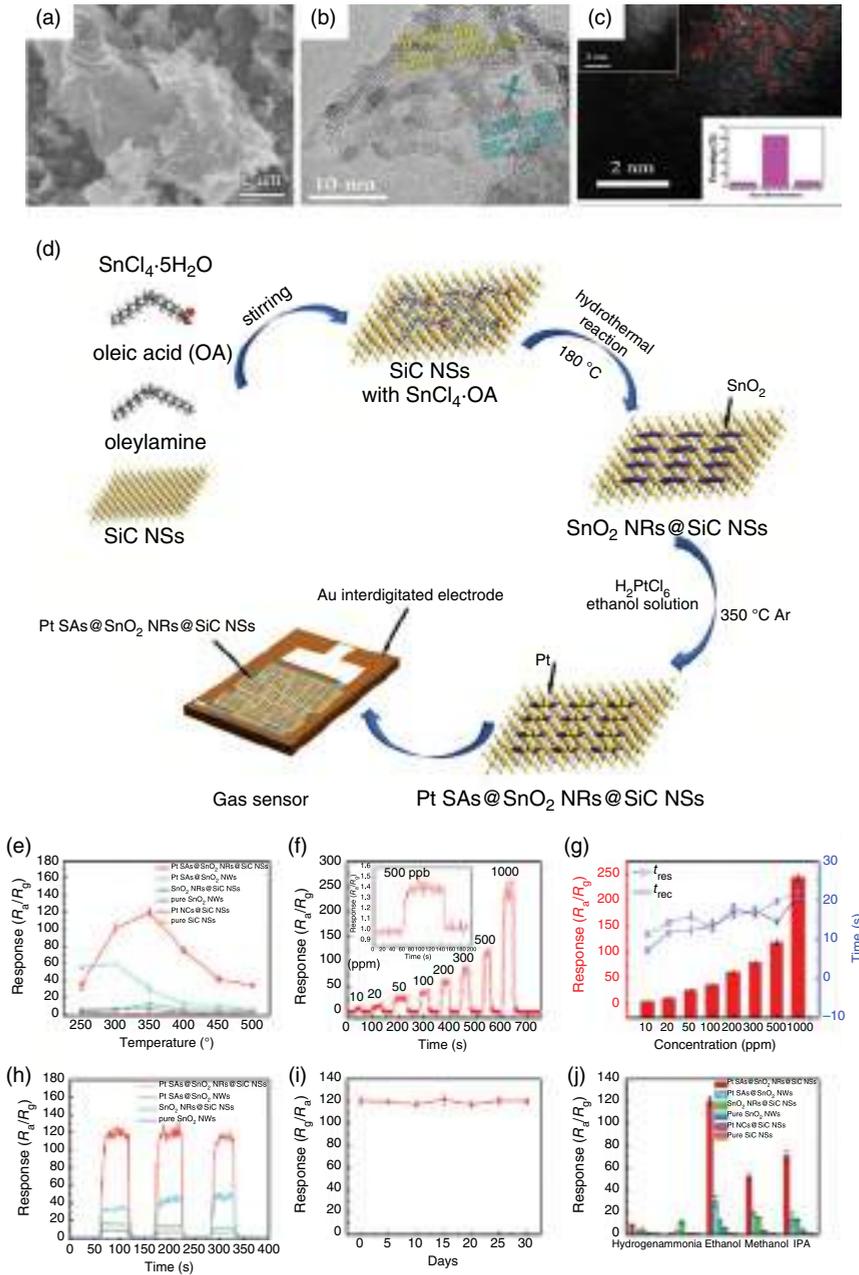
Figure 11.7 (a) SEM image, (b) TEM image, and (c) high-resolution HAADF-STEM images of Pt single atoms-decorated SnO_2 nanorods loaded on SiC nanosheets. (d) The sketch of the process to synthesize the composite and assemble the gas sensor. (e–j) The corresponding gas-sensing performances of the sensors based on the synthesized sensing materials at 350 °C. Source: Sun et al. [76], Reproduced with permission from American Chemical Society.

could be another positive factor for the gas adsorption and diffusion, which would further improve the gas-sensing performance. It was reported that the heterojunctions between $NiCo_2O_4$ and α-MoO_3 would promote the chemical adsorption of oxygen molecules on MoO_3 due to the existence of an electron accumulation layer with a high electron concentration. Then more electrons were captured in MoO_3, and this process would also make more electrons transferred from $NiCO_2O_4$, increasing the hole concentration of holes in the side of $NiCO_2O_4$ and resulting in the low resistance of the composite in air. When the ethanol was introduced, the reaction between the promoted chemisorbed oxygen species and the ethanol would release more electrons back to the composite than the pure MoO_3, significantly decreasing the hole concentration in $NiCO_2O_4$ and improving the sensor response of the composite. In the research, the effect of the content of the decorated $NiCO_2O_4$ was not reported, an important factor to fully understand the sensing performance of the composite. The sensor based on the composited with optimal content of $NiCO_2O_4$ might be exhibited a higher sensor response to ethanol at a lower working temperature (Figure 11.8).
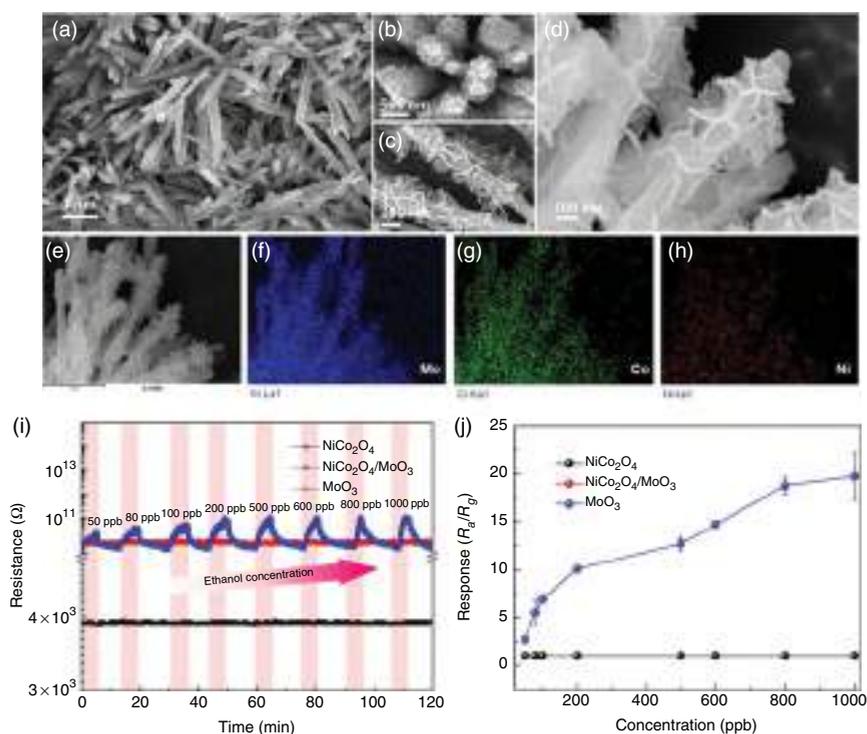
Figure 11.8 (a–d) SEM images, (e) TEM image, and (f–h) corresponding elemental mapping images of MoO_3 nanorods decorated with porous $NiCo_2O_4$ nanosheets. (i) Dynamic sensing performance of pure MoO_3 nanorods, bare $NiCo_2O_4$ nanosheets, or the $NiCo_2O_4$-decorated MoO_3 nanorods to 50–1000 ppb to ethanol at 350 °C. The assembled sensor is similar to that shown in the inset in Figure 11.6c. (j) The corresponding concentration-dependent gas sensor response of $NiCo_2O_4$-decorated MoO_3 nanorods. Source: Xu et al. [77], Reproduced with permission from Elsevier.

The study of Xu et al. showed that the novel heterostructure of Co_3O_4 nanowire array modified with $ZnSnO_3$ nanosheets was fabricated in situ on flat alumina substrates with Pt interdigitated electrodes and Pt heaters via a simple hydrothermal method without seed layers [78]. The gas-sensing measurement revealed that the Co_3O_4–$ZnSnO_3$ composite arrays showed a sensor response of 5.57 (R_{gas}/R_{air}) toward 100 ppm ethanol at 300 °C, which was 2.04 times higher than that of Co_3O_4 nanowire arrays. A similar structure of Co_3O_4 nanowires decorated with $NiMoO_4$ nanosheets was also established via a similar method by the same team [79]. The sensor based on the $NiMoO_4$-decorated Co_3O_4 nanowire array was also exhibited a higher sensor response of 17.12 toward 100 ppm trimethylamine at 250 °C, 3.91 times higher than that of Co_3O_4 arrays (4.39).

The work of Wang and his team revealed that the composite film of few-layer black phosphorus nanosheets and ZnO nanowires could be utilized to detect NO_2 at room temperature [80]. The black phosphorus nanosheets were synthesized via an exfoliation method, and the composite was prepared via mixing the black phosphorus nanosheets and the ZnO nanowires. The sensor response ($\Delta R/R_{air}$*100%, $\Delta R = R_{gas} - R_{air}$) of the pure black phosphorus nanosheets was reported to be only 37.7% to 50 ppb NO_2 at 25 °C. Then the sensing performance of the composite was effectively enhanced with a higher sensor response of 74% to the NO_2 with the same concentration.

The g-C_3N_4 nanosheets were also applied to modify the SnO_2 nanorods to successfully improve their ethanol sensing response [81]. The flower-like SnO_2/g-C_3N_4 nanocomposites were synthesized via a facile hydrothermal method with the source materials of $SnCl_4 \cdot 5H_2O$ and urea. It was found that the composite with the content of g-C_3N_4 being 7 wt% showed a better sensing performance toward ethanol compared with that of the one composited with the content of g-C_3N_4 being 0, 5, or 9 wt%. The composite with the optimal content exhibited a sensor response (R_{air}/R_{gas}) of 1150–500 ppm ethanol at 340 °C, three times higher than that of the pure SnO_2 (43). In addition, the working temperature was also decreased from the original 360 °C for the pure SnO_2 nanowires to 340 °C for the composite.

These researches illustrated that a majority of the reported 1D/2D hybrids could be effectively assembled via a two-step method. And the sensing response and the working temperature of the 1D sensing material were successfully improved through decorated 2D sheet-like materials. However, there are still some challenges remaining to be overcome to improve the gas-sensing performance of the 1D/2D composite, which would be discussed in detail in the following texts.

11.3 Remain Challenges and Possible Effective Ways to Explore High-Performance Gas Sensor

In general, the sensor responses of a majority of the sensors based on the 1D/2D hybrids always increase with increasing the working temperature. The highest value of the sensor response of the sensor could be obtained at an optimal working temperature. Then the sensor response would decrease with further increasing the

working temperature over the optimal value. However, the 1D/2D hybrids could only exhibit a high sensor response to target gas at a relatively high optimal working temperature. For example, the sensor response of the RGO-loaded CuO nanofibers was improved to 11.7–100 ppm H_2S of at the optimal working temperature of 300 °C [82]. The sensor based on the ZnO nanofibers loaded by RGO with the weight percent being 0.44 wt% presented the optimal NO_2-sensing performance at 400 °C [83]. As discussed in the section of **Introduction**, there would be a high risk of explosion when the concentration of the gas was increased to be in the explosive limit. The high working temperature would make the explosion more likely to take place and increase the power consumption of the gas sensor. The low working temperature might not provide enough energy that makes the oxygen species react with the target gas, but the high working temperature might accelerate the desorption of the oxygen species or the target gas, which was responsible for the highest sensor response at an optimal working temperature [47]. Further modification of the sensing material with certain catalysts might be possible to decrease the energy required to trigger the reaction between the oxygen species and the target gas. The Pt or Pd has been successfully used to decrease the working temperature of the sensor based on metal oxides. The optimal working temperature of the MoO_3 was decreased from 250 to 175 °C with the decoration of Pt and graphitic-carbon nitride (g-CN) [84]. Even though the decoration of noble metal nanoparticles might increase the cost of production, the low working temperature could decrease the power consumption and effectively reduce the explosion risk during the operating of the gas sensors based on the 1D/2D hybrids.

Another challenge for the reported sensors based on the 1D/2D hybrids is that they are still significantly affected by the humidity. It was reported that the adsorbed oxygen species or the target gas molecules on the surface of the sensing materials played an important role in the sensing response. The reaction between the oxygen species and the target gas was responsible for the sensing response of the sensor. The sensor response always decreased with increasing humidity, widely described as water vapor poisoning [79, 85]. When the sensor worked under high humidity, the adsorption of water molecules on the surface of the sensing material would decrease the active site for the adsorption of oxygen molecules in the air, then the number of the adsorbed oxygen species would decrease and fewer target molecules would consume during the sensing process, leading to the decrease in the sensor response. Meanwhile, the adsorbed water molecules might directly react with oxygen species (O^-) to form terminal hydroxyl groups on the surface of the sensing material, and the target gas molecule would also have to compete with the adsorbed water molecule and the target molecule, another factor responsible for the decreased sensor response under high humidity. Additionally, the sensor response of the 1D metal oxide-based sensor was found to be slightly weakened in 30–60 days, reported in several references [36, 86]. This might also be attributed to the decreased active sites on the surface of the sensing material with the fluctuation of humidity and the adsorptions of water molecules. The method of designing the corresponding compensating circuit, doping metal oxides with metal atom, coating the sensing material with hydrophobic polymer, or functionalizing the

sensing substrate with metal nanoparticles might be possible and successful to minimize or reduce the effect of humidity on the gas sensing performance of the 1D metal oxides composited with 2D materials [87–90]. The structure of the gas-sensing device would become complex to some extent, but the negative effects of the humidity on the gas-sensing properties of metal oxides-based sensors could be effectively limited or even eliminated. It should be noted that there were few reports systematically investigating the effective strategy to improve the stability of the metal oxide-based sensor under high humidity. More efforts should be made to study and explore the method to possibly avoid the effects of humidity on the gas-sensing performance of 1D/2D hybrids, meaningful to further promote the application of gas sensors.

Our discussions aforementioned revealed that the gas-sensing performance of 1D semiconducting material with the morphology of nanorod, nanowire, or nanofiber could be successfully enhanced through compositing with 2D nanosheets of graphene, GO, MoS_2, WS_2, ZnO, NiO, SnO, or $NiCO_2O_4$. It was clear that only a few kinds of 2D nanosheets were used to improve the 1D metal oxide. The sheet-like BN, In_2O_3, TiC, Co_3O_4, or InSe were also reported to be potential gas-sensing materials [91–95]. These 2D nanosheets might be applied to decorated 1D metal oxides to improve their gas-sensing responses. With more and more 1D/2D composite designed and constructed, it might be possible to assemble the gas sensor with high sensor response, short response/recovery time, and outstanding long-term stability at low working temperature and under high humidity. The relatively poor sensing performance of some reported 1D/2D composite might also indicate that the selected sensing material was not the optimal one. The latest 2D sheet-like materials could be a candidate to assemble potential sensing substrate to exhibit promising gas-sensing performance.

Recently, the method of machine learning and high-throughput computing has been widely and popularly used to efficiently explore possible high-performance materials in the area of drug discovery, diagnostic system for complex diseases, toxicity assessment, or gas sensors [96–99]. Meanwhile, machine learning was also applied to explore the selectivity of E-nose with plenty of data labeled under various circumstances [100–102]. The work of Salhi et al. suggested that machine learning was effective to develop high-performance smart e-nose with seven sensors to realize the early detection of gas leakage [103]. The trained smart e-nose was reported to be successful in selectively sensing LPG, CO, CO_2, smoke, or flame under different humidity conditions with the accuracy being almost 100%. Therefore, the potential sensing material could be effectively selected from the database with high-throughput screening certain conditions. The selected sensing substrate would test to label enough data under various environments to obtain a dataset. The assembled sensor might be likely to exhibit high sensor response and short response/recovery time with promising selectivity with further training of the collected dataset. According to the discussions aforementioned, the method of machine learning combined with high-throughput computing could be a successful method to effectively screen potential sensing materials and train the dataset to further improve their gas-sensing properties [104, 105]. More attention should be paid to this efficient strategy to develop high-performance gas sensors to better meet the

requirements of practical applications. The gas sensor based on 1D/2D hybrids is now in the ascendant, and one can envision a bright prospect for the development of this promising composite.

11.4 Conclusions

The 1D metal oxide with the structure of nanowire, nanorod, or nanofiber has been widely applied as sensing material to detect various gases. And their gas-sensing performance could be effectively enhanced through compositing them with 2D sheet-like materials. The typical 2D material of graphene-based nanosheets, MoS_2, WS_2, NiO, ZnO, SnO_2, SiC, $NiCO_2O_4$, or g-C_3N_4 have been successfully decorated on the 1D sensing material to improve their sensing responses. The high special surface area, the establishment of heterojunction, and the modulation of the potential barrier are mainly responsible for the enhanced gas-sensing performances of 1D semiconducting nanostructures decorated with 2D materials. The relatively high working temperature and the weakened gas-sensing property under high humidity might limit the further application of the 2D material-decorated 1D metal oxide in practices. The high-throughput computing with further machine learning could be a possible strategy to screen more effective gas-sensing material to exhibit more outstanding gas-sensing performance.

Acknowledgments

References

1 Ma, X., Jia, H., Sha, T. et al. (2019). Spatial and seasonal characteristics of particulate matter and gaseous pollution in China: implications for control policy. *Environ. Pollut.* 248: 421–428.

2 Wen, M., Li, G., Liu, H. et al. (2019). Metal–organic framework-based nanomaterials for adsorption and photocatalytic degradation of gaseous pollutants: recent progress and challenges. *Environ. Sci.: Nano* 6: 1006–1025.

3 Guan, W., Tang, N., He, K. et al. (2020). Gas-sensing performances of metal oxide nanostructures for detecting dissolved gases: a mini review. *Front. Chem.* 8: 76.

4 Cho, S.H., Suh, J.M., Eom, T.H. et al. (2021). Colorimetric sensors for toxic and hazardous gas detection: a review. *Electron. Mater. Lett.* 17: 1–17.

5 Buckley, D.J., Black, N.C., Castanon, E.G. et al. (2020). Frontiers of graphene and 2D material-based gas sensors for environmental monitoring. *2D Mater.* 7: 032002.

6 Umar, A., Ibrahim, A.A., Nakate, U.T. et al. (2021). Fabrication and characterization of CuO nanoplates based sensor device for ethanol gas sensing application. *Chem. Phys. Lett.* 763: 138204.

7 Vanotti, M., Poisson, S., Soumann, V. et al. (2021). Influence of interfering gases on a carbon monoxide differential sensor based on SAW devices functionalized with cobalt and copper corroles. *Sens. Actuators, B* 332: 129507.

8 Yang, S., Lei, G., Xu, H. et al. (2019). A DFT study of CO adsorption on the pristine, defective, In-doped and Sb-doped graphene and the effect of applied electric field. *Appl. Surf. Sci.* 480: 205–211.

9 Zou, M., Aono, Y., Inoue, S., and Matsumura, Y. (2020). Response of palladium and carbon nanotube composite films to hydrogen gas and behavior of conductive carriers. *Materials* 13: 4568.

10 Dong, M., Zheng, C., Miao, S. et al. (2017). Development and measurements of a mid-infrared multi-gas sensor system for CO, CO_2 and CH_4 detection. *Sensor* 17: 2221.

11 Tang, H., Sacco, L.N., Vollebregt, S. et al. (2020). Recent advances in 2D/ nanostructured metal sulfide-based gas sensors: mechanisms, applications, and perspectives. *J. Mater. Chem.* 8: 24943–24976.

12 Zhao, C., Gong, H., Niu, G., and Wang, F. (2020). Ultrasensitive SO_2 sensor for sub-ppm detection using Cu-doped SnO_2 nanosheet arrays directly grown on chip. *Sens. Actuators, B* 324: 128745.

13 Li, K., Luo, Y., Liu, B. et al. (2019). High-performance NO_2-gas sensing of ultrasmall $ZnFe_2O_4$ nanoparticles based on surface charge transfer. *J. Mater. Chem.* 7: 5539–5551.

14 Lou, C., Yang, C., Zheng, W. et al. (2021). Atomic layer deposition of ZnO on SnO_2 nanospheres for enhanced formaldehyde detection. *Sens. Actuators, B* 329: 129218.

15 Arafat, M., Dinan, B., Akbar, S.A., and Haseeb, A. (2012). Gas sensors based on one dimensional nanostructured metal-oxides: a review. *Sensor* 12: 7207–7258.

16 Fu, X., Yang, P., Xiao, X. et al. (2019). Ultra-fast and highly selective room-temperature formaldehyde gas sensing of Pt-decorated MoO_3 nanobelts. *J. Alloys Compd.* 797: 666–675.

17 Kumar, R., Al-Dossary, O., Kumar, G., and Umar, A. (2015). Zinc oxide nanostructures for NO_2 gas–sensor applications: a review. *Nano-Micro Lett.* 7: 97–120.

18 Park, K.-R., Cho, H.-B., Lee, J. et al. (2020). Design of highly porous SnO_2-CuO nanotubes for enhancing H2S gas sensor performance. *Sens. Actuators, B* 302: 127179.

19 Seiyama, T., Kato, A., Fujiishi, K., and Nagatani, M. (1962). A new detector for gaseous components using semiconductive thin films. *Anal. Chem.* 34: 1502–1503.

20 Miller, D.R., Akbar, S.A., and Morris, P.A. (2014). Nanoscale metal oxide-based heterojunctions for gas sensing: a review. *Sens. Actuators, B* 204: 250–272.

21 Govardhan, K. and Grace, A.N. (2016). Metal/metal oxide doped semiconductor based metal oxide gas sensors-a review. *Sens. Lett.* 14: 741–750.

22 Wang, Z., Hu, Y., Wang, W. et al. (2012). Fast and highly-sensitive hydrogen sensing of Nb_2O_5 nanowires at room temperature. *Int. J. Hydrogen Energy* 37: 4526–4532.

23 Song, Y.G., Park, J.Y., Suh, J.M. et al. (2018). Heterojunction based on Rh-decorated WO_3 nanorods for morphological change and gas sensor application using the transition effect. *Chem. Mater.* 31: 207–215.

24 Tao, K., Han, X., Yin, Q. et al. (2017). Metal-organic frameworks-derived porous In_2O_3 hollow nanorod for high-performance ethanol gas sensor. *ChemistrySelect* 2: 10918–10925.

25 Wang, C., Cui, X., Liu, J. et al. (2016). Design of superior ethanol gas sensor based on Al-doped NiO nanorod-flowers. *ACS Sens.* 1: 131–136.

26 Wang, X., Wang, T., Si, G. et al. (2020). Oxygen vacancy defects engineering on Ce-doped α-Fe_2O_3 gas sensor for reducing gases. *Sens. Actuators, B* 302: 127165.

27 Tonezzer, M. (2019). Selective gas sensor based on one single SnO_2 nanowire. *Sens. Actuators, B* 288: 53–59.

28 Liu, W., Xu, L., Sheng, K. et al. (2018). A highly sensitive and moisture-resistant gas sensor for diabetes diagnosis with Pt@ In_2O_3 nanowires and a molecular sieve for protection. *NPG Asia Mater.* 10: 293–308.

29 Li, Z. (2017). Supersensitive and superselective formaldehyde gas sensor based on NiO nanowires. *Vacuum* 143: 50–53.

30 Naama, S., Hadjersi, T., Keffous, A., and Nezzal, G. (2015). CO_2 gas sensor based on silicon nanowires modified with metal nanoparticles. *Mater. Sci. Semicond. Process.* 38: 367–372.

31 Yang, S., Lei, G., Xu, H. et al. (2021). Metal oxide based heterojunctions for gas sensors: a review. *Nanomaterials* 11: 1026.

32 Ge, L., Mu, X., Tian, G. et al. (2019). Current applications of gas sensor based on 2-D nanomaterial: a mini review. *Front. Chem.* 7: 839.

33 Kumar, R., Liu, X., Zhang, J., and Kumar, M. (2020). Room-temperature gas sensors under photoactivation: from metal oxides to 2D materials. *Nano-Micro Lett.* 12: 1–37.

34 Choi, S.-J. and Kim, I.-D. (2018). Recent developments in 2D nanomaterials for chemiresistive-type gas sensors. *Electron. Mater. Lett.* 14: 221–260.

35 Wang, C.N., Li, Y.L., Gong, F.L. et al. (2020). Advances in doped ZnO nanostructures for gas sensor. *Chem. Rec.* 20: 1553–1567.

36 Moon, D.-B., Bag, A., Lee, H.-B. et al. (2021). A stretchable, room-temperature operable, chemiresistive gas sensor using nanohybrids of reduced graphene oxide and zinc oxide nanorods. *Sens. Actuators, B* 345: 130373.

37 Zhao, Y., Li, H., Li, Y. et al. (2021). Layered SnO_2 nanorods arrays anchored on reduced graphene oxide for ultra-high and ppb level formaldehyde sensing. *Sens. Actuators, B* 346: 130452.

38 Xu, K., Yang, L., Yang, Y., and Yuan, C. (2017). Improved ethanol gas sensing performances of a ZnO/Co_3O_4 composite induced by its flytrap-like structure. *Phys. Chem. Chem. Phys.* 19: 29601–29607.

39 Novoselov, K.S., Geim, A.K., Morozov, S.V. et al. (2004). Electric field effect in atomically thin carbon films. *Science* 306: 666–669.

40 Chatterjee, S.G., Chatterjee, S., Ray, A.K., and Chakraborty, A.K. (2015). Graphene–metal oxide nanohybrids for toxic gas sensor: a review. *Sens. Actuators, B* 221: 1170–1181.

41 Toda, K., Furue, R., and Hayami, S. (2015). Recent progress in applications of graphene oxide for gas sensing: a review. *Anal. Chim. Acta* 878: 43–53.

42 Majhi, S.M., Mirzaei, A., Kim, H.W., and Kim, S.S. (2021). Reduced graphene oxide (rGO)-loaded metal-oxide nanofiber gas sensors: an overview. *Sensor* 21: 1352.

43 Rafiee, Z., Roshan, H., and Sheikhi, M.H. (2021). Low concentration ethanol sensor based on graphene/ZnO nanowires. *Ceram. Int.* 47: 5311–5317.

44 Minh Triet, N., Thai Duy, L., Hwang, B.-U. et al. (2017). High-performance Schottky diode gas sensor based on the heterojunction of three-dimensional nanohybrids of reduced graphene oxide–vertical ZnO nanorods on an AlGaN/GaN layer. *ACS Appl. Mater. Interfaces* 9: 30722–30732.

45 Yang, S., Wang, Z., Zou, Y. et al. (2017). Remarkably accelerated room-temperature hydrogen sensing of MoO_3 nanoribbon/graphene composites by suppressing the nanojunction effects. *Sens. Actuators, B* 248: 160–168.

46 Abideen, Z.U., Kim, H.W., and Kim, S.S. (2015). An ultra-sensitive hydrogen gas sensor using reduced graphene oxide-loaded ZnO nanofibers. *Chem. Commun.* 51: 15418–15421.

47 Yan, C., Lu, H., Gao, J. et al. (2018). Improved NO_2 sensing properties at low temperature using reduced graphene oxide nanosheet-In_2O_3 heterojunction nanofibers. *J. Alloys Compd.* 741: 908–917.

48 Galstyan, V., Ponzoni, A., Kholmanov, I. et al. (2018). Reduced graphene oxide-TiO_2 nanotube composite: comprehensive study for gas-sensing applications. *ACS Appl. Nano Mater.* 1: 7098–7105.

49 Sun, Z., Huang, D., Yang, Z. et al. (2015). ZnO nanowire-reduced graphene oxide hybrid based portable NH_3 gas sensing electron device. *IEEE Electron Device Lett.* 36: 1376–1379.

50 Meng, H., Yang, W., Ding, K. et al. (2015). Cu_2O nanorods modified by reduced graphene oxide for NH_3 sensing at room temperature. *J. Mater. Chem. A* 3: 1174–1181.

51 Chu, X., Hu, T., Gao, F. et al. (2015). Gas sensing properties of graphene–WO_3 composites prepared by hydrothermal method. *Mater. Sci. Eng., B* 193: 97–104.

52 Bai, S., Chen, C., Luo, R. et al. (2015). Synthesis of MoO_3/reduced graphene oxide hybrids and mechanism of enhancing H_2S sensing performances. *Sens. Actuators, B* 216: 113–120.

53 Xia, Y., Wang, J., Xu, J.-L. et al. (2016). Confined formation of ultrathin ZnO nanorods/reduced graphene oxide mesoporous nanocomposites for high-performance room-temperature NO_2 sensors. *ACS Appl. Mater. Interfaces* 8: 35454–35463.

54 Wang, T., Sun, Z., Huang, D. et al. (2017). Studies on NH_3 gas sensing by zinc oxide nanowire-reduced graphene oxide nanocomposites. *Sens. Actuators, B* 252: 284–294.

55 Fang, W., Yang, Y., Yu, H. et al. (2017). An In_2O_3 nanorod-decorated reduced graphene oxide composite as a high-response NOx gas sensor at room temperature. *New J. Chem.* 41: 7517–7523.

56 Reddeppa, M., Park, B.-G., Kim, M.-D. et al. (2018). H_2, H_2S gas sensing properties of rGO/GaN nanorods at room temperature: effect of UV illumination. *Sens. Actuators, B* 264: 353–362.

57 Amarnath, M. and Gurunathan, K. (2021). Selective ammonia sensing response of vanadium doped cerium oxide nanorods wrapped reduced graphene oxide electrodes at room temperature. *Sens. Actuators, B* 336: 129679.

58 Kumar, R.R., Murugesan, T., Dash, A. et al. (2021). Ultrasensitive and light-activated NO_2 gas sensor based on networked MoS_2/ZnO nanohybrid with adsorption/desorption kinetics study. *Appl. Surf. Sci.* 536: 147933.

59 Viet, N.N., Dang, T.K., Phuoc, P.H. et al. (2021). MoS_2 nanosheets-decorated SnO_2 nanofibers for enhanced SO_2 gas sensing performance and classification of CO, NH_3 and H_2 gases. *Anal. Chim. Acta* 1167: 338576.

60 Liu, A., Lv, S., Jiang, L. et al. (2021). The gas sensor utilizing polyaniline/MoS_2 nanosheets/SnO_2 nanotubes for the room temperature detection of ammonia. *Sens. Actuators, B* 332: 129444.

61 Bai, X., Lv, H., Liu, Z. et al. (2021). Thin-layered MoS_2 nanoflakes vertically grown on SnO_2 nanotubes as highly effective room-temperature NO_2 gas sensor. *J. Hazard. Mater.* 416: 125830.

62 Zhang, D., Jiang, C., Li, P., and Sun, Y.e. (2017). Layer-by-layer self-assembly of Co_3O_4 nanorod-decorated MoS_2 nanosheet-based nanocomposite toward high-performance ammonia detection. *ACS Appl. Mater. Interfaces* 9: 6462–6471.

63 Zhao, S., Wang, G., Liao, J. et al. (2018). Vertically aligned MoS_2/ZnO nanowires nanostructures with highly enhanced NO_2 sensing activities. *Appl. Surf. Sci.* 456: 808–816.

64 Zhao, P., Tang, Y., Mao, J. et al. (2016). One-dimensional MoS_2-decorated TiO_2 nanotube gas sensors for efficient alcohol sensing. *J. Alloys Compd.* 674: 252–258.

65 Zhao, S., Li, Z., Wang, G. et al. (2018). Highly enhanced response of MoS_2/porous silicon nanowire heterojunctions to NO_2 at room temperature. *RSC Adv.* 8: 11070–11077.

66 Dwiputra, M.A., Fadhila, F., Imawan, C., and Fauzia, V. (2020). The enhanced performance of capacitive-type humidity sensors based on ZnO nanorods/WS_2 nanosheets heterostructure. *Sens. Actuators, B* 310: 127810.

67 Suh, J.M., Kwon, K.C., Lee, T.H. et al. (2021). Edge-exposed WS_2 on 1D nanostructures for highly selective NO_2 sensor at room temperature. *Sens. Actuators, B* 333: 129566.

68 Wang, B., Zheng, Z.Q., Zhu, L.F. et al. (2014). Self-assembled and Pd decorated Zn_2SnO_4/ZnO wire-sheet shape nano-heterostructures networks hydrogen gas sensors. *Sens. Actuators, B* 195: 549–561.

69 Liu, F., Chen, X., Wang, X. et al. (2019). Fabrication of 1D Zn_2SnO_4 nanowire and 2D ZnO nanosheet hybrid hierarchical structures for use in triethylamine gas sensors. *Sens. Actuators, B* 291: 155–163.

70 Wang, X. and Cho, H.J. (2018). p-CuO nanowire/n-ZnO nanosheet heterojunction-based near-UV sensor fabricated by electroplating and thermal oxidation process. *Mater. Lett.* 223: 170–173.

71 Lu, Y., Ma, Y., Ma, S., and Yan, S. (2017). Hierarchical heterostructure of porous NiO nanosheets on flower-like ZnO assembled by hexagonal nanorods for high-performance gas sensor. *Ceram. Int.* 43: 7508–7515.

72 Hoa, L.T., Tien, H.N., and Hur, S.H. (2014). Fabrication of novel 2D NiO nanosheet branched on 1D-ZnO nanorod arrays for gas sensor application. *J. Nanomater.* 2014.

73 Nakate, U.T., Yu, Y., and Park, S. (2021). High performance acetaldehyde gas sensor based on pn heterojunction interface of NiO nanosheets and WO_3 nanorods. *Sens. Actuators, B* 130264.

74 Wang, Z., Zhi, M., Xu, M. et al. (2021). Ultrasensitive NO_2 gas sensor based on Sb-doped SnO_2 covered ZnO nano-heterojunction. *J. Mater. Sci.* 56: 7348–7356.

75 Wang, B., Wang, Y., Lei, Y. et al. (2016). Vertical SnO_2 nanosheet@ SiC nanofibers with hierarchical architecture for high-performance gas sensors. *J. Mater. Chem. C* 4: 295–304.

76 Sun, L., Wang, B., and Wang, Y. (2020). High-temperature gas sensor based on novel Pt single atoms@ SnO_2 nanorods@ SiC nanosheets multi-heterojunctions. *ACS Appl. Mater. Interfaces* 12: 21808–21817.

77 Xu, K., Wei, W., Sun, Y. et al. (2019). Design of $NiCO_2O_4$ porous nanosheets/α-MoO_3 nanorods heterostructures for ppb-level ethanol detection. *Powder Technol.* 345: 633–642.

78 Xu, K., Zhao, W., Yu, X. et al. (2020). Enhanced ethanol sensing performance using Co_3O_4-$ZnSnO_3$ arrays prepared on alumina substrates. *Phys. E* 117: 113825.

79 Xu, K., Tang, Q., Zhao, W. et al. (2020). In situ growth of Co_3O_4@ $NiMoO_4$ composite arrays on alumina substrate with improved triethylamine sensing performance. *Sens. Actuators, B* 302: 127154.

80 Wang, Y., Zhou, Y., Ren, H. et al. (2020). Room-temperature and humidity-resistant trace nitrogen dioxide sensing of few-layer black phosphorus nanosheet by incorporating zinc oxide nanowire. *Anal. Chem.* 92: 11007–11017.

81 Wang, Y., Cao, J., Qin, C. et al. (2017). Synthesis and enhanced ethanol gas sensing properties of the g-C_3N_4 nanosheets-decorated tin oxide flower-like nanorods composite. *Nanomaterials* 7: 285.

82 Kim, J.-H., Mirzaei, A., Zheng, Y. et al. (2019). Enhancement of H_2S sensing performance of p-CuO nanofibers by loading p-reduced graphene oxide nanosheets. *Sens. Actuators, B* 281: 453–461.

83 Abideen, Z.U., Katoch, A., Kim, J.-H. et al. (2015). Excellent gas detection of ZnO nanofibers by loading with reduced graphene oxide nanosheets. *Sens. Actuators, B* 221: 1499–1507.

84 Chaudhary, V. and Nehra, S.P. (2021). Pt-sensitized MoO_3/mpg-CN mesoporous nanohybrid: a highly sensitive VOC sensor. *Microporous Mesoporous Mater.* 315: 110906.

85 Wang, L., Fu, H., Jin, Q. et al. (2019). Directly transforming SnS_2 nanosheets to hierarchical SnO_2 nanotubes: towards sensitive and selective sensing of acetone at relatively low operating temperatures. *Sens. Actuators, B* 292: 148–155.

86 Li, X., Zhou, Y., Tai, H. et al. (2020). Nanocomposite films of p-type MoS_2 nanosheets/n-type ZnO nanowires: sensitive and low-temperature ppb-level NO_2 detection. *Mater. Lett.* 262: 127148.

87 Hsu, L.C., Ativanichayaphong, T., Cao, H. et al. (2007). Evaluation of commercial metal-oxide based NO_2 sensors. *Sens. Rev.*

88 Kwak, C.-H., Kim, T.-H., Jeong, S.-Y. et al. (2018). Humidity-independent oxide semiconductor chemiresistors using terbium-doped SnO_2 yolk–shell spheres for real-time breath analysis. *ACS Appl. Mater. Interfaces* 10: 18886–18894.

89 Qu, F., Zhang, S., Huang, C. et al. (2021). Surface functionalized sensors for humidity-independent gas detection. *Angew. Chem., Int. Ed.* 60: 6561–6566.

90 Kondalkar, V.V., Duy, L.T., Seo, H., and Lee, K. (2019). Nanohybrids of Pt-functionalized Al_2O_3/ZnO core–shell nanorods for high-performance MEMS-based acetylene gas sensor. *ACS Appl. Mater. Interfaces* 11: 25891–25900.

91 Sajjad, M. and Feng, P. (2014). Study the gas sensing properties of boron nitride nanosheets. *Mater. Res. Bull.* 49: 35–38.

92 Ma, J., Fan, H., Zhang, W. et al. (2020). High sensitivity and ultra-low detection limit of chlorine gas sensor based on In_2O_3 nanosheets by a simple template method. *Sens. Actuators, B* 305: 127456.

93 Raghu, A.V., Karuppanan, K.K., Nampoothiri, J., and Pullithadathil, B. (2019). Wearable, flexible ethanol gas sensor based on TiO_2 nanoparticles-grafted 2D-titanium carbide nanosheets. *ACS Appl. Nano Mater.* 2: 1152–1163.

94 Deng, S., Liu, X., Chen, N. et al. (2016). A highly sensitive VOC gas sensor using p-type mesoporous Co_3O_4 nanosheets prepared by a facile chemical coprecipitation method. *Sens. Actuators, B* 233: 615–623.

95 Zhang, L., Li, Z., Liu, J. et al. (2020). Optoelectronic gas sensor based on few-layered InSe nanosheets for NO_2 detection with ultrahigh antihumidity ability. *Anal. Chem.* 92: 11277–11287.

96 Patel, L., Shukla, T., Huang, X. et al. (2020). Machine learning methods in drug discovery. *Molecules* 25: 5277.

97 Karthik, S. and Sudha, M. (2018). A survey on machine learning approaches in gene expression classification in modelling computational diagnostic system for complex diseases. *Int. J. Eng. Technol.* 8: 182–191.

98 Zhang, Y., Wong, Y.S., Deng, J. et al. (2016). Machine learning algorithms for mode-of-action classification in toxicity assessment. *BioData Min.* 9: 1–21.

99 Acharyya, S., Jana, B., Nag, S. et al. (2020). Single resistive sensor for selective detection of multiple VOCs employing SnO_2 hollowspheres and machine learning algorithm: a proof of concept. *Sens. Actuators, B* 321: 128484.

100 Jaeschke, C., Glöckler, J., El Azizi, O. et al. (2019). An innovative modular eNose system based on a unique combination of analog and digital metal oxide sensors. *ACS Sens.* 4: 2277–2281.

101 Peng, G., Tisch, U., Adams, O. et al. (2009). Diagnosing lung cancer in exhaled breath using gold nanoparticles. *Nat. Nanotechnol.* 4: 669–673.

102 Liao, Y.-H., Shih, C.-H., Abbod, M.F. et al. (2020). Development of an E-nose system using machine learning methods to predict ventilator-associated pneumonia. *Microsyst. Technol.* 1-11.

103 Salhi, L., Silverston, T., Yamazaki, T., and Miyoshi, T. (2019). Early detection system for gas leakage and fire in smart home using machine learning. In: *2019 IEEE International Conference on Consumer Electronics (ICCE)*, 1–6. IEEE.

104 Yaqoob, U. and Younis, M.I. (2021). Chemical gas sensors: recent developments, challenges, and the potential of machine learning-a review. *Sensor* 21: 2877.

105 Lekha, S. and Suchetha, M. (2020). Recent advancements and future prospects on E-Nose sensors technology and machine learning approaches for non-invasive diabetes diagnosis: a review. *IEEE Rev. Biomed. Eng.* 14: 127–138.

12

Recent Advancement in the Development of Optical Modulators Based on 1D and 2D Materials

Kavintheran Thambiratnam, Norazriena Yusoff, Siti N. Aidit, Muhamad Z. Samion, Nur A. Azali, and Harith Ahmad

Universiti Malaya, Photonics Research Centre, Kuala Lumpur, 50603, Malaysia

12.1   Introduction

Over the past few years, the use of one-dimensional (1D) and two-dimensional (2D) materials for interdisciplinary research has been attracting a wide range of interests, reflecting a general trend in the scientific world. Particularly, the use of 1D materials in the form of nanoparticles has been widely considered for the development of high-end photonic devices due to their various advantages in size control, high aspect ratio, and physical and chemical qualities [1–3]. These include the utilization of various types of carbon nanotubes (CNTs) [4–6], metals [7–9], and also metal oxides [10, 11] for this particular application. Apart from these materials, the emergence of 2D materials for photonics applications has also been growing at a significant pace since the discovery of graphene in 2004. Since then, 2D-structured materials such as transition metal-based chalcogenides (TMDs) [12–15], topological insulators (TIs) [12, 16, 17], and MXenes [18–23] have also been widely explored. The recent appearance of these materials has greatly assisted in the advancement of nonlinear photonics due to these materials having an outstanding nonlinear optical characteristics. A huge amount of scientific studies has been conducted on this foundation, and various unique materials then been explored and extensively employed as optical modulators. Of particular interest in the field of nonlinear photonics is the development of optical modulators for fiber lasers. The performance and applications of fiber lasers have substantially increased since the discovery of 1D and 2D materials, and fiber laser-related research has also progressed rapidly as a result of this discovery.

In this chapter, recent research on the advancement of optical modulators based on 1D- and 2D-structured materials will be examined, with a focus on manufacturing methods, optical properties, and their applications in fiber lasers. The potential

future advancements of these structured materials will also be identified by summarizing the scientific achievements that have been achieved from these research works. The first section of this chapter provides a brief introduction of 1D and 2D materials. The second section discusses the operations of optical modulation in fiber lasers. The structure, properties, fabrication methods, and applications of 1D- and 2D-structured materials are discussed in the third and fourth section, respectively. Section 12.5 presents the material configuration in fiber lasers and optical modulation based on 1D materials as well as 2D materials. Finally, the conclusion, challenges, and future perspectives are also discussed.

12.2 Optical Modulation in Fiber Lasers

12.2.1 Q-Switching Operation

Lasers can operate in either the continuous-wave (CW) or Q-switching regimes that produce optical power which is limited by a maximum obtainable pump power. Q-switching can be simplified to when the output energy supplied is concentrated in a single pulse of light, while for the case of the CW beam the output energy is supplied in a constant stream of light [24]. The Q-switching technique was first described by Hellwarth in 1961, where it was predicted that a laser can generate short pulses if cavity losses were suddenly switched. In 1962, Hellwarth with his partner, McClung, had showed Q-switching as a technique allows the generation of a pulse of light with a short duration and high pulse energy [25]. Thus, Q-switching is used to obtain high energy and short pulses, which gives benefits in several applications such as medicine, remote sensing, and material processing [26, 27]. The process is known as Q-switching because the quality factor, Q, of the fiber laser is altered when the technique is applied.

Generally, Q-switching is achieved by inserting a shutter inside the laser cavity. The shutter acts as the medium to control the laser output to the cavity. There will be no feedback received from the mirror in the cavity if the shutter is closed, even though enough power supply is given to the gain medium. In this case, the laser action is prohibited because no stimulated emission occurs in the gain medium. Since the power supply is on however, population inversion still occurs, where more atoms can excite from the lower energy levels to the higher energy levels. The volume of the population inversion is greater than the threshold population that would be reached in the absence of the shutter for the similar laser operation. Then if the shutter is suddenly opened, the spontaneous emissions will begin to bounce back and forth through the gain medium. The laser beam then increases and utilizes the population inversion which causes it to reduce quickly and in turn reduces the power of the laser beam. These techniques involve the switching of the quality factor or Q-factor, in which high losses show a low Q-factor while low losses show a high Q-factor. Thus, the Q-factor can be increased quickly if the shutter is kept closed at the beginning and rapidly opened it, and this is called Q-switching.

Q-switching can be categorized as either active and passive Q-switching. Active Q-switching can be generated by using an external signal such as acousto optic

modulator (AOM) and electro-optic modulator (EOM), which act to modulate the losses of the laser. Acousto optic Q-switching can be achieved by using the acousto optic effect. The propagating acoustic wave or standing wave inside the medium changes the refractive index of the material periodically because of the periodic straining in the medium and results in the diffraction of the optical wave. In the presence of standing wave, the medium acts as phase grating. In this case, when the acousto optic is placed inside the cavity, it will diffract the light beam, thus producing low Q-factor. The Q-factor can be increased by changing the acoustic wave [28]. The EOM method on the other hand basically works in combination with polarizer. The lasing pulse can be generated when the EO switch becomes transparent by the application of a voltage; thus, the Q-factor is switched high.

Passive Q-switching is commonly achieved by using a saturable absorber (SA). The intensity of incident light is increased when the SA is placed inside the resonator and thus decreases the absorption coefficient of the material; this is due to the saturation of a transition. In the beginning, the intensity level inside the resonator is small and keeps the Q-factor low. However, when the pumping of the active medium increases, the intensity level inside the resonator increases and the SA is bleached and becomes transparent. This results to switching the Q-factor to a high value and producing a short pulse of light [29].

12.2.2 Mode-Locking Operation

Mode-locking is a technique used generally to produce pulses of light in the order of picoseconds or femtosecond range, which are shorter compared to the pulses produced through Q-switching. Mode-locking was first demonstrated by Hargrove et al. by utilizing an AOM in a He–Ne laser [30]. It can be achieved by the phase-locking of many longitudinal cavity modes oscillating within the cavity into a fixed mode relationship with each other. Mode-locked pulses generate pulses with a high repetition rate with a narrow pulse width from a fiber laser. The mode-locked output of the generated light in the temporal domain can be described as the summation of all the oscillating modes as shown below:

$$e(t) = \sum_n E_n e^{j\left[(\omega_o + n\omega_R)t + \Phi_n\right]}$$

whereby the equation describes the amplitude, E_n, phase of the nth mode, Φ_n, and the referenced center for the oscillating frequency, ω_0.

Similar to the Q-switching techniques, there are two methods for generating mode-locked pulses, either by using active or passive mode-locking. For active mode-locking, a modulator device is used and placed inside the cavity to make the round-trip phase change and reduce modulation losses. A passive mode-locking can be achieved by the presence of SA or self-synchronization using polarization controller [31]. The SA plays an important role in the passive technique as it acts to absorb the light entering linearly into the cavity until it reaches at certain intensity. The SA is a nonlinear optical component such as 1D and 2D materials, which the absorption coefficient decreases when the optical intensity increases. When the

cavity achieved certain level of intensity, the SA will be saturated and produced pulse train with high peak intensity.

12.3   1-Dimensional Structured Materials

In the past few decades, a broad range of low-dimensional material particularly 1D-structured materials have been extensively studied. Due to their exceptional electronic, optical, and structural properties, 1D materials has demonstrated distinctive performances and excelled in various fields of application in particular optoelectronics and photonics applications [4]. Generally, 1D materials can be defined as material (metal or semimetals, oxides, sulfides, halides, etc.) that possess a dimension within the range of 1–100 nm and comes in a variety of structures, for instance nanotubes, nanowires, and nanorods. Figure 12.1 shows some examples of 1D materials that have been categorized based on different structure, including nanotubes, nanowires, and nanorods.

A 1D nanotube, which can be either a CNT or an inorganic nanotube, is known to be a material that is elongated in one dimension and possess a ration of length-to-diameter of about 132 000 000 : 1. Nanotubes direct electrons along the elongated axis and can exist in different arrangements inclusive of single-walled nanotubes (SWNTs) with micrometers long and 1–2 nm in diameter, double-walled nanotubes (DWNTs), multi-walled nanotubes (MWNTs) with diameter ranging from 50 to
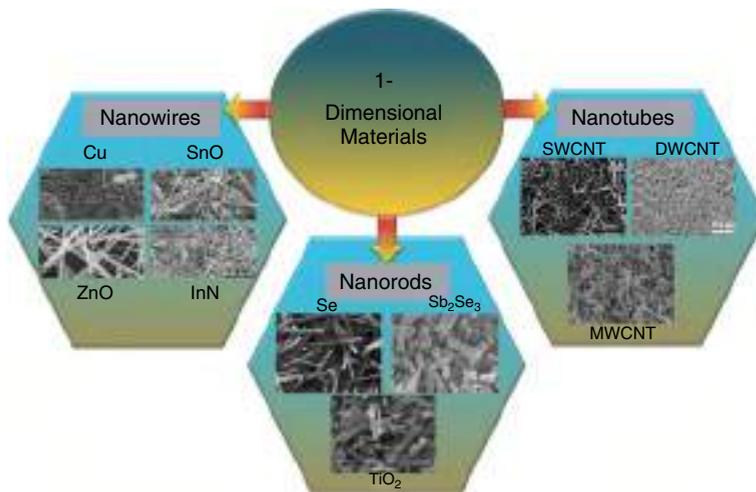
Figure 12.1   1D materials in the form of different structures, including nanotubes [32–34], nanorods [35–37], and nanowires [38–41]. Sources: Velayati et al. [37], Reproduced with permission from Elsevier; Cheng et al. [36], Reproduced with permission from Elsevier; Khizir et al. [35], Reproduced with permission Elsevier; Mohammadian et al. [33], MDPI, CC BY 4.0; Muangrat et al. [34], Reproduced with permission from Elsevier; Abdul Rahim et al. [32], MDPI, CC BY 4.0; Scardaci [38], MDPI, CC BY 4.0; Zheng et al. [39], MDPI, CC BY 4.0; Chen et al. [40], MDPI, CC BY 4.0; Li et al. [41], MDPI, CC BY 4.0.

100 nm, chiral nanotubes, armchair nanotubes, and zigzag nanotubes. Nanowires are another established 1D material which is also referred to as quantum wires. Similar to nanotubes, nanowires are also elongated in one direction but with a much lower ration of width to length that is approximately 1 : 1000. Nanowires have become one of the ideal materials for numerous applications in view of the fact that they demonstrate different quantum effects which alongside their unidirectional electron movement. The most common nanowires are made up from various semiconducting materials such as zinc oxide (ZnO) [42], tin oxide (SnO_2) [43], silicon carbide (SiC) [44], silicon (Si) [45], gallium nitride (GaN) [46], and boron nitride (BN) [47]. Apart from nanotubes and nanowires, 1D material can also come in the form of nanorods morphology in which their dimensions are in the range of 1–100 nm. Nanorods may have the standard aspect ratios, that is the length divided by width is in the range of 3–5. In building up the nanorods structure, a combination of ligands has played a role as shape control agents and attached to different facets of the nanorods with varying strengths. As a result, different faces of the nanorods are allowed to grow at various rates, hence forming an elongated object. Nanorods may be fabricated from metals or semiconducting materials such as gold (Au) [48], silver (Ag) [49], or palladium (Pd) [50].

12.3.1 Synthesis Method of 1D Materials

Several methods that have been reported can be performed to synthesize 1D material in which different approaches were taken in order to obtain desired structures of 1D materials. Generally, there are two different approaches to the synthesis of 1D materials that referred to as top-down (destruction) and bottom-up (construction) approach. In top-down approach, material in smaller scale (nanoscale) is synthesized by breaking down the bulk material, hence reducing the scale from bulk materials into smaller unit. Laser ablation, metal-assisted chemical etching (MACE), mechanical milling, electro-explosion, and sputtering are some examples of top-down approach for the synthesis of 1D material. In contrast to the top-down approach, the bottom-up approach is related to the molecular recognition and chemical self-assembly of molecules which led to the formation of structures with various sizes lay out in between several nanometers to few microns. Vapor-phase growth, template-assisted etching, liquid-phase growth, and electrospinning are some of the examples of methodologies under the bottom-up approach. The chemical vapor deposition (CVD) technique has been widely utilized to grow 1D nanotubes, particularly CNTs with single, double, and multiple-walled. Thermal CVD (T-CVD), floating catalyst thermal CVD (FCT-CVD), and microwave plasma-enhanced CVD (MPE-CVD) are examples of methods that are commonly adopted in CVD technique in order to obtain the 1D nanotubes material [33]. For years, the CVD technique has become one of the promising and scalable approaches for growing CNT on different types of surface or substrate. The growth methods in obtaining 1D nanowires are very much influenced by the Wagner's vapor–liquid–solid crystal methods [51]. In this method, metal nanoparticles have been introduced in order to determine the diameter of the produced

nanowires. The growth of 1D crystal was originated from the formation of the solid–liquid interface, which next ratifies the early nucleation stage at the nanometer scale for all of the vapor–liquid–solid processes. This nanowire growth mechanism has revealed that the single-crystal semiconductor nanowire is possibly synthesized in a predictable manner for the first time by implementing a general concept of nanoparticle-catalyzed growth. These early studies contributed to the groundwork for the predictable growth of nanowires with many different compositions. Recent progress in the development of 1D nanowires has validated that nanowires can be synthesized by various methods, for instance by thermal decomposition, laser ablation, CVD, electroless deposition, cation exchange, selected-control reaction, arc discharge, and conventional template-assisted solution phase growth [52].

12.3.2 Properties of 1D Materials

The existence of low-dimensional materials is related to the confinement of the electronic state wave function in one of the three dimensions. The thin film (2D) and nanowire (1D) structures are formed as the dimensions of the materials are decreasing to the nanoscale in one and two directions, respectively. Therefore, the low-dimensional materials exhibiting quantum size effects have significantly altered their electronic properties and deeply modified their photonic and optoelectronic performances as opposed to their bulk counterpart. As such, the study on 1D materials has been growing exponentially over the past several decades and has stimulated interest from diverse scientific and engineering disciplines which are attributable to their intriguing properties. 1D nanomaterials, particularly the nanotubes, nanowires, and nanorods, have been fascinated very much in both academia and industry because of their potential application in various fields. As an example, CNTs have been extensively explored and utilized as an SA material for the generation of mode-locked fiber lasers. This is due to the merits of CNT such as fast recovery, deep modulation depth, low saturation intensity, broad operation bandwidth, polarization insensitivity, excellent environmental stability, and easy in fabrication. The third-order nonlinear polarizability measured by pump-probe spectroscopy is about 10^{-7} to 10^{-10} esu ($1\,\text{esu} = 1.11 \times 10\text{–}9\,\text{m}^2/\text{V}^2$). The recovery time was a fast intraband carrier relaxation time of 0.3–1.2 ps and a slow recombination process of 5–20 ps. Besides that, multi-walled carbon nanotube (MWCNT) material has shown outstanding thermal property which is a favorable feature for the development of high-power ultrafast laser. Moreover, MWCNTs also possess a Young modulus of around 1000 GPa and the thermal conductivity of about 3000 W/m K which can be considered as high [14]. Interestingly, the multiple-walled structure of MWCNTs which takes the form of a stack of concentrically rolled graphene sheets has made it less sensitive to the environment compared to SWCNT and DWCNT. The thermal or laser damage threshold of MWCNTs is considerably high due to the fact that the outer walls of MWCNTs can protect the inner walls from damage or oxidation [53].

12.4   2D-Structured Materials

In recent years, 2D materials are described to be interesting materials that have been excellently venturing in ultrafast photonics field. This field encompasses a wide variety of crucial applications, such as optical communications, optical modulation by optical limiting/mode-locking, photodetectors, and integrated miniature. As compared to their bulk form, 2D materials appeared to have distinctive performances in all-optical photonics devices due to the peculiar optical, electronic, and structural properties which arise resulting from the quantum confinement effects. In general, 2D materials can be classified into several groups, including 2D monoelements, 2D chalcogenides, TIs, and MXenes. Each of these groups of 2D material possesses their own unique properties that are beneficial in numerous specific applications, especially in photonics and optoelectronics applications. Figure 12.2 shows the example of 2D materials arranged according to their group.

12.4.1   2D Monoelements

2D graphene has attracted numerous attentions since 2004 due to its unique honeycomb atomic structure and band structure which led to the rise of excellent physical properties including ultrahigh mobility, Dirac electronic behavior, and quantum
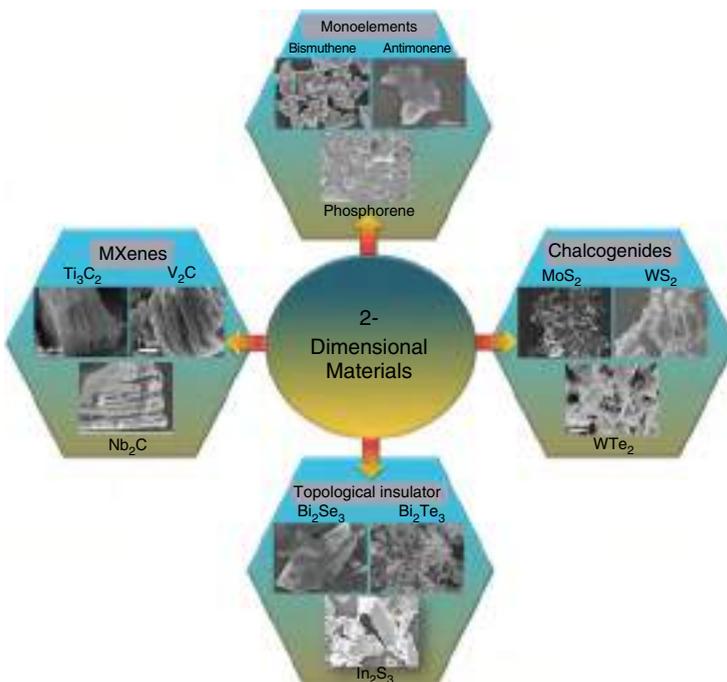
Figure 12.2   Example of 2D-structured materials: monoelements [54–56], chalcogenides [57–59], topological insulators [60–62], and MXenes [63–65]. Sources: [54–65], Reproduced with permission from Elsevier.

Hall effect. Inspired by the discovery of graphene, researchers have speculated that similar 2D honeycomb-structured materials comprised of other elements can be experimentally produced. The 2D monoelement materials also known as 2D Xenes materials have the form of graphene-like structure with intra-layer covalent bond and weak van der Waals forces that bind the layers together. Similar to graphene, 2D Xenes materials composed of group IIIA–VIA atoms that arranged in a 2D honeycomb lattice nanostructure. The degree of bucking is different depending on the interplay of sp^2 and sp^3 hybrid bonds. Elements in the group IIIA (borophene), group IVA (silicene, germanene, and stanine), group VA (phosphorene, arsenene, antimonene, and bismuthene), and group VIA (selenene and tellurene) of the periodic table are the examples of materials classified as the 2D MXenes [66, 67]. It is important to note that each type of 2D Xenes possesses unique structures with special crystal forms and spatial arrangements depending on their fabrication methods.

In general, the method in synthesizing 2D Xenes materials can be divided by two approaches namely top-down and bottom-up approach. Physical vapor deposition (PVD), CVD, and wet chemical reaction are the examples of synthesis techniques that used the bottom-up approach. The aforementioned methods required harsh condition and are able to fabricate products with high purity and designed structures. On the contrary, top-down approach which includes mechanical cleavage, thermal oxidation etching, and liquid-phase exfoliation in a solvent such as *N*-methyl-2-pyrrolidone (NMP) are ease in operation yet difficult to control regular structures with narrow distribution in consequences of complex variables, and the production yield by this method is also generally low. Typically, the mechanical or chemical exfoliation approaches are the most convenient method to fabricate 2D Xenes honeycomb structure because of the weak van der Waals force that binds the interlayer of the monoelements. Recently, the epitaxial growth approach has been reported to be one of the effective synthesis methods of bismuthene [68]; however, this technique required some improvement in term of its scalability. Recently, researchers have utilized the electrochemical method to exfoliate the layered material, thus obtaining the few-layer 2D Xenes. This method has been reported to be a straightforward technique which is able to produce high mass product, having extra merit over other chemical and physical techniques.

Current research has been committed to the development of emerging and investigating potential applications of 2D Xenes in various fields. Theoretically, it is predicted that once the layer thickness is on lower order of the Fermi wavelength, the semi-metal bismuth might have converted to semiconductors as a result of quantum confinement effect. Besides that, the 2D Xenes materials also demonstrate a tunable layer-dependent bandgap which means that the bandgap can be manipulated according to the desired optical absorption ranging from the ultraviolet (UV) to near-infrared (NIR). This is beneficial for good optical imaging capability in tumor location as example. Due to their intriguing properties such as excellent physical, chemical, electronic, and optical properties, 2D Xenes have become a promising catalyst, electrode material, energy storage materials in batteries or superconductors, SA material, optical modulator, etc., that can be applied in wide range of applications.

12.4.2   2D Chalcogenides

Another group of 2D materials are chalcogenides, and are made up of one or multiple chalcogen elements such as sulfur (S), selenium (Se), and tellurium (Te). These chalcogen elements that have been commercialized are usually incorporated with other element to form a new 2D chalcogenide materials such as germanium (Ge), gallium (Ga) [69], silicon (Si) [70], antimony (Sb) [71], tin (Sn) [72], molybdenum (Mo) [73], tungsten (W) [74], and aluminum (Al) [75]. 2D chalcogenide materials have atomic layers of X–M–X or X–M–M–X, which M represents the metal atom and X is the chalcogen atom. The stacked units of the atomic layers produce a close-packed structure. There are van der Waals force along the crystallographic c-direction that acts as the gap for the sandwich unit between one another. The atomic layers are strongly bonded by covalent bonds with several electrostatic contributions which present according to the ionicity of the M—X bonds. The metals are commonly found in a trigonal prismatic coordination for the covalent bond formation to optimize the covalent overlap, while the octahedral coordination is more favored for ionic to minimize the electrostatic repulsion [76].

The discovery of 2D chalcogenide materials including metal monochalcogenides (MMs) and transition metal dichalcogenides (TMDs) gives benefits for the development of 2D materials in the photonics application, and the materials acts as the SAs for the generation of passively Q-switched and mode-locked pulses [77–79]. MMs materials have general formula of MX which made up of two elements from group IVA or IIIA (M = Si, Ge, Sn, Ga, etc.) and the chalcogen atom (X = S, Se, or Te). 2D MMs have highly anisotropic structure with the monolayer structure of orthorhombic crystal structure (*Pnma*) space group with low crystal symmetry C_{2v}. It is predicted that various fascinating phenomena can take place in monolayer of MMs such as spontaneous polarization and bulk photovoltaic effect [80], giant piezoelectricity [81], ferroelasticity [82], and ferroelectricity [83]. The MMs have inspiring characteristics, such as large carrier mobility and good photoconductivity and have tunable energy gap based on the number of layers and unique 2D structure with large surface area. The 2D MMs materials have attracted worldwide interest in recent decades due to their unique qualities and other features such as low cost, earth-abundant, and ecologically benign, and their use in diverse fields of applications has been swiftly studied. For example, a study conducted by Qiu et al. [84] highlighted the promise of tin selenide (SnS), one of the MMs materials, for gas sensor applications. This is owing to SnS's distinctive 2D monolayer and excellent oxidation resistance, as well as its huge active surface area, which is useful for increasing gas molecule adsorption. Brent et al. reported the electronic characteristics of monolayer or few-layer MMs by theoretical and experimental works in another paper [85]. Their findings revealed that SnS has a direct and indirect bandgap in the 1.0–2.3 eV region, which covers a portion of the infrared and visible spectrum. Furthermore, MMs materials have considerable nonlinear optical properties, as demonstrated by studies undertaken by Zhou et al. [86]. They discovered that germanium sulfide (GeS) has a broadband nonlinear optical absorption ranging from 400 to 800 nm, as well as an excellent nonlinear optical response that is

dependent on wavelength and excitation intensity. Results of this study demonstrate that few-layer GeS is a potential option in nanophotonic application, especially for the advancement of SAs and optical diodes. Furthermore, a number of researches have explored the suitability of 2D MMs materials for implementation as transistors, sensors, and photodetectors.

TMDs, the most representative member of 2D chalcogenide materials, have recently piqued the curiosity of researchers due to their intriguing characteristics. TMDs are represented by the generic formula MX_2, where M is the transition metal atom of group IVB (Ti, Zr, Hf) or group VIB (Mo, W) and X denotes the chalcogen atom, which is either S, Se, or Te, and so offers a diverse range of materials with various properties. TMD materials have a layered structure with strong X—M—X bonds, with one transition metal atom (M) sandwiched between two chalcogen atoms (X) that are securely bound together by powerful interaction of covalent bonding. Meanwhile, the individual MX_2 layers are held together by interlayer van der Waals forces that are relatively much weaker. TMD's electrical and optical characteristics, like those of other 2D materials, may be altered with regard to its layer thickness. Layered TMD materials, as opposed to its bulk equivalents, have a direct optical bandgap with strong light–matter interaction, good stability, and a high nonlinear optical sensitivity. TMDs also have the unique properties of nonzero bandgap and third-order optical nonlinearity. The current study findings have acknowledged the use of 2D TMDs material in a variety of applications such as photodetector, transistor, energy storage, and nonlinear optical devices. TMDs have been extensively explored in recent years to exhibit ultrafast electron relaxation and broadband nonlinear optical response, allowing them to be utilized as passive Q-switches, optical limiters, and mode-lockers. TMDs offer a wide range of applications due to its unique features, including electronics, optoelectronics, sensing, and energy storage.

12.4.3 2D Topological Insulators

Discovery of new elements with unique quantum mechanical characteristics proved to be an important research avenue for the advancement of condensed matter physics. Thanks to their unusual charge and spin behavior at the surface, TIs have received a lot of attention across the last decade. TI showed gapless metallic states on its surface owing to its high spin–orbit coupling and time reversal symmetry [87, 88]. Furthermore, the occurrence of the quantum spin Hall effect in 2D TI materials has been demonstrated without the presence of an external magnetic field [89]. For its exceptional electrical characteristics, TI is a highly promising material for the advancement of next-generation electronics technology. Following that, the application of TI has expanded to the realm of photonics [90]. For instance, with the introduction of Dirac materials as nonlinear SAs, TI has been widely employed to modulate the CW laser in the temporal domain and generate Q-switched or mode-locked lasers [91–93]. In comparison to graphene, TI-based SAs have lower saturation intensity and a broader effective bandwidth. TIs are defined as materials with an insulating gap in the bulk and yet

gapless at the edge (surface). Despite the fact that their unique electrical characteristics have been extensively investigated, their nonlinear optics property has received comparatively little attention. The combination of the narrow bandgap bulk and the gapless surface enables TI to operate with a broad bandwidth of saturable absorption. Bismuth selenide (Bi_2Se_3) has a relatively low saturation intensity, which can be significant in the development of low-threshold pulsed lasers. In its surface state, TI, like graphene, has a band structure with Dirac-like linear dispersion. Multiple materials, such as Bi_2Te_3, Bi_2Se_3, and Sb_2Te_3, have been confirmed experimentally as three-dimensional TI with a single Dirac cone in its surface state. Within these three materials, Bi_2Se_3 has a slightly higher bulk bandgap (0.3 eV) than the other TI compounds and is regarded as a potential optical material for room-temperature applications [91].

12.4.4 2D MXenes

Recently, a new member of 2D family has been discovered and named as MXene, which is based on the transition metal nitrides, carbonitrides, or carbides. $M_{n+1}X_nT_x$ is the general configuration of MXene where n takes the number between 1 and 3, M refers to the transition metals, such as titanium (Ti), vanadium (V), chromium (Cr), molybdenum (Mo), niobium (Nb), and tantalum (Ta), X represents the carbon (C) and/or nitrogen (N), and T_x (where x is a variable) denotes the surface terminations group on the outer transition metal layers such as fluorine (–F), oxygen (–O), or hydroxyl (–OH) terminations. For MXene with nonfunctional group, it has a hexagonal crystal structure where the M atoms are placed in the outer layer and the X atoms located in between M atoms in the arrangement of M(1)–X–M(2)–X–M(1). In contrast, MXene with functional group would have three types of atomic structure subject to the distribution of T_x functional group [94]: (i) T_x functional groups are attached on each sides of the M_3X_2 sheet, and it is located above the M(2) atoms that is near to three X atoms; (ii) T_x functional groups are attached on each sides of the M_3X_2 sheet and it is located above the X atoms; and (iii) combination of both types where the T_x group distributed on M_3X_2 where one side is opposite to M(2) atoms and opposite to the X atoms for another side.

As of today, several methods have been reported can be performed to successfully synthesize MXene, and the most common method is by selectively etching the A layers from their $M_{n+1}AX_n$ phase precursors, where A is an A group and IIIA and IVA elements have been typically used. In order to etch the A atomic layer from their corresponding 3D MAX-phase element, the wet chemical etching process is carried out to obtain MXene. Due to the weak bonding between layer-to-layer in MAX phase as compared to their intra-layer, the A layer is lot easier to be removed with the assistance of strong etchant element. It has been reported that the synthesis method together with the etching agent have a strong influence on the structural defects, morphology, and surface groups of MXene. In the standard procedure, the bonds between the M and A element is broken by immersing the MAX phase in an acid solution, where hydrofluoric (HF) acid and hydrochloric (HCl) acid have been practically used. In spite of its simplicity route, majority of the established synthesis

methods trigger the generation of intercalated water, poisonous gases, and abundant hydroxyl groups on the MXene surfaces. This is because it mainly depends on water as the main solvent and fluoride-based compounds as etchants for selective etching process [95]. On this account, several alternative approaches have been commenced to overcomes these issues by considering an effective and greener exfoliation process and with abundant terminations-containing MXene. The fluoride-containing acidic solutions and its derivative methods [96], CVD methods [97], hydrothermal synthesis [95], and alkali-etching methods [98] are some of the examples of alternative ways to synthesize MXene. Regardless of its aforementioned drawback, the acid etching and its derivative methods are still being widely performed in current research by reason of its simple process.

In principle, MXenes are built up with an infinite lateral dimensions and thicknesses of an atomic scale, and each member of MXene family exhibits different properties owing to the termination of selected elements on the surface. MXene are regarded as a type of 2D materials with exceptional mechanical, electric, and optical properties comprising unique optical, electromagnetic, mechanical, and gas-sensitive properties [99, 100]. Apart from that, MXene displays properties that merge the aspects of both metals and ceramics such as high damage tolerant, resistant to thermal shock, and readily machinable [101]. According to the study of MXene conducted experimentally and theoretically, it have been revealed that these excellent characteristics of MXene arise due to various factors, in particular, the elemental abundance, diverse chemical compositions, tunable surface functionalities, high electrical conductivity, large surface dimensional ratio, and exceptional strength and stability [102]. Owing to the hybrid properties of good hydrophilicity and high electrical conductivities shown by MXene, it has become one of the promising candidates for various potential applications including energy storage application, electromagnetic interference shielding, and transparent conductive electrodes. Interestingly, due to their adjustable nonlinear optical properties with large nonlinear absorption coefficient (10^{-13} esu), MXenes have shown remarkable capabilities as an optical modulator in producing the Q-switched and mode-locked pulsed laser [103]. In the theoretical study conducted by Huang et al., they have found that Nb_2C (one of the member in MXene family) possesses an electron–phonon scattering at 300 K with intensities near to phonon–phonon scattering. This finding implies that there is a significant reduction in the lattice thermal conductivity [104]. In another report, Gao et al. [105] have investigated the nonlinear optical performance and carrier dynamic of Nb_2C MXene where the ultrafast relaxation time of 37.43 fs and slow relaxation time of 0.5733 ps have been obtained. Besides that, they have found that the nonlinear optical parameters of Nb_2C MXene are better compared to other 2D materials; thus, they are possibly applicable in wide range of ultrafast photonics applications. Taking advantage of the peculiar and fascinating properties of MXenes, it has been revealed that MXenes are one of the promising materials to explore in diverse applications, particularly in optoelectronics, energy storage, spintronics and catalysis, and environmental and biological fields [106]. Moreover, MXenes have wide range of applications, for example in photoluminescent quantum dots [107], conversion of

light-to-heat for energy harvesting [108], photothermal therapy [109], biosensors, chemical catalysts [110], water purification [111], composite reinforcement [112], electromagnetic interference shielding [113], and electrochemical capacitors [114].

12.5   1D and 2D Material-Based Saturable Absorbers for Fiber Lasers

12.5.1   Configuration of 1D and 2D Materials as Optical Modulators in Fiber Lasers

For optical modulation in fiber lasers, various configurations could be utilized to integrate 1D and 2D materials as SAs. Generally, 1D and 2D materials are fabricated as nanomaterials, which make them unfitting for direct application into laser cavities. As such, the 1D and 2D materials must be applied in a way that improves light–material interaction to obtain the desired effect. One of the most common and simple method to integrate 1D and 2D materials in fiber lasers is by placing the material between the surfaces of two fiber ferrules to create a closed system, as shown in Figure 12.3a. These materials are typically in the film form so that light propagating in the fiber core will directly interact with the material. The light will then be transmitted to the connecting optical fiber. For this configuration, the materials can be cut in a small size, as long as they are enough to sufficiently cover the fiber core, which is approximately 9 µm in diameter. There are also some instances that the optical deposition technique is used to deposit the material onto the surface of the ferrule [118]. Although these methods may seem straightforward and convenient, the low optical damage threshold of materials in the film form must be properly considered. This direct interaction between the light and the material may cause a high heat accumulation that could damage the material. Hence, this method of integration limits the use of 1D and 2D materials in high-power fiber lasers.

A different method to integrate 1D and 2D materials as SAs is by utilizing a reflective mechanism. This is achieved by having a silver- or gold-coated mirror with the materials plated in between. This is shown in Figure 12.3b. To achieve an efficient light–material interaction, the emitted light output from the fiber must be perpendicular to the surface of the mirror. This, however, may accidentally cause scratches on the mirror surfaces since the fiber and the mirror come into contact. Another method or solution is the use of photonic crystal fibers (PCFs), as shown in Figure 12.3c. The 1D and 2D materials could be dropped or filled into the hollow area of the PCF to allow a direct light–material interaction. However, this method also faces some challenges, since the core and air hole are smaller compared to single-mode fibers. This makes the drying of the solvent inside the core of the PCF to be an obstacle, as the unwanted solvent will result in higher insertion loss and will deteriorate the performance of the generated laser. Furthermore, it is also similarly difficult to splice PCFs and single-mode fibers (SMFs) together, which would also
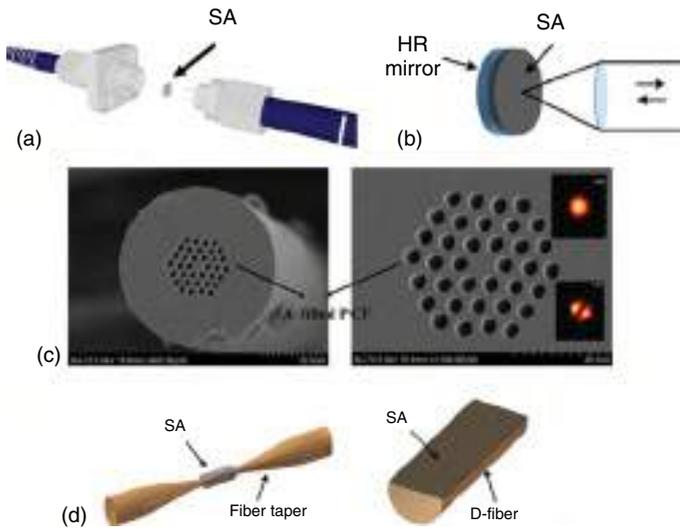
Figure 12.3 Possible arrangements of 1D and 2D materials as SAs. (a) Sandwiched between two fiber ferules. Source: Ahmad et al. [115]/Springer Nature/Public Domain. (b) Reflective mechanism. Source: Huang et al. [116]/De Gruyter/Public Domain. (c) The use of PCF. Source: Chen et al. [117], MDPI, CC BY 4.0. (d) Evanescent field interaction. Source: Huang et al. [116]/De Gruyter/Public Domain.

induce high losses. For this reasons, PCF-based structure is challenging to be assuredly reproduced.

Recently, a new method of integrating materials in fiber lasers has been attracting a lot of interest from researchers. This method utilizes the interaction between the Evanescent field of the propagating light with the 1D or 2D materials. Figure 12.3d shows that the SA materials can be deposited onto the surface of an exposed fiber such as microfibers or side-polished fibers (SPFs). The risk of the material being optically damaged is less, since there is an indirect interaction between the light and the material. This method also allows for a longer operation with less issue of heat accumulation and has been demonstrated for high-power operation in fiber laser technologies.

12.5.2 Optical Modulation in Fiber Lasers Using 1D Material-Based SAs

12.5.2.1 Q-Switching Operation

The excellent nonlinear properties of the 1D materials such as carbon-based, metal, and metal oxide nanoparticles make them excellent SAs for Q-switched fiber laser generation. A wide range of 1D materials has been investigated as SAs, including CNTs, copper (Cu), Ag, Au, Al, bismuth oxide (Bi_2O_3), nickel oxide (NiO), and iron oxide (Fe_3O_4). The Q-switched laser performances based on these 1D materials are summarized in Table 12.1 and are classified in terms of emission wavelength, repetition rate, pulse width, and pulse energy.

Table 12.1 Summary of Q-switched fiber lasers based on 1D materials.

Region (µm)	1D material	SA platform	Central wavelength (nm)	Rep. rate (kHz)	Pulse width (µs)	Pulse energy (nJ)	References
1.0	Carbon	Fiber ferrule	1060.2	24.27	12.18	143.5	[119]
	Cu	Fiber ferrule	1035.4	104	2.2	192	[120]
	Ag	Fiber ferrule	1033.3	184.8	1.01	58.3	[121]
	Au	Fiber ferrule	1064.5	61.88	4.23	50.74	[122]
1.55	Carbon	Fiber ferrule	1568.6	47	4.6	102.1	[123]
			1533.6	33.62	4.2	531	[124]
	Al	Fiber ferrule	1567.6	48.8	2.17	11.29	[125]
	Bi_2O_3	Fiber ferrule	1564	49.5	1.55	21.31	[126]
	Ag	Side-polished fiber	1558	66.74	6.12	139.08	[127]
	NiO	Fiber ferrule	1561.2	52.18	5.2	31.5	[128]
	Cu	Fiber ferrule	1560	83	2.6	66	[129]
	Au	Fiber ferrule	1561	23	9.6	—	[130]
			1559.2	41.17	5.69	403.2	[131]
2.0	Au	Fiber ferrule	1969	21.95	2.6	89.8	[132]
			1891	49.64	2.38	120	[133]
			1940	52.75	2.4	180	[134]
	Fe_3O_4	Side-polished fiber	1943	87	0.88	14.2	[135]

CNTs, which possess outstanding optical properties such as having a high third-order susceptibility and a broadband operation, were among the first of 1D materials to attract the attention of the photonics community. They are classified into three broad types: SWCNTs, DWCNTs, and MWCNTs. Some exceptional performances of Q-switching operation based on MWCNTs have been obtained, delivering a pulse with maximum energy of 531 nJ [124]. Stable Q-switching operation with CNTs was also realized in 1.0 µm region, generating a maximum pulse energy of 143.5 nJ [119]. The broadband operation of CNTs-based SA is due to the different electronic transitions of nanotubes which vary with the tube diameter and chirality [136].

Metal nanoparticles have also drawn much attention attributed to the multiple excellent properties and advantages that are well fitted with the requirements of a good SA. Several works have reported the uses of metal nanoparticles as SAs for Q-switching operation in different fiber lasers. For example, the Q-switched lasers at 1.0 and 1.55 µm have been investigated by using Ag and Cu nanoparticles-based SAs. The results of Q-switched ytterbium-doped fiber laser using Ag as SA are shown in Figure 12.4a–e. Broadband Q-switched pulse generation was reported from 1.0, 1.55, and 2.0 µm fiber laser systems using Au SA. The results of Q-switched
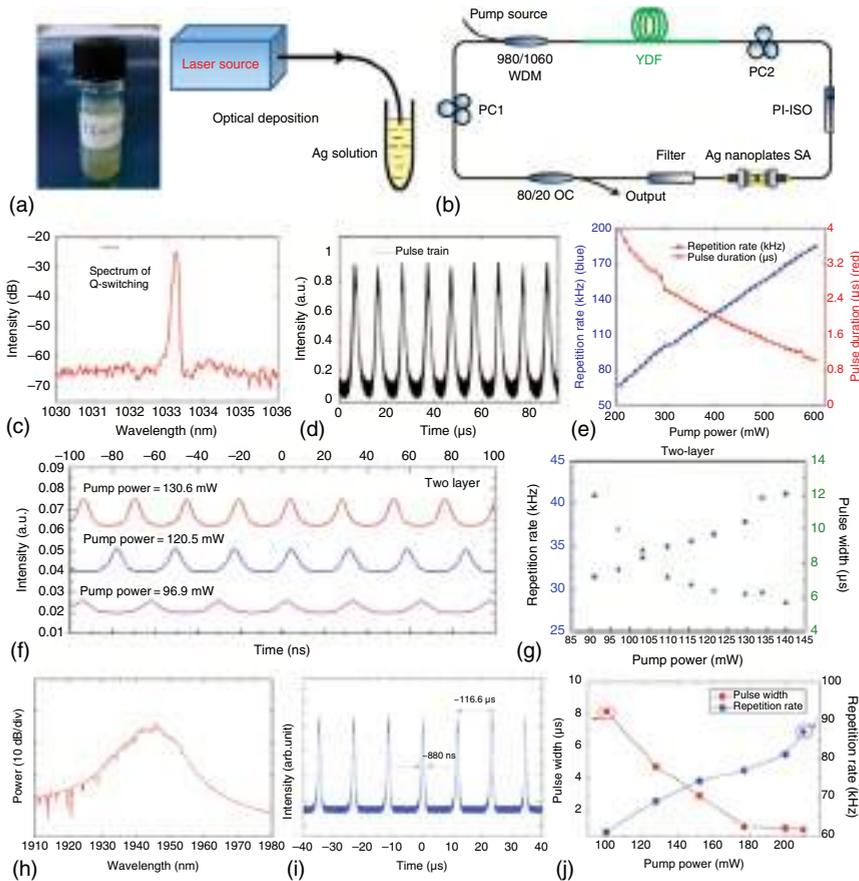
Figure 12.4 Q-switching fiber lasers with various 1D SAs. (a–e) Ag. (a) Ag solution and optical deposition method setup. (b) Schematic of Q-switched ytterbium-doped fiber laser. (c) Optical spectrum at 1.0 μm. (d) Pulse train. (e) Evolutions of the pulse repetition rate and the pulse width against pump power at 1.0 μm. Source: Fu et al. [121], Walter de Gruyter GmbH, CC BY 4.0. (f–g) Au. (f) Pulse train. (g) Evolutions of the pulse repetition rate and the pulse width against pump power at 1.55 μm. Source: Lee et al. [131]/Springer Nature/Public Domain. (h–j) Fe_3O_4. (h) Optical spectrum at 2.0 μm. (i) Pulse train. (j) Evolutions of the pulse repetition rate and the pulse width against pump power at 2.0 μm. Source: Koo et al. [135]/ with permission of Elsevier.

fiber operating at 1.55 μm are depicted in Figure 12.4f,g. In an investigation into the saturation property of metal nanoparticles, Kim et al. found that the origin of the saturation effect is correlated to the intensity-dependent intrinsic dielectric function of nanoparticles, which causes a shift in the plasmonic resonance, as a result, a decrease in the effective nonlinear coefficients [137]. It is also found that the saturation behavior is strongest near the surface plasmon resonance [138–140]. There are other works reported that the ground-state plasmon bleaching, which is connected to the intrinsic electron dynamics in metal nanoparticles, causes the saturation effect of the metal nanoparticles [141–143]. Besides, it is also well known that metal

nanoparticles SA exhibit broad saturable absorption property which ranges from UV region to infrared region due to the sensitivity of plasmon resonance toward the shape and size of the metallic nanoparticles [144–148].

12.5.2.2 Mode-Locking Operation

Compared to Q-switched fiber lasers, mode-locked fiber lasers have significant advantages in delivering high-frequency pulse with high peak power. It has been proven as one of the most effective tools for a wide variety of applications in medical diagnosis, astronomical detection, ultraprecision manufacturing, etc., because of their extremely narrow pulse width and large peak power. The remarkable optical nonlinearity of 1D materials has also been studied in generating mode-locked pulses. The incorporation of 1D material-based SAs in the laser cavity is able to modulate the circulating light in the laser cavity which results in a fixed phase between most of the longitudinal modes, thus generating a mode-locked pulse train in a time domain. Several works have reported the generation of mode-locked fiber lasers using 1D materials as SAs, and the performances are shown in Table 12.2.

Table 12.2 Summary of mode-locked fiber lasers based on 1D materials.

Region (μm)	1D material	SA platform	Central wavelength (nm)	Repetition rate (MHz)	Pulse width (ps)	Pulse energy (nJ)	References
1.0	Carbon	Fiber ferrule	1025.5	21.2	0.3	—	[149]
1.55	Cu	Fiber ferrule	1563.3	1.86	17 300	9.15	[9]
	CuO	Fiber ferrule	1560	0.98	1.7	1.29	[11]
	Carbon	Fiber ferrule	1533.6	15.3	1.8	0.28	[150]
			1555	358.6	0.55	0.001	[151]
			1560.5	17.4	0.49	—	[152]
		PCF	1566.36	9.1	1.003	0.66	[153]
		Microfiber	1557.1	5.41	0.82	2.36	[154]
	Au	Microfiber	1552	4.76	0.88	—	[155]
		Fiber ferrule	1559.9	11.7	3.4	2.34	[131]
		D-shaped fiber	1560	25.72	0.59	—	[156]
	MgO	Fiber ferrule	1569.1	3.5	5.6	2.17	[157]
2.0	Au	Microfiber	1943.5	25.66	0.4	1.78	[158]
		Fiber ferrule	1982	37.49	4.02	—	[159]
		D-shaped fiber	1950	27.66	0.37	—	[156]
	Co_3O_4	Fiber ferrule	1958.1	11.36	1.39	0.02	[160]
	Carbon	Fiber ferrule	1902	14.83	0.9	—	[161]
			1928.5	56.37	0.5	0.5	[6]

1D materials, in addition to its usual sandwiched structure, lends itself well to integration with microstructure optical fibers such as D-shaped fibers, SPFs, or photonics crystal fibers (PCFs). The former structure is normally classified as the transmission-type SA, while the latter is categorized in the evanescent field-type SA. The evanescent field-type SA employs the evanescent wave to interact with saturable absorption materials on the surface of D-shaped fibers or tapered fibers as well as inside the cladding holes of PCFs. In view of recent development on the 1D materials-based mode-locking fibers, either transmission-type SA or evanescent field-type SA has been studied. For example, Li et al. demonstrated mode-locked erbium-doped fiber lasers by filling short SWCNTs into cladding holes of grapefruit-type of PCF [153], as shown in Figure 12.5a–c. Stable mode-locked pulse with a duration of 1.003 ps operating at 1566.36 nm was generated. Cui et al. employed the Au nanorods deposited onto a D-shaped fiber to induce mode-locking in the thulium-doped fiber laser with a repetition rate of 27.66 MHz, a central wavelength of 1950 nm, a pulse width of 370 fs, and a signal-to-noise ratio (SNR) of 67 dB [156]. Wang et al. deposited Au nanorods onto the microfiber as a mode-locker for erbium-doped fiber laser [155]. These Au nanorods-deposited microfiber-based passively mode-locked erbium-doped fiber lasers generated ~887 fs optical pulse at 1552 nm. Khaleel et al. utilized the magnesium oxide (MgO)/polyvinyl alcohol (PVA) thin film as the SA to mode-lock the erbium-doped fiber laser at 1569.1 nm with a repetition rate of 3.5 MHz and pulse width of 5.6 ps, as shown in Figure 12.5g–i. There are also other works that reported the use of 1D materials–polymer composite SA to mode-lock the fiber lasers such as Cu [9], CuO [11], and Co_3O_4 [160].

Based on the previous reported works, it is clear that 1D materials play a crucial role on initiating mode-locking operation in the fiber laser systems. Additionally, it is assure that the 1D materials are excellent candidates for broadband SA, since they cover a wide wavelength range from 1000 to 2500 nm.

12.5.3 Optical Modulation in Fiber Lasers Using 2D Material-Based SAs

12.5.3.1 Q-Switching Operation

Graphene is the most well-known 2D material, consisting of a single layer of carbon atoms arranged in a 2D honeycomb lattice. Categorized as a 2D monoelement, graphene has been widely used as a SA for all types of fiber lasers owing to its distinctive optical properties, such as broad tuning range. The saturable absorption property of graphene was first studied by two independent groups from Singapore and United Kingdom [162, 163]. Following those reports, several studies have reported the use of graphene as SA in generating Q-switched fiber laser. For instance, Zhang et al. demonstrated a Q-switched erbium-doped fiber laser using graphene-deposited microfiber as SA, delivering Q-switched pulse with a minimum duration of 13.6 μs [164]. Q-switched fiber lasers based on graphene thin film have also been reported in 2.0 μm region [165, 166]. The ultra-wideband absorption shown by graphene is ascribed to its zero-bandgap structure. Unlike
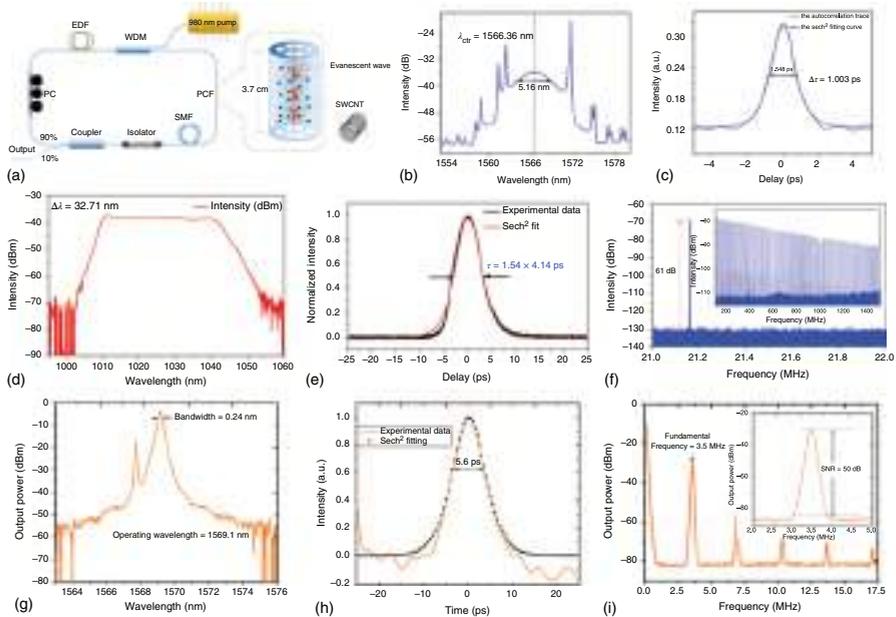
Figure 12.5 Mode-locked fiber lasers with various 1D SAs. (a–c) CNTs-PCF. (a) Schematic of mode-locked erbium-doped fiber laser using PFC filled with SWCNT as SA. (b) Optical spectrum 1.55 μm. (c) Autocorrelation trace. Source: Li et al. [153]/Optical Express/Public Domain. (d–f) CNTs. (d) Optical spectrum at 1.0 μm. (e) Autocorrelation trace. (f) RF spectrum. Source: Hou et al. [149]/Optical Express/Public Domain. (g–i) MgO. (g) Optical spectrum at 1.55 μm. (h) Autocorrelation trace. (i) RF spectrum. Source: Khaleel et al. [157]/Elsevier.

CNTs, graphene requires no bandgap optimization or diameter/chiral adjustment, making the broadband SA preparation process easier. Antimonene, another 2D monoelement material has gradually become known and studied. Yuan et al. has successfully employed antimonene SA in erbium-doped fiber laser [55]. Q-switched fiber laser with center wavelength of 1558 nm and pulse width of 1.42 μs was realized, as shown in Figure 12.6a–c. Since the first discovery of graphene SA, the number of 2D materials-based SA such as TMDs, Tis, and MXenes has been growing continuously. A summary of Q-switched fiber lasers based on these 2D materials is shown in Table 12.3.

The second most widely studied 2D material is probably TMDs, a class of nonlinear optical materials that include a wide range of transition metal elements. The nonlinear optical performance of layered TMDs is significantly better than that of bulk TMDs because they have a direct bandgap ranging from 1 to 2.5 eV, depending on the chemical compositions. Among TMDs, the saturable absorption of layered MoS_2 was first investigated in 2013 [181]. Following this report, Luo et al. proposed and demonstrated 1.0, 1.55, and 2.0 μm passively Q-switched fiber lasers by exploiting a few-layer MoS_2 as SA [170]. One of the lasers is able to produce Q-switched pulse with large energy of ~1 μJ and pulse width of 1.76 μs. Layered WS_2 also possesses remarkable optical properties, including high optical nonlinear susceptibility and broadband working wavelength range. The saturable absorption property of layered WS_2 was studied by Zhang et al. in ytterbium-doped fiber laser [167], as shown in Figure 12.6d–h. The laser generated stable Q-switched pulse at 1030 nm with pulse width of 3.2 μs and pulse energy of 13.6 nJ. The same WS_2 SA was then incorporated in the erbium-doped fiber laser, generating a Q-switched pulse centered at 1558 nm with a minimum pulse width of 2.38 μs and maximum pulse energy of 195 nJ [167], as depicted in Figure 12.6i–k.

Following the success of MoS_2 and WS_2, a vast number of layered TMD materials have emerged and investigated as Q-switchers such as $MoSe_2$ [176], TiS_2 [177], ReS_2 [178], PdS_2 [174], and $PtTe_2$ [169]. Remarkably, the operating photon energy of the reported works is observed to be much lower that the bandgap of the TMDs SAs. This could be attributed to the sub-bandgap absorption arises from edge-induced sub-bandgap states [182–184]. The state at the material's edges, in particular, plays a crucial role in enabling absorption by exciting the electrons to the edge states level within the bandgap, resulting in saturable absorption at high incident intensity through Pauli blocking. Moreover, the wideband saturable absorption of TMDs materials could be explained by a distribution of edge-induced states within the bandgap.

Ascribing to its small indirect bulk bandgap of 0.2–0.3 eV, TIs exhibit effective wideband nonlinear optical response spanning from visible to the mid-IR region. Among the various TIs, Bi_2Se_3 is the most used TI as SA for Q-switching generation [60, 171, 179]. Recently, a new class of 2D materials, known as MXenes, has widely investigated. Several reported works have confirmed that it could be utilized as SA to achieve Q-switched pulse output in fiber lasers [22, 103, 168, 180], as shown in Figure 12.6l–n.
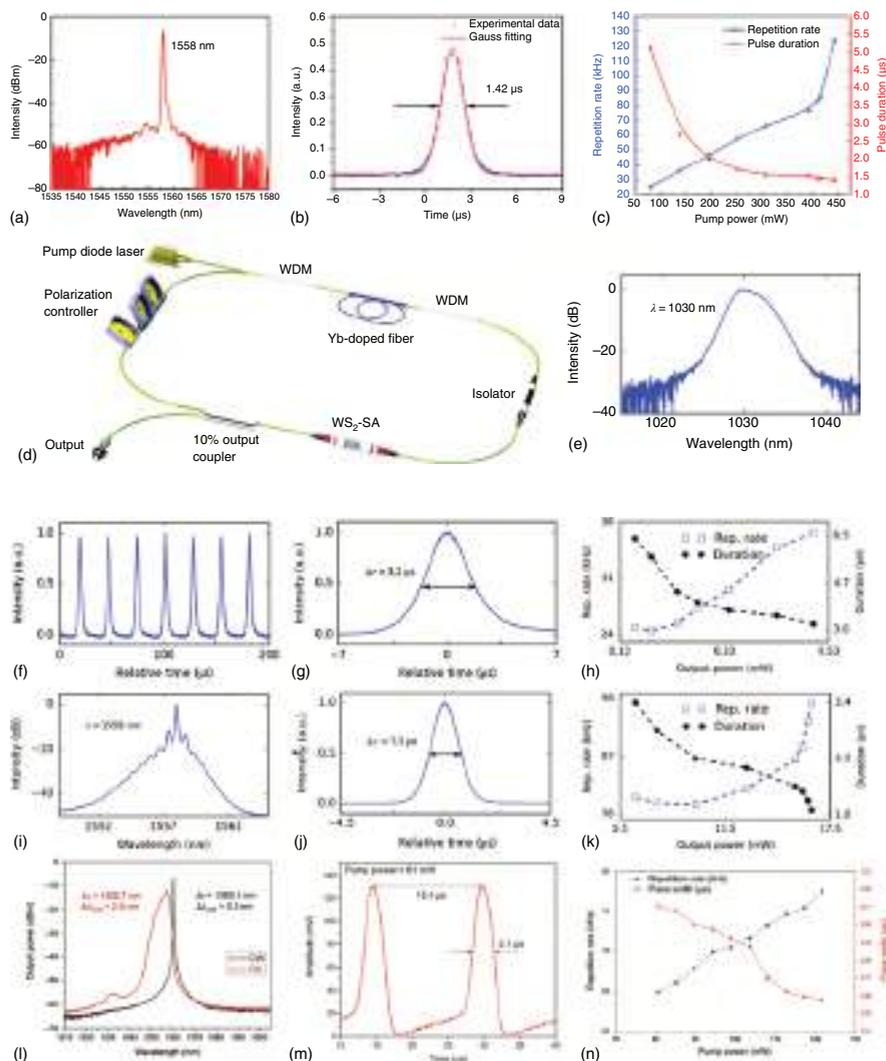
Figure 12.6 Q-switched fiber lasers with various 2D SAs. (a–c) Antimonene. (a) Optical spectrum at 1.55 μm. (b) Single-pulse profile. (c) Evolutions of the pulse repetition rate and the pulse width against pump power. Source: Yuan et al. [55]/Elsevier. (d–k) WS$_2$. (d) Schematic of ytterbium-doped fiber laser using WS$_2$ SA. (e) Optical spectrum at 1.0 μm. (f) Oscilloscope trace. (g) Single-pulse profile. (h) Evolutions of the pulse repetition rate and the pulse width against pump power at 1.0 μm. (i) Optical spectrum at 1.55 μm. (j) Single-pulse profile. (k) Evolutions of the pulse repetition rate and the pulse width against pump power at 1.55 μm. Source: Zhang et al. [167]/Springer Nature/Public Domain. (l–n) Ti$_3$C$_2$T$_x$ MXene. (l) Optical spectrum. Source: Jafry et al. [168]/with permission of Elsevier.

12.5.3.2 Mode-Locking Operation

The excellent nonlinear properties of the novel layered 2D materials such as graphene, bismuthene, TMDs, TIs, and MXenes have also been proved effective to induce mode-locking operation in fiber lasers. Examples of successful

Table 12.3 Summary of Q-switched fiber lasers based on 2D materials.

Region (µm)	2D material	SA platform	Central wavelength (nm)	Rep. rate (kHz)	Pulse width (µs)	Pulse energy (nJ)	References
1.0	PtTe$_2$	Fiber ferrule	1066	33.5	5.2	74	[169]
	WS$_2$	Fiber ferrule	1030	36.7	3.2	13.6	[167]
	MoS$_2$	Fiber ferrule	1066.5	28.9	5.8	32.6	[170]
	Bi$_2$Se$_3$	Fiber ferrule	1050.4	46	5.44	89	[60]
			1057.8	1.2	3.48	13.3	[171]
1.55	Graphene	Microfiber	1558.6	39.1	13.6	251.9	[164]
			—	69.32	2.2	93.76	[172]
	Antimonene	Fiber ferrule	1558	124.1	1.42	54	[55]
			1559.63	76.7	1.58	37.9	[173]
	PdS$_2$	Fiber ferrule	1567	26	4.5	15.1	[174]
	WS$_2$	Fiber ferrule	1560	60.88	2.38	195	[175]
			1558	97	1.3	179.6	[167]
	MoSe$_2$	Fiber ferrule	1562.3	32.8	30.4	57.9	[176]
	MoS$_2$	Fiber ferrule	1565	27	5.4	63.2	[170]
	TiS$_2$	Microfiber	1560.2	50.7	4.01	9.5	[177]
	ReS$_2$	Fiber ferrule	1557.3	19	5.49	62.8	[178]
	Bi$_2$Se$_3$	Fiber ferrule	1560	68.2	2.4	47.1	[179]
			1560.33	62.5	2.1	6.1	[60]
	Ti$_3$C$_2$T$_x$	Fiber ferrule	1563	48.74	1.18	82.06	[22]
		D-shaped fiber	1556.7	77.52	2.58	134.2	[168]
	Nb$_2$C	Fiber ferrule	1558.73	75.19	13.3	15.63	[103]
2.0	Graphene	Fiber ferrule	1932	36.29	6.8	11.03	[165]
			1976	43	1.41	—	[166]
	MoS$_2$	Fiber ferrule	2032	48.1	1.76	1000	[170]
	Ti$_3$C$_2$T$_x$	Fiber ferrule	1996	33.3	3.55	111	[180]

implementation of these 2D materials in generation of mode-locked fiber lasers are summarized in Table 12.4.

Bismuthene, which is a 2D monoelement material similar to graphene, has attracted a huge interest due to its unique electronic transport, semi-metallic bonding, and enhanced long-term stability. It is also found that a few layers of bismuthene have a direct bandgap ranging from 0.36 to 0.99 eV making it a perfect SA for developing near- to mid-infrared mode-locked fiber lasers [198]. Guo et al. demonstrated a mode-locked fiber laser using bismuthene-deposited on microfiber as SA. The fiber laser generated a 193 fs mode-locked pulse centered at 1561 nm with a

Table 12.4 Summary of mode-locked fiber lasers based on 2D materials.

Region (μm)	2D material	SA platform	Central wavelength (nm)	Rep. rate (MHz)	Pulse width (ps)	Pulse energy (pJ)	References
1.0	Bismuthene	Microfiber	1035.8	21.74	46	—	[185]
	PdS_2	D-shaped fiber	1033	24.4	375	640	[186]
	SnS_2	Fiber ferrule	1062.66	39.33	0.65	—	[187]
	Ti_2CT_x	D-shaped fiber	1051.08	11.2	164.4	—	[188]
1.55	Graphene	Microfiber	1563.8	26.3	1.94	—	[172]
	Bismuthene	Microfiber	1561	8.85	0.19	—	[189]
			1531	4	1.3	350	[190]
			1557.5	22.74	0.62	—	[191]
	PdS_2	D-shaped fiber	1565.8	12.1	0.8	—	[174]
	$MoSe_2$	Microfiber	1558.35	16.33	1	—	[192]
		Fiber ferrule	1560	8.8	0.58	91.3	[193]
	TiS_2	Microfiber	1563.3	22.7	1.25	25.3	[177]
	ReS_2	Fiber ferrule	1558.6	5.48	1.6	—	[178]
	Bi_2Te_3	Fiber ferrule	1570.45	13.14	0.5	—	[194]
		Microfiber	1560.8	18.55	0.43	27	[195]
	Bi_2Se_3	Fiber ferrule	1562.4	22.6	0.63	15.6	[179]
	Ti_2CT_x	D-shaped fiber	1565.4	8.25	5.3	—	[188]
	Nb_2C	Microfiber	1559	14.12	0.77	212.7	[65]
2.0	Graphene	Sandwiched	1913.7	19.97	—	20	[166]
	MoS_2	Sandwiched	1926	13.9	1.33	—	[196]
	$MoSe_2$	D-shaped fiber	1912.6	18.21	0.92	—	[197]
	Bi_2Te_3	Microfiber	1909.5	21.5	1.26	—	[17]

repetition rate of 8.85 MHz [189], as shown in Figure 12.7a–c. Another work on mode-locking operation in 1.0 μm region using bismuthene SA has been demonstrated by Feng et al. [185].

In 2020, Cheng et al. fabricated an SA device based on a pentagonal TMD material, PdS_2 [186]. The PdS_2 was deposited on a D-shaped fiber creating all-fiber SA device for mode-locking operation in the ytterbium-doped fiber laser. A highly stable mode-locked pulse was realized operating at 1033 nm with pulse duration of 375 ps and repetition rate of 21.74 MHz, as shown in Figure 12.7d–f. The wideband saturable absorption of PdS_2 was also confirmed by the same group when they managed to observe mode-locked erbium fiber laser using PdS_2 SA [174]. TIs such as Bi_2Te_3 and Bi_2Se_3 were also used as SAs to demonstrate the 1.55 μm [179, 194, 195] and 2.0 μm [17] mode-locked fiber lasers. The performances of mode-locked erbium-doped fiber laser using Bi_2Te_3 deposited onto a microfiber are depicted in Figure 12.7g–k.
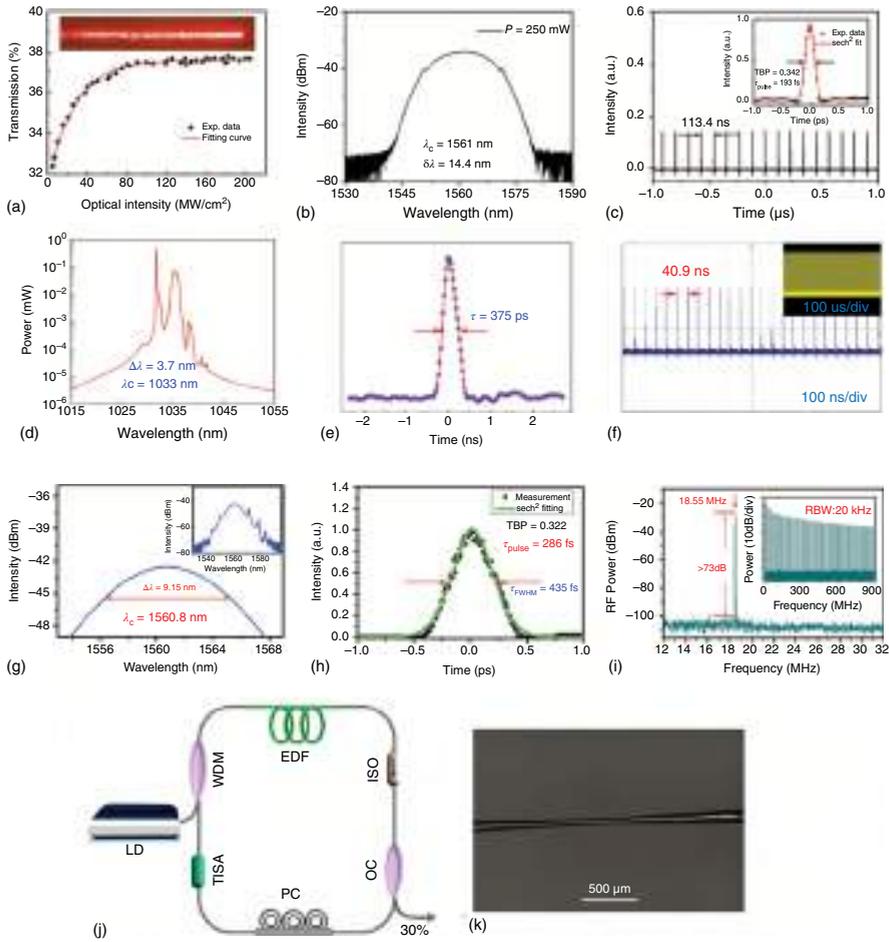
Figure 12.7 Mode-locked fiber lasers with various 2D SAs. (a–c) Bismuthene. (a) The nonlinear saturable absorption curve of the microfiber-based bismuthene device. Inset shows the evanescent field of red light source. (b) Optical spectrum 1.55 μm. (c) Pulse train. Inset show autocorrelation trace. Source: Guo et al. [189], Optica Publishing Group, CC BY 4.0. (d–f) PdS$_2$. (d) Optical spectrum at 1.0 μm. (e) Autocorrelation trace. (f) Pulse train. Source: Cheng et al. [186], MDPI, CC BY 4.0. (g–k) Bi$_2$Te$_3$. (g) Optical spectrum. (h) Autocorrelation trace. (i) RF spectrum. (j) Schematic of mode-locked erbium doped fiber laser with Bi$_2$Te$_3$ microfiber SA. (k) Side view of microfiber coated with Bi$_2$Te$_3$. Source: Yan et al. [195], Springer Nature, CC BY 4.0.

12.6 Conclusion, Challenges, and Future Perspectives

The utilization of 1D- and 2D-structured materials as optical modulators in fiber lasers has increased dramatically since the discovery of CNTs and graphene. Optical modulation based on these materials has advanced in practically every aspect that includes theoretical studies, fabrication and integration methods, and also different configurations of the laser cavities. In the area of nonlinear photonics, research

related to 1D and 2D materials has evolved at a rapid pace. This is owing to the ongoing advancements in the technology of material fabrication, which has a direct effect on the enhancement of the general and nonlinear properties of 1D and 2D materials. Although it is widely accepted that the utilization of 1D and 2D materials could not be a mean in overcoming issues and problems related to the development of optical modulators in fiber lasers, they have contributed in making photonics devices close to a commercial status. In this chapter, the significance of 1D- and 2D-structured materials in the advancement of optical modulators has been comprehensively discussed. Although the development and the research of this topic are still in keeping with the present trend of scientific investigation, difficulties in implementing the outcome of the research for practical purposes still remain. This, however, may open up various possibilities in coming out with solutions, which could serve as a new driving purpose in this area.

To date, the field of nonlinear photonics has grown tremendously due to the emergence of novel 1D and 2D materials that have been a key contributor with the added efforts of scientific researchers. One of the remaining challenges is the technology's industrialization or commercialization, as the materials used would have a significant impact on the functionality of the developed optical modulators. If the optical modulators based on the 1D and 2D materials are robust and reliable as conventional SAs, commercialization would then be a reality. Another challenge that must be overcome is the photothermal effect generated by the light–material interaction. Although some approaches for overcoming the photothermal effect have been demonstrated [43–49], other optical modulators based on 1D and 2D materials remain vulnerable to optical damage. As a result, it is critical to find new approaches to address this problem.

Some of the future perspectives in the advancement of optical modulators are proposed as follows. As of now, there have various demonstrations of optical modulators in fiber lasers that are able to generate pulses with a high peak power and pulse energy using 1D and 2D materials. Further improvement could be made to generate pulses with shorter pulse widths in order to have outputs with higher peak powers. This could be obtained by having an optimized fabrication technique to have a low-loss material and also by having an improved design of the laser cavities. In addition, further research could be extended for the generation of Q-switched as well as mode-locked lasers in the longer wavelengths from 2.1 to 4 μm regions, which are useful for medical and other industrial-related applications. Up till now, most of the research using 1D and 2D materials have been focused on the shorter wavelengths of 1–2 μm, with little works touching in the longer wavelengths. The proposed study is expected to be one of the major research focuses in the near future.

In addition, other nonlinear optical phenomena in optical fibers could be explored using 1D and 2D materials, such as four-wave mixing (FWM), second-harmonic generation (SHG), and also multi-soliton molecules in fiber lasers. It is consequently critical to conduct additional research into the optical nonlinearity of 1D and 2D materials. As the current works and investigations on other nonlinear optical phenomena are still scarce, focus on this research topic will be greatly beneficial on the advancement of 1D and 2D materials for other photonics and optoelectronics applications.

References

1 Liao, Q., Xu, Z., Zhong, X. et al. (2014). An organic nanowire waveguide exciton--polariton sub-microlaser and its photonic application. *J. Mater. Chem. C* 2 (15): 2773–2778.

2 Yan, R., Gargas, D., and Yang, P. (2009). Nanowire photonics. *Nat. Photonics* 3 (10): 569–576.

3 Shi, Y.L. and Wang, X.D. (2021). 1D organic micro/nanostructures for photonics. *Adv. Funct. Mater.* 31 (7): 1–20.

4 Avouris, P., Freitag, M., and Perebeinos, V. (2008). Carbon-nanotube photonics and optoelectronics. *Nat. Photonics* 2 (6): 341–350.

5 Avouris, P. (2009). Carbon nanotube electronics and photonics. *Phys. Today* 62 (1): 34–40.

6 Sobon, G., Duzynska, A., Świniarski, M. et al. (2017). CNT-based saturable absorbers with scalable modulation depth for thulium-doped fiber lasers operating at 1.9 μm. *Sci. Rep.* 7 (February): 1–9.

7 Xiong, X., Zou, C.-L., Ren, X.-F. et al. (2013). Silver nanowires for photonics applications. *Laser & Photonics Rev.* 7 (6): 901–919.

8 Kassab, L.R.P. and De Araujo, C.B. (2018). *Metal Nanostructures for Photonics*. Elsevier.

9 Ismail, E.I., Ahmad, F., Shafie, S. et al. (2020). Copper nanowires based mode-locker for soliton nanosecond pulse generation in erbium-doped fiber laser. *Results Phys.* 18: 103228.

10 Choi, S. and Aharonovich, I. (2015). Zinc oxide nanophotonics. *Nanophotonics* 4 (4): 437–458.

11 Sadeq, S.A., Harun, S.W., and Al-Janabi, A.H. (2018). Ultrashort pulse generation with an erbium-doped fiber laser ring cavity based on a copper oxide saturable absorber. *Appl. Opt.* 57 (18): 5180–5185.

12 Wu, K., Chen, B., Zhang, X. et al. (2018). High-performance mode-locked and Q-switched fiber lasers based on novel 2D materials of topological insulators, transition metal dichalcogenides and black phosphorus: review and perspective. *Opt. Commun.* 406: 214–229.

13 Chen, B., Zhang, X., Wu, K. et al. (2015). Q-switched fiber laser based on transition metal dichalcogenides MoS_2, $MoSe_2$, WS_2, and WSe_2. *Opt. Express* 23 (20): 26723–26737.

14 Chen, H., Yin, J., Yang, J. et al. (2017). Transition-metal dichalcogenides heterostructure saturable absorbers for ultrafast photonics. *Opt. Lett.* 42 (21): 4279–4282.

15 Ahmad, H., Aidit, S.N., Mohanraj, J. et al. (2018). Mixed transition metal dichalcogenide as saturable absorber in ytterbium, praseodymium, and erbium fiber laser. *IEEE J. Quantum Electron* 54 (3): 1600409.

16 Lee, J. and Lee, J.H. (2018). Femtosecond Tm–Ho co-doped fiber laser using a bulk-structured Bi_2Se_3 topological insulator. *Chinese Phys. B* 27 (9): 94219.

17 Yin, K., Zhang, B., Li, L. et al. (2015). Soliton mode-locked fiber laser based on topological insulator Bi 2 Te 3 nanosheets at 2 μm. *Photonics Res.* 3 (3): 72–76.

18 Dong, Y., Chertopalov, S., Maleski, K. et al. (2018). Saturable absorption in 2D Ti_3C_2 MXene thin films for passive photonic diodes. *Adv. Mater.* 30: 1705714.

19 Wang, C., Xu, J., Wang, Y. et al. (2021). MXene ($Ti_2 NT_x$): synthesis, characteristics and application as a thermo-optical switcher for all-optical wavelength tuning laser. *Sci. China Mater.* 64 (1): 259–265.

20 Jiang, X., Liu, S., Liang, W. et al. (2018). Broadband nonlinear photonics in few-layer MXene $Ti_3C_2T_x$ (T = F, O, or OH). *Laser Photon. Rev.* 12 (2): 1700229.

21 Wu, Q., Jin, X., Chen, S. et al. (2019). MXene-based saturable absorber for femtosecond mode-locked fiber lasers. *Opt. Express* 27 (7): 10159–10170.

22 Ahmad, H., Albaqawi, H.S., Yusoff, N. et al. (2020). Tunable passively Q-switched erbium-doped fiber laser based on $Ti_3C_2T_x$ MXene as saturable absorber. *Opt. Fiber Technol.* 58: 102287.

23 Li, J., Zhang, Z., Du, L. et al. (2019). Highly stable femtosecond pulse generation from a MXene $Ti_3C_2T_x$ (T = F, O, or OH) mode-locked fiber laser. *Photonics Res.* 7 (3): 260–264.

24 Fründel, F.B.A. (2014). *Optical Pulses-Lasers-Measuring Techniques*. Academic Press.

25 McClung, F.J. and Hellwarth, R.W. (1962). Giant optical pulsations from ruby. *Appl. Opt.* 1 (101): 103–105.

26 Paschotta, R., Häring, R., Gini, E. et al. (1999). Passively Q-switched 01-mJ fiber laser system at 153 μm. *Opt. Lett.* 24 (6): 388.

27 Popa, D., Sun, Z., Hasan, T. et al. (2001). Graphene Q-switched, tunable fiber laser. *Appl. Phys. Lett.* 98.

28 Ion, J. (2005). *Laser Processing of Engineering Materials: Principles, Procedure and Industrial Application*. Elsevier.

29 Saha, A. and Manna, N. (2011). *Optoelectronics and Optical Communication*. Laxmi Publications.

30 Hargrove, L.E., Fork, R.L., and Pollack, M.A. (1964). Locking of He–Ne laser modes induced by synchronous intracavity modulation. *Appl. Phys. Lett.* 5 (1): 4–5.

31 Tamura, K., Ippen, E.P., Haus, H.A., and Nelson, L.E. (1993). 77-fs pulse generation from a stretched-pulse mode-locked all-fiber ring laser. *Opt. Lett.* 18 (13): 1080–1082.

32 Abdul Rahim, Z., Yusof, N.A., Mohammad Haniff, M.A.S. et al. (2018). Electrochemical measurements of multiwalled carbon nanotubes under different plasma treatments. *Materials (Basel).* 11 (10): 1902.

33 Mohammadian, N., Ghoreishi, S.M., Hafeziyeh, S. et al. (2018). Optimization of synthesis conditions of carbon nanotubes via ultrasonic-assisted floating catalyst deposition using response surface methodology. *Nanomaterials* 8 (5): 316.

34 Muangrat, W., Obata, M., Htay, M.T. et al. (2021). Nitrogen-doped graphene nanosheet-double-walled carbon nanotube hybrid nanostructures for high-performance supercapacitors. *FlatChem* 29: 100292.

35 Khizir, H.A. and Abbas, T.A.-H. (2021). Hydrothermal synthesis of TiO_2 nanorods as sensing membrane for extended-gate field-effect transistor (EGFET) pH sensing applications. *Sensors Actuators A Phys.* 113231.

36 Cheng, Y., Xin, C., Zhao, J. et al. (2022). Constructing lateral sulfur-gradient Sb_2 (S_xSe_{1-x}) 3 heterostructures for Sb_2Se_3 nanorod photocathodes with enhanced photoelectrochemical properties. *Electrochim. Acta* 403: 139610.

37 Velayati, M., Hassani, H., and Darroudi, M. (2021). Green synthesis of Se-nanorods using poly anionic cellulose (PAC) and examination of their photocatalytic and cytotoxicity effects. *Inorg. Chem. Commun.* 133: 108935.

38 Scardaci, V. (2021). Copper nanowires for transparent electrodes: properties, challenges and applications. *Appl. Sci.* 11 (17): 8035.

39 Zheng, B.-C., Shi, J.-B., Lin, H.-S. et al. (2020). Growth of less than 20 nm SnO nanowires using an anodic aluminum oxide template for gas sensing. *Micromachines* 11 (2): 153.

40 Chen, C., Zhou, P., Wang, N. et al. (2018). UV-assisted photochemical synthesis of reduced graphene oxide/ZnO nanowires composite for photoresponse enhancement in UV photodetectors. *Nanomaterials* 8 (1): 26.

41 Li, H., Zhao, G., Wang, L. et al. (2016). Morphology controlled fabrication of InN nanowires on brass substrates. *Nanomaterials* 6 (11): 195.

42 Yoo, K., Lee, W., Kang, K. et al. (2020). Low-temperature large-area fabrication of ZnO nanowires on flexible plastic substrates by solution-processible metal-seeded hydrothermal growth. *Nano Converg.* 7 (1): 1–10.

43 Song, Z., Xu, S., Li, M. et al. (2016). Solution-processed SnO_2 nanowires for sensitive and fast-response H_2S detection. *Thin Solid Films* 618: 232–237.

44 Hu, P., Dong, S., Zhang, X. et al. (2017). Synthesis and characterization of ultralong SiC nanowires with unique optical properties, excellent thermal stability and flexible nanomechanical properties. *Sci. Rep.* 7 (1): 1–10.

45 Ren, L., Li, H., and Ma, L. (2011) The Selective Growth of Silicon Nanowires and Their Optical Activation. Nanowires-Implementations Appl.

46 Suo, G., Jiang, S., Zhang, J. et al. (2014). Synthetic strategies and applications of GaN nanowires. *Adv. Condens. Matter Phys.* 2014: 456163.

47 Chen, Y.J., Zhang, H.Z., and Chen, Y. (2006). Pure boron nitride nanowires produced from boron triiodide. *Nanotechnology* 17 (3): 786.

48 Chueaiarrom, C., Loedsapchinda, N., Puttharugsa, C. et al. (2020). Gold nanorod-optical fiber for sensing biomolecular interaction. *Key Eng. Mater.* 853: 81–86.

49 Rekha, C.R., Nayar, V.U., and Gopchandran, K.G. (2018). Synthesis of highly stable silver nanorods and their application as SERS substrates. *J. Sci. Adv. Mater. Devices* 3 (2): 196–205.

50 Chen, Y.-H., Hung, H.-H., and Huang, M.H. (2009). Seed-mediated synthesis of palladium nanorods and branched nanocrystals and their use as recyclable Suzuki coupling reaction catalysts. *J. Am. Chem. Soc.* 131 (25): 9114–9121.

51 Garnett, E., Mai, L., and Yang, P. (2019). Introduction: 1D nanomaterials/nanowires. *Chem. Rev.* 119 (15): 8955–8957.

52 Bao, R., Jiao, K., He, H. et al. (2007). Fabrication of metal oxide nanowires templated by SBA-15 with adsorption-precipitation method. *Stud. Surf. Sci. Catal.* 267–270.

53 Lin, X.C., Zhang, L., Tsang, Y.H. et al. (2013). Multi-walled carbon nanotube as a saturable absorber for a passively mode-locked Nd: YVO_4 laser. *Laser Phys. Lett.* 10 (5): 55805.

54 Chen, H., Zhou, M., Zhang, P. et al. (2022). Passively Q-switched Nd: GYAP laser at 1.3 μm with bismuthene nanosheets as a saturable absorber. *Infrared Phys. Technol.* 104023.

55 Yuan, J., Liu, G., Xin, Y. et al. (2021). Passively Q-switched modulation based on antimonene in erbium-doped fiber laser with a long term stability. *Opt. Mater. (Amst).* 118: 111256.

56 Aftab, W., Khurram, M., Jinming, S. et al. (2020). Highly efficient solar-thermal storage coating based on phosphorene encapsulated phase change materials. *Energy Storage Mater.* 32: 199–207.

57 Li, L., Zhou, L., Li, T. et al. (2020). Passive mode-locking operation of a diode-pumped Tm: YAG laser with a MoS_2 saturable absorber. *Opt. Laser Technol.* 124: 105986.

58 Wang, X., Xu, J., You, Z. et al. (2016). Tri-wavelength passively Q-switched Yb^{3+}: $GdAl_3 (BO_3)_4$ solid-state laser based on WS2 saturable absorber. *Opt. Mater. (Amst).* 62: 621–625.

59 Xia, D., Wang, Z., Yang, S. et al. (2021). Enhancing electrocatalytic hydrogen evolution of WTe_2 by formation of amorphous phosphate nanoshells. *Electrochim. Acta* 385: 138409.

60 Haris, H., Harun, S.W., Muhammad, A.R. et al. (2017). Passively Q-switched erbium-doped and ytterbium-doped fibre lasers with topological insulator bismuth selenide (Bi_2Se_3) as saturable absorber. *Opt. Laser Technol.* 88: 121–127.

61 He, X., Zhang, H., Wei, R. et al. (2016). Nonlinear saturable absorption of nanoscaled Bi_2Te_3/PMMA composite film. *Phys. E Low Dimens. Syst. Nanostruct.* 81: 71–76.

62 Ma, X., Chen, W., Tong, L. et al. (2022). In_2S_3-based saturable absorber for passively harmonic mode-locking in 2 μm region. *Opt. Laser Technol.* 145: 107476.

63 Chen, Y., Gu, W., Tan, L. et al. (2021). Photocatalytic H_2O_2 production using Ti_3C_2 MXene as a non-noble metal cocatalyst. *Appl. Catal. A Gen.* 618: 118127.

64 Lv, W., Wu, G., Li, X. et al. (2022). Two-dimensional V_2C@ Se (MXene) composite cathode material for high-performance rechargeable aluminum batteries. *Energy Storage Mater.*

65 Ahmad, H., Ramli, R., Yusoff, N. et al. (2021). Performance of Nb_2C MXene coated on tapered fiber as saturable absorber for the generation of mode-locked erbium-doped fiber laser. *Infrared Phys. Technol.* 114: 103647.

66 Yang, Q.-Q., Liu, R.-T., Huang, C. et al. (2018). 2D bismuthene fabricated via acid-intercalated exfoliation showing strong nonlinear near-infrared responses for mode-locking lasers. *Nanoscale* 10 (45): 21106–21115.

67 Beladi-Mousavi, S.M., Pourrahimi, A.M., Sofer, Z., and Pumera, M. (2019). Atomically thin 2D-arsenene by liquid-phased exfoliation: toward selective vapor sensing. *Adv. Funct. Mater.* 29 (5): 1807004.

68 Sun, S., You, J.Y., Duan, S. et al. (2022). Epitaxial growth of ultraflat bismuthene with large topological band inversion enabled by substrate-orbital-filtering effect. *ACS Nano.* 16 (1): 1436–1443.

69 Siddique, S., Gowda, C.C., Tromer, R. et al. (2021). Scalable synthesis of atomically thin gallium telluride nanosheets for supercapacitor applications. *ACS Appl. Nano Mater.* 4 (5): 4829–4838.

70 Chandra Mondal, K., Roy, S., Dittrich, B. et al. (2015). A soluble molecular variant of the semiconducting silicondiselenide. *Chem. Sci.* 6 (9): 5230–5234.

71 Hu, N., Cheney, M.A., Hanifehpour, Y. et al. (2017). Synthesis, characterization, and catalytic performance of Sb_2Se_3 nanorods. *J. Nanomater.* 2017: 5385908.

72 Tyagi, A., Karmakar, G., Wadawale, A. et al. (2018). Facile one-pot synthesis of tin selenide nanostructures using diorganotin bis(5-methyl-2-pyridylselenolates). *J. Organomet. Chem.* 873: 15–21.

73 Luo, L., Shi, M., Zhao, S. et al. (2019). Hydrothermal synthesis of MoS_2 with controllable morphologies and its adsorption properties for bisphenol A. *J. Saudi Chem. Soc.* 23 (6): 762–773.

74 Sharma, P., Kumar, A., Bankuru, S. et al. (2020). Large-scale surfactant-free synthesis of WS_2 nanosheets: An investigation into the detailed reaction chemistry of colloidal precipitation and their application as an anode material for lithium-ion and sodium-ion batteries. *New J. Chem.* 44 (4): 1594–1608.

75 Wehmschulte, R.J. and Power, P.P. (1996). Low-temperature synthesis of aluminum sulfide as the solvate $Al_4 S_6 (NMe_3)_4$ in hydrocarbon solution. *Cryst. data J. Am. Chem. Soc* 35 (8).

76 Julien, C., Pereira-Ramos, J.-P., and Momchilov, A. (2012). *New Trends in Intercalation Compounds for Energy Storage.* Springer Science & Business Media.

77 Ahmad, H., Ramli, R., Samion, M.Z., and Yusoff, N. (2021). Mode-locked thulium/holmium co-doped fiber laser using WTe_2-covered tapered fiber. *Optik (Stuttg).* 245: 167723.

78 Ahmad, H., Ramli, R., Ahmad Kamely, A. et al. (2020). GeSe evanescent field saturable absorber for mode-locking in a thulium/holmium fiber laser. *IEEE J. Quantum Electron.* 56 (5): 1–8.

79 Ahmad, H., Azmy, N.F., Yusoff, N. et al. (2021). $MoTe_2$-PVA as saturable absorber for passively Q-switched thulium-doped fluoride and erbium-doped fiber laser. *Optik (Stuttg).* 243.

80 Rangel, T., Fregoso, B.M., Mendoza, B.S. et al. (2017). Large bulk photovoltaic effect and spontaneous polarization of single-layer monochalcogenides. *Phys. Rev. Lett.* 119 (6).

81 Fei, R., Li, W., Li, J., and Yang, L. (2015). Giant piezoelectricity of monolayer group IV monochalcogenides: SnSe, SnS, GeSe, and GeS. *Appl. Phys. Lett.* 107 (17).

82 Wu, M. and Zeng, X.C. (2016). Intrinsic ferroelasticity and/or multiferroicity in two-dimensional phosphorene and phosphorene analogues. *Nano Lett.* 16 (5): 3236–3241.

83 Panday, S.R., Barraza-Lopez, S., Rangel, T., and Fregoso, B.M. (2019). Injection current in ferroelectric group-IV monochalcogenide monolayers. *Phys. Rev. B* 100 (19).

84 Qiu, P., Qin, Y., Bai, Y. et al. (2021). Gas selectivity regulation of monolayer SnS by introducing nonmetallic dopants: a combined theoretical and experimental investigation. *Appl. Surf. Sci.* 570: 151155.

85 Brent, J.R., Lewis, D.J., Lorenz, T. et al. (2015). Tin (II) sulfide (SnS) nanosheets by liquid-phase exfoliation of herzenbergite: IV–VI main group two-dimensional atomic crystals. *J. Am. Chem. Soc.* 137 (39): 12689–12696.

86 Zhou, L., Wang, Y., Dong, Y. et al. (2021). Femtosecond carrier dynamics and saturable absorption in few layer germanium sulfide. *Optik (Stuttg).* 229: 166226.

87 Yuan, J., Ma, W., Zhang, L. et al. (2017). Infrared nanoimaging reveals the surface metallic plasmons in topological insulator. *ACS Photonics* 4 (12): 3055–3062.

88 Chang, C.-Z. and Li, M. (2016). Quantum anomalous hall effect in time-reversal-symmetry breaking topological insulators. *J. Phys. Condens. Matter* 28 (12): 123002.

89 Murakami, S. (2011). Quantum spin hall systems and topological insulators. *New J. Phys.* 13 (10): 105007.

90 Khanikaev, A.B. and Shvets, G. (2017). Two-dimensional topological photonics. *Nat. Photonics* 11 (12): 763–773.

91 Lin, Y.-Y., Song, W.-H., Lee, P. et al. (2018). Dynamic cavity effects in topological insulator Bi_2Te_3 based passive Q-switched solid state laser. *J. Phys. Commun.* 2 (12): 125007.

92 Yu, H., Zhang, H., Wang, Y. et al. (2013). Topological insulator as an optical modulator for pulsed solid-state lasers. *Laser Photon. Rev.* 7 (6): L77–L83.

93 Bonaccorso, F. and Sun, Z. (2014). Solution processing of graphene, topological insulators and other 2d crystals for ultrafast photonics. *Opt. Mater. Express* 4 (1): 63–78.

94 Dong, L.M., Ye, C., Zheng, L.L. et al. (2020). Two-dimensional metal carbides and nitrides (MXenes): preparation, property, and applications in cancer therapy. *Nanophotonics* 9 (8): 2125–2145.

95 Wang, L., Zhang, H., Wang, B. et al. (2016). Synthesis and electrochemical performance of $Ti_3C_2T_x$ with hydrothermal process. *Electron. Mater. Lett.* 12 (5): 702–710.

96 Ghidiu, M., Lukatskaya, M.R., Zhao, M.-Q. et al. (2014). Conductive two-dimensional titanium carbide 'clay' with high volumetric capacitance. *Nature* 516 (7529): 78–81.

97 Xu, C., Wang, L., Liu, Z. et al. (2015). Large-area high-quality 2D ultrathin Mo_2C superconducting crystals. *Nat. Mater.* 14 (11): 1135–1141.

98 Li, T., Yao, L., Liu, Q. et al. (2018). Fluorine-free synthesis of high-purity $Ti_3C_2T_x$ (T=OH, O) via alkali treatment. *Angew. Chemie Int. Ed.* 57 (21): 6115–6119.

99 Maleski, K.A. (2019). *Solution Processing and Optical Properties of 2D Transition Metal Carbides (MXenes)*. Drexel University.

100 Kim, S.J., Koh, H.-J., Ren, C.E. et al. (2018). Metallic $Ti_3C_2T_x$ MXene gas sensors with ultrahigh signal-to-noise ratio. *ACS Nano* 12 (2): 986–993.

101 Naguib, M., Mochalin, V.N., Barsoum, M.W., and Gogotsi, Y. (2014). 25th anniversary article: MXenes: a new family of two-dimensional materials. *Adv. Mater.* 26 (7): 992–1005.

102 Amrillah, T., Hermawan, A., Alviani, V.N. et al. (2021). MXenes and their derivatives as nitrogen reduction reaction catalysts: recent progress and perspectives. *Mater. Today Energy* 100864.

103 Ahmad, H., Yusoff, N., Albaqawi, H.S. et al. (2021). Niobium carbide (Nb_2C) MXene as a saturable absorber to assist in the generation of a wavelength tunable passively Q-switched fiber laser. *Laser Phys. Lett.* 18 (6): 65101.

104 Huang, Y., Zhou, J., Wang, G., and Sun, Z. (2019). Abnormally strong electron–phonon scattering induced unprecedented reduction in lattice thermal conductivity of two-dimensional Nb_2C. *J. Am. Chem. Soc.* 141 (21): 8503–8508.

105 Gao, L., Chen, H., Zhang, F. et al. (2020). Ultrafast relaxation dynamics and nonlinear response of few-layer niobium carbide MXene. *Small Methods* 4 (8): 2000250.

106 Khazaei, M., Mishra, A., Venkataramanan, N.S. et al. (2019). Recent advances in MXenes: from fundamentals to applications. *Curr. Opin. Solid State Mater. Sci.* 23 (3): 164–178.

107 Guan, Q., Ma, J., Yang, W. et al. (2019). Highly fluorescent Ti 3 C 2 MXene quantum dots for macrophage labeling and Cu^{2+} ion sensing. *Nanoscale* 11 (30): 14123–14133.

108 Li, R., Zhang, L., Shi, L., and Wang, P. (2017). MXene Ti_3C_2: an effective 2D light-to-heat conversion material. *ACS Nano* 11 (4): 3752–3759.

109 Huang, Z., Cui, X., Li, S. et al. (2020). Two-dimensional MXene-based materials for photothermal therapy. *Nanophotonics* 9 (8): 2233–2249.

110 Sinha, A., Zhao, H., Huang, Y. et al. (2018). MXene: an emerging material for sensing and biosensing. *TrAC Trends Anal. Chem.* 105: 424–435.

111 Al-Hamadani, Y.A.J., Jun, B.-M., Yoon, M. et al. (2020). Applications of MXene-based membranes in water purification: a review. *Chemosphere* 254: 126821.

112 Gong, K., Zhou, K., Qian, X. et al. (2021). MXene as emerging nanofillers for high-performance polymer composites: a review. *Compos. Part B Eng.* 108867.

113 Iqbal, A., Kwon, J., Kim, M.-K., and Koo, C.M. (2021). MXenes for electromagnetic interference shielding: experimental and theoretical perspectives. *Mater. Today Adv.* 9: 100124.

114 Zhu, Q., Li, J., Simon, P., and Xu, B. (2020). Two-dimensional MXenes for electrochemical capacitor applications: Progress, challenges and perspectives. *Energy Storage Mater.*

115 Ahmad, H., Kamely, A.A., Yusoff, N. et al. (2020). Generation of Q-switched pulses in thulium-doped and thulium/holmium-co-doped fiber lasers using MAX phase (Ti_3AlC_2). *Sci. Rep.* 10 (1).

116 Huang, L., Zhang, Y., and Liu, X. (2020). Dynamics of carbon nanotube-based mode-locking fiber lasers. *Nanophotonics* 9 (9): 2731–2761.

117 Chen, Y.-S., Yan, P.-G., Chen, H. et al. (2015). Harmonic mode-locked fiber laser based on photonic crystal fiber filled with topological insulator solution. *Photonics* 2 (2): 342–354.

118 Martinez, A., Fuse, K., Xu, B., and Yamashita, S. (2010). Optical deposition of graphene and carbon nanotubes in a fiber ferrule for passive mode-locked lasing. *Opt. Express* 18 (22): 23054–23061.

119 Kasim, N., Al-Masoodi, A.H.H., Ahmad, F. et al. (2014). Q-switched ytterbium doped fiber laser using multi-walled carbon nanotubes saturable absorber. *Chinese Opt. Lett.* 12 (3): 31403.

120 Al-Masoodi, A.H.H., Abdulghafoor, O.B., Alani, I.A.M. et al. (2020). Passively Q-switched pulses from ytterbium-doped fiber laser (YDFL) using copper oxide (CuO) nanoparticles as a saturable absorber. *Opt. Mater. Express* 10 (11): 2896–2908.

121 Fu, B., Wang, P., Li, Y. et al. (2020). Passively Q-switched Yb-doped all-fiber laser based on Ag nanoplates as saturable absorber. *Nanophotonics* 9 (12): 3873–3880.

122 Ahmad, M.T., Muhammad, A.R., Haris, H. et al. (2019). Q-switched ytterbium doped fibre laser using gold nanoparticles saturable absorber fabricated by electron beam deposition. *Optik (Stuttg).* 182: 241–248.

123 Mohammed, D.Z. and Al-Janabi, A.H. (2016). Passively Q-switched erbium doped fiber laser based on double walled carbon nanotubes-polyvinyl alcohol saturable absorber. *Laser Phys.* 26 (11): 115108.

124 Ahmed, M.H.M., Ali, N.M., Salleh, Z.S. et al. (2015). Q-switched erbium doped fiber laser based on single and multiple walled carbon nanotubes embedded in polyethylene oxide film as saturable absorber. *Opt. Laser Technol.* 65: 25–28.

125 Salman, A.A. and Al-Janabi, A.H. (2019). Aluminum nanoparticles saturable absorber as a passive Q-switcher for erbium-doped fiber laser ring cavity configuration. *Laser Phys.* 29 (4): 45102.

126 Ahmad, H., Aidit, S.N., and Yusoff, N. (2018). Bismuth oxide nanoflakes for passive Q-switching in a C-band erbium doped fiber laser. *Infrared Phys. Technol.* 95: 19–26.

127 Ahmad, M.T., Rusdi, M.F.M., Jafry, A.A.A. et al. (2019). Q-switched erbium-doped fiber laser using silver nanoparticles deposited onto side-polished D-shaped fiber by electron beam deposition method. *Opt. Fiber Technol.* 53: 101997.

128 Nady, A., Ahmed, M.H.M., Latiff, A.A. et al. (2017). Nickel oxide nanoparticles as a saturable absorber for an all-fiber passively Q-switched erbium-doped fiber laser. *Laser Phys.* 27 (6): 65105.

129 Sadeq, S.A., Al-Hayali, S.K., Harun, S.W., and Al-Janabi, A. (2018). Copper oxide nanomaterial saturable absorber as a new passive Q-switcher in erbium-doped fiber laser ring cavity configuration. *Results Phys.* 10: 264–269.

130 Jiang, T., Qin, G., Qin, W., and Zhou, J. (2014). Passively Q-switched erbium-doped fiber laser based on gold nanorods. *Optik (Stuttg).* 125 (19): 5789–5793.

131 Lee, Y.-W., Chen, C.-M., Chuang, W.-H. et al. (2021). Highly efficient mode-locked and Q-switched Er^{3+}−doped fiber lasers using a gold nanorod saturable absorber. *Sci. Rep.* 11 (1): 1–8.

132 Muhammad, A.R., Zakaria, R., Ahmad, M.T. et al. (2019). Pure gold saturable absorber for generating Q-switching pulses at 2 μm in thulium-doped fiber laser cavity. *Opt. Fiber Technol.* 50: 23–30.

133 Rosol, A.H.A., Jafry, A.A.A., Mokhtar, N. et al. (2021). Gold nanoparticles film for Q-switched pulse generation in thulium doped fiber laser cavity. *Optoelectron. Lett.* 17 (8): 449–453.

134 Li, S., Kang, Z., Li, N. et al. (2019). Gold nanowires with surface plasmon resonance as saturable absorbers for passively Q-switched fiber lasers at 2 μm. *Opt. Mater. Express* 9 (5): 2406–2414.

135 Koo, J., Jeong, K., Yu, B.-A., and Shin, W. (2019). Evanescent field interaction with Fe_3O_4 nano-particle for passively Q-switched thulium-doped fiber laser at 1.94 μm. *Opt. Laser Technol.* 119: 105579.

136 Kataura, H., Kumazawa, Y., Maniwa, Y. et al. (1999). Optical properties of single-wall carbon nanotubes. *Synth. Met.* 103 (1–3): 2555–2558.

137 Kim, K.-H., Husakou, A., and Herrmann, J. (2010). Saturable absorption in composites doped with metal nanoparticles. *Opt. Express* 18 (21): 21918–21925.

138 Kyoung, M. and Lee, M. (1999). Nonlinear absorption and refractive index measurements of silver nanorods by the Z-scan technique. *Opt. Commun.* 171 (1–3): 145–148.

139 Elim, H.I., Yang, J., Lee, J.-Y. et al. (2006). Observation of saturable and reverse-saturable absorption at longitudinal surface plasmon resonance in gold nanorods. *Appl. Phys. Lett.* 88 (8): 83107.

140 Rangel-Rojo, R., McCarthy, J., Bookey, H.T. et al. (2009). Anisotropy in the nonlinear absorption of elongated silver nanoparticles in silica, probed by femtosecond pulses. *Opt. Commun.* 282 (9): 1909–1912.

141 Gurudas, U., Brooks, E., Bubb, D.M. et al. (2008). Saturable and reverse saturable absorption in silver nanodots at 532 nm using picosecond laser pulses. *J. Appl. Phys.* 104 (7): 73107.

142 Seo, J.T., Yang, Q., Kim, W.-J. et al. (2009). Optical nonlinearities of Au nanoparticles and Au/Ag coreshells. *Opt. Lett.* 34 (3): 307–309.

143 Philip, R., Kumar, G.R., Sandhyarani, N., and Pradeep, T. (2000). Picosecond optical nonlinearity in monolayer-protected gold, silver, and gold-silver alloy nanoclusters. *Phys. Rev. B* 62 (19): 13160.

144 Link, S., Mohamed, M.B., and El-Sayed, M.A. (1999). Simulation of the optical absorption spectra of gold nanorods as a function of their aspect ratio and the effect of the medium dielectric constant. *J. Phys. Chem. B* 103 (16): 3073–3077.

145 Sönnichsen, C., Franzl, T., Wilk, T. et al. (2002). Drastic reduction of plasmon damping in gold nanorods. *Phys. Rev. Lett.* 88 (7): 77402.

146 Link, S. and El-Sayed, M.A. (1999). Spectral properties and relaxation dynamics of surface plasmon electronic oscillations in gold and silver nanodots and nanorods. *J. Phys. Chem. B* 103 (40): 8410–8426.

147 Pietrobon, B., McEachran, M., and Kitaev, V. (2009). Synthesis of size-controlled faceted pentagonal silver nanorods with tunable plasmonic properties and self-assembly of these nanorods. *ACS Nano* 3 (1): 21–26.

148 Xie, Y., Carbone, L., Nobile, C. et al. (2013). Metallic-like stoichiometric copper sulfide nanocrystals: phase-and shape-selective synthesis, near-infrared surface plasmon resonance properties, and their modeling. *ACS Nano* 7 (8): 7352–7369.

149 Hou, L., Guo, H., Wang, Y. et al. (2018). Sub-200 femtosecond dispersion-managed soliton ytterbium-doped fiber laser based on carbon nanotubes saturable absorber. *Opt. Express* 26 (7): 9063–9070.

150 Ahmed, M.H.M., Ali, N.M., Salleh, Z.S. et al. (2014). All fiber mode-locked erbium-doped fiber laser using single-walled carbon nanotubes embedded into polyvinyl alcohol film as saturable absorber. *Opt. Laser Technol.* 62: 40–43.

151 Sotor, J., Sobon, G., Jagiello, J. et al. (2015). Repetition frequency scaling of an all-polarization maintaining erbium-doped mode-locked fiber laser based on carbon nanotubes saturable absorber. *J. Appl. Phys.* 117 (13): 133103.

152 Li, D., Jussila, H., Wang, Y. et al. (2018). Wavelength and pulse duration tunable ultrafast fiber laser mode-locked with carbon nanotubes. *Sci. Rep.* 8 (1): 1–8.

153 Li, Y., Gao, L., Huang, W. et al. (2016). All-fiber mode-locked laser via short single-wall carbon nanotubes interacting with evanescent wave in photonic crystal fiber. *Opt. Express* 24 (20): 23450–23458.

154 Lau, K.Y., Ng, E.K., Bakar, M.H.A. et al. (2018). Low threshold linear cavity mode-locked fiber laser using microfiber-based carbon nanotube saturable absorber. *Opt. Laser Technol.* 102: 240–246.

155 Wang, X.-D., Luo, Z.-C., Liu, H. et al. (2014). Microfiber-based gold nanorods as saturable absorber for femtosecond pulse generation in a fiber laser. *Appl. Phys. Lett.* 105 (16): 161107.

156 Cui, L., Liu, J., Li, N. et al. (2020). Passively mode-locked Er^{3+} and Tm^{3+}−doped fiber lasers by using a common gold nanorods/D-shaped fiber as saturable absorber. *Laser Phys. Lett.* 17 (11): 115104.

157 Khaleel, W.A., Sadeq, S.A., Alani, I.A.M., and Ahmed, M.H.M. (2019). Magnesium oxide (MgO) thin film as saturable absorber for passively mode locked erbium-doped fiber laser. *Opt. Laser Technol.* 115: 331–336.

158 Kang, Z., Liu, M., Tang, C. et al. (2018). Microfiber coated with gold nanorods as saturable absorbers for 2 μm femtosecond fiber lasers. *Opt. Mater. Express* 8 (12): 3841–3850.

159 Kang, Z., Liu, M.Y., Gao, X.J. et al. (2015). Mode-locked thulium-doped fiber laser at 1982 nm by using a gold nanorods saturable absorber. *Laser Phys. Lett.* 12 (4): 45105.

160 Ahmad, H., Samion, M.Z., and Yusoff, N. (2018). Soliton mode-locked thulium-doped fiber laser with cobalt oxide saturable absorber. *Opt. Fiber Technol.* 45: 122–127.

161 Dai, R., Meng, Y., Li, Y. et al. (2019). Nanotube mode-locked, wavelength and pulsewidth tunable thulium fiber laser. *Opt. Express* 27 (3): 3518.

162 Bao, Q., Zhang, H., Wang, Y. et al. (2009). Atomic-layer graphene as a saturable absorber for ultrafast pulsed lasers. *Adv. Funct. Mater.* 19 (19): 3077–3083.

163 Hasan, T., Sun, Z., Wang, F. et al. (2009). Nanotube–polymer composites for ultrafast photonics. *Adv. Mater.* 21 (38–39): 3874–3899.

164 Zhang, R., Wang, J., Liao, M. et al. (2019). Tunable Q-switched fiber laser based on a graphene saturable absorber without additional tuning element. *IEEE Photonics J.* 11 (1): 1–10.

165 Ahmad, H., Samion, M.Z., Sharbirin, A.S. et al. (2018). Graphene-PVA saturable absorber for generation of a wavelength-tunable passively Q-switched thulium-doped fiber laser in 2.0 μm. *Laser Phys.* 28 (5): 55105.

166 Luo, Z., Li, Y., Huang, Y. et al. (2016). Graphene mode-locked and Q-switched 2-μm Tm/Ho codoped fiber lasers using 1212-nm high-efficient pumping. *Opt. Eng.* 55 (8): 81310.

167 Zhang, M., Hu, G., Hu, G. et al. (2015). Yb- and Er-doped fiber laser Q-switched with an optically uniform, broadband WS_2 saturable absorber. *Sci. Rep.* 5 (1): 17482.

168 Jafry, A.A.A., Krishnan, G., Kasim, N. et al. (2020). MXene $Ti_3C_2T_x$ as a passive Q-switcher for erbium-doped fiber laser. *Opt. Fiber Technol.* 58: 102289.

169 Cheng, P.K., Tang, C.Y., Wang, X.Y. et al. (2019). Passively Q-switched ytterbium-doped fiber laser based on broadband multilayer platinum ditelluride ($PtTe_2$) saturable absorber. *Sci. Rep.* 9 (1): 1–7.

170 Luo, Z., Huang, Y., Zhong, M. et al. (2014). 1-, 1.5-, and 2-μm fiber lasers Q-switched by a broadband few-layer MoS_2 saturable absorber. *J. Light. Technol.* 32 (24): 4077–4084.

171 Al-Masoodi, A.H.H., Ahmad, F., Ahmed, M.H.M. et al. (2017). Q-switched ytterbium-doped fiber laser with topological insulator-based saturable absorber. *Opt. Eng.* 56 (5): 56103.

172 Wang, R., Liu, Y., Jiang, M. et al. (2017). Passively Q-switched and mode-locked fiber laser research based on graphene saturable absorbers. *Opt. Quantum Electron.* 49 (4): 137.

173 Hu, P., Liu, Y., Guo, L. et al. (2019). Passively Q-switched erbium-doped fiber laser based on antimonene as saturable absorber. *Appl. Opt.* 58 (28): 7845–7850.

174 Cheng, P.K., Tang, C.Y., Wang, X.Y. et al. (2020). Passively Q-switched and femtosecond mode-locked erbium-doped fiber laser based on a 2D palladium disulfide (PdS_2) saturable absorber. *Photonics Res.* 8 (4): 511–518.

175 Li, L., Wang, Y., Wang, Z.F. et al. (2018). High energy Er-doped Q-switched fiber laser with WS2 saturable absorber. *Opt. Commun.* 406: 80–84.

176 Ahmad, H., Suthaskumar, M., Tiu, Z.C. et al. (2016). Q-switched erbium-doped fiber laser using $MoSe_2$ as saturable absorber. *Opt. Laser Technol.* 79: 20–23.

177 Zhu, X., Chen, S., Zhang, M. et al. (2018). TiS_2-based saturable absorber for ultrafast fiber lasers. *Photonics Res.* 6 (10): C44–C48.

178 Mao, D., Cui, X., Gan, X. et al. (2017). Passively Q-switched and mode-locked fiber laser based on an ReS_2 saturable absorber. *IEEE J. Sel. Top. Quantum Electron.* 24 (3): 1–6.

179 Haris, H., Arof, H., Muhammad, A.R. et al. (2019). Passively Q-switched and mode-locked erbium-doped fiber laser with topological insulator bismuth selenide (Bi_2Se_3) as saturable absorber at C-band region. *Opt. Fiber Technol.* 48: 117–122.

180 Buntat, M.A., Rosol, A.H.A., Rusdi, M.F.M. et al. (2021). $Ti_3C_2T_x$ thin film as a saturable absorber for passively generating Q-switched pulses in thulium-doped fiber laser cavity. Наносистемы: физика, химия, математика 12 (4): 436–441.

181 Wang, K., Wang, J., Fan, J. et al. (2013). Ultrafast saturable absorption of two-dimensional MoS_2 nanosheets. *ACS Nano* 7 (10): 9260–9267.

182 Zhang, M., Howe, R.C.T., Woodward, R.I. et al. (2015). Solution processed MoS_2-PVA composite for sub-bandgap mode-locking of a wideband tunable ultrafast Er: fiber laser. *Nano Res.* 8 (5): 1522–1534.

183 Woodward, R.I., Howe, R.C.T., Hu, G. et al. (2015). Few-layer MoS_2 saturable absorbers for short-pulse laser technology: current status and future perspectives. *Photonics Res.* 3 (2): A30–A42.

184 Woodward, R.I., Howe, R.C.T., Runcorn, T.H. et al. (2015). Wideband saturable absorption in few-layer molybdenum diselenide ($MoSe_2$) for Q-switching Yb-, Er- and Tm-doped fiber lasers. *Opt. Express* 23: 20051–20061.

185 Feng, T., Li, X., Chai, T. et al. (2019). Few-layer bismuthene for 1-μm ultrafast laser applications. *Beilstein Arch.* 2019 (1): 28.

186 Cheng, P.K., Liu, S., Ahmed, S. et al. (2020). Ultrafast Yb-doped fiber laser using few layers of PdS_2 saturable absorber. *Nanomaterials* 10 (12): 2441.

187 Li, J., Zhao, Y., Chen, Q. et al. (2017). Passively mode-locked ytterbium-doped fiber laser based on SnS_2 as saturable absorber. *IEEE Photonics J.* 9 (6): 1–7.

188 Yi, J., Du, L., Li, J. et al. (2019). Unleashing the potential of Ti_2CT_x MXene as a pulse modulator for mid-infrared fiber lasers. *2D Mater.* 6 (4): 45038.

189 Guo, B., Wang, S.-H., Wu, Z.-X. et al. (2018). Sub-200 fs soliton mode-locked fiber laser based on bismuthene saturable absorber. *Opt. Express* 26 (18): 22750–22760.

190 Guo, P., Li, X., Chai, T. et al. (2019). Few-layer bismuthene for robust ultrafast photonics in C-band optical communications. *Nanotechnology* 30 (35): 354002.

191 Wang, C., Wang, L., Li, X. et al. (2018). Few-layer bismuthene for femtosecond soliton molecules generation in Er-doped fiber laser. *Nanotechnology* 30 (2): 25204.

192 Zhang, R.-L., Wang, J., Zhang, X.-Y. et al. (2019). Mode-locked fiber laser with $MoSe_2$ saturable absorber based on evanescent field. *Chinese Phys. B* 28 (1): 14207.

193 Ahmad, H.B., Aidit, S.N., Hassan, N.A. et al. (2016). Generation of mode-locked erbium-doped fiber laser using $MoSe_2$ as saturable absorber. *Opt. Eng.* 55 (7): 76115.

194 Jiang, G., Zhou, Y., Wang, L., and Chen, Y. (2018). PMMA sandwiched Bi_2Te_3 layer as a saturable absorber in mode-locked fiber laser. *Adv. Condens. Matter Phys.* 2018: 7578050.

195 Yan, P., Lin, R., Ruan, S. et al. (2015). A practical topological insulator saturable absorber for mode-locked fiber laser. *Sci. Rep.* 5 (1): 1–5.

196 Cao, L., Li, X., Zhang, R. et al. (2018). Tm-doped fiber laser mode-locking with MoS_2-polyvinyl alcohol saturable absorber. *Opt. Fiber Technol.* 41: 187–192.

197 Lee, J., Koo, J., Lee, J. et al. (2017). All-fiberized, femtosecond laser at 1912 nm using a bulk-like $MoSe_2$ saturable absorber. *Opt. Mater. Express* 7 (8): 2968–2979.

198 Pumera, M. and Sofer, Z. (2017). 2D monoelemental arsenene, antimonene, and bismuthene: beyond black phosphorus. *Adv. Mater.* 29 (21): 1605299.

Z

13

1D and 2D Semiconducting Hybrid Nanostructures for Advanced Photodiodes

Norazriena Yusoff[1], Tamil M. Thandavan[1], Harith Ahmad[1], and Kavintheran Thambiratnam[1]

[1] *Universiti Malaya, Photonics Research Centre, Kuala Lumpur, 50603, Malaysia*

13.1 Introduction

Photodetectors (PDs) are light-sensing devices that turn light into an electric current. PDs are critical components in a wide range of devices that we use on a daily basis. The electromagnetic spectrum goes from the very short X-ray to radio waves that can be thousands of meters long. The optical part of the spectrum runs from 0.01 to 1000 m and includes ultraviolet (UV), visible, and infrared (IR) radiation. PDs are radiation detectors that are suitable for use in these areas [1–3]. All PDs are designed to detect a certain wavelength or a broad range of radiant light and produce an output signal proportionate to the amount of energy absorbed. PDs are used in a variety of applications in our daily lives, including electro-optical displays, photography, environmental monitoring, optical communication, military, safety control, and many more [4–6]. Good photoresponsivity, fast reaction time, high sensitivity, and high efficiency are the main qualities of an ideal PDs. PDs can be distinguished in a variety of ways based on wavelength spectra (IR to UV detectors) and structural characteristics. The PDs can be classified as a UV detector, visible detector, IR detector, or Terahertz detector based on its detection range. According to the bandgap of the semiconductor materials, we can employ them for these detecting ranges.

Gain is proportional to the mobility of the transistor channel and the carrier lifetime. The origin of very high gain is often due to the very long lifetimes will likely prevent the PDs from addressing a real-world application. Thus, efforts toward gain improvement should be focused on increasing carrier mobility rather than prolonging carrier lifetime, and the ultimate figure of merit to be looked upon is the gain bandwidth product, and not the gain itself. In photodiodes or graphene-based p–n

junction detectors, the speed of a photodetector is of paramount importance, especially in time-of-flight remote sensing or data communications [7]. Again, the reports on the speed of the detector have to be documented at relevant conditions and followed by a full characterization of the detector in achieving high speed without sacrificing other key figures of merit such as the quantum efficiency and the sensitivity. A fast PD must also be sensitive enough and operate at realistically relevant conditions (in terms of temperature, form factor, etc.).

Silicon (Si) has traditionally been the material of choice in the application of PDs [8]. Complementary metal oxide semiconductor (CMOS) technology may easily integrate such Si-based PDs [9]. Si-based devices have become less expensive because of the aggressive scaling; hence they have a wider range of applications. Despite the fact that Si-based PDs have evolved and improved throughout time, however, the indirect nature of the Si bandgap limits their performance. The absorption of Si is restricted to the electromagnetic spectrum of visible and near-IR regions. Furthermore, because of the indirect bandgap characteristics of Si, phonon production occurs to conserve the momentum throughout the light-assisted transition of carriers process from lower energy to higher energy. The scattering of the carriers caused by these phonons reduces the effectiveness of Si-based PDs. Furthermore, Si in bulk form is a poor light absorber, thus reducing the efficiency of Si-based PDs. The limitations of Si-based PDs have led to a search for other materials in the research community.

Intensive efforts should continue apace in the direction of PDs with distinct advantages over old technology. The goal of the PDs technological landscape is to create devices with a form factor that cannot be achieved with normal single-crystalline technologies or devices that are cost- and performance-competitive with present technologies. The former has been showed in a number of cases using low-dimensional PDs and hybrid heterojunction PDs with modulation bandwidths exceeding 60 GHz [10]. Over the past few years, PDs based on low-dimensional semiconductors have attracted researchers' interest due to their merits of quantum performance, small scale, low energy utilization, and better strength [11, 12]. Low-dimensional materials, particularly 1D and 2D materials, can demonstrate their added value in two ways by achieving extremely high modulation frequencies (important for data transfer applications) or by achieving extremely high sensitivity (relevant for imaging, remote sensing, and spectrometry applications).

In the work conducted by Sarkar and coworkers, they successfully synthesized 1D zinc oxide crystals (ZCs) via a simple wet chemical approach (Figure 13.1a) [13]. The prepared 1D ZCs sample demonstrates a great UV absorption by the presence of a sharp absorption peak at 369 nm. It also displays a photoluminescence (PL) behavior with a sharp emission peak at 384 nm. By using the prepared sample, a UV PD device was fabricated and its photoconductivity with a significant change in resistance was observed during UV exposure. Figure 13.1b displays the current versus voltage (*I–V*) characteristics of the 1D ZC-based UV PD in which an increase in the current and slope can be observed; thus, it implies the excellent photoconductivity of the 1D ZC under the UV exposure. Other than 1D-based structure of PDs, the development of PDs using 2D materials has received emerging research study
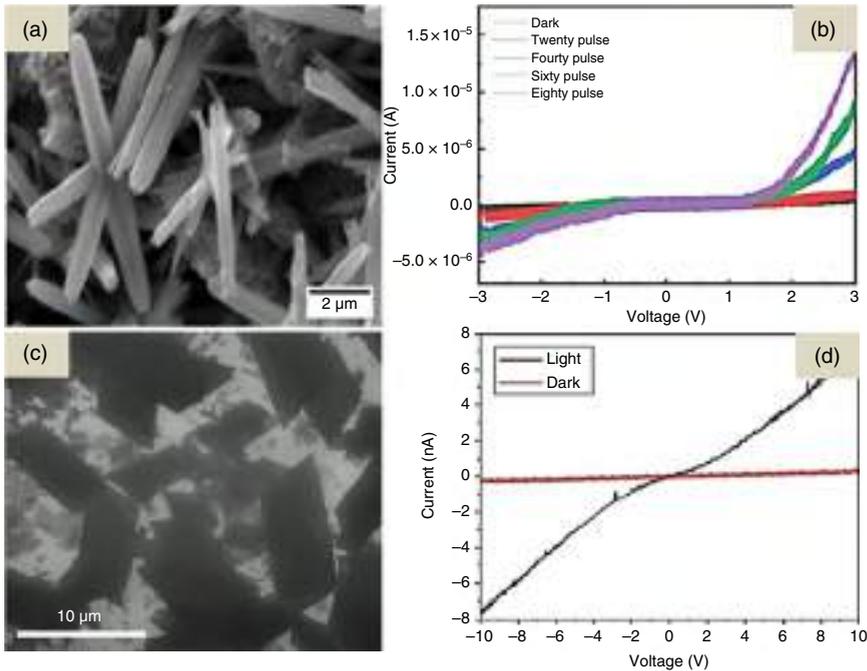
Figure 13.1 (a) A high magnification SEM image of 1D ZC with a smooth outer wall surface. (b) Comparative I–V characteristics of the 1D ZC-based UV PD at various numbers of applied UV pulses. (c) SEM image of Sb_2Se_3 nanosheets. (d) The I–V characteristics of Sb_2Se_3 under dark condition and under the irradiation of 405 nm laser. Source: Refs [13, 14], Elsevier.

in the past few years. For instance, Wang et al. have demonstrated the fabrication of PD using antimony selenide (Sb_2Se_3) nanosheets which have been synthesized via highly facile hydrothermal method. The scanning electron microscopy (SEM) image of Sb_2Se_3 and its I–V characteristics obtained under dark condition and an irradiation of 405 nm laser were depicted in Figure 13.1c,d, respectively. Based on the obtained result, the I–V characteristic curve of the device is linear with symmetrical left and right ends, showing that the nanosheet has good Ohmic contact with the metal electrodes. The photoelectric properties of fabricated Sb_2Se_3-based PD exhibits a better response to visible light with a "ON/OFF" ratio of 10.8, short response/recovery periods (0.40/0.12 seconds), and long-term durability [14]. This study provides evidence of the applicability of 2D materials for high-performance PD fabrication.

Researchers have recently become interested in mixed-dimensional hetero-structures such as one-dimensional (1D)–2D [15], two-dimensional (2D)–2D [16], and three-dimensional (3D)–2D [17] due to their unique features obtained by combining nanomaterials of different dimensionalities. Heterostructures made up of diverse materials have distinct tunable energy band structures, allowing them to produce intriguing electrical and optoelectronic features. This chapter will focus on the construction of 1D semiconductor nanostructures grown on 2D

nanomaterials hybrid nanostructures for PDs application. The basic principle of PDs was presented in Section 13.2. The few types and applications of PDs were discussed in Sections 13.3 and 13.4, respectively. Meanwhile, Sections 13.5 and 13.6 introduce few common techniques on the device fabrication method and device characterization method. The current status of 1D/2D hybrid nanostructures PDs was discussed in Section 13.7, followed by the conclusion made from the discussed topic of this chapter.

13.2 Principle of Photodetector

PDs convert light signals to electrical wave forms. There are three types of PDs:
  (a) Photoemissive
  (b) Photoconductive
  (c) Photovoltaic
      i. PN junction photodetector
      ii. PIN photodiode
      iii. Avalanche photodiode

PDs are typically employed as an optical receiver, converting light signals that strike a junction into voltage or electric current. The light photons are absorbed by an illumination window with an anti-reflect coating. In the depletion area, photon absorption results in the formation of electron–hole pairs. Photodiodes and phototransistors are examples of PDs. Solar cells, which collect light and convert it to energy, are another optical device comparable to photodetectors. The LED is a comparable but distinct optical device that works in the opposite direction of a photodiode, converting voltage or current to light instead of light to voltage or current. The photoelectric effect, which is the action of light on a circuit, is the principle that applies to PDs. Max Planck was a German physicist who, in 1900, found that energy is radiated in small discrete units known as quanta; he also discovered the Planck's constant, which is a universal constant of nature. Planck's discoveries gave rise to quantum mechanics, a new branch of physics based on the equation $E = h\nu$, which is Planck's constant multiplied by the frequency of radiation. The photoelectric effect occurs when light strikes a metal surface in a vacuum, causing electrons to be expelled from the surface. This explains the basic theory of light energy that enables PDs to work. PDs are extensively employed in houses as safety devices in the form of smoke detectors, as well as in security systems alongside other optical devices.

Figure 13.2 shows the general working principle of PDs. Covalent bonds are ionized when a light is used to illuminate the PN junction. This produces electron and hole pairs. The creation of electron–hole pairs produces photocurrents. When photons with energies more than 1.1 eV collide with the diode, electron–hole pairs emerge. When a photon penetrates the depletion zone of a diode, it has a strong energy impact on the atom. As a result, an electron is released from the atom
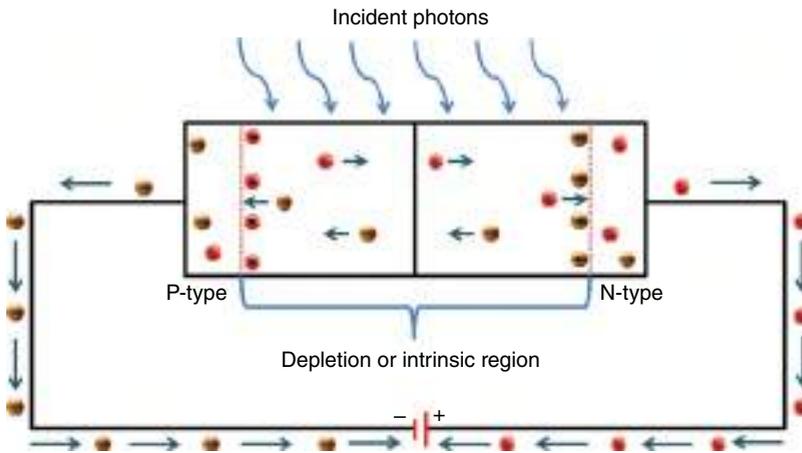
Figure 13.2 Photodiode working principle.

structure. Free electrons and holes are formed as a result of the electron release. A negative charge is assigned to an electron, while a positive charge is assigned to a hole. There will be an electric field integrated into the depletion energy. Electron–hole pairs travel away from the junction as a result of the electric field. To produce photocurrent, holes migrate to the anode and electrons to the cathode. The intensity of photon absorption and the energy of photons are directly related. When the energy of the pictures is lower, the absorption is higher. Inner photoelectric effect is the name given to this entire process. The two methods of photon excitation are intrinsic and extrinsic excitations. When a photon excites an electron in the valence band to the conduction band, this is known as intrinsic excitation.

13.3   Types of Photodetectors

PDs are sometimes referred to as photon detectors, since they make use of the photo-excitation of electric carriers in some way. PDs typically produce an electrical output signal that is proportionate to the incident optical power, such as a voltage or electric current. This section will discuss about several types of PDs, including photodiodes, PIN photodiode, avalanche photodiode, and phototransistor.

13.3.1   Photodiodes

The photodiode is a typical PD that has been widely used. A photodiode is made up of a semiconductor sample with a junction of oppositely doped areas (PN junction). This leads to a charge carrier-depleted area with high impedance. The high impedance permits detectors made of silicon and germanium to function at low temperatures with high sensitivity. An illumination window is used to operate the

photodiode, allowing light to be used as an external input. The diode is worked under reverse bias conditions, since light is employed as an input. When no light is available, the current across the junction is zero under the reverse bias condition, allowing the diode to be employed as a switch or relay when enough light is present. Because silicon produces crystal lattice vibrations known as phonons when photons are absorbed to produce electron–hole pairs, photodiodes are mostly manufactured of gallium arsenide (GaAs) rather than silicon. GaAs may form electron–hole pairs without the slow-moving phonons, allowing for faster switching between on and off states. Besides that, GaAs also are highly responsive toward the intensity of light. Once charge carriers are generated in the diode material, they will move to the junction through the diffusion process. If operated in conjunction with appropriate electronics, such devices can be very compact, quick, and highly linear, with a high quantum efficiency (i.e. generate nearly one electron per incident photon) and a wide dynamic range. Quantum efficiency, current, and capacitance are among the important photodiode properties. There are few common types of photodiodes that have been categorized based on their construction and principles of operation, for example PIN photodiode and avalanche photodiode.

13.3.1.1 PIN Photodiode
A PIN photodiode is a form of photodiode that has an intrinsic layer between the P and N types of materials. Figure 13.3 shows the schematic diagram of PIN photodiode. Due to the intrinsic layer's high resistivity, the PIN must be reverse bias. The depletion region of the PIN is larger, allowing more electron–hole pairs to form at a lower capacitance. Because electron mobility is larger than hole mobility, the illumination window for a PIN is on the P-side of the diode, resulting in better frequency

Figure 13.3 Schematic diagram of PIN photodiode.

responsiveness. In compared to the PN photodiode, it has a higher breakdown voltage, allowing it to be employed with a bias voltage of around 100, resulting in a faster response time. In order to have large photocurrent generation, the thickness of the depletion layer can be tuned. The surface area on which light falls grows as the thickness of the depletion layer increases. As a result, a photodiode's conversion efficiency improves, and more photocurrent is produced. One of the advantages of the PIN photodiode is its high-frequency response, which is greater than that of the cadmium sulfide photodetector. Aside from that, it is cheap, and the response time is measured in nanoseconds, making it ideal for electronic circuitry. The spectral response of these diodes is broad and has the ability to process very weak signals. As PIN photodiodes need a lot of reverse bias to work which might lower the signal-to-noise ratio, this has become one of the drawbacks of PIN diode. Because of their ability to detect weak signals, PIN photodiodes have been widely employed in laser pulse detection, ultrafast switching circuits, and logic circuits.

13.3.1.2 Avalanche Photodiode

Avalanche photodiode is another type of PD in which impact ionization generates more electron–hole pairs. Figure 13.4 shows the schematic diagram of avalanche photodiode. It works similarly to a P–N or PIN photodiode in that electron–hole pairs are formed by photon absorption, but the avalanche photodiode employs the impact ionization principle to boost photocurrent magnitude. Impact ionization is the process by which a high-kinetic-energy carrier strikes a bounded energy carrier and transfers its energy to it, allowing the bounded energy carrier to move freely. This results in a higher concentration of energy carriers and, as a result, a larger current magnitude. When an avalanche photodiode is operated at reverse bias near the breakdown, photostimulated charge carriers accelerate in the depletion area and avalanche to produce additional carriers. Due to the high current-gain

Figure 13.4 Schematic diagram of avalanche photodiode.

bandwidth product, this type of photodiode has the advantage of being able to detect very weak signals. However, the construction of an avalanche photodiode, on the other hand, is quite intricate, and special attention must be paid to the junction. A guard ring must be used in order to protect the diode against edge breakdown, and the junction should be uniform. Avalanche photodiodes have been utilized in fiber optic communication systems because of its capacity to detect low-level signals. A silicon avalanche photodiode with suitable design can have a response time of roughly 1 ns. Besides that, avalanche photodiodes are also suitable for fiber optic systems requiring low light levels and a quantum efficiency greater than 100%.

13.3.2 Phototransistor

The phototransistor is a semiconductor device that can detect light levels and adjust the current flowing between the emitter and collector based on the amount of light received. A phototransistor is similar to a photodiode with the exception that it has an extra n-type region. Both phototransistors and photodiodes are capable of sensing light, but the phototransistor is more sensitive due to the gain supplied by the bipolar transistor. As a result, phototransistors are better suited for a variety of applications. A phototransistor works in the same way as a photodiode with an amplifying transistor does. When light strikes a phototransistor's base terminal, it causes a small current to flow, which is amplified by the action of a conventional transistor, resulting in a massive current. Figure 13.5 shows the typical structure of phototransistor in which it has been designed to provide a large area to the incident light. In general, when compared to a similar photodiode, a phototransistor generates 50–100 times the current of the photodiode. A semiconductor material is used to make the phototransistor. Once light strikes the material, charge carriers in the semiconductor
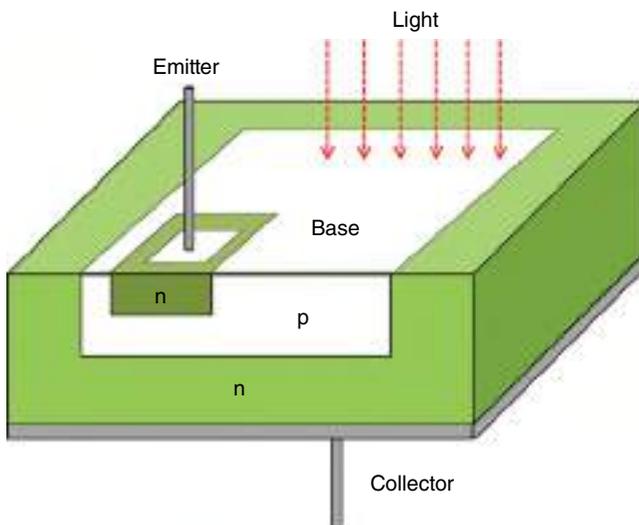
Figure 13.5 Typical structure of phototransistor.

material, such as holes or electrons, can cause current to flow inside the base area. This can be utilized for transistor biasing in the base region. Phototransistors have several advantages, including being highly sensitive, inexpensive, less complex, and providing a large quantity of current with a high gain. In addition, it is less noisy than avalanche-type photodiodes and has higher gain, current, and response time when compared to photodiodes. Due to their advantages, phototransistor has been used in several applications such as lighting control, alarm systems, proximity detectors, and punch-card readers.

13.4   Applications of Photodetectors

PDs are employed in a variety of applications, including radiation detection, smoke detection, flame detection, and switching on street lighting relays. Depending on the desired operation, photodiode circuits use either usually closed or normally open contacts. The photodiode in a smoke detector circuit is connected to a relay switch, which is ordinarily closed and connected to the fire alarm. When the photodiode conducts, it detects the relay switch and opens the typically closed switch, preventing the alarm from being activated. The typically closed contact activates the alarm when the photodiode fails to conduct. Photodiodes are also utilized as a safety feature in modern oil-burning furnaces. The photodiode is made of lead sulfide and is used to detect the boiler's flame. If the flame goes out or fails to occur, the photodiode opens the circuit, cutting power to the motor and step-up transformer. Street lights are another typical application. When the photodiode in the circuit fails to conduct, it activates switch-on relays, which turn on the street lights and turn them off when there is enough light. Atomic force microscope (AFM) is another use in which a laser beam is directed from a laser diode (LD) onto the rear of the cantilever and reflected to a photodiode. As the probes of the cantilever scrape across the material's surface, the position of the light beam on the diode determines the material's (x,y,z) position. This produces a 3D image of the scanned surface. Photodiodes and lasers are also employed to create security systems. A security alarm is triggered when the light projected by a laser to the photodiode is broken.

A set of key performance indicators characterizes the potential of a PD, and one important figure of merit is the detector's sensitivity, which must be measured carefully under the same experimental conditions and reported as a function of electrical bandwidth, temperature, and optical wavelength. These are the detector's quantum efficiency, responsivity, and noise current. The quantum efficiency is important because it determines how many primary electrical carriers are created per single incident photon and is usually limited to unity (100%) until multicarrier creation or avalanche phenomena occur. In the presence of a photoconductive gain mechanism, the responsivity can reach extremely high levels. The combination of a detector's sensitivity and noise current, however, is what ultimately defines its sensitivity. It is worth noting that the latter is frequently estimated at the shot noise limit in published literature, a condition that is rarely encountered in PDs, particularly photoconductive detectors. Furthermore, the presence of 1/f or flicker noise in
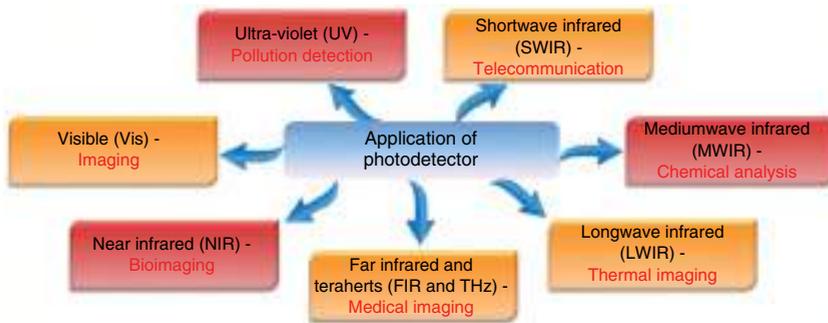
Figure 13.6 Application of PDs in various spectral ranges.

graphene and 2D materials is already widely documented, and it is the most common source of noise in such devices. Figure 13.6 shows some of the application of PDs in various spectral ranges.

13.5 Device Fabrication Methods

Various experimental techniques and methods were employed to achieve the desired materials that will facilitate the fabrication of PDs. Some of the methods are vapor-phase transport, drop-casting, thermal oxidation, e-beam vaporization, direct current (DC) sputtering, and spin coating. The brief discussions on each method were presented in this section.

13.5.1 Vapor-Phase Transport

In the commercial manufacturing of commercial powders, such as oxide and non-oxide powders, vapor-phase technologies play a key role. The gas-phase condensation technique, in which a solid is vaporized by Joule heating to generate a supersaturated vapor, from which small-scale particles condense, dominates this category. Other methods such as electron beam evaporation, laser ablation, magnetic sputtering, and arc discharge can produce supersaturated vapor with a variety of particle sizes, shapes, and compositions. Chemical reaction, mass transfer, nucleation, coagulation, and condensation are the physical processes involved. The process enables for the creation of nanocrystalline powders with excellent purity and controlled particle size distribution without the requirement for a later calcination phase. The type of powder generated is determined by the gas employed. In this situation, a high-temperature annealing step is frequently necessary to complete the oxidation.

In the work presented by Tamil Many et al. [18], they utilized the vapor-phase transport method assisted by thermal evaporation of brass and further allowed the flow of argon gas through methanol solution in order to deposit zinc oxide (ZnO) layer and hybrid carbon–zinc oxide (C-ZnO) layers on an n-Si substrate.
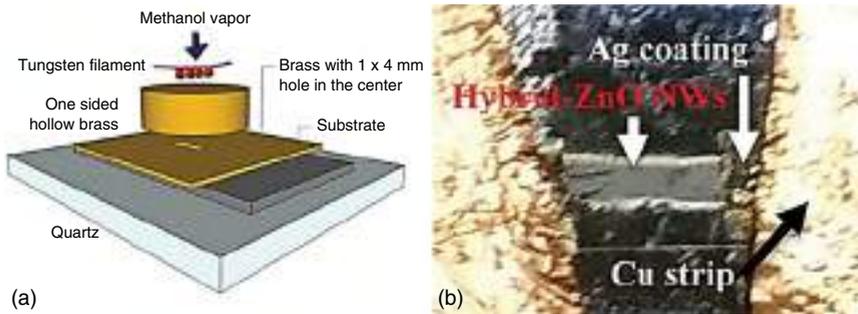
Figure 13.7 Experimental setup of vapor phase transport deposition of C-ZnO and (b) fabricated hybrid C-ZnO-based PD.

Figure 13.7a displays the schematic diagram of experimental setup for vapor-phase transport method which consists of the quartz plate, n-silicon (Si) layer, brass plate with a hole, one-sided hollow brass plate, and tungsten filament. In order to complete the fabrication process, the prepared C–ZnO thin film was held against SiO_2/p-Si substrate with a paper clip and followed by the formation of source and drain electrodes by applying a silver (Ag) conducting paste to the n–Si and p–Si junctions. The fabricated hybrid C-ZnO-based PD is shown in Figure 13.7b.

13.5.2 Drop-Casting

Drop-casting is the process of forming a thin solid film by dropping a solution onto a flat surface and then evaporating it by drying at ambient temperature or in the furnace at the necessary temperatures according to the material specifications. This technique is used to make tiny coatings on small surfaces. A small amount of solvent is required for this process. Multiple droplets formed by this technique offer a distinctive environment to manage the direction of shrinkage and the rate of evaporation of the droplets. This approach involves pouring the solution in drops onto the substrate and allowing it to dry without spreading. The liquid spreads on the surface from the drop locations when the droplets are pushed onto the substrate due to interfacial forces that tend to move the droplet outward. When the edges of numerous droplets come into contact with each other on the substrate surface, they mix and form a non-circular drop with a concave contact line. Because of the uneven drying conditions and lack of control, the films produced by this process are nonuniform. The center of these films is thicker, and their edges are thinner. Drop-casting is a process for making polymer semiconductors, which are expensive and have low solubility. The following diagram illustrates the use of the drop-casting process to create a boron nitride (BN)/GO composite layer on the designed Ag electrode configuration on SiO_2/Si substrate heated to 550 °C on a hotplate as reported by Harith et al. [19]. In this work, the drop-casting technique was utilized to deposit BN/GO layer onto a SiO_2/Si substrate (Figure 13.8), and the fabricated BN/GO-based PD device was further used to facilitate photodetection in the UV and visible range laser and light sources.
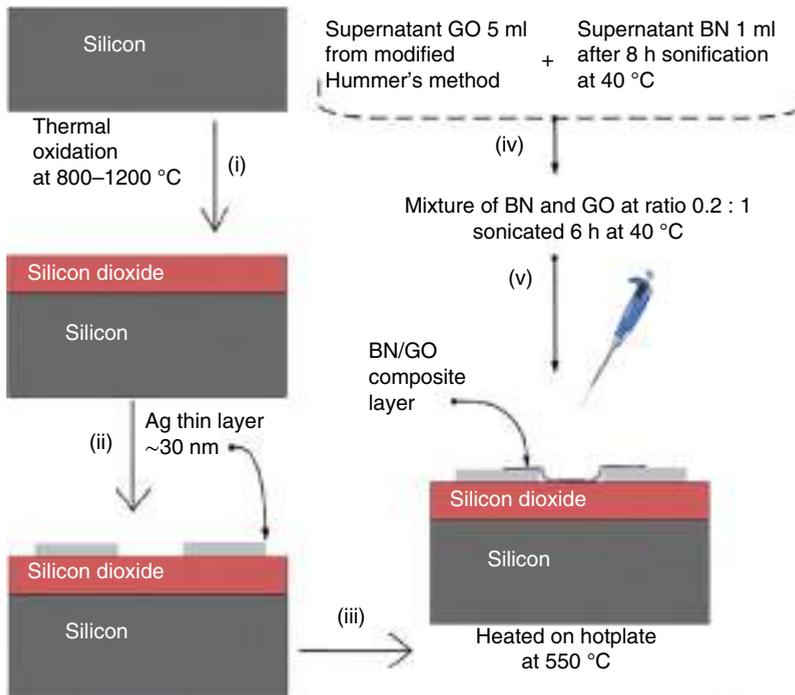
Figure 13.8 Schematic diagram shows the preparation of BN/GO composite layer on SiO_2/Si substrate. Source: Ahmad et al. [19]/with permission of Elsevier.

13.5.3 Thermal Oxidation

The process of generating a thin layer of oxide on the surface of a wafer is known as thermal oxidation. Thermal oxidation is a complicated process in which oxidants diffuse, a chemical reaction occurs, and the volume increases in order to convert the silicon substrate into SiO_2. The oxidant species used, the oxidation environment (temperature and pressure), and the crystal orientation of the substrate all have a significant impact on this process. These factors can be used to manage the quality and growth of the oxide during the manufacturing process. For instance, thermal evaporation allowed deposition of silicon dioxide insulating layer on top of p-type silicon is illustrated in [20]. In this work, a thermal oxidation method at temperatures ranging from 800 to 1200 °C was used to create an insulating SiO_2 layer with a thickness of 1500 nm on a p-Si. The considerable thickness was chosen to avoid direct contact between the p-Si and the 2D material on the SiO_2 surface.

13.5.4 Electron Beam (E-Beam) Evaporation

Electron beam evaporation or E-beam evaporation is a type of physical vapor deposition which involved the targeted material being hit by an electron beam that is originated from a charged tungsten filament. The targeted material will be evaporated and transform to a gaseous state for deposition on the material to be coated.
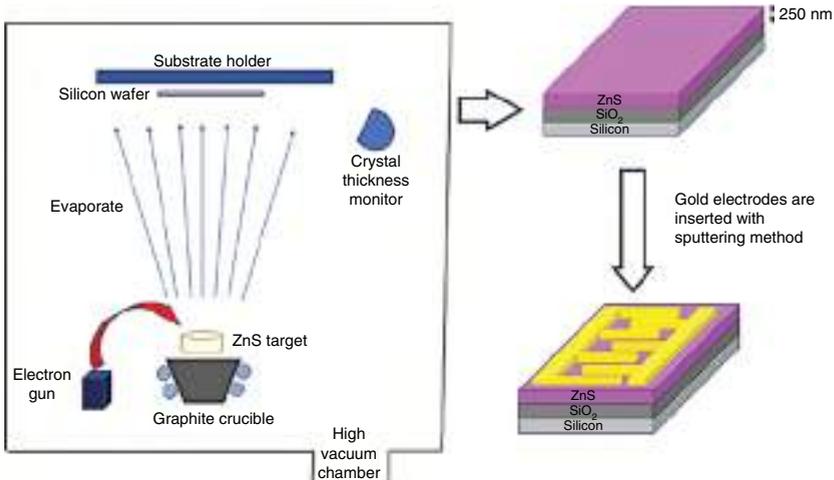
Figure 13.9 Schematic diagram of E-beam evaporation technique used to deposit ZnS onto the Si substrate and the ZnS-based PD fabrication. Source: Hajimazdarani et al. [21]/ with permission of Elsevier.

These atoms or molecules in the vapor phase subsequently precipitate and create a thin film coating on the substrate in a high vacuum chamber. The two most popular methods of physical vapor deposition are E-beam evaporation, which is a thermal evaporation technique, and sputtering. The E-beam deposition approach, out of the two, has various distinct advantages for a variety of applications. E-beam evaporation allows much greater deposition rates, ranging from 0.1 to 100 nm per minute, resulting in higher density film coatings with improved substrate adherence. By focusing the energy on the target rather than the entire vacuum chamber, it is possible to limit the risk of heat damage to the substrate while also reducing the degree of contamination from the crucible. Due to its merit, E-beam evaporation technique has been widely used for PD device fabrication. For example, in order to fabricate the Schottky metal–semiconductor–metal (MSM) photodetector, the E-beam evaporation method was utilized to deposit zinc sulfide (ZnS) and zinc sulfide–europium oxide (ZnS–Eu_2O_3) onto a Si substrate as reported by Hajimazdarani et al. [21]. The schematic of the steps of ZnS deposition on the Si substrate by the E-beam evaporation technique and the fabrication of the PD in this project was illustrated in Figure 13.9.

13.5.5 Direct Current (DC) Sputtering

DC sputtering is a thin film physical vapor deposition technique in which an ionized gas molecule bombards a target material to be coated, forcing atoms to "Sputter" off into the plasma. These vaporized atoms are then deposited when they condense as a thin film on the substrate to be coated. Figure 13.10a shows the DC sputtering system used for deposition of metal electrodes, and Figure 13.10b shows the example of deposited Ag metal electrodes on Si substrate obtained using DC sputtering technique.
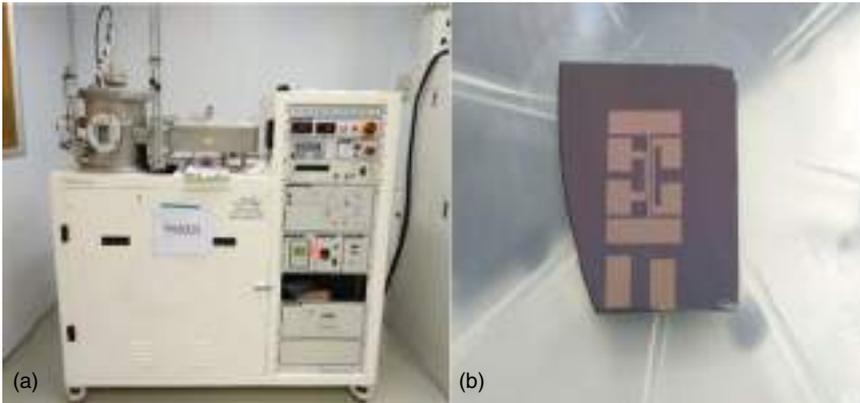
Figure 13.10 (a) DC sputtering system used for deposition of metal electrodes and (b) deposited Ag metal electrodes on Si substrate.

13.5.6 Spin Coating

The machine used for the spin coating process is called a spin coater (Figure 13.11), or simply spinner. The spin coater rotates while the fluid spins off the edges of the

Figure 13.11 Spin coater.

substrate until the desired thickness of the film is achieved. The applied solvent is usually volatile and simultaneously evaporates. Spin coating allows for the formation of multilayered GO thin film on polymer membrane as for example.

13.6 Device Characterizations

13.6.1 Electrical Characterizations

The current–voltage dependence and photoresponsivity of the photodetector were characterized by applying a DC bias voltage across the positive (+ve) and negative (−ve) electrodes. Here, various light sources were used to continuously illuminate on the sample. They include UV, white light ranging from 400 to 700 nm, and laser sources ranging from 600 to 980 nm. A cooled Oclaro LC96A74P, 20R butterfly LD, was mounted on a CLD1015LD controller. The laser was emitted through a Nufern PM980-HP/XP single-mode fiber which is spliced to an FC-FC/UPC/SM/Φ0.9 single-mode pigtail fiber. The end of the ferrule was positioned in perpendicular at various distances above the prepared photodetector surface. Current–voltage (I–V) characterization also performed at room temperature using a Keithley 2410 Source Meter. It was useful in obtaining results of swept voltages and step-up voltages. The photoresponsivity and rise (τ_r) and fall (τ_f) time of the GO photodetector were studied by applying frequency modulation by means of 30 MHz DS345 Synthesized Function Generator which is connected to the LD pump. The frequency response of the photodetector analyzed against various illumination laser pulse modulated frequencies using a YOKOGAWA DLM2054 Mixed Signal Oscilloscope unit. Figure 13.12 shows the example of Keithley source meter 2410 for I–V characterization and oscilloscope for temporal measurement to determine the rise and fall time.

Figure 13.13 depicts the diagrams of the temporal measurement setup (Figure 13.13a) and I–V characterization (Figure 13.13b) of BN/GO composite layer planar structure [19].

13.6.2 Photocurrent Behavior

The I–V characteristics deliver information about the behavior of the photodetector. It can be Ohmic or Schottky. In the study reported by Tien et al. [22], the photocurrent (i_p) responses of a 1D gallium telluride (GaTe) nanowire and 2D GaTe nanosheet have been studied, and comparison between both nanostructures has been made. Figure 13.14 shows the results obtained under the excitation wavelengths of 325, 405, 532, 633, and 808 nm with 1 V of bias voltage by various illumination intensities. These results reveal that both 1D and 2D GaTe respond to a broad spectral range illumination ranging from UV to NIR region, in which the 2D GaTe device demonstrates a higher photocurrent in contrast to the 1D GaTe device.
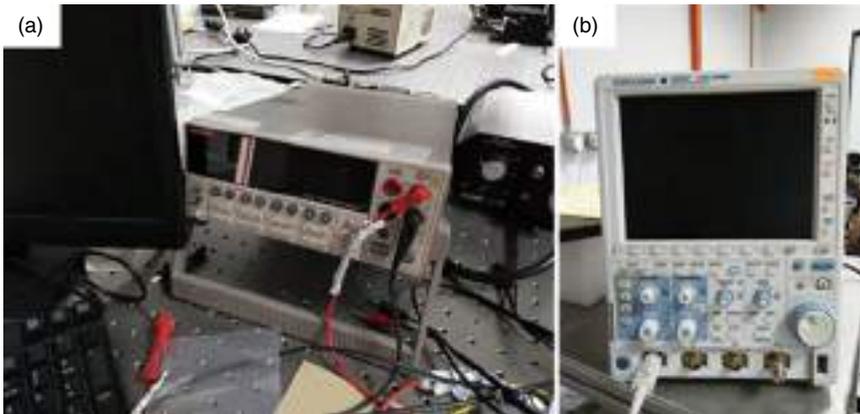
Figure 13.12 (a) Keithley source meter 2410 for *I–V* characterization and (b) oscilloscope for temporal measurement to determine the rise and fall time.
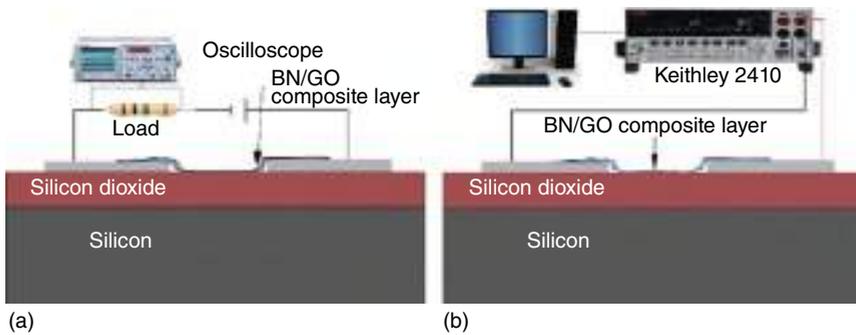
Figure 13.13 (a) Temporal measurement setup of graphene in planar structure and (b) *I–V* characterization of BN/GO composite layer planar structure. Source: Ahmad et al. [19]/with permission of Elsevier.

13.6.3 Responsivity and External Quantum Efficiency (EQE) Characteristics of Photodetector

Based on the *I–V* results, external quantum efficiency (EQE) and photoresponsivity in the sample were determined. Photoresponsivity calculated based on formula (13.1):

$$R_\lambda = \frac{I_{pd} - I_{dk}}{P} \tag{13.1}$$

The EQE was calculated using formula (13.2):

$$\mathrm{EQE}\left(\%\right) = \frac{hc\,R_\lambda}{e\lambda} \tag{13.2}$$
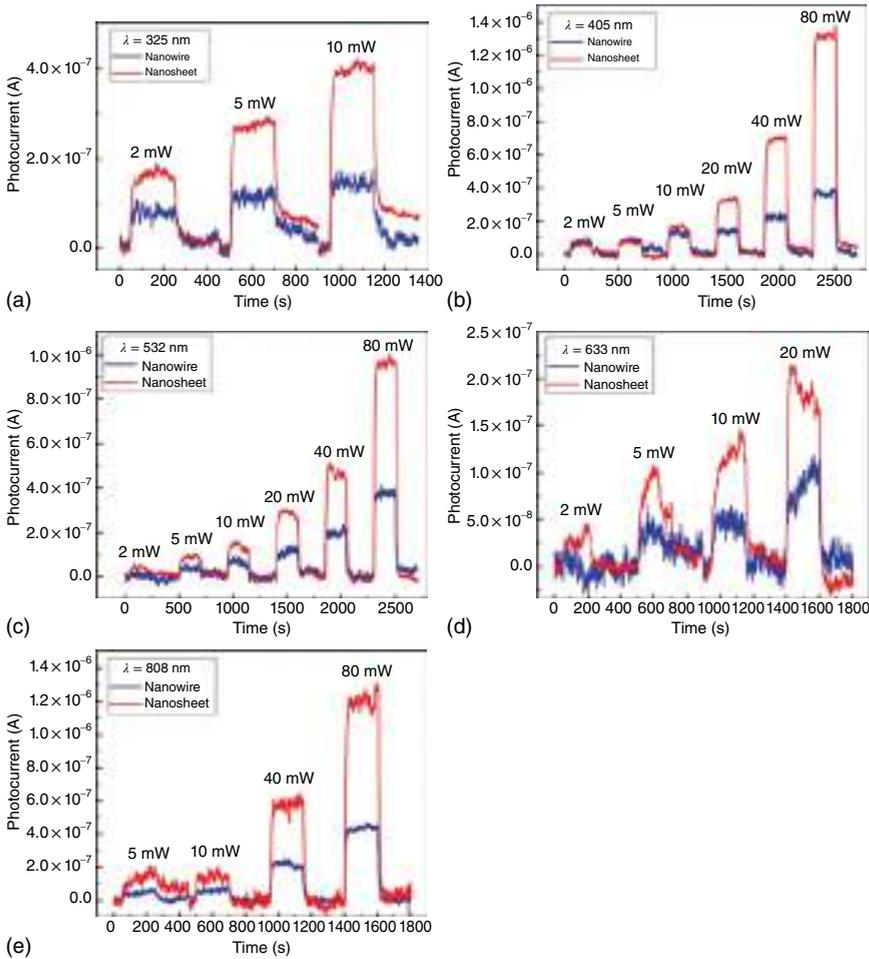
Figure 13.14 Photocurrent responses of a 1D GaTe nanowire (blue) and 2D GaTe nanosheet (red) obtained at the wavelengths of (a) 325 nm, (b) 405 nm, (c) 532 nm, (d) 633 nm, and (e) 808 nm under different excitation intensities. Source: Tien et al. [22]/with permission of Elsevier.

Figure 13.15 shows the responsivity and EQE (inset) of BN/GO composite photodetector [19], responsivity of WS_2 thin film [23], responsivity of p-Si/MoS_2 PN junction, and EQE of p-Si/MoS_2 PN heterojunction PD [24].

Other than responsivity, the detectivity D^* is also an important parameter to signify the detection performance of PDs with different materials and geometries:

$$D^* = \left(\frac{\left(A\Delta f \right)^{1/2}}{\text{NEP}} \right)$$
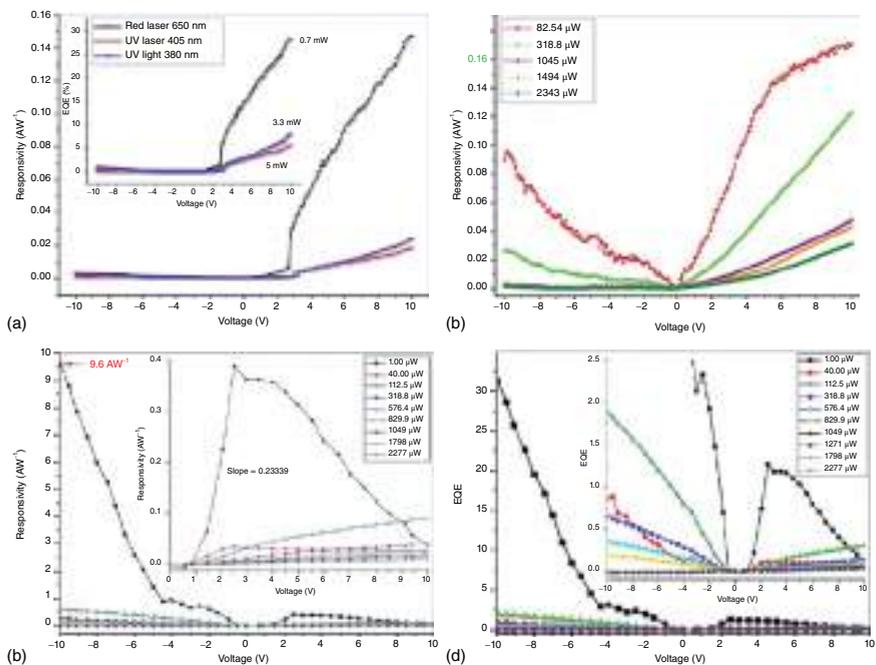
Figure 13.15 (a) Responsivity and EQE (inset) of BN/GO composite photodetector, (b) responsivity of WS$_2$ thin film, (c) responsivity of p-Si/MoS$_2$ PN, and (d) EQE of p-Si/MoS$_2$ PN heterojunction PD. Source: Ahmad et al. [19]/with permission of Elsevier.

where A is the device area of the PD, Δf is its bandwidth, and NEP is the noise equivalent power of the PD. By assuming the shot noise from dark current dominates the total noise of a PD, the equation can be simplified as:

$$D^* = \left(\frac{A^{1/2} R}{\left(2eI_d \right)^{1/2}} \right)$$

13.6.4 Temporal Response of Photodetector

The rise time duration for the responsivity to increase from 10% to 90% and the fall time to decrease from 90% to 10% were evaluated as shown in Figure 13.16 [19].

The rise and fall time for the photodetectors found to be profound as compared to the other reported value elsewhere. Rise and fall curves were detected due to boisterous signals due to low bias voltage at high-frequency modulations 3000 and 5000 Hz. The consistency of fast response of the photodetector is found to be varied as the frequency modulation and DC bias voltage increased. An increase in rise time was noted for increased frequency modulation from 100 to 500 Hz and subsequently decreases as the frequency modulation further increased to 1000, 3000, and 5000 Hz. Modulated laser at 500 Hz exhibits high rise time for various DC bias voltages.
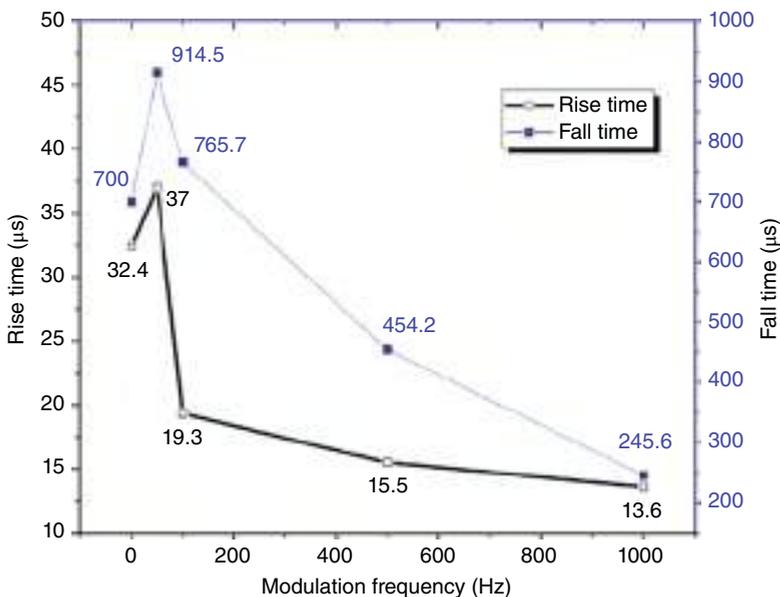
Figure 13.16 Temporal measurement of BN/GO composite layer. Source: Ahmad et al. [19]/ with permission of Elsevier.

13.7 Current Status of 1D/2D Hybrid Nanostructures Photodetectors

13.7.1 1-Dimensional Materials-Based Photodetectors

Due to their unique shapes, compositions, doping states, and chemical and physical properties, 1D nanostructures have become the focus of contemporary nanotechnology research. 1D nanostructures may now be rationally manufactured in single-crystal form in with all critical factors, such as chemical composition, morphologies, doping state, diameter, and length, being controlled. They are the smallest structures that are capable of successfully transporting electrical carriers, making them excellent for nanoscale electronics and optoelectronics fabrication. With significant surface-to-volume ratios and Debye lengths equivalent to their small size, 1D nanostructures' electronic properties are substantially impacted by surface processes, resulting in higher sensitivity than thin films.

Carbon nanotubes (CNTs) and inorganic semiconductor nanowires are the two most common types of 1D material. Other than that, nanofiber, nanorod, and nanofilament can also been categorized as 1D material. Zhang et al. [25] have developed a fully printed flexible photodetectors using a 1D single-wall carbon nanotubes (SWCNTs), and their electrical characteristics under laser illumination have been studied. The schematic diagram of a fully produced back-gated thin film transistor employed in this investigation is shown in Figure 13.17a. The optical micrograph of the printed transistor with the well-defined channel region and gate, source, and drain electrodes is shown in Figure 13.17b. In addition, a SEM image of the printed SWCNT network in the channel is presented to demonstrate its uniformity. The transfer ($I_{DS}-V_{GS}$) and output ($I_{DS}-V_{DS}$) properties of the transistor with (dashed lines) and without (solid lines) laser illumination on the channel area are shown in Figures 13.17c,d, respectively. It can be summarized that the device exhibit gate-voltage-dependent photoresponse with the positive photocurrent or semiconductor-like behavior (conductivity increases at elevated temperatures) under positive gate biases and the negative photocurrent or metal-like behavior (conductivity decreases at elevated temperatures) under negative gate biases. These properties of photoresponse were resulted from the photothermal effect and the use of high-purity 1D semiconducting SWCNTs.

13.7.2 2D Materials-Based Photodetectors

In recent years, 2D materials have gotten a lot of interest as well for photonics applications. This group of materials has quickly established itself as exciting building blocks for a variety of nanoelectronic devices with promising applications in next-generation optoelectronics, such as photodetectors (PDs) [26]. Furthermore, the number of layers can be changed to alter their optoelectronic performance. They have showed exceptional light absorption, allowing PD to detect light ultrafast and ultrasensitively, especially in their single-layer structure. Graphene [27], black phosphorus [28], and transition metal dichalcogenides (TMDs) [29] have all proven
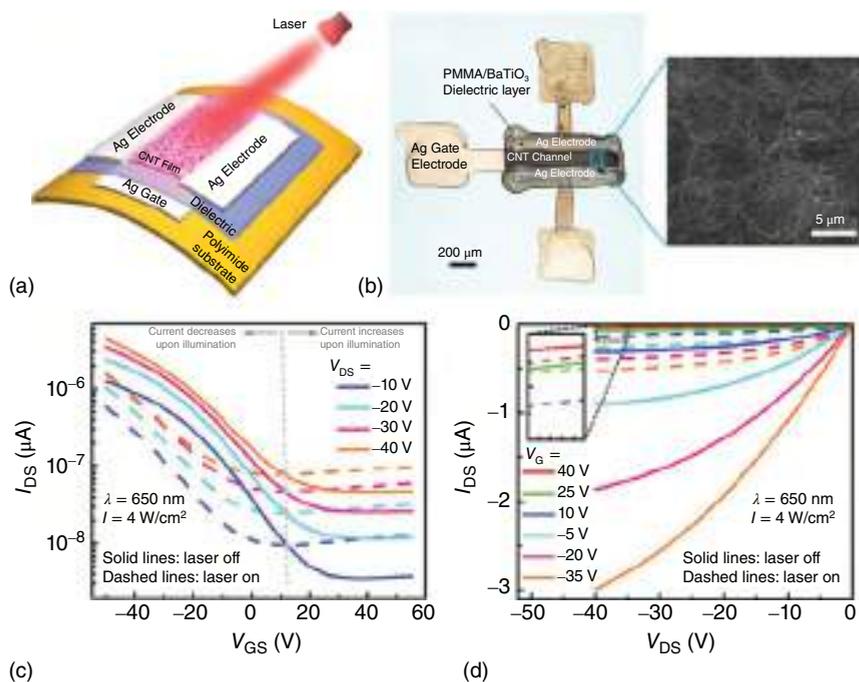
Figure 13.17 (a) Illustration of a fully printed flexible photodetector based on SWCNT material. (b) Image of the printed transistor obtained from optical microscope. Inset: SEM image of the printed SWCNT network on top of the PMMA/BaTiO$_3$ gate dielectric layer. (c) Transfer characteristics of the fully printed transistor with and without laser illumination. (d) Output characteristics of the fully printed transistor with and without laser illumination. The inset shows a zoomed in view for I_{DS} from 0 to −0.2 μA and V_{DS} from −40 to −35 V. Source: Zhang et al. [25]/with permission of AIP Publishing.

outstanding performance in PD, thanks to their atomic thickness, strong light–matter interaction, and variable band alignment.

MPX$_3$ (M = Fe, Co, Ni, Mn; X = S, Se) transition metal thiophosphates have recently emerged as a novel type of 2D intrinsic van der Waals (vdW) magnetic semiconducting materials. Monolayer MnPSe$_3$ is expected to offer great visible light absorption and high carrier mobility as a member of the MPX$_3$ family. Recently, in a study led by Lui and coworkers, they have successfully synthesized a high-quality MnPSe$_3$ crystals via a chemical vapor transport method and the performance of photodetector based on 2D MnPSe$_3$ has been investigated [30]. Figure 13.18a displays the low-resolution transmission electron microscop (TEM) image of MnPSe$_3$ in which the clear 2D lamellar morphologies with different thicknesses were observed. The I_{ds}−V_{ds} characteristics of the MnPSe$_3$ photodetector measured in the dark and under different light intensities with the thickness of 110 nm were depicted in Figure 13.18b. They discovered that the manufactured device has a low dark current (0.15 pA) and a high photoresponsivity (426 mA W^{-1}) without gate bias, as well as strong photoswitching stability toward short-wavelength light based on the obtained results. Their findings have suggested that thicker MnPSe$_3$ layers allow for
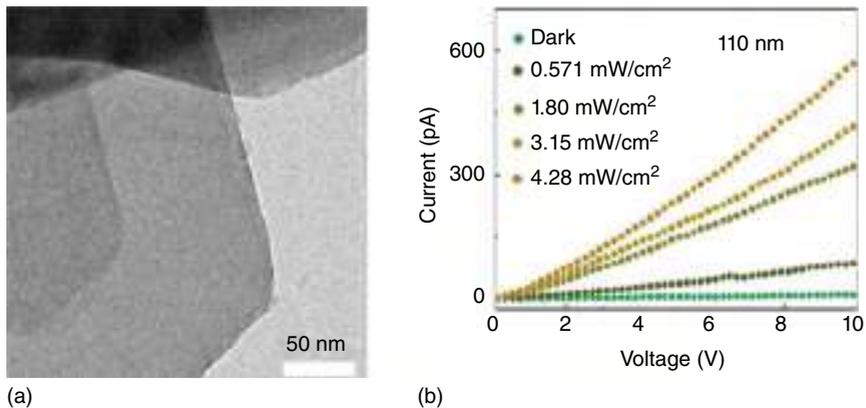
Figure 13.18 (a) TEM image of 2D-layered MnPSe$_3$. (b) I_{ds}–V_{ds} characteristics of the MnPSe$_3$ photodetector measured in the dark and under different light intensities with the thickness of 110 nm. Source: Liu et al. [30], Elsevier.

higher photo-absorption efficiency and more carrier generation, which leads to higher photoresponsivity.

13.7.3 1D/2D Hybrid Nanostructures-Based Photodetectors

In addition to individual low-dimensional material, their hybrid systems could be very interesting for photodetectors applications. In recent years, 1D–2D vdWs mixed-dimensional heterostructures with atomically sharp interfaces, high quality, and outstanding compatibility have gotten a lot of attention. Heterojunctions between 1D and 2D materials can cause a rectifying behavior in the dark current output characteristic. As a result, photodetectors of this sort can operate in reverse bias mode and have a high light on/off ratio. Hybrid nanostructures, which are made up of two or more components with different functions, usually have improved optoelectronic performance due to the combination of unique features of separate elements [31]. Hybrid nanostructures have been extensively researched and used as building blocks for PDs, which have outstanding properties such as high sensitivity, fast reaction speed, and broad photoresponse [32].

They have proposed a study on a mixed-dimensional vdW heterojunction photodetector with high-performance 1D p-type tellurium (Te) and 2D n-type ReS$_2$ nanowires deposited on ReS$_2$ nanoflake using the dry transfer method [33]. At the end of the study, they summarized that the Te/ReS$_2$ heterojunction photodetector outperforms pure Te and ReS$_2$ photodetectors, with good responsivity (180 A/W), high specific detectivity (10^9), and a quick photoresponse time (5 ms) (Figure 13.19). The responsivity and response time of the Te/ReS$_2$ heterojunction photodetector are one order of magnitude higher than the ReS$_2$-alone device. The benefits of type II band alignments, enhanced light absorption, and the passivate surface effect of heterojunction, which also swiftly separates the photogenerated electron–hole pairs, account for these improvements. The performance enhancements described in this
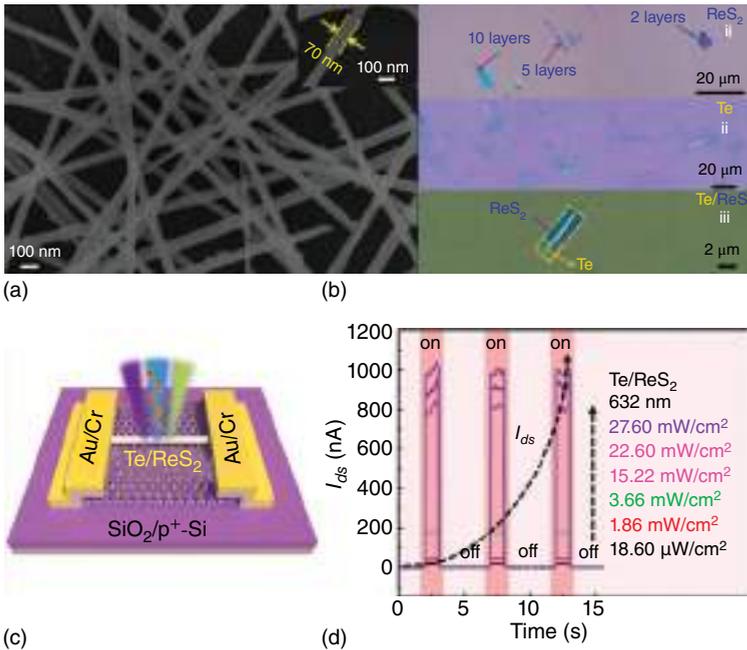
Figure 13.19 (a) Te NWs SEM image. The matching enlarged photos of the single Te NW are shown in the inset. (b) Optical microscope views of (i) varied thicknesses of 2D ReS$_2$ NFs, (ii) different lengths of single 1D Te NWs, and (iii) a typical 1D Te/2D ReS$_2$ mixed-dimensional heterojunction. (c) The built 1D Te/2D ReS2-based PD device's schematic structure. (d) Time-dependent photocurrent response for Te/ReS$_2$ during switched-on/off light irradiation with various power intensities at V_d 2V and V_g 0V. Source: Tao et al. [33]/ with permission of American Chemical Society.

study could lead to a mixed-dimensional vdWs heterojunction production approach for optoelectronic applications.

13.8 Conclusion

Extensive research efforts have been recently dedicated to the growth of 1D nanostructure on 2D layers for various applications, particularly for PD device application. From these researches, it has evident the potential of building a variety of flexible devices, with the individual components alleviating the drawback of device performance due to nonuniformity. However, the characterization of individual nanostructures has never been seriously investigated, because the variation in device performance between individual 1D/2D junctions is significantly larger than the value that is tolerable in conventional electronic and optoelectronic circuits. It has been stated that this is linked to the variation in defects (such as vacancies, impurities, threading dislocations, and lattice distortions) between individual nanomaterials and their heterointerfaces. This constraint brought to mind the need of uniform and high-quality epitaxial growth of both components on the wafer scale,

as well as the suppression of uncontrollable defect production. Even with 1D nano-structures that have been extensively researched, such as the first vertically aligned Si whisker created in 1964, exact control of size, orientation, position, and defects are still required (including thread dislocation in the tiny footprint). Given that experimental studies of 2D materials have a very limited history and uniform crystal formation of 2D materials has only recently begun for a few materials, it is clear that their growth can be much improved.

The most significant benefit of the bottom-up technique for 1D/2D hybrid nano-materials is the ease with which completely distinct nanomaterials and nanostruc-tures can be combined on the same substrate, allowing multifunctional nanosystems to be created. By addressing various nanostructure heterostructures in a controlled manner, the use of a mix of 1D- and 2D-based electronics would enable the fabrica-tion of flexible and stretchable nanomaterials, as well as multifunctional nanode-vices and nanosystems. A multifunctional flexible nanochip for wearable or implantable sensors, for example, is made up of numerous nanodevices such as sensors, transistors, and energy harvesting devices. 2D nanomaterials and their het-erostructures can be used in device applications such as nanotransistors, pressure sensors, and power generators. Many more nanosystems made up of 1D nanostruc-ture devices and 2D nanomaterial devices can also be made for a variety of flexible device applications.

In order to ensure the successful deployment of 1D and 2D material-based tech-nologies in production lines, a coherent and persuasive road map is required. The unusual form factor of 1D/2D hybrid materials and the requirements of nonstand-ardized integration techniques, especially in CMOS, are crucial when it comes to disruptive innovations and their entry into existing markets or opening new mar-kets. Although current PD technologies have the potential to be strengthened or even replaced, significant efforts are still needed to address nonuniform doping, batch-to-batch variability arising from growth or even transfer variability issues, as well as hysteretic effects that can occur in 1D and 2D materials due to their interac-tion with their local environment. Solutions to those problems should also be scal-able and not add to the manufacturing process' complexity. It is expected that the 1D and 2D materials to play a crucial role in the next generation of PDs, image sensors, optical transceivers, spectrometers and other potential applications. Whether or not this becomes a reality will be determined mainly by the success of those initial demonstrators in terms of technology and manufacturing readiness, which will be achieved through collaboration between researchers and important industrial partners.

References

1 Yang, S., Peng, J., Huang, H. et al. (2022). The tunable bandgap of phosphorus-arsenic alloys for mid-and long-infrared regime photodetectors. *Mater. Sci. Semicond. Process.* 144: 106552.

2 Kuang, D., Li, Y., Gao, Y. et al. (2022). Performance improvement of flexible ultraviolet photodetectors based on ZnO nanorod arrays by hydrothermal method with assistance of polyethyleneimine. *J. Alloys Compd.* 899: 163185.

3 Zhang, J., Zhang, X., Li, J. et al. (2022). Simultaneous visible and ultraviolet photoresponse improvement of MoS_2/ZnO heterostructure photodetector via direct resonant coupling of Au nanoparticles localized surface plasmon resonance. *Opt. Mater.* 124: 111997.

4 Bandyopadhyay, A. and Deen, M.J. (2001). Photodetectors for optical fiber communications. In: *Photodetectors and Fiber Optics* (ed. H.S. Nalwa), 307–368. Cambridge Massachusetts, United States: Academic Press.

5 You, J.-H., Oh, S., Park, J.-E. et al. (2021). A novel LiDAR sensor alignment inspection system for automobile productions using 1-D photodetector arrays. *Measurement* 183: 109817.

6 Xiong, D., Deng, W., Tian, G. et al. (2022). Controllable in-situ-oxidization of 3D-networked $Ti_3C_2T_x$-TiO_2 photodetectors for large-area flexible optical imaging. *Nano Energy* 93: 106889.

7 Wang, G., Zhang, M., Chen, D. et al. (2018). Seamless lateral graphene p–n junctions formed by selective in situ doping for high-performance photodetectors. *Nat. Commun.* 9: 1–9.

8 Thahe, A.A., Bakhtiar, H., Bidin, N. et al. (2018). High-performance nanoporous silicon-based photodetectors. *Optik* 168: 424–431.

9 Liu, D., Li, T., Tang, B. et al. (2022). A near-infrared CMOS silicon avalanche photodetector with ultra-low temperature coefficient of breakdown voltage. *Micromachines* 13: 47.

10 Konstantatos, G. (2018). Current status and technological prospect of photodetectors based on two-dimensional materials. *Nat. Commun.* 9: 1–3.

11 Averin, S., Kuznetsov, P., Zhitov, V. et al. (2015). Electrically tunable spectral responsivity in metal–semiconductor–metal photodetectors based on low-dimensional ZnCdS/ZnMgS/GaP, ZnCdS/ZnS/GaP heterostructures. *Solid-State Electron.* 114: 135–140.

12 Paul, P., Biswas, J., Chattopadhyay, S., and Kabi, S. (2022). Analytical modelling for the dark current of TiO_2/ZnS core shell quantum dot (CSQD) photodetectors. *Mater. Today Proc.* .

13 Sarkar, S.K. and Gupta, D. (2021). Easily prepared one dimensional zinc oxide crystals, characterization and application in UV photodetector. *Mater. Today Proc.* 47: 4712–4717.

14 Wang, J., Rehman, S.U., Xu, Y. et al. (2022). Two-dimensional antimony selenide (Sb_2Se_3) nanosheets prepared by hydrothermal method for visible-light photodetectors. *Sol. Energy* 233: 213–220.

15 Liang, F.-X. and Luo, L.-B. (2017). 1D/2D material-based photodetectors driven by ferroelectrics. *Sci. China Phys. Mech. Astron.* 60: 037031.

16 Ahn, J., Kang, J.-H., Park, M.-C., and Hwang, D.K. (2020). All 2D WSe_2/MoS_2 heterojunction photodiode and its image sensor application. *Opt. Lett.* 45: 4531–4534.

17 Liu, X., Luo, J., Lin, Y. et al. (2021). High-performance photodetectors using a 2D MoS_2/3D-AlN structure. *ACS Appl. Electron. Mater.* 3: 5415–5422.

18 Ahmad, H. and Tamil, T. (2018). High responsivity, self-powered carbon–zinc oxide hybrid thin film based photodetector. *Appl. Nanosci.* 8: 1755–1765.

19 Ahmad, H. and Tamil, T. (2018). Enhancement of broadband ultraviolet visible photodetection by boron nitride nanoparticles in bulk graphene oxide layer. *Opt. Mater.* 86: 18–23.

20 Ahmad, H. and Thandavan, T. (2020). High photoresponsivity and external quantum efficiency of ultraviolet photodetection by mechanically exfoliated planar multi-layered graphene oxide sheet prepared using modified Hummer's method and spin coating technique. *Mater. Express* 10: 998–1009.

21 Hajimazdarani, M., Ghasali, E., Naderi, N., and Orooji, Y. (2020). Enhanced optical properties and photodetection behavior of ZnS thin film deposited by electron beam evaporation upon doping with europium oxide. *Ceram. Int.* 46: 28382–28389.

22 Tien, L.-C., Shih, Y.-C., Chen, C.-Y. et al. (2021). Broadband photodetectors based on layered 1D GaTe nanowires and 2D GaTe nanosheets. *J. Alloys Compd.* 876: 160195.

23 Ahmad, H. and Thandavan, T.M.K. (2019). Ultraviolet photoconduction in tungsten disulphide based Schottky heterostructure photodetector. *Opt. Mater.* 92: 255–261.

24 Ahmad, H., Thandavan, T.M.K., and Thambiratnam, K. (2019). Dual characteristics of molybdenum disulfide based PN heterojunction photodetector prepared via drop-cast technique. *Optik* 188: 8–11.

25 Zhang, S., Cai, L., Wang, T. et al. (2017). Fully printed flexible carbon nanotube photodetectors. *Appl. Phys. Lett.* 110: 123105.

26 Jiayi, L., Yi, D., Zhang, D.W., and Peng, Z. (2019). Photodetectors based on two-dimensional materials and their van der Waals heterostructures. *Acta Phys. Chim. Sin.* 35: 1058–1077.

27 Schuler, S., Muench, J.E., Ruocco, A. et al. (2021). High-responsivity graphene photodetectors integrated on silicon microring resonators. *Nat. Commun.* 12: 1–9.

28 Guo, Q., Pospischil, A., Bhuiyan, M. et al. (2016). Black phosphorus mid-infrared photodetectors with high gain. *Nano Lett.* 16: 4648–4655.

29 Kang, D.H., Kim, M.S., Shim, J. et al. (2015). High-performance transition metal dichalcogenide photodetectors enhanced by self-assembled monolayer doping. *Adv. Funct. Mater.* 25: 4219–4227.

30 Liu, P. and Pu, Y. (2021). High-performance photodetector based on few-layered 2D $MnPSe_3$. *Results Phys.* 29: 104750.

31 Hong, Y.J., Saroj, R.K., Park, W.I., and Yi, G.-C. (2021). One-dimensional semiconductor nanostructures grown on two-dimensional nanomaterials for flexible device applications. *APL Mater.* 9: 060907.

32 Han, L., Yang, M., Wen, P. et al. (2021). A high performance self-powered photodetector based on a 1D Te–2D WS_2 mixed-dimensional heterostructure. *Nanoscale Adv.* 3: 2657–2665.

33 Tao, J.-J., Jiang, J., Zhao, S.-N. et al. (2021). Fabrication of 1D Te/2D ReS_2 mixed-dimensional van der waals pn heterojunction for high-performance phototransistor. *ACS Nano* 15: 3241–3250.

Index